



JAEA Takasaki Annual Report 2012

(Ed.) Takuji KOJIMA

Takasaki Advanced Radiation Research Institute

March 2014

Japan Atomic Energy Agency

日本原子力研究開発機構

本レポートは独立行政法人日本原子力研究開発機構が不定期に発行する成果報告書です。
本レポートの入手並びに著作権利用に関するお問い合わせは、下記あてにお問い合わせ下さい。
なお、本レポートの全文は日本原子力研究開発機構ホームページ (<http://www.jaea.go.jp>)
より発信されています。

独立行政法人日本原子力研究開発機構 研究技術情報部 研究技術情報課
〒319-1195 茨城県那珂郡東海村白方白根 2 番地 4
電話 029-282-6387, Fax 029-282-5920, E-mail: ird-support@jaea.go.jp

This report is issued irregularly by Japan Atomic Energy Agency.
Inquiries about availability and/or copyright of this report should be addressed to
Intellectual Resources Section, Intellectual Resources Department,
Japan Atomic Energy Agency.
2-4 Shirakata Shirane, Tokai-mura, Naka-gun, Ibaraki-ken 319-1195 Japan
Tel +81-29-282-6387, Fax +81-29-282-5920, E-mail: ird-support@jaea.go.jp

JAEA Takasaki Annual Report 2012

(Ed.) Takuji KOJIMA

Takasaki Advanced Radiation Research Institute

Japan Atomic Energy Agency

Watanuki-machi, Takasaki-shi, Gunma-ken

(Received December 9, 2013)

JAEA Takasaki annual report 2012 describes research and development activities performed from April 1, 2012 to March 31, 2013 mainly with Takasaki Ion Accelerators for Advanced Radiation Application (TIARA, four ion accelerators), and electron/gamma-ray irradiation facilities (an electron accelerator and three ^{60}Co gamma-ray irradiation facilities) at Takasaki Advanced Radiation Research Institute, Japan Atomic Energy Agency (JAEA Takasaki). These activities are classified into four research fields: 1) Space, Nuclear and Energy Engineering, 2) Environmental Conservation and Resource Exploitation, 3) Medical and Biotechnological Application, and 4) Advanced Materials, Analysis and Novel Technology.

This annual report contains 164 reports consisting of 156 research papers and 8 status reports on operation/maintenance of the irradiation facilities described above, a list of publications, patents, related press-releases, television broadcasting, and the type of research collaborations as appendices.

Keywords: TIARA, Ion Accelerator, Electron Accelerator, Gamma-ray Facility, Nuclear and Energy Engineering, Environmental Conservation, Resource Exploitation, Medical Application, Biotechnological Application, Advanced Materials, Novel Technology, Materials for Space, Semiconductors, Inorganic Materials, Organic Materials, Functional Materials, Radiation Chemistry, Radiation Biology, Radioisotope Production, Material Analysis, Solid State Physics, Beam Technology, Accelerator Technology, Facility Operation, Safety Control

(Editorial committee) Takuji KOJIMA, Hisayoshi ITOH, Atsushi TANAKA,
Watalu YOKOTA, Shimpei MATSUHASHI, Yasuyuki Haruyama,
Hiroshi YOSHIDA and Yoshiteru NAKAMURA

高崎量子応用研究所研究年報 2012

日本原子力研究開発機構 高崎量子応用研究所
(編) 小嶋 拓治

(2013 年 12 月 9 日受理)

高崎量子応用研究所研究年報 2012 は、同研究所にある TIARA 施設（イオン加速器 4 基）及び電子・ガンマ線照射施設（電子加速器 1 基、 ^{60}Co ガンマ線照射施設 3 棟）等を利用して 2012 年 4 月 1 日から 2013 年 3 月 31 日までの間に行われた研究・技術開発成果をまとめたものである。この研究年報には、1) 宇宙・原子力・エネルギー、2) 環境保全・資源利用、3) 医療・バイオ技術応用、4) 先端材料・分析・基盤技術の 4 分野に分類した 156 編の論文及び 8 編の施設の運転・管理状況報告からなる合計 164 編を収録する。また、論文リスト、出願特許、新聞発表、テレビ放映及び研究実施形態・利用施設の一覧表を付録として含む。

高崎量子応用研究所：〒370-1292 群馬県高崎市綿貫町 1233

編集委員：(著者代表) 小嶋 拓治、伊藤 久義、田中 淳、横田 渉、
松橋 信平、春山 保幸、吉田 宏、中村 義輝

PREFACE

This report covers activities of research and development using TIARA (Takasaki Ion Accelerators for Advanced Radiation Application), an electron accelerator and Co-60 gamma-ray irradiation facilities in Takasaki Advanced Radiation Research Institute, JAEA, from April 2012 to March 2013.

This annual report contains 164 papers in the following research fields:

- 1) Space, Nuclear and Energy Engineering,
- 2) Environmental Conservation and Resource Exploitation,
- 3) Medical and Biotechnological Application,
- 4) Advanced Materials, Analysis and Novel Technology,
- 5) Status of Irradiation Facilities.

In the field of Space Engineering, radiation tolerance of solar cell components and various types of electronic devices has been examined in connection with their space application. R&Ds of new functional devices have been also performed by using ion irradiation technique. For Nuclear and Energy Engineering, practically available results were obtained for radiation stability of Cs or Sr adsorbents, radiation effects in cement solidification form, zeolite, and sludge used for radioactive waste treatment, and radiation resistance of polymer materials and optical devices applied for nuclear facilities. As for structural materials used in light water, fast and fusion reactors, radiation induced microstructural change has been intensively studied using ion beams for pressure vessel steels, fuel claddings and blanket materials at TIARA. High performance polymer electrolyte membranes suitable for fuel cell application and ion exchange membranes used for hydrogen production have been developed by radiation grafting and cross-linking technique.

In the field of Environmental Conservation and Resource Exploitation, radiation grafting technique using electron beams was used to develop fibrous catalysts producing biodiesel fuels as well as adsorbents removing radioactive Cs ions in water. Using the latter material, water purifier was fabricated and its high performance on Cs removal was demonstrated. Improvement of thermal and mechanical properties of various biodegradable polymers has been studied with radiation crosslinking technique for their industrial applications. Experimental and theoretical investigations of wastewater treatment due to gamma-ray irradiation showed that ionizing radiation was quite useful for decomposition of chlorinated antibiotics in water. Hydro-gels produced by crosslinking of hydroxypropyl cellulose were investigated to be effective for immobilizing denitrifying bacteria useful for environmental purification.

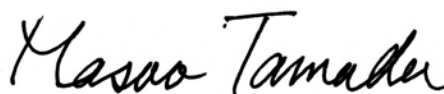
In the field of Medical and Biotechnological Application, radiation sensitivity of higher

plants and microorganisms has been investigated and new knowledge was provided. Obvious gamma-ray sensitivity was found in the seeds of flavonoid-less mutants in *Arabidopsis*, meanwhile grown-medium dependent increase of survival was observed in *E.coli* cells. Radiation-induced bystander effects on normal human lung fibroblasts were investigated. Following co-culture between irradiated cells and non-irradiated cells for 24 h, non-irradiated bystander cells were cultured for 14 days to count colonies formed. The dose-response curve of carbon ions (LET=108 keV/ μ m) was similar to that of γ -rays (0.2 keV/ μ m), indicating that radiation-induced bystander cell-killing effect is independent of LET. On the other hand, the ion microbeam analysis with particle-induced X-ray/Gamma-ray emission (micro-PIXE/PIGE) system for elemental mapping of bio-medical samples was widely utilized to study about the risk of cigarette smoking, Gadolinium neutron capture therapy, participation to the pulmonary alveolar proteinosis of asbestos suction, functions of plant tissue and so on. In order to expand the potential for cancer diagnosis and therapy using radionuclides, generating a radio-peptide drug for targeting oncoprotein such as the human epidermal growth factor receptor type 2 (Her2), was investigated. A new labeling technique for radiohalogenating of peptide has been successfully developed to synthesize the F(p-¹³¹I)MARSGL, which is a radioiodinated linear peptide consisting of six amino acids as an anti-Her2 peptide. The radionuclides are also applied to the plant studies on plant functions, absorption of various nutrients and pollutants from the environment, which is crucial for the human society. New experimental methods were developed for production of a ¹³N-labeled N₂ gas tracer with high radioactivity, for analysis of cadmium transport in a whole plant body, and for live-imaging of radiocesium movement using a specially-designed gamma camera. The ion beam breeding has been applied for many kinds of plants and microorganisms such as chrysanthemum, rice, poplar, and entomopathogenic fungi to obtain new useful varieties. A candidate gene was identified for high ethyle caproate production in the sake yeast generated by the ion beam breeding. Study on mutational effect of carbon ion beams in *Arabidopsis* suggested that the frequency of large DNA deletions is affected by LET.

In the field of Advanced Materials and Analysis, applying ion- or electron-irradiation effect leads to creation of various materials such as Gasochromic MoO₃ film, protein or polyvinylpyrrolidone nanowire/fiber, Platinum nanoparticles, SiC membrane/nanotubes, Zeolite membrane, PMMA, fluoropolymer, SU-8 and UV curable resin with micro structures. Analyses of characteristics of various materials with and without irradiation were performed using conventional methods, photospectrometry (PL, CL), microscopy (TEM, AFM, MFM, and ESR) and radiation-applied analysis, e.g. PIGE, ILUMIS, EELS, AICM, XRD, XMCD-PEEM, positron annihilation spectroscopy, and SPM. As for the Novel Technology, radiation chemistry studies on radiolysis of water or organics were carried out using

continuous or pulsed MeV heavy ion beams. Different kinds of radiation measurements were also studied on the basis of TOF method, wall-less TE proportional counter, fluorescent screen, and CR-39 detector. Characteristics of rock-salt, ice, PMMA, Gafchromic film, CVD diamond film, and scintillator were examined as new detectors. The fundamental studies on the interaction between MeV/atom cluster ions and target materials for C_2 - C_{60} were performed on the basis of the measurement of secondary ions/electrons or luminescence emitted from materials, and theoretical estimation of energy deposition/loss. Technical developments at AVF cyclotron for single-hit irradiation and wide uniform irradiation were in progress besides quick beam change for microbeam and phase bunching analysis for higher quality of beams. Development of a compact focusing system for 300 keV gaseous ion microbeam and microwave ion source with long-life was also in progress as off-line experiments.

About the Status of Irradiation Facilities, all the accelerators in TIARA, the AVF cyclotron, the 3-MV tandem accelerator, the 3-MV single ended accelerator and the 400-kV ion implanter, were operated steadily and safely as well as MeV-electron and Co-60 gamma-ray irradiation facilities. Total operation times of the tandem accelerator, the single-ended accelerator and the ion implanter were 38,671, 44,064 and 34,305 hours, respectively, since the beginning of their operation. The total number of experiments made by various users using the AVF cyclotron was 9,788 from the first beam extraction in 1991 to March 2013, as a result of continuous efforts such as regular maintenance and trouble shooting.



Masao Tamada,
Director General
Takasaki Advanced Radiation Research Institute
Japan Atomic Energy Agency

This is a blank page.

Contents

1. Space, Nuclear and Energy Engineering	1
1-01 Radiation Tolerance of New Coverglass for Space Solar Sheet	5
1-02 Proton Induced Degradation of Triple Junction Amorphous Silicon Thin Film Solar Cells	6
1-03 Applicability of the Improved Radiation Hardness Techniques for Angle Irradiation in DICE Latches on a 65 nm Bulk CMOS Process	7
1-04 Influence of Generated Charge by High Energy Ion Irradiation on Soft Error Rate in SOI SRAM	8
1-05 Radiation Damage in $\text{Si}_{1-x}\text{Ge}_x$ Source/Drain p-type MOSFETs	9
1-06 Anomalous Charge Collection from 4H-SiC Schottky Barrier Diodes	10
1-07 Atomic and Electronic Structure Analysis of the Interface between $\alpha\text{-SiO}_2$ and 4H-SiC(11-20)	11
1-08 Proton Irradiation Effects on Nitride Semiconductor-based Light Emitting Device	12
1-09 Evaluation of Radiation Tolerance of FRAM Microprocessor for Heavy Ion Irradiation	13
1-10 Experimental Study on Radiation Effects on Magnetic Tunnel Junctions 2	14
1-11 Ion Beam Induced Luminescence (IBIL) from Diamond Induced by Various Single Ion with High Energy	15
1-12 Fabrication of Strongly Coupled Pair of NV Centers in Diamond by Ion Implantation	16
1-13 Radiolytic Stabilities of Hydrophilic and Lipophilic Ligands for Mutual Separation of Am/Cm/Ln	17
1-14 Characterization of Composite Adsorbent for Minor Actinides by Micro-PIXE Method	18
1-15 Radiolytic Stability of Metal Hexacyanoferrate as Adsorbent for Recovery of Cesium Ion	19
1-16 Study on Durability of Strontium Adsorbents against Gamma Irradiation	20
1-17 Effect of Gamma-ray Irradiation on De-oxygenation of Salt-containing Water by Hydrazine	21
1-18 Evaluation of Hydrogen Gas Generation from Cement Solidification Form by Gamma-ray Irradiation II	22
1-19 Studies of Irradiation Effects on Surface Structure of Zeolites after Decontamination of Radioactive Water	23
1-20 Evaluation of Radiation Resistance of Activated Sludge Used for Nitrate Ion Decomposition	24
1-21 Radiation Resistance Test of Insulation for Instrumentation Wire of JT-60SA Magnet	25
1-22 Radiation Resistant Evaluation of Sealing Coat Using Super Quick Hardening Type Polyurethane and Polyurea	26

1-23	Study of Radiation Resistance of Optical Fibers for Remote Imaging and Spectroscopy	27
1-24	Study of Radiation-resistant LED Lighting	28
1-25	Creation of Database of Radiation Resistance on Polymer Materials and Equipment	29
1-26	Evaluation of High-temperature Irradiation Resistance of ODS Ferritic Steel for Fast Reactor Application	30
1-27	Irradiation Hardening Behavior of SUS316L and F82H Steels in Heavy Irradiation Fields up to 250 dpa	31
1-28	Radiation-induced Hardening for SUS316L with Bending Deformation	32
1-29	Irradiation Hardening of Extra High Purity Ni-base Superalloy under External Stress	33
1-30	Irradiation Hardening of G-Phase Strengthened Ni-base Alloy under Multi-ion Irradiation	34
1-31	Precipitate Stability and Swelling Resistance of High-Nickel Alloy during Irradiation	35
1-32	Effects of Displacement Damage and Gas Atoms on Radiation Hardening and Microstructure in F82H Weldment	36
1-33	Corrosion Tests of Steels Used for Reactor Pressure Vessel and Primary Containment Vessel	37
1-34	Corrosion Resistance of Tank Material Used for Flock Storage	38
1-35	Investigation of Microstructure in SiC Made by Nano-infiltration Transient Eutectic Process after Triple Ion Beam Bombardment	39
1-36	Ionizing Dose Dependences of Radiation-induced Conductivity and Radiation-induced Electrical Degradation of Chemical Vapor Deposited Silicon Carbides under Gamma-ray Irradiation	40
1-37	Surface Morphology of He Implanted CeO ₂ Thin Film	41
1-38	A Macroporous SiC Material Synthesized from Preceramic Polymer with Direct Foaming and Radiation Curing	42
1-39	Alkaline Durable Anion Exchange Membranes Synthesized by Radiation-induced Grafting for Hydrazine Hydrate Fuel Cell	43
1-40	Preparation of Anion-Exchange Membranes for Fuel Cell Applications by γ -ray Pre-irradiation Grafting: Effect of the Carbon Dioxide in the Air	44
1-41	Poly(ether ether ketone) (PEEK)-based Graft Type Polymer Electrolyte Membrane: Relative Humidity Dependence for Fuel Cell Application	45
1-42	Preparation of Novel Polymer Electrolyte Membranes by Combination of Radiation Induced Grafting and Atom Transfer Radical Polymerization	46
1-43	Preparation of Platinum Nanoparticle Catalysts for Fuel Cell Applications by Ion Implantation	47
1-44	Ion Content of Ion Exchange Membrane in HI-I ₂ -H ₂ O Mixture	48
1-45	Applied-voltage Dependence on Conductometric Track Etching of Poly(vinylidene fluoride)	49

1-46	Microscopic Evaluation of the Absolute Fluence Distribution of an Ion Beam Using a Track Etching	50
2.	Environmental Conservation and Resource Exploitation	51
2-01	Homogeneous Transesterification Kinetics of Triglyceride to Biodiesel Using Grafted Fibrous Catalyst	53
2-02	Effect of Initial Radical Concentration on Radiation-induced Graft Polymerization on Polyethylene Nonwoven Fabric	54
2-03	Development of the Water Purifier with Grafted Adsorbent for Cs Removal	55
2-04	Development of a Grafted Filter for Radioactive Cesium	56
2-05	The Influence on the Vulcanized Rubber Physical Properties by Radiation Grafting	57
2-06	Radiation-induced Crosslinking of Poly(butylene adipate-co-terephthalate)	58
2-07	Effect of Gamma-rays Irradiation on Concentrated Aqueous Solutions of BSA, DNA and Their Mixture	59
2-08	Treatment of Chlorinated Antibiotics by Oxidative/Reductive Species under Ionizing Radiation	60
2-09	Immobilization of Denitrifying Bacteria to HPC Gel Medium Synthesized by EB Irradiation	61
3.	Medical and Biotechnological Application	63
3-01	Estimation of Damage Localization in DNA Irradiated with Ionizing Radiations in Water	69
3-02	The Effect of Radiation Quality on Growth-medium Dependent Survival in <i>Escherichia coli</i>	70
3-03	Gamma-ray Sensitivity in <i>Arabidopsis thaliana</i> Exhibiting Different Flavonoid Accumulation Patterns	71
3-04	Target Irradiation of Individual Cells Using Focusing Heavy-ion Microbeam of JAEA-Takasaki (IV): An Improvement of Control Pathway of Scanned Beam Irradiation for “Actual” Cell Sample Irradiation	72
3-05	Microbeam Irradiation Response of the Salt Chemotaxis in Mock-conditioned <i>C. elegans</i>	73
3-06	Radiation-induced Bystander Cell-killing Effect is Dependent on Dose of Carbon Ions and γ -rays but Independent of LET	74
3-07	Mechanisms for the Induction of Radioadaptive Response by Radiation-induced Bystander Response	75
3-08	Analysis of Bystander Cell Signaling Pathway Activated by Heavy Ion-microbeam IV	76
3-09	Fluence-dependent Chromosomal Aberrations via Bystander Effect in Normal Human Fibroblasts Induced by C-, Ne- and Ar-ion Microbeams	77

3-10	Ion Beam Irradiation Has Different Influences on the Expression of Bax in Cultured Human Retinal Vascular Endothelial Cells Exposed to L-dopa among ^{20}Ne , ^{12}C , and ^4He	78
3-11	Radiosensitivity is Affected by the Dependence of DNA Double-strand Break Repair on LET	79
3-12	Epigenetic Modifier as a Potential Radiosensitizer for Heavy-ion Therapy on Malignancy	80
3-13	Apoptotic Cell Death of the Heavy Ion Irradiated Silkworm Egg after Cellular Blastoderm Stage	81
3-14	Promotion of Miss-differentiation of Testis-ova in p53 Deficient Medaka Testis by Micro-beam Irradiation of Carbon-ions	82
3-15	Polythene Chromosome Abberation as a Possible Marker for Assessing DNA Damage upon Ionizing Radiation in the Sleeping Chironomid Larvae	83
3-16	Effects of Carbon-ion Microbeam Irradiation on Pharyngeal Pumping in <i>Caenorhabditis elegans</i>	84
3-17	Electron-spin Relaxation Times of Irradiated Fructose Measured with Pulsed ESR	85
3-18	Relaxation Times of Radicals Induced in Irradiated Foods Using Pulse-ESR and CW-ESR	86
3-19	Three-dimensional Distribution Measurement of Eu in a <i>Paramecium Bursaria</i>	87
3-20	Approaches to Isolation and Culture of Mice LMECs, and Effects of Nicotine on Trace Elements Distribution in LMECs	88
3-21	Measurement of Fluorine Distribution in Root Dentin under Fluoride-containing Coating Materials	89
3-22	Imaging of Metallofullerene Distribution Using Micro-PIXE for Gadolinium NCT	90
3-23	Elemental Analysis of Lung Tissue Particles and Intracellular Iron Content of Alveolar Macrophages in Pulmonary Alveolar Proteinosis	91
3-24	Analysis of Erythrocytes in Hepatitis C Patients Treated with Peg-interferon Using In-Air Micro-PIXE	92
3-25	Trial for Targeting of Anticancer Drugs, Using Radiosensitive Immunolabelled Microcapsules	93
3-26	Development of Method for Plant Material Analysis by Micro-PIXE (Particle Induced X-ray Emission)	94
3-27	Sensitivity of Micro Beam PIXE System in TIARA for Several Trace Elements and Determination of Elemental Abundances in a Small Organism	95
3-28	Synthesis of Radiohalogen-labeled Peptide with High Affinity to HER2/neu Receptor	96
3-29	Complexation of Lutetium-177 with Bifunctional Chelators in the Presence of Competing Metals	97

3-30	Production of ^{13}N -labeled Nitrogen Gas Tracer for the Imaging of Nitrogen Fixation in Soybean Nodules	98
3-31	Analysis of the Effect of O_2 Partial Pressure on Nitrogen Fixation in Soybean Plant Using Positron-emitting Tracer	99
3-32	RI Imaging Method to Analyze a Process of Radiocesium Contamination of Plants and to Develop Phytoremediation Techniques	100
3-33	Whole-plant Imaging of ^{107}Cd Distribution Using Positron-emitting Tracer Imaging System	101
3-34	Development of Ion Beam Breeding Technology in Plants and Creation of Useful Plant Resources	102
3-35	Ion Beam Breeding of Rice for the Mutation Breeding Project of the Forum for Nuclear Cooperation in Asia (FNCA)	103
3-36	Generating New Chrysanthemum Plant Varieties Using Ion Beams	104
3-37	Mutational Effects of Carbon Ions near the Range End in Arabidopsis	105
3-38	Homologous Recombination Induced by Low-dose Radiations in Arabidopsis	106
3-39	Screening of Salt Tolerant Mutants by Combination of Radiation Mutagenesis and <i>In vitro</i> Regeneration in Lombardy Poplar (<i>Populus nigra</i>)	107
3-40	Effects of Gamma-ray Irradiation on Oxalate Metabolism in <i>Rumex obtusifolius</i> L.	108
3-41	Determination of the Carbon Ion Beam Irradiation Condition for Barley	109
3-42	Mutagenic Effect of Carbon Ion Beams in <i>Deinococcus radiodurans</i>	110
3-43	Genetic Analysis of Novel DNA Cross-link Repair Genes Common to <i>Deinococcus</i> and <i>Thermus</i>	111
3-44	Molecular Analysis of Heavy Ion Induced Mutations in Budding Yeast <i>S. cerevisiae</i>	112
3-45	Improvement of Endophytic Bacteria Using Ion Beams and Application of Bio-pesticide with Plant Growth Promoter Made from Oligo-chitosan	113
3-46	Identification of DNA Mutation Sites in a High Temperature Tolerant Mutant of <i>Bradyrhizobium japonicum</i> USDA110 Generated by Ion-beam Irradiation	114
3-47	Simultaneous Saccharification and Fermentation from Ionic Liquid-pretreated Biomass Using Ionic Liquid-tolerant Yeast Mutant	115
3-48	Benomyl-tolerant Mutation of Entomopathogenic Fungi Induced by Carbon Ion Beams	116
3-49	Mutation Analysis of High Ethyl Caproate Producing Sake Yeasts Generated by Ion Beam Breeding	117
3-50	Role of DNA Repair and Effect of Herbal Extract on LOH Induced by Ion Beam Radiations in <i>Saccharomyces cerevisiae</i>	118
4.	Advanced Materials, Analysis and Novel Technology	119
4-01	Preparation of Gasochromic MoO_3 Films by Reactive Sputtering Deposition	123
4-02	1D Protein and Sugar Nanostructures by Single Particle Reactions	124

4-03	Formation of Ag Nanoparticles on Poly(vinylpyrrolidone) Nanowire Fabricated by SPNT	125
4-04	Formation of Poly(vinylpyrrolidone) Nanofiber Containing Platinum Particles	126
4-05	Production of Nano-sized Platinum-particle Films Using Low Energy Electron Beams	127
4-06	Wetting Phenomena of Polycarbosilane Solution	128
4-07	Investigation of Permeation Mechanism through Zeolite Membranes by Using Ion Beam Irradiation	129
4-08	Control of Spatial Crosslinking Reaction in Polymer Film by Ion and Electron Beam Irradiation	130
4-09	Effect of Irradiation Ions on Critical Fluence of Changing to Amorphous from Crystalline SiC Nanotubes	131
4-10	Thermo-Optic Switch Consisting of Mach-Zehnder Polymer Waveguide Drawn Using Proton Beam Writing	132
4-11	Hydriding Property of Hydrogen Storage Alloy by Charged Particle Under Different Irradiation Environment	133
4-12	Micropatterning on Fluoropolymer Surface Using Proton Beam Writing and Nitrogen Ion Beam Irradiation	134
4-13	Fabrication of a Flexible Dielectrophoretic Device Using Proton Beam Writing	135
4-14	Li-ion Battery Characterization by Ion Beam Analysis	136
4-15	Atomistic Transformation Processes Induced by the Interaction of Implanted N-ions with Ti Thin Films	137
4-16	Ion Beam Analysis of Quaternary Heusler Alloy $\text{Co}_2(\text{Mn}_{1-x}\text{Fe}_x)\text{Si}(111)$ Epitaxially Grown on Ge(111)	138
4-17	Non-thermal Equilibrium Crystal Structure of FeRh Intermetallic Compound Irradiated with Energetic Heavy Ions	139
4-18	Magnetic Patterning of FeRh Thin Films by Energetic Light Ion Microbeam Irradiation and Their XMCD-PEEM Observation	140
4-19	Transmission Properties of a 4-MeV C^+ Ion Beam Entering a Curved Insulating Channel	141
4-20	Cathodoluminescence of He^+ -ion-implanted Feldspars	142
4-21	Control of Photoluminescent Properties of Si-O-C Materials by Irradiation of Various Particle Beams	143
4-22	Contribution of Aeolian Dust in Ichinomegata Estimated from Electron Spin Resonance Signal Intensity and Crystallinity of Quartz	144
4-23	Development of Spin-polarized Positron Beam and Its Application to Spintronics Study	145
4-24	Complementary Study of Vacancy Defects in Si Substrates by Using SPM and EBIC Method	146
4-25	Positron Annihilation Lifetime Study of Cation Vacancies in Electroceramics	147

4-26	Yield of Transient Species in NaBr Aqueous Solution Irradiated with Pulsed H^+ , C^{5+} and Ne^{8+} Ions	148
4-27	Transient Absorption Spectra of Biphenyl-Dodecane Solution Measured by Microsecond Ion Pulse Radiolysis	149
4-28	Observation of Scintillation Behavior under Pulsed Ion Beam Irradiation	150
4-29	Solvent Effect on Copolymerization of Maleimide with Styrene Induced by Ion Beam Irradiation	151
4-30	Measurements of Low Energy Neutron Spectra Using the TOF Method in Quasi-monoenergetic Neutron Fields at TIARA	152
4-31	Measurement of Lineal Energy Distributions for Energetic Ion Beams Using a Wall-less Tissue Equivalent Proportional Counter	153
4-32	Fabrication of UV Curable Resin Based Microscopic Devices Using External Scanning Proton Microbeam	154
4-33	Preliminary Study on 3D Proton Lithography Using 300 kV Compact Focused Gaseous Ion Beam System	155
4-34	Research and Development of an Ultra-high-energy Neutrino Detector Using Radar Reflection in Rock Salt and Ice	156
4-35	Effect of Low Irradiation Temperature on the Gamma-ray Response of Clear Polymethylmethacrylate Dosimeter, Radix W	157
4-36	Analysis of Phase Bunching in AVF Cyclotron	158
4-37	Status Report on Technical Developments of Electrostatic Accelerators	159
4-38	Fast Single-ion Hit System for Heavy-ion Microbeam at TIARA Cyclotron (VI)	160
4-39	Development of a Microwave Ion Source for Industrial Applications	161
4-40	Beam Intensity Distribution Measurement Using a Fluorescent Screen for Formation of a Uniform Ion Beam	162
4-41	Response of Gafchromic Films to Energetic Ion Beams	163
4-42	Development of Scintillator for Detention of Single-ion	164
4-43	Focused Microbeam Irradiation Effects in Transmission CVD Diamond Film Detectors	165
4-44	Development of a New Ion Microbeam Analysis Technique: Ion Luminescence Microscopic Imaging and Spectroscopy	166
4-45	Coulomb Explosion Process in Collision of a Swift Cluster Ion with Gas Target	167
4-46	Study of Ion Induced Luminescence from Sapphire Irradiated with Swift Cluster Ion Beams	168
4-47	Electronic Stopping Power of Al and Si for Swift Carbon Cluster Ions with Average Charge Reduction	169
4-48	Comparison of Positive Secondary Ion Emission Yields for PMMA between Low Energy Bi and C_{60} Ion Impacts	170
4-49	Vicinage Effect on Secondary-electron Yield from Carbon Foils Bombarded with 62.5-250-keV/u H_2^+ and C_2^+ Ions	171

4-50	Production of Fast C ₆₀ Microbeam Using the Capillary-beam Focusing Method	172
4-51	Ion Tracks in Amorphous Si ₃ N ₄ Films Produced by Sub MeV C ₆₀ Ion	173
5.	Present Status of Irradiation Facilities 2011	175
5-01	Utilization Status at TIARA Facility	177
5-02	Operation of the AVF Cyclotron	178
5-03	Operation of Electrostatic Accelerators	179
5-04	Operation of the Electron Accelerator and the Gamma-ray Irradiation Facilities	180
5-05	Utilization Status of the Electron Accelerator and the Gamma-ray Irradiation Facilities	181
5-06	Radiation Control in TIARA	182
5-07	Radioactive Waste Management in TIARA	183
5-08	FACILITY USE PROGRAM in Takasaki Advanced Radiation Research Institute	184
	Appendices	185
Appendix 1	List of Publication	186
Appendix 2	List of Related Patents	205
Appendix 3	List of Related Press-release and Television Broadcasting	207
Appendix 4	Type of Research Collaboration and Facilities Used for Research	210
Appendix 5	Examples of Typical Abbreviation Name for Organizations in Japan Atomic Energy Agency (JAEA)	212

1. Space, Nuclear and Energy Engineering

1-01	Radiation Tolerance of New Coverglass for Space Solar Sheet	5
	K. Shimazaki, Y. Kobayashi, M. Takahashi, M. Imaizumi, S. Sato and T. Ohshima	
1-02	Proton Induced Degradation of Triple Junction Amorphous Silicon Thin Film Solar Cells	6
	S. Sato and T. Ohshima	
1-03	Applicability of the Improved Radiation Hardness Techniques for Angle Irradiation in DICE Latches on a 65 nm Bulk CMOS Process	7
	A. Maru, H. Shindou, S. Kuboyama, T. Tamura, H. Abe and T. Ohshima	
1-04	Influence of Generated Charge by High Energy Ion Irradiation on Soft Error Rate in SOI SRAM	8
	M. Hazama, S. Abo, F. Wakaya, T. Makino, S. Onoda, T. Ohshima, T. Iwamatsu, H. Oda and M. Takai	
1-05	Radiation Damage in $\text{Si}_{1-x}\text{Ge}_x$ Source/Drain p-type MOSFETs	9
	K. Takakura, I. Tsunoda, M. Yoneoka, T. Nakashima and M. Sugiyama	
1-06	Anomalous Charge Collection from 4H-SiC Schottky Barrier Diodes	10
	T. Makino, M. Deki, N. Iwamoto, S. Onoda, N. Hoshino, H. Tsuchida and T. Ohshima	
1-07	Atomic and Electronic Structure Analysis of the Interface between $\alpha\text{-SiO}_2$ and 4H-SiC(11-20)	11
	A. Miyashita and M. Yoshikawa	
1-08	Proton Irradiation Effects on Nitride Semiconductor-based Light Emitting Device	12
	H. Okada, Y. Okada, H. Sekiguchi, A. Wakahara, S. Sato and T. Ohshima	
1-09	Evaluation of Radiation Tolerance of FRAM Microprocessor for Heavy Ion Irradiation	13
	Y. Chiba, E. Asai, H. Tomioka, R. Shimazu, T. Kameda, T. Ohshima, S. Onoda and T. Makino	
1-10	Experimental Study on Radiation Effects on Magnetic Tunnel Junctions 2	14
	D. Kobayashi, Y. Kakehashi, K. Hirose, S. Ikeda, M. Yamanouchi, H. Sato, E.-C. Enobio, T. Endoh, H. Ohno, S. Onoda, T. Makino and T. Ohshima	
1-11	Ion Beam Induced Luminescence (IBIL) from Diamond Induced by Various Single Ion with High Energy	15
	S. Onoda, H. Abe, T. Makino and T. Ohshima	
1-12	Fabrication of Strongly Coupled Pair of NV Centers in Diamond by Ion Implantation	16
	T. Yamamoto, S. Onoda, H. Abe, S. Sato, T. Ohshima, J. Isoya and T. Umeda	
1-13	Radiolytic Stabilities of Hydrophilic and Lipophilic Ligands for Mutual Separation of Am/Cm/Ln	17
	Y. Sugo, Y. Sasaki and N. S. Ishioka	

1-14	Characterization of Composite Adsorbent for Minor Actinides by Micro-PIXE Method	18
	Y. Takahatake, M. Nakamura, Y. Nakajima, Y. Koma, K. Sano, T. Arai, T. Satoh and M. Koka	
1-15	Radiolytic Stability of Metal Hexacyanoferrate as Adsorbent for Recovery of Cesium Ion	19
	M. Arisaka, M. Watanabe, M. Ishizaki, M. Kurihara, R. Chen and H. Tanaka	
1-16	Study on Durability of Strontium Adsorbents against Gamma Irradiation	20
	Y. Itoh, Y. Saitoh and T. Terunuma	
1-17	Effect of Gamma-ray Irradiation on De-oxygenation of Salt-containing Water by Hydrazine	21
	T. Motooka, T. Sato and M. Yamamoto	
1-18	Evaluation of Hydrogen Gas Generation from Cement Solidification Form by Gamma-ray Irradiation II	22
	T. Nakayama , Y. Kawato , S. Suzuki and Y. Meguro	
1-19	Studies of Irradiation Effects on Surface Structure of Zeolites after Decontamination of Radioactive Water	23
	R. Nagaishi, K. Morita, S. Tashiro, R. Saito and I. Yamagishi	
1-20	Evaluation of Radiation Resistance of Activated Sludge Used for Nitrate Ion Decomposition	24
	A. Nakagawa, T. Kogawara, T. Onizawa, K. Hanada, T. Nakayama and Y. Meguro	
1-21	Radiation Resistance Test of Insulation for Instrumentation Wire of JT-60SA Magnet	25
	H. Murakami, A. Sukegawa and K. Yoshida	
1-22	Radiation Resistant Evaluation of Sealing Coat Using Super Quick Hardening Type Polyurethane and Polyurea	26
	I. Funakawa, M. Kito, K. Horie, K. Watanabe, T. Numao, Y. Saegusa T. Masuda, K. Higashi, K. Shidomi and R. Yamagata	
1-23	Study of Radiation Resistance of Optical Fibers for Remote Imaging and Spectroscopy	27
	H. Naito, C. Ito, K. Imaizumi, A. Nagai and K. Tobita	
1-24	Study of Radiation-resistant LED Lighting	28
	M. Kamikawa, K. Oka, R. Yamagata M. Kawasaki and K. Izumi	
1-25	Creation of Database of Radiation Resistance on Polymer Materials and Equipment	29
	A. Shimada, M. Sugimoto, A. Miyashita and M. Yoshikawa	
1-26	Evaluation of High-temperature Irradiation Resistance of ODS Ferritic Steel for Fast Reactor Application	30
	S. Ohtsuka, T. Tanno, N. Ohkubo, S. Jitsukawa, S. Yamashita, Y. Yano, T. Kaito and T. Sawai	

1-27	Irradiation Hardening Behavior of SUS316L and F82H Steels in Heavy Irradiation Fields up to 250 dpa	31
	N. Okubo, N. Ishikawa and S. Ohnuki	
1-28	Radiation-induced Hardening for SUS316L with Bending Deformation	32
	N. Ishikawa, N. Okubo and K. Kondo	
1-29	Irradiation Hardening of Extra High Purity Ni-base Superalloy under External Stress	33
	I. Ioka, G. H. Kim and T. Inoue	
1-30	Irradiation Hardening of G-Phase Strengthened Ni-base Alloy under Multi-ion Irradiation	34
	N. Okubo, I. Ioka, G. H. Kim and T. Inoue	
1-31	Precipitate Stability and Swelling Resistance of High-Nickel Alloy during Irradiation	35
	S. Yamashita, T. Inoue, Y. Sekio, T. Hayashi, I. Yamagata, T. Yoshitake and T. Kaito	
1-32	Effects of Displacement Damage and Gas Atoms on Radiation Hardening and Microstructure in F82H Weldment	36
	M. Ando and H. Tanigawa	
1-33	Corrosion Tests of Steels Used for Reactor Pressure Vessel and Primary Containment Vessel	37
	J. Nakano and T. Tsukada	
1-34	Corrosion Resistance of Tank Material Used for Flock Storage	38
	Y. Sano , H. Ambai, M. Takeuchi and Y. Koma	
1-35	Investigation of Microstructure in SiC Made by Nano-infiltration Transient Eutectic Process after Triple Ion Beam Bombardment	39
	K. Ozawa, T. Taguchi T. Nozawa, M. Ando and H. Tanigawa	
1-36	Ionizing Dose Dependences of Radiation-induced Conductivity and Radiation-induced Electrical Degradation of Chemical Vapor Deposited Silicon Carbides under Gamma-ray Irradiation	40
	B. Tsuchiya, T. Shikama, S. Nagata, K. Saito and S. Yamamoto	
1-37	Surface Morphology of He Implanted CeO ₂ Thin Film	41
	H. Serizawa, S. Yamamoto and T. Hakoda	
1-38	A Macroporous SiC Material Synthesized from Preceramic Polymer with Direct Foaming and Radiation Curing	42
	A. Idesaki, M. Sugimoto and M. Yoshikawa	
1-39	Alkaline Durable Anion Exchange Membranes Synthesized by Radiation-induced Grafting for Hydrazine Hydrate Fuel Cell	43
	K. Yoshimura, H. Koshikawa, T. Yamaki, H. Shishitani, S. Yamaguchi, H. Tanaka and Y. Maekawa	
1-40	Preparation of Anion-Exchange Membranes for Fuel Cell Applications by γ -ray Pre-irradiation Grafting: Effect of the Carbon Dioxide in the Air	44
	H. Koshikawa, K. Yoshimura, T. Yamaki, M. Asano and Y. Maekawa	

1-41	Poly(ether ether ketone) (PEEK)-based Graft Type Polymer Electrolyte Membrane: Relative Humidity Dependence for Fuel Cell Application	45
	S. Hasegawa, H. Koshikawa, J. Chen and Y. Maekawa	
1-42	Preparation of Novel Polymer Electrolyte Membranes by Combination of Radiation Induced Grafting and Atom Transfer Radical Polymerization	46
	S. Sawada, S. Hasegawa and Y. Maekawa	
1-43	Preparation of Platinum Nanoparticle Catalysts for Fuel Cell Applications by Ion Implantation	47
	S. Kato, T. Yamaki, S. Yamamoto, T. Hakoda, K. Kawaguchi, T. Kobayashi, Y. Maekawa, A. Suzuki and T. Terai	
1-44	Ion Content of Ion Exchange Membrane in HI-I ₂ -H ₂ O Mixture	48
	N. Tanaka, T. Yamaki, M. Asano, T. Terai and K. Onuki	
1-45	Applied-Voltage Dependence on Conductometric Track Etching of Poly(vinylidene fluoride)	49
	N. Nuryanthi, T. Yamaki, H. Koshikawa, A. Kitamura (Ogawa), S. Sawada, M. Asano, S. Hasegawa, Y. Maekawa and Y. Katsumura	
1-46	Microscopic Evaluation of the Absolute Fluence Distribution of an Ion Beam Using a Track Etching	50
	A. Kitamura (Ogawa), T. Yamaki, Y. Yuri, S. Sawada and T. Yuyama	

1 - 01

Radiation Tolerance of New Coverglass
for Space Solar Sheet

K. Shimazaki^{a)}, Y. Kobayashi^{a)}, M. Takahashi^{a)}, M. Imaizumi^{a)},
S. Sato^{b)} and T. Ohshima^{b)}

^{a)}Aerospace Research and Development Directorate, JAXA,

^{b)}Environment and Industrial Materials Research Division, QuBS, JAEA

Space solar sheet (SSS) being currently under development is a quite unique and Japan's original devise for generating electricity in space¹⁾. There are two kinds of SSS: one is a film-type SSS using transparent polymer film and the other is glass-type SSS (G-SSS) using a coverglass. Space solar sheet basically possesses 15 paper-like III-V multi-junction solar cells connected in five series and three parallel rows. The cells are laminated with the transparent polymer film or coverglass. To realize G-SSS, features of flexibility, toughness (not crack easily) and high radiation tolerance are inevitably required for the coverglass. Optical degradation of the coverglass caused by space radiation is particularly important since it decreases the amount of transmitted sunlight falling on solar cells and degrades the cell output power. Hence, we evaluated a radiation tolerance of a new coverglass for G-SSS.

Space radiations are omnidirectional charged particles and have energies that range from near-zero up to several hundred million electron volts. However, the present ground tests are different from the actual space radiation environment. Ground tests usually utilize the monoenergetic and normal incident charged particles. For simulating the same level of degradation as the actual space radiation environment, we calculated the energies deposited in the sample using PHITS (Particle and Heavy Ion Transport code System)^{2,3)}. The interest sample was a new coverglass with 50 μm thickness. Figure 1 illustrates the calculated depth profiles of the deposited energies by space radiations and ground-based monoenergetic irradiations. The assumed space environments and conditions were low-earth orbit for 5 years and geostationary orbit for 10 years. The 1-MeV electron was selected for ground test because its electron completely penetrates the sample. Calculation results show that the required fluences of 1-MeV electron were approximately 2×10^{14} and 2×10^{16} e/cm^2 for simulating the degradation due to space radiation at Low Earth Orbit (LEO) and Geostationary Orbit (GEO).

Figure 2 depicts the results of irradiation tests. Changes in transmittance due to the irradiations were evaluated as an effective transmittance which corresponded to the relative changes in calculated short-circuit current of the solar cells. The remaining factors of effective transmittance of the coverglass were 98% and 97% at fluences of 2×10^{14} and 2×10^{16} e/cm^2 . The degradation behavior seems to be saturated as the fluence increases. In addition, the coverglass showed same degree of the degradation between

LEO and GEO conditions although the total dose of GEO was larger than that of LEO by two orders of magnitude. It is expected that the optical properties of the coverglass is stable at different radiation environment. The transmittance loss of the coverglass will be only 3% when it is utilized on geostationary orbit for 10 years. These results demonstrate the developed coverglass exhibit an excellent performance in space and has a high potential for applying to G-SSS.

References

- 1) T. Takamoto et al., Proc. 35th IEEE PVSC (2010) 412-7.
- 2) H. Iwase et al., J. Nucl. Sci. Technol. **39** (2002) 1142.
- 3) K. Niita et al., Radiat. Meas. **41** (2006) 1080.

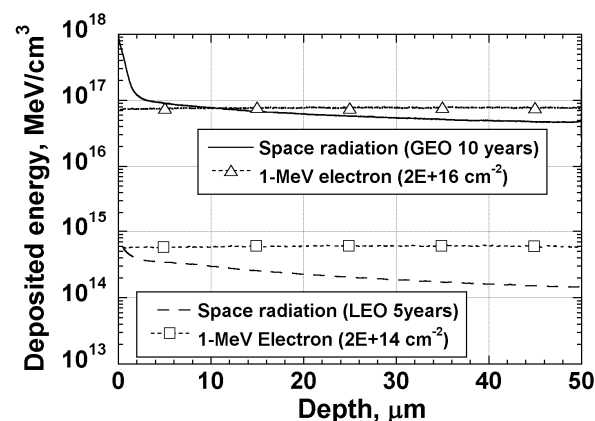


Fig. 1 Calculated depth profiles of deposited energies in coverglass.

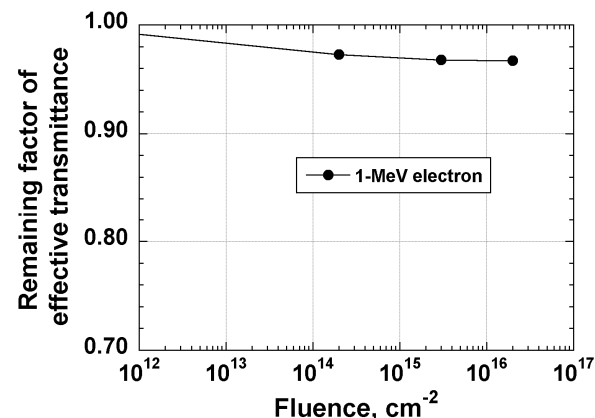


Fig. 2 Changes in effective transmittance of coverglass irradiated with 1-MeV electrons at Takasaki, JAEA.

1 - 02

Proton Induced Degradation of Triple Junction Amorphous Silicon Thin Film Solar Cells

S. Sato and T. Ohshima

Environment and Industrial Materials Research Division, QuBS, JAEA

I. Introduction

Amorphous silicon (a-Si) thin film solar cells are one of the major candidates for flexible space solar cells, since it is known they have not only good radiation tolerance, but also many distinct advantages: high specific power, high flexibility, ruggedness, and tight rollup feature for stowage¹⁾. Additionally, they also have the potential for reductions of both cost and stowage volume. Recently, the specific power of 1200 W/kg has been attained by triple-junction (TJ) amorphous silicon alloy solar cells using roll-to-roll processing²⁾. However, systematic knowledge of the radiation degradation of a-Si solar cells is still insufficient compared to other types of solar cells, such as crystalline Si and III-V compounds.

II. Experimental

Samples used in this study were a-Si/a-Si_{0.8}Ge_{0.2}/a-Si_{0.6}Ge_{0.4} TJ solar cells. Proton irradiation was performed at TIARA. Current-voltage (*I*-*V*) characteristics under air mass zero (AM0), 1 sun light illumination were measured *in-situ* in an irradiation chamber. In this study, proton beam flux, temperature during irradiation, and elapsed time between irradiation and measurement were carefully controlled in order to compare the degradation behavior accurately. The proton beam flux and the irradiation temperature were $1.4 \times 10^{10} \text{ cm}^{-2}\text{s}^{-1}$ and 298 K, respectively, and the *I*-*V* measurement was done 1 minute after irradiation was stopped. The cells were kept under dark conditions except when the *I*-*V* measurement was performed.

III. Results and Discussion

Figure 1 shows short-circuit current (*I*_{sc}) variations of the cells as a function of proton fluence (degradation curve). The degradation of *I*_{sc} was larger as the proton energy was lower, except the results of 10 keV and 20 keV proton irradiations. Protons with energies of 10 keV and 20 keV stop in the top (a-Si) and middle (a-Si_{0.8}Ge_{0.2}) subcells respectively and deposit all of their energies in the cell. However, their proton energy itself was less than 40 keV and thus, their induced damage was also lower.

Figure 2 shows the degradation curves of *I*_{sc} which are scaled using the displacement damage dose (DDD). DDD is defined as the product of NIEL³⁾ (Non-Ionizing Energy Loss, MeV·cm²/g) and the proton fluence. In order to consider the deposited energy distribution as a function of depth in the device structure, NIEL per unit depth was calculated using TRIM code and the average value in the whole region of the cell was used. The result clearly show

that a universal curve is drawn using DDD scaling, indicating that the degradation is mainly attributed to the displacement damage effect, which is the same mechanism as the degradation of crystalline silicon solar cells and is very different from the light-induced degradation so commonly occurring in a-Si solar cells⁴⁾.

We would like to thank Dr. Kevin Beernink of United Solar Ovonic LLC for fabricating the samples.

References

- 1) S. G. Bailey et al., Proc. 34th IEEE PVSC (2009) 001909-13.
- 2) A. Banerjee et al., Proc. 34th IEEE PVSC (2009) 002651-55.
- 3) I. Jun et al., IEEE Trans. Nucl. Sci. **50** (2003) 1924-28.
- 4) D. L. Staebler et al., Appl. Phys. Lett. **31** (1977) 292-4.

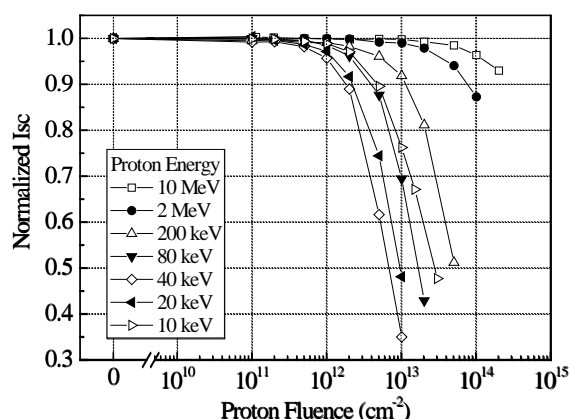


Fig. 1 Degradation of *I*_{sc} due to proton irradiation. The ordinate axis is normalized by the value before irradiation.

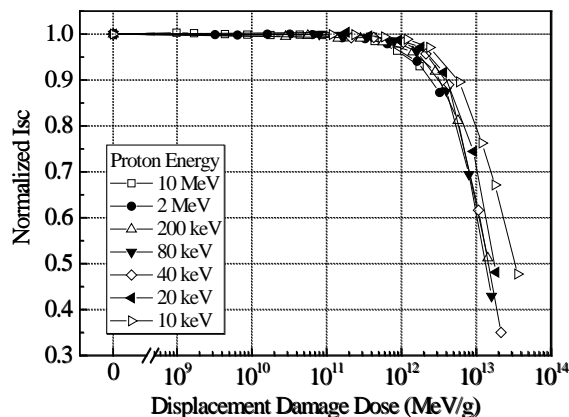


Fig. 2 Displacement damage dose (DDD) scaling for the degradation curves of *I*_{sc}.

1 - 03 **Applicability of the Improved Radiation Hardness Techniques for Angle Irradiation in DICE Latches on a 65 nm Bulk CMOS Process**

A. Maru^{a)}, H. Shindou^{a)}, S. Kuboyama^{a)}, T. Tamura^{a)}, H. Abe^{b)} and T. Ohshima^{b)}

^{a)}Aerospace Research and Development Directorate, Japan Aerospace Exploration Agency (JAXA),

^{b)}Environment and Industrial Materials Research Division, QuBS, JAEA

Recently, due to the requirements for higher density integration and device scaling, logical circuits have been fabricated with the process technologies less than 100 nm. Single-Event Upset (SEU) and Single-Event Transient (SET) phenomena are considered serious problems for those integrated circuits, because their supply voltage and the threshold to the phenomena are also decreasing. It was reported that Dual Interlocked Storage Cell (DICE) circuit is the hardened topology against SEU^{1),2)}. The DICE circuit keeps data using two memory nodes, and if data inversion occurs by incident particles on the one hand memory node, the correct data is rewritten by the other hand memory node. Therefore, DICE circuit has excellent radiation tolerance. However, in highly integrated circuits, it was found that two neighboring transistors were simultaneously inverted by an incident particle due to the charge sharing mechanism³⁾. Therefore, it is important for the design of highly integrated DICE circuits used in space to estimate the extent of the charge sharing.

In the past study⁴⁾, we evaluated the effectiveness of the Radiation Hardness By Design (RHBD) approach for 90 nm CMOS process, by using heavy ions from AVF cyclotron at JAEA. The DICE memory test circuit was fabricated by using 90 nm bulk CMOS process and the angled irradiation testing was performed with this circuit. As a result, SEUs were observed in the DICE memory circuit when heavy ions were irradiated with grazing angles. This result can be explained by the simultaneous inversion of a critical transistor pair which triggers SEU in the DICE memory. Due to the penetration of a single heavy ion into the critical transistor pair, SEUs were observed in the previous experiments. To mitigate this, we proposed three node DICE circuits. Figure 1 shows a schematic diagram of our

designed three node DICE circuit. Extra p-type transistors were inserted to the normal DICE circuit. In addition, the critical three transistors were arranged so as not to align in a straight line, and thus, a single ion could not penetrate these critical transistors in this circuit, simultaneously.

In the latest study, we applied this technique to the 65 nm bulk CMOS process and designed the three node DICE circuits. The layout designing indicates an advantage of the circuits area compared with the same circuits on the 90 nm bulk CMOS process: Higher integrated devices used for space are expected to be fabricated by using the 65 nm CMOS process. Table 1 shows a comparison of the circuit area.

The test samples, which were fabricated by using Taiwan Semiconductor Manufacturing Company (TSMC), were evaluated by using heavy ions with LET of 3.4 ~ 68.8 MeV/(mg/cm²). The results indicated that the test circuits exhibited almost the same single event tolerance compared to the circuits fabricated on the 90 nm bulk CMOS process. Therefore, the 65 nm bulk CMOS process is found to be applied to the devices used for space. However, some SEUs were still observed in the three node DICE circuit. There is the possibility to improve SEU tolerance by modifying transistor layout. We continue evaluating newly developed DICE circuits, and will modify the transistor layout in next stage.

References

- 1) M. P. Baze et al., IEEE Trans. Nucl. Sci. 55 (2008) 3295.
- 2) K. Wang et al., Can. Conf. Electr. Comput. Eng. (2009) 1076.
- 3) A. Amusan, et al., IEEE Trans. Nucl. Sci. 53 (2006) 3253.
- 4) A. Maru et al., IEEE Trans. Nucl. Sci. 57 (2010) 3602.

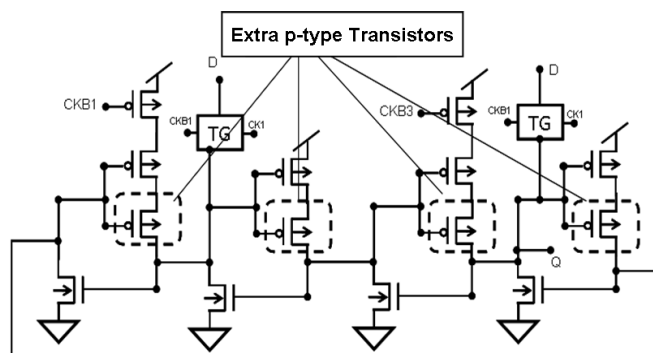


Fig. 1 Schematic diagram of three node DICE memory cell.

Table 1 Comparison of the circuit area for the conventional DICE and the three node DICE circuits.

Circuit name	90 nm	65 nm
DICE	53.40[um ²]	19.44[um ²]
Three node DICE	70.71[um ²]	46.08[um ²]

1 - 04 **Influence of Generated Charge by High Energy Ion Irradiation on Soft Error Rate in SOI SRAM**

M. Hazama^{a)}, S. Abo^{a)}, F. Wakaya^{a)}, T. Makino^{b)}, S. Onoda^{b)}, T. Ohshima^{b)},
T. Iwamatsu^{c)}, H. Oda^{c)} and M. Takai^{a)}

^{a)}Center for Quantum Science and Technology under Extreme Conditions, Osaka University,

^{b)}Environment and Industrial Materials Research Division, QuBS, JAEA,

^{c)}Renesas Electronics Corporation

When a semiconductor device is irradiated with a high energy particle, originated from a cosmic ray, electron-hole pairs are generated along its track due to energy consumption of the particle and flow to the circuit, resulting in a soft error. In recent years, a size of a semiconductor device is shrunk for low power consumption and high speed operation. Therefore the amount of charge which induces soft errors (critical charge) for an advanced device has decreased as compared with that for a conventional device. A silicon-on-insulator (SOI) device can suppress the soft errors. Because an active region of the SOI device is separated from a substrate by a buried oxide (BOX) layer, the small amount of charge is generated by the high energy particle in the active region of the SOI device. However the soft errors occur by a floating body effect in the partially depleted (PD) SOI device with the electrically floated active region from the substrate, even if the amount of the generated charge in the SOI body is less than the critical charge. When the electron-hole pairs are generated in the SOI body of an n-channel Metal-Oxide-Semiconductor Field-Effect Transistor (MOSFET), the generated electrons move to the source and drain electrodes and the generated holes move to the neutral region at the bottom of the SOI body. The accumulated holes at the neutral region increase the body potential of the SOI MOSFET, resulting in the abnormal drain current and the soft error. The body-tie structure was invented to suppress the floating body effect, in which the highly doped p-type region is fabricated at the bottom side of the active region of the n-channel SOI MOSFET and connects to the ground potential. The accumulated holes can be retrieved through the highly doped p-type region and the body electrode. In this study, the influence of the amount of the generated charge on the soft error rates (SERs) in the body-tie SOI Static Random Access Memories (SRAMs) are investigated by various ion probes to clarify the effect of the floating body on the soft error.

In order to generate the various amounts of charge, the SOI SRAM with body-tie structure was irradiated with H, He, Li, Be, C, and O, accelerated up to a few tens of MeV by the tandem accelerator. The thicknesses of SOI and BOX layers are 75 nm and 145 nm, respectively. The critical charge of the experimental PD SOI SRAM with a technology node of 90 nm was 1.8 fC. The number of the incident particles to SOI SRAM is counted by a solid state detector (SSD) before and after ion irradiation. The less number of particles than the number of SRAM cells were

used to avoid multi hits to the single SRAM cell. The generated charge in the SOI layer was calculated by The Stopping and Range of Ions in Matter (SRIM) simulator¹⁾.

Figure 1 shows SERs as a function of the generated charge in the SOI body by H, He, Li, Be, C and O ion probes. SERs in the SOI SRAM increased with increasing the amount of generated charge below the critical charge. These errors were induced by the floating body effect. SERs which occurred at the amount of the generated charge exceeds the critical charge were almost constant. These errors were induced by the flowed charge and the floating body effect.

The amount of generated charge in the SOI body depends on the kind and energy of the incident particles. Therefore, it is necessary to make measures according to the expected incident particles for realizing the soft-error-free PD SOI devices.

Reference

- 1) J. Ziegler, The Stopping and Range of Ions in Matter (SRIM2008) <<http://www.srim.org>>.

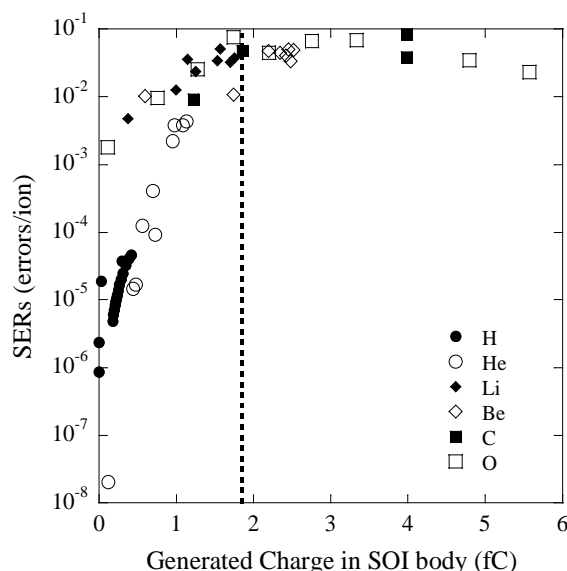


Fig. 1 SERs as a function of amount of the generated charge in the SOI body by using H, He, Li, Be, C and O ion probes for 90 nm node PD SOI-SRAM. The vertical dotted line shows the critical charge of 1.8 fC.

1 - 05 Radiation Damage in Si_{1-x}Ge_x Source/Drain p-type MOSFETs

K. Takakura^{a)}, I. Tsunoda^{a)}, M. Yoneoka^{a)}, T. Nakashima^{b,c)} and M. Sugiyama^{d)}

^{a)}Kumamoto National College of Technology, ^{b)}University of Miyazaki,

^{c)}Chuo Denshi Kogyo Co. Ltd., ^{d)}Tokyo University of Science

The development of semiconductor devices, which can operate in a radiation-harsh environment, is extensively taking place in a global context. This has been driven by multiple factors, including the high-energy particle accelerators and artificial satellites. Moreover, in the frame of high mobility substrates, new channel materials and/or promising methods to create strained channels are required^{1,2)}. In line with this, we have investigated the degradation of the device performances of Si_{1-x}Ge_x S/D (source/drain) p-channel metal oxide semiconductor field effect transistors (p-MOSFETs) irradiated electrons. The purpose of this study is to investigate Ge content dependence on radiation damage of Si_{1-x}Ge_x S/D p-MOSFETs.

Si_{1-x}Ge_x (x = 0, 0.3 and 0.35) S/D p-MOSFETs were fabricated at interuniversity microelectronics center (imec) at Belgium. The Si_{1-x}Ge_x S/D region depth of x = 0.3 and 0.35 samples is 40 nm, and gate length and gate width of all samples are 0.25 μ m and 10 μ m. Subsequently, these were irradiated by 2-MeV electrons for a fluence of 1×10^{17} and 5×10^{17} e/cm² at room temperature, using the electron accelerator at Takasaki Advanced Radiation Research Institute, JAEA. Before and after electron irradiation, input (I_{DS} - V_{GS}) characteristic was measured with a drain voltage at -25 mV and gate voltages ranging from -1.2 to 0.5 V, enabling to estimate the hole-mobility³⁾.

Before irradiation, the drain current increases with increasing Ge content. After irradiation, the drain current decreases with increasing electron fluence for all Ge content. Figure 1 shows the Ge content dependence of the maximum

hole mobility before and after electron irradiation. The hole mobility enhancement effect by SiGe stressor is clearly observed by x = 0.3 and 0.35 samples before irradiation. These results indicate that the change of the drain current with Ge content can be mainly attributed to the increase of the hole mobility due to the compressive strain in the Si-channel. After electron irradiation, the hole mobility decreases with increasing electron fluence for all Ge content. This result suggests that the lattice defects are introduced by electron irradiation in the Si channel.

The damage factor of maximum hole mobility ($D_F = \mu_{\text{max-after}} / \mu_{\text{max-before}}$; where $\mu_{\text{max-before}}$ and $\mu_{\text{max-after}}$ are the maximum hole mobility in before and after electron irradiation) was summarized in Fig. 2 as a function of the Ge content. The damage factor decreases with increasing electron fluence for all Ge content. Moreover, Ge content dependence in the damage factor does not observed. It also indicates that the degradation of hole mobility by electron irradiation does not corresponds to compressive strain in the channel.

References

- 1) M. Kodera et al., Jpn. J. Appl. Phys. **47** (2008) 2506.
- 2) K. Rim et al., IEEE IEDM Tech. Dig. (1995) 517.
- 3) T. Nakashima et al., Thin Solid Films **520** [8] (2012) 3337.

Acknowledgement

Part of this work was supported by Inter-University Laboratory for the Joint Use of JAEA Facilities.

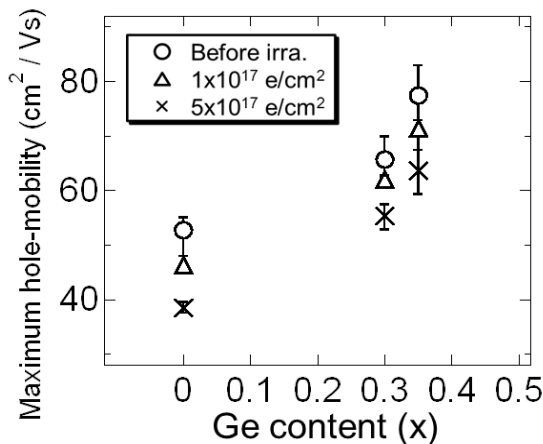


Fig. 1 Hole-mobility before and after electron irradiated Si_{1-x}Ge_x-S/D p- MOSFETs as a function of the Ge content.

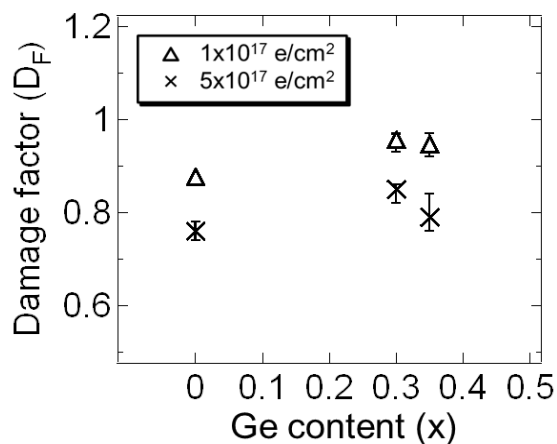


Fig. 2 The damage factor of electron irradiated Si_{1-x}Ge_x-S/D p- MOSFETs as a function of the Ge content.

1 - 06 Anomalous Charge Collection from 4H-SiC Schottky Barrier Diodes

T. Makino^{a)}, M. Deki^{b)}, N. Iwamoto^{a)}, S. Onoda^{a)}, N. Hoshino^{c)},
H. Tsuchida^{c)} and T. Ohshima^{a)}

^{a)}Environment and Industrial Materials Research Division, QuBS, JAEA,

^{b)}The University of Tokushima,

^{c)}Central Research Institute of Electric Power Industry (CRIEPI)

Silicon carbide (SiC) are regarded as a promising candidate for a material of electronic devices requiring high radiation tolerance (rad-hard devices). Some results indicate that electronic devices fabricated with SiC have a superior radiation tolerance from the point of view of Total Ionizing Dose effects (TIDs)¹⁻³⁾. For the development of rad-hard SiC devices, it is necessary to understand the response of their performance when dense charge is generated in them by an incident ion, resulting in Single Event Effects (SEEs). Silicon carbide can endure an electric field about eight times greater than silicon or GaAs before exhibiting avalanche breakdown. High breakdown electric fields allow for very high-voltage, high-power devices. Permanent malfunctions can be induced in power devices by SEEs, and the probability of SEEs increases with increasing electric field in the device. Since the electric field in SiC power devices must be higher than in Si power devices, it is very important to elaborate the SEEs in SiC devices. Recently, several Schottky Barrier Diodes (SBDs) have become commercially available due to the improvement in crystalline quality. At present, experimental data for understanding the exact mechanisms of SEEs in SiC-SBDs are very scarce and Single Event Burnout (SEB) mechanisms of SiC-SBDs have not been fully understood.

In this study, heavy-ion induced charge collection is demonstrated for thick epi-layer. To reveal SEB mechanisms, the applied bias dependence of the charge collection in SiC-SBDs has been investigated here.

SiC-SBDs used in this study were fabricated on an n-type 4H-SiC epi-layer. The thickness of the epi-layer is 30 μm . A molybdenum (Mo) contact with a thickness of 50 nm was used as the anode of SiC-SBD. The bonding pad on the Mo-contact was made of Al (2 μm thick). The bonding pad area is 1 mm^2 . We measured the collected charge induced by heavy ions in SiC-SBD from its cathode. SiC-SBD was mounted on a chip carrier with two strip-lines with short bonding wires. The anode was grounded and the cathode biased from +100 V to +1,000 V with 50 V to 200 V steps by a high-voltage supply via a charge-sensitive preamplifier (ORTEC Model 142C). Collected charge signals from the pre-amplifier were analyzed by a Pulse-Height Analyzer (PHA). The pulse-height distribution analyzed by PHA basically corresponds to the collected charge distribution.

Figure 1 shows the collected charge spectra from SiC-SBD at different bias conditions. The vertical axes are ion induced pulse generation cross-section. The horizontal axis corresponds to the collected charge. Normally the collected charge spectrum might have a mono-peak similar to that found in a Si-SSD spectrum. In fact, an ion-induced mono-peak in SiC-SBD was observed in a previous study⁴⁾.

However, here two major peaks under bias conditions higher than 300 V are observed as shown in Fig. 1. The first peak exists at a value of 6.2 pC in every bias condition. The first peak increases with the reverse bias applied to the cathode, and finally saturates, because the depletion width in the epi-layer increases with the reverse bias and finally saturates. The upper limit of the first peak (6.2 pC) corresponds to the fully-stopped 300 MeV of Kr ion induced charge in 4H-SiC. Here, the mean electron-hole pair creation energy is 7.8 eV in 4H-SiC, while the second peaks are observed as anomalous charge collection beyond 6.2 pC.

Anomalous collected charge peaks (2nd peaks) has been

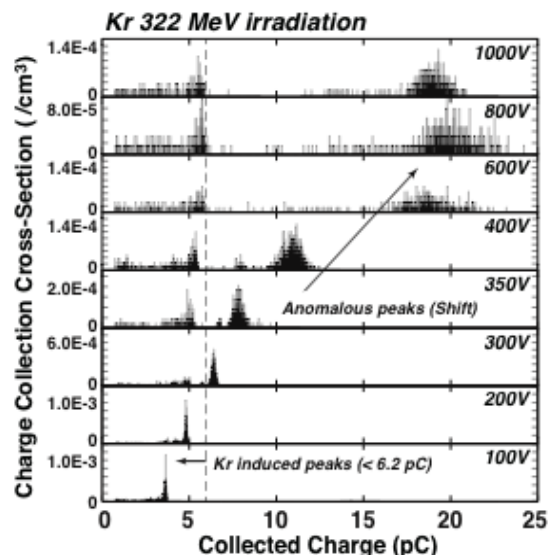


Fig. 1 Collected charge spectra from the SiC-SBD⁵⁾.

observed for the first time⁵⁾. Previous results suggest that the high electric-field induced by incident ion on SiC-SBD may be a possible reason for the charge enhancement. The higher electric-field may enhance the ion-induced charge due to impact ionization and/or the trap assisted tunneling. However, from these results, we cannot identify the mechanisms of the anomalous charge collection. Therefore, more studies are needed in order to reveal the effective parameter for the anomalous charge collection on SiC-SBD, since an increase of the collected charge may trigger SEB in any devices whatever the charge collection mechanism.

References

- 1) T. Ohshima et al., J. Appl. Phys. 90 (2001) 3038.
- 2) Y. Tanaka et al., Mater. Sci. Forum 645-648 (2010) 941.
- 3) S. Onoda et al., IEEE Trans. Nucl. Sci. 56 (2009) 3218.
- 4) S. Kuboyama et al., IEEE Trans. Nucl. Sci. 53 (2006) 3343.
- 5) T. Makino et al., IEEE Trans. Nucl. Sci. 60 (2013) 2647.

1 - 07

Atomic and Electronic Structure Analysis of the Interface between α -SiO₂ and 4H-SiC(11-20)

A. Miyashita and M. Yoshikawa

Environment and Industrial Materials Research Division, QuBS, JAEA

In the silicon carbide (SiC) trench-gate metal-oxide-semiconductor field-effect transistors (MOS-FETs) which is fabricated on the 4H-SiC(0001) substrate, a (11-20) face is used as a sidewall of the trench-gate (Fig. 1). Recent years, a high channel mobility was obtained on (11-20) face compared with (0001) face¹⁾. The channel mobility is degraded by the defects which exist at the interface between gate oxide film and the SiC substrate. As the component of the gate oxide film is amorphous SiO₂ (α -SiO₂), we have developed large-scale simulation techniques of α -SiO₂/SiC interface for investigation of MOS-FETs and successfully obtained the theoretical α -SiO₂/4H-SiC(0001) interfacial model (Si-face model)²⁾. In this work, to determine the reason for a high channel mobility at the interface between the α -SiO₂ layers and the 4H-SiC(11-20) substrate, we generated the theoretical α -SiO₂/4H-SiC(11-20) interfacial model (A-face model) with the computer simulation and compared the atomic and the electronic structure of the A-face model with those of the Si-face model.

The heating and the quenching method was used for the generation of A-face model²⁾. In the atomic structure model before heating (initial model), the β crystal was connected on 4H-SiC(11-20) substrate. The obtained A-face model had an abrupt interface. The theoretical data from the analysis of the radial distribution function (RDF) of α -SiO₂ layers were corresponding to the experimental data of the silica (Fig. 2), and therefore the SiO₂ layers had an excellent amorphous structure. On the other hand, the band gap energy which had been derived from the density of

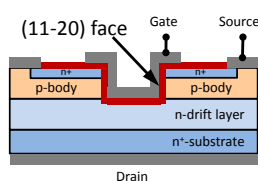


Fig. 1 Schematic cross section of trench-gate MOSFET.

states (DOS) of the A-face model was 3.6 eV, which is larger than 3.2 eV known as an experimental data of the band gap energy of 4H-SiC crystal. To obtain an accurate band

gap energy, we tried to stabilize the electronic structure of the entire A-face model by increasing the thickness of the SiC layers from five layers to eight layers. As a result, a band gap energy of 3.3 eV, which is almost equal to the experimental data, was successfully obtained. The defect levels which had been observed from the electronic structure of improved theoretical A-face model were not quite different from those obtained from the past analysis of Si-face model.

The A-face model with rough interface (rA-face model) was generated after the heating and quenching process using the modified initial model. In the modified initial model, to make interatomic reaction actively during the heating and quenching process, additional O was arranged next to the dangling-bond of C at the interface. In the generated rA-face model, C-C bond and a lot of other defects appeared in the band gap (Fig. 3). The energy levels of the defects were almost equal to those which had been obtained from the Si-face model with rough interface (rSi-face model). Some of the defect levels appeared in the rSi-face model, however, were not generated in rA-face model. Those defect levels were mainly generated from interfacial Si. Especially, in rSi-face model, the defect level, which is originated in the expanding Si-C bond at the interface, generated with Si in the SiC layer decreases the channel mobility very much because the defect has energy level just below the conduction band of 4H-SiC. On the other hand, in rA-face model, it is considered that the distortion of the defect is reduced easily compared with the case of rSi-face model since Si-C bond is on the surface of the SiC layer. Therefore, the defect level did not appear in the band gap in rA-face model. It is suggested that the cause of high mobility on 4H-SiC(11-20) is a lack of this defect level.

References

- 1) H. Yano et al., Appl. Phys. Lett. **90** (2007) 042102.
- 2) A. Miyashita et al., JAEA Takasaki Annu. Rep. 2011 (2013) 12.

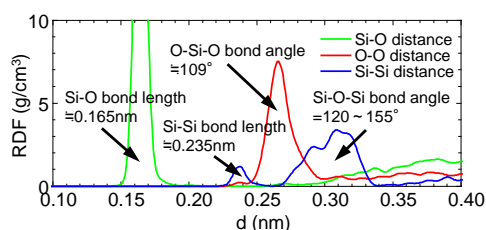


Fig. 2 RDF spectrum of the α -SiO₂ layers of A-face model. (In the experimental data of silica, Si-O bond length, O-Si-O bond angle and Si-O-Si bond angle are 0.165 nm, 109.5 deg and 145±10 deg, respectively.)

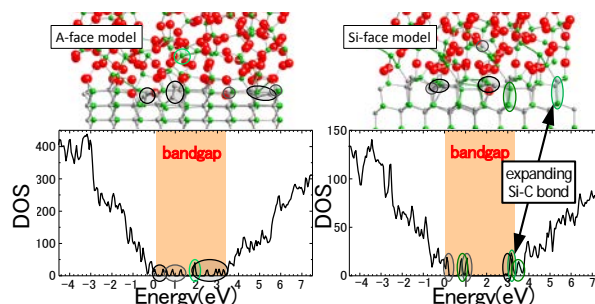


Fig. 3 Side view of the interfacial rA-face and rSi-face models and corresponding DOS.

1 - 08

Proton Irradiation Effects on Nitride Semiconductor-based Light Emitting Device

H. Okada^{a)}, Y. Okada^{a)}, H. Sekiguchi^{a)}, A. Wakahara^{a)}, S. Sato^{b)} and T. Ohshima^{b)}^{a)}Department of Electrical and Electronic Information Engineering, Toyohashi University of Technology, ^{b)}Environment and Industrial Materials Research Division, QuBS, JAEA

Three hundred eighty keV proton irradiation effects on GaN-based light emitting device (LED) were investigated by characterizing two-terminal resistance of p- and n-contacts on both types of layers in LED wafer. After the proton irradiation, in the range of 1×10^{14} – 1×10^{15} cm⁻², two-terminal resistance on n-layer kept its initial value. On the other hand, the p-layer showed the drastic increase in resistance, indicating hole traps were introduced in GaN. The results suggest that the radiation effects on GaN-based device is mainly governed by introduction of the hole traps.

窒化ガリウム(GaN)などの窒化物半導体は、広いバンドギャップに加えて機械的、化学的安定性を有するなど過酷な環境でも動作する半導体デバイスとして期待されている。窒化物半導体のデバイス応用の代表ともいえる LED などの発光デバイスは、近年、高効率な青色および蛍光体との組み合わせによる白色光源として広く用いられている。こうした発光デバイスの耐放射線性や劣化メカニズムを解明することは、宇宙空間でのシステム構築やより耐久性の優れたデバイス開発のために重要である。しかし、窒化物半導体デバイスの耐放射線性の系統的な理解に向けた取り組みや、特に、p 型 GaN についての報告は少ない¹⁾。電子と正孔の両方のキャリアを用いる LED などのバイポーラデバイスの放射線照射効果や、それに基づく特性劣化予測を得るには、半導体デバイスの構成要素のそれぞれの照射効果の実験評価を行い、その知見に基づいたデバイス全体の特性の解明を行う必要がある。そこで今回は、GaN 系 LED 構造の n 型層および p 型層それぞれに対する陽子線照射効果を評価した。

今回は、市販されている InGaN 量子井戸を発光層にもつ GaN LED 構造(発光ピーク波長 $\lambda=450$ nm)の陽子線照射効果を検討した。(Fig.1) この構造の p 型層および n 型層それぞれの電気的特性変化を評価するために、リソグラフィ工程によりウェハの一部を誘導性結合反応性エッチング(ICP-RIE)によりエッチングして n 型層を露出させ、p 層および n 層に同心円状のオーミック電極を形成した。ここでは、p 型層のオーミック電極には Ag、n 型層には Ti/Al/Ti/Au を蒸着し、熱処理によりオーミック特性を得た。それぞれの蒸着金属の厚さは 200-300 nm である。デバイス作製後、TIARA のイオン注入装置を用いて、真空中、室温にて 380 keV の陽子線照射を行った。SRIM を用いたシミュレーションから 380 keV の陽子線照射でのプロトンの侵入長は 2-3 μ m と見積もられ、n 型および p 型層を十分に突き抜けることから、水素注入による影響はほとんどないと予想される。照射濃度は 1×10^{14} cm⁻² および 1×10^{15} cm⁻² とし、熱処理などは施さず室温での電流-電圧特性を評価した。

試料上の同一の電極の組み合わせについて陽子線照射前後の抵抗を測定し、照射量に対してプロットした結果を Fig.2 に示す。n 型層においては、 1×10^{14} cm⁻² 照射後でも初期の抵抗値が維持された。 1×10^{15} cm⁻² の照射後では抵抗の増加が観測されたが、その変化は 1 桁以下であった。これに対し p 型層においては、 1×10^{14} cm⁻² 照射後に明らかな抵抗増加が観測され、 1×10^{15} cm⁻² の照射後には 6 桁以上の顕著な抵抗増加が生じた。即ち、p 型層と n 型層で

は照射効果に差異が現れた。また、 1×10^{15} cm⁻² 照射後の p-n 接合に LED の順方向バイアスを印加したが、照射前に比べて低バイアス領域での再結合電流の増加、ならびに大きな順バイアス領域での順方向電流の低下が電流-電圧特性に現れるとともに、発光特性の著しい劣化が観測された。

我々は AlGaIn/GaN ヘテロ構造に 380 keV の陽子線照射を行い、シートキャリア密度が 1×10^{14} cm⁻² のプロトン照射においても変化しないことを報告している²⁾。構造が異なるため単純な比較は困難だが、陽子線照射によって形成されたホールトラップが GaN 系 LED の照射劣化を支配している可能性がある。

References

- 1) A. Y. Polyakov et al., J. Mat. Chem. C **1** (2013) 877.
- 2) H. Okada et al., J. Phys.: Conf. Ser. **352** (2011) 012010.

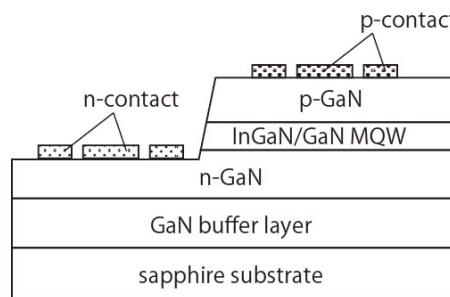


Fig. 1 Sample structure for characterization of proton irradiation effects on GaN-based LED.

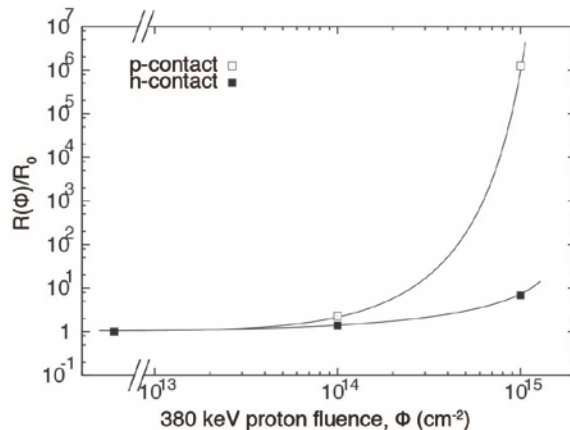


Fig. 2 Proton fluence dependence of two-terminal resistance in p- and n-contact.

1 - 09

Evaluation of Radiation Tolerance of FRAM Microprocessor for Heavy Ion Irradiation

Y. Chiba^{a)}, E. Asai^{b)}, H. Tomioka^{a)}, R. Shimazu^{a)}, T. Kameda^{c)},
T. Ohshima^{d)}, S. Onoda^{d)} and T. Makino^{d)}

^{a)}School of Science and Engineering, University of Tsukuba,

^{b)}Graduate School of Systems and Information Engineering, University of Tsukuba,

^{c)}Faculty of Engineering, Information and Systems, University of Tsukuba,

^{d)}Environment and Industrial Materials Research Division, QuBS, JAEA

1. Introduction

Ferroelectric Random Access Memory (FRAM) attracts notice as a superior radiation tolerant device in aerospace field. In micro-satellite field, although the various challenging missions are performed by universities, companies *etc.*, even now new type microprocessors such as FRAM built-in processors are not utilized due to limited radiation tolerance data and no previous actual operation achievements in space environment. The authors investigate radiation tolerance of commonly used microprocessor with conventional memory, PIC16F877A (PIC) and new type microprocessor with FRAM, MSP430FR5739 (MSP) to evaluate whether the FRAM built-in micro-processors can be used in the micro satellites.

2. Experimental

Table 1 shows a device property of processors under the irradiation experiment. In the experiment, heavy ions were irradiated by using JAEA facility, the AVF cyclotron of the Takasaki Ion Accelerations for advanced Radiation Application (TIARA). The heavy ions irradiated to the PIC were 150 MeV-⁴⁰Ar⁸⁺, 322 MeV-⁸⁴Kr¹⁷⁺ and 454 MeV-¹²⁹Xe²⁵⁺. Those irradiated to the MSP were 75 MeV-²⁰Ne⁴⁺, 150 MeV-⁴⁰Ar⁸⁺, 322 MeV-⁸⁴Kr¹⁷⁺ and 454 MeV-¹²⁹Xe²⁵⁺. To evaluate their radiation tolerance, the single event upsets (SEUs) were counted after ion irradiation, and the SEU cross section of each device was calculated. The Linear Energy Transfer (LET) dependence of the SEU cross section $\sigma_{hi}(L)$ (cm²/bit) is derived from the equation:

$$\sigma_{hi}(L) = \sigma_s \left[1 - \exp \left\{ - \left(\frac{L - L_{th}}{W} \right)^s \right\} \right] \quad (1)$$

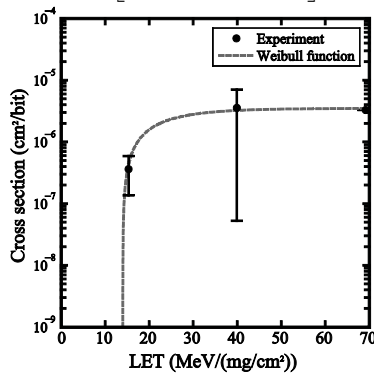


Fig. 1 Relationship between SEU cross-section and LET by irradiating ⁴⁰Ar⁸⁺, ⁸⁴Kr¹⁷⁺ and ¹²⁹Xe²⁵⁺ ions toward PIC16F877A.

where σ_s and L_{th} are a saturated cross section and a threshold LET, respectively. W and s are the constants determining the shape of Weibull function. The LETs of the used heavy ions were obtained by SRIM software.

3. Results and Discussion

LET-SEU cross section relationships for the PIC and MSP are shown in Figs. 1 and 2, respectively. According to the results, the saturated cross section of MSP is approximately 10⁻² smaller than that of PIC, and the threshold LET of MSP is approximately 1/2 of that of PIC.

The SEU frequencies of the both devices on the planned orbit (400 km altitude, 65 degrees inclination) were evaluated by the online software, CRÈME 96¹⁾. The frequencies of the PIC and MSP were 2.33×10^{-7} SEUs/bit/day and 3.40×10^{-9} SEUs/bit/day, respectively. It was confirmed that the SEU frequency of the MSP is 10⁻² smaller than that of PIC. According to SEU simulation on the planned orbit, FRAM microprocessors were shown to have high radiation tolerance sufficient for actual space application.

Reference

- 1) A. J. Tylka et al., IEEE Trans. Nucl. Sci. 44 (1997) 2150.

Table 1 Device property of PIC and MSP.

Device	PIC	MSP
Voltage (V)	5	3.3
Observed Data buffer (byte)	256	64
Memory type	SRAM and EEPROM	FRAM

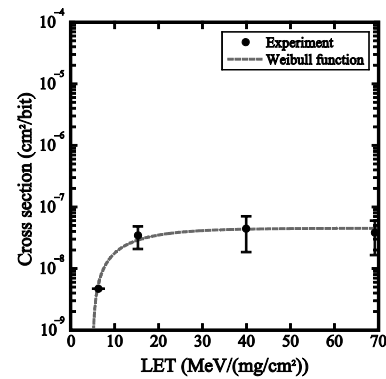


Fig. 2 Relationship between SEU cross-section and LET by irradiating ²⁰Ne⁴⁺, ⁴⁰Ar⁸⁺, ⁸⁴Kr¹⁷⁺ and ¹²⁹Xe²⁵⁺ ions toward MSP430FR5739.

1 - 10

Experimental Study on Radiation Effects on
Magnetic Tunnel Junctions 2

D. Kobayashi^{a)}, Y. Takehashi^{a)}, K. Hirose^{a)},
S. Ikeda^{b)}, M. Yamanouchi^{b)}, H. Sato^{b)}, E.-C. Enobio^{b)}, T. Endoh^{b)}, H. Ohno^{b)},
S. Onoda^{c)}, T. Makino^{c)} and T. Ohshima^{c)}

^{a)} Institute of Space and Astronautical Science, JAXA,

^{b)} Center for Spintronics Integrated Systems, Tohoku University,

^{c)} Environment and Industrial Materials Research Division, QuBS, JAEA

Magnetic tunnel junctions or MTJs are investigated in terms of their tolerance to radiation. The MTJ is a non-volatile digital memory device, which is programmable between high and low resistance states, playing a key role in spintronics, i.e., an emerging semiconductor device technology that utilizes the spin of the electron. Tested structure is a perpendicular-anisotropy MTJ that consists of CoFeB ferromagnetic metals and an ultra-thin MgO insulator, initialized to the low resistance condition before irradiation. It exhibits no resistance change after irradiation by 15-MeV Si ions. It is also demonstrated that constant bias voltage fed to the sample during the Si irradiation has no influence on the radiation tolerance.

プロセッサに代表される半導体集積回路は情報エレクトロニクス機器の心臓部である。計算速度を上げるために回路素子の微細化が進められてきたが、その弊害として消費電力の増大と放射線耐性の低下が深刻になっており、それらをいかに克服するかが課題となっている。この課題を解決する技術として、電子が持つ磁石としての性質であるスピンを活用した、新しい半導体集積回路技術「スピントロニクス」が注目されている。

磁気トンネル接合「MTJ (Magnetic Tunnel Junction)」はこの技術の中核を担う素子である。二つの強磁性金属を電極として持ち、それらによって薄い絶縁体を挟みこんだ二端子構造からなる。可変抵抗として機能し、その抵抗値はスピンの向きに依存したトンネル効果に従って決まる。具体的には、二つの強磁性金属の磁化の相対的な向き、すなわち、平行か反平行かに応じて、高抵抗または低抵抗の値を安定的に取ることができる。スピントロニクスでは、主に、この二つの抵抗値をデジタル信号に割り当てることで、MTJ をデジタルな不揮発性メモリ素子として活用する。

MTJ は原理的に放射線に耐性があると言われており、いくつかの論文でそれを支持する実験結果も報告されている。しかし、近年開発されている MTJ は、それらで調べられているものに比べて、ずっと小さい素子サイズになっている上に、新しい磁化制御方式が導入されているため、これまで通り放射線耐性があるかどうか疑問である。そこで、我々は 2011 年度より日本原子力研究開発機構の施設共用制度を利用して、この素子に対する放射線照射効果を追求している¹⁾。

試料は東北大学にて作製したものであり、直径 70 nm の円柱形である。電気特性を評価するために上層配線と下層配線を直交するように配置し、MTJ をその交点で二層を垂直に繋ぐように作製した。作製した MTJ は強磁性金属に CoFeB、絶縁体に MgO を採用しており、垂直磁気異方性をもつことが特徴である²⁾。すなわち、磁化の向きは円柱の円盤面に垂直に揃う。放射線を円盤面に垂直となるよう照射し、照射前後で抵抗値が変化するか調べた。照射試験にはタンデム加速器を利用した。

まず TA 照射ポートを用いて 3 MeV シリコンを照射した所、昨年度の試験結果と合わせて、素子に選択的に照射し、

なおかつ、チャンバから取り出すことなく特性を評価することが望ましいという結論を得た。

この結論を踏まえて、TB ポートによるマイクロビームを利用して次の実験を行なった。まず、素子を低抵抗状態、つまり、二つの強磁性金属の磁化の向きを平行に揃えた状態に初期化し、これを半導体デバイス微小領域照射装置の真空チャンバに接続した。同装置にて 1.6 μm 径に集束した 15 MeV シリコンイオンマイクロビームを 0.8 μm ステップでずらしながら MTJ を含む 40 μm 角四方をスキャンした。各ステップでの滞留時間を調整することで MTJ に照射される粒子数を調整し、1 または 100 となるようにした。照射時には、素子の二つの電極をソースメーターに接続してバイアスを印加した。印加したバイアスの種類は 0 V (短絡)、 ± 0.1 V、 ± 0.5 V の 5 種類である。これらは初期化した抵抗状態を反転させるに至らない大きさである。照射前後で直流抵抗を測定し比較した。

測定の結果、いずれの照射条件でも抵抗値は測定のばらつきの範囲で一致した。低抵抗状態が放射線照射によって高抵抗に反転する、シングルイベントアップセットは、少なくとも本試験の範囲では確認されなかった。バイアス印加状態での MTJ の重イオン耐性を明らかにしたのは、本研究が初めてである。本内容をまとめ国際会議 RADECS に投稿した³⁾。今後の展望として、高抵抗状態に初期化して同様の照射試験を実施し、保持している抵抗値によらずシングルイベント耐性があることを確認したい。また、本研究では DC 特性を評価しているので、過渡的な特性についても確認が望ましい。

References

- 1) D. Kobayashi et al., JAEA Takasaki Annu. Rep. 2011 (2013) 15.
- 2) S. Ikeda et al., Nature Materials **9** (2010) 721.
- 3) D. Kobayashi et al., Conf. Radiat. Eff. Comp. Syst. (RADECS), (2013)G-1.

1 - 11 Ion Beam Induced Luminescence (IBIL) from Diamond Induced by Various Single Ion with High Energy

S. Onoda, H. Abe, T. Makino and T. Ohshima

Environment and Industrial Materials Research Division, QuBS, JAEA

When a high energy heavy ion strikes a semiconductor device, the destructive or non-destructive events occur. To identify the sensitive region of device, a single ion irradiation and mapping techniques are required. For this aim, we are developing the Ion Photon Emission Microscopy (IPEM) system. To observe a map of sensitive region by using IPEM, the position where an ion strikes a scintillator placed over a device is recorded together with the ion induced event detected by a semiconductor device. Since the spatial resolution is determined by the spot size of the Ion Beam Induced Luminescence (IBIL), the scintillator is one of the most important parts of IPEM. Branson et al. suggested that YAG:Ce is the most promising candidate for IPEM scintillator¹⁾. In the previous report, however, we proposed a diamond containing dense Nitrogen-Vacancy (NV) centers as a scintillator with high spatial resolution²⁾. On the other hand, it is required that the scintillator is able to detect the wide variety of ion species and energies. In this report, we will show the results of the high energy ion irradiation to the diamond containing NV centers.

The sample is created by following procedure. First, we prepare the type Ib High Presser High Temperature (HPHT) single crystal diamond, which contains dense Nitrogen (N) impurities. The shape of HPHT diamond is sphere. Its diameter is about 1 mm. Next, the electron irradiation with the energy of 2 MeV is carried out. During electron irradiation, dense vacancies are created. The subsequent annealing at 1,000 °C in vacuum for 2 hours is performed, in order to combine N with vacancy. Finally we observe the diamond containing NV centers. Its color is changed to pink. The uniformity of NV centers is confirmed by Ultra-Violet (UV) light illumination as shown in Fig. 1.

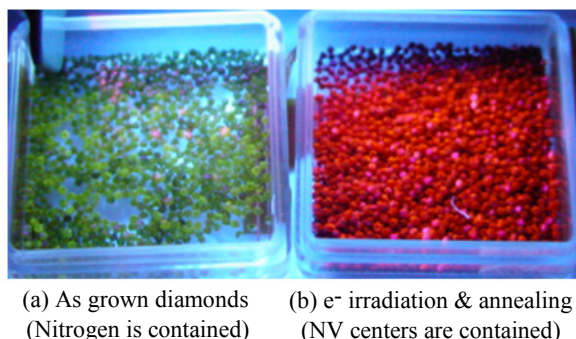


Fig. 1 Photograph of type Ib HPHT single crystal before electron irradiation (a) and after electron irradiation with subsequent annealing (b). The diamonds are illuminated by UV light with the wavelength of 254 nm.

After the diamond is mounted on the sample holder of IPEM system, Nitrogen (N), Neon (Ne), Argon (Ar), Krypton (Kr), and Xenon (Xe) with the energies of 56, 75, 150, 322 and 454 MeV are irradiated to the diamond containing NV centers. The luminescence from the diamond is detected by the GaAsP Image Intensifier (I.I.) (Hamamatsu, C8600) and the cooled Charge Coupled Device (CCD) camera (Hamamatsu, C4880-50-26A). The Quantum Efficiencies (QEs) of these detectors (the sensitive wavelength is ranging from 350 to 750 nm) match the IBIL emission spectrum from NV centers (the luminescence wavelength is ranging from 550 to 800 nm).

Typical CCD images are shown in Fig. 2. The dashed circles highlight the ion induced spots. It is found that the spots are detected for all cases. In this study we successfully demonstrate that the diamond containing NV centers can be used to detect a wide variety of ion species and energies. It is debatable whether the spot size and intensity of IBIL depends on the ion species and energies. According to these results, we therefore conclude that a diamond containing NV centers is a rival candidate of a YAG:Ce for IPEM scintillator applications.

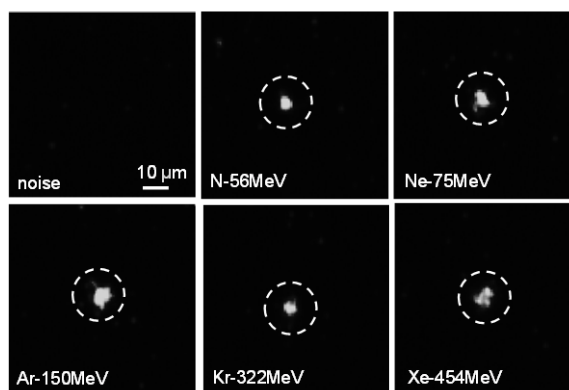


Fig. 2 CCD images when various ions with various energies penetrate the diamond.

Acknowledgment

The part of this study was carried out as “Strategic Japanese-German Joint Research Project” supported by JST and DFG (FOR1482). Collaborator is J. Isoya (University of Tsukuba).

References

- 1) J. V. Branson et al., Nucl. Instrum. Meth. B 269 (2011) 2326-29.
- 2) S. Onoda et al., Trans. Mater. Res. Soc. Jpn. 37[2] (2012) 241-44.

1 - 12 Fabrication of Strongly Coupled Pair of NV Centers in Diamond by Ion Implantation

T. Yamamoto^{a)}, S. Onoda^{a)}, H. Abe^{a)}, S. Sato^{a)}, T. Ohshima^{a)}, J. Isoya^{b)} and T. Umeda^{b)}

^{a)}Environment and Industrial Materials Research Division, QuBS, JAEA,

^{b)}Research Center for Knowledge Communities, University of Tsukuba

Negatively charged nitrogen-vacancy (NV⁻) centers in diamond consists of a substitutional nitrogen with a vacancy at an adjacent lattice site and have an S=1 ground state. Unique properties such as long coherence time (T_2), optical readout and optical preparation make NV⁻ centers promising for solid-state quantum information devices operated at room temperature (RT). An array of NV⁻ centers coupled coherently through dipole-dipole interaction between each neighboring NV⁻ centers is a promising architecture of scalable solid-state quantum register, in which single qubit rotation gates and two-qubit CNOT gates comprise a universal set. In the present work, we demonstrate a fabrication of strongly coupled pair of NV⁻ centers with long T_2 which is prerequisite for 2-qubit CNOT gate of high fidelity.

High-purity, 99.998% ^{12}C enriched single-crystal (SC) CVD diamond was co-implanted with 20 keV N_2^+ ion ($2.5 \times 10^7/\text{cm}^2$) and 20 keV $^{12}\text{C}^+$ ion ($1.4 \times 10^{11}/\text{cm}^2$) at RT and subsequently annealed at 1,000 °C for 2 h in vacuum. The scanning CFM (confocal microscopy), ODMR (optically detected magnetic resonance) and pulsed ODMR such as Hahn echo decay and DEER (double electron electron resonance) were measured at RT by using a home-built set up of University of Ulm.

Two nitrogen implants from a 20 keV $^{15}\text{N}_2^+$ molecular ion are located within a distance of $d < 20$ nm (41% probability for $d \leq 11$ nm) in diamond lattice. After annealing, two nitrogen atoms from a $^{15}\text{N}_2^+$ molecular ion might form either just one $^{15}\text{NV}^-$, or $^{15}\text{NV}^-$ - $^{15}\text{NV}^-$ pair, or no $^{15}\text{NV}^-$ at all.

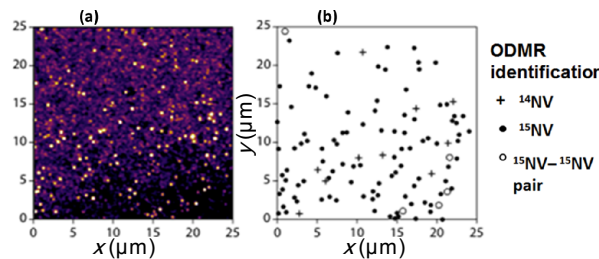


Fig. 1 (a) CFM map of 99.998% ^{12}C enriched SC CVD diamond co-implanted with $^{15}\text{N}_2^+$ and $^{12}\text{C}^+$ and subsequently annealed at 1,000 °C. (b) ODMR identification of each fluorescence spot to be either ^{14}NV , or ^{15}NV , or $^{15}\text{NV}^-$ - $^{15}\text{NV}^-$ pair. ^{14}NV is formed from pre-existing nitrogen impurity. Nitrogen has two stable isotopes, ^{14}N ($I=1$, natural abundance 99.63%) and ^{15}N ($I=1/2$, 0.37%) and ODMR can distinguish between $^{15}\text{NV}^-$ and $^{14}\text{NV}^-$. For an implantation site where no NV is formed from a N_2^+ ion, no fluorescent spot is observed.

Table 1 The yield of $^{15}\text{NV}^-$ and $^{15}\text{NV}^-$ - $^{15}\text{NV}^-$ pair from $^{15}\text{N}_2^+$ (totally 156 ions) implanted in a region of $25\text{ }\mu\text{m} \times 25\text{ }\mu\text{m}$.

	$^{15}\text{NV}^-$	$^{15}\text{NV}^-$ - $^{15}\text{NV}^-$ pair	No NV ⁻	$^{14}\text{NV}^-$
$^{15}\text{N}_2^+$ only	62 (40%)	1 (0.6%)	93 (60%)	0
co-implantation	100 (64%)	5 (3.2%)	51 (33%)	10

Each of 115 fluorescent spots in the CFM map of Fig. 1 (a) is identified by ODMR to be either ^{14}NV , or ^{15}NV , or $^{15}\text{NV}^-$ - $^{15}\text{NV}^-$ pair [Fig. 1 (b)]. The results are summarized in Table 1, together with those for implantation of N_2^+ ion only. Since the resolution of CFM is $\sim 0.3\text{ }\mu\text{m}$, the distances of $^{15}\text{NV}^-$ - $^{15}\text{NV}^-$ pairs have been obtained by DEER measurements of the dipole-dipole interactions (Fig.2). One of five pairs exhibits a strong dipole-dipole interaction (55 ± 1 kHz, the distance 13 nm) and both NV have long T_2 (0.65 ± 0.10 ms, 0.63 ± 0.10 ms, respectively, measured by Hahn echo decay). The high ratio (~ 70) between the coherence time and the expected gate time suggests that this pair is suitable for demonstrating high fidelity 2-qubit CNOT gate. It should be noted that co-implantation, novel annealing condition and high-quality ^{12}C -enriched SC substrate which enable high yield and long T_2 for implanted NV⁻ are crucial for fabricating the NV⁻ pair of excellent properties.

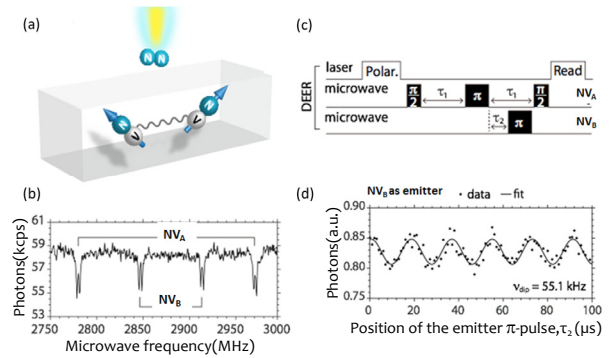


Fig. 2 (a) Schematics of fabrication of dipole-coupled NV⁻ pairs by molecular ion implantation. (b) ODMR of $^{15}\text{NV}_\text{A}$ - $^{15}\text{NV}_\text{B}$ pair. (c) Pulse sequence of DEER. In the Hahn echo of NV_A , the position of π pulse of NV_B is scanned. (d) The dipolar interaction has been measured to be 55 kHz.

This study was carried out as “Strategic Japanese-German Joint Research Project” supported by JST and DFG (FOR1482). Collaborators are T. Teraji (NIMS), C. Müller, L. P. McGuinness, B. Naydenov, F. Jelezko (University of Ulm) and J. Wrachtrup (University of Stuttgart).

1 - 13 Radiolytic Stabilities of Hydrophilic and Lipophilic Ligands for Mutual Separation of Am/Cm/Ln

Y. Sugo^{a,b)}, Y. Sasaki^{b)} and N. S. Ishioka^{a)}

^{a)}Medical and Biotechnological Application Division, QuBS, JAEA,

^{b)}Division of Chemistry for Nuclear Engineering, NSED, JAEA

1. Introduction

Mutual separation of americium (Am), curium (Cm), and lanthanides (Ln) is important to develop the partitioning process of high-level radioactive liquid waste (HLW), because the different disposal methods will be proposed¹⁾. The mutual separation of Am/Cm/Ln is quite difficult to establish due to their very similar chemical behavior, same oxidation state, and similar ionic radii.

We have developed various amidic ligands for the separation of Am and Cm from HLW, as shown in Fig. 1. These ligands can be easily synthesized by condensation of the corresponding carboxylic acid and dialkylamine, and tailored to have hydrophilicity and lipophilicity by using dialkylamine having short or long alkyl chains. Recently, a new technique using the combination of the hydrophilic and lipophilic ligands dissolved in aqueous and organic phases has been reported²⁻⁴⁾. This technique is very useful for the mutual separation of Am/Cm/Ln, due to the multiplier effect. In order to evaluate the applicability of the hydrophilic and lipophilic ligands to the partitioning process of HLW, it is essential to investigate radiolytic stabilities of these ligands.

2. Experimental

Several kinds of hydrophilic (C2: R=C₂H₅) and lipophilic (C6: R=n-C₆H₁₃, C8: R=n-C₈H₁₇, C12: R=n-C₁₂H₂₅) derivatives of diglycolamide (DGA), dioxaoctanediamide (DOODA), and nitrilotriacetamide (NTA) were synthesized and dissolved in water or *n*-dodecane. These aqueous and organic solutions were irradiated with ⁶⁰Co γ -rays at an absorbed dose rate of 5 kGy h⁻¹. The concentration of each ligand before and after irradiation was determined using a capillary gas chromatography equipped with a flame ionization detector.

3. Results and Discussion

In order to compare the radiolytic stabilities of the amidic ligands having different structure, the aqueous and organic solutions of DGA, DOODA, and NTA at concentration of 0.1 M were irradiated under the same condition. The decay curves of the concentration of each ligand dissolved in water and *n*-dodecane are illustrated in Figs. 2 and 3, respectively.

The slopes of the decay curves are approximately equal in each graph. It is suggested that the radiolytic stabilities are not correlated with the differences in the alkyl chain length at the amidic N and in the structure of the central framework.

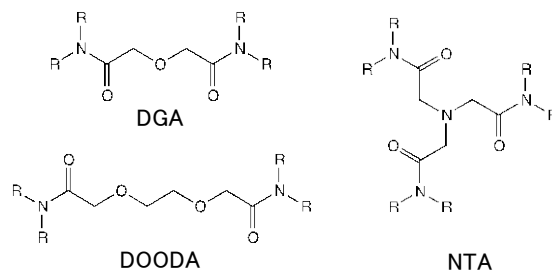


Fig. 1 The representative amidic ligands for the separation of minor actinides (R=alkyl).

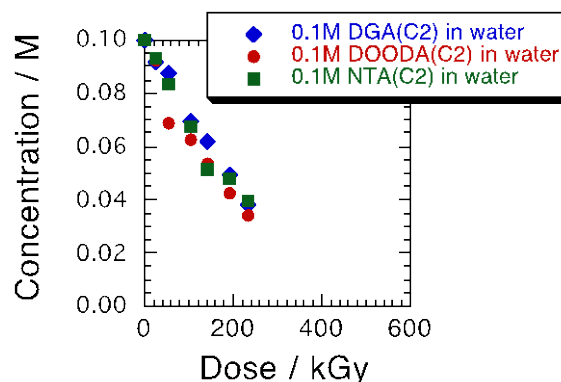


Fig. 2 Changes in concentrations of hydrophilic ligands dissolved in water by γ -irradiation.

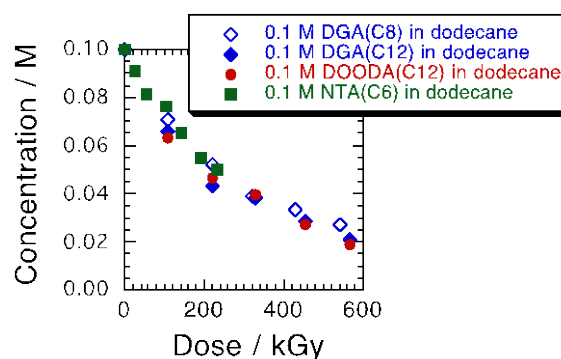


Fig. 3 Changes in concentrations of lipophilic ligands dissolved in *n*-dodecane by γ -irradiation.

References

- 1) "Actinide and Fission Product Partitioning and Transmutation", VI. General information, 2012 NEA Annu. Rep. (2012).
- 2) Y. Sasaki et al., Solv. Extr. Res. Dev. Jpn. 18 (2011) 93.
- 3) Y. Sasaki et al., Procedia Chem. 7 (2012) 380.
- 4) Y. Sasaki et al., Solv. Extr. Ion Exch. 31(2013)401.

1 - 14

Characterization of Composite Adsorbent for Minor Actinides by Micro-PIXE Method

Y. Takahatake^{a)}, M. Nakamura^{a)}, Y. Nakajima^{a)}, Y. Koma^{a)}, K. Sano^{b)}, T. Arai^{b)},
T. Satoh^{c)} and M. Koka^{c)}

^{a)}Department of Fukushima Technology Development, NFCEL, JAEA, ^{b)}Shibaura Institute of Technology, ^{c)}Department of Advanced Radiation Technology, TARRI, JAEA

JAEA has been developing the extraction chromatography technology for minor actinides (MA; Am and Cm) recovery from spent fast reactor fuels. The adsorbent consists of three materials; namely the adsorbent is prepared by impregnating an extractant into the support of porous silica particle coated with styrene-divinylbenzene polymer as a binder (referred as SiO₂-P). In some cases, recovery rate of the target metals was found to be insufficient, and it suggests that a part of the target metals was retained in the adsorbents. It is supposed that mobile phase diffuses slowly inside the adsorbent, and as a result of repeated adsorption/elution cycles the target metals were localized to lower their recovery rate. Analyzing metal distribution inside the particle will bring an insight to optimize the adsorbent structure for better separation. The Micro-PIXE analysis enables to detect some elements inside a particle, therefore applicability of the method to the silica-based particle was examined.

The support of the adsorbents is made of SiO₂, and it was afraid that characteristic X-ray of Si which would be dominant interferes detection of target metals, typically lanthanides. At first, the adsorbent that adsorbed neodymium as a stand-in of MA was examined in order to confirm feasibility of analysis. Next, several adsorbents prepared by adsorption/elution sequence were analyzed by Micro-PIXE at TIARA.

The extractant used was *N,N,N',N'*-tetra-*n*-octyl-diglycolamide (TODGA). The SiO₂-P is ca. 50 μm in its diameter. Degree of cross linkage of the polymer was 15% by controlling the ratio of divinylbenzene to styrene when polymerization, and amount of TODGA impregnated were 33.3 wt% of adsorbents. Neodymium was once absorbed from the neodymium nitrate solution ([Nd] = 10 mM, [H⁺] =

5 M) and eluted with the 0.01M nitric acid solution for varied time by batchwise procedure at room temperature. The particle was fixed on a polycarbonate film and irradiated with proton beam to obtain an image of 128×128. The count ratio of Nd/Si X-ray was calculated.

Figure 1 shows the image of TODGA/SiO₂-P adsorbent with neodymium. The peak of Si was remarkable at low energy region in the spectra obtained, and that of Nd was successfully discriminated from that of Si. It was confirmed that neodymium distribution on the adsorbent was uniform after batchwise adsorption.

Figure 2 shows the relationship the count ratio of Nd/Si as a function of elution time. Nd/Si ratio decreased with the increase of elution time, and this suggests that diffusion of metal complexed with TODGA is not fast and the adsorption structure would need some improvements. The ratios for each elution time were rather scattered especially for 60 minutes. Therefore it is considered that the internal micro structure of each adsorbent particle is not uniform, and this leads to one cause of low recovery rate. Fragmentations of adsorbents were included in the TODGA/SiO₂-P adsorbents as shown in Fig. 1, and the small fragmentations uphold comparatively less metallic cations. By removing such fragmentations, an improved chromatogram and better separation will be obtained.

The findings above show a certain applicability of Micro-PIXE analysis to the composite material; inorganic silica, heavy metals, and organic polymer, and the dispersion of Nd/Si count ratio will be further studied in order to establish the optimum structure of the adsorbent. Besides analysis for depth distribution inside the adsorbent will be pursued to confirm localization of metals.

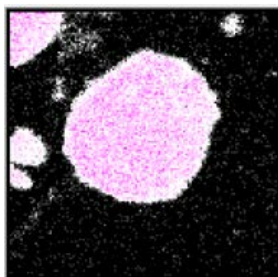


Fig. 1 The image of Micro-PIXE analysis for the TODGA/SiO₂-P adsorbent. Both width and height of the picture are 100 μm. White color shows silicon (principal matrix of the adsorbent), red color shows neodymium adsorbed by complexing with TODGA.

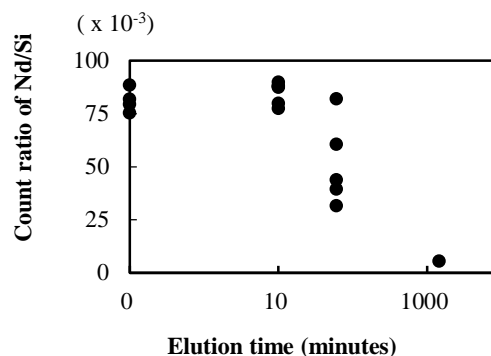


Fig. 2 The relationship count ratio of Nd/Si as a function of the elution time. Nd/Si ratio was calculated with Si and Nd counts obtained by Micro-PIXE analysis.

1 - 15 Radiolytic Stability of Metal Hexacyanoferrate as Adsorbent for Recovery of Cesium Ion

M. Arisaka^{a)}, M. Watanabe^{a)}, M. Ishizaki^{b)}, M. Kurihara^{b)}, R. Chen^{c)} and H. Tanaka^{c)}

^{a)}Division of Chemistry for Nuclear Engineering, NSED, JAEA, ^{b)}Department of Material and Biological Chemistry, Faculty of Science, Yamagata University, ^{c)}Nanosystem Research Institute, National Institute of Advanced Industrial Science and Technology

Introduction

In nuclear industry, one of the most important tasks is the management of high level radioactive wastes (HLW). It is expected, by removal of cesium (Cs) from HLWs, that the volume of vitrified wastes decrease because the amount of HLWs stuffed into vitrified wastes is limited by the decay heats of such nuclides as ¹³⁷Cs and ⁹⁰Sr from a viewpoint of safe disposal. In addition, the handling of HLWs would become easier because the bulk of radioactivity of HLWs comes from ¹³⁷Cs and ⁹⁰Sr for several hundred years after reprocessing of spent fuels.

Metal hexacyanoferrate, MHCF, is known as an adsorbent for selective adsorption of Cs ion in solutions. Applications of MHCF (M=Fe, Cu or Ni) to recovery of Cs from HLWs have been studied. Recently, we reported an electrochemical application of MHCF for Cs recovery from nitric acid (HNO₃) solutions^{1,2)}. It has been commonly accepted that the selectivity of MHCF to Cs ions are caused by regular lattice spaces surrounded by cyanide-bridged metals. However, the intrinsic mechanism of Cs ion adsorption still has not been made clear. So far, we have revealed that synthesized FeHCF, obtained as a charge-compensated salt (Fe^{III}₄[Fe^{II}(CN)₆]₃), has much higher Cs adsorption ability than that of commercially purchased FeHCF, i.e., prussian blue having ideal perfect lattice. The higher ability is attributed to the presence of lattice defect sites³⁾.

In this study, the influence of irradiation with gamma-rays to MHCF having lattice defect sites on Cs adsorption ability and stability in HNO₃ solutions was investigated for application of MHCF to practical Cs separation process.

Experimental

Irradiated sample is a mixture of MHCF and 1.0 M HNO₃ solution. MHCF used in this study is as follows; Fe^{III}₄[Fe^{II}(CN)₆]₃ (FeHCF), Cu^{II}₃[Fe^{III}(CN)₆]₂ (CuHCF), Ni^{II}₃[Fe^{III}(CN)₆]₂ (NiHCF).

Irradiation with gamma-rays was done at the Co-60 gamma ray irradiation facilities in Takasaki Advanced Radiation Research Institute of JAEA. Samples in glass tubes were intermittently irradiated with gamma-rays from 1.0 × 10¹⁶ Bq ⁶⁰Co source at an absorbed dose rate of 10 kGy h⁻¹ in air at room temperature for a maximum of 27 hours. A dose absorbed by each sample was corrected for an electron density. Absorbed doses were calibrated by a cellulose triacetate film dosimeter.

Results and Discussion

First, the adsorption experiment for Cs was performed using the irradiated MHCF as the adsorbent. The distribution coefficients of Cs onto MHCF were constant independent of the total absorbed dose. This indicates that the Cs adsorption ability of MHCF was maintained under the absorbed dose conditions (50-300 kGy).

Second, the radiolytic degradation of MHCF was evaluated by determination of the amount of M (=Fe, Cu, Ni) in HNO₃ solution, which is separated from the sample by filtration after gamma-ray irradiation. The result for CuHCF was shown in Fig. 1 as an example. It was found that the weight percent of Fe and Cu in the solutions to initial weight of CuHCF increased slightly with an increase of the total absorbed dose. The increase was attributed to radiolytic decomposition of CuHCF. Under the condition in this study, the weight percent of Fe and Cu in the solutions to initial weight of CuHCF was less than 0.05%.

From the viewpoint of usage for a long period, it suggests that the CuHCF is fully stable. Moreover, the composition of carbon, nitrogen and hydrogen in CuHCF is constant independent of the total absorbed dose.

Acknowledgement

Present study includes the result of "Compact and reusable cesium recovery system by electrochemical adsorption/desorption" entrusted to JAEA and AIST by Japan Science and Technology Agency (JST).

References

- 1) R. Chen et al., *Electrochem. Commun.*, **25**, (2012) 23.
- 2) R. Chen et al., *Electrochim. Acta*, **87**, (2013) 119.
- 3) M. Ishizaki et al., *Phys. Chem. Chem. Phys.*, **42**(2013)16049.

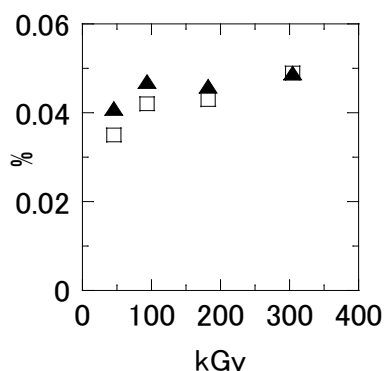


Fig. 1 Weight percent of Fe (filled triangle) and Cu (opened square) to initial weight of CuHCF in HNO₃ solutions after irradiation with gamma-rays.

1 - 16 Study on Durability of Strontium Adsorbents against Gamma Irradiation

Y. Itoh, Y. Saitoh and T. Terunuma

Tokai Reprocessing Technology Development Center, NFCEL, JAEA

Treatment of Low-level radioactive liquid wastes (LLW) generated from Tokai reprocessing plant are planned in low-level radioactive waste treatment facility (LWTF).

By treatment of co-precipitation and ultra-filtration in the LWTF, the LLW consist of highly concentrated sodium nitrate containing low level radioactive ^{137}Cs and ^{90}Sr . Subsequently, READ-Sr adsorbents, which made from sodium titanate and polyacrylonitrile (PAN), are used in the ^{90}Sr removal process. However, the READ-Sr adsorbents have some problems in the maximum adsorption capacity and irradiation durability.

In our previous study, the distribution coefficient ($K_{d,\text{Sr}}$) and maximum adsorption capacity (Q_{max}) of Sr^{2+} for A and X type of zeolites were investigated by batch adsorption experiment¹⁾. It was confirmed that $K_{d,\text{Sr}}$ onto the A type of zeolite (A51-JHP adsorbents) was nearly equal to the READ-Sr adsorbents and the A51-JHP adsorbents had large adsorption capacity comparing to the READ-Sr adsorbents.

In this study, durability of the A51-JHP adsorbents against gamma-ray irradiation were investigated and compared to the READ-Sr adsorbents.

Each A51-JHP and READ-Sr adsorbents were contacting with simulated LLW (5 M NaNO_3 solution) in a vial, and they were irradiated at room temperature with Co-60 gamma-rays at a dose rate of around 3 kGy/h. The maximum accumulated dose of each adsorbent was around 2.5 MGy. After the gamma irradiation, the adsorbents separated from the sodium nitrate solution and the supernatant were analyzed by ICP-AES. The $K_{d,\text{Sr}}$ and Q_{max} of Sr onto the irradiated adsorbents were also examined by the batch uptake experiment after washing and drying of the adsorbents.

As shown in Fig. 1, the $K_{d,\text{Sr}}$ and Q_{max} of Sr onto the READ-Sr adsorbents decreased with the increase of absorbed dose. After an irradiation of 2.5 MGy, the Q_{max} of Sr to that of non-irradiated one was decreased to be around 1/2. In the A51-JHP adsorbents, the $K_{d,\text{Sr}}$ and Q_{max} of Sr nearly kept constant even after irradiation. And also the Q_{max} of Sr was 0.65 mmol/g, the A51-JHP indicated large adsorption capacity comparing to the READ-Sr.

Figure 2 shows SEM images of the READ-Sr adsorbents before and after irradiation. The surface alteration such as cracking was clearly observed after irradiation of 0.3 MGy, and the PAN of the surface came off after irradiation of 2.5 MGy. Thus, it is considered that decrease of adsorption capability is due to degradation of PAN in the adsorbents by gamma radiation.

Therefore, it was confirmed that the A51-JHP adsorbents had large adsorption capacity and durability against gamma

irradiation comparing to the READ-Sr adsorbents.

Acknowledgements

We would like to thank Professor Dr. Hitoshi Mimura, Mr. Shunsuke Susa of Tohoku University and Mr. Ryohei Yamagata at Irradiation Service Section in TARRI for their advice and assistance on the experiment.

Reference

- 1) S. Susa et al., WM2013 Conf. 13127 (2013).

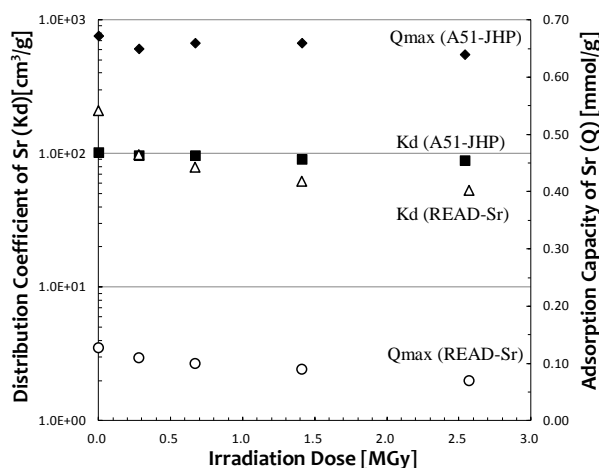


Fig. 1 Distribution coefficient and maximum adsorption capacity of Sr onto A51-JHP and READ-Sr adsorbents in 5 M NaNO_3 solution.

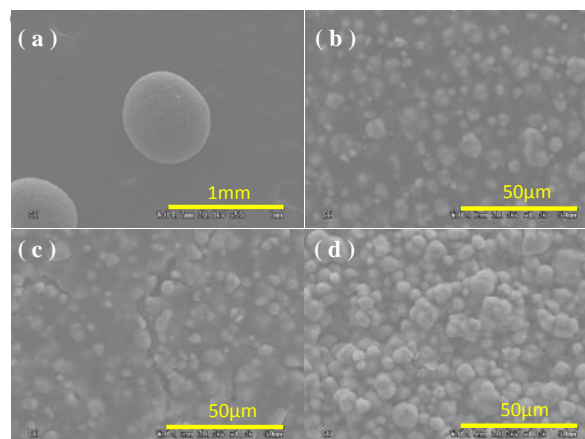


Fig. 2 SEM images of non-irradiated sample (a) of READ-Sr adsorbent, (b) was magnified image (1,000 times) of the sample (a), and magnified image after irradiation : 0.3 MGy (c), 2.5 MGy (d).

1 - 17 Effect of Gamma-ray Irradiation on De-oxygenation of Salt-containing Water by Hydrazine

T. Motooka, T. Sato and M. Yamamoto

Division of Fuels and Materials Engineering, NSED, JAEA

After the 2011 Tohoku Earthquake and Tsunami, the cooling systems at the Fukushima Daiichi nuclear power station failed. As an emergency measure, seawater was poured into the spent fuel pools to cool the spent fuels. In the current cooling system, oxygen from the air dissolves in pool water. To reduce the amount of dissolved oxygen (DO), after May 2011, Tokyo Electric Power Co. added hydrazine (N_2H_4) to inhibit the corrosion of the materials.

In thermal power plants, N_2H_4 is used as a deoxidant for high-temperature water, but it is known that the deoxygenation effect is weak for room temperature water. It has been reported that the gamma radiolysis products of N_2H_4 react with oxygen molecules, and the DO concentration in a sample of irradiated water is reduced as a result of N_2H_4 addition. However, these data were not obtained for salt-containing water, but for distilled water. The deoxygenation behavior of N_2H_4 for DO in salt-containing water is not known.

Therefore, in this study, the reaction of DO and N_2H_4 was studied in salt-containing water exposed to gamma-ray irradiation. A small amount of N_2H_4 was added to the salt-containing water, and the water was irradiated at room temperature. After irradiation, the reaction of DO and N_2H_4 was evaluated via quantitative analysis of both DO and N_2H_4 . Herein is presented a discussion of the effect of gamma-ray irradiation on the reaction of DO and N_2H_4 in salt-containing water.

The test solutions (distilled water, 1/8 artificial seawater, and artificial seawater with 32 ppm N_2H_4) were irradiated at dose rates of 0.1 to 10 kGy/h for 1 h. The concentration of

DO before and after irradiation is shown in Fig. 1. For comparison, the concentration of DO in samples allowed to sit for 1 h in the absence of gamma radiation (0 Gy/h) is also plotted. As can be seen in the figure, the concentration of DO in the non-irradiated samples was nearly the same as that in the samples before the tests. In contrast, the concentration of DO in the irradiated samples decreased markedly with increasing dose rate and was less than 1 ppm at dose rates above 1 kGy/h. Notably, at a dose rate of 0.1 kGy/h, the decrease in the DO concentration in the artificial seawater (ASW) was less than that in the distilled water and 1/8 ASW.

Samples of distilled water, 1/8 ASW, and ASW with 32 ppm N_2H_4 were irradiated at a dose rate of 1 kGy/h, and the change in the concentration of DO with time is plotted in Fig. 2. It can be seen in the figure that the DO concentration decreased with increasing irradiation time and was reduced to less than 1 ppm in 10 min for the distilled water and 1/8 ASW samples and in 30 min for the ASW sample. Deoxygenation using N_2H_4 was clearly slower in the ASW.

As shown in Fig. 2, the rate of decrease in the concentration of DO during gamma-ray irradiation was lower in the ASW than in the distilled water. This result suggests that the salts in the ASW affected the deoxygenation.

The deoxygenation of salt-containing water with N_2H_4 is suppressed by chloride ions.

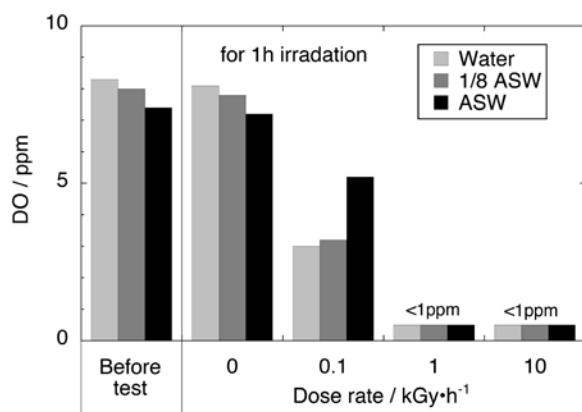


Fig. 1 Comparison of dissolved oxygen concentrations with and without irradiation at different dose rate for 1 h. Water, distilled water; ASW, artificial seawater; 1/8 ASW, distilled water/ASW = 1:7. Initial $[\text{N}_2\text{H}_4] = 32$ ppm.

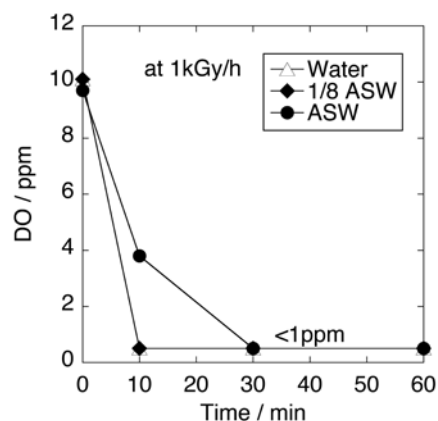


Fig. 2 Change in dissolved oxygen concentration with irradiation time at 1 kGy/h. Initial $[\text{N}_2\text{H}_4] = 32$ ppm.

1 - 18 Evaluation of Hydrogen Gas Generation from Cement Solidification Form by Gamma-ray Irradiation II

T. Nakayama, Y. Kawato, S. Suzuki and Y. Meguro

Nuclear Cycle Backend Technology Development Unit, NCBD, JAEA

Radioactive combustible wastes generated in Japan Atomic Energy Agency (JAEA) are incinerated and the ash obtained by incineration will be solidified with cement. After conditioning, the cement solidification forms which include radioactive waste will continuously generate hydrogen gas by radiolysis of water. Therefore amount of hydrogen gas generated from the waste form should be understood in order to evaluate the safety during its storage.

It is thought that the hydrogen gas generation is strongly influenced by the condition and amount of water in the form. In a previous study, the amount of hydrogen gas from a cement solidification form of incinerated ash was larger than that from a cement paste form without incinerated ash¹⁾. Much amount of water was needed for kneading of the incinerated ash with cement than for that of cement itself due to reactions of water with the ash, and then much free water remaining in the cement solidification form of incinerated ash would result in increase of the amount of hydrogen gas. In this study, influence of dose rate, ash filling rate, water cement ratio, amount of water-reducing admixture, and free water on the hydrogen gas generation was investigated by irradiation tests.

Incinerated ash of nonradioactive wastes, ordinary portland cement (OPC) and a high-range water-reducing admixture were employed to make several cement solidification forms and their composition are shown in Table 1. Sample No 10 was prepared by heating sample No 1 at 378 K for 24 h. The composition was expressed as "Ash filling rate / Water cement ratio - Water-reducing admixture ratio". The solidified sample was cut to a piece of ca. 8 mm wide, 8 mm long, and 40 mm high and was sealed in a 15 mm diameter quartz ampule. A cement paste sample using OPC (No 8) and a water sample (No 9) were also prepared. Irradiation tests were performed in Co-60 Gamma-ray Food Irradiation Facility No 1 cell, and the

samples were irradiated by ⁶⁰Co γ-rays at 5 Gy/h for 500 h. The No 1 type samples were irradiated at 5 Gy/h, 28 Gy/h, and 45 Gy/h, in which the absorbed dose was adjusted to be 2 kGy. The hydrogen gas in the ampule was determined by gas chromatography.

Results of irradiation test are summarized in Table 1. The amount of hydrogen gas is normalized into the value for 1 g of sample and 1 kGy of absorbed dose. Although the variability in the amount of hydrogen gas was large, remarkable relationship of the hydrogen gas amount to the ash filling rate (No 2, 3, 4), water cement ratio (No 3, 6, 7), amount of water-reducing admixture (No 1-1, 3, 5), and absorbed dose rate (No 1-1, -2, -3) was not observed. On the other hand, it found out that amount of hydrogen generation of the dried sample (No 10) decreased greatly.

Because the cement solidification form of incinerated ash and the cement paste form (No 8) differed in amount of water used for preparation, the amount of free water in the forms were determined, and G-values for the free water were calculated and compared with G-value of pure water (No 9). Here, the amount of free water was determined by weight change of the forms after heating at 378 K for 70 h. The free water ratio and G-value for the free water in sample were summarized in Table 1. The G-value of all cement solidification forms including dried one (No 10) shows almost same value. The G-value became large in the order of water, the cement paste, the solidification form. It suggests that cement has a property to promote hydrogen gas generation by radiolysis and moreover incinerated ash does.

Reference

- 1) T. Nakayama et al., JAEA Takasaki Annu. Rep 2011 (2013) 20.

Table 1 Conditions of samples for irradiation test and results of hydrogen gas yield and G-value.

Sample		Conditions					Results		
		Ash /wt%	Water / wt%	Cement / wt%	Water-reducing admixture / wt% *	Radiation does rate / Gy h ⁻¹	H2 yield / mL g ⁻¹ kGy ⁻¹	Free water ratio	G-value / molecule 100 eV ⁻¹
No 1-1	30/1.4-0	30	41	29	0	5	(7.3±0.0)×10 ⁻³	27.4	11
No 1-2	30/1.4-0	30	41	29	0	28	(6.2±1.5)×10 ⁻³	27.4	9.2
No 1-3	30/1.4-0	30	41	29	0	45	(5.0±0.4)×10 ⁻³	27.4	7.4
No 2	25/1.2-2	25	41	34	2	5	(5.4±0.0)×10 ⁻³	26.9	8.1
No 3	30/1.4-2	30	41	29	2	5	(8.6±0.5)×10 ⁻³	27.1	13
No 4	35/1.7-2	35	41	24	2	5	(6.9±1.1)×10 ⁻³	28.1	9.8
No 5	30/1.4-1	30	41	29	1	5	(6.7±3.5)×10 ⁻³	26.6	10
No 6	30/1.3-2	30	40	30	2	5	(5.8±0.6)×10 ⁻³	26.1	9.0
No 7	30/1.2-2	30	39	32	2	5	(5.7±1.5)×10 ⁻³	24.1	9.7
No 8	OPC paste	0	77	23	0	5	(1.5±0.6)×10 ⁻³	9.7	6.2
No 9	Water	0	100	0	0	5	(1.4±0.1)×10 ⁻³	100	0.54
No 10	30/1.4-0	30	41	29	0	5	(0.4±0.1)×10 ⁻³	2.1	8.5

* Water-reducing admixture was added to cement weight.

1 - 19 Studies of Irradiation Effects on Surface Structure of Zeolites after Decontamination of Radioactive Water

R. Nagaishi, K. Morita, S. Tashiro, R. Saito and I. Yamagishi

Fukushima Project Team, NSRI, JAEA

Radioactive water emitted in the Fukushima Dai-ichi NPS accident has been decontaminated by the adsorption¹⁾ and/or the coagulation sedimentation of radioactive nuclides, in which radioactive wastes of adsorbents and sludge after the decontamination are accumulated and stored inside the NPS until their disposal methods will be decided. Figure 1 shows estimated hydrogen (H_2) production rates (a) and total doses (b) absorbed in the Cs adsorption vessels as a function of time course after the accident. The H_2 production rates will decrease, while the doses will increase, leading to making the degradation of zeolites more serious. The degradation would affect the H_2 production, Cs retention state and thermal conduction inside the vessel²⁾. Thus we irradiated zeolites by using electron beams (EB) to study the irradiation effects on the surface structure of zeolites.

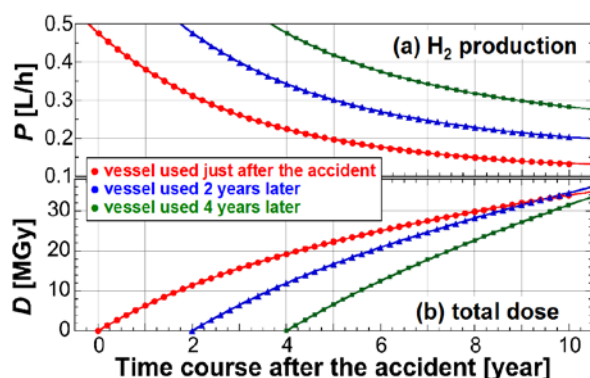


Fig. 1 Estimated hydrogen production rates (a) and total doses (b) absorbed in the Cs adsorption vessels (decay heat: 300W), depending on their decontamination time.

Two types of zeolites, which were examined to remove Cs from radioactive water¹⁾, were used: one mordenite (MOR) and two chabazites (CHA-1, CHA-2). The dried zeolites and wet ones immersed in pure water or seawater were prepared as irradiation samples. Each sample was put into a Ti-petri dish, covered with a Kapton film, and then irradiated vertically on water-cooling SUS plate, where the sample height was almost same as extrapolated range of EB in the sample. The incident energy of EB was set as 1.0 MeV, which is comparable to averaged energy of β -ray from Y-90, and the current was 1.0 mA. Temperature change in the sample during the irradiation was measured within 1.0 degree²⁾. After the irradiation, the sample was separated into aqueous solution and zeolites. The irradiated zeolites were washed with pure water, dried in vacuum at more than 597.15 K, and then applied to the surface analysis by gas adsorption. The adsorption gases (adsorbates) used in the analysis were nitrogen (measured at

77 K), argon (87.3 K) and water vapor (298.15 K).

The sample was irradiated at absorbed dose of 10 MGy. It means that the damp zeolite wastes have been kept in the adsorption vessel for about one year as shown in Fig. 1. Figure 2 shows adsorption behaviors of water vapor on three zeolites at 298.15 K, where relative pressure (P/P_0) in horizontal axes corresponds to relative humidity (RH). In Fig. 2(a), the rapid increases of adsorption at P/P_0 lower than 0.2 indicates that inside zeolites, micro pores with size smaller than 2 nm are well developed, and the gradual ones at P/P_0 of 0.2-0.9 means that the zeolites can hold 10-30 wt% of water in themselves at normal RH of 20-90 %.

The change of adsorption behavior by the irradiation can be seen in Fig. 2(b). Adsorbed water in the zeolites increased by the irradiation, especially at $P/P_0 < 0.2$. This suggests that the degradation of zeolites is originated from the inner damage of micro pore, and that in the damage, destruction of inner wall and invasion of water into new pores take place together with generation of finely divided powder. It can be noted that "pore volume" is a suitable parameter in the adsorption behavior rather than "surface area" when discussing the irradiation effects quantitatively.

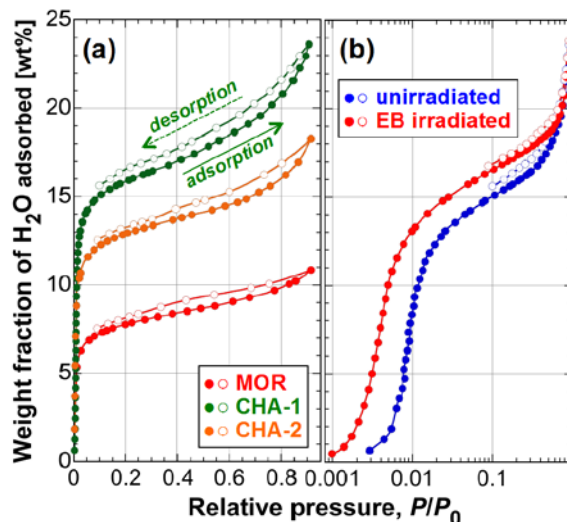


Fig. 2 Adsorption of water vapor on zeolites at 298.15 K. (a) isotherms of MOR, CHA-1 and CHA-2 before EB irradiation. (b) isotherms of CHA-1 after EB irradiation. Saturated pressure (P_0) of water vapor is 3.169 kPa at 298.15 K.

References

- 1) Database, "Contaminated liquid water treatment for Fukushima Dai-ichi NPS", Atom. Ener. Soc. Jpn. (2011).
- 2) R. Nagaishi, Biannu. J. Jpn. Soc. Radiat. Chem. 92 (2011) 15; R. Nagaishi et al., JAEA Takasaki Annu. Rep. 2011 (2013) 21.

1 - 20 Evaluation of Radiation Resistance of Activated Sludge Used for Nitrate Ion Decomposition

A. Nakagawa, T. Kogawara, T. Onizawa, K. Hanada, T. Nakayama and Y. Meguro

Nuclear Cycle Backend Technology Development Unit, NCBD, JAEA

Highly concentrated sodium nitrate liquid waste is generated from liquid waste processing, off-gas treatment and so on in the nuclear fuel reprocessing facility. Because nitrate compounds are hazardous materials, technology development for removal of nitrate from the waste prior to its disposal is important. Decomposition of nitrate ion is one of the nitrate removal methods, and so the authors have developed a biological nitrate ion decomposition method by using activated sludge¹⁾. In this development, it is considered that capability of the activated sludge on degradation of nitrate ion is influenced by radiation. In this study, gamma-ray irradiation test was conducted and gamma-ray resistance of activated sludge was evaluated.

Assuming that nitrate ion in an intermediate radioactive liquid waste generated from the reprocessing facility of Japan Atomic Energy Agency is decomposed using a cubic container of 5 m³, gamma-ray absorbed dose rate at the central part of container was calculated to be 0.1 Gy/h using ORNL Isotope Generation and Depletion Code (ORIGEN 2.1) and Point Kernel Code for Dose Equivalent (QAD-CGGP2). In this experiment, absorbed dose rates were set 1, 10, and 100 Gy/h from ⁶⁰Co source in the Food Irradiation Facility. Radiation resistance was confirmed on severer conditions than the calculated one. Irradiation time per day was 20 hours and accumulated time was 250 hours.

An experimental apparatus is shown in Fig. 1. The activated sludge was in a decomposition vessel, a sodium nitrate solution was fed to the decomposition vessel, and the processed liquid was transferred to a waste vessel through a membrane module separately from the sludge. The sodium nitrate solution was a mixture of a 0.42 mol/L sodium nitrate solution, a carbon source (0.34 mol/L acetic acid solution) and a nutrient (NH₄Cl and KH₂PO₄ solution). The liquid feed rate was 0.608 L/day and the amount of activated sludge was 1 L. In this condition, nitrate ion

decomposition rate was 3.5 kg-N/m³/day. The temperature of activated sludge in the decomposition vessel was maintained at 24-28 °C with a heater. The pH value in the vessel was measured and a sulfuric acid solution was added for making pH condition neutral when the pH increased by nitrate ion decomposition. Nitrogen gas was introduced to the decomposition vessel by a diffuser to make the activated sludge anaerobic condition. The processed liquid was sampled and the nitrate ion concentration was determined by ion chromatography.

The activated sludge was irradiated with gamma-ray in the course of decomposition of nitrate ion. Nitrate ion decomposition rate was defined as the percentage of the nitrate ion concentration in the sample to that in the decomposition vessel calculated from the sodium nitrate solution amount supplied. The decomposition rate to the absorbed dose in this irradiation test is shown in Fig. 2. In this figure, triangle, square and diamond were results of 1, 10 and 100 Gy/h tests, respectively. The decomposition rate was over 90% until 600 Gy independent of the absorbed dose rate. From this result, the activated sludge used in this experiment will be able to employed over 5,000 hours when the dose rate is the value estimated (0.1 Gy/h). In the irradiation test with 1 Gy/h, the variability of decomposition rate was large and the absorbed doses was much smaller than 600 Gy. Therefore, it is considered that more specific irradiation test in the low dose rate region is needed.

Acknowledgment

This work was funded by ANRE: Agency for Natural Resources and Energy, of METI: Ministry of Economy, Trade and Industry, of Japan at FY 2012.

Reference

- 1) K. Takahashi et al., JAEA-Technol. (2008) 084.

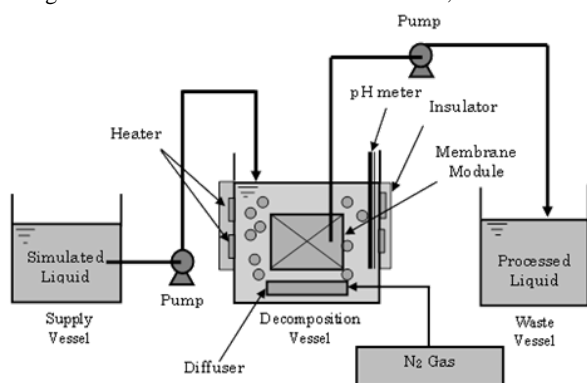


Fig. 1 Experimental apparatus of gamma-ray irradiation on activated sludge.

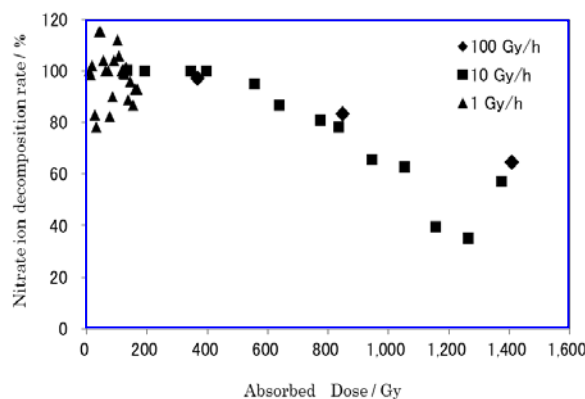


Fig. 2 Relationship between nitrate ion decomposition rate and accumulated absorbed dose.

1 - 21

Radiation Resistance Test of Insulation for Instrumentation Wire of JT-60SA Magnet

H. Murakami, A. Sukegawa and K. Yoshida

Tokamak System Technology Unit, FRDD, JAEA

The modifying of the JT-60U magnet system to the superconducting coils (JT-60SA) is progressing as a satellite facility for ITER by both parties of Japanese government (JA) and European Union (EU) in the Broader Approach agreement¹⁾. The superconducting magnet²⁾ is used for initiating and controlling plasma in JT-60SA. The insulation for instrumentation wire of fusion magnet withstands high voltage, cryogenic temperature and high dose such as 21 kV, 4 K, 20 kGy for the cryogenic magnet and 600 kGy for the room temperature (RT) magnet of JT-60SA.

The insulation material for an instrumentation wire withstands high dose more than 10 MGy can use Polyimide or PEEK (polyetheretherketone) insulation³⁾. They are very hard for handling instrumentation wires. On the other hand, the PTFE (polytetrafluoroethylene) for the insulator in instrumentation wires, which is common used for cryogenic devices because of good mechanical and electrical properties and easy handling, can withstand up to only 0.7 kGy.

The ETFE (ethylenetetrafluoroethylene) insulation is candidate material for instrumentation wire in cryogenic

usage. The ETFE insulation is similar mechanical and electrical properties of PTFE insulator. The ETFE insulated wire as shown in Fig. 1 was cool downed from RT to cryogenic temperature several times and after that the 21 kV high voltage test was conducted. The ETFE insulated wire can use in cryogenic temperature since the withstand voltage of cool downed ETFE wire was more than 21 kV.

The tensile test was performed using ETFE insulation samples irradiated up to 2 MGy at the Cobalt 60 irradiation facility in JAEA Takasaki Institute as a radiation resistance test. The test results are shown in Fig. 2. The acceptance criterion is more than 50 % of elongation. The test results show the elongation is more than 50 % until 1 MGy. The broken samples after tensile test are shown in Fig. 3. The color of 2 MGy radiated sample was changed to dark brown. These results indicate that the ETFE can use up to 1 MGy.

The irradiation test revealed that the ETFE insulated wire can be replaced with Polyimide or PEEK insulated wire for the cryogenic devices under the middle irradiation range condition (up to 1 MGy) including the JT-60SA magnet system.

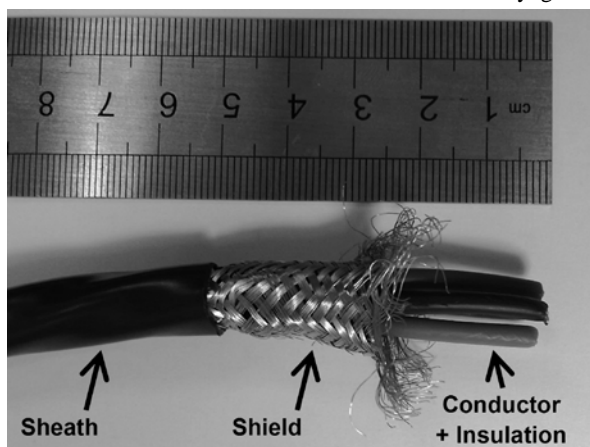


Fig. 1 ETFE insulated wire for high voltage sensor.

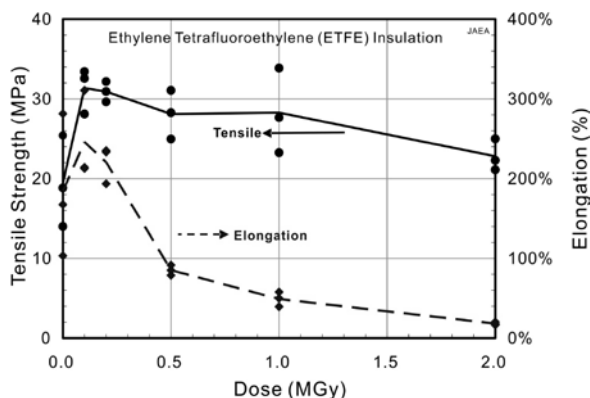


Fig. 2 Tensile test results under room temperature.

References

- 1) S. Ishida et al., Nucl. Fusion 51, (2011) 094018.
- 2) K. Yoshida et al., IEEE Trans. Appl. Superconduct. 22, 3 (2012) 4200304.
- 3) Center for Proton Accelerator Facilities Planning Group, JAERI-Data/Code 2003-015 (2003).

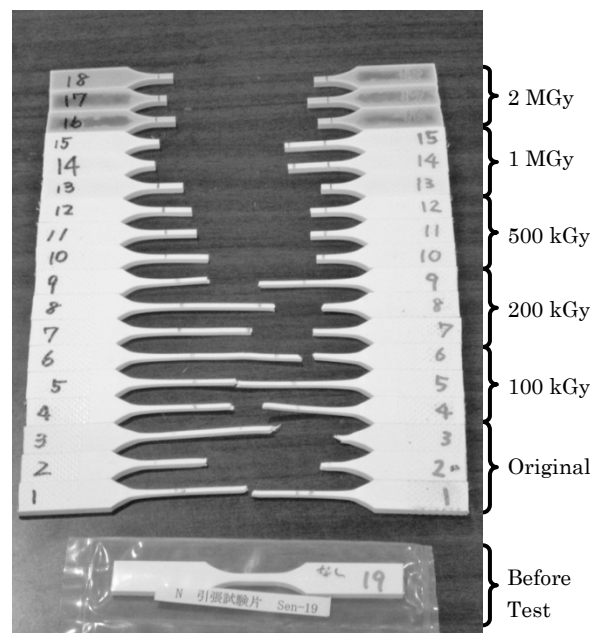


Fig. 3 Broken sample after tensile test.

1 - 22 Radiation Resistant Evaluation of Sealing Coat Using Super Quick Hardening Type Polyurethane and Polyurea

I. Funakawa^{a)}, M. Kito^{a)}, K. Horie^{a)}, K. Watanabe^{b)}, T. Numao^{c)}, Y. Saegusa^{d)}
T. Masuda^{e)}, K. Higashi^{e)}, K. Shidomi^{f)} and R. Yamagata^{f)}

^{a)}International Structure Maintenance Technology Association, ^{b)}Structures Technology Division, Railway Technical Research Institute, ^{c)}Department of Urban & Civil Engineering, Ibaraki University, ^{d)}JR Freight Real Estate Development, ^{e)}Dyflex Co. Ltd., ^{f)}Department of Advanced Radiation Technology, TARRI, JAEA

As for evaluating radiation tolerance as basic performance of the high-performance waterproofing mechanic by the need of safekeeping facilities of the waste including the radioactive material definitely, it is with an extremely important problem. Super quick hardening type polyurethane and the polyurea are adopted as the field of engineering works, the waterproofing materials in the field of building, water blocking material, a concrete protective material. In addition, it is applied to the large-scale waste disposal ground based on these results. The radiation resistance for these materials was evaluated under the gamma ray environment in this experiment. As a result, it was revealed that polyurea resin showed high radiation tolerance than polyurethane resin.

放射性物質を含む廃棄物の保管施設設置の必要性により、高性能な遮水・防水工の基本性能として、放射線耐性を正しく評価することは極めて重要な課題となる。ここで、ポリウレタン、ポリウレアは、その連続膜の形成と高い物理性能により土木、建築分野における防水材料、遮水材料として幅広く認知・採用されている。これらの実績をもとに大規模な廃棄物処分場への応用なども実用化されるに至っている。本報では合成高分子樹脂材料である超速硬化型ポリウレタン、ポリウレアについて、ガンマ(γ)線環境下における性能評価実験について報告する。

本研究における放射線照射は、高崎量子応用研究所コバルト 60 照射施設にて実施した。使用材料は、2 液反応硬化型 超速硬化ポリウレア樹脂(A)および 2 液反応硬化型 超速硬化ポリウレタン樹脂(B)とした。試験項目を Table 1 に示す。各種の合成高分子材料でシート形状に成形した試験体に Co-60 γ 線を空間線量率 10 kGy/h の照射条件で、約 1、3、5、7、10 MGy までの照射を行った。

照射後、試験体を取り出し、各種の物性試験を実施した。シート形状の試験体より引張試験の場合は、JIS K 6251 3 号型 ダンベルで打ち抜き、23 °C で引張速度 500 mm/min での引張強度、破断時の伸び率を測定した。また、引裂試験の場合は、JIS K 6252 切込みなしアングル形ダンベルで打ち抜き、23 °C で引張速度 500 mm/min での引裂強度を測定した。なお、試験体数は、それぞれ 3 本ずつとした。

引張強度および引張強度の保持率の比較を Fig. 1, 2 にそれぞれ示す。引張強度の保持率は、A では 1 MGy 時で 60%以上、3 MGy を過ぎると 50~60%程度で推移していた。B では、3 MGy 以降で 30%程度であった。伸び率および伸び率の保持率の比較を Fig. 3, 4 にそれぞれ示す。照射前においては B が A より伸び率は大きなものであるが、3 MGy の照射後では、同等の伸び率となっていた。また、伸び率の保持率は 5 MGy 時では A が高いものとなっている。

引裂強度の保持率は、A は 5 MGy において 60%程度、B は 35%程度まで低下していた。ヤング係数の保持率は、A、B ともに放射線による変化はさほどない。表面硬度の保持率は、A、B ともにほぼ一定であった。重量変化率の比較を Fig. 5 に示す。各材料とも放射線による重量減少が明らか

Table 1 Testing requirement and method.

Requirement	Method
(1) Tensile strength	JIS K 6251
(2) Elongation	JIS K 6251
(3) Tear strength	JIS K 6252
(4) Young's modulus	JIS K 6251 $E=\sigma/\epsilon$
(5) Surface hardness	JIS K 6253 Type D Durometer
(6) Weight variation rate	Rate of change of the weight before and after the irradiation

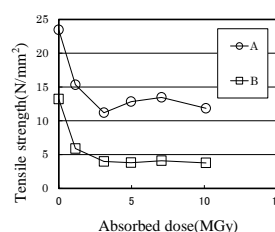


Fig. 1 Tensile strength.

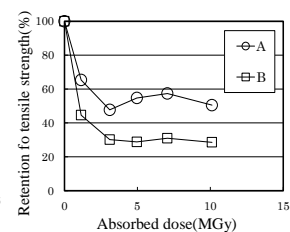


Fig. 2 Retention of tensile strength.

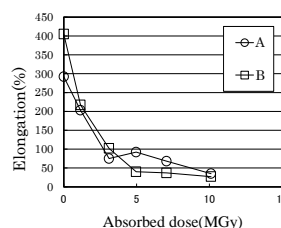


Fig. 3 Elongation.

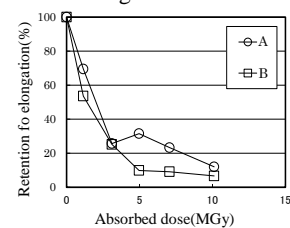


Fig. 4 Retention of elongation.

かであるが、B では 3 MGy において重量減少が進むのに対し、A では 5 MGy まで重量損失が起らない良好な結果となった。

以上より、ポリウレタン樹脂よりもポリウレア樹脂の方が、良い放射線耐性を示すことが明らかとなった。

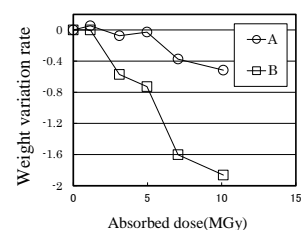


Fig. 5 Weight variation rate.

1 - 23 Study of Radiation Resistance of Optical Fibers for Remote Imaging and Spectroscopy

H. Naito^{a,b)}, C. Ito^{a,b)}, K. Imaizumi^{a)}, A. Nagai^{a)} and K. Tobita^{a)}

^{a)}Experimental Fast Reactor Department, ORDC, JAEA, ^{b)}Fukushima Project Team, ORDC, JAEA

A new probing technique is under development to inspect the damaged boiled water reactors (BWRs) of the Fukushima Daiichi Nuclear Power Station¹⁾. The nuclear fuel debris could be distributed from the reactor pressure vessel (RPV) to the primary containment vessel (PCV) in the meltdown nuclear reactor core of Fukushima Daiichi Nuclear Power Station. The probing system needs to be mounted on a remote-controlled robotic arm to insert into a pedestal in the PCV, which consists of a water-proof view scope, optics of laser induced breakdown spectroscopy (LIBS,) radiation resistant optical fibers, radiation detector, etc. The system is expected to apply to examination under high radiation dose environment such as 10^2 - 10^4 Sv/h. The radiation resistance of the optical fiber is improved by increasing the amount of up to 1,000 ppm hydroxyl in pure silica fibers²⁾ or by using infrared.

In order to evaluate the radiation resistance of optical fibers which contains 1,000 ppm hydroxyl in the pure silica core, we carried out the gamma-ray irradiation test under 5×10^3 Gy/h using a ^{60}Co source. The irradiation length of the tested fiber was about 10 m and the numbers of image fiber cores were 2,000. Both ends of the fiber were outside of the irradiation room and we measured the transmitted light power during irradiation by an optical spectrum analyzer and a halogen lamp. In addition, we took images of 1) visible light images using a color CCD camera and 2) infrared images using a monochromatic CCD camera with an infrared transmitting filter.

The wavelength spectrum is shown in Fig. 1 and the photographs are shown in Fig. 2. There is a large peak by the non-bridging oxygen hole center (NBOHC) and a peak tail of E' center, but is no large absorption in infrared region except an OH absorption peak of 945 nm. In visible light

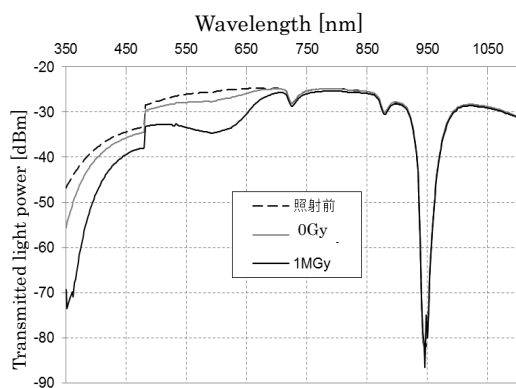


Fig. 1 Wavelength spectrum for transmitted light power of image fiber which contains 1,000 ppm hydroxyl in the pure silica core.

images, the image was darkened at 1.1×10^6 Gy. The edge of the image circle became darker than the center of image circle. In infrared images, the image was not changed between before irradiation and after irradiation. The infrared images were fuzzier than the visible images because the light leakage to the neighbor core was large in infrared region. The clad thickness of the tested fiber was about $3.6 \mu\text{m}$ and we found that it was needed to increase for an infrared imaging.

We have confirmed that the optical fiber which contains 1,000 ppm hydroxyl in the pure silica core had enough radiation resistance and the infrared imaging was effective for observation under high radiation doses. We progress the development of the probing system using this optical fiber and practical application for the observation in RPV/PCV.

References

- 1) C. Ito et al., Proc. Int. Conf. Laser Appl. Nucl. Eng. (LANE '13), LANE2-4, (2013) 12.
- 2) H. Naito et al., JAEA Takasaki Annu. Rep. 2010 (2012) 23.

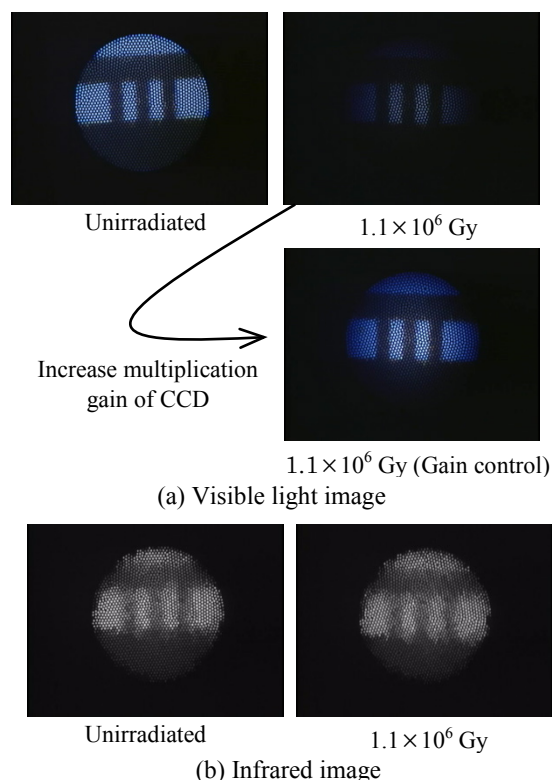


Fig. 2 Images of the zebra chart transmitted through the image fiber. The number of the image fiber cores is 2,000.

1 - 24

Study of Radiation-resistant LED Lighting

M. Kamikawa ^{a)}, K. Oka ^{b)}, R. Yamagata ^{c)} M. Kawasaki ^{a)} and K. Izumi ^{a)}^{a)} Kandenko Co., Ltd.,^{b)} Laser Application Technology Division, QuBS, JAEA,^{c)} Department of Advanced Radiation Technology, TARRI, JAEA

There are a lot of restrictions of electric installations in a high radiation environment. It is no exception about the lighting setup. In late years a long-lived LED light attracts attention. The gamma-ray irradiation examination of the LED lighting is not reported until now. This paper reports on examination of gamma-ray irradiation conditions for LED lighting. We aim at “Development of the Radiation-resistant LED lighting” for use in high radiation environment.

1. はじめに

加速器施設・核融合施設・原子炉施設・核燃料再処理施設等は、高放射線環境下となるエリアを有する。高放射線環境下では、多くの電気設備は寿命が著しく短くなる。照明器具も例外ではない。これまでに、高放射線環境に適用できる照明器具(HID タイプ)の開発 ¹⁾がなされている。一方、近年、長寿命である LED 照明は市場に多く取り入れられており、高放射線環境下での利用は大変重要である。

そこで本研究では、「耐放射線性 LED 照明」の開発を目標とし、本課題では、LED 照明に γ 線照射試験を行い、基礎データを測定した。

2. 光源の選定

試験体は、メーカ 3 社の既製品と既製品を独自に改良を施したものとした。光源の種類については、表面実装型(SMD: Surface Mount Device)と砲弾型を選定した。

3. γ 線照射試験

高崎量子応用研究所 Co-60 照射施設第 7 照射室内に試験体を設置し、 γ 線を照射した (Fig. 1 参照、線量率: 0.405~4.32 kGy/h)。また、試験体は、「点灯状態」と「消灯状態」のものとし、各試験体の電気的特性[照度・絶縁抵抗(抵抗)]について、初期状態からの変化値を確認した。

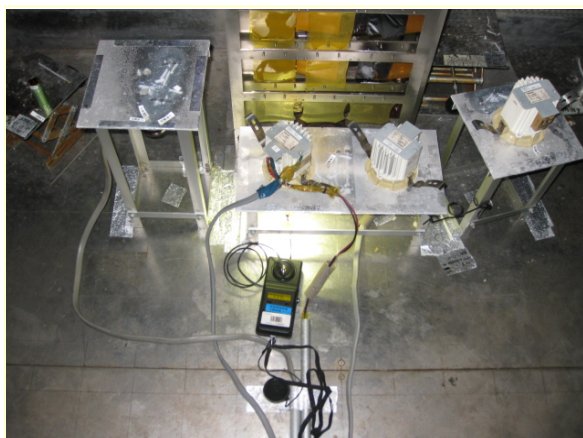


Fig. 1 The view of LED lighting irradiation.

4. 試験結果

LED 照明についての照射試験結果概要を、Table 1 に示す。この試験において、既製品の LED 照明器具(表面実装型)は、 γ 線吸収線量 206~830 Gy (数分~十数分間

程度)で点灯しなくなった。B 社製の砲弾型の光源は、 γ 線吸収線量 0.58 MGy で初期照度の 8%程度まで低下した。

また、点灯しなくなった器具について、そのまま γ 線照射を継続した結果、周辺材料及び、絶縁材料が著しく劣化していることを確認できた。

一方、独自に改良を施した LED 照明(表面実装型)は、 γ 線吸収線量 4.07 MGy において初期照度の 70%程度であったが、使用可能であることを確認できた。

Table 1 Result of gamma-ray irradiation damage of LED lightings.

Sample No.	Sample No.1	Sample No.2	Sample No.3	Sample No.4	Sample No.5	Sample No.6
Manufacturer	Company A	Company A	Company B	Company C	Company A	Company A
LED Type	SMD	SMD	Cannonball type	SMD	SMD	SMD
State of LED irradiating	Lighting	Lighting	Lights out	Lighting	Lighting	Lighting
Absorbed dose (Gy)	360 Gy	4.07 MGy	0.58 MGy	830 Gy	206 Gy	215 Gy
luminous flux maintenance rate (%)	Die down	70% Initial ratio	8% Initial ratio	Die down	Die down	Die down
Others	Ready-made	Remodeling	Ready-made	Ready-made	Ready-made	Ready-made

5. おわりに

本試験において、LED 照明の γ 線照射試験の基礎データを測定する事ができた。

今後は、今回測定した基礎データを基にして、より最適な絶縁材料を選定した上で、「耐放射線性 LED 照明」の試験を行い、 γ 線照射試験を実施する。

本研究が実証できれば、メンテナンス頻度の低減により、人体被曝の低減、放射性廃棄物の減容化に貢献できる。さらに放射線環境下への設置促進や、早期の福島復興支援にも寄与できるものと考ええる。

Reference

- 1) T. Tsuchida et al., JAEA Takasaki Annu. Rep. 2010 (2012) 27.

1 - 25

Creation of Database of Radiation Resistance on Polymer Materials and Equipment

A. Shimada, M. Sugimoto, A. Miyashita and M. Yoshikawa

Environment and Industrial Materials Research Division, QuBS, JAEA

Various materials and equipment are considered to be used for the operations of decommissioning of Tokyo Electric Power Company Fukushima Dai-ichi Nuclear Power Plants (1F). For the safety and reliable operation of decommissioning, it is important to examine the radiation resistance of materials and equipment used in severe radiation environments in 1F. In Japan Atomic Energy Agency (JAEA), the radiation resistance has been studied for various materials and equipment and a lot of knowledge of radiation resistance has been accumulated as reports, papers and so on.

In order to make use of the knowledge accumulated in JAEA, our research group has developed a database by the name of “Database of Radiation Resistance on Polymer Materials and Equipment (DRRPME)”, which is a useful tool specially designed for the reference to the knowledge of radiation resistance.

So much knowledge regarding radiation resistance of materials and equipment, which are used in J-PARC (Japan Proton Accelerator Research Complex), nuclear fusion reactors, nuclear power plants, γ -ray irradiation facilities, waste treatment facilities, nuclear fuel reprocessing plants and so on, are compiled in DRRPME. Specifically speaking, total of 878 data for radiation resistance of materials and equipment are collected, involving 423 data of polymer materials, 223 data of equipment and parts, 103 data of oils, fats and paint coatings and 129 data of organic composite materials, which are summarized from 33 JAEA reports, 38 scholarly papers, 30 congress materials and 9 other reports.

Figure 1 shows the console image of DRRPME produced in a personal computer. As seen in Fig. 1, there are five criteria menu such as broad category, narrow category, species of radiation, irradiation atmosphere and name of materials and equipment to narrow down to a candidate out of 878 data. By the combination of the five criteria, user of DRRPME can easily obtain the data of radiation resistance of materials and equipment as well as the information of references which the data is described in. In case of data described in JAEA reports, uniform resource locator (URL) is available for getting JAEA web site which shows the original report containing data of radiation resistance.

The program code of DRRPME is created by Microsoft Access 2010 and is easily operated on Microsoft Windows operation system. So the user can obtain the information of radiation resistance of materials and equipment even if the user is in the work site without connecting internet.

The procedure to obtain the software of DRRPME is different from between JAEA staffs and persons who do not

belong to JAEA. Although JAEA staffs can obtain from JAEA intra-net, the persons who do not belong to JAEA have to get DRRPME through “Research Organization for Information Science and Technology (RIST)”.

Such type of database program was not released yet, so we announced the contents of DRRPME in a press release on June 1, 2012. It is expected that DRRPME is a useful tool not only for the decommissioning of 1F for several decades but also for the selection and manufacture of materials and equipment for the general nuclear power plants and accelerator facilities.

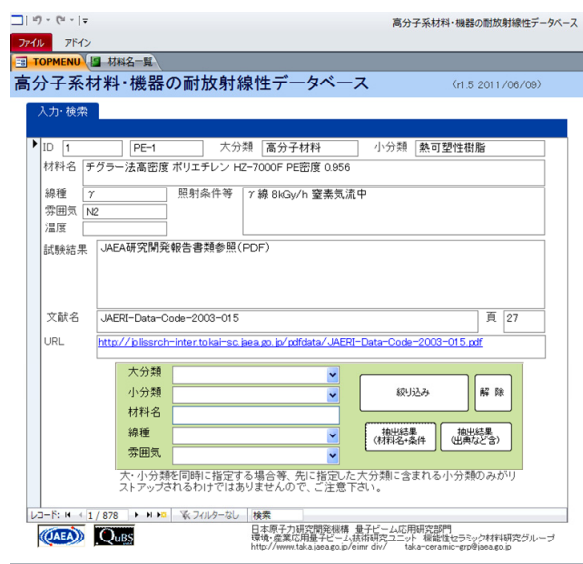


Fig. 1 Console image of DRRPME.

Five search criteria of this database

- Broad category (“daibun-rui”) : polymer materials equipments and parts, oils, fats and paint coatings, organic composite materials.
- Narrow category (“syoubun-rui”) : (for example, polymer materials) epoxy resins, elastomers, thermoplastics resins and so on.
- Species of radiation (“sensyu”) : γ -ray, electron beam, ion beam and so on.
- Atmosphere (“hun-iki”) : air, N_2 , O_2 and so on
- Name of materials and equipment (“zairyomei”) : input by keyboard.

URL for obtaining software of DRRPME

- JAEA staffs
<http://drpme.taka.jaea.go.jp/>
- Persons who do not belong to JAEA
<http://www.rist.or.jp/nucis/>

1 - 26 Evaluation of High-temperature Irradiation Resistance of ODS Ferritic Steel for Fast Reactor Application

S. Ohtsuka^{a)}, T. Tanno^{a)}, N. Ohkubo^{b)}, S. Jitsukawa^{b)}, S. Yamashita^{a)},
Y. Yano^{a)}, T. Kaito^{a)} and T. Sawai^{c)}

^{a)}Fast Reactor Fuels and Materials Technology Development Unit, ANSRD, JAEA, ^{b)}Division of Fuels and Materials Engineering, NSED, JAEA, ^{c)}Advanced Science Research Center, JAEA

Research and development (R&D) of fast breeder reactor (FBR) cycle system have been internationally carried out. This system can remarkably increase the efficiency of uranium utilization, which produces huge amount of energy with little CO₂ emission. It is also beneficial to reduce the volume and activity of radioactive nuclear waste. In the R&D of FBR cycle system, development of long-life fuel cladding tube is a critical issue for enhancing the reactor performance (safety and economical performance), and the transmutation efficiency of minor actinide. Japan Atomic Energy Agency (JAEA) has been developing oxide dispersion strengthened (ODS) steels as a primary candidate of the long-life fuel cladding tube. The FBR fuel cladding tube will be exposed to the high-temperature up to 700 °C and high-dose neutron irradiation up to 250 dpa in normal operation condition. In the off-normal events, the cladding temperature up to 830 °C is permitted. Thus, evaluating the irradiation response of ODS steel at high-temperature is very important. The authors had carried out the neutron irradiation test of ODS ferritic steel cladding tube to neutron dose of 50 dpa at irradiation temperature of 400- 830 °C using JOYO¹⁾ and BOR-60²⁾. Since it takes long time to derive the high dose neutron irradiation data, the simulation irradiation technique using ion-accelerator is effective to evaluate the radiation tolerance of nuclear materials. This study uses the heavy ion beam, Fe-ion beam, for producing cascade damage. The irradiation test results using ion-beam and neutron of ODS ferritic steel reported so far are summarized in Table 1. Though irradiation data are not plentiful, the ODS ferritic steels developed by JAEA, JAEA-ODS, have been reported to have good microstructure stability. However, there are some reports indicating the irradiation-induced instability of dispersed oxide particles in the steels other than JAEA-ODS. This study carries out the simulation irradiation using Fe-ion beam to evaluate the high-dose irradiation response of JAEA-ODS, especially stability of nano-sized oxide particle, in FBR high burn-up core condition.

Irradiation temperatures were 400 °C and 700 °C, which are the operation temperatures at the bottom and top of fuel column, respectively in normal operation. The specimens were irradiated with Fe⁺³ ion (self-ion) beams at TIAAR. The ODS steels used for the irradiation tests are JAEA-9Cr and 11Cr-ODS steels, whose chemical compositions are Fe-9wt%Cr-0.13C-2W-0.2Ti-0.35Y₂O₃ and Fe-11wt%Cr-0.13C-1.4W-0.4Ni-0.2Ti-0.35Y₂O₃, respectively. For each steel, two types of heat treatments were adopted: normalizing-and-tempering (NT; 1,050 °C × 1 h, AC => 800 °C × 1 h, AC), and furnace-cooling (FC; 1,050 °C × 1 h => furnace-cooling at 30 °C/h). The normalizing-and-tempering produces the duplex matrix constituting of

tempered martensite and residual-α ferrite, which is favored in terms of irradiation resistance. The furnace cooling produces the constitution of transformed-α ferrite and residual-α ferrite, which is advantageous to ductility. Traditional 11Cr heat-resistant steel, PNC-FMS, was also irradiated as a reference material. To date, Fe-ion irradiations up to 60 dpa were completed at 400 °C and 80 dpa at 700 °C, on the five types of specimens described above. The nano-indentation tests were carried out for the NTed 9Cr-ODS steel and the NTed 11Cr-ODS steel, both of which were irradiated to 60 dpa at 400 °C. The test results indicated that both specimens have the irradiation hardening with the increasing rate of approximately 20%. Hereafter, the tests for the rest of irradiated steels will be completed. Transmission electron microscope (TEM) observation will be carried out on the specimens appropriately chosen on the basis of the nano-indentation test results, thus characterizing the radiation damage microstructure. The ion-irradiation tests will be continued until the displacement damage reaches 250 dpa to systematically study the effects of chemical composition, especially Cr concentration, and type of matrix structure on microstructure stability under high-dose irradiation of ODS steel cladding tube.

References

- 1) S. Yamashita, Y. Yano, S. Ohtsuka, et al, J. Nucl. Mater. doi: <http://dx.doi.org/10.1016/j.jnucmat.2013.04.051>.
- 2) T. Kaito, Y. Yano, S. Ohtsuka et al, J. Nucl. Sci. Technol. 50 (4) (2013) 387-99.
- 3) T. R. Allen et al, J. Nucl. Mater. 375 (2008) 26-37.
- 4) S. Yamashita et al., J. Nucl. Mater. 367-370 (2007) 202-07.
- 5) I. Monnet et al, J. Nucl. Mater. 335 (2004) 311-21.

Table 1 Previously-carried-out test results on the stability of oxide particles under irradiation^{1,3-5)}.

Alloy	Irradiation particles	Temp. (°C)	Dose (dpa)	Stability of nano-sized oxide particles	Ref.
JAEA-ODS (9/12Cr-ODS)	Neutron	410~830	15~30	Stable	1)
JAEA-ODS (9Cr-ODS)	Ni-ion	500~700	150	Increase in number density	3)
INCO MA957 (14Cr-ODS)	Neutron	500~700	100	Decrease in number density	4)
DT2203Y05 (13Cr-ODS)	Neutron	400~580	30~80	Disappearance of fine oxide particles	5)
EM10-Y ₂ O ₃ (9Cr-ODS)	Ar-ion	400	30	Slight decrease in size	5)
	Electron	400		decrease in size	
EM10-MgO (9Cr-ODS)	Ar-ion	400	30	Slight decrease in size	5)
	Electron	400		decrease in size	

1 - 27

Irradiation Hardening Behavior of SUS316L and F82H Steels in Heavy Irradiation Fields up to 250 dpa

N. Okubo^{a)}, N. Ishikawa^{a)} and S. Ohnuki^{b)}

^{a)}Division of Fuels and Materials Engineering, NSED, JAEA,

^{b)}Faculty of Engineering, Hokkaido University

Austenitic stainless steels SUS316L and reduced activated ferritic steels F82H were irradiated at considerably high damage level up to 250 dpa at irradiation temperature of 300 °C by means of self-ion irradiation. The hardening behavior of the irradiated SUS316L steels indicated that the hardness was saturated at about 50 dpa and was kept constant at higher dose of irradiation. In the case of F82H, however, no saturation of hardening behavior was observed under irradiation at considerably high fluence of 250 dpa.

In future commercial fusion system and ADS target components, the structural materials will be heavily irradiated under severe conditions, where displacement damage, high concentration of He and H atom accumulations will simultaneously occur by high energy neutron irradiations. Degradation of mechanical properties after irradiation should be suppressed within a range permissible for reactor design. High fluence neutron irradiation experiments over a few hundred dpa are practically difficult due to long time irradiation and high cost. Ion irradiation experiments are powerful techniques for high fluence irradiation, but only a few papers about swelling¹⁾ have been reported so far.

In this report, we address irradiation hardening of SUS316L and F82H steels in the case of self-ion irradiation without simultaneous irradiation of helium and/or hydrogen in order to assess only the effect of displacement damage at considerably high levels.

At TIARA, ion irradiation of 10 MeV-Fe³⁺ to the SUS316L (solution annealed) and F82H (IEA Heat) was conducted at 300 °C in order to investigate the irradiation-hardening behavior up to 250 dpa. The irradiation rate was 1.2×10^{-3} dpa/s. After the irradiation, the micro-hardness was measured by using nanoindentation technique. To suppress the variation of surface morphology and original hardness among the specimens, the identical specimen was irradiated for SUS316L and F82H after intermittent hardness measurements over 100 dpa.

Dependence of irradiation hardening on the displacement damage to SUS316L and F82H is shown in Fig. 1. In the case of SUS316L, the irradiation hardening increased gradually as increasing the damage up to 50 dpa. The slope appeared to be decreasing around 50 dpa and subsequently saturating. The value of power obtained from the log-log plots of ΔH_v vs. dpa data was about 0.02 for SUS316L. In the case of F82H, however, no saturation of hardening behavior was observed under irradiation at considerably high fluence of 250 dpa. In future, it is necessary to observe the microstructures with TEM to answer what the difference between SUS316L and F82H is.

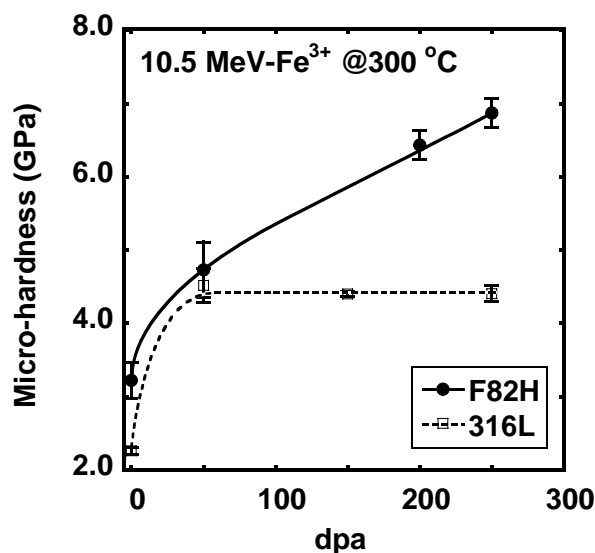


Fig. 1 Dependence of irradiation hardening on displacement damage in F82H.

Reference

- 1) F. A. Garner et al., Book of abst. 2nd joint IAEA-EC meeting, 2012.

1 - 28 Radiation-induced Hardening for SUS316L with Bending Deformation

N. Ishikawa, N. Okubo and K. Kondo

Division of Fuels and Materials Engineering, NSED, JAEA

Irradiation assisted stress corrosion cracking (IASCC) is one of the important phenomena that are found in in-core components in light water reactor. In spite of extensive studies over a long period of time it is not yet fully understood. One of the keys to solve the problem is to understand the effect of welding. It should be noted that the phenomenon is often found at welded zones, where strong stress may affect the irradiation behaviour. In this study, the effect of stress on irradiation-induced hardening is investigated.

An austenitic stainless steel (SUS316L) specimen with bending and that without bending were simultaneously irradiated with 12 MeV Ni^{3+} ions at 330 °C. The configuration of the sample holder was shown in the previous annual report ¹⁾. Specimen holder for the specimen with bending deformation is such that the curvature radius is 12.5 mm to give about 2% plastic strain into a 0.5 mm thick specimen. Half of the specimen was masked with aluminum foils during the irradiation, so that hardness for unirradiated area and that for irradiated area can be easily compared without influenced by a possible difference of specimen conditions. After the irradiation, the micro-hardness was measured by using nanoindenter (ENT-1100a, ELIONIX) for both irradiated area and unirradiated area of the specimen. The hardness was measured by fixing the indentation depth of 0.3 μm , which is much smaller than the projected range of the ion (3.2 μm).

As shown in Fig. 1 the increase in hardness was found for irradiations to 2 and 15 dpa. The hardness of the specimen without bending does not depend on the lateral position of the specimen, indicating that the hardness does not depend on the position of the specimen, but depends on the irradiation-induced defect density. However, the data for the bended specimens show that the hardness depend on the position of the measurement. Since the specimen is bended, it is suspected that the load was not applied perpendicular to the surface of the specimen. This may make inappropriate loading condition of the indenter. The only position where the appropriate indentation condition is satisfied is the boundary of the unirradiated and irradiated area, where the load was applied perpendicular to the surface. Therefore, it is concluded that the effect of irradiation-induced hardness change is not affected by bending with 2% plastic strain. (Here, only the data near the boundary are compared.) The data appeared in Ref. 1) was

measured only for the position approximately 2 mm distant from the boundary. Therefore, the difference in the hardness due to bending during the irradiation found in Ref. 1) was not due to bending itself but due to inappropriate measurement condition.

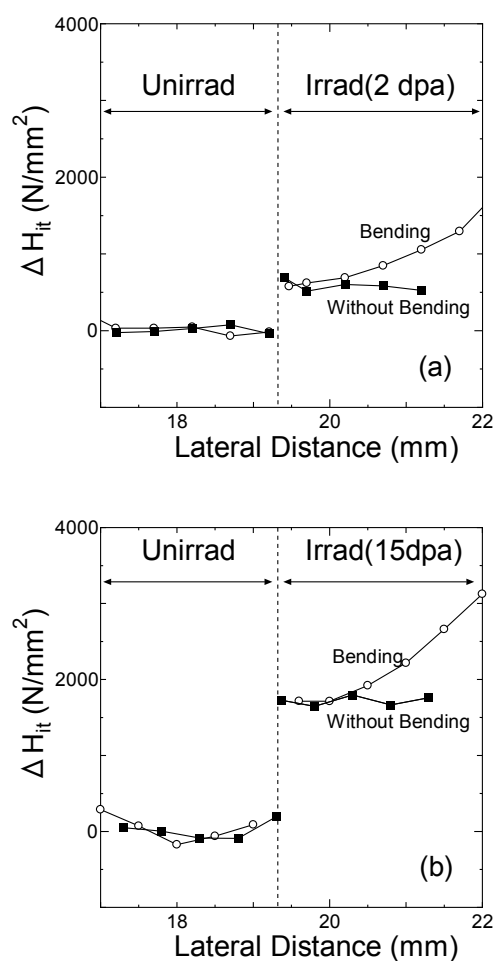


Fig. 1 Change in hardness for unirradiated area and for irradiated area. The data for the specimen with bending and those for the specimen without bending are shown in the same figure.

Reference

- 1) N. Ishikawa et al., JAEA Takasaki Annu. Rep. 2011 (2013) 25.

1 - 29 Irradiation Hardening of Extra High Purity Ni-base Superalloy under External Stress

I. Ioka^{a)}, G. H. Kim^{b)} and T. Inoue^{c)}

^{a)}Division of Fuels and Materials Engineering, NSED, JAEA, ^{b)}Tokamak Eng. Dept., National Fusion Res. Inst., ITER Korea, ^{c)}Fast Reactor Fuels and Materials Technology Development Unit, ANSRD, JAEA

An extra high purity (EHP) Ni-base superalloy has been developed as MA doped MOX fuel claddings for sodium cooled fast reactors. In EHP alloys, impurities, such as C, O, N, P and S were reduced to less than 100 ppm in total to improve workability, irradiation embrittlement and intergranular corrosion resistance. The cladding materials suffer from stress (external pressure, thermal stress) under the operation. There have been many irradiation experiments done under external stress to investigate stress effects on microstructural evolution of 300 series austenitic stainless steels. It is reported that the total nucleation rate of Frank loops increased with increasing external stress¹⁾. However, there are few studies on the effect of external stress on microstructural evolution of Ni-base superalloy under irradiation. The purpose of this study is to evaluate the effect of external stress on irradiation hardening of EHP Ni-base superalloy.

The material used in this study was W-rich silicide phase strengthened EHP Ni-base alloy, so called EHP(WSi) alloy. The EHP(WSi) alloy was manufactured by the multiple refined melting process. The ingot was solution-treated at 1,498 K for 1 h and then aged at 1,123 K for 24 h. The chemical composition of the alloy is given in Table 1. The materials were cut to small coupon type specimens ($20 \times 5 \times 0.5$ mm³). Specimens were plastically deformed by mean of a special bending holder during the irradiation as shown in Fig. 1. Tensile strain on the surface of bent specimens was calculated to be about 2%, so that the initial stress was over 0.2% offset stress level. Both deformed and undeformed specimens were simultaneously irradiated using the holder. Irradiation was performed under triple ($\text{Ni}^{3+} + \text{He}^+ + \text{H}^+$) ion beams at 673 K in the TIARA facility at JAEA. Ions of 12 MeV Ni^{3+} , 1.05 MeV He^{2+} and 380 keV H^+ were injected to simulate a FaCT core irradiation environment. The peak depth of displacement damage was calculated to be 2 μm by SRIM-2000. The mean displacement damage at depth of 1.5 μm was changed from 1 to 27 dpa. The injection rates for He and H were 1 appmHe/dpa and 15 appmH/dpa, respectively. The surface temperature of the both specimens was measured by two-dimensional infrared pyrometer and kept to be constant under irradiation. The microhardness was measured by using a nanoindenter. The hardening behaviour of the irradiated specimens was evaluated by indentation depth of

400 nm in consideration of the damage depth. The microhardness was calculated from mean values of 10 points per each specimen.

The dependence of microhardness on the irradiation damage was evaluated for EHP(WSi) alloy with and without bending deformation. Figure 2 shows the change in irradiation hardening at 823 K as a function of dose. In both of deformed and undeformed specimens, the microhardness increased immediately up to 5 dpa and was saturated around 10 dpa. Although variation of data was large, the difference in the microhardness change of both specimens was small. Therefore, there is no effect of external stress on microhardness of EHP(WSi) alloy in this study. However, the microhardness of deformed specimens was slightly higher than that of undeformed ones from initial condition at 673 K²⁾. The difference may be caused by the stress relaxation at 823 K. The residual stress of deformed specimens before and after the irradiation will be measured to examine the stress relief.

References

- 1) H. Tanigawa et al., Nucl. Instrum. Meth. Phys. Res. B 102 (1995) 151.
- 2) I. Ioka et al., JAEA Takasaki Annu. Rep. 2011 (2013) 26.

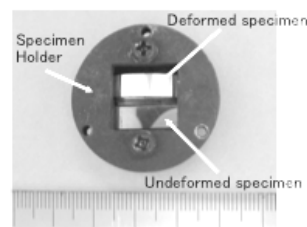


Fig. 1 Special bending holder for ion irradiation.

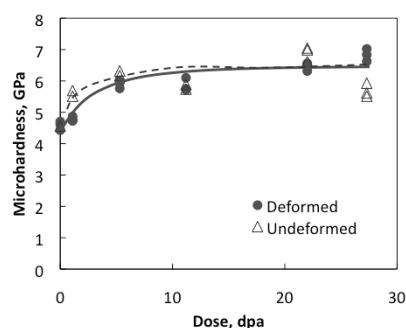


Fig. 2 Dependence of microhardness on irradiation damage at 823K for EHP(WSi) alloy.

Table 1 Chemical composition of EHP(WSi) alloy (wt%).

Fe	Ni	Cr	W	Si	C	P	S	O	N
bal.	42.8	25.35	10.24	2.75	0.004	0.0005	<0.0005	<0.0005	0.0006

1 - 30 Irradiation Hardening of G-Phase Strengthened Ni-base Alloy under Multi-ion Irradiation

N. Okubo^{a)}, I. Ioka^{a)}, G. H. Kim^{b)} and T. Inoue^{c)}

^{a)}Division of Fuels and Materials Engineering, NSED, JAEA,

^{b)}Tokamak Engineering Department, National Fusion Research Institute, ITER Korea,

^{c)}Fast Reactor Fuels and Materials Technology Development Unit, ANSRD, JAEA

1. Introduction

Precipitation-strengthened Ni-base alloys have been considered for fuel cladding in advanced reactors. Because these alloys have not only excellent properties at high temperature, but also very good performance with respect to swelling and creep resistance during irradiation. The main factor of high temperature strength in these alloys is the formation of ordered phase γ' [$\text{Ni}_3(\text{Ti}, \text{Al})$] or γ'/γ'' [Ni_3Nb] in the matrix¹⁾. However, many studies reported that these alloys exhibited the significant ductility loss due to irradiation at high temperature¹⁻³⁾. The reasons of poor ductility were believed to be the re-distribution of ordered phase γ' and solute segregation during irradiation at defect sink sites, such as grain boundary, void surface and dislocation.

From this viewpoint, we have developed an alternative Ni-base alloy strengthened by W-rich silicide (G phase), which has a good stability at high temperature. The aim of this work is to evaluate the ductility of the G phase strengthened Ni-base alloy irradiated at various temperatures. The ductility is evaluated from microhardness of ion-irradiated material. The microhardness of G phase strengthened Ni-base alloy is compared with that of ordered phase γ' in Nimonic PE16, which is a representative commercial alloy of precipitation-strengthened Ni-base alloys.

2. Experimental

G phase strengthened Ni-base alloy (Fe-43Ni-25Cr-10W-2.7Si) under extra high purity grade so-called EHP(WSi) alloy was used for the ion-beam irradiation experiments. To estimate irradiation hardening, ion-irradiation were performed at TIARA under triple ($\text{Ni}^{3+} + \text{He}^+ + \text{H}^+$) ion beams at 100 dpa and at temperatures ranging from 773 K to 973 K, which was the range of operation temperature for cladding material of JSFR. Twelve MeV Ni^{3+} was injected to produce radiation damage and ions of 1.05 MeV He^{2+} and 380 keV H^+ were implanted through Al degrader foils to simulate a FaCT core irradiation environment. The peak depth of displacement damage was calculated to be 2 μm by SRIM-2000. The mean displacement damage at depth of 1.5 μm was selected to be 100 dpa. The injection rates for He and H were 1 appm/dpa and 15 appm/dpa, respectively.

The surface temperature of the specimens was measured by two-dimensional infrared pyrometer and kept to be constant under irradiation. The microhardness was measured by using a nanoindenter. The hardening behaviour of the

irradiated specimens was evaluated by indentation depth of 400 nm in consideration of the damage depth.

3. Results and discussion

The dependence of microhardness on irradiation temperature was evaluated for EHP(WSi) and Nimonic PE16. The change in microhardness is shown in Fig. 1. In both specimens, the microhardness decreased with the increase of irradiation temperature, except the data of Nimonic PE16 at 973 K. It seems that the decrease in microhardness is attributed to thermal recovery of irradiation defects. For the increase of microhardness of Nimonic PE16 at 973 K, the authors reported that the general features of microstructure were γ' coarsening and γ' precipitation on dislocations, void surfaces and grain boundaries from TEM observation of irradiated specimen at 973 K⁴⁾. It is considered that the reason of the increase may be re-precipitation of γ' on dislocations, void surfaces and grain boundaries. The detailed microstructural evaluation with TEM is essential issue for interpreting the increase.

References

- 1) W. J. S. Yang et al., J. Nucl. Mater. 132 (1985) 249.
- 2) W. J. S. Yang, J. Nucl. Mater. 108&109 (1982) 339.
- 3) D. J. Mazey et al., J. Nucl. Mater. 160 (1988) 153.
- 4) G. H. Kim et al., JAEA Takasaki Annu. Rep. 2011 (2013) 27.

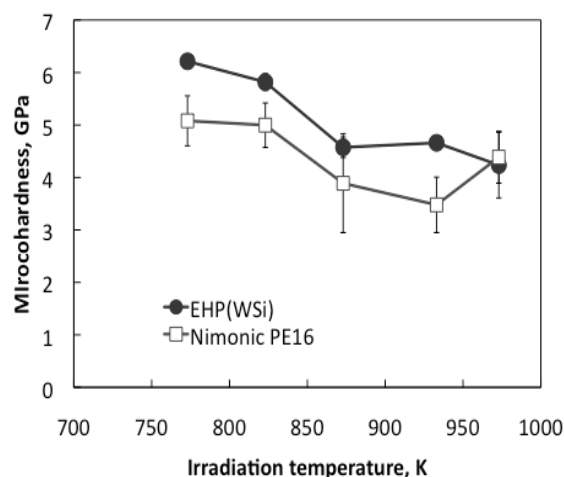


Fig. 1 Change in microhardness of Nimonic PE16 and EHP(WSi) irradiated at 100 dpa as a function of irradiation temperature.

1 - 31

Precipitate Stability and Swelling Resistance of High-Nickel Alloy during Irradiation

S. Yamashita^{a,b)}, T. Inoue^{a,c)}, Y. Sekio^{c)}, T. Hayashi^{c)}, I. Yamagata^{a,c)},
T. Yoshitake^{a,c)} and T. Kaito^{a,c)}

^{a)}Fast Reactor Fuels and Materials Technology Development Unit, ANSRD, JAEA, ^{b)}Fukushima Project Team, ORDC, JAEA, ^{c)}Fukushima Fuels and Materials Department, ORDC, JAEA

1. Introduction

Precipitation-strengthened high-nickel alloys have been developed for fuel cladding material in advanced reactor because of their intrinsic superior swelling property. In most case, these alloys are strengthened by an intermetallic compound such as ordered phase γ' [$\text{Ni}_3(\text{Ti}, \text{Al})$] formed in the matrix. The most important issue in development of high-nickel alloy is considered to be the improvement of mechanical properties at elevated temperature; the significant ductility loss due to irradiation at high temperature. The cause of this problem was believed to be the re-distribution of ordered phase γ' and solute segregation to defect sink sites, such as grain boundary, dislocation and void surface, during irradiation. In this study, several types of precipitation-strengthened high-nickel alloys were developed and then the phase stability (precipitate stability and swelling resistance) in these alloys during irradiation was evaluated by utilizing TIARA facility.

2. Experimental

The materials used in this study were two types of high nickel alloys and one austenitic stainless steel for the comparison; carbo-nitride phase strengthened high-nickel alloy (8NK_A, 22NK-28), γ'/γ'' [Ni_3Nb] phase strengthened high-nickel alloy (1543G) and Ti-modified SUS316 stainless steel (PNC316).

Small coupons specimens ($6 \times 3 \times 0.3 \text{ mm}^3$) were irradiated at the TIARA facility by 10.5 MeV Fe^{3+} ions with 1.05 MeV He^+ ions and 0.38 MeV H^+ ions. He^+ and H^+ ions implantation was performed using aluminum foil energy degraders. The irradiation was performed to 100 dpa at the depth of 1.0 μm and the damage rate was about 1.0×10^{-3} dpa/s at this depth. The implantation rates for He and H were 1 appmHe/dpa and 15 appm/dpa, respectively.

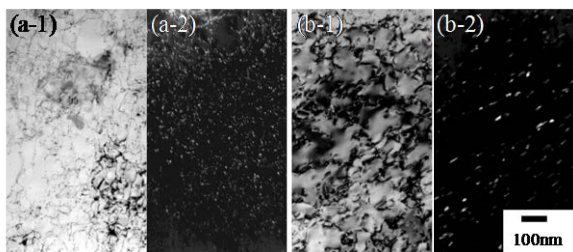


Fig. 1 Bright field and Dark field TEM images of precipitates observed in 8NK-A (a-1, a-2) and 1543G (b-1, b-2) before irradiation. Each precipitate is identified as a MC type of carbide for 8NK_A and γ'/γ'' phase for 1543G from the respective diffraction pattern analyses.

Thin foils for transmission electron microscopy (TEM) were fabricated using a focused ion beam (FIB) instrument. TEM observations for phase stability evaluation of ion-irradiated high-nickel alloys were carried out with a JEM-4000FX operated at 400 kV.

3. Results and Discussion

Bright field and Dark field TEM images of typical precipitates observed in 8NK-A (a-1, a-2) and 1543G (b-1, b-2) are shown in Fig. 1. As can be seen in Fig. 1 there were finely distributed precipitates in the matrix before irradiation. However, it was revealed from TEM observation of ion-irradiated specimens that disappearance or coarsening of precipitates happened locally and that the re-distribution of precipitates progressed.

Figure 2 shows irradiation temperature dependence of void swelling of high-nickel alloys (8NK_A, 1543G, 22NK-28) and austenitic stainless steel (PNC316). This result indicated that swelling peak temperature was around 600 °C and that swelling resistance of carbo-nitride phase strengthened high-nickel alloy (8NK_A, 22NK-28) was better than that of Ti-modified SUS316 stainless steel (PNC316) under this irradiation condition. Simultaneously, it was confirmed that γ'/γ'' [Ni_3Nb] phase strengthened high-nickel alloy (1543 G) had superior swelling resistant property.

References

- 1) W. J. S. Yang et al., J. Nucl. Mater. 132 (1985) 249.
- 2) D. J. Mazey et al., J. Nucl. Mater. 160 (1988) 153.

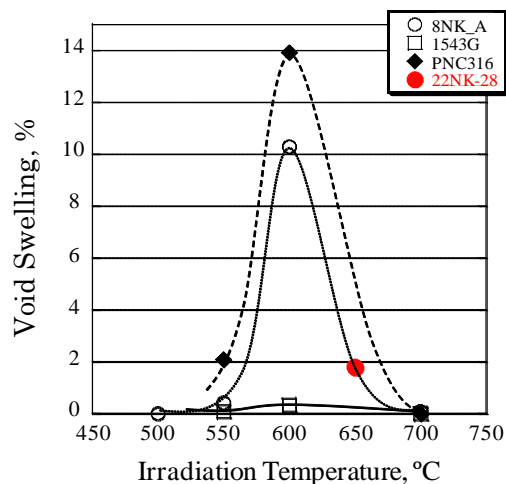


Fig. 2 Irradiation temperature dependence of void swelling in triple beam ion-irradiated high-nickel alloys. Void swelling of each specimen is estimated from the microstructure at the depth of 0.75-1.25 μm .

1 - 32 **Effects of Displacement Damage and Gas Atoms on Radiation Hardening and Microstructure in F82H Weldment**

M. Ando and H. Tanigawa

Division of Rokkasho BA Project, FRDD, JAEA

Reduced activation ferritic/martensitic steel (RAFs) is the most promising candidate for the blanket structural material in fusion reactor¹⁾. This blanket contains many joints of F82H plates using tungsten inert gas (TIG) welding, electron beam (EB) welding, hot isostatic pressing (HIP) and so on. These joints will be also exposed to high neutron flux irradiation in fusion reactor. Neutron irradiation experiments are being performed at HFIR, JMTR and so on. Some data of modified F82H and welded F82H are also obtained from post irradiation experiment. On the other hand, the effect of transmutation helium on mechanical properties and void swelling in RAFs is also an important subject. Multi ion irradiation method contributed to this subject in F82H base metal because this method can easily simulate the ratio of displacement damage and helium/hydrogen production²⁾. However study of helium/hydrogen gas effect on F82H welded joints is not enough.

The objective of this study is to evaluate radiation hardening and void swelling behavior of multi-ion irradiated F82H weldments up to 20 dpa.

The material used in this study was reduced activation ferritic/martensitic steel (F82H IEA; Fe-8Cr-2W-0.2V-0.04Ta-0.1C). This steel was normalized at 1,040 °C for 0.63 h and tempered at 750 °C for 1 h. The specimens of TIG and EB weld metal (WM) were annealed at 720 °C for 1 h (PWHT; post weld heat treatment). More details are reported elsewhere³⁾. Small coupons of specimens (6×3×0.8 mm³) were irradiated in the TIARA facility by 10.5 MeV Fe³⁺ ions with/without 1.05 MeV He⁺ ions and 0.38 MeV H⁺ ions. He⁺ and H⁺ ions implantation was

performed using aluminum foil energy degraders. The irradiation was performed to 20 dpa at the depth of 1.0 μm and the damage rate was about 1×10^{-3} dpa/s at this depth. Post-irradiation experiments were performed at IFERC DEMO R&D building in Rokkasho. The irradiated specimens were made into thin films, with a Hitachi FB-2100 focused ion beam (FIB) processing system. The microstructural examination was carried out using a JEOL JEM-2100F transmission electron microscope (TEM) operating at 200 kV.

Figure 1 a)-c) show examples of microstructure images for F82H IEA, EB-WM and TIG-WM at 470 °C up to 20 dpa by triple ion beam irradiation. For 470 °C irradiation in these F82H, cavities are observed at the depth from about 0.7 to 1.6 μm (damage level ~20 dpa at 1.0 μm) from an irradiation surface. The void swelling in F82H IEA, EB-WM and TIG-WM was ~0.6%, ~0.3% and ~0.6%, respectively. The swelling decreased at EB-WM region, slightly. On the other hand, few cavities were observed in the same region at 400 °C irradiation.

Further microstructural examinations with irradiated F82H specimens will be performed and then we will obtain the temperature of a void swelling peak for dose rate of 10^{-3} dpa/s.

References

- 1) H. Tanigawa et. al., J. Nucl. Mater. 417 (2011) 9-15.
- 2) E. Wakai et.al., J. Nucl. Mater. 318 (2003) 270.
- 3) K. Shiba, Proc. IEA Work. Group Meet. Ferritic/Martensitic Steels, Switzerland, ORNUM-4939 (1995).

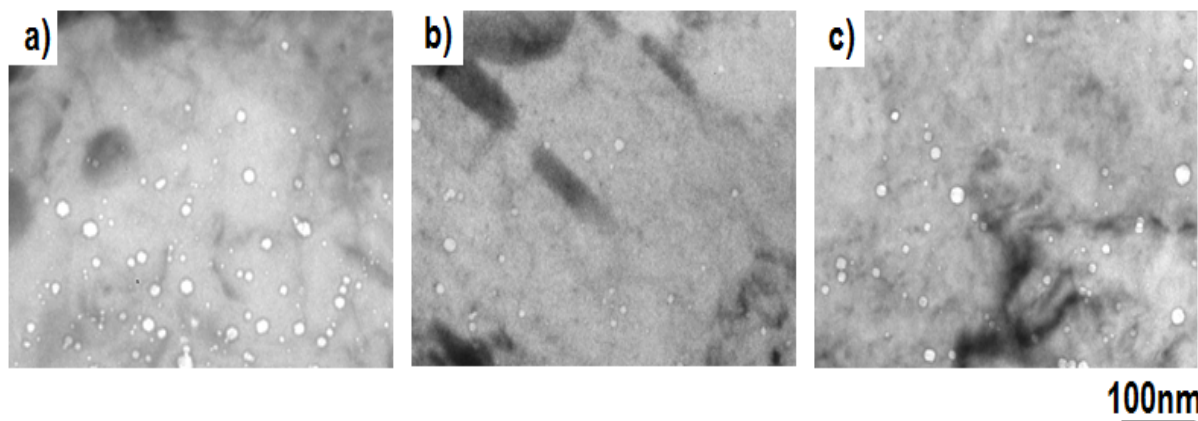


Fig. 1 Microstructure images of cavities in F82H irradiated at 470 °C, 20 dpa by triple beam irradiation (Around 1.0 μm from surface). a) F82H IEA, b) F82H EB-WM, c) F82H TIG-WM.

1 - 33 Corrosion Tests of Steels Used for Reactor Pressure Vessel and Primary Containment Vessel

J. Nakano and T. Tsukada

Fukushima Project Team, NSRI, JAEA

After the great east Japan earthquake on March 11, 2011, Tsunami attacked the Fukushima Daiichi Nuclear Power Plant (NPP). To cool the reactor cores in the Unit 1, 2 and 3 of the Fukushima Daiichi NPP, the seawater was injected into the reactors. Low alloy steel and carbon steel which have relatively low corrosion resistance, are used as the reactor pressure vessel (RPV) and primary containment vessel (PCV), respectively. Since melted nuclear fuel fell down from the RPVs, the high dose of radiation has been continuing in the PCVs. When water is irradiated by gamma rays, oxygen, hydrogen peroxide, radicals, etc. are produced by water radiolysis. The species are chemically active and it is considered that corrosion on RPV and PCV might be assisted.

Therefore, we are carrying out the research related to the corrosion issues which may affect the integrity of the RPV and PCV to evaluate the effects of the gamma rays irradiation on corrosion of steels.

Corrosion tests under gamma rays irradiation and an

irradiation facility at the Takasaki advanced radiation research institute are shown in Fig. 1. Sheet type specimens of 40 mm×10 mm×2 mm were immersed in diluted artificial seawater with chloride concentration of 100 ppm at 323 K (50 °C). Subsequently, ^{60}Co source of gamma rays was lifted from a pool under a floor and the specimens were irradiated. Duration of corrosion tests under gamma rays irradiation were 50, 100 and 500 h.

Equipment for corrosion tests arranged in the irradiation room is shown in Fig. 2. The flasks were placed close to ^{60}Co source and dose rate of 4.4 kGy/h was estimated in the flasks containing water.

Visual inspection of the specimens before and after corrosion test for 50 h is shown in Fig. 3. Formation of oxide layer is observed on their surface. Weight loss will be estimated after oxide layer removal treatment.

In the next step, corrosion tests in diluted artificial seawater containing corrosion inhibitor will be performed as countermeasure for degradation of the steel components.

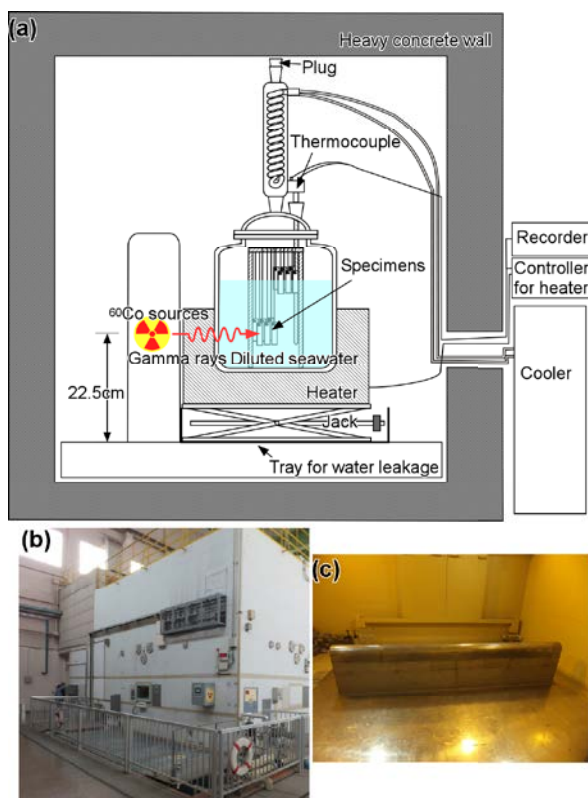


Fig. 1 Corrosion tests under gamma rays irradiation and an irradiation facility at the Takasaki advanced radiation research institute, (a) schematic illustration of corrosion tests, (b) external view of an irradiation room and (c) cover of ^{60}Co source in the irradiation room.

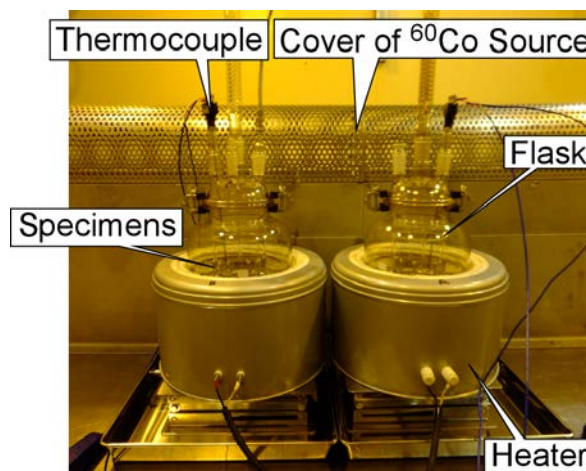


Fig. 2 Equipment for corrosion tests arranged in the irradiation room.

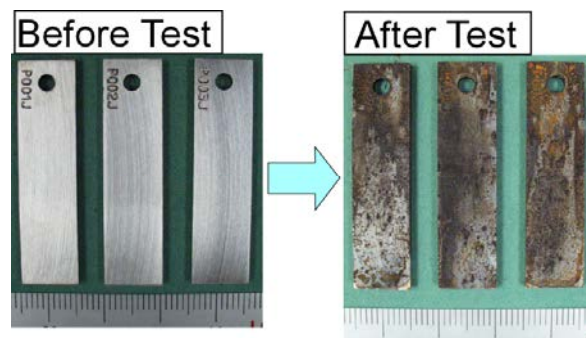


Fig. 3 Visual inspection of specimens before and after corrosion test for 50 h in diluted seawater at 323 K.

1 - 34 Corrosion Resistance of Tank Material Used for Flock Storage

Y. Sano, H. Ambai, M. Takeuchi and Y. Koma

Department of Fukushima Technology Development, NFCEL, JAEA

Introduction

The flock, which was generated in the coagulation process for radioactive contaminated water from the Fukushima Daiichi nuclear power plant, contains the sea water. When storing the flock until its processing it was anticipated to make a crevice on the surface of its storage tank. Concerning durability of tank material, it is important to evaluate not only uniform corrosion but also local corrosion. In addition, the effect of radiation from the flock should be considered. In this study, we investigated these effects on the corrosion of SS400 as the material of the storage tank, to which the flock will be transferred in the future¹⁾, in the settling condition.

Experimental

Based on the information on the flock storage condition¹⁾, electrochemical tests, in which corrosion potentials and polarization curves were recorded, were carried out with SS400 under several conditions for discussing major corrosion factors and possibility of local corrosion. Immersion tests were performed subsequently on the selected conditions and average corrosion rates were estimated by the weight loss of the coupons after the immersion for 1,230 hours. In addition, the surfaces of the coupons were observed by microscopy for evaluating the local corrosion. During these tests, γ -ray of ^{60}Co was irradiated at Takasaki to flock solution at different absorbed dose rates. In all of these tests, the flock supplied from Tokyo Electric Power Company (TEPCO) as a surrogate and artificial sea water (Aquamarine supplied from Yashima Chemical Co.) were used.

Results and discussion

In the electrochemical tests, no change of corrosion potential was observed with γ -ray irradiation, and the polarization curves suggested the corrosion would proceed uniformly. Figure 1 shows the change of corrosion current densities estimated by Tafel plot with absorbed dose rates of γ -ray. The corrosion current density increased at the high absorbed dose rate. Figure 2 summarized the average corrosion rates in the immersion tests with the parameters of absorbed dose rates of γ -ray, pH and sea water concentration of the flock solution which were estimated to be major corrosion factors from the results of the electrochemical tests. Although the corrosion rates changed slightly in some conditions as suggested by the electrochemical tests, e.g. increasing at the high absorbed dose rate, they were around 0.1 mm/y, which was the almost same as the corrosion rate of SS400 in sea water²⁾. Microscopic analysis of the immersed coupons showed no severe corrosion including local corrosion occurred. The increase of the corrosion rate at the high absorbed dose rate will be caused by significant generation of H_2O_2 which acts as an oxidizer in the flock solution.

References

- 1) TEPCO, "Report on our facility management plan for Units 1-4 of Fukushima Daiichi Nuclear Power Station based on the "Policy on the Mid-term Security" (2012).
- 2) Fushoku-Boshoku Handbook, Maruzen, Tokyo (2000).

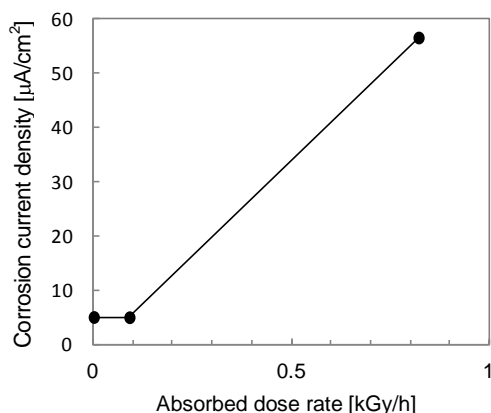


Fig. 1 Change of corrosion current densities with absorbed dose rates of γ -ray.

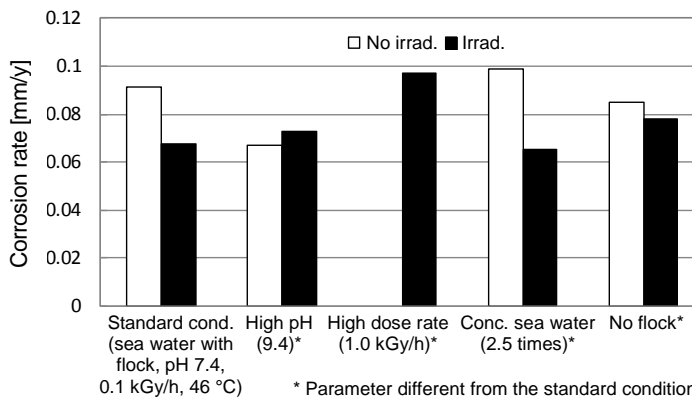


Fig. 2 Effects of corrosion factors on corrosion rates of SS400 (Immersion time: 1,230 h, Irradiation time: 1,050 h).

1 - 35

Investigation of Microstructure in SiC Made by Nano-infiltration Transient Eutectic Process after Triple Ion Beam Bombardment

K. Ozawa^{a)}, T. Taguchi^{b)}, T. Nozawa^{a)}, M. Ando^{a)} and H. Tanigawa^{a)}

^{a)}Division of Rokkasho BA Project, FRDD, JAEA,

^{b)}Materials Science Research Division, QuBS, JAEA

Silicon carbide (SiC) and its composites (SiC/SiC) are attractive candidate materials for nuclear fusion energy application because of their superior irradiation performance and thermo-physical, -chemical, and -mechanical properties^{1,2)}. To realize the use of such composites, the effect of transmuted helium (He) and hydrogen (H) under fusion environment needs to be clarified in terms of dimensional stability of SiC. However, the information after irradiation is quite limited about SiC containing secondary phases composed of sintering additives as impurities, such as matrix of nano-infiltration transient eutectic (NITE) sintering process³⁾, in contrast to high purity SiC made by the chemically vapor infiltration method⁴⁾. Therefore, the irradiation effect on dimensional stability of the NITE-SiC has been previously examined^{5,6)}. In the following two fiscal years, microstructural evolution of the NITE-SiC after ion irradiation to a relatively high-dose with a special emphasis on the transmuted H effects was investigated.

Monolithic SiC ceramics via the NITE method were irradiated at Takasaki Ion Accelerators for Advanced Radiation Application (TIARA) facility of Japan Atomic Energy Agency. Simultaneous dual or triple ion irradiation was conducted to ~30 dpa at 1000 °C in order to simulate the synergetic transmuted He/H effects. Microstructure was evaluated with transmission electron microscopy (TEM)

for a specimen thinned by focused ion beam.

After dual and triple ion irradiation to 10 dpa with 130 appmHe/dpa, small cavities (~2 nm) were formed in the SiC grains (Fig. 1), and larger ones (~15 nm) formed along yttrium-aluminum-garnet (YAG)/SiC grain boundaries. Based on the TEM micrograph analysis results shown in Fig. 2 and Table 1, under fusion environmental condition (40 appmH/dpa), no remarkable negative effects of hydrogen on cavity formation was found under the condition studied. Additionally, cavity swelling was also small even under the excessive H implanted condition (~0.06% for the cavities in grain interiors and ~0.05% for the ones at grain boundaries after 400 appmH/dpa (Triple × 10) irradiation). Further detailed observation and analysis for the specimens irradiated to ~30 dpa are underway.

References

- 1) T. Nozawa et al., J. Nucl. Mater. 386-388 (2009) 622.
- 2) Y. Katoh et al., J. Nucl. Mater. 367-370 (2007) 659.
- 3) Y. Katoh et al, Fusion Eng. Des. 61-62 (2002) 723.
- 4) L. L. Snead et al., J. Nucl. Mater. (2007) 329.
- 5) T. Nozawa et al., JAEA Takasaki Annu. Rep. 2009 (2011) 138.
- 6) T. Nozawa et al., JAEA Takasaki Annu. Rep. 2010 (2012) 131.

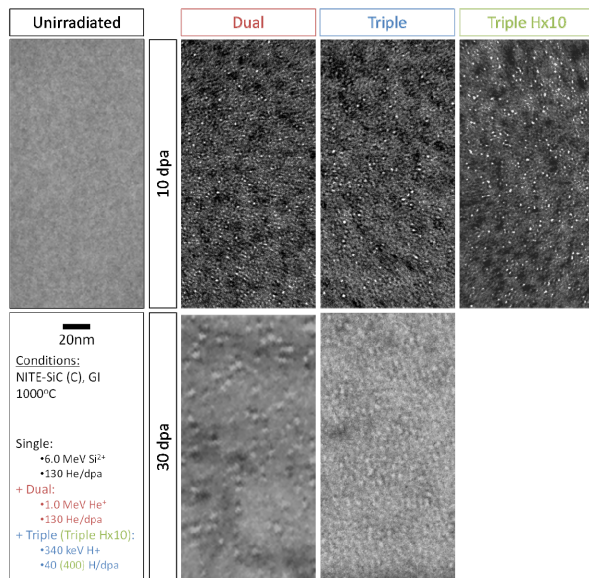


Fig. 1 TEM micrographs showing cavity formation after ion irradiation to 10 and 30 dpa at 1000 °C with varied He/dpa and H/dpa conditions (Dual, Triple, Triple×10).

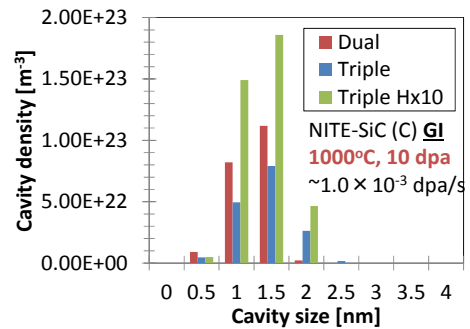


Fig. 2 TEM image analysis for cavity diameter distribution in NITE-SiC grain interior after 10 dpa irradiation at 1000 °C.

Table 1 The results in Fig. 2 for average cavity diameter (d), number density (n), and cavity swelling ($\Delta V/V$).

Condition	d (nm)	n (/m ³)	$\Delta V/V$ (%)
Dual	1.5	2.1×10^{23}	0.025
Triple	1.7	1.6×10^{23}	0.029
Triple H×10	1.6	3.9×10^{23}	0.060

1 - 36 Ionizing Dose Dependences of Radiation-induced Conductivity and Radiation-induced Electrical Degradation of Chemical Vapor Deposited Silicon Carbides under Gamma-ray Irradiation

B. Tsuchiya^{a)}, T. Shikama^{b)}, S. Nagata^{b)}, K. Saito^{b)} and S. Yamamoto^{c)}

^{a)} Department of General Education, Faculty of Science and Technology, Meijo University,

^{b)} Institute for Materials Research, Tohoku University,

^{c)} Environment and Industrial Materials Research Division, QuBS, JAEA

Silicon carbides (SiCs) are potential candidates as insulating materials in nuclear fusion systems such as separators or insulating flow channel inserts, between tritium breeding and neutron multiplier materials composing Li-Pb blanket modules. So far, it has been reported that the electrical properties of insulating ceramics are dynamically modified by electrons that are excited from valence bands to conduction bands by the so-called dynamic radiation effects^{1,2)}. In fact, for CVD-SiC materials with high purity and density, synthesized by the chemical vapor deposition technique, the radiation enhanced phenomena such as radiation induced conductivity (RIC) and radiation induced electrical conductivity (RIED)-like behavior has been observed by in situ radiation experiments under gamma-ray and fast neutron irradiations³⁾. The RIC and RIED-like behavior according to radiation-induced modification of the electrical property occurred with essentially no displacement damage, but ionizing effects (radiolysis). However, it has not been clarified fully, yet. It is significant important to investigate the radiation damage process and physical mechanism on the degradation of the electrical property by radiation in more detail by combining in situ radiation experiments with post-irradiation examinations.

Figures 1(a)-(d) show SEM (SEI: secondary electron image) micrographs of unirradiated, gamma-ray-irradiated CVD-SiC samples at approximately 0.24, 1.13, and 1.47 MGy, respectively. It seems to be the melting formation for the surface morphology of the gamma-ray-irradiated CVD-SiC sample. The result shows the radiation damage due to ionizing effects. The microstructures for the unirradiated, gamma-ray-irradiated samples have been shown by XRD patterns of Fig. 2. There is essentially no change in the XRD patterns before and after irradiation, indicating no significant loss in crystallinity. The RIED-like behavior²⁾ may be attributed to changes in electronic structure by breaking the bond between Si and C atoms and distortion of the structure, which is due not to the atomic displacements but the electronic excitation essentially. As the results, it is concluded that the covalent nature of SiC extremely makes it sensitive to radiolysis; defects production by ionizing radiation.

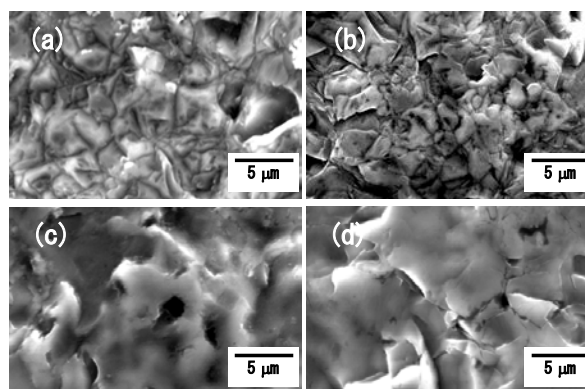


Fig. 1 SEM (SEI: secondary electron image) micrographs of (a) unirradiated and gamma-ray-irradiated CVD-SiC samples at approximately (b) 0.24, (c) 1.13, and (d) 1.47 MGy.

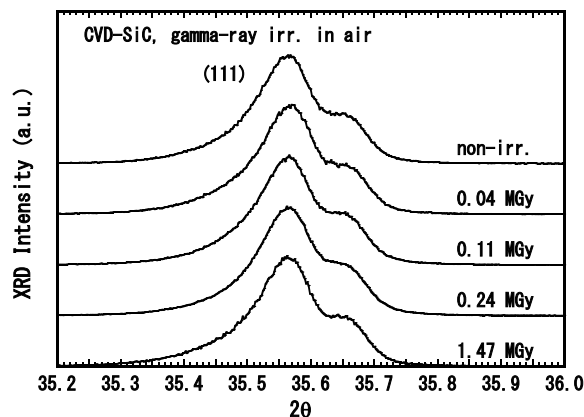


Fig. 2 XRD patterns of unirradiated, gamma-ray (1.47 MGy) and fast neutron ($8.4 \times 10^{19} \text{ n/m}^2$)-irradiated CVD-SiC samples.

References

- 1) E. R. Hodgson, Nucl. Instrum. Meth. Phys. Res. B 191 (2002) 744.
- 2) S. J. Zinkle, E. R. Hodgson, J. Nucl. Mater. 191-194 (1992) 58.
- 3) B. Tsuchiya et al., Fusion Eng. Des. 86 (2011) 2487.

1 - 37 Surface Morphology of He Implanted CeO₂ Thin Film

H. Serizawa^{a)}, S. Yamamoto^{b)} and T. Hakoda^{b)}

^{a)} Division of Fuels and Materials Engineering, NSED, JAEA,

^{b)} Environment and Industrial Materials Research Division, QuBS, JAEA

Recent investigation made by JAEA showed that a gas bubble bounded by facets is formed in UO₂ during a process of a precipitation of helium followed by injection with HIP.

The interesting phenomena they found is that the shape of the negative crystal changes depending on the inner pressure of cavity, which implies that the shape of the cavity can be transformed by controlling the condition of helium release followed by the injection. They call the shape controllable negative crystal image crystal¹⁾. In case of UO₂, helium was injected by HIP successfully since a solubility of helium is relatively high. However the injection method may or may not be suitable for other ceramics in which helium solubility is low. Therefore, we decided to examine other injection method. This paper addresses the gas bubble formation in CeO₂ thin film by helium injected by ion bombardment.

Pieces of CeO₂(100) thin film was heat treated at 1,273 K for 2 h. The channeling effect of the film was examined by RBS. The minimum yield was as low as 2.3%, which means that the film is regarded as a single crystal. The oriented growth of the surface (100) was confirmed by X-ray diffraction. The films were irradiated with 70-keV He⁴⁺ and 130-keV He⁴⁺ ions from 400-kV ion implanter of TIARA. The ion doped film was heat treated at 1,273 K for 1 h. The heating rate (H. R.) was varied from 5 to 10 K/min to examine the surface morphology. After the heat treatment, the surface of the film was examined by confocal laser scanning microscopy. Figure 1 shows the surface morphology of the annealed film. It was found that the precipitated helium forms gas bubble in the film. The gas bubble formed in the near surface region forms blister. The force of accumulated gas opens the lid of the blister. The surface morphology of the film varies depending on the anneal condition. Many broken blisters are observed on the film helium injected with low energy. The surface morphology is also affected by heating rate. Almost no defect is seen for the sample with H. R.: 5 K/min (Fig. 1[B]), while the surface morphology with H. R.: 10 K/min is rough. The figures indicate that the gas bubble tends to be formed in the near surface region when H. R. is high. The aim of this study is to develop new functional thin film. So, the formation of blister on the surface is undesirable. The results of this study imply that we can produce thin ceramic film without damaged surface successfully by selecting the appropriate annealing condition followed by helium ion injection.

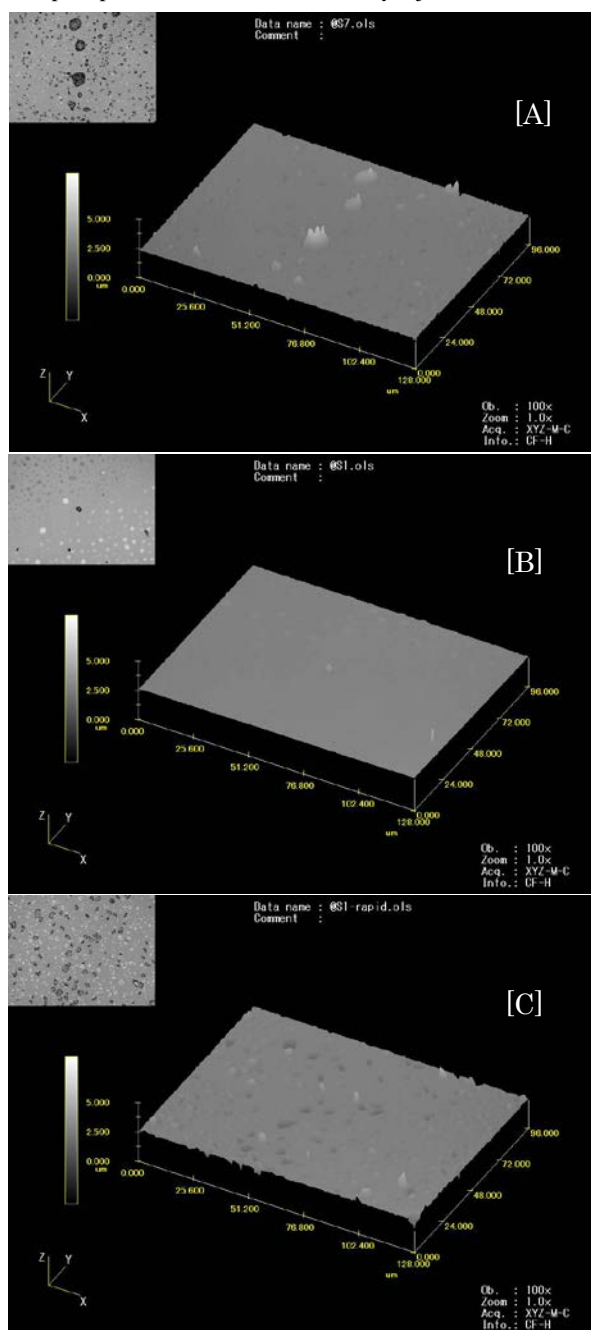


Fig. 1 Morphology of film surface examined by confocal laser scanning microscopy. [A] 70-keV He⁴⁺ H.R.: 5 K/min, [B] 130-keV He⁴⁺ H.R.:5 K/min, [C] 130-keV He⁴⁺ H.R.:10 K/min.

Reference

- 1) H. Serizawa et al., Cryst. Growth Des. 13 (2013) 2815.

1 - 38

A Macroporous SiC Material Synthesized from Preceramic Polymer with Direct Foaming and Radiation Curing

A. Idesaki, M. Sugimoto and M. Yoshikawa

Environment and Industrial Materials Research Division, QuBS, JAEA

Porous ceramic materials which possess low density, high specific surface area, high liquid/gas permeability and low thermal conductivity as well as intrinsic properties of ceramic materials are utilized as catalyst supports, hot gas filters, molten metal filters, thermal insulation, and so on, in wide industrial fields. In order to expand these applications more, it is important to develop porous ceramic materials with enhanced properties such as thermal resistance, corrosive resistance, strength, and so on. Silicon carbide (SiC) which possesses excellent resistance for heat, oxidation and corrosion can give porous ceramic materials available under severe conditions. Several fabrication processes of porous SiC materials have been proposed: “sacrificial template method” using polymeric spheres, polymeric foams and freeze-casting of slurry or solution and “direct foaming method” using blowing agents or CO₂ gas. While SiC ceramic powders and preceramic polymers are used in these processes, the fabrication process using preceramic polymers is advantageous in comparison with powder-sintering process because the preceramic polymers possess high formability, low processing temperature and controllability of compositions with addition of fillers. We have synthesized a variety of SiC products such as fibers, micro parts, membranes for gas separation from preceramic polymers with radiation curing. In this work, fabrication of a porous SiC material from polycarbosilane (PCS) was examined with following processes (Fig. 1): (1) direct foaming process; PCS is heated to melt and simultaneously blowing agent is thermally decomposed to generate gases for foaming, (2) radiation curing process; the foamed body is irradiated by gamma-rays in air to fix the foamed shape and (3) pyrolysis process; the cured body is converted to a porous SiC

material by firing at 1,000 °C in an inert atmosphere. In the direct foaming process, PCS is heated to melt and simultaneously the blowing agent is thermally decomposed to generate gases for the foaming. Because an optimum blowing agent for PCS should be selected to obtain a porous SiC material, biurea which decomposes in a temperature range of 180-340 °C evolving NH₃, CO₂ and N₂ with the amount of 90 mL/g was used in this work.

A mixture of PCS and biurea of 1 wt% put into an aluminum pan was heated to 230 °C with a heating rate of 200 °C/h and hold for 2 h, and then heated to 280 °C with the heating rate of 200 °C/h under Ar atmosphere. The sample was not held at the foaming temperature and cooled in the furnace to obtain a foamed PCS body. The foamed PCS body was irradiated by ⁶⁰Co gamma-rays with dose of 1 MGy at room temperature in air. After the irradiation, the foamed PCS body was heat-treated at 250 °C for 1 h in Ar to complete curing process. The cured PCS body was pyrolyzed at 1,000 °C for 1 h in Ar. Obtained porous SiC material showed an average cell size of 0.5 mm, total porosity of 74% and compressive strength of 3.2 MPa (Fig. 2).

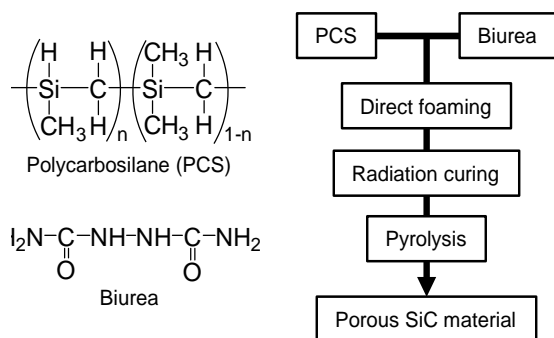


Fig. 1 Chemical structures of starting materials and fabrication process of a porous SiC material in this work.

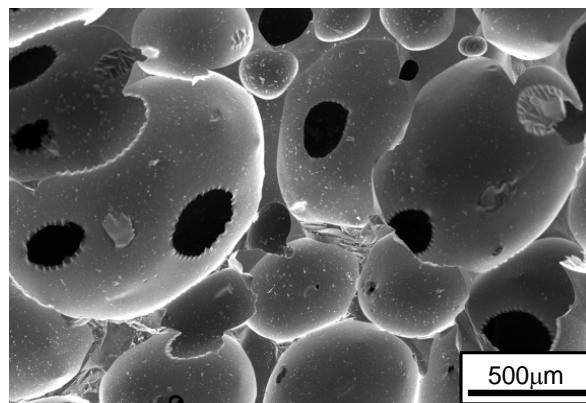


Fig. 2 SEM image of porous SiC material synthesized from PCS and biurea with direct foaming and radiation curing.

As a conclusion, it was found that biurea is very useful agent for the foaming of PCS. A porous SiC material which possesses high open porosity and high compressive strength was synthesized from PCS and biurea. This material is expected to be applied for a catalyst support, a hot gas filter or a molten metal filter although evaluation and optimization of specific surface area and gas/liquid permeability are required.

1 - 39

Alkaline Durable Anion Exchange Membranes Synthesized by Radiation-induced Grafting for Hydrazine Hydrate Fuel Cell

K. Yoshimura^{a)}, H. Koshikawa^{a)}, T. Yamaki^{a)}, H. Shishitani^{b)}, S. Yamaguchi^{b)},
H. Tanaka^{b)} and Y. Maekawa^{a)}

^{a)}Environment and Industrial Materials Research Division, QuBS, JAEA,

^{b)}Daihatsu Motor Co., Ltd.

Anion exchange membrane fuel cells (AEMFC) have recently received considerable attention due to their potential advantages of over proton exchange membrane fuel cells (PEMFC). The AEMFC works under alkaline condition, where the electrochemical reactions are more facile than in acidic medium, and non-precious metals such as nickel, cobalt and iron can replace platinum as the catalyst. Additionally, aqueous solution of methanol or hydrazine hydrate can be used as fuels^{1,2)}.

An anion exchange membrane (AEM) is one of the key materials for AEMFC. Previously, we prepared AEM with an imidazolium cation (AEM1) by radiation-induced grafting (Fig. 1). AEM1 showed moderate conductivity and water-uptake compared with the corresponding trimethylammonium group containing AEM. However, the conductivity of AEM1 decreased rapidly under the alkaline condition at elevated temperature (1 M KOH, 60 °C). In this work, we developed alkaline durable properties of AEMs by introducing poly(N-vinylimidazolium hydroxide) by a radiation-induced grafting method for direct hydrazine fuel cells (Fig. 1, AEM2 and AEM3).

The ETFE films were irradiated with a ⁶⁰Co γ -ray source (JAEA Takasaki) at room temperature in argon atmosphere to a total dose of 50 kGy at a dose rate of 17 kGy h⁻¹. The pre-irradiated ETFE films were immediately immersed into the argon-purged monomer solution consisting of 50 wt% N-vinylimidazole (NVI) or a mixture of NVI/styrene (8 : 2 weight ratio) in xylene. The imidazole pendant groups in the grafted ETFE were quaternarized using propyliodide and the resultant AEMs were immersed in 1 M KOH solution at 60 °C for 170 h to convert into the hydroxide form, completely. The ionic conductivity of fully hydrated AEMs was measured by two-point probe AC impedance spectroscopy.

The poly(NVI)- and copoly(NVI/styrene)-grafted ETFE films (precursors of AEM2 and AEM3) were prepared with grafting degrees of 52 and 85%, respectively.

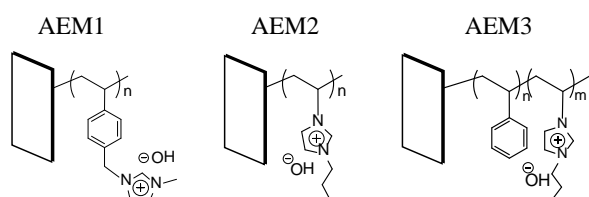


Fig. 1 Chemical structures of AEMs.

The copolymerized AEM3 was synthesized for prevention of the excessive water uptake of membrane and for reduction of electrostatic repulsion between adjacent imidazolium cations. The quaternization reaction for AEM2 proceeds quantitatively, thus molar ratio of NVIm and styrene in AEM3 can calculate from weight gain after quaternization. The molar ratio of NVIm and styrene in AEM3 was calculated to be 1 : 1. The ionic conductivities at 60 °C of AEM2 and AEM3 were 10 and 27 mS/cm, respectively.

The alkaline stability of AEMs was evaluated by monitoring the change in conductivity of AEMs in 1 M KOH at 60 °C (Fig. 2). The conductivity of AEM1 disappeared within a few hours while AEM2 and AEM3 kept the conductivity for longer periods. Especially, AEM3, possessing copolymer grafts of N-vinylimidazolium hydroxide and styrene showed excellent alkaline stability with keeping conductivity of more than 20 mS/cm after 10 days. The above results strongly indicate that the alteration of anion exchange groups from benzyl- to alkyl-imidazolium hydroxide in the AEMs drastically enhances the alkaline durability in alkaline solutions at elevated temperatures. Accordingly, the alkylimidazolium groups in copolymer grafts in AEMs are promising an anion exchange group for highly alkaline durable direct hydrazine fuel cells.

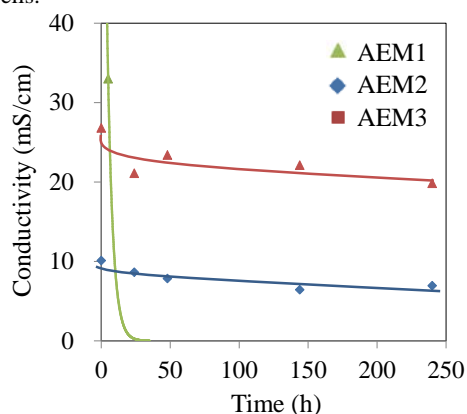


Fig. 2 The AEM conductivities after being immersed in 1 M KOH at 60 °C.

References

- 1) A. Serov et al., *Appl. Catal B-Environ.* 98 (2010) 1.
- 2) K. Asazawa et al., *Angew. Chem. Int. Ed.* 46 (2007) 8024.

1 - 40

Preparation of Anion-Exchange Membranes for Fuel Cell Applications by γ -ray Pre-irradiation Grafting: Effect of the Carbon Dioxide in the Air

H. Koshikawa, K. Yoshimura, T. Yamaki, M. Asano and Y. Maekawa

Environment and Industrial Materials Research Division, QuBS, JAEA

Widespread commercialization of fuel cells has been hindered by economic problems associated with the extensive use of platinum. In order to overcome such difficulties, researchers have so far developed anion-exchange membrane fuel cells (AEMFCs), which do not need expensive platinum catalysts in the electrodes. Our recent focus has been the preparation of new hydroxide (OH)-conducting membranes for applications to “hydrazine-fueled” AEMFCs¹⁾ by the γ -ray pre-irradiation grafting method^{2,3)}. Generally, carbon dioxide (CO_2) is dissolved in the AEM, thereby resulting in the transformation from the OH to bicarbonate (HCO_3) ions. We investigated here the effect of CO_2 in the air on the exchange between OH and HCO_3 ions in the AEM.

Our AEM preparation involved the grafting of chloromethylstyrene (CMS) into poly(ethylene-co-tetrafluoroethylene) (ETFE) films and subsequent quaternization (Fig. 1)^{2,3)}. A 50 μm -thick ETFE film was pre-irradiated with ^{60}Co γ -rays at 30 kGy and then immersed in the CMS/xylene 33/67 vol% grafting solution in Ar at 60 $^\circ\text{C}$ for 4 h. The quaternization of the ETFE-g-CMS film occurred in a 30% trimethylamine (TMA) aqueous solution at room temperature for 10 h, followed by the washing in a 1 M HCl solution and in deionized water (AEM-Cl). The AEM-Cl film was immersed in a 1 M KOH solution at room temperature for 6 h to give the AEM in the hydroxide form (AEM-OH). This anion exchange process was entirely performed in N_2 -bubbled water. The transformation of the AEM-OH to HCO_3 form (AEM- HCO_3) was examined in the

air at room temperature, by a thermogravimetric analysis (TGA) method.

Figure 2 shows the first deviations of the TGA profiles of (a) AEM-OH, AEM-OH after exposure to the air for (b) 0.5, (c) 1.25, and (d) 10 h, and (e) AEM- HCO_3 membranes. The bicarbonate conversion ratio in the AEM can be estimated by dividing the height of the peak of 180 $^\circ\text{C}$ by that of 240 $^\circ\text{C}$. The ratio increased from 0.6 (AEM-OH) continuously to 3.5 during the course of exposure to the air. The ratio of the heights at 0.5 h is the half of that in AEM- HCO_3 . This result shows that the salt formation of the AEM with hydroxide anions, even at room temperature in ten hours, transform to more stable bicarbonate form following the absorption of moisture in the air⁴⁾.

References

- 1) K. Asazawa et al., J. Electrochem. Soc. 156 (2009) B509.
- 2) H. Koshikawa et al., Proc. RadTech Asia 2011 (2011) 240.
- 3) T. Yamaki, Maku (Membrane) 36 (2011) 240.
- 4) H. Koshikawa et al., Macromol. Chem. Phys., 214(2013)1756.

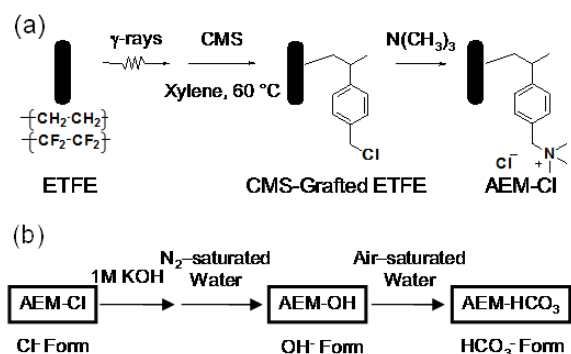


Fig. 1 Preparation scheme for AEM. (a) Radiation-induced graft polymerization of CMS into ETFE films and subsequent quaternization of the poly(CMS) grafts. (b) Anion-exchange reactions of AEM-OH with hydroxide and bicarbonate anions.

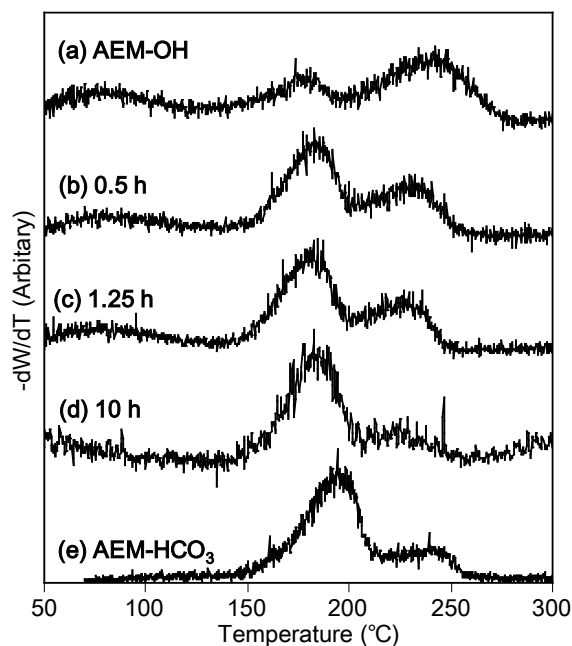


Fig. 2 First deviations of the TGA profiles of the graft-type AEMs: (a) AEM-OH, (b)–(d) AEM-OH after exposure to air for 0.5, 1.25, and 10 h, (e) AEM- HCO_3 .

1 - 41 Poly(ether ether ketone) (PEEK)-based Graft Type Polymer Electrolyte Membrane: Relative Humidity Dependence for Fuel Cell Application

S. Hasegawa, H. Koshikawa, J. Chen and Y. Maekawa

Environment and Industrial Materials Research Division, QuBS, JAEA

A pre-irradiation grafting method is a fascinating technique for direct introduction of new functional graft polymers (grafts) into polymer substrates without any damages. The radiation technique has been widely applied to the preparation of high performance fuel cell polymer electrolyte membranes (PEMs) for mobile electricities, vehicles, and domestic co-generation systems. The PEMs of aromatic hydrocarbon polymers, so-called “super engineering plastics” including poly (ether ether ketone) (PEEK), have useful characteristics such as high mechanical strength, gas barrier property, and radiation resistance¹⁾. Thus, in this work, we investigated the humidity dependence of proton conductivity and mechanical strength at 80 °C and relative humidity (RH) from 30 to 95%, which are the most important characteristics for power generation efficiency and durability under real operating conditions in fuel cell systems.

Graft polymerization was conducted by the γ -rays irradiation of PEEK films (crystallinity: 11%) with 30-160 kGy, followed by the immersion in 50 wt% ethyl 4-styrenesulfonate (E4S) in 1,4-dioxane to obtain E4S-grafted PEEK films (grafted-PEEK) with grafting degrees (GDs) of 39-133%. The grafted-PEEK films were hydrolyzed in aqueous solution at 95 °C for 24 hours to give poly (styrenesulfonic acid) grafted PEEK films (PEEK-PEM) with ion exchange capacities (IECs) of 1.19 - 2.83 mmol/g.

Figure 1 shows the proton conductivities of all the PEEK-PEMs in a RH range from 30 to 95% at 80 °C. Under a humid condition (95% RH), the proton conductivities increased from 0.061 to 0.34 S/cm with the increases of GD. With the decreases of RH from 95 to 30%, the proton conductivities decreased by two order of magnitudes, which were much smaller than those of other aromatic hydrocarbon-type PEMs.

Proton conductivities of PEEK-PEMs under 30% RH and tensile strengths (TSs) under 100% RH at 80 °C are plotted as a function of GD together with those of Nafion-212 as a reference in Fig. 2 (a) and 2 (b), respectively. The PEEK-PEM with a GD of 133% exhibited a compatible proton conductivity (0.0069) S/cm and two times higher TS (21 MPa) compared with those of Nafion.

In conclusion, the PEEK-PEMs possess the proton conduction character being less dependent on RH than other aromatic hydrocarbon type PEMs and superior mechanical properties because hydrophilic grafted polymers show clearer phase separation from the hydrophobic substrate,

thereby maintaining conducting channels even under dry conditions and higher TS owing to the crystal structures of the PEEK substrates.

Reference

- 1) S. Hasegawa et al., Polymer **54** (2013) 2895-900.

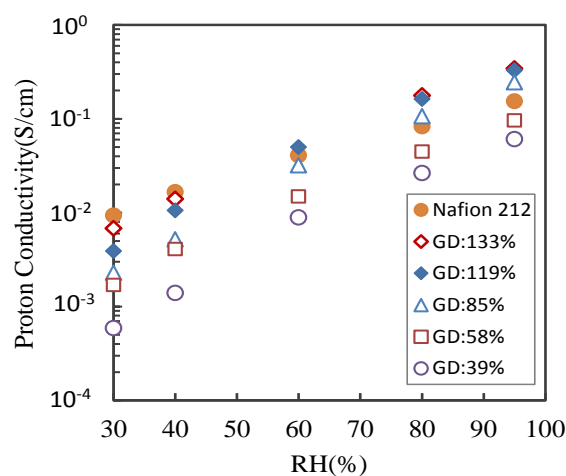


Fig. 1 Plots of proton conductivities with various PEEK-PEM samples as a function of RH at 80 °C.

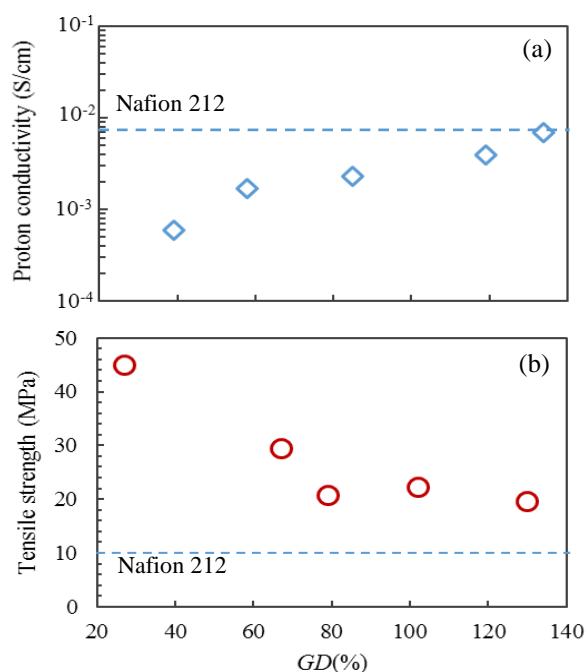


Fig. 2 Plots of proton conductivity under 30% RH (a) and stress under 100% RH (b) at 80 °C as a function of GD.

1 - 42 Preparation of Novel Polymer Electrolyte Membranes by Combination of Radiation Induced Grafting and Atom Transfer Radical Polymerization

S. Sawada, S. Hasegawa and Y. Maekawa

Environment and Industrial Materials Research Division, QuBS, JAEA

We have recently tried to prepare the novel polymer electrolyte membranes (PEMs) for fuel cell applications by combination of the radiation-induced grafting polymerization (RIGP) and atom transfer radical polymerization (ATRP) methods¹⁾ (see Fig. 1). The base ETFE films were irradiated with 15-kGy γ -ray in an Ar atmosphere, and then immersed in styrene (St) / chloromethylstyrene (CMS) mixtures for the RIGP. The degree of St/CMS grafting, DOG_1 , was estimated by: $DOG_1 = (W_1 - W_0) \times 100 / W_0$, where W_0 and W_1 are the weights of the original ETFE and St/CMS-grafted films, respectively. Next, for the ATRP, the films were immersed in ethylstyrenesulfonate (ETSS) solutions, which contained CuBr and N,N,N',N'',N'''-Pentamethyldiethylenetriamine (PMDETA) as ATRP catalyst and ligand, respectively. The ETSS graft chains were elongated from the Cl atoms in CMS units. The degree of ETSS grafting, DOG_2 , was estimated by: $DOG_2 = (W_2 - W_1) \times 100 / W_1$, where W_2 is the weight of the ETSS grafted film. Finally, the films were hydrolyzed in pure water to introduce sulfonic acid groups.

Holmberg *et al.* previously prepared the PEMs by the RIGP of CMS into PVDF films; the ATRP of St from CMS units; and sulfonation of St units²⁾. What should be noticed in their work is that the ATRP temperature was 100-130 °C. At such high temperature, the following thermal polymerization would take place. After the RIGP, some part of the radicals produced by irradiation should remain and react with oxygen in the air to form peroxides. These peroxides were likely decomposed to produce radicals at above 100 °C, initiating the polymerization. Accordingly, we are sure that not only the ATRP but also the unexpected thermal polymerization occurred in their experiment, which made the molecular architecture uncontrollable.

To prohibit the thermal polymerization, the ATRP temperature was fixed at 50 °C. Figure 2 shows the DOG_2 as a function of the reaction time. With no CuBr and PMDETA, the DOG_2 was almost 0% regardless of the reaction time, indicating no thermal polymerization. In contrast, when the concentration of CuBr and PMDETA was 0.04 M and 0.08 M, respectively, the DOG_2 dramatically increased with time. This was the first experimental demonstration that only the ATRP occurred inside the polymer films.

The ion exchange capacity (IEC) of the obtained PEMs was estimated by a base-acid titration. Figure 3 shows the IEC as a function of the DOG_2 . The IEC increased with the DOG_2 , and reached the maximum value of 2.8 meq/g. Our future work is to investigate the structures and various

properties of these RIGP/ATRP PEMs.

References

- 1) S. Sawada et al., JAEA Takasaki Annu. Rep. 2011 (2013) 34.
- 2) S. Holmberg et al., J. Polym. Sci.: Part A: Polym. Chem. 40 (2002) 591.

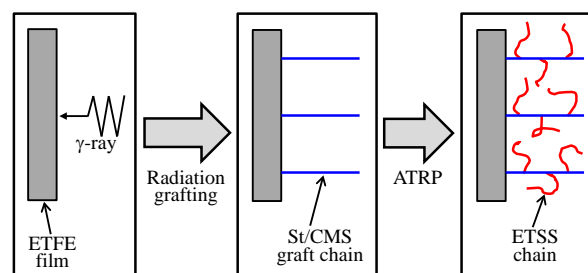


Fig. 1 Scheme of radiation grafting of St/CMS and ATRP of ETSS into a base polymer film.

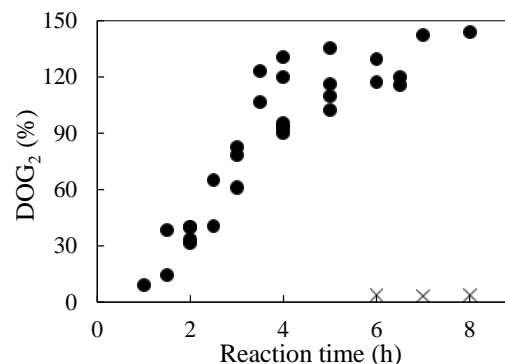


Fig. 2 DOG_2 as a function of the reaction time in the ATRP at 50 °C. The monomer solutions contained (●) 0.04 M CuBr and 0.08 M PMDETA and (×) no CuBr and PMDETA.

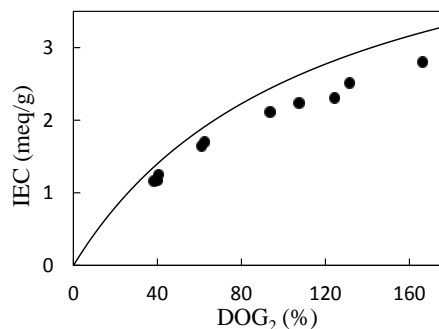


Fig. 3 IEC as a function of the DOG_2 . The solid curve is based on the assumption that all the ETSS units are hydrolyzed.

1 - 43

Preparation of Platinum Nanoparticle Catalysts for Fuel Cell Applications by Ion Implantation

S. Kato^{a,b)}, T. Yamaki^{b)}, S. Yamamoto^{b)}, T. Hakoda^{b)}, K. Kawaguchi^{b,c)},
T. Kobayashi^{d)}, Y. Maekawa^{b)}, A. Suzuki^{a)} and T. Terai^{a)}

^{a)}Department of Nuclear Engineering and Management, The University of Tokyo,

^{b)}Environment and Industrial Materials Research Division, QuBS, JAEA,

^{c)}Department of Chemistry and Materials Technology, Kyoto Institute of Technology,

^{d)}Atomic Physics Laboratory, Advanced Science Institute, RIKEN

Syntheses of platinum (Pt) nanoparticles have been intensively studied for their application to polymer electrolyte fuel cells (PEFCs), in which a sluggish oxygen reduction reaction (ORR) on a cathode is one of the biggest issues. In this research, Pt nanoparticles were prepared by ion implantation in glassy carbon (GC) substrates for the first time^{1,2)}. We expect that ion implantation and the subsequent thermal treatment can achieve efficient growth of the particles leading to high-performance catalysts with less amount of expensive noble metal. This report describes our preparation procedure and morphological properties of the formed Pt particles.

Figure 1 shows the preparation procedure involving Pt⁺ implantation in a mirror polished GC substrate followed by electrochemical etching and thermal treatment. The implantation of 100 keV Pt⁺ was performed at nominal fluences up to 4×10^{16} ions/cm² in an IA1 chamber at the TIARA 400-kV ion implanter^{1,2)}. The depth profiles of the implanted Pt were estimated by Rutherford backscattering spectra with 2 MeV He⁺ from the TIARA 3-MV single-ended accelerator. The Pt concentration maximum was found at a depth of ca. 35 nm.

The electrochemical etching made the embedded Pt exposed on the surface so that it could function as PEFC catalyst. The surface carbon layer was electrochemically

etched by anodization in a 0.1 M NaOH aqueous solution³⁾. In our experiment, the etching rate was estimated to be 50 nm/min. Finally, the Pt atoms on the surface would be agglomerated during the thermal treatment at 400 °C in a N₂ atmosphere to form particles.

Figure 2 shows a surface field emission-scanning electron microscope (FE-SEM) image of the Pt-implanted GC after the electrochemical etching and thermal treatment. The bright-dot structures were clearly observed throughout the entire image; importantly, these were not observed in an unimplanted GC. Therefore, we can attribute them to the resulting Pt nanoparticles. Their diameters were mostly a few tens of nanometers. Electrochemical analysis in an acidic solution is now in progress. The cyclic voltammogram⁴⁾ exhibited characteristic peaks due to hydrogen adsorption/desorption onto a metal-Pt surface. The ORR activity was found as saturation current in a hydrodynamic voltammogram using a rotating disk electrode system⁵⁾.

References

- 1) S. Kato et al., Trans. Mat. Res. Soc. Jpn. 38 (2013) 81.
- 2) S. Kato et al., Nucl. Instrum. Meth. Phys. Res. B (2013) in press.
- 3) G.K. Kiema et al., J. Electrochem. Soc. 151 (2004) C142.
- 4) T. Yamaki et al., Mater. Res. Soc. Symp. Proc. 1217 (2010) 151.
- 5) T. Hakoda et al., Appl. Surf. Sci. 257 (2010) 1556.

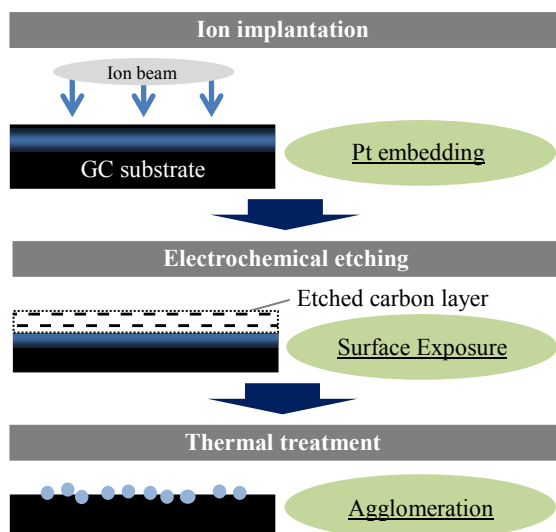


Fig. 1 Schematic drawing of catalyst nanoparticle synthesis by using ion implantation.

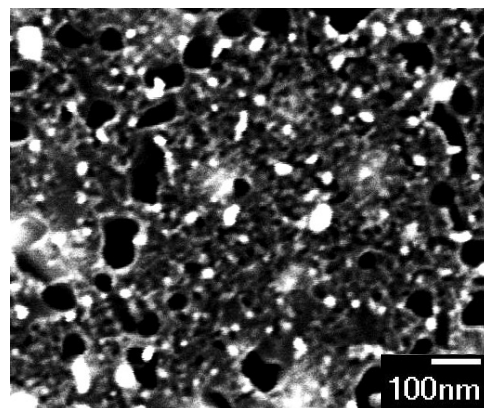


Fig. 2 Surface FE-SEM image of the Pt implanted GC substrate after the electrochemical etching and thermal treatment.

1 - 44

Ion Content of Ion Exchange Membrane in HI-I₂-H₂O Mixture

N. Tanaka^{a,b)}, T. Yamaki^{c)}, M. Asano^{c)}, T. Terai^{b)} and K. Onuki^{a)}

^{a)}Hydrogen Application Research and Development Division, NHARC, JAEA,

^{b)}Department of Nuclear Engineering and Management, The University of Tokyo,

^{c)}Environment and Industrial Materials Research Division, QuBS, JAEA

JAEA has been conducting R&D on a hydrogen production thermochemical water-splitting Iodine-Sulfur (IS) process as a heat utilization system using HTGR (High Temperature Gas-cooled Reactor)¹⁾. In the IS process, a new cation-exchange membrane using the radiation-induced graft polymerization method has been applied to the electro-electrodialysis (EED) in order to enhance the hydrogen iodide (HI) in HI-I₂-H₂O mixture (HIx solution)^{2,3)}. An EED model⁴⁾ for membrane permeation mechanism claimed that the ion contents of the ion-exchange membrane immersed in the HIx solution were important factors for the optimized membrane design. In this paper, the I⁻ content of the HIx solution absorbed in a styrene-grafted poly(ethylene-co-tetrafluoroethylene) (ETFE-St) membrane and Nafion 212 was experimentally evaluated.

The determination of constitutions in the evaluated membranes for HIx solution absorption was performed as follows: the ETFE-St membranes (ion exchange capacity (IEC): 1.1, 1.4, and 1.6 mmol/g) prepared by the radiation-grafting method²⁾ and Nafion 212 (Du Pont, IEC: 0.86 mmol/g) were used. The membranes dried for at least 24 h in a vacuum oven at 313 K. Each membrane was immersed in the HIx solution for 4 h at 313 K. The HI molality of the immersed HIx solution was varied as: 1, 4, 7, 10, 12, 13, or 15 mol/kg while the molar ratio of I₂ to HI was fixed at 1. The membrane was then removed from the immersed solution and placed into an aqueous 0.5 mol/L KI solution at 313 K for 1 h for extracting H⁺ and I₂. The resulting solution was titrated; the H⁺ content could be determined from the NaOH titration, and the I₂ content was determined from iodometry. The I⁻ content corresponds to the difference between the H⁺ content and IEC.

Figure 1 shows the variation of I⁻ content as a function of HI molality in the immersed HIx solution. The content (y-axis) was normalized by IEC, thereby enabling us to evaluate the I⁻ content per unit sulfonate group in the membrane. The respective ETFE-St membranes exhibited a same level of I⁻/IEC ratio. The I⁻ content of the ETFE-St membranes increased with an increase in HI molality up to 7 mol/kg and then leveled off, whereas the I⁻ absorption of Nafion 212 was minimal, irrespective of HI molality.

The noticeable difference between the evaluated membranes would be ascribed to the I₂ absorption of membranes. Figure 2 plots the I₂ content per unit IEC of membranes as a function of HI molality in the immersed HIx solution. The I₂ content of ETFE-St membranes steadily increase with an increase in HI molality, whereas

the I₂ absorption of Nafion 212 was hardly observed. The difference between membranes was explained by the difference of the affinity of membranes for I₂: the strong affinity of the ETFE-St membranes was attributed to the formation of the charge-transfer complex between I₂ and the St species, which was precluded in Nafion 212⁴⁾. In addition, I₂ was known to form the I₃⁻ complex, which indicates that I⁻ in the ETFE-St membranes that can accumulate plentiful I₂ could be stabilized as I₃⁻ complex in comparison with Nafion 212.

References

- 1) S. Kubo et al., Nucl. Eng. Des. 233 (2004) 355.
- 2) N. Tanaka et al., J. Membr. Sci. 346 (2010) 136.
- 3) T. Yamaki et al., Polymer 45 (2004) 6569.
- 4) N. Tanaka et al., J. Membr. Sci. 411-412 (2012) 99.

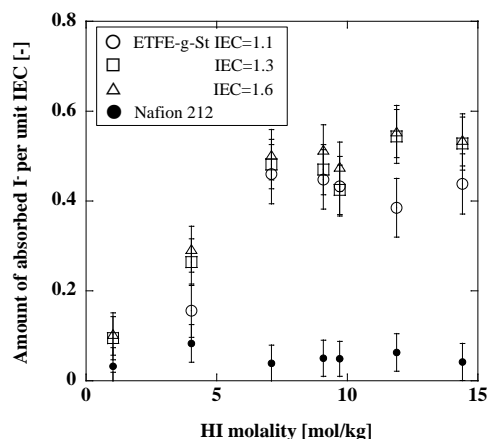


Fig. 1 HI molality dependence of I⁻ content per unit IEC.

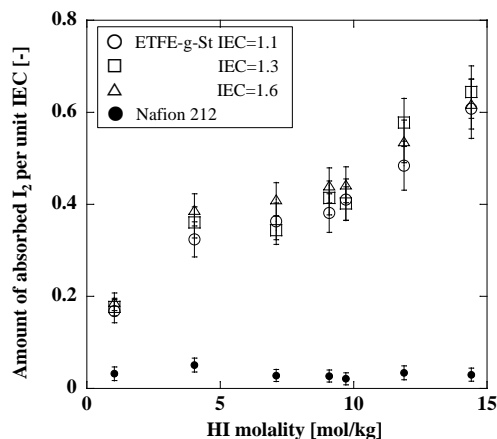


Fig. 2 HI molality dependence of I₂ content per unit IEC.

1 - 45 Applied-voltage Dependence on Conductometric Track Etching of Poly(vinylidene fluoride)

N. Nuryanthi^{a,b)}, T. Yamaki^{a)}, H. Koshikawa^{a)}, A. Kitamura (Ogawa)^{c)}, S. Sawada^{a)},
M. Asano^{a)}, S. Hasegawa^{a)}, Y. Maekawa^{a)} and Y. Katsumura^{b)}

^{a)}Environment and Industrial Materials Research Division, QuBS, JAEA,

^{b)}Department of Nuclear Engineering and Management, The University of Tokyo,

^{c)}Department of Advanced Radiation Technology, TARRI, JAEA

Our efforts have been focused on ion-track etched membranes of poly(vinylidene fluoride) (PVDF)¹⁻³⁾. In order to monitor the chemical development of heavy-ion tracks, we have performed conductometric track etching, in which the electrical conductance through the membrane is analyzed during the course of etching. Fortunately, this etching/analysis method gave us another option for investigating the etching behavior, that is, the effect of the voltage level applied to a conductometric cell. Our first experiments in this regard using surface scanning electron micrograph (SEM) observations demonstrated that the etching under the voltage application led to larger pore diameters than that without the applied voltage^{4,5)}. We examined here the influence of the applied voltage on the etching characteristics of heavy-ion-irradiated PVDF films, using the parameters extracted directly from the conductometric curves⁶⁾.

A PVDF film 25 μm in thickness was irradiated with 450 MeV ^{129}Xe ions at a fixed fluence of 3×10^7 ions/ cm^2 . The irradiation was performed in a vacuum chamber of the LD beamline at the TIARA cyclotron. The chemical etching was then performed in a 9 mol dm^{-3} KOH aqueous solution at 80 $^{\circ}\text{C}$ in a conductometric cell. A 1 kHz AC voltage was applied at an amplitude ranging from 0.1 to 3.0 V between the Pt electrodes. Assuming the cylindrical pores, we calculated the effective pore diameter, d_{eff} , at any given time from the measured conductance.

Figure 1 shows a curve of the d_{eff} value versus etching time. As clearly shown in an inset, the breakthrough time was approximately twice shorter at 3.0 V than at 0.1 V, meaning that a track etch rate increased by the same rate as the breakthrough time.

We employed moderate etching conditions, that is, a pure KOH aqueous solution without any oxidant additives, thereby evaluating the process of pore evolution and growth precisely¹⁻³⁾. The final stage of etching reached dissolution outside the latent track (i.e., bulk etching), where the d_{eff} did not appear to increase because of a negligibly-low bulk etch rate. In other words, the d_{eff} value in this stage can be regarded as representative of the completion of the etching process. Additionally, the etching time required to reach the final d_{eff} is extracted and defined as T_E .

The T_E value seemed to depend largely on the applied voltages although the final d_{eff} was constant at about 270 nm for all the curves. It was difficult for us to estimate the exact value of T_E by using the curves of Fig. 1, and so we

calculated the time derivative of d_{eff} , i.e., a radial etch rate. Toward the final etching stage, the radial etch rate decreased slowly and finally reached to zero; a period between the beginning of etching and this moment corresponds to T_E . We found that the T_E value was reduced by half with an increase in the applied voltage levels from 0.1 to 3.0 V. This reduction would result from the shortened breakthrough time followed by the enhanced pore growth represented by the higher radial etch rate. The observed promotional effects of the etching process can be rationalized by considering the electrophoretic migration of dissolved species in and out of each pore⁷⁾. Accordingly, conductometric etching under different voltage conditions offers the ability to control pore geometries by optimizing the etching process in the transverse direction as well as in the thickness direction.

References

- 1) N. Nuryanthi et al., *Electrochemistry* 78 (2010) 146.
- 2) T. Yamaki et al., *ECS Trans.* 35 (2011) 1.
- 3) T. Yamaki et al., *Trans. Mater. Res. Soc. Jpn.* 37 (2012) 223.
- 4) N. Nuryanthi et al., *JAEA Takasaki Annu. Rep.* 2011 (2013) 35.
- 5) N. Nuryanthi et al., *Trans. Mater. Res. Soc. Jpn.* 38 (2013) 105.
- 6) N. Nuryanthi et al., *Nucl. Instrum. Meth. Phys. Res. B* 314(2013)95.
- 7) T. W Cornelius et al., *Nucl. Instrum. Meth. Phys. Res. B* 265 (2007) 553.

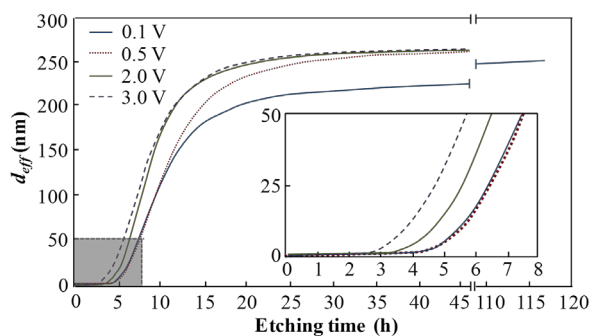


Fig. 1 Plot of the d_{eff} value as a function of etching time. Inset: an initial stage of etching for comparing the breakthrough time.

1 - 46

Microscopic Evaluation of the Absolute Fluence Distribution of an Ion Beam Using a Track Etching

A. Kitamura (Ogawa)^{a)}, T. Yamaki^{b)}, Y. Yuri^{a)}, S. Sawada^{b)} and T. Yuyama^{a)}

^{a)}Department of Advanced Radiation Technology, TARRI, JAEA,

^{b)}Environment and Industrial Materials Research Division, QuBS, JAEA

A uniform-beam formation/irradiation system using multipole magnets has been developed at TIARA¹⁾. For the evaluation of the beam uniformity, the relative intensity distribution is obtained from the optical density of a radiochromic film (Gafchromic HD-810, Ashland Inc.). However, the absolute fluence distribution is unknown since it cannot be estimated easily and precisely from the Gafchromic film. The actual fluence and its distribution would be crucial to beam applications in materials and biological research. In this study, the absolute particle fluence distribution was evaluated on the microscopic level using the track-etching technique, which involves the irradiation of a material with energetic heavy ions followed by preferential chemical etching of the ion tracks²⁾.

Polyethylene terephthalate (PET) films (25 μm in thickness) and Gafchromic films were irradiated in air with a 520-MeV ^{40}Ar uniform beam at TIARA. The kinetic energy on the surface of the sample was estimated to be approximately 330 MeV. The irradiated area was approximately $50 \times 50 \text{ mm}^2$ and the average fluence was $1.0 \times 10^8 \text{ ions/cm}^2$, which was estimated from the beam current, the irradiation time, and the coloration of the Gafchromic film. A perturbed, non-uniform beam with a different distribution was also employed for comparison. The irradiated PET films were etched in a 1 M NaOH aqueous solution at 80 $^\circ\text{C}$ for 10 min. After drying in a vacuum, the samples were equally divided into 64 sections of 6 mm square. The number of track-etched pores in the central region ($12 \times 17 \text{ }\mu\text{m}^2$) of each section was counted with a scanning electron microscope (SEM). The irradiated Gafchromic films were read using a flat-bed scanner in order to digitize them into TIFF images with 16-bit RGB color intensity values at a resolution of $500 \times 500 \text{ }\mu\text{m}^2$. The optical density d was determined from the red color value. A total of 64 square-grid optical densities were extracted at intervals of 6 mm from the original measured data so that the intensity distribution could be directly compared to that of the PET film. For both the track-etched PET and Gafchromic films, the uniformity of the intensity distribution was evaluated by taking the relative standard deviations (RSD) of the pore density and the d value over the 64 sections.

Figure 1 shows the absolute fluence distribution obtained from the microscopic track-pore densities of the PET film irradiated with the uniform Ar beam. The density was exactly the same as the absolute fluence, because the track-pores formed on the PET film were the evidence of the incident ions. It was found that the average track-pore

density for all the 64 sections was $0.9 \times 10^8 \text{ ions/cm}^2$, and the RSD of the distribution was 12%, which was in good agreement with the RSD obtained for the Gafchromic film despite the large difference in the observation resolution for the two films. From this result, it was revealed that for the uniform beam formed in the system used in this study, the uniformity observed in a microscopic region of $10^2 \text{ }\mu\text{m}^2$ was the same as that in a relatively macroscopic region of $10^5 \text{ }\mu\text{m}^2$.

The intensity distribution was also investigated using an intentionally perturbed non-uniform beam for verification with a different distribution. The average of the absolute fluence was estimated to be $0.9 \times 10^8 \text{ ions/cm}^2$. The maximum and minimum were $0.5 \times 10^8 \text{ ions/cm}^2$ and $1.6 \times 10^8 \text{ ions/cm}^2$, respectively. The RSD on the PET film deteriorated to 23%, which was again very close to that on the Gafchromic film (22%).

On the basis of these observations, the present microscopic technique for evaluating the beam intensity distribution using the track pores was statistically validated and confirmed to be highly reliable. Thus, the uniform intensity distribution was microscopically revealed in our uniform-beam formation system using the track-etching technique.

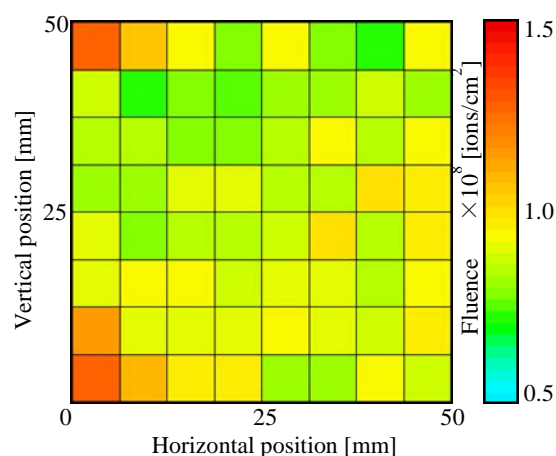


Fig. 1 Microscopic fluence distribution of the PET film irradiated with the uniform beam.

References

- 1) Y. Yuri et al., Nucl. Instrum. Meth. Phys. Res. A **642** (2011) 10-17.
- 2) A. Kitamura (Ogawa) et al, Nucl. Instrum. Meth. Phys. Res. B 314(2013)47.

2. Environmental Conservation and Resource Exploitation

2-01	Homogeneous Transesterification Kinetics of Triglyceride to Biodiesel Using Grafted Fibrous Catalyst	53
	Y. Ueki and N. Seko	
2-02	Effect of Initial Radical Concentration on Radiation-induced Graft Polymerization on Polyethylene Nonwoven Fabric	54
	S. Saiki, K. Okaya and N. Seko	
2-03	Development of the Water Purifier with Grafted Adsorbent for Cs Removal	55
	T. Shibata, N. Seko, N. Kasai, S. Saiki, A. Iwanade, H. Hoshina, Y. Ueki, M. Nakano and T. Mikami	
2-04	Development of a Grafted Filter for Radioactive Cesium	56
	M. Nakano, T. Mikami, T. Shibata, N. Kasai and N. Seko	
2-05	The Influence on the Vulcanized Rubber Physical Properties by Radiation Grafting	57
	H. Saito, N. Mizote, Y. Ueki and N. Seko	
2-06	Radiation-induced Crosslinking of Poly(butylene adipate-co-terephthalate)	58
	N. Nagasawa, M. Akaoka, M. Tamada, H. Mitomo and M. Taguchi	
2-07	Effect of Gamma-rays Irradiation on Concentrated Aqueous Solutions of BSA, DNA and Their Mixture	59
	H. Okamura, N. Nagasawa, K. Furusawa and T. Dobashi	
2-08	Treatment of Chlorinated Antibiotics by Oxidative/Reductive Species under Ionizing Radiation	60
	A. Kimura and M. Taguchi	
2-09	Immobilization of Denitrifying Bacteria to HPC Gel Medium Synthesized by EB Irradiation	61
	T. Yanagisawa, Y. Kamata, N. Nagasawa, M. Taguchi and T. Tanaka	

This is a blank page.

2 - 01 Homogeneous Transesterification Kinetics of Triglyceride to Biodiesel Using Grafted Fibrous Catalyst

Y. Ueki and N. Seko

Environment and Industrial Materials Research Division, QuBS, JAEA

Biodiesel fuel (BDF), which is defined as the monoalkyl ester of fatty acid derived from transesterification of triglyceride (TG) with alcohol, has been regarded as a promising alternative to petroleum diesel fuel because of its qualities such as carbon neutral, renewable and environment friendly resources. We succeeded in developing an efficient and productive fibrous catalyst for BDF production in previous study¹⁾. The objective of this study is to investigate the mechanism and kinetics of homogeneous transesterification using the grafted fibrous catalyst.

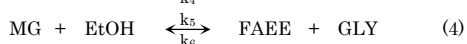
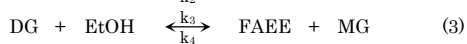
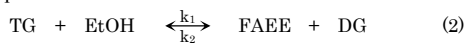
The grafted fibrous catalyst with 3.6 mmol-TMA/g-catalyst was used as a heterogeneous basic catalyst, and its catalytic performance was evaluated through the transesterification of triolein (purity: 60%) in ethanol (EtOH) with a cosolvent such as decane. The detailed preparation and batch-wise transesterification procedures are described in our previous paper¹⁾.

Generically, the transesterification of TG with EtOH using a basic catalyst consists of three consecutive reversible reactions. TG is converted stepwise to diglyceride (DG), monoglyceride (MG), and finally fatty acid ethyl ester (FAEE) and glycerol (GLY) as following equations:

Overall Reaction:



Stepwise Reactions:



where k_1 , k_3 , and k_5 are the forward rate constants and k_2 , k_4 , and k_6 are the reverse rate constants. Although many researchers have studied the kinetics of transesterification, the majority of numerical models were derived from the transesterification in a two-phase liquid system²⁾. On the other hand, in this paper, decane was used as a cosolvent in order to form a single-phase mixture and to accelerate transesterification. Therefore, the kinetic model of two-phase liquid system couldn't be applicable to the kinetic model of single-phase liquid system. In this batch-wise test, both DG and MG, which were intermediate products, weren't included in the crude triolein as well as during the transesterification. That is to say, the reverse reaction of Eq. (2) was not taken into account; the rate constant k_2 was considered negligible. Consequently, the reaction rate of TG could be defined as follows:

$$-r_{\text{TG}} = -\frac{d[\text{TG}]}{dt} = k_1[\text{TG}][\text{EtOH}] \quad (5)$$

where $-r_{\text{TG}}$ is the reaction rate (conversion rate) of TG and $[\text{TG}]$ and $[\text{EtOH}]$ are the concentration of TG and EtOH in a

reaction mixture.

If the homogeneous transesterification using the grafted fibrous catalyst is the irreversible second-order reaction with respect to TG, a straight line plot can be obtained by plotting the $\{1/([\text{EtOH}]_0 - [\text{TG}]_0) \times \ln([\text{TG}]_0[\text{EtOH}]/[\text{TG}][\text{EtOH}]_0)\}$ versus transesterification time, and the slope of the line is equal to the rate constant k_1 . As shown in Fig. 1, it was indicated that this homogeneous transesterification using the grafted fibrous catalyst was an irreversible second-order reaction with respect to TG, because of its linearity. The rate constant k_1 of the grafted fibrous catalyst and DIAION PA306S were estimated to be 0.1194 and 0.0463 L/mol h, respectively. The rate constant k_1 of the grafted fibrous catalyst reached 2.5 times higher than that of DIAION PA306S, although the same quaternized amine groups (TMA-type) were introduced onto the surface of catalytic materials. Furthermore, the linearity of the plot of the grafted fibrous catalyst was maintained until finishing transesterification almost completely. On the other hand, the slope of DIAION PA306S was non-linear (curved), and the value of y-axis was gradually decreased with the lapse of transesterification time. This difference in the rate constant k_1 was thought to be due to the difference in the reactant-transfer mechanism of each catalyst. Briefly, in the case of the grafted fibrous catalyst, the reactants could be easily and immediately transported to the functional groups by convective flow. Whereas, in the case of the granular resin, the most functional groups of the granular resin were immobilized onto the micropores, and the reactants were slowly transported to the functional groups by diffusion.

References

- 1) Y. Ueki et al., Int. J. Org. Chem. **1**(2) (2011) 20-25.
- 2) H. Nouredini et al., J. Am. Oil Chem. Soc. **74** (1997) 1457-63.

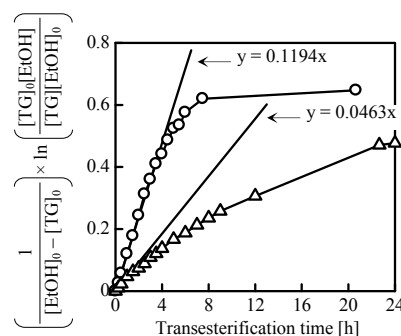


Fig. 1 Relationship between reactant concentration and transesterification time.

○: grafted fibrous catalyst, △: Granular resin.

2 - 02

Effect of Initial Radical Concentration on Radiation-induced Graft Polymerization on Polyethylene Nonwoven Fabric

S. Saiki^{a)}, K. Okaya^{a,b)} and N. Seko^{a)}^{a)}Environment and Industrial Materials Research Division, QuBS, JAEA,^{b)}Graduate School of Engineering, The University of Tokyo

Radiation-induced graft polymerization has been applied for many fields, for example heavy metal ion adsorbent, deodorant and surface modification and so on. Especially for industrial manufacture pre-irradiation method, which separates the synthetic procedure of graft adsorbents into irradiation process and grafting process, is often adopted because homo-polymer is little produced and these processes can be conducted at different places. Between irradiation and grafting process for pre-irradiation method, irradiated trunk polymers should be kept at low temperature not to diminish radicals produced in the trunk polymer. It has been already known that the radicals in irradiated trunk polymers inactivate gradually at high temperature and that the amount of radicals has a large effect on the degree of grafting.

In this study, focusing on polyethylene nonwoven fabric as a model of trunk polymer, the radical decay kinetics in the irradiated trunk polymer were studied by ESR method, and compared with the results of grafting experiments to show the guideline for sample preservation at radiation grafting.

A few pieces of nonwoven fabric cut into 3 mm×3 cm for ESR measurements and 2 cm square for grafting experiments, were irradiated with a dose of 50 kGy by an electron beam in polyethylene bags purged by nitrogen gas and were kept in constant temperature unit at 20 °C. ESR spectra of the samples after keeping for given time were measured by ESR method (JEOL JES-TE300, Modulation width 0.1 mT, Time constant 0.1 s, Sweep time 2 min, Power 10 μW). Radiation grafting was conducted in a monomer solution prepared by mixing glycidyl methacrylate (GMA), water, and Tween 80 at 333 K for 2 h by putting into a water bath. The resulting sample was dried under reduced pressure and weighed.

As a result of ESR measurements, ESR spectrum of irradiated polyethylene nonwoven fabric were identified as alkyl radicals of polyethylene¹⁾. These spectra were decayed as storage time in the air at 20 °C in Fig. 1. The radical decay in polyethylene has ever been interpreted as first-order decay, second-order decay and so on²⁾. However, the radical decay of our results didn't obey first-order decay and either second-order decay, but obeyed the sum of two different pseudo-first order decays as a following equation in Fig. 2;

$$y = y_0 \{a \exp(-k_1 t) + (1-a) \exp(-k_2 t)\} \quad (1)$$

The results of grafting experiments showed the same tendency as the radical decays that the degree of grafting

decreased with the storage time. Compared with the result of the amount of radicals and grafting experiments, these values were one-to-one relation. This means that the degree of grafting can be calculated by the storage time and eq. (1) in the case of the same preserving condition and grafting procedure. From this experiment results and calculation, up to 32 h the polyethylene nonwoven fabric can be kept at 20 °C in the air to obtain 100% of the degree of grafting.

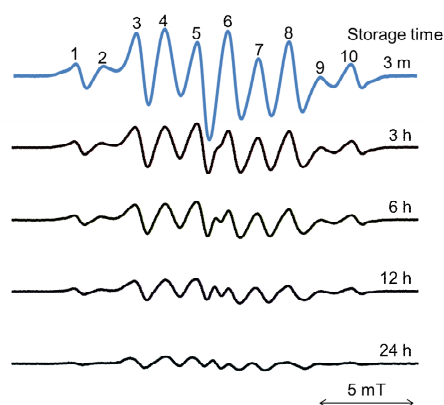


Fig. 1 The decay of alkyl radical of polyethylene as storage time.

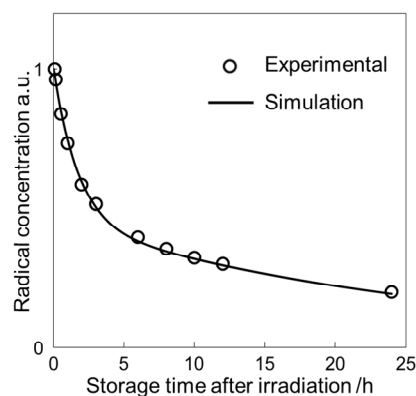


Fig. 2 Radical decay (Experimental) and simulation curve by the sum of 2 pseudo-first order decay (Simulation) at 20 °C with the dose of 50 kGy.

References

- 1) S. Shimada et al., Jpn. J. Appl. Phys., 8 (1969) 145.
- 2) D. C. Waterman et al., J. Phys. Chem., 74 (1970) 1913.

2 - 03

Development of the Water Purifier with Grafted Adsorbent for Cs Removal

T. Shibata^{a)}, N. Seko^{a)}, N. Kasai^{a)}, S. Saiki^{a)}, A. Iwanade^{a)}, H. Hoshina^{a)},
Y. Ueki^{a)}, M. Nakano^{b)} and T. Mikami^{b)}

^{a)}Environment and Industrial Materials Research Division, QuBS, JAEA,

^{b)}Kurashiki Textile Manufacturing. Co., Ltd.

Although more than two years has elapsed since the accident of the Fukushima Daiichi Nuclear Power Plant, the decontamination activity has been carried out presently. The region except the on-site, radioisotopes such as ¹³⁴Cs, ¹³⁷Cs and etc. in environment water has been low concentration. However, results of monitoring investigation of drinking water in Fukushima, which resource is well water and stream water, showed ¹³⁷Cs was detected 6 of 436 samples¹⁾. Therefore, securing safety life water is demand.

We have developed immediately a grafted adsorbent for removing Cs just after this accident²⁾. This adsorbent has sufficient results to remove radioactive Cs in the environmental water almost completely. However, ammonium 12-molybdophosphate (AMP) which introduces as the adsorbent functional group releases easily. It is not problems because there is not standard of Mo for wastewater treatment and environment. In the case of applying it to drinking water, it becomes potential impediments. In this study, the improvement of adsorbent by introducing bridge structure for hardly to elute AMP was developed. Introducing bridge structure was investigated by adding crosslinking reagent to a monomer as follows.

The adsorbent was synthesized by the following procedure; nonwoven fabric irradiated with an electron beam of 50 kGy was grafted in a monomer composed 10 wt% of glycidyl methacrylate (GMA), 90 wt% of dimethyl sulfoxide (DMSO), 0.8 wt % of Tween 80, 0.4 mol%/GMA of AMP and from 1 to 10 mol%/GMA of polyethylene glycol dimethacrylate (4G, 9G or 14G) or triallyl isocyanurate (TAIC) as the crosslinking reagent.

The efficiency of synthesized adsorbent was investigated by batch experiment, in which it cut into 1 cm² (0.02 g) was immersed in 50 mL of 50 ppb Cs solution and stirred for 24 h. Figure 1 shows the results of batch experiment of each adsorbent. It was clarified that amount of eluted Mo from adsorbents introduced with bridge structure was less than that without the bridge structure. Further, amount of adsorbed Cs of most adsorbents introduced with bridge structure was more than that without the bridge structure, and some of adsorption rate were over than 97%.

As the results of investigation by the external organization, this adsorbent developed satisfies the food sanitation law and the water supply law. Figure 2 shows the water purifier manufactured. The original cartridge was replaced with incorporated adsorbent developed. Monitoring test of the developed adsorbent attached to

faucets of common household has been carried out in Fukushima, in which natural water like well water and stream water is used for life water because there is not public water service, with the cooperation of the public office for one year from March 2013.

References

- 1) Ministry of the Environment (2012) in press.
(<http://www.env.go.jp/press/press.php?serial=15678>).
- 2) A. Iwanade et al., J. Radioanal. Nucl. Chem. 293 (2012) 703-9.

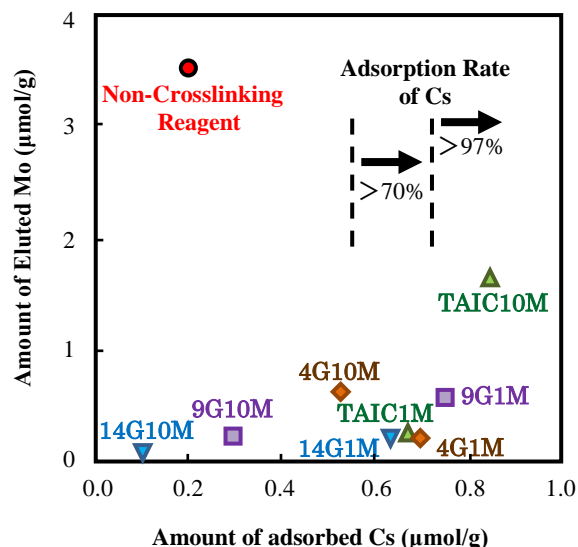


Fig. 1 Results of adsorption and elution in batch experiment. The notation in a figure shows name of crosslinking reagent and amount of addition of it.

ex.)

9G 1M

Name of crosslinking
reagent

Amount of addition
(mol%/GMA)

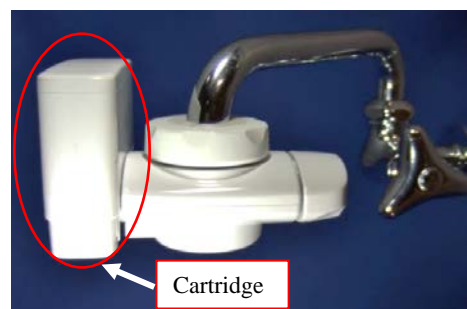


Fig. 2 The photograph of water purifier incorporated graft polymerization adsorbent.

2 - 04 Development of a Grafted Filter for Radioactive Cesium

M. Nakano^{a)}, T. Mikami^{a)}, T. Shibata^{b)}, N. Kasai^{b)} and N. Seko^{b)}

^{a)}Kurashiki Textile Manufacturing. Co., Ltd.,

^{b)}Environment and Industrial Materials Research Division, QuBS, JAEA

The filtration media to remove radioactive cesium in water has been developed by radiation graft polymerization technology. In this study, ammonium phosphomolybdate having cesium adsorptivity is grafted onto nonwoven fabrics to be the filtration media, and the media can rapidly adsorb cesium ion from water. The performance is featured particularly when applied to purification at extremely low concentration and it could adsorb down to the detection limit concentration (< 10 Bq/L). Based on these results, a water purifier with the grafted filter was developed, and monitoring test of it has been carried out for one year in Fukushima.

現在、広範に飛散した放射性物質を除染する復旧作業が進められ、警戒区域から避難指示解除準備区域や居住制限区域などに変更される地域が増えてきている。これらの区域では、生活(宿泊)はできないものの、帰宅のための片付けや修繕などが許可されており、清掃用などの生活用水の確保が重要となっている。また、既に解除された区域においても、安心した水の供給が求められている状況にある。そこで、放射線グラフト重合技術を活用して、極微量で水中に溶存するセシウムイオンを高効率に捕集可能な除染材料を開発し、浄水器用のフィルターとして適応した成果について報告する。

除染材料(捕集材)は、操作性や加工性が良く、作業の前後で2次の汚染が発生しない材料が望まれるため、これらの要素を満たす既存の高分子材料にセシウムを捕集可能な機能を付与した。捕集材の合成では、高分子基材の不織布繊維に窒素雰囲気下で電子線を50 kGy照射し、次いで、モノマーとしてグリシジルメタクリレート(GMA)をグラフト重合させた。モノマー溶液は、GMA 10 wt%にリンモリブデン酸アンモニウム(AMP)を0.4 mol%-GMAを加えたものに架橋剤としてのトリアリルイソシアヌレート(TAIC) 5 mol%-GMAを加えて調整し、40 °Cで2時間反応させ、目的物を得た。

作製した放射性セシウム捕集材料の評価は、80 Bq/Lの放射性セシウムが検出された井戸水を0.45 µm及び0.1 µm径の市販濾過膜と市販のアニオン及びカチオンタイプのイオン交換ろ紙で処理を行い除去できずに残存した56 Bq/Lのセシウムが溶存している井戸水を対象にして進めた。吸着除去性能は、セシウムとの接触状態が異なるバッチ吸着試験とカラム吸着試験を行い、処理前後のセシウム濃度を測定して評価した。バッチ吸着試験では、円形(φ35 mm, 0.18 g)に切り出した捕集材を井戸水を採取したポリ瓶に投入し、17時間浸漬攪拌を行った。また、カラム吸着試験ではφ9 mmに切り出した捕集材1.3 mLをカラムに見立てた注射器に充填し、井戸水を吸引して捕集材に接触させた(Fig. 1)。その結果、バッチ吸着試験では、17時間接触後の井戸水中にはセシウムは検出されなかった。また、カラム吸着試験においても、バッチ吸着試験に比較して約4倍量の井戸水を通液し、使用した捕集材量が約1/2、接触時間は約1/100であったにもかかわらず、検出限界値以下まで除去することができた(Table 1)。これは、開発したグラフト捕集材が、短時間で高効率にセシウムを除去できることを示している。そこで、これらの利点を特徴付けた水処理用の製品として家庭用浄水器の製作に展開した。浄

水器として活用するためには、部材からの滲出物を検査する食品衛生法と水質基準を満たす水道法の規制に従う必要がある。開発した捕集材は強固にAMPを固定できていることが確認でき、また、基材の不織布繊維からの滲出も規制値以下であることを確認した後、浄水器に組み込むためのカートリッジの製作に着手した。カートリッジは、既に汎用品として使用されている家庭用浄水器のハウジングを利用し、単にカートリッジ部分に開発した捕集材を充填するだけで使用を可能にしたので、安価で操作性の良い浄水器として製作することができた(Fig. 2)。

開発した浄水器は、現在福島県内でモニター試験を実施中であり、定期的に交換し、放射性セシウムの捕集状態などを確認した後、最終的な商品の販売を目指している。



Fig. 1 The batch mode adsorption test (left: Test 1) and column model test (right: Test 2).

Table 1 Results of adsorption test for Cs removal.

	Conc. of radioactive Cs ion (Bq/L)
Well water sample	88.0
Test 1 (batch)	N.D.
Test 2 (column mode)	N.D.



Fig. 2 The photograph of water purifier.

2 - 05 The Influence on the Vulcanized Rubber Physical Properties by Radiation Grafting

H. Saito^{a)}, N. Mizote^{a)}, Y. Ueki^{b)} and N. Seko^{b)}

^{a)}Mitsuba Corporation,

^{b)}Environment and Industrial Materials Research Division, QuBS, JAEA

In this study, a hydrophilic monomer, namely, methacrylic acid (MAA) was grafted on vulcanized rubber surface by simultaneous electron beam irradiation. With the surface-modified rubber, we measured the abrasive wear resistance, mechanical characteristic and thermal resistance, and found that the mechanical characteristic and thermal resistance decreased compared to the initial rubber. There is little difference in initial rubber and grafted rubber, when degree of grafting is equal to or lower than 2%.

我々はこれまでに放射線グラフト重合法を用いて、ゴムの表面改質に関する研究に取り組み、摩擦変動が少なく、かつ耐摩耗性に優れた新規表面改質ゴムの開発に成功した。さらにある条件下においては表面改質ゴムの摩擦が初期に対して 1/30 にまで低減する程の特異的な水潤滑摩擦特性を見出した¹⁾。本研究では、特異的な摩擦傾向を示す新規水潤滑ゴムの機械的特性について確認した。

ゴム基材にはカーボンブラックを配合した NBR シートを用いた。そのシートにメタクリル酸 (MAA) を接触させた後、加速電圧 2 MV、電流値 1 mA、照射線量 5~15 kGy の条件で電子線同時照射グラフト重合を行った。次いで、水酸化カリウムでアルカリ処理を行い、目的とする表面改質親水性ゴムシートを得た。得られたゴムシートを用いて、耐摩耗性試験、Wet condition での破断強度測定試験、永久歪試験を実施した。

Figure 1 は MSE (Micro Slurry Erosion) 法による耐摩耗性評価を示したものである。本試験は 1 μm のアルミナ粒子を水と混合させた状態で噴射させた時の摩耗深さにて評価している。グラフト処理品は水存在下で低摩擦化すると同時に軟化傾向を示す。ピンオンディスク試験では低摩擦化の影響で軟化している処理品の方が耐摩耗性は高かった¹⁾ のに対して、本試験では材料強さが摩耗量に直結するため処理後の方が耐摩耗性は低かった。この結果は摩耗のさせ方により、結果は大きく変わることを示している。

Figure 2 はグラフト率と破断強度の関係について示したものである。Wet condition での破断強度について注目するとグラフト率 2% 程度までは初期の値と同等であるが、2% を境目に急激に低下している。これは Wet では軟化傾向を示

し、グラフト率の増加に伴い、表面粗度の上昇があいまって、発生した窪み同士がつながっていく形でクラックが進展していく為、急激に低下すると推察される。

Figure 3 はグラフト率と永久歪の関係について示したものである。グラフト率の増加と共に永久歪は低下しているが、グラフト率 2% 程度までは初期の水準を維持していた。

以上の結果よりグラフト率 2% 程度までであれば、破断強度や永久歪といったゴムの物性に影響を及ぼさないことが確認された。

Reference

- 1) H. Saito et al., JAEA Takasaki Annu. Rep. 2011 (2013) 45.

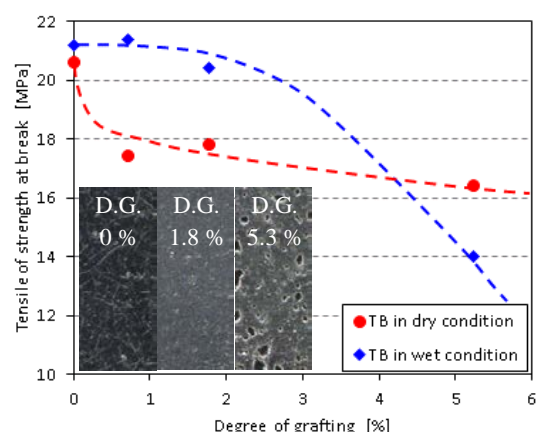


Fig. 2 Relationship between the degree of grafting and the tensile of strength at break.

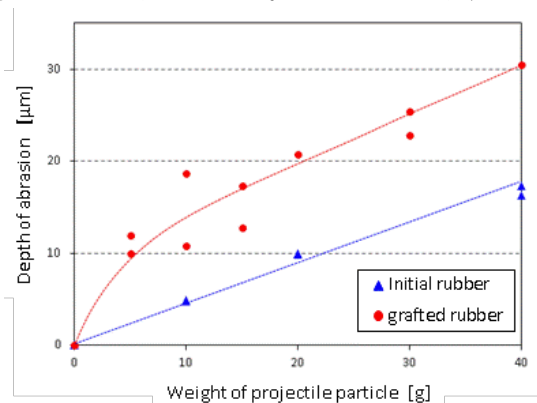


Fig. 1 Relationship between the weight of projectile particle and the depth of abrasion.

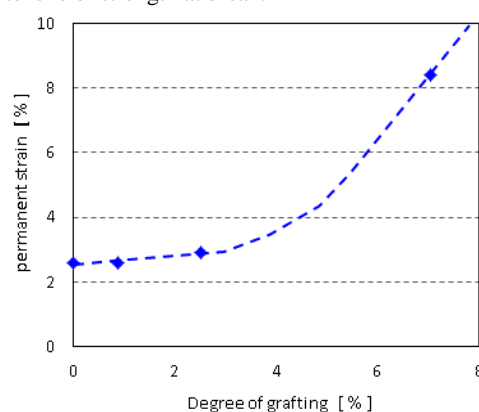


Fig. 3 Relationship between the degree of grafting and the permanent strain.

2 - 06

Radiation-induced Crosslinking of
Poly(butylene adipate-co-terephthalate)N. Nagasawa^{a)}, M. Akaoka^{b)}, M. Tamada^{a)}, H. Mitomo^{b)} and M. Taguchi^{a)}^{a)}Environment and Industrial Materials Research Division, QuBS, JAEA,^{b)}Faculty of Engineering, Gunma University

Poly (butylene adipate-co-terephthalate) (PBAT) synthesized by polycondensation is a completely biodegradable aliphatic and aromatic polyester. PBAT is decomposed into harmless water and carbon dioxide by microorganisms in the soil. Therefore, PBAT is expected to be utilized for applications in trash bags and disposable packages. The high thermal stability is, however, necessary for expanding their applications.

Radiation-induced crosslinking is an effective method for improvement of heat stability of polymer materials. Therefore, this technique was applied to produce the crosslinked poly(L-lactic acid) PLLA and polyamide11 (PA11) with crosslinking agent, triallyl isocyanurate (TAIC)^{1,2)}. To improve the thermal stability, radiation effect on crosslinking of PBAT with TAIC was investigated.

PBAT and TAIC were supplied by BASF Japan Ltd., and Nippon Kasei Chemical Co, Ltd., Japan, respectively. PBAT was dried in vacuum at 40 °C for 12 h before use in the experiments. PBAT was mixed at different concentrations of TAIC at 180 °C for 10 min in a Laboplastomill model 50C150 (Toyo Seiki Seisaku-sho, Ltd., Japan) at a rotor speed of 60 rpm. The PBAT films with and without TAIC were prepared by hot-pressing at 180 °C for 5 min. The films were enclosed in polythene-nylon bags and vacuum-sealed and irradiated at different doses up to 200 kGy with an electron beam (EB) accelerator. The acceleration energy and beam current were 2 MeV and 2 mA, respectively.

The gel content was estimated by weighing insoluble part

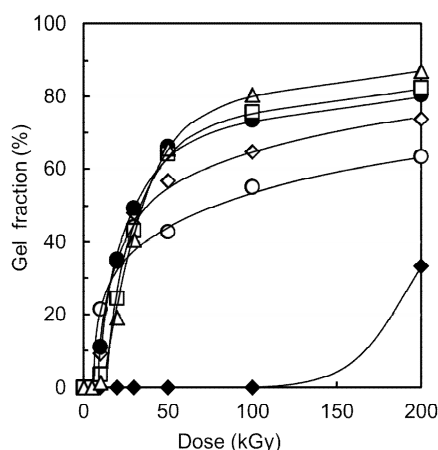


Fig. 1 Relationship between irradiation dose and gel fraction of PBAT films with various concentration of TAIC. ◆:TAIC 0 wt%, ○:TAIC 0.5 wt%, ◇:TAIC 1.0 wt%, ●: TAIC 2.0 wt%, □: TAIC 3.0 wt%, △:TAIC 5.0 wt%.

of the crosslinked PBAT film after immersion in chloroform for 48 h. The crosslinking structures are formed in PBAT films without TAIC (0 wt%) irradiated at 200 kGy. However, in the presence of TAIC, gel fraction of the films represented to the crosslinking density increased with TAIC content and radiation dose as shown in Fig. 1. Gelation of the irradiated PBAT with TAIC is higher than that of PBAT without TAIC at the investigated dose range from 10 to 200 kGy, indicating that the crosslinking structures are effectively formed with TAIC. The thermal stability of the crosslinked PBAT films was estimated by a thermo-mechanical analyzer (TMA). The crosslinked PBAT films have excellent properties as demonstrated by retention of original shape even at temperatures higher than melting point (115 °C) as shown in Fig. 2. The biodegradability, which was estimated by enzyme test using Lipase AK (incubation at 55 °C, pH 7.0), of the crosslinked PBAT film was similar to that of non-irradiated one. As a result, the crosslinked PBAT after usage would undergo biodegradation by naturally existing microorganisms. Therefore, the crosslinked PBAT with TAIC by EB-irradiation was found to be thermally stable and keep biodegradation enough for expanding applications.

References

- 1) N. Nagasawa et al., Nucl. Instrum. Meth. Phys. Res. B **236** (2005) 611.
- 2) T. Tago et al., JAEA Takasaki Annu. Rep. 2011 (2013) 48.

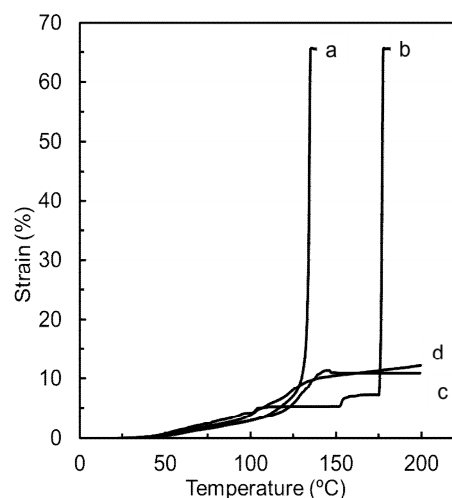


Fig. 2 TMA heating curves of PBAT film with 3.0 wt% TAIC after EB-irradiation under the vacuum. a) 0 kGy, b) 30 kGy, c) 50 kGy, d) 100 kGy.

2 - 07 Effect of Gamma-rays Irradiation on Concentrated Aqueous Solutions of BSA, DNA and Their Mixture

H. Okamura^{a)}, N. Nagasawa^{b)}, K. Furusawa^{c)} and T. Dobashi^{a)}

^{a)}Department of Chemistry and Chemical Biology, Graduate School of Science and Technology, Gunma University,

^{b)}Environment and Industrial Materials Research Division, QuBS, JAEA,

^{c)}Faculty of Advanced Life Science, Hokkaido University

We have prepared BSA (bovine serum albumin) - DNA gel particles using gamma-rays irradiation in aqueous concentrated solutions of DNA and BSA mixture. The turbid and UV absorption suggest formation of nano-sized particles by irradiation in aqueous solutions of BSA and BSA-DNA mixture.

ナノサイズのカプセルや粒子は、がんや感染症などの薬物治療において、薬物輸送担体としての利用が期待されている。このような材料に必要とされる条件として、生体にとって有害でないこと、高い安定性を持つことなどが挙げられる。ナノサイズの微粒子作製方法の一つとして、ゼラチン希薄水溶液に γ 線を照射することによりナノゲルが形成されることが報告されている¹⁾。このゼラチンナノゲルの形成は 1.0×10^{-3} wt%と、かなり希薄な水溶液で行われているため、生産効率が低い。工業的に応用する場合には、より高濃度でナノゲルを形成できるような系の構築が望ましい。一方、他の生体高分子でもこのようなナノゲルを形成するかどうかは、多様な機能を有するナノゲルの作製という観点から大変興味深い。そこで、本研究では、生体高分子として、様々な応用が期待できる牛血清アルブミン(BSA)とDNAの水溶液、それらの混合水溶液に対する γ 線の照射効果について調べた。

BSA (Cohn Fraction V, pH=7.0, 和光純薬) の 1 wt% 水溶液と、サケ白子由来 DNA (Mw=259 kDa, マルハニチロ) の 0.1 wt% 水溶液を等量混合し、BSA/DNA 混合水溶液を調製した。この混合水溶液に線量率 10 kGy/h、線量 5 ~ 20 kGy の範囲で ⁶⁰Co- γ 線で照射を行った。また、比較対照として 1 wt% BSA 水溶液と 0.1 wt% DNA 水溶液を調製し、同様の条件で照射を行った。照射試料について目視観察するとともに、紫外吸収スペクトルの測定を行った。

Figure 1(a) ~ (c) は γ 線照射後の各水溶液の写真である。(a) の BSA 水溶液では、15 kGy 以上で白濁化が観察されたが長時間静置しても沈殿することはなかった。このことはナノサイズの安定な構造が形成されたことを示唆する。一方、(b) の DNA 水溶液では目視による変化は見られなかった。(c) の DNA と BSA を混合した水溶液では、同じ線量で照射した BSA 水溶液よりも低い吸収線量で白濁化することがわかった。 γ 線照射によって白濁した試料は、孔径 220 nm のメンブレンフィルターでろ過してもすべて白濁したままであった。このことは、220 nm よりも小さな大きさの微粒子が形成されていることを示唆している。また、高分子の濃度と線量を変化することにより、大きさの異なるナノサイズの粒子が観察された。

次に、混合水溶液の照射試料に対する紫外吸収スペクトルから未照射試料の紫外吸収スペクトルを引いた差スペクトルを Fig. 2 に示す。この結果から、線量の増加とともに測定範囲の波長での吸収が全体的に増大することがわかった。これは、目視で白濁が観察されなかった 5 kGy であっても何らかの構造体が形成され、DNA を含有しているこ

とを示唆している²⁾。

以上の結果から、照射条件の制御により、高収量でナノサイズの BSA/DNA 複合粒子の作製が可能であることが分かった。いくつかの抗がん剤は DNA にインターカレートすることが知られていることから³⁾、開発した DNA を含有する複合粒子は薬物輸送担体としての応用が期待される。

References

- 1) K. Furusawa et al., Colloid Polym. Sci. **283** (2004) 229-33.
- 2) K. Furusawa et al., J. Biomater. Sci. **19** (2008) 1159-70.
- 3) V. A. Bloomfield et al., University Science Books, Sausalito, California, (2000) 535-96.

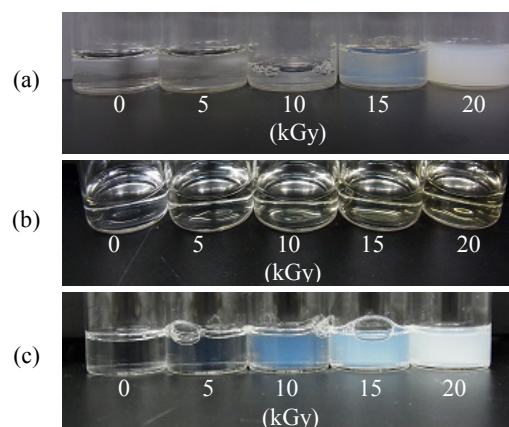


Fig. 1 Photographs of samples irradiated with different doses; (a) BSA solutions, (b) DNA solutions, (c) BSA/DNA mixture.

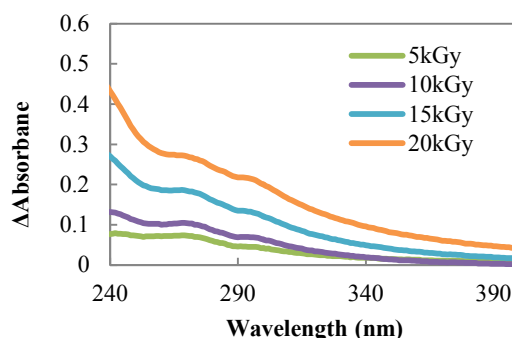


Fig. 2 Differential spectra of BSA/DNA mixture before and after gamma-rays irradiation.

2 - 08 Treatment of Chlorinated Antibiotics by Oxidative/Reductive Species under Ionizing Radiation

A. Kimura and M. Taguchi

Environment and Industrial Materials Research Division, QuBS, JAEA

Drug resistant bacteria, which have low chemo sensitivity, proliferate in the water environment exposing to high concentration of chemotherapeutic drugs, especially antibiotics, from household, domestic animals, medical treatment site, waste disposal plant and so on¹⁾. The concentrations of the antibiotics in the water environment increased gradually because of the population growth and diversification of advanced medical worldwide. The antibiotics have been also detected at the downstream of water treatment facilities, indicating that the physical-chemical treatment and activated sludge system could not remove them completely. Advanced oxidation technologies (AOTs) such as ionizing radiation method, ozone / UV photolysis, Fenton-type oxidation and so on are investigated for effective decomposition of the persistent antibiotics in real wastewater. The ionizing radiation can produce oxidative and reductive species homogeneously in particular. The purpose of this work is to treat persistent chlorinated antibiotics by the ionizing radiation method. Rate constants of the antibiotics with radiation-induced reactive species were investigated by a competition reaction method and pulse radiolysis method in the previous study²⁾. Decomposition efficiency of chlorinated antibiotics in real wastewater by the ionizing radiation methods was simulated using the experimental results.

Chloramphenicol (CP) was selected as experimental samples because it is consumed a lot for the domestic animals and medical treatment site, and detected in the water environment¹⁾. CP was dissolved under aerated condition in real wastewater at the amount of total organic carbon at about 50 mgC dm⁻³, which was collected at an influent of the water treatment facility of Gunma Prefectural Sewerage Management General Office. The γ -ray irradiations were carried out at 293 K at Japan Atomic Energy Agency (JAEA), Takasaki to the doses in the range from 50 to 1,000 Gy. CP in the wastewater was treated by combination of the activated sludge system and the ionizing radiation method, and its decomposition behavior is calculated on the basis of chemical kinetics.

Concentration of chloramphenicol (CP) was reduced almost zero at 1 kGy as shown in Fig. 1, on the other hand, sulfa drugs as typical antibiotics were eliminated in real wastewater at 0.5 kGy of γ -ray irradiation²⁾. CP is considered to have a lower reactivity with hydroxyl (OH) radicals than the other aromatic antibiotics because it has phenyl ring substituted chlorine and nitro groups as electron accepters. Decomposition efficiencies of CP by the radiation-induced OH radicals would be interfered by the organic carbons (OC) in the wastewater, and decreases in

the concentrations of CP in the wastewaters were simulated by use of the rate constant of CP with OH radicals ($1.6 \times 10^{10} \text{ mol}^{-1} \text{ dm}^3 \text{ s}^{-1}$) obtained in the previous work²⁾. G-value of OH radical is set at 2.7 molecules 100^{-1} eV^{-1} ³⁾, and the concentration of total organic carbons is set at 50 mgC dm⁻³ near to the average value of real wastewater samples in this experiment. The rate constants of many organic compounds with OH radicals are reported to be about $10^6 - 10^{10} \text{ mol}^{-1} \text{ dm}^3 \text{ s}^{-1}$ ³⁾, and the rate constant of OC with OH radicals in the simulation is assumed to be $1 \times 10^8 \text{ mol}^{-1} \text{ dm}^3 \text{ s}^{-1}$. Simulation curve for the decomposition of CP in wastewater by OH radicals is shown by dashed line in Fig. 1, and the result is not agreement with the experimental ones. The other AOTs use OH radicals for decomposition of antibiotics, so they also need the similar OH radical concentrations corresponding to 3,000 Gy by γ -rays. The γ -ray irradiations produced hydrated electrons as well as OH radicals, and the former attacks on chlorine of CP. The rate constant of CP with hydrated electrons is reported to be $3.6 \times 10^{10} \text{ mol}^{-1} \text{ dm}^3 \text{ s}^{-1}$ ²⁾. The rate constant of OC with hydrated electrons is assumed to be $1.0 \times 10^7 \text{ mol}^{-1} \text{ dm}^3 \text{ s}^{-1}$ because the rate constants of many organic compounds with hydrated electrons are reported to be about $10^4 - 10^{10} \text{ mol}^{-1} \text{ dm}^3 \text{ s}^{-1}$ ³⁾. The simulation curve considering the reaction of CP with OH radicals and hydrated electrons fits well with the experimentally obtained CP concentrations as shown by solid line in Fig. 1.

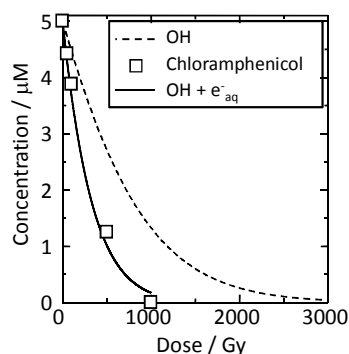


Fig. 1 Decomposition of chloramphenicol in real wastewater by ionizing radiation (square) and its simulation curves by hydroxyl radicals (dashed line), and hydroxyl radicals and hydrated electrons (solid line).

References

- 1) M. Sasaki et al., Miyagi Pref. Inst. Pub. Heal. Environ. Ann. Rep. 26 (2008) 31-34.
- 2) A. Kimura et al., JAEA Takasaki Annu. Rep. 2011 (2013) 50.
- 3) G. V. Buxton et al., J. Phys. Chem. Ref. Data 17 (1988) 513.

2 - 09

Immobilization of Denitrifying Bacteria to
HPC Gel Medium Synthesized by EB IrradiationT. Yanagisawa^{a)}, Y. Kamata^{a)}, N. Nagasawa^{b)}, M. Taguchi^{b)} and T. Tanaka^{a)}^{a)}Department of Civil and Environmental Engineering, Maebashi Institute of Technology,^{b)}Environment and Industrial Materials Research Division, QuBS, JAEA

A gel medium for denitrifying bacteria was developed using a radiation-induced crosslinking technology of polysaccharide. The gel medium consisted of the culture solution for denitrifying bacteria and hydroxypropylcellulose (HPC). The gel was readily insolubilized by the electron beam irradiation level of 20 kGy. The denitrification experiments were carried out using the HPC gel. The experimental results showed that denitrifying bacteria was selectively immobilized to the HPC gel medium.

下水や畜産廃水などは一般に、その安定性や簡便性から生物学的プロセスにより処理されている。しかしながら、微生物の機能を利用する処理方法については、余剰汚泥が大量に発生すること、栄養塩類の除去能が有機物のそれに比較して低いこと、ランニングコストが比較的高いことなどの問題が以前より指摘されている。余剰汚泥発生量の低減化や栄養塩除去能の改善に対しては、反応槽における微生物量を増加させることが有効であり、活性汚泥法に関しては、これまで微生物担体を反応槽に直接投入する担体投入型活性汚泥法などの高度化プロセスが提案されている。担体の材質としては、プラスチックやポリエチレンなどが一般に知られている。本研究では、放射線加工で作製したHPCゲルを微生物担体として用いることを提案し、その特性について実験的に検討した。ヒドロキシプロピルセルロース(HPC)ゲルの電子顕微鏡による観察¹⁾、ゲル分率や膨潤率の測定^{2,3)}、および硝化細菌の固定化実験⁴⁾の結果より、放射線加工 HPC ゲルは担体として利用可能と考えられた。ここでは、HPC 担体への脱窒細菌の選択的固定化の可能性について検討した。

HPCと脱窒細菌用培地を練り混ぜて、放射線を照射してHPC ゲル担体を作製した。HPC 濃度は30%、線量は電子線20 kGyとした。電子線架橋により、水溶性のHPCが不溶性のゲル様物質へと変化するとともに、微生物が固定化されやすい細やかな網目状の構造が形成された。上記の照射条件において、ゲル分率:86.5%、膨潤率:13.1%であった²⁾。

次に、ガラス製の反応器(有効容量:約1リットル)に、調製したゲルを縦:0.5 cm、横:0.5 cm、長さ:10 cmの大きさに成形し、形状が崩れないように直径約1 cmのメッシュ状のプラスチック筒に挿入してから充填した。HPC ゲルは、比表面積(反応器の有効容量に対する担体ゲルの総表面積)が約70 m²/m³となるように成形ゲルを36セット充填した。

HPC ゲル担体への微生物の固定化は、上記の反応器(担体充填後)を約550 mLの下水二次処理水で満たして行った。このとき、再曝気による溶存酸素(DO)濃度の上昇を抑制するため、反応器の上面をパラフィルムで覆って密閉状態で行った。固定化の期間は先の実験⁴⁾と同様に26日とした。その後、反応器内の溶液を下水二次処理水から硝酸塩溶液へと交換し、同様に密閉状態で脱窒実験を行った。脱窒実験は、水温25℃の条件で行った。サンプリングは実験開始から0、1、3、7、15、21日後に反応器より行った。サンプリング試料について、イオンクロマトグラフ

イを用いて亜硝酸イオン(NO₂⁻)および硝酸イオン(NO₃⁻)の濃度などを測定した。

脱窒実験の結果(NO₃⁻、NO₂⁻濃度の経時変化)を Fig. 1に示す。実験開始から7日目までは、NO₃⁻濃度は減少した。これは、脱窒反応によりNO₃⁻がN₂まで還元された結果と考えられる。7日以降、NO₃⁻濃度の減少は確認されなかった。実験開始時と実験終了時では約15%のNO₃⁻が減少した。DO濃度が増加する前まではNO₃⁻濃度の減少が確認できたことから、DO濃度の上昇が脱窒反応の進行を抑制したと考えられる。また、実験開始後3～7日にかけてNO₂⁻濃度の上昇が確認されたことから、反応器内では硝酸塩還元反応が進行していたと考えられる。

References

- 1) 杉山拓也、田中恒夫:放射線加工による微生物担体の創製、前橋工科大学卒業論文、(2009)、1-6.
- 2) 吉池友則、田中恒夫:放射線による微生物担体の加工、前橋工科大学卒業論文、(2010)、1-6.
- 3) 池上直斗、田中恒夫:HPC担体による選択培養の可能性、前橋工科大学卒業論文、(2011)、1-8.
- 4) T. Yanagisawa et al., JAEA Takasaki Annu. Rep. 2011 (2013) 52.

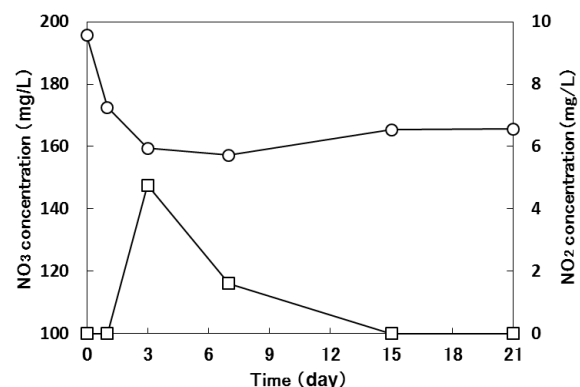


Fig. 1 Changes in NO₃⁻ and NO₂⁻ concentrations treated by denitrifying bacteria immobilized to HPC gel medium.
○: NO₃⁻, □: NO₂⁻.

This is a blank page.

3. Medical and Biotechnological Application

3-01	Estimation of Damage Localization in DNA Irradiated with Ionizing Radiations in Water	69
	K. Akamatsu and N. Shikazono	
3-02	The Effect of Radiation Quality on Growth-medium Dependent Survival in <i>Escherichia coli</i>	70
	M. Sakai, M. Takahashi, N. Shikazono and K. Awazu	
3-03	Gamma-ray Sensitivity in <i>Arabidopsis thaliana</i> Exhibiting Different Flavonoid Accumulation Patterns	71
	S. Kitamura and I. Narumi	
3-04	Target Irradiation of Individual Cells Using Focusing Heavy-ion Microbeam of JAEA-Takasaki (IV): An Improvement of Control Pathway of Scanned Beam Irradiation for “Actual” Cell Sample Irradiation	72
	T. Funayama, Y. Yokota, T. Sakashita and Y. Kobayashi	
3-05	Microbeam Irradiation Response of the Salt Chemotaxis in Mock-conditioned <i>C. elegans</i>	73
	T. Sakashita, M. Suzuki, Y. Hattori, H. Ikeda, Y. Mutou, Y. Yokota, T. Fuyanama, N. Hamada, K. Fukamoto and Y. Kobayashi	
3-06	Radiation-induced Bystander Cell-killing Effect Is Dependant on Dose of Carbon Ions and γ -rays but Independent of LET	74
	Y. Yokota, T. Funayama, H. Ikeda, M. Suzuki, T. Sakashita and Y. Kobayashi	
3-07	Mechanisms for the Induction of Radioadaptive Response by Radiation-induced Bystander Response	75
	H. Matsumoto, M. Tomita, K. Otsuka, M. Hatashita, M. Maeda, T. Funayama, Y. Yokota, Y. Mutou, M. Suzuki, T. Sakashita and Y. Kobayashi	
3-08	Analysis of Bystander Cell Signaling Pathway Activated by Heavy Ion-microbeam IV	76
	M. Tomita, H. Matsumoto, K. Otsuka, M. Maeda, T. Funayama, Y. Yokota, M. Suzuki, T. Sakashita and Y. Kobayashi	
3-09	Fluence-dependent Chromosomal Aberrations via Bystander Effect in Normal Human Fibroblasts Induced by C-, Ne- and Ar-ion Microbeams	77
	M. Suzuki, N. Autavapromporn, T. Funayama, Y. Yokota, Y. Mutou, M. Suzuki, H. Ikeda, Y. Hattori and Y. Kobayashi	
3-10	Ion Beam Irradiation Has Different Influences on the Expression of Bax in Cultured Human Retinal Vascular Endothelial Cells Exposed to L-dopa among ^{20}Ne , ^{12}C , and ^4He	78
	K. Akeo, T. Funayama, Y. Kobayashi and Y. Akeo	
3-11	Radiosensitivity is Affected by the Dependence of DNA Double-strand Break Repair on LET	79
	A. Takahashi, M. Kubo, H. Ma, A. Nakagawa, Y. Yoshida, T. Kanai, T. Ohno, Y. Furusawa, T. Funayama, Y. Kobayashi and T. Nakano	

3-12	Epigenetic Modifier as a Potential Radiosensitizer for Heavy-ion Therapy on Malignancy	80
	K. Saito, T. Funayama, Y. Kobayashi and T. Murakami	
3-13	Apoptotic Cell Death of the Heavy Ion Irradiated Silkworm Egg after Cellular Blastoderm Stage	81
	K. Shirai, T. Funayama, T. Sakashita, Y. Yokota and Y. Kobayashi	
3-14	Promotion of Miss-Differentiation of Testis-ova in p53 Deficient Medaka Testis by Micro-beam Irradiation of Carbon-ions	82
	T. Yasuda, S. Oda, T. Watanabe-Asaka, T. Funayama, Y. Yokota, Y. Mutou, H. Ikeda, Y. Kobayashi and H. Mitani	
3-15	Polythene Chromosome Abberation as a Possible Marker for Assessing DNA Damage upon Ionizing Radiation in the Sleeping Chironomid Larvae	83
	O. Gusev, S. Shimura, R. Cornette, T. Kikawada, T. Sakashita, T. Funayama, Y. Kobayashi and T. Okuda	
3-16	Effects of Carbon-ion Microbeam Irradiation on Pharyngeal Pumping in <i>Caenorhabditis elegans</i>	84
	M. Suzuki, Y. Hattori, T. Sakashita, T. Funayama, Y. Yokota, H. Ikeda and Y. Kobayashi	
3-17	Electron-spin Relaxation Times of Irradiated Fructose Measured with Pulsed ESR	85
	M. Kikuchi, H. Kameya, Y. Shimoyama, M. Ukai and Y. Kobayashi	
3-18	Relaxation Times of Radicals Induced in Irradiated Foods Using Pulse-ESR and CW-ESR	86
	K. Kishita, S. Kawamura, M. Kikuchi, H. Nakamura, Y. Kobayashi and M. Ukai	
3-19	Three-dimensional Distribution Measurement of Eu in a <i>Paramecium Bursaria</i>	87
	T. Satoh, M. Koka, W. Kada, A. Yokoyama, T. Ohkubo, A. Yamazaki, Y. Ishii, T. Kamiya and N. Kozai	
3-20	Approaches to Isolation and Culture of Mice LMECs, and Effects of Nicotine on Trace Elements Distribution in LMECs	88
	E. Sakurai, E. Sakurai K. Yanai, K. Ishii, S. Yamauchi, S. Koshio, S. Matsuyama, M. Koka, T. Satoh and T. Kamiya	
3-21	Measurement of Fluorine Distribution in Root Dentin under Fluoride-containing Coating Materials	89
	K. Okuyama, H. Yamamoto, H. Komatsu, S. Oki, Y. Matsuda, N. Hashimoto, Y. Iwami, M. Hayashi, M. Nomachi, K. Yasuda, T. Satoh and M. Koka	
3-22	Imaging of Metallofullerene Distribution Using Micro-PIXE for Gadolinium NCT	90
	Y. Yamamoto, K. Nakai, F. Yoshida M. Shirakawa, Endo, A. Matsumura, Y. Horiguchi and Y. Nagasaki	

3-23	Elemental Analysis of Lung Tissue Particles and Intracellular Iron Content of Alveolar Macrophages in Pulmonary Alveolar Proteinosis	91
	K. Dobashi, Y. Shimizu, S. Matsuzaki, N. Yanagitani, T. Satoh, M. Koka, A. Yokoyama, T. Ohkubo, Y. Ishii, T. Kamiya and M. Mori	
3-24	Analysis of Erythrocytes in Hepatitis C Patients Treated with Peg-interferon Using In-Air Micro-PIXE	92
	S. Tomioka, T. Nagamine, T. Akutsu, T. Satoh, M. Koka and T. Kamiya	
3-25	Trial for Targeting of Anticancer Drugs, Using Radiosensitive Immunolabelled Microcapsules	93
	S. Harada, S. Ehara, K. Ishii, T. Satoh, T. Kamiya and M. Koka	
3-26	Development of Method for Plant Material Analysis by Micro-PIXE (Particle Induced X-ray Emission)	94
	T. Yamamoto, H. Noda, J. Furukawa and S. Satoh	
3-27	Sensitivity of Micro Beam PIXE System in TIARA for Several Trace Elements and Determination of Elemental Abundances in a Small Organism	95
	Y. Iwata, M. Katada, T. Kamiya and T. Satoh	
3-28	Synthesis of Radiohalogen-labeled Peptide with High Affinity to HER2/neu Receptor	96
	I. Sasaki, K. Yamada, S. Watanabe, H. Hanaoka, Y. Sugo, H. Oku and N. S. Ishioka	
3-29	Complexation of Lutetium-177 with Bifunctional Chelators in the Presence of Competing Metals	97
	S. Watanabe, K. Hashimoto and N. S. Ishioka	
3-30	Production of ¹³ N-labeled Nitrogen Gas Tracer for the Imaging of Nitrogen Fixation in Soybean Nodules	98
	S. Ishii, M. Igura, Y.-G. Yin, N. V. P. Hung, N. Suzui, N. Kawachi, A. Koyanagi, T. Ohyama and S. Fujimaki	
3-31	Analysis of the Effect of O ₂ Partial Pressure on Nitrogen Fixation in Soybean Plant Using Positron-emitting Tracer	99
	N. V. P. Hung, S. Ishii, N. Suzui, N. Kawachi, Y. G. Yin, A. Koyanagi, T. Ohyama and S. Fujimaki	
3-32	RI Imaging Method to Analyze a Process of Radiocesium Contamination of Plants and to Develop Phytoremediation Techniques	100
	N. Kawachi, Y.-G. Yin, N. Suzui, S. Ishii, H. Watabe, S. Yamamoto and S. Fujimaki	
3-33	Whole-plant Imaging of ¹⁰⁷ Cd Distribution Using Positron-emitting Tracer Imaging System	101
	N. Suzui, Y.-G. Yin, M. Igura, S. Ishii, N. Kawachi, S. Ishikawa and S. Fujimaki	
3-34	Development of Ion Beam Breeding Technology in Plants and Creation of Useful Plant Resources	102
	Y. Hase, S. Nozawa, I. Asami, Y. Tanokashira, Y. Matsuo, A. Kanazawa, K. Honda and I. Narumi	

3-35	Ion Beam Breeding of Rice for the Mutation Breeding Project of the Forum for Nuclear Cooperation in Asia (FNCA)	103
	A. Tanaka, S. Nozawa, Y. Hase, I. Narumi, H. Ishikawa and A. Koike	
3-36	Generating New Chrysanthemum Plant Varieties Using Ion Beams	104
	A. Zaiton, A. H. Affrida, S. Shakinah, M. Nurul Hidayah, S. Nozawa, I. Narumi, Y. Hase and Y. Oono	
3-37	Mutational Effects of Carbon Ions near the Range End in Arabidopsis	105
	Y. Hase, S. Nozawa and I. Narumi	
3-38	Homologous Recombination Induced by Low-dose Radiations in Arabidopsis	106
	T. Uchida, M. Teranishi, Y. Hase, M. Endo, S. Toki, J. Hidema and A. N. Sakamoto	
3-39	Screening of Salt Tolerant Mutants by Combination of Radiation Mutagenesis and <i>In vitro</i> Regeneration in Lombardy Poplar (<i>Populus nigra</i>)	107
	K. K. Biswas, Y. Hase, I. Narumi and Y. Oono	
3-40	Effects of Gamma-ray Irradiation on Oxalate Metabolism in <i>Rumex obtusifolius</i> L.	108
	S. Kitano, A. Miyagi, Y. Oono, Y. Hase, I. Narumi, H. Uchimiya and M. Kawai-Yamada	
3-41	Determination of the Carbon Ion Beam Irradiation Condition for Barley	109
	T. Iimure, T. Hoki, Y. Hase, S. Nozawa, I. Narumi, M. Kihara and K. Ogushi	
3-42	Mutagenic Effect of Carbon Ion Beams in <i>Deinococcus radiodurans</i>	110
	K. Satoh, T. Onodera, K. Takeda and I. Narumi	
3-43	Genetic Analysis of Novel DNA Cross-link Repair Genes Common to <i>Deinococcus</i> and <i>Thermus</i>	111
	T. Onodera, K. Satoh, T. Ohta and I. Narumi	
3-44	Molecular Analysis of Heavy Ion Induced Mutations in Budding Yeast <i>S. cerevisiae</i>	112
	Y. Matuo, Y. Izumi, Y. Hase, A. N. Sakamoto, S. Nozawa, I. Narumi and K. Shimizu	
3-45	Improvement of Endophytic Bacteria Using Ion Beams and Application of Bio-pesticide with Plant Growth Promoter Made from Oligo-chitosan	113
	M. Aino, K. Satoh, I. Narumi, N. Nagasawa, F. Yoshii and M. Taguchi	
3-46	Identification of DNA Mutation Sites in a High Temperature Tolerant Mutant of <i>Bradyrhizobium japonicum</i> USDA110 Generated by Ion-beam Irradiation	114
	K. Takeda, K. Satoh, I. Narumi, N. Ohkama-Ohtsu and T. Yokoyama	
3-47	Simultaneous Saccharification and Fermentation from Ionic Liquid-pretreated Biomass Using Ionic Liquid-tolerant Yeast Mutant	115
	K. Ninomiya, S. Omote, K. Satoh, I. Narumi and N. Shimizu	
3-48	Benomyl-tolerant Mutation of Entomopathogenic Fungi Induced by Carbon Ion Beams	116
	T. Saito, Y. Fitriana, K. Satoh and I. Narumi	

3-49	Mutation Analysis of High Ethyl Caproate Producing Sake Yeasts Generated by Ion Beam Breeding	117
	T. Masubuchi, R. Ueda, O. Kamiyama, H. Ikenaga, K. Satoh and I. Narumi	
3-50	Role of DNA Repair and Effect of Herbal Extract on LOH Induced by Ion Beam Radiations in <i>Saccharomyces cerevisiae</i>	118
	T. Nunoshiba, Y. Sakata, A. Yamauchi, K. Satoh, T. Onodera and I. Narumi	

This is a blank page.

3 - 01 Estimation of Damage Localization in DNA Irradiated with Ionizing Radiations in Water

K. Akamatsu and N. Shikazono

Medical and Biotechnological Application Division, QuBS, JAEA

1. Introduction

It is known that DNA lesions induced by ionizing radiation and chemicals can cause mutation and carcinogenesis. In particular, 'clustered damage' site, that is a DNA region with multiple lesions within one or two helical turns, is believed to be hardly repaired. This damage is considered to be induced, e.g., around high-LET ionizing radiation tracks. However, detail of the damage is not known. We have already developed a method for estimating degree of localization of apurinic/aprimidinic (AP) sites on DNA using Förster resonance energy transfer (FRET). The FRET efficiency (E) was calculated using the donor fluorescence intensities before/after enzymatic digestion of the labeled AP-DNA¹⁾. Now we have tried to apply the method to $^4\text{He}^{2+}$ - and ^{60}Co γ -irradiated DNA.

2. Experiments

● Sample preparation and He beam irradiation

Plasmid DNA digested by Sma I was used (linear formed). One hundred microliters of the DNA aq. (0.5 g/L) was transferred to an irradiation chamber (Fig. 1), and was irradiated at TIARA with $^4\text{He}^{2+}$ beam at room temperature with the linear energy transfer (LET) of ~ 70 keV/ μm (TC), which was controlled by a depth-tunable cell irradiation equipment. ^{60}Co γ -rays (Kyoto University Research Reactor Institute: KURRI) were also used as a standard radiation source.

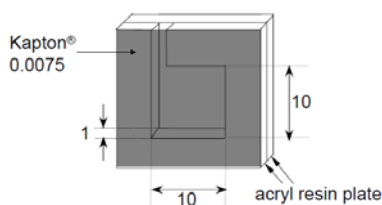


Fig. 1 A prototype of irradiation chamber (mm).

● Preparation of fluorophore-labeled irradiated DNA and the fluorescence spectroscopy for FRET observation

The irradiated DNA (10 μL in water) and 10 μL of 100 mM Tris-HCl (pH 7.5) were mixed in a microtube. Two microliters of a mixture containing AF350 (donor fluorescent probe) and AF488 (acceptor one) with a given molar ratio was added to the DNA solution and was incubated for 24 h at 37 $^{\circ}\text{C}$. The fluorophore-labeled DNA was purified by ethanol precipitation. Twenty microliters of water was added to the residue. The fluorescence intensities were measured both at 449 nm (ex. 347 nm for AF350) and at 520 nm (ex. 460 nm for AF488). After the measurement, the enzyme cocktail containing DNase I and phospho- diesterase I was added to the solution, and it was incubated for 2 h at 37 $^{\circ}\text{C}$. FRET efficiencies (E) were calculated from the donor intensity before/after the digestion.

3. Results and Discussion

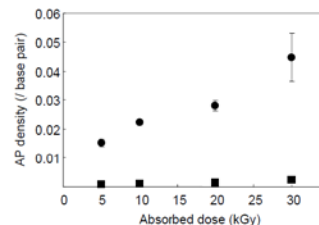


Fig. 2 Relationship between absorbed dose and AP density for He ion beam (■) and ^{60}Co γ -rays (●).

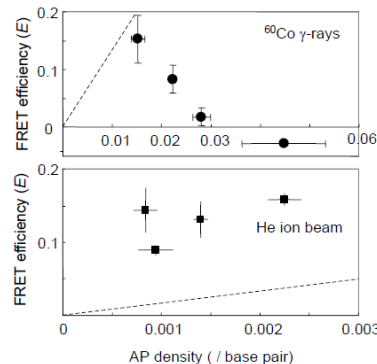


Fig. 3 Relationship between AP density and FRET efficiency for He ion beam (■) and ^{60}Co γ -rays (●). The dashed lines indicate theoretical lines for randomly-distributed AP in DNA.

The He beam is stopped completely by DNA aq. (1 mm depth, see Fig. 1), and all of the energy is transferred into the solution. It should be noted that the energy deposition may not be homogeneous although diffusion of DNA molecules can be promoted by vibration of the chamber during irradiation. Figure 2 shows clear difference in the AP density (the number of AP sites produced/total DNA base pairs in the solution) between these radiation sources. Elimination of OH radicals by recombination would be responsible for the low level AP production for the high-LET He beam. In Fig. 3, decrease of E for ^{60}Co γ -rays would be caused by gross fragmentation of DNA due to the numerous lesions. More data of lower dose region are needed. The E values for He beam are much higher than those for randomly-distributed AP. He beam seems to produce clustered AP regions more frequently than random case. However, deeper consideration in heterogeneity of the energy deposition should be important for more proper estimation of the damage localization. Improvement of the irradiation system may also be needed.

4. Acknowledgments

We would like to gratefully thank Dr. Takeshi Saito (KURRI) for supporting ^{60}Co γ -ray irradiation experiments.

Reference

- 1) K. Akamatsu, N. Shikazono, Anal. Biochem. **433** (2013) 171-80.

3 - 02 The Effect of Radiation Quality on Growth-medium Dependent Survival in *Escherichia coli*

M. Sakai^{a, b)}, M. Takahashi^{b)}, N. Shikazono^{b)} and K. Awazu^{a)}

^{a)} Division of Sustainable Energy and Environmental Engineering, Graduate School of Engineering, Osaka University, ^{b)} Medical and Biotechnological Application Division, QuBS, JAEA

Clustered damage is induced by ionizing radiation and is considered to lead to deleterious effects¹⁾. Their yields and configurations likely depend on the radiation qualities, which is defined by the ionization density along the particle track, in most cases characterized by LET (linear energy transfer)^{1, 2)}. Although medium dependence of survival after X-ray exposure has been found in *Escherichia coli*³⁾, to what extent the medium-dependent effect is affected by the ionizing density of a radiation, which is usually related to the linear energy transfer (LET), remains unclear. In this project, we aim to find out whether radiation quality affects the medium-dependent survival. Here, the results of the effect of growth medium on survival of *Escherichia coli* after exposure to He ions or X-rays are presented.

The cells of CSH100 (wild type *E. coli*) were incubated in rich liquid medium (LB) at 37 °C. Cells ($2\text{--}3 \times 10^8$) were filtered through a nitrocellulose membrane of a diameter of 1.3 cm. To prevent cells from drying, the membrane was placed on a filter paper pre-wetted with 300 μL of 0.15 M NaCl solution with 20% glycerol. Subsequently, the membrane was placed on 0.15 M NaCl agar in a Petri dish, and then the dish was covered with a polyimide film (Kapton film, 7.5 μm thickness). Cells were irradiated with He ions (at dose rates of 1~4 Gy/sec) or with X-rays (at a dose rate of 0.47 Gy/sec). The LET of He ions was altered by placing a Ni foil with a thickness of 300 μm in front of the sample. The LET of the sample was estimated to be 89 keV/ μm by the ELOSS code. After irradiation, cells were either directly plated on rich/minimal plates or plated on rich/minimal plates after incubation in liquid medium. Survival of cells was determined from dividing the number of survived clones after irradiation by the number of clones that was mock irradiated.

The survival of *E. coli* wild-type cells plated immediately after irradiation decreased exponentially with increasing dose of both X-rays and He ions (Fig. 1). The survivals were not significantly different between the two types of radiation, except that there was a rich medium-dependent increase of survival after X-irradiation but not after He ion radiation. To find out the duration of medium-dependent radioresistance, we next looked at the survival of cells incubated in liquid rich medium after irradiation. The numbers of unirradiated cells increased approximately 10-fold in liquid rich medium (data not shown). The growth rate was reduced with increasing dose of radiation, probably due to both cell death and growth arrest. Cells that were incubated for 2 h after X-irradiation showed no enhancement of medium-dependent survival (Fig. 2).

It is noteworthy that the growth-medium dependent

increase of survival was observed only when cells were incubated in rich medium both pre- and post-irradiation, and not when cells were grown in minimal medium either pre- or post-irradiation (data not shown). This indicates that a specific physiological state is induced by X-rays in rich medium. The absence of medium-dependent increase of survival after 2 h post-irradiation incubation indicates that the induced state is sustained for no longer than 2 h. The lack of medium-dependent resistance after He-irradiation lead us to suggest that the physiological state is unchanged by irradiation or that the induced state can only cope with less complex X-ray induced DNA damage.

References

- 1) N. Shikazono et al., J. Radiat. Res. 50 (2009) 27.
- 2) H. Nikjoo et al., Radiat. Res. 156 (2001) 577.
- 3) N. Sargentini et al., Radiat. Res. 93 (1983) 364.

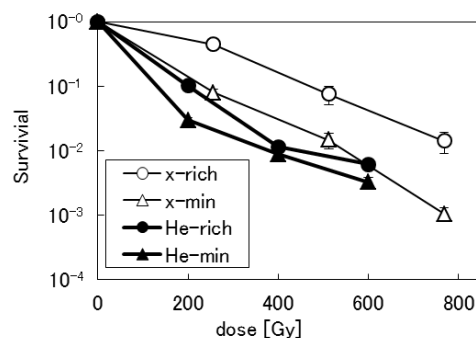


Fig. 1 Survival of cells plated immediately after irradiation. Wild-type CSH100 cells exposed to X-rays were plated on rich (○) or glucose minimal (Δ) plates. CSH100 cells exposed to He ions were also plated on rich (●) or glucose minimal (▲) plates.

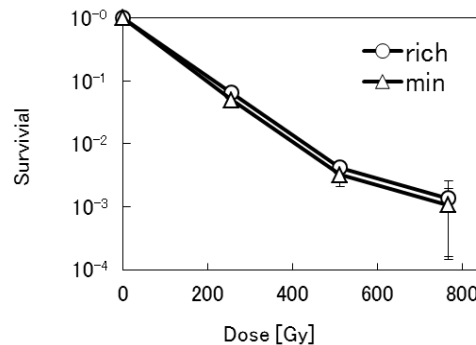


Fig. 2 Survival of cells plated after 2 h postirradiation incubation in rich liquid medium. CSH100 cells exposed to X-rays were plated on rich (○) or glucose minimal (Δ) plates.

3 - 03 **Gamma-ray Sensitivity in *Arabidopsis thaliana* Exhibiting Different Flavonoid Accumulation Patterns**

S. Kitamura and I. Narumi*

Medical and Biotechnological Application Division, QuBS, JAEA,

*Present affiliation: Faculty of Life Sciences, Toyo University

Flavonoids are one of the major secondary metabolites in plants, and have various and important physiological functions such as pigments, pathogen defense compounds, UV-absorbing agents, and regulators for auxin transport. In addition, it is also known that flavonoids have features that can scavenge reactive oxygen species (ROSs). However, it remains to be unraveled whether the flavonoids can reduce cellular and molecular damages by ionizing radiation in plants. To understand more deeply the physiological functions of flavonoids in plants, we analyze here the responses to gamma-irradiation in *Arabidopsis thaliana* exhibiting different flavonoid accumulation patterns.

Arabidopsis flavonoid mutants (*transparent testa* [*tt*]) and the wild type (WT) were used in this study. Mature dry seeds and 3-day-old seedlings were exposed to ⁶⁰Co gamma-rays at Food Irradiation Facility, JAEA. The seeds exposed to different doses of gamma-rays were surface-sterilized, sown on nutrient plates, and germinated in a chamber controlled at 23 °C with continuous light. Survival plants showing greenish true leaves were counted at 2 weeks after germination. For seedling irradiation, 3-day-old seedlings grown vertically on the nutrient plates in the chamber were exposed to gamma-rays. After exposure, the plates were set vertically, as the case of pre-exposure condition. Root length and fresh weight were measured for 3 days and 3 weeks after exposure, respectively.

When dry seeds were exposed to gamma-rays, obvious differences in gamma-ray sensitivities were detected between WT and a complete flavonoid-less mutant, *tt4*. For example, survival rate of *tt4* at 1,200 Gy was about 37%, whereas that of WT at 1,200 Gy was nearly 100% (Fig. 1, left). When the seedlings were exposed, such a difference in gamma-ray sensitivity was not observed, based on the root growth during 3 days after exposure (Fig. 1, right) and the fresh weight at 3 weeks after exposure (data not shown). These results indicate that flavonoids have an impact on gamma-ray sensitivity on dry seeds but not on young seedlings.

Arabidopsis dry seed composes of inner embryo (plant body) and outer seed coat, both of which can accumulate flavonoids. Although *tt4* seeds show high sensitivity to gamma-rays, the *tt4* seed cannot accumulate flavonoids in both tissues, due to complete lack of flavonoids in any tissues. To address which flavonoid-accumulating tissues in dry seeds are involved in gamma-ray sensitivity, genetic approach was conducted using seed coat-specific flavonoid mutants. *tt12* mutant shows a flavonoid-less phenotype in

seeds but a normal flavonoid phenotype in embryo¹⁾. When dry seeds of *tt12* were exposed to gamma-rays, a survival curve was depicted between those of WT and *tt4* (Fig. 2). This result suggests that seed coat flavonoids have an impact on gamma-ray sensitivity of inner embryo growth.

To know the relationship between gamma-ray sensitivity and radical scavenging activity of flavonoids, ROS scavenging ability in dry seeds was determined for each genotype. As a result, WT and *tt4* seed extracts showed the highest and lowest abilities, respectively, and *tt12* extract showed an intermediate between them. This is clearly correlated with gamma-ray sensitivities in dry seeds. Although further analysis is necessary, these results suggest that flavonoids would contribute ROS scavenging within irradiated seeds, even in the case where the flavonoid accumulating tissues are apart from the rudimentary plant body, an embryo.

Reference

- 1) K. Marinova et al., Plant Cell 19 (2007) 2023.

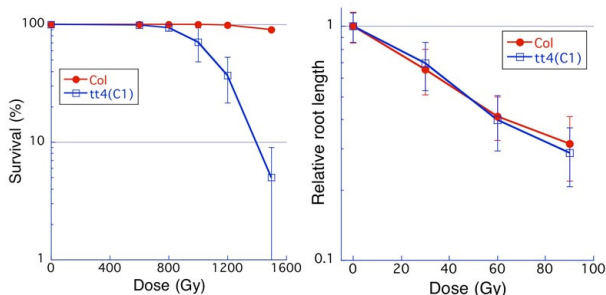


Fig. 1 Effects of gamma-rays on seed growth (left) and seedling growth (right). Average \pm SD were shown.

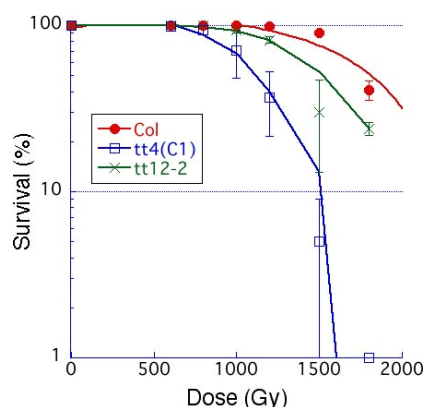


Fig. 2 Survival curves of seeds exposed to gamma-rays (Average \pm SD).

3 - 04 Target Irradiation of Individual Cells Using Focusing Heavy-ion Microbeam of JAEA-Takasaki (IV): An Improvement of Control Pathway of Scanned Beam Irradiation for “Actual” Cell Sample Irradiation

T. Funayama, Y. Yokota, T. Sakashita and Y. Kobayashi

Medical and Biotechnological Application Division, QuBS, JAEA

Heavy-ion has higher biological effectiveness, and that was caused by the non-uniform energy distribution along with heavy-ion tracks. This property of heavy-ion radiation raised three major subjects to be studied in radiation biological field: bystander effect, single ion hit effect, and clustered DNA damage. To explore these three issues, a target irradiation of individual cells using heavy-ion microbeam is a useful means. Therefore, we have developed a collimating heavy-ion microbeam system under a vertical beam line of an AVF cyclotron of JAEA-Takasaki¹⁾, and explored various effects of heavy-ion hit on biological materials²⁾. However, there are limitations of the collimating system in the size of the microbeam spot and in the irradiation speed that cannot be overcome in principle.

Thus, we started the development of a new focusing microbeam system for target-irradiating individual cells more precisely than the collimating system. Using the system, we established a method to irradiate finer heavy-ion microbeam on individual HeLa cells³⁾, and also succeeded to draw a cell distribution pattern on CR-39 film using scanned heavy-ion microbeam⁴⁾.

Nevertheless, the protocol of scanned beam irradiation is inefficient, because the control system of beam scanner and microscope uses different PCs and software. For that reason, the protocol for scanned beam irradiation is still complex for practical biological experiment: concretely speaking, to irradiate cell sample with a scanned microbeam, we first take a picture with microscope PC, then extract coordinates, calculate applied voltages, copy data to beam PC, input to the scanner software, and then irradiate samples.

Thus, we improved the irradiation control pathway, which become able to control overall cell irradiation procedure with a single PC and single software. As shown in Fig. 1a, the original pathway of the scanned beam irradiation needed two PCs for control irradiation, and need manual operation in the transfer of coordinate data and the setting of the ion count to the counter. To establish a basis for full automatic irradiation with scanned beam with simple experimental protocol, we developed measurement-system control software for microscope control PC and a control box for the P-chopper (Fig. 1b). The software for controlling measurement system was integrated into the Camera Control software, which has managed stage, microscope, and CCD camera, and makes the scanned beam

irradiation automatic. A control box was designed to regulate P-chopper control signals with on/off triggers that came separately from PC and measurement system. By developing them, we become able to irradiate the target sample with a scanned beam with single software on a single PC. Thus, we conclude that this improvement of irradiation control pathway is a significant progress in the establishment of the protocol for irradiating “actual” cell sample with scanned beam.

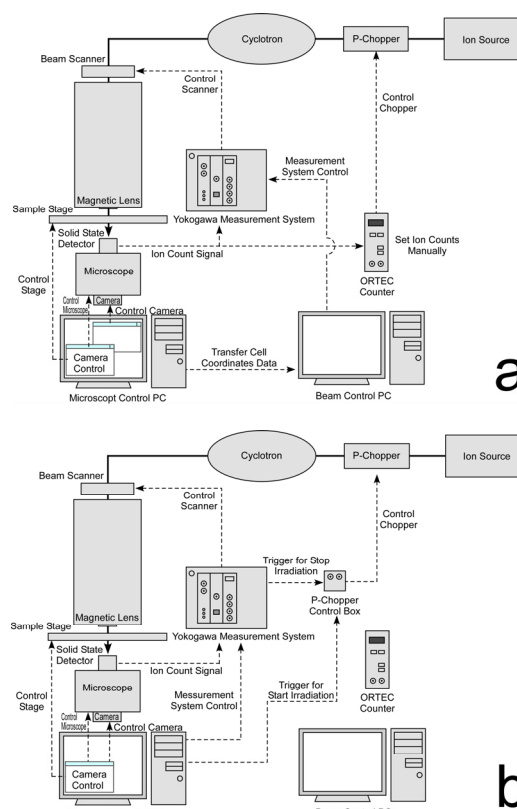


Fig. 1 Improvement of scanned beam irradiation control pathway, (a) the original control pathway, (b) the pathway after improvement.

References

- 1) T. Funayama et al., J. Radiat. Res. 49 (2008) 71-82.
- 2) T. Funayama et al., IEEE T. Plasma. Sci. 36 (2008) 1432.
- 3) T. Funayama et al., JAEA Takasaki Annu. Rep 2010 (2012) 65.
- 4) T. Funayama et al., JAEA Takasaki Annu. Rep 2011 (2013) 63.

3 - 05

Microbeam Irradiation Response of the Salt Chemotaxis in Mock-conditioned *C. elegans*

T. Sakashita^{a)}, M. Suzuki^{a)}, Y. Hattori^{a)}, H. Ikeda^{a)}, Y. Mutou^{a)}, Y. Yokota^{a)},
T. Fuyanama^{a)}, N. Hamada^{b)}, K. Fukamoto^{c)} and Y. Kobayashi^{a)}

^{a)}Medical and Biotechnological Application Division, QuBS, JAEA,

^{b)}Radiation Safety Research Center, Central Research Institute of Electric Power Industry,

^{c)}Faculty of Textile Science and Technology, Shinshu University

An increasing body of data indicates that ionizing radiation affects the nervous system and alters its function¹⁾. Recently, we reported that chemotaxis of *C. elegans* during the salt chemotaxis learning was modulated by carbon ion irradiation²⁾. However, we had no direct evidence for the interaction of ionizing radiation with the central neuronal tissue (nerve ring) in *C. elegans*. Microbeam irradiation is useful to analyze direct radiation effects at a cellular or tissue level. Thus, we applied the microbeam irradiation (¹²C, 18.3 MeV/u, LET = 119 keV/μm) to the *C. elegans* nerve ring and examined the effect on the salt chemotaxis learning. Our preliminary results showed the modulatory response of the salt chemotaxis learning to targeted carbon-ion irradiation³⁾. Here, we present the effects of targeted carbon-ion irradiation on the salt chemotaxis of mock-conditioned animals. Mock conditioning means the same conditioning as salt chemotaxis learning except salt stimulation.

Well-fed adults of *C. elegans* grown at 20 °C on the plate spread with *E. coli* OP50 were used in all experiments. The areas of nerve ring (Head) and the counter part (Tail) of mock-conditioned *C. elegans* in a ditch filled with the wash-buffer (5 mM KPO₄ [pH 6.0], 1 mM CaCl₂, 1 mM MgSO₄, and 0.5% gelatin) of the micro device⁴⁾ were irradiated with 12,000 carbon ions corresponding to 500 Gy at 20 μmφ micro-aperture area (Fig. 1).

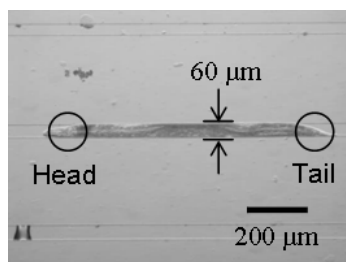


Fig. 1 *C. elegans* in a ditch of the micro device. Circles show the areas of nerve ring (Head) and Tail.

On the other hand, whole-body carbon ion irradiation by the broad beam irradiation facility was carried out. Immediately after irradiation, chemotaxis to NaCl was measured. Using the assay plate with a gradient of NaCl concentration, we evaluated chemotaxis based on the chemotaxis index (CI) that was calculated as {(number of animals at the high-concentration spot) – (number of animals at the control spot)} / (total number of animals in the

assay plate)²⁾. The positive CI indicates moving towards a higher concentration of chemical compounds. The results of CI were evaluated as mean ± 95% confidential interval. Statistical test was carried out by the chi-square test with a Yates' correction.

As shown in Fig. 2, we demonstrate the effects of target and broad beam irradiation of mock-conditioned animals (CI: 0.83 ± 0.09 in non-irradiated animals, 0.86 ± 0.08 in broad beam irradiated animals, 0.51 ± 0.13 in the Head locally irradiated animals, and 0.82 ± 0.11 in the Tail locally irradiated animals).

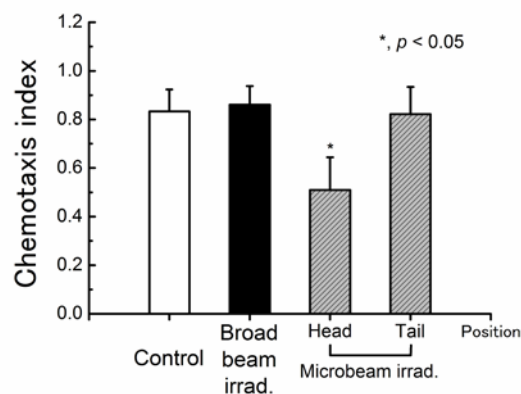


Fig. 2 Effects of carbon ion broad and microbeam irradiation on the salt chemotaxis of mock-conditioned *C. elegans*. Error bars show the 95% confidence intervals, and asterisks indicate the significant differences in CI.

Intriguingly, the Head targeted irradiation of *C. elegans* demonstrated the decrease of the salt chemotaxis, whereas broad and Tail targeted irradiations did not induce such a decrease in CI. In the previous report³⁾, we found that the modulatory response of the salt chemotaxis learning was induced by both Head and Tail microbeam irradiation. To understand the microbeam irradiation response of the mock-conditioned *C. elegans*, we are planning the mutant analysis of *C. elegans* in the near future.

References

- 1) T. Sakashita et al., J. Radiat. Res. 51 (2010) 107-21.
- 2) T. Sakashita et al., Biol. Sci. Space 26 (2012) 21-25.
- 3) T. Sakashita et al., JAEA Takasaki Annu. Rep. 2011 (2013) 64.
- 4) S. R. Lockery et al., J. Neurophysiol. 99 (2008) 3136-43.

3 - 06

Radiation-induced Bystander Cell-killing Effect is Dependant on Dose of Carbon Ions and γ -rays but Independent of LET

Y. Yokota^{a)}, T. Funayama^{a)}, H. Ikeda^{a,b)}, M. Suzuki^{a)}, T. Sakashita^{a)} and Y. Kobayashi^{a)}

^{a)}Medical and Biotechnological Application Division, QuBS, JAEA,

^{b)}Gunma University Graduate School of Medicine

Radiation-induced bystander effect manifests cell killing and other effects in cells that are not irradiated but are close to irradiated cells via intercellular and intracellular signaling. It is necessary to clear the mechanism of bystander effect in order to estimate the potential risks of low dose radiation accurately. In the present study, we thus investigate the dose and LET dependencies of bystander cell-killing effect using carbon ion broadbeam and ^{60}Co γ -rays to shed light on the mechanism of bystander effect and update our data previously reported^{1,2)}.

Normal human lung fibroblasts WI-38 cell line was cultured with MEM medium supplemented with 10% fetal bovine serum. Cells inoculated in porous membrane-based inserts were irradiated with carbon ion broadbeam (LET = 108 keV/ μm) and γ -rays (0.2 keV/ μm), and the inserts were then placed on corresponding companion plates, in which non-irradiated cells were cultured in the same way as irradiated cells. The ratio of irradiated cells and non-irradiated cells was almost 1:2.

Following co-culture between irradiated cells and non-irradiated cells for 24 h, non-irradiated bystander cells were trypsinized, counted, and then diluted to a suitable cell density with culture medium. Diluted cell suspension was transferred into a tissue culture dish and cultured for 14 days to count colonies formed. Colonies comprising 50 or more cells were regarded as survivors. Survival of bystander cells co-cultured with cells irradiated by γ -rays decreased

with increasing dose and its reduction was saturated at 0.5 Gy or higher doses (Fig. 1). The dose-response curve of carbon ions was similar to that of γ -rays, indicating that bystander cell-killing effect is independent of LET.

Next, the concentration of nitrite was measured using Saltzman's method to elucidate the mechanism of bystander effect mediated via nitric oxide (NO) radicals (Fig. 2). NO radicals are produced in irradiated cells and oxidized to yield nitrite and nitrate in the medium. Then the amount of nitrite is determined photometrically using Saltzman's reagent comprising n-1-naphthylethylene-diamine and sulfanilic acid which forms an azo dye specifically with nitrite. The concentration of induced nitrite increased with increasing dose up to 0.25 Gy and saturated at higher doses. The saturation levels of induced nitrite tended to be higher in carbon ions than in γ -rays. Taking the results of survival and induced nitrite together, it is concluded that NO radicals released from irradiated cells promote bystander cell-killing effect but the effective concentration of NO radicals has an upper threshold.

References

- 1) Y. Yokota et al., JAEA Takasaki Annu. Rep. 2010 (2012) 67.
- 2) Y. Yokota et al., JAEA Takasaki Annu. Rep. 2011 (2013) 65.

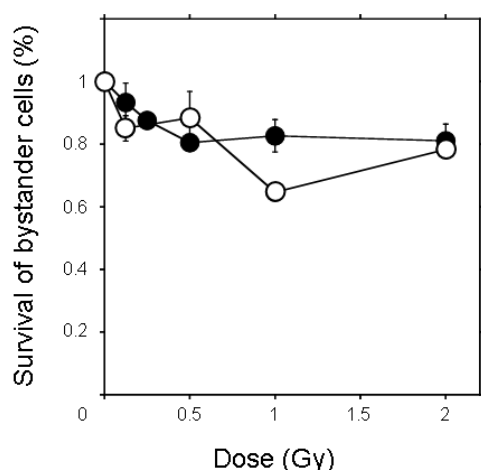


Fig. 1 Survival of bystander cells co-cultured with cells irradiated by carbon ions (open circle) or γ -rays (closed circle). Data are mean \pm SEM of 3-6 independent beam times except for 1 and 2 Gy of carbon ions (N = 2).

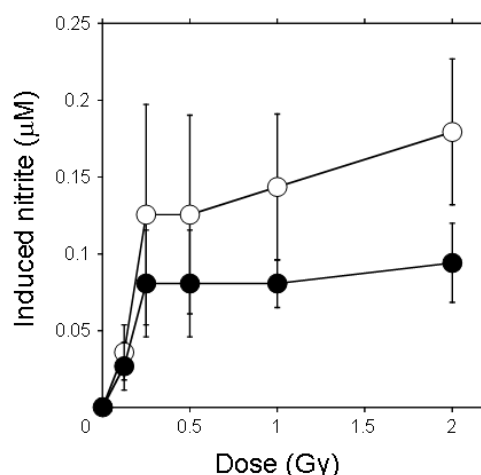


Fig. 2 Concentration of induced nitrite in the medium where irradiated cells and bystander cells were co-cultured. Data are mean \pm SEM of 3-4 independent beam times of carbon ions (open circle) or γ -rays (closed circle).

3 - 07 Mechanisms for the Induction of Radioadaptive Response by Radiation-induced Bystander Response

H. Matsumoto^{a)}, M. Tomita^{b)}, K. Otsuka^{b)}, M. Hatashita^{c)}, M. Maeda^{c)}, T. Funayama^{d)},
Y. Yokota^{d)}, Y. Mutou^{d)}, M. Suzuki^{d)}, T. Sakashita^{d)} and Y. Kobayashi^{d)}

^{a)}Biomedical Imaging Research Center, University of Fukui, ^{b)}Central Research Institute of Electric Power Industry, ^{c)}The Wakasa Wan Energy Research Center, ^{d)}Medical and Biotechnological Application Division, QuBS, JAEA

The objective of this project is to elucidate molecular mechanisms for the induction of radioadaptive response by radiation-induced bystander responses induced by low dose/low dose rate radiation using heavy ion microbeams in JAEA.

We performed the exhaustive analysis of gene expression, when radioadaptive response has been induced, using RT² ProfilerTM PCR Array System. We found several genes induced specifically and preferentially when radioadaptive response could be induced. We confirmed that *iNOS* expression was specifically induced only when radioadaptive response could be induced. Our findings strongly suggested that radioadaptive response can be induced by NO-mediated bystander responses evoked by low dose/low dose rate radiation, and that the induction of specific gene expression is required for the induction of radioadaptive response.

低線量/低線量率放射線に対して生物が示す特異的な応答様式には、放射線適応応答、放射線誘発バイスタンダー応答、放射線超高感受性、遺伝的不安定性等がある¹⁾。我々は、日本原子力研究開発機構において開発された細胞局部照射装置(HZ1)および深度制御種子照射装置(HY1)を用いて、この放射線誘発バイスタンダー応答の放射線適応応答への寄与を明らかにすることを計画した。

1. 実験方法

- (1) 細胞: *p53* 欠損ヒト非小細胞肺癌細胞(H1299細胞)へ正常型 *p53* 遺伝子を導入した H1299/wtp53 細胞を用いた。
- (2) 培養: 35 mm ディッシュの内面中央に 2.0×10^6 cells/mL の細胞懸濁液 5 μ L を 1 箇所スポットし(1.0×10^4 cells/colony)、15~20 時間培養したものを照射実験に供した。
- (3) 照射: Funayama ら²⁾の方法に従って、中央にスポットしたコロニーの 10 個の細胞に 5 粒子の 520 MeV $^{40}\text{Ar}^{14+}$ を HZ1 ポートにおいて照射した。一定時間(3~6 時間)培養後、520 MeV $^{40}\text{Ar}^{14+}$ を HY1 ポートにおいて 5 Gy 照射した。実験群は下記の通りである。
Group 1: 非照射細胞(対照群)
Group 2: HZ1 照射→HY1 照射(放射線適応応答誘導群)
Group 3: HZ1 照射のみ
Group 4: HY1 照射のみ
- (4) 全 RNA の抽出: 各実験群において最終照射から 6 時間後に細胞を回収し、全 RNA をキット(RNeasy Plus Mini Kit, キアゲン)を用いて抽出した。
- (5) 各実験群の全 RNA を RT² First Strand Kit(キアゲン)を用いて cDNA に変換し、RT² ProfilerTM PCR Array System の中の DNA Damage Signaling Pathway PCR Array および Nitric Oxide Signaling Pathway PCR Array を用いて、各実験群において特異的に発現誘導されている遺伝子を網羅的に解析した。

2. 結果および考察

- (1) HZ1 照射のみ(Group 3)あるいは HY1 照射のみ(Group 4)と HZ1 照射→HY1 照射(適応応答誘導群、Group 2)との比較: RT² ProfilerTM PCR Array System の中の DNA Damage Signaling Pathway PCR Array および Nitric Oxide Signaling Pathway PCR Array を用いて、上記 2 群を比較した結果、放射線適応応答誘導群(Group 2)に特異的に発現誘導されている遺伝子が数種見出された。これらの遺伝子は、細胞周期調節あるいは DNA 損傷修復に関わる遺伝子であった。また放射線適応応答のポジティブ・コントロールとなる *iNOS* 遺伝子の発現誘導³⁾は放射線適応応答誘導群 3(Group 2)においてのみ確認された。
- (2) HZ1 照射のみ(Group 3)と HY1 照射のみ(Group 4)の比較: RT² ProfilerTM PCR Array System の中の DNA Damage Signaling Pathway PCR Array を用いて、上記 2 群を比較した結果、HZ1 照射のみ(Group 3)あるいは HY1 照射のみ(Group 4)に特異的に発現誘導されている遺伝子が数種見出された。詳細については現在解析中である。

以上の結果より、放射線適応応答の誘導に必要と考えられる遺伝子が数種確認された。これらの遺伝子について、さらに精査することにより、放射線誘発バイスタンダー応答による放射線適応応答の誘導のメカニズム、特に NO を介したメカニズムの解明⁴⁾を目指す。

References

- 1) H. Matsumoto et al., J. Radiat. Res. 48 (2007) 97.
- 2) T. Funayama et al., Radiat. Res. 163 (2005) 241.
- 3) H. Matsumoto et al., Cancer Res. 67 (2007) 8574.
- 4) H. Matsumoto et al., Curr. Mol. Pharmacol. 4 (2011) 126.

3 - 08 Analysis of Bystander Cell Signaling Pathway Activated by Heavy Ion-microbeam IV

M. Tomita^{a)}, H. Matsumoto^{b)}, K. Otsuka^{a)}, M. Maeda^{a)}, T. Funayama^{c)},
Y. Yokota^{c)}, M. Suzuki^{c)}, T. Sakashita^{c)} and Y. Kobayashi^{c)}

^{a)}Central Research Institute of Electric Power Industry, ^{b)}University of Fukui,
^{c)}Medical and Biotechnological Application Division, QuBS, JAEA

Radiation-induced bystander responses are defined as responses in cells that have not been directly targeted by radiation but are in the neighborhood of cells that have been directly exposed. In our study, we aim to clarify the cell signaling pathway activated by high-LET radiation in the bystander cells. Normal human fibroblast WI-38 cells were irradiated with 520 MeV ⁴⁰Ar-ion microbeams or broadbeams. We found that NF-κB-dependent signaling pathway involving Akt and COX-2 plays an important role in the NO-mediated bystander response. Additionally, we started the study of bystander response using 3D tissue culture system.

低粒子数の重イオン線による生物影響を解明する上で、DNA 初期損傷量に依存しない「非標的効果」が注目されている。特に、放射線に直接曝露された細胞の近傍に存在する全く放射線に曝露されていない細胞において観察される「放射線誘発バystanダー応答」は、最も特徴的な非標的効果である¹⁾。本研究は、原子力機構の細胞局所照射装置(HZ1)と深度制御種子照射装置(HY1)を利用し、バystanダー細胞に生じるシグナル伝達経路の変化を、ヒト正常細胞を用いて明らかにすることを目的とする。これまでの研究において、Ar イオンマイクロビーム照射により、バystanダー細胞に細胞の生存シグナル伝達に関与する Akt のリン酸化、炎症反応に関与する COX-2 の蓄積が生じ、一酸化窒素(NO)の消去剤によって抑制されることを見出した。これらの現象は、転写因子である NF-κB を介するシグナル伝達機構に関与することから、NF-κB を解析した。今年度は、データの追加と再現性の確認を行った。

ヒト正常線維芽細胞 WI-38 を、6 穴プレート内に入れた直径 25 mm のカバーガラス上で 1 週間培養し、コンフルエントにした。照射 2 時間前に 60 mm ディッシュにカバーガラスを移した後、新しい培地もしくは NO の消去剤である carboxy-PTIO(c-PTIO, 20 μM)を添加した培地を加え培養した。マイクロビームの照射は、HZ1 ポートにおいて行い、5 粒子の 520 MeV ⁴⁰Ar¹⁴⁺を 5 細胞のみに照射した²⁾。対照実験として、HY1 ポートにおいてブロードビーム 5 Gy を全体に照射した。照射後にカバーガラス上の全細胞を回収した後、western blotting による解析を行った。

照射 6 時間後に回収した細胞を用いて解析した結果、Akt のリン酸化と COX-2 の蓄積誘導が生じるのに対し、NF-κB p65 の Ser536 のリン酸化は、照射細胞においてわずかに増加していたが、バystanダー細胞では変化は認められなかった(Fig. 1)。そのため、NF-κB のリン酸化がより早い時間に生じている可能性を考え、照射 3 時間後に細胞を回収して解析を行った(Fig. 2)。その結果、NF-κB p65 および Akt のリン酸化がバystanダー細胞において増加し、c-PTIO によって抑制されることを見出した。以上の結果から、高 LET 重イオン線によるバystanダー応答は、照射細胞から放出された NO により、バystanダー細胞において NF-κB、Akt が活性化し、COX-2 を誘導することによって生じることが明らかになった。

次に、WI-38 細胞を 3 次元培養することにより、スフェロイドを形成する方法を開発した。低接着性の U 字底の 96 穴

プレートに細胞を播種すると、スフェロイドを形成し、3 次元で細胞が融合している様子が観察された(Fig. 3)。今後はスフェロイドに加え、3 次元皮膚モデルも用いて検討を進める予定である。

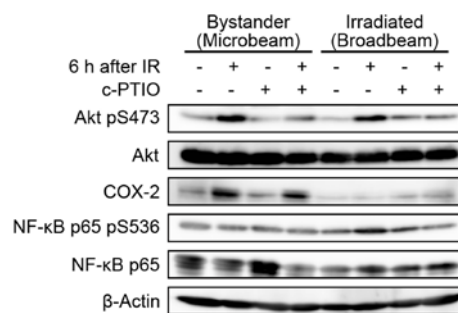


Fig. 1 Phosphorylation of Akt and NF-κB and accumulation of COX-2 in Ar-ion-irradiated or bystander WI-38 cells 6 h after irradiation. IR: Ar-ion irradiation; c-PTIO: carboxy-PTIO (20 μM).

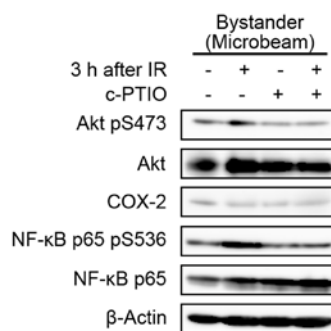


Fig. 2 Phosphorylation of Akt and NF-κB in bystander WI-38 cells 3 h after irradiation.

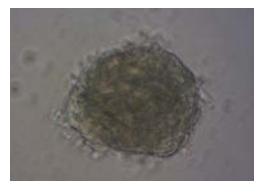


Fig. 3 Spheroid formation of WI-38 cells.

References

- 1) H. Matsumoto et al., Curr. Mol. Pharmacol. 4 (2011) 126.
- 2) T. Funayama et al., Radiat. Res. 163 (2005) 241.

3 - 09 Fluence-dependent Chromosomal Aberrations via Bystander Effect in Normal Human Fibroblasts Induced by C-, Ne- and Ar-ion Microbeams

M. Suzuki^{a)}, N. Autsavaporn^{a)}, T. Funayama^{b)}, Y. Yokota^{b)}, Y. Mutou^{b)}, M. Suzuki^{b)}, H. Ikeda^{b)}, Y. Hattori^{b)} and Y. Kobayashi^{b)}

^{a)} Research Center for Charged Particle Therapy, National Institute of Radiological Science,

^{b)} Medical and Biotechnological Application Division, QuBS, JAEA

We have been studying the radiation-quality dependent bystander cellular effects using heavy-ion microbeams with different ion species, such as C, Ne and Ar ions. From our observations so far, the bystander cell-killing effect via gap-junction mediated cell-cell communication was induced by carbon ions, but not neon and argon ions¹⁾. We continued to examine micronucleus formation induced by the bystander effect via either gap-junction mediated cell-cell communication or secreted factor(s) to culture medium from the irradiated cells. This year we focused on the fluence-dependent micronucleus formation using C-, Ne- and Ar-ion microbeams.

Early passage (passage number 6-10) normal human skin fibroblasts obtained from the Riken BioResource Center were irradiated with C-ion ($^{12}\text{C}^{5+}$ 220 MeV), Ne-ion ($^{20}\text{Ne}^{7+}$ 260 MeV) or Ar-ion ($^{40}\text{Ar}^{13+}$ 460 MeV) microbeams at the HZ1 port. Approximately 6×10^5 cells were inoculated into each of microbeam dish, which was made of acrylic resin ring with 36 mm diameter and attached 7.5 μm -thick polyimide film on the bottom of the ring, 2 days before the microbeam irradiation. Irradiations were carried out using the 256 (16 \times 16)-cross-stripe irradiation method described in the previous report²⁾. In this irradiation method we can estimate that the percentage of direct irradiated cells by the microbeams in the 256-cross-stripe irradiation method is around 0.04% of total cells on the dish, when comparing to areas of the cell and the dish. The beam size of each ion microbeam was 20 μm in diameter and the irradiations in each point were carried out to deliver 2, 4, 8, 16, 20 ions for carbon, 1, 2, 4, 5 ions for neon and 1, 2 ions for argon. The fraction of micronucleated cells was examined using the same method with the cytokinesis block technique in the previous report³⁾. At least 500 cells were examined for each data point and ion, and only micronuclei in binucleated cells were detected as a damaged cell. In order to investigate the mechanism(s) of the bystander effect, half of the sample dishes were treated with 18- α -glycyrrhetic acid (AGA), which was a specific inhibitor of gap-junction mediated cell-cell communication, 30 min prior to irradiations³⁾.

Figure 1 shows the fluence-dependent formation of micronuclei induced by carbon-, neon- and argon-ion microbeams. In any ion species, the percent of the micronuclei formation in the absence of AGA clearly showed fluence-dependent manner and was suppressed when using the presence of AGA. The percent of the

formation of micronuclei was ranging from 2-10% in the absence of AGA and 1-4% in the presence of AGA and the results shown were beyond our expectation, because only 0.04% of total cells in the dish was directly hit by the ions. This is clear evidence that two different mechanisms play a critical role in inducing bystander effect in chromosomal damage, such as gap-junction mediated cell-cell communication in the case of the absence of AGA and secreted factor(s) to culture medium from the irradiated cells in the case of the presence of AGA.

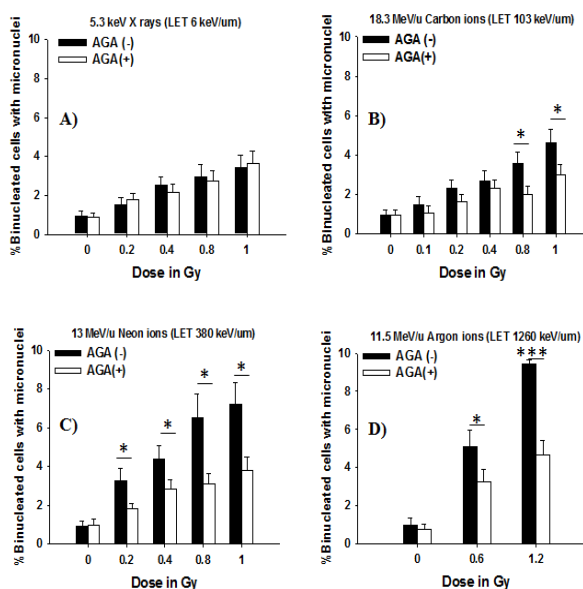


Fig. 1 The fluence-dependent formation of micronuclei in normal human fibroblasts irradiated with carbon (B), neon (C) and argon (D) ion microbeams. The data of X-ray microbeams (A) were carried out at Photon Factory in High Energy Accelerator Research Organization. The results were the means and standard deviations from the 3 independent beam times.

References

- 1) M. Suzuki et al., JAEA Takasaki Annu. Rep. 2010 (2012) 72.
- 2) M. Suzuki et al., JAEA Takasaki Annu. Rep. 2006 (2008) 107.
- 3) M. Suzuki et al., JAEA Takasaki Annu. Rep. 2011 (2013) 69.

3 - 10 **Ion Beam Irradiation Has Different Influences on the Expression of Bax in Cultured Human Retinal Vascular Endothelial Cells Exposed to L-dopa among ^{20}Ne , ^{12}C , and ^4He**

K. Akeo^{a),b)}, T. Funayama^{c)}, Y. Kobayashi^{c)} and Y. Akeo^{a)}

^{a)}Akeo Eye Clinic, ^{b)}Keio University School of Medicine,

^{c)}Medical and Biotechnological Application Division, QuBS, JAEA

Deficiency of L-dopa causes degeneration of the substantia nigra in the brain and L-dopa is used in the treatment of Parkinson's disease. We proved that L-dopa produced NO and superoxide, and had the cytotoxic effects on the retinal pigment epithelial cells¹⁾. GPx3, a plasma antioxidant enzyme, maintains genomic integrity by inactivating these reactive oxygen species, known DNA-damaging agents²⁾. Bcl-2 (B-cell lymphoma 2) is the founding member of the Bcl-2 family of apoptosis regulator protein encoded by the BCL2 gene³⁾. These proteins govern mitochondrial outer membrane permeabilization and can be either pro-apoptotic or anti-apoptotic including Bcl-2 proper. The increase of outer mitochondrial membrane permeability (MMP) is a central event in apoptotic cell death, since it releases several apoptogenic factors such as cytochrome c into the cytoplasm that activate the downstream destructive processes. The voltage-dependent anion channel (VDAC) plays an essential role in the increase of MMP, and is regulated by the Bcl-2 family of proteins via direct interaction. Anti-apoptotic Bcl-2 family members close the VDAC, whereas some pro-apoptotic members, that is, Bax genes (Bcl-2-associated X protein), interact with the VDAC to generate a protein-conducting channel through which cytochrome c can pass⁴⁾. In the absence of any apoptotic/oxidant stimulus, Faucher et al. measured the expression of Bax and Bcl-2 in a human endothelial like cell-line overexpressing the organic hydroperoxide-scavenging enzyme, glutathione peroxidase (GPx), which is able to change the protein Bax levels without affecting those of p53 and Bcl-2⁵⁾.

We previously reported that exposure to L-dopa inhibited the expression of GPx3 in human retinal endothelial (RE) cells in vitro. Ion beam irradiations both of He and C decreased GPx3 more remarkably than Ne. The expression of GPx3 incubated with L-dopa decreased significantly after irradiation to both He and C. The irradiation of Ne increased the expression of GPx3 incubated with L-dopa after the exposure of the irradiation significantly⁶⁾. The expression of p53 was not significantly influenced by L-dopa, but increased just after the irradiation both of Ne and He in those cells incubated with L-dopa⁷⁾. There were no significant differences of Bcl-2 gene expression among the irradiation of Ne, C, and He. L-dopa significantly inhibited the expression of anti-apoptotic Bcl-2. The expression of Bcl-2 in RE cells incubated with L-dopa decreased significantly after the irradiation of C. We considered the different accumulation of the energy irradiated at a point by various ions could be concerned with the effects on the expression of Bcl-2 in RE cells incubated with L-dopa as well as GPx3 or p53⁸⁾.

Ion beam irradiation caused the induction of apoptosis in RE cells that affected by inactivating the reactive oxygen species because of exposure to L-dopa. We investigated how L-dopa influenced the expression of pro-apoptotic Bax genes in RE cells. We applied the ion beams as the induction of the oxidative stress that might influenced this pro-apoptotic Bax gene, and measured the expression using a real time-reverse-transcriptase polymerase chain reaction (RT-PCR). Human RE cells incubated with 250 μM L-dopa were exposed to an ionization radiation (350 MeV Ne, 220 MeV C, and 50 MeV He). We obtained the cells after the irradiation and extracted total cellular RNA and cDNA was synthesized. We designed the primers for RT-PCR amplification of the cDNA of Bax. The reactions were carried out at the following temperature: 95 °C, for denaturation; 60 °C, for annealing; and 72 °C. After mixing the cDNA, primer, and SYBR green, the expression of 18s RNA and Bax was measured using the LightCycler system as RT-PCR. The technology of this system is extremely innovative and enables rapid and simultaneous evaluation PCR experiments. Fluorometric analysis of the formed PCR products was performed as a real-time measurement either continuously or at specifically defined time points during each PCR cycle.

There were no significant differences of Bax gene expression without L-dopa among the irradiation of Ne, C, and He. However, Exposure to L-dopa for 2 h significantly inhibited the expression of Bax in human RE cells in vitro. The expression of Bax in RE cells incubated with L-dopa decreased significantly after 4, 8, 24 h of irradiation in case of Ne, and after 0 and 8 h of irradiation in case of C. We speculated that L-dopa had no significant effects on the expression of p53 in human RE cells in vitro because L-dopa damaged both expression of anti-apoptotic Bcl-2 genes and pro-apoptotic Bax genes in mitochondria. We considered that it was possible for the long duration of the exposure to the irradiation of C to augment the effects on the pro-apoptotic Bax genes in human RE cells in vitro.

References

- 1) K. Akeo et al., *Pigment Cell Res.* 13 (2000) 80.
- 2) B. Chen et al., *Cancer Lett.* 309 (2011) 37.
- 3) Y. Tsujimoto, et al., *Science*. 228 (1985) 1440.
- 4) Y. Tsujimoto, et al., *Biochimie*. 84 (2002) 187.
- 5) K. Faucher et al., *Mol. Cell Biochem.* 277 (2005) 81.
- 6) K. Akeo et al., *Tiss. Cult. Res. Commun.* 32 (2013) 195.
- 7) K. Akeo et al., *JAEA Takasaki Annu. Rep.* 2009 (2011) 95.
- 8) K. Akeo et al., *JAEA Takasaki Annu. Rep.* 2011 (2013) 71.

3 - 11 Radiosensitivity is Affected by the Dependence of DNA Double-strand Break Repair on LET

A. Takahashi^{a,b)}, M. Kubo^{b)}, H. Ma^{b)}, A. Nakagawa^{b)}, Y. Yoshida^{c)}, T. Kanai^{c)}, T. Ohno^{c)}, Y. Furusawa^{d)}, T. Funayama^{e)}, Y. Kobayashi^{e)} and T. Nakano^{b,c)}

^{a)}Advanced Scientific Research Leaders Development Unit, Gunma University, ^{b)}Department of Radiation Oncology, Gunma University, ^{c)}Gunma University Heavy Ion Medical Center, ^{d)}Research Center for Charged Particle Therapy, National Institute of Radiological Sciences, ^{e)}Medical and Biotechnological Application Division, QuBS, JAEA

Ionizing radiation induces DNA double-strand breaks (DSBs) and DSBs are potentially lethal lesions and a threat to cell survival. There are two major pathways for the repair of DSBs: homologous recombination (HR) and non-homologous end-joining (NHEJ). Higher levels of cell death are induced by high-linear energy transfer (LET) radiation when compared with low-LET radiation, even at the same doses. This reflects the higher relative biological effectiveness (RBE) of high LET radiation resulting from less effective or less efficient DNA repair. Reports have shown that heavy-ion-induced DSBs are repaired more slowly than X-ray-induced DSBs¹⁾. In particular, carbon-ion beams have a high LET value and a high RBE in the Bragg peak region. When targeting appropriate tumors, this might confer an additional advantage for the use of radiation in cancer therapy. However, it is unclear whether high-LET radiation specifically inhibits one repair pathway or both repair pathways.

To clarify the relationship between DSB repair and radiosensitivity in the presence of radiation with different LET values, knock-out (KO) embryonic fibroblasts were constructed. The genes targeted in these KO cells were designed to result in no repair activity from a KO of the NHEJ-related *LIG4* gene and/or the HR-related *Rad54* gene. Results in these KO mice were compared to activity in the parental (wild-type) cells which were provided by Dr. F.W. Alt (Howard Hughes Medical Institute, USA). Cells were irradiated with X-rays and carbon-ion beams at Gunma University (13, 50 and 70 keV/μm) and TIARA (108 keV/μm), and iron-ion beams at the NIRS

(200 keV/μm). The surviving fractions were analyzed with colony formation assays (Fig. 1). RBE ratios were calculated using the 10% survival doses (Fig. 2).

In addition, the sensitization ratios were also calculated using the 10% survival doses from wild-type cells and KO cells for DSB repair (Fig. 3).

Wild-type cells and *Rad54* KO cells were more sensitive with increasing LET

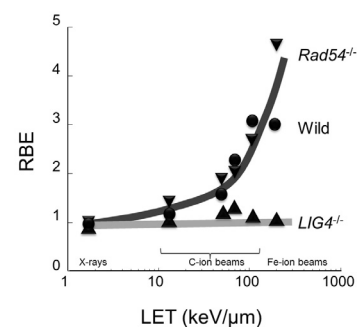
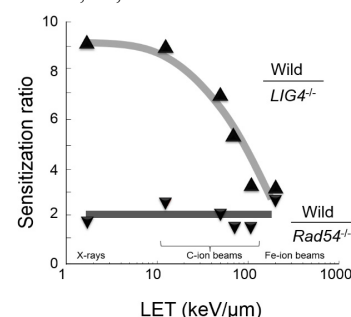


Fig. 2 LET-RBE curves. ●, wild-type cells; ▲, *LIG4*-KO cells; ▼, *Rad54*-KO cells.



values. *LIG4* KO cells showed exactly the same sensitivities in response to different LET values (Fig. 1). Wild-type cells and *Rad54*-KO cells, i.e. NHEJ proficient cells, exhibited high RBE values with increasing LET values (Fig. 2). Although a deficient HR (wild/*Rad54*-KO) exhibited an almost constant sensitization ratio, a deficient NHEJ (wild/*LIG4*-KO) exhibited a high sensitization ratio when compared to a deficient HR, even with increasing LET values (Fig. 3).

These results suggest that: (1) the determining factor leading to a high RBE in the presence of high LET radiation may be the suppression and/or the inefficacy of NHEJ repair; and (2) targeting NHEJ repair yields a high radiosensitivity in the presence of carbon-ion beams when compared to suppressing HR. Further analysis of these results is currently underway.

Reference

1) A. Takahashi et al., J. Radiat. Res. 49 (2008) 645-52.

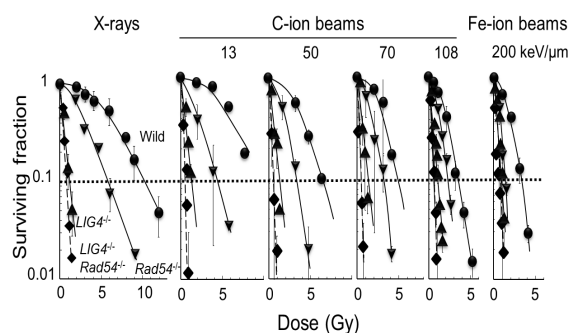


Fig. 1 The effect of DSB repair on radiosensitivity after exposure to radiation with different LET values. ●, wild-type cells; ▲, *LIG4*-KO cells; ▼, *Rad54*-KO cells; ◆, *LIG4*- and *Rad54*-KO cells.

3 - 12 Epigenetic Modifier as a Potential Radiosensitizer for Heavy-ion Therapy on Malignancy

K. Saito^{a,b,c)}, T. Funayama^{b,c)}, Y. Kobayashi^{b,c)} and T. Murakami^{a)}

^{a)}Faculty of Pharmacy, Takasaki University of Health and Welfare, ^{b)}Medical and Biotechnological Application Division, QuBS, JAEA, ^{c)}Graduate School of Medicine, Gunma University

Introduction

Malignant melanoma is one of the most common cutaneous malignancies and its incidence worldwide has been increasing at a greater rate than that of any other cancer. Unfortunately, it resists often various authentic therapies including chemotherapy and radiation therapy, and it is well characterized by very low objective clinical responses, representing lethal disease.

Epigenetic modifiers have emerged recently as promising anticancer agents and it has been expected that epigenetic modifiers may enhance the effect of other cancer therapeutics including radiotherapy¹⁾. In addition, the biological effects of the high linear energy transfer (LET) heavy-ion radiation are more pronounced than the low-LET radiation (e.g., γ -ray or X-ray). These accumulating evidences allowed us to investigate whether the use of epigenetic modifiers could sensitize melanoma cells for the heavy-ion therapy.

Materials and methods

Cell and cell culture

Murine B16F10 melanoma cells were purchased from the American Type Culture Collection (Manassas, VA, USA). Cells were cultured in Dulbecco's Modified Eagle Medium (Invitrogen, Carlsbad, CA, USA) supplemented with 10% fetal bovine serum (MP Biomedicals, Santa Ana, CA, USA) and 1% antibiotic-antimycotic (GIBCO, Carlsbad, CA, USA) at 37 °C in a humidified atmosphere with 5% CO₂.

Radiation exposure

The ⁶⁰Co γ -ray irradiation was performed in Room No.1 of the food irradiation facility at JAEA-Takasaki. The heavy-ion irradiation groups were exposed to carbon ions accelerated by the AVF cyclotron and generated with the HY1 port of TIARA at JAEA-Takasaki. Control groups were sham-irradiated and handled in parallel with the test groups.

Clonogenic survival assay

Cells in exponential growth were seeded at a density 1×10^6 cells per 35 mm culture dish 20-24 h before irradiation. Cells were treated with investigational or comparator epigenetic modifier for 16.5 h and then irradiated. The concentration of modifier was selected that required to reduce colony formation by 10% alone. After irradiation, cells were trypsinized and plated after appropriate dilution onto 100 mm culture dishes. Cells (between 100 and 10,000) were seeded per dish in order to obtain between 30 and 100 single well-separated colonies per dish. After

9 (± 1) days, colonies were fixed with 2% formalin and followed by crystal violet staining. Colonies generated more than 50 cells were counted as clonogenic survivors and the number of colonies was normalized to that observed for unirradiated controls. Three dishes were counted per point. Data presented are the mean \pm SE from at least three independent experiments. For statistics evaluation, *P* values were analyzed with two-way ANOVA test.

Results and discussion

Treatment of B16F10 melanoma cells with an epidemic modifier in combination with heavy-ion radiation provided enhanced inhibition of colony formation (Fig. 1). These data suggest that combination of these drugs with heavy-ion therapy may provide improved therapeutic response in melanoma patients.

Reference

- 1) L. S. Kristensen et al., Eur. J. Pharmacol. 625 (2009) 131-42.

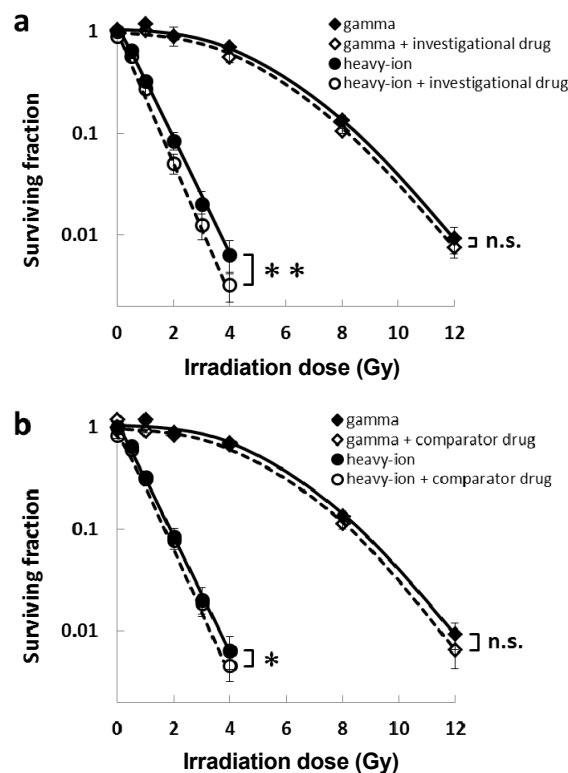


Fig. 1 The effect of epigenetic modifiers on radiosensitivity for melanoma cells by clonogenic assay. (a) investigational drug (b) comparator drug. **P* < 0.05; ***P* < 0.01; n.s., not significant.

3 - 13

Apoptotic Cell Death of the Heavy Ion Irradiated Silkmoth Egg after Cellular Blastoderm Stage

K. Shirai^{a)}, T. Funayama^{b)}, T. Sakashita^{b)}, Y. Yokota^{b)} and Y. Kobayashi^{b)}^{a)}Faculty of Textile Science and Technology, Shinshu University,^{b)}Medical and Biotechnological Application Division, QuBS, JAEA

Until now, we reported that the heavy ion irradiated silkworm egg (10 Gy of carbon ions) restart the development after short time delay, in spite of imperfect repair of the DNA damage. Then, the egg having damaged DNA is thought to die at 14 hours after oviposition, because the damaged nuclei disappear at the time. However, the elimination mechanism of the damaged nuclei is unknown. So, we examined the timing and mechanisms of the elimination for the irradiated nuclei.

In the irradiated egg, a part of nuclei reached front part of egg at 12 hours after oviposition. But the nuclei in about half of the eggs were hardly detected under microscope at this time. These results indicate the timing of elimination of the damaged nuclei is at 12-14 hours after oviposition. Moreover, the positive signals of TUNEL staining were detected in the eggs. These results indicate the damaged nuclei in the irradiated egg degrade (just) after cellular blastoderm stage by apoptosis.

著者らは、10 Gy の $^{12}\text{C}^{5+}$, 220 MeV イオン照射をカイコ受精卵に行った場合、約 2 時間の発生停止後、すぐに発生(分裂)を再開する一方で、ほとんどの卵が孵化することなく、発生途中で致死することを明らかにしている。

昨年度は、致死卵の中で全体の約 6 割を占める胚帯形成前に発生停止した卵において卵の周辺細胞質に到達した後、核が崩壊している可能性を示した。そこで本年度は、分裂核の崩壊機構をさらに詳細に追究した。

重イオン照射には、TIARA 施設の $^{12}\text{C}^{5+}$, 220 MeV イオンを用い、照射線量は昨年度と同じ 10 Gy とした。照射は卵の産下 2 時間 10 分後に行い、照射後 10 時間から 18 時間まで 1 時間ごとに、それ以降は 1-3 日ごとに卵をサンプリングし解析に用いた。

最初、受精直後に照射する目的で産下 2 時間後に重イオン照射を行っていたが、これらの卵はほとんど発生することなく死滅する結果となった。そこで凍結切片を作成し観察したところ、ほとんどの卵において分裂核が認められず、発生が全く進んでいないことが示唆された。原因は現在のところ不明であるが、カイコ系統や照射準備室内温度の僅かな変化により、発生速度が変化した可能性がある。そこで照射時間を 10 分間遅らせ照射を試みたところ、このような現象は認められなくなった。この受精前や直後における照射が受精に与える影響については今後追究する予定である。

照射卵における分裂核の崩壊ステージとその機構を調査した。Figure 1 はその結果である。A および B は産下 13 時間後の照射卵の核を DAPI 染色で検出したものである。図 A では周辺細胞質に到達した分裂核が観察される。照射卵の約半数はこの後も発生を続け、一部は孵化する。しかしながら、この様な卵の染色体も傷害は完全には修復していないものが多数あると考えられ、一部の個体では染色体切断を示唆する「まだら」状の幼虫斑紋が観察された(データ省略)。一方、図 B では明確な同じステージにもかかわらず核が明確に観察されず、代わりに卵殻周辺にモヤ状の物質が染色された。非照射の対照区の孵化率から不受精卵とは考えられないことから、この卵の核はアポトーシスにより崩壊し、排除されつつあると考えられた。そこで分裂核のアポトーシスの検出を試みた(図 C)。その結果、崩壊しつつあると思われる分裂核が TUNEL 陽性として

検出された。

以上、本研究により昨年度の予想通り、重イオン照射を受けたカイコ初期発生卵の分裂核が周辺細胞質への到達後、速やかにアポトーシスにより崩壊し、その後排除されることが確認された。

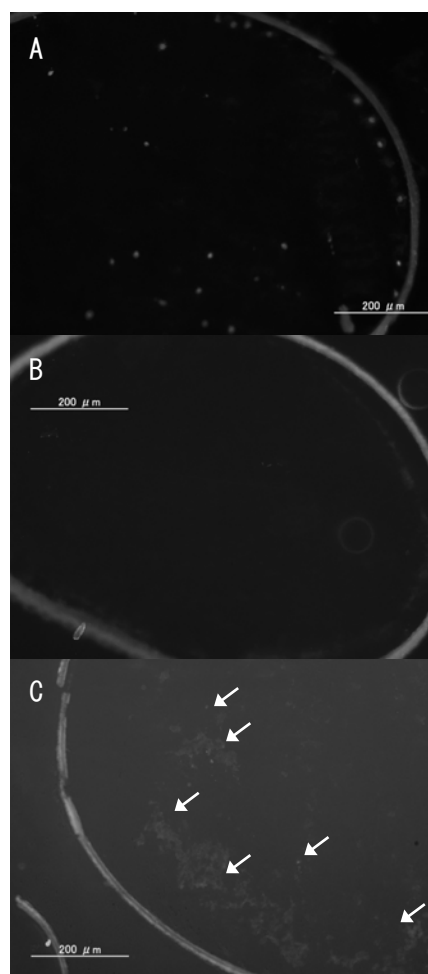


Fig. 1 Heavy ion irradiated silkworm egg at 13 hour after oviposition. A and B: DAPI staining of the nuclei, C: Detection of apoptotic nuclei by TUNEL.

3 - 14 Promotion of Miss-differentiation of Testis-ova in p53 Deficient Medaka Testis by Micro-beam Irradiation of Carbon-ions

T. Yasuda^{a)}, S. Oda^{a)}, T. Watanabe-Asaka^{a)}, T. Funayama^{b)}, Y. Yokota^{b)}, Y. Mutou^{b)},
H. Ikeda^{b)}, Y. Kobayashi^{b)} and H. Mitani^{a)}

^{a)}Graduated School of Frontier Sciences, The University of Tokyo,

^{b)}Medical and Biotechnological Application Division, QuBS, JAEA

In our previous study, we found that a small number of oocyte-like cells (testis-ova) differentiated spontaneously in the cysts of spermatogonia in the p53-deficient testes, in contrast to the wild-type testes in which testis-ova were never found. Furthermore, ionizing radiation (IR) irradiation temporarily increased the number of testis-ova in p53 deficient testes, testis-ova size, and proceeded up to premature meiosis. In the present study, we applied 10 - 15 targeted irradiation of testes in living adult medaka with carbon-ion micro-beam (diameters of 250 μm). And the analysis that is the differentiation of testis-ova in the p53-deficient medaka testes 7 days after irradiation, is underway to validate the availability of the testis-ova phenotype as an indicator of the irradiation.

p53 遺伝子を欠損したオスメダカ精巣では、精原幹細胞に混在して卵原細胞が存在し、ガンマ線の照射によってこれら卵原細胞の卵細胞 (testis-ova) への分化・成長が顕著に促進される¹⁾。ガンマ線 (5 Gy) の照射 3 日後から卵細胞の分化・成長が促進され始め、照射 2 週間後までに減数分裂複糸期の途中まで進行するとともに testis-ova はそのサイズを増大させ、ガンマ線照射後 1 週間前後に極めて特徴的な精巣組織像を見せる。異常分化を起こした testis-ova はその後死滅して排除され、照射 28 日後には精巣の組織像は非照射時の正常な組織像に戻る¹⁾。野生型メダカ精巣および非照射時の p53 遺伝子欠損メダカ精巣においてはこのような組織像は見られないことから、p53 遺伝子欠損メダカ精巣における testis-ova の分化・成長は、放射線照射によって一過的に誘導されるものであり、放射線照射の明瞭な指標となるものと期待できる。

我々は過去に炭素重粒子線マイクロビームを用いてメダカ成魚の精巣を選択的に照射する手法を開発した。今回、p53 遺伝子欠損メダカ精巣において testis-ova の分化・成長を指標として、精巣選択的照射法の有効性を検証するとともに、ブロードビーム照射による影響と比較することによって放射線の組織応答の研究におけるマイクロビーム照射法の有用性を確認した。

照射実験では、p53 遺伝子欠損メダカオス成魚に MS222 麻酔を施し、 $^{12}\text{C}^{6+}$, 320 MeV マイクロビーム (照射範囲の直径 250 μm , 5 Gy および 10 Gy、各々 3 尾) を精巣が位置する胴体部 10-15 ヶ所 (Fig. 1 の赤丸印) へ照射した。また、別のオスメダカに対して、ブロードビームを用いて全身照射を行った。照射 7 日後に精巣を単離し、Davidson 固定後テクノビット樹脂包埋し、精巣中央部の組織切片 (7 μm 厚) を作成後、HE 染色を施し検鏡した。

炭素重粒子線 5 Gy 及び 10 Gy をブロードビーム照射した群の精巣では、ガンマ線照射時と同様、分化・成長が進行した卵母細胞が多数個観察された (Fig. 2A, C 矢印)。一方、精巣組織のみを狙ってマイクロビーム照射した場合、10 Gy 照射群ではブロードビーム照射群に比して成長が進行していない小さな卵母細胞が誘導され (Fig. 2D 矢印)、5 Gy マイクロビーム照射群では卵母細胞はほとんど誘導されず、ブロードビーム照射群と明瞭な差が認められた。これ

らの結果は、精巣組織のみを選択的に照射した場合、全身照射した場合より放射線の組織影響が小さいことを示しており、組織選択的に照射された場合の組織応答の解明におけるマイクロビームの有効性を示すものであると考えられる。

Reference

- 1) T. Yasuda et al., Cell death & disease (2012) 3, e395.

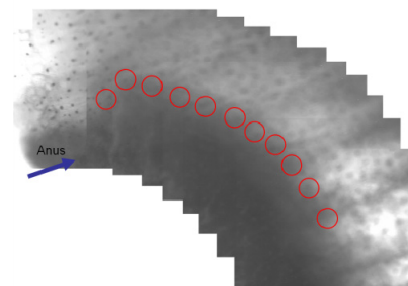


Fig. 1 Testis in abdomen of adult medaka was irradiated with 10 or more shots (red circles) of carbon-ion micro-beam.

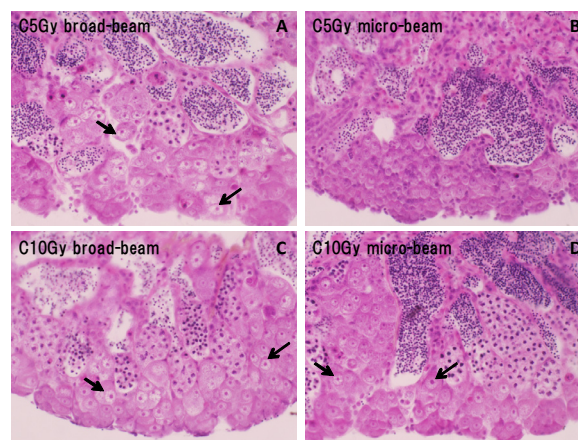


Fig. 2 Induction of testis-ova in p53 deficient medaka testis by carbon-ion broad- and micro-beam irradiation at 7 days after irradiation.

3 - 15 Polythene Chromosome Abberation as a Possible Marker for Assessing DNA Damage upon Ionizing Radiation in the Sleeping Chironomid Larvae

O. Gusev^{a,c)}, S. Shimura^{a)}, R. Cornette^{a)}, T. Kikawada^{a)}, T. Sakashita^{b)}, T. Funayama^{b)}, Y. Kobayashi^{b)} and T. Okuda^{a)}

^{a)}Anhydrobiosis Research Group, National Institute of Agrobiological Sciences,

^{b)}Medical and Biotechnological Application Division, QuBS, JAEA,

^{c)}Department of Invertebrate Zoology, Kazan Federal University

The Sleeping Chironomid, *Polypedilum vanderplanki* can stand complete desiccation (anhydrobiosis) and also shows radio-resistance¹⁾. A comet assay revealed that both desiccation and heavy ion irradiation cause severe DNA damage in cells of the larvae and that post-anhydrobiosis and post-irradiation recovery of nucleic acids takes at least a few days²⁾. Non-irradiated dry larvae after revival also possessed cells with severely damaged DNA, with a level of fragmentation comparable to those exposed to 70 Gy ⁴He ions. ROS generated upon dehydration of cells are probably a major cause of the DNA fragmentation. Three major participants of the ROS-elimination system, i.e. catalase, Cu/Zn-superoxide dismutase and glutathione peroxidase were found to be abundant in the EST database prepared from the larvae entering anhydrobiosis³⁾. Gamma-rays irradiation increased expression of these 3 genes within the first few hours after irradiation. We also recognized the expression of two other genes involved in DNA-damage recognition and repair upon anhydrobiosis and irradiation, i.e. *Rad23* which plays a central role both in proteosomal degradation of misfolded proteins, DNA excision repair, and recognition of different types of DNA damage; and *Rad51* which participates in common DNA-damage response pathway and are associated with the activation of homologous recombination and double-strand breaks repair.

P. vanderplanki larva has a giant polythene chromosome which could be a good tool to assess the DNA damage and its repair in relation to anhydrobiosis and irradiation stress. Now it is the right time to establish this method because it has many applications in the future. As an example influence of radioactive contamination in Chernobyl regions has been successfully monitored by observing the morphological changes in the polythene chromosome of chironomid larvae⁴⁾. By using the dehydrated *P. vanderplanki* larvae similar radiation monitoring system can be applied in Fukushima and International Space station.

The *P. vanderplanki* karyotype contains 2n=8 and the chromosome I has characteristic puffs which specifically appear upon anhydrobiosis (Fig. 1 and 2). We will further complete all the chromosome band patterns and also identify the corresponding genes do by FISH and genome analysis.

References

- 1) M. Watanabe et al., Int. J. Radiat. Biol. 82 (2006) 587-92.
- 2) O. Gusev et al., PLoS ONE 5, (2010) e14008.
- 3) R. Cornette et al., J. Biol. Chem. 285 (46) (2010) 35889-99.
- 4) Petrova & Zhironov, Rus. J. Genet: Appl. Res. 2 (2012) 127.

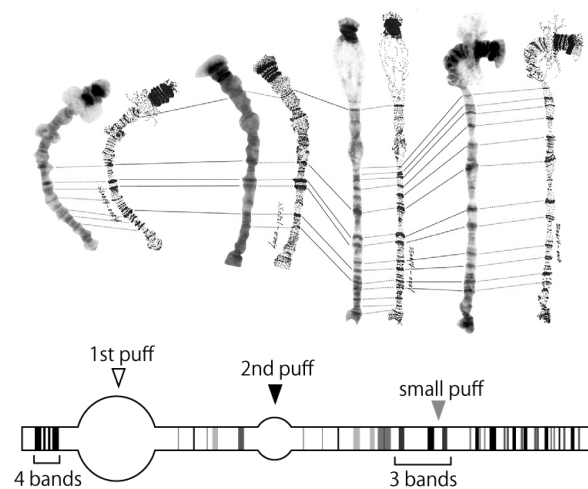


Fig. 1 *Polypedilum vanderplanki* polythene chromosome 1 (up) and the schematic picture (bottom) of active larvae.



Fig. 2 *P. vanderplanki* polythene chromosome 1 from a larva just rehydrated. An arrow indicates post-anhydrobiosis specific puff.

3 - 16

Effects of Carbon-ion Microbeam Irradiation on Pharyngeal Pumping in *Caenorhabditis elegans*

M. Suzuki^{a)}, Y. Hattori^{a,b)}, T. Sakashita^{a)}, T. Funayama^{a)}, Y. Yokota^{a)},
H. Ikeda^{a,c)} and Y. Kobayashi^{a,c)}

^{a)}Medical and Biotechnological Application Division, QuBS, JAEA,

^{b)}Graduate School of Engineering, Hiroshima University,

^{c)}Gunma University Graduate School of Medicine

We recently reported that locomotion in the nematode *Caenorhabditis elegans* using body-wall muscles was significantly reduced after broad-beam irradiation of the whole body¹⁾, and slightly reduced after region-specific microbeam irradiation (500 Gy) of local regions of the body²⁾. This suggested that radiation delivered to a very limited region of the body is sufficient to reduce locomotion²⁾. To investigate the radiation effects on different types of movement using different muscles, we subsequently focused on pumping motion (chewing and swallowing) which is a rapid periodic motion involving the use of the pharyngeal muscles, and found that the proportion of animals in which the pumping motion stopped had increased after broad-beam irradiation³⁾. In the present study, we examined whether or not the same effects on pharyngeal pumping motion could be induced by region-specific microbeam irradiation.

Young adult wild-type *C. elegans* were used in the experiments. To investigate the effects of region-specific microbeam irradiation, we used energetic carbon ions ($^{12}\text{C}^{5+}$, 18.3 MeV/u, LET=119 keV/ μm) generated at the HZ1 port of TIARA at JAEA. *C. elegans* was enclosed in a polydimethylsiloxane microfluidic device⁴⁾ with buffer to inhibit locomotion during irradiation (Fig. 1). The 'head' region including the pharynx, 'middle' region around the intestine, and 'tail' region were targeted independently; these regions were irradiated with 12,000 carbon ions corresponding to 500 Gy at a 20 μm micro-aperture region. *C. elegans* was placed on an agar dish with a bacterial lawn (food) immediately after irradiation, and 60-continuous shots of the pharyngeal pumping motion, each of 1 s duration, were obtained using a high-speed camera. The frequency of the pumping strokes per 1 s duration, used as an evaluation standard of the pumping motion, was manually counted.

As shown in Fig. 2, all in all the distribution of the frequencies of the pumping motion in each group of the region-specific microbeam-irradiated animals was similar to that in the non-irradiated animals, though the proportion of animals in which the pumping motion had stopped increased slightly in the group irradiated in the head region. These findings suggested that a region-specific microbeam irradiation at a dose of 500 Gy did not affect the pharyngeal pumping motion differently from the whole-body irradiation. Further studies involving the effects of microbeam irradiation on pumping motion in *C. elegans* are in progress.

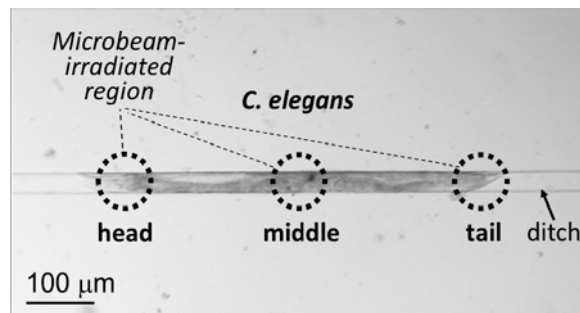


Fig. 1 A *C. elegans* enclosed in a microfluidic device. The dotted circle represents the microbeam-irradiated region.

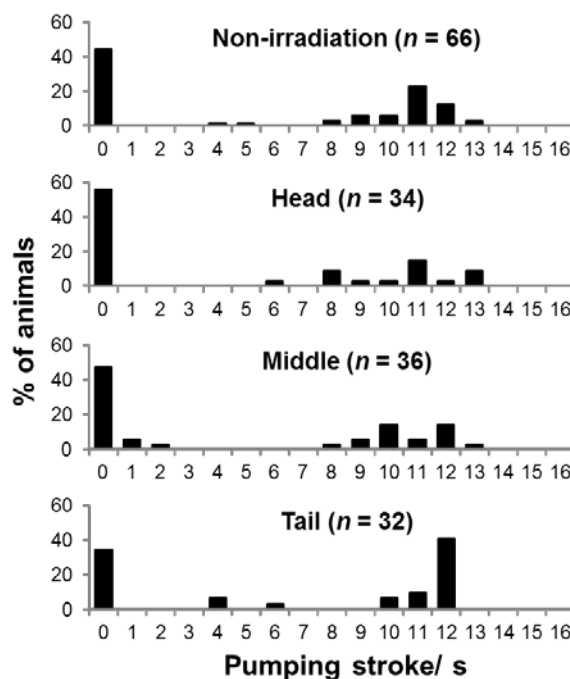


Fig. 2 Pharyngeal pumping motion in *C. elegans* after microbeam irradiation. *n* represents the number of animals.

References

- 1) T. Sakashita et al., Biol. Sci. Space 26 (2012) 7-11.
- 2) M. Suzuki et al., JAEA Takasaki Annu. Rep. 2011 (2013) 77.
- 3) M. Suzuki et al., JAEA Takasaki Annu. Rep. 2010 (2012) 80.
- 4) Lockery et al., J. Neurophysiol. 99 (2008) 3136-43.

3 - 17 Electron-spin Relaxation Times of Irradiated Fructose Measured with Pulsed ESR

M. Kikuchi^{a)}, H. Kameya^{b)}, Y. Shimoyama^{a)}, M. Ukai^{c)} and Y. Kobayashi^{a)}

^{a)}Medical and Biotechnological Application Division, QuBS, JAEA,

^{b)}National Food Research Institute, ^{c)}Hokkaido University of Education

Electron spin resonance (ESR) spectroscopy has been authorized worldwide as an irradiated food detection method. We had established a procedure for radiation-induced radicals in irradiated fresh fruits^{1, 2)}. However, detectable periods of the radicals depend on their lifetime. The lifetime is related to the interactions with neighboring unpaired electrons. One of the physical interactions is electron-spin relaxation times: spin-lattice relaxation time T_1 and spin-spin relaxation time T_2 .

In this study, the relaxation times of unpaired electrons in radiation-induced radicals concerning irradiated foods were directly measured using pulsed ESR to reveal the strength of interaction with the neighboring dipoles. The specimen is fructose, edible pure chemicals, and mainly contained in fruits.

The powder of fructose crystal was exposed to ^{60}Co γ -rays at room temperature by changing the radiation dose levels from 1 to 100 kGy. ESR spectroscopy was performed with a continuous wave (CW) ESR (Jeol RE-3X) and a pulsed ESR (Bruker ESP-380E) at room temperature using the X-band microwave frequency.

ESR spectra of irradiated fructose crystals by CW ESR were essentially same at tested dose levels, as shown in Fig. 1. While, ESR spectra by pulsed ESR were drastically different according to dose levels (Fig. 2). We detected four signals, of which the g -factor was same (Figs. 1 and 2).

Main peak observed at 1 kGy was broad on pulsed ESR. Increasing with the dose levels, main peak was clearly split to two peaks (LM & RM in Fig. 2). Furthermore, relative heights of side peaks (LS & RS in Fig. 2) increased as the increasing of dose levels. It is suggested that CW ESR can measure all of the unpaired electrons, while pulsed ESR can detect the interactions based upon neighboring unpaired electrons as the electron-spin echo swept in magnetic field.

Figure 3 shows the relationship between the dose level and the relaxation times. T_1 showed no changes, however, T_2 decreased as with the increases of the dose levels. The reduction of T_2 means the stronger spin-spin interactions. The stronger interactions could be caused by accumulation of radicals in the irradiated fructose crystals. Moreover, these responses may be affected by differences in the environment of the radicals in fructose molecules. T_2 of the side peaks were longer than those of the main peaks in fructose, indicating that radicals of the side peaks interact less with neighboring dipoles than do those of the main peaks³⁾.

References

- 1) M. Kikuchi et al., Spectrochim. Acta A 75 (2010) 310.
- 2) M. Kikuchi et al., Radiat. Phys. Chem. 80 (2011) 664.
- 3) M. Kikuchi et al., Radiat. Phys. Chem. 81 (2012) 1639.

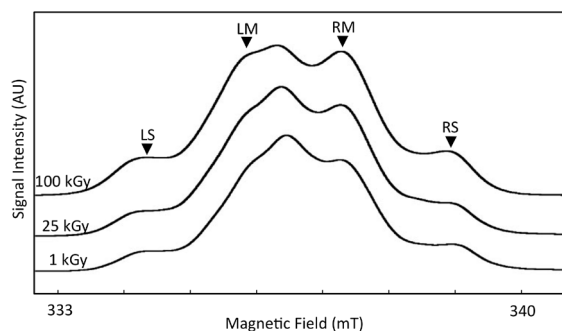


Fig. 1 CW ESR spectra of γ -irradiated fructose. LS, RS, LM and RM are designated from left and right side peaks, and left and right main peaks of pulsed ESR spectrum, respectively.

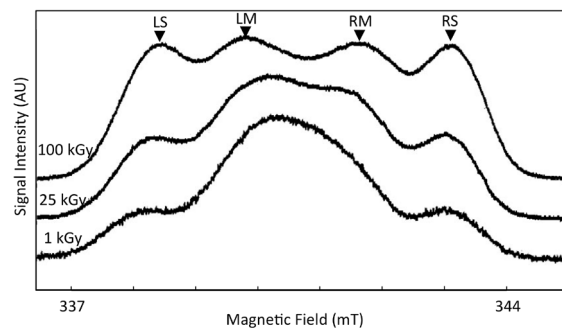


Fig. 2 Field-swept spectra of electron spin echo signals in γ -irradiated fructose using pulsed ESR.

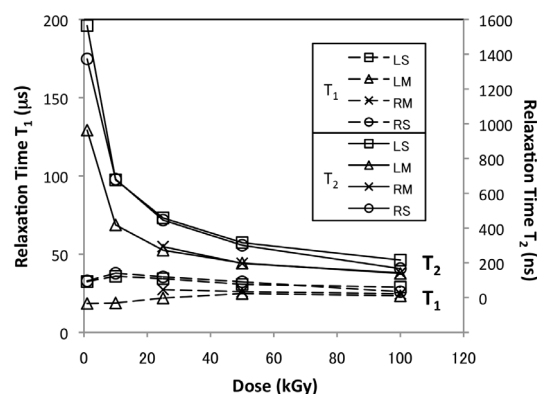


Fig. 3 Dose responses of electron spin relaxation time T_1 and T_2 in γ -irradiated fructose.

3 - 18 Relaxation Times of Radicals Induced in Irradiated Foods Using Pulse-ESR and CW-ESR

K. Kishita^{a)}, S. Kawamura^{a)}, M. Kikuchi^{b)}, H. Nakamura^{a)},
Y. Kobayashi^{b)} and M. Ukai^{a)}

^{a)}Hokkaido University of Education,

^{b)}Medical and Biotechnological Application Division, QuBS, JAEA

Using pulse-ESR and CW-ESR, we attempted the measurement of relaxation times (T_1 , T_2) of radicals induced in irradiated foods. The specimens were black pepper and hard wheat flour. We succeeded in measurement of the field swept echo signal of irradiated specimen and in direct analysis of relaxation times (T_1 , T_2). T_1 of irradiated black pepper was 33 μ s, and T_1 of irradiated hard wheat flour was 21 μ s. T_2 of irradiated black pepper was 420 ns, and T_2 of irradiated hard wheat flour was 260 ns. We also succeeded in measurement of the signal of irradiated specimens by CW-ESR. We detected the strong singlet signal from irradiated pepper, and the broad complicated signal from irradiated hard wheat flour. It suggested that the radiation-induced radicals of these two specimens are different.

食品照射は、衛生的な食品を安定的に供給し、腐敗や食害による食糧の損失を防ぐための殺菌・殺虫技術の一つであり、その利用は世界的に広がっている。ヨーロッパ連合では照射食品の標準検知法として電子スピン共鳴分光法 (Electron Spin Resonance Spectroscopy; ESR) が採択されている。日本では平成 24 年 9 月付けで ESR が採択¹⁾された。

ESR による分析には Continuous wave-ESR; CW-ESR (連続波 ESR) と Pulse-ESR (Pulse 波 ESR) がある。検知法では CW-ESR による計測を行い、得られる信号強度から照射処理の有無を判別する。

ラジカルの緩和時間には、スピン-格子緩和時間(T_1)とスピン-スピン緩和時間(T_2)の 2 種があり²⁾、ラジカル種が異なる場合、ESR 計測で得られる緩和時間に違いが生じると推察される。ラジカルの緩和時間(T_1 , T_2)は Pulse-ESR の計測により直接求めることができるが、照射食品中に誘導されるラジカルについて、Pulse-ESR 計測による報告は少ない。CW-ESR では Pulse-ESR とは異なり、直接ラジカルの緩和時間を求めることができない為、Lund らの算出方法³⁾を用いて、ESR 信号から得られるパラメータにより、緩和時間を算出する。

緩和時間を比較検討することにより、照射誘導ラジカル種の違いを明らかにすることを目的とし、実際に放射線照射した小麦粉(強力粉)及び黒コショウを実験試料として計測した。

照射強力粉及び照射黒コショウの Pulse-ESR の測定に成功した。Figure 1 は黒コショウの信号である。また CW-ESR 計測において照射黒コショウでは有機フリーラジカル由来のシャープな 1 本線信号が観測された。照射強力粉では、複雑な信号が観測された(Fig. 2)。これは有機フリーラジカル由来の singlet 信号と ^{14}N 由来の triplet 信号が重なったものと推察される。照射強力粉の場合 T_1 は Pulse-ESR 測定でも CW-ESR 測定でもほぼ同じ値を示した。照射黒コショウの場合、 T_1 は計測値に比べ、算出値が著しく減少し、桁数が異なった(Table 1)。黒コショウの T_2 は、桁数では数百 ns オーダーで同じだが、算出値は低くなる傾向にあった。照射強力粉の T_2 では、算出値が著しく減少し、桁数が異なった。以上のことから、緩和時間を算出する場合、Lund 法を用いて算出するのは、簡単な CW-ESR 計測で得られることから有用である。しかし、含有する成分によ

って、CW-ESR 信号が与えるパラメータに差異が生じ、算出値にばらつきができることが明らかになった。照射強力粉と照射黒コショウでは T_1 , T_2 の値が異なることから、含有する成分の影響があると推察された。

References

- 1) 平成 24 年 9 月 10 日付け食安発 0910 第二号、<http://www.mhlw.go.jp/topics/yunyu/other/2012/dl/120910-02.pdf>.
- 2) 石津和彦、実用 ESR 入門—生命科学へのアプローチ—、講談社、東京 (1981) 19-24.
- 3) A. Lund et al., Radiat. Res. **172**(6) (2009) 753-60.

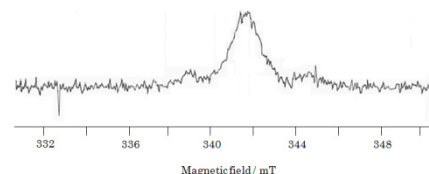


Fig. 1 A field swept echo spectrum of irradiated black pepper at 25 kGy.

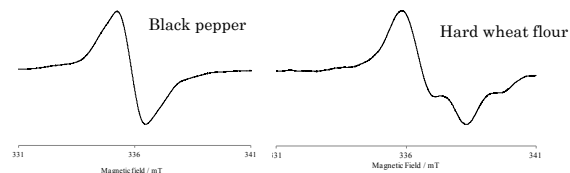


Fig. 2 ESR spectra of irradiated foods at 50 kGy.

Table 1 The relaxation time of irradiated black pepper and irradiated hard wheat flour at 50 kGy.

	black pepper		hard wheat flour	
	$T_1(\mu\text{s})$	$T_2(\text{ns})$	$T_1(\mu\text{s})$	$T_2(\text{ns})$
Pulse-ESR	33	420	21	260
CW-ESR	3.4	160	16	15

3 - 19 Three-dimensional Distribution Measurement of Eu in a *Paramecium Bursaria*

T. Satoh^{a)}, M. Koka^{a)}, W. Kada^{b)}, A. Yokoyama^{a)}, T. Ohkubo^{a)}, A. Yamazaki^{c)}, Y. Ishii^{a)},
T. Kamiya^{a)} and N. Kozai^{d)}

^{a)}Department of Advanced Radiation Technology, TARRI, JAEA, ^{b)}Faculty of Science and Technology, Gunma University, ^{c)}Research Facility Center for Science and Technology, University of Tsukuba, ^{d)}Advanced Science Research Center, JAEA

Introduction

Three-dimensional analysis technique for trace elements in a minute sample such as a single biological cell of 100 μm or less has been developed using PIXE (particle induced X-ray emission)-CT (computed tomography) in this study. Scanning transmission ion microscopy (STIM)-CT is performed as well as PIXE-CT for three-dimensional measurement of major elements' distributions, which are required for corrections of X-ray yields due to energy losses of projectiles and absorption of X-rays¹⁾. Moreover, ML-EM (maximum likelihood expectation maximization)²⁾ algorithm has been introduced to three-dimensional reconstruction because higher spatial resolution can be obtained even with less X-ray yields. On the strength of these, three-dimensional measurement of trace elements in a minute biological cell has been successfully achieved³⁾. As a second step, we performed the three-dimensional analysis of a single cell of *paramecium busaria* incubated with yeast in europium solution to visualize how the microorganisms accumulate heavy elements.

Experiment

Three-MeV proton microbeam with a diameter of 1 μm at TIARA was used in this study. The scanning area was 128×128 pixels corresponding to $100 \times 100 \mu\text{m}^2$. For STIM-CT experiment, a surface barrier detector was placed at just behind the sample, while a Faraday cup was placed at the same position in the case of PIXE-CT analysis. The distance and the angle of the lithium-drifted silicone detector for PIXE-CT analysis were 22 mm from the target and 140° to beam axis, respectively. A target was placed on an automatic rotation stage, which made a full turn by rotating 9° at a step in vacuum. As a result, we could obtain forty projections per a sample. It is very difficult to place a sample on the center of axis precisely though the precise alignment of the rotation axis with the center of the scanning area is very important for suppression of artifacts in the image reconstruction. To solve this problem, another linear motion stage was used for lateral alignment. The sample position on every angle was adjusted to scan over the whole of the sample. The measuring times of PIXE and STIM were respectively about 10 and 5 minutes per a projection. After the both measurements of STIM-CT and PIXE-CT, the center of gravity in each projection was calculated from the PIXE projection on phosphorus, and was defined an imaginary axis of rotation in the three-dimensional

reconstruction of STIM and PIXE.

A dried cell of *Paramecium bursaria* was used as a target. The pre-cultured cells with yeast in europium solution were fixed with a fixative and then washed with purified water repeatedly. The cells were subsequently dried on a carbon foil in air at room temperature. One of dried cells was fixed on the top of a Kapton tube with inner diameter of 500 μm and wall thickness of 25 μm using vinyl acetate emulsion adhesive as in Fig. 1.

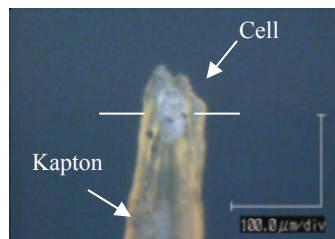


Fig 1 Microphotograph of the sample of a cell, *Paramecium bursaria*. White lines indicate the position of tomograms in Fig. 2.

Result

The tomograms obtained using the ML-EM reconstruction about phosphorus and europium at the white line in Fig. 1 is shown in Fig. 2. Phosphorus distributed itself uniformly over the cell because of the major element of cytoskeleton protein. The distribution of europium was seen inside that of phosphorus. It is demonstrated that europium taken into the cell has been successfully visualized.

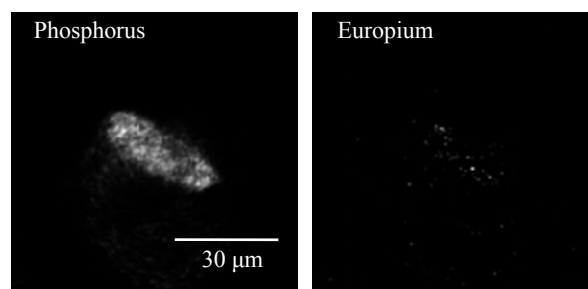


Fig. 2 Tomograms of the cell of *paramecium busaria* on phosphorus and europium.

References

- 1) T. Satoh et al., Nucl. Instrum. Meth. B267 (2009) 2125.
- 2) K. Lange et al., J. Compt. Assist. Tomogr. 8 (1983) 306.
- 3) T. Satoh et al., Int. J. PIXE. 22 (2012) 73.

3 - 20 Approaches to Isolation and Culture of Mice LMECs, and Effects of Nicotine on Trace Elements Distribution in LMECs

E. Sakurai^{a,b)}, E. Sakurai^{c)}, K. Yanai^{b)}, K. Ishii^{c)}, S Yamauchi^{c)}, S. Koshio^{c)},
S. Matsuyama^{c)}, M. Koka^{d)}, T. Satoh^{d)} and T. Kamiya^{d)}

^{a)}Faculty of Pharmacy, Iwaki Meisei University,

^{b)}Department of Pharmacology, Tohoku University School of Medicine,

^{c)}Department of Quantum Science and Energy Engineering, Tohoku University,

^{d)}Department of Advanced Radiation Technology, TARRI, JAEA,

^{e)}Faculty of Pharmaceutical Sciences, Tokushima Bunri University

Cigarette smoking is a risk factor for cancer, cardiovascular disease, diabetes and Chronic Obstructive Pulmonary Disease (COPD). Lung microvascular endothelial cells (LMECs) has an important rule about efficient protective systems for maintains homeostasis. It is known that two different transendothelial pathway (diffusive nonvesicular flux pathway and vesicle-mediated pathways) can be utilized for the passage of solutes. Naturally, trace elements should be present in the LMECs. However, there is no report about the distribution of trace element in LMECs. We already became successful to take rats LMECs. This time, we tried to isolation and culture of mice LMECs in two kinds of mice strains for the first time.

In this report, we measured change of the trace elements in LMECs by nicotine treatment using in air micro particle induced x-ray emission method. In-air micro-PIXE was developed at the Takasaki Ion Accelerators for Advanced Radiation Application (TIARA), JAEA. Micro-PIXE allows analyzing the spatial distribution of the elements quantitatively.

Three weeks old male C57BL/6J or ICR mice purchased from Japan SLC. Mice LMECs were isolated using a modification of the technique described by Magee et al¹⁾. The cell suspensions were seeded onto collagen coated culture flasks (225 cm²) in medium of DMEM/F-12 in a humidified atmosphere of 5% of CO₂ in air. Secondary subculture cells were grown on collagen-coated polycarbonate film (2.54 cm²) for microanalysis. The cells were washed two times with 1mL of Krebs buffer, and pre-incubated with 0.9 mL of Krebs buffer at 37 °C for 5 min. Then, 0.1 mL of Krebs buffer containing 0.02, 0.2 or 2 mM nicotine was added to the each film, and cells were incubated for 15 min. The cells on the 5 µm polycarbonate films were washed 7 times with THAM buffer. The specimens were promptly dipped into 2-methylbutane and chilled with liquid nitrogen and then freeze-dried overnight in the vacuum stage²⁾.

We became successful to isolate C57BL/6J or ICR mice LMECs. However, LMECs from ICR mice were difficult to culture. This cause is still unclear.

Figure 1 show Zinc image LMECs from C57BL/6J mice treated with nicotine final dose of 2, 20 and 200 µM in the polycarbonate film image in region of 100 × 100 µm².

When the LMECs were treated with nicotine, the amount of zinc decreased dose dependent manner. Whole on the other hands, calcium levels were increased dose dependent manner. Such changes of the trace elements levels in the LMECs were shown in Fig. 2.

This is a preliminary result of nicotine effects for mice LMECs. We will need further experiments and present results near future.

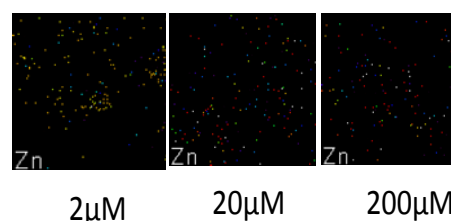


Fig. 1 Microgram of PIXE sample and Zinc image (100 × 100 µm) of LMECs from C57BL/6J mice treated with nicotine final dose of 2, 20, 200 µM.

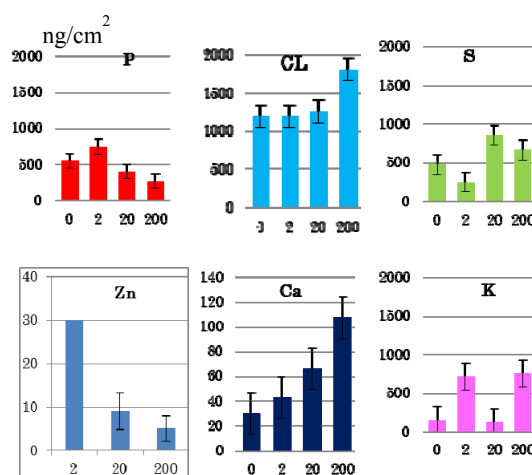


Fig. 2 Effects of nicotine on the trace element levels in LMCs.

References

- 1) E. Sakurai et al., Am. J. Physiol. Lung Cell Mol. Physiol. 282 (2002): L1192-7.
- 2) E. Sakurai et al., JAEA Takasaki Annu. Rep. 2006 (2008) 182.

3 - 21 Measurement of Fluorine Distribution in Root Dentin under Fluoride-containing Coating Materials

K. Okuyama^{a)}, H. Yamamoto^{b)}, H. Komatsu^{a)}, S Oki^{a)}, Y. Matsuda^{a)}, N. Hashimoto^{a)}, Y. Iwami^{b)}, M. Hayashi^{b)}, M. Nomachi^{c)}, K. Yasuda^{d)}, T. Satoh^{e)} and M. Koka^{e)}

^{a)}Graduate School of Dental Medicine, Hokkaido University, ^{b)}Graduate School of Dentistry, Osaka University, ^{c)}Graduate School of Science, Osaka University, ^{d)}The Wakasa wan Energy Research Center, ^{e)}Department of Advanced Radiation Technology, TARRI, JAEA

Introduction

Fluoride-containing coating materials (FCCMs) is available to control hypersensitivity and prevent dental caries, but it is easily removed by physical force. It is important for clinical use to keep its ability to prevent dental caries even after removal from the tooth surface. The purpose of this study is to evaluate fluorine (F) distribution in dentin under FCCMs after removing from surface in pH-cycling by means of an in-air micro-PIGE/PIXE system at TIARA.

Materials and Methods

Six extracted human teeth were used in this study. Four 200- μ m thick longitudinal sections were obtained from each tooth. The polished surfaces, except the outer surface, were covered with wax. Two FCCMs (CTX2 varnish: CT and MI varnish: MI) and a glass ionomer cement (fluoride-containing) (Fuji III: F3) were applied on the root dentin surface. No treated specimens were used as a control (NO). Twenty-four hours after material application to root surface, these materials were removed from surface. The pH-cycling (pH 6.8-4.5) was carried out for 4 weeks for preparing artificial carious dentin using an automatic pH-cycling system¹⁾. After pH-cycling, fluorine and calcium distributions of the outer dentin under materials in specimen were evaluated using micro-PIGE/PIXE system at TIARA²⁾. The outermost surface of the dentin was defined at the position containing 5% of the calcium concentration in intact dentin. For the comparison of fluorine uptake, the average fluorine concentration in each specimen was calculated at area of 70 μ m from the defined surface.

Results

Table 1 shows the average fluorine concentration (ppm) in dentin under materials at area of 70 μ m from the surface. For the materials before pH-cycling, there was no significant difference in F uptake among all groups ($p > 0.05$, Games-Howell test). For the materials after pH-cycling, F uptake from F3 was showed higher value than that of NO ($p < 0.05$). There was no significant difference in F uptake among three materials ($p > 0.05$). On F uptake from MI or F3, the F concentration of "after pH-cycling" was higher than that value of "before pH-cycling" ($p < 0.05$).

Discussion

To estimate caries prevention effect of fluoride-containing dental materials, the F uptake was investigated in enamel around materials during pH-cycling³⁾ as the F uptake resulted from the precipitation of fluorapatite $\text{Ca}_{10}(\text{PO}_4)_6\text{F}_2$ (i.e., remineralization). For dentin under fluoride-containing coating materials (FMMCs), F uptake was analyzed same as enamel. Therefore, it is speculated that these two FMMCs were effective in reducing the dental caries, since F uptake was shown on group CT and MI.

Fluorine measurement values indicated that the MI varnish facilitates F uptake even after removing from the dentin surface. This difference between FCCMs is due to the different amount levels of calcium, phosphate and the base materials. MI only includes casein phosphopeptide-amorphous calcium phosphate (CPP-ACP) and polyvinyl acetate.

Conclusion

After removing of Fluoride-containing coating materials from the dentin surface, F uptake was observed. These kind materials would be effective for preventive dentistry.

References

- 1) Y. Matsuda et al., Dent. Mater. J. 24 (2006) 280.
- 2) H. Yamamoto et al., Nucl. Instrum. Meth. Phys. Res. B 210 (2003) 388.
- 3) H. Komatsu et al., Nucl. Instrum. Meth. Phys. Res. B 269 (2011) 2274.

Table 1 The average fluorine concentration (ppm) in dentin under materials at area of 70 μ m from the surface.

	Before pH-cycling	After pH-cycling
NO	369 \pm 227	385 \pm 151
CT	186 \pm 65	1842 \pm 1766
F3	643 \pm 127	1541 \pm 514
MI	420 \pm 145	3760 \pm 3000
		Mean \pm SD, n=6.

3 - 22

Imaging of Metallofullerene Distribution Using Micro-PIXE for Gadolinium NCT

Y. Yamamoto^{a)}, K. Nakai^{a)}, F. Yoshida^{a)}, M. Shirakawa^{a)}, Endo^{a)}, A. Matsumura^{a)},
Y. Horiguchi^{b)} and Y. Nagasaki^{c)}

^{a)}Graduated School of Comprehensive Human Sciences, University of Tsukuba,

^{b)}Department of Neurosurgery, Faculty of Medicine, University of Tsukuba,

^{c)}Graduate School of Pure and Applied Sciences, University of Tsukuba

Neutron Capture Therapy (NCT) is a characteristic radiation therapy for malignant tumors, which uses nuclear reactions of thermal neutron and the NCT agent. These agents have large cross-section to capture neutrons, accumulate selectively to the malignant tumor cells. For example, ^{10}B has large cross section (3,838 barn) and nuclear capture and fission reactions $^{10}\text{B}(n, \alpha)^7\text{Li}$ generate high LET particles. Though these particles have 5 to 9 μm pathway only, surrounding normal cells could escape from the radiation damage. For the ideal NCT treatment, NCT agents should have high accumulation into tumor cells and have low accumulation into surrounding normal cells. In the Clinical BNCT trial, there are only two boron compound were used, but tumor/normal boron concentration ratios were not sufficient to achieve cure of invasive malignant tumors. Gadolinium-157 has high cross-section (254,000 barn) and MRI contrast agent containing Gadolinium is widely used as a diagnostic drug. But still useful gadolinium compound for NCT has not been developed because of toxicity. Fullerene is a class of sphere-shaped molecule made exclusively of carbon atoms. Metallofullerene is the complexes of metal-containing fullerene¹⁾. According to the previous studies, Gd@C82 is a type of metallofulleren which is encapsulated gadolinium atom inside fullerene, and is a potentially useful gadolinium compounds for NCT²⁾. To clarify the bio-distribution of the Gd-containing-fulleren, micro-particle induced X-ray emission (Micro-PIXE) has used.

Cultured undifferentiated colon carcinoma cells (CT 26) were injected subcutaneously to rt. thigh of BALB/c mice.

After the tumor growth, Gd@C82 was injected intravenously via tail vein. Forty-eight hours after the administration, the tumor was removed. The samples were cryosectioned and attached on polycarbonate film and freeze dried. Micro-PIXE analysis was performed at Takasaki Ion Accelerators for Advanced Radiation Application (Takasaki, Japan). These samples were irradiated with proton beam (3 MeV).

The distribution of Phosphorus in tumor samples was shown in Fig. 1A. The distribution of Potassium and Gadolinium in tumor samples was shown in Fig.1B and 1C. Tumor cells showed highly distribution of P and K, and especially, cell nucleus revealed the high distribution of P. Fig.1C showed the distribution of Gd@C82, and merged image showed the Gd distribution was matched the tumor cell.

The biodistribution of gadolinium compounds in tumor cells is very important information to develop a new NCT agents and essential information for effective NCT^{3, 4)}. Micro-PIXE technique is useful for imaging the biodistribution of gadolinium, and Gd@C82 is potentially useful gadolinium carrier for NCT.

References

- 1) J. Meng et al., J Nanosci. Nanotechnol. 10(12) (2010) 8610-16.
- 2) Y. Horiguchi et al., Sci. Technol. Adv. Mater. 12 (2011) 044607.
- 3) GD. Stasio et al., Canc. Res. 61 (2001) 4272-77.
- 4) K. Endo et al., Oncol. Res. 16 (2006) 57-65.

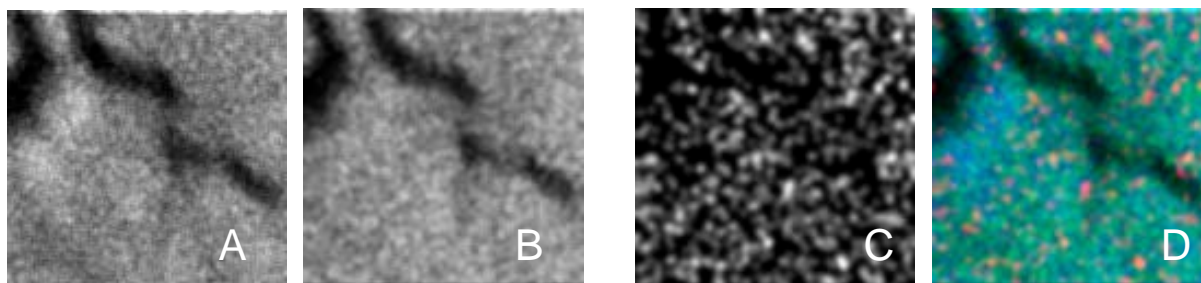


Fig. 1 The distribution of Phosphorus atoms in tumor samples (A), Potassium (B) and Gadolinium (C), (50 $\mu\text{m} \times 50 \mu\text{m}$). D is showing merged image of P (blue), K (green), Gd (red), (50 $\mu\text{m} \times 50 \mu\text{m}$).

3 - 23 Elemental Analysis of Lung Tissue Particles and Intracellular Iron Content of Alveolar Macrophages in Pulmonary Alveolar Proteinosis

K. Dobashi^{a)}, Y. Shimizu^{b,c)}, S. Matsuzaki^{b)}, N. Yanagitani^{b)}, T. Satoh^{d)}, M. Koka^{d)},
A. Yokoyama^{d)}, T. Ohkubo^{d)}, Y. Ishii^{d)}, T. Kamiya^{d)} and M. Mori^{b)}

^{a)}Gunma University Graduate school of Health Sciences,

^{b)}Department of Medicine and Molecular Science, Graduate School of Medicine, Gunma University,

^{c)}Department of Pulmonary Medicine, Maebashi Red Cross Hospital,

^{d)}Department of Advanced Radiation Technology, TARRI, JAEA

Pulmonary alveolar proteinosis (PAP) is a rare disease occurred by idiopathic (autoimmune) or secondary to particle inhalation. The aim of this study was to assess the secondary PAP due to inhalation of harmful particles by employing in-air micro-PIXE analysis in TIARA for particles and intracellular iron in tissue specimens obtained from a PAP patient comparing with normal lung tissue. The elements composing particles and their locations in the PAP specimens could be identified by in-air micro-PIXE analysis, with magnesium (Mg), aluminum (Al), silicon (Si), phosphorus (P), sulfur (S), scandium (Sc), potassium (K), calcium (Ca), titanium (Ti), chromium (Cr), copper (Cu), manganese (Mn), iron (Fe), and zinc (Zn) being detected. Si was the major component of the particles. Serial sections stained by Berlin blue revealed accumulation of sideromacrophages that had phagocytosed the particles. The intracellular iron content of alveolar macrophage from the surfactant-rich area in PAP was higher than normal lung tissue in control lung by both in-air micro-PIXE analysis and Berlin blue staining. The results suggest that secondary PAP is associated with exposure to inhaled particles and accumulation of iron in alveolar macrophages.

1. 背景と目的

アスベストの吸入は、肺線維症や肺がんの原因となり、しかも発病まで数 10 年とかかることから、「静かな時限爆弾」とも言われ、大変な社会問題である。早期診断や病態解明には、肺内のアスベストの種類、量、分布などを人肺組織内で特定する必要があるが、簡単でなかった。我々は、独立行政法人日本原子力研究開発機構との共同研究で、同機構が TIARA において開発した大気マイクロ PIXE 分析技術を応用して、数 mg の肺組織の中のケイ素や金属元素の二次元分布を 1 μm の解像度で画像化する分析法を開発し、世界で初めて、吸入したアスベストを肺組織中に存在したままで画像化することに成功した。肺胞蛋白症はまれな疾患であるが、原因として自己免疫が関与する場合と吸入粒子が関与する場合が考えられている。今回、我々は、肺胞蛋白症の患者から採取したパラフィン包埋肺組織を使用し、肺内に存在する元素を分析することにより本症の発症に粉塵吸入の関与の有無を検討した。

2. 方法

肺胞蛋白症の患者から、胸腔鏡下肺生検にて採取した肺組織をパラフィン包埋して作製した組織切片にイオンビームを照射した。さらに連続する切片に H-E 染色、ベルリンブルー染色（組織中の鉄分を染める）を行った。これらについて正常肺組織のデータと比較した。

3. 結果と考察

肺胞蛋白症の肺組織中には、Mg、Al、Si、P、S、Sc、K、Ca、Ti、Cr、Cu、Mn、Fe、Zn などが検出された。粒子の形成成分は Si が主体であった。Fe の沈着が Si に一致して認められた。さらに強拡大では、肺胞蛋白症の肺組織中のサーファクタントの多い部位の肺胞マクロファージでは、細胞内に Fe の沈着が認められた。しかもこの Fe を含むマクロファージの分布は、サーファクタントの分布と一致していた。正常肺組織ではマ

クロファージの中に Fe の集積は認められなかった (Fig. 1)。

2 次性の肺胞蛋白症は、吸入粒子と病変部のマクロファージ内に Fe の集積が見られ、これらが本症の発症に関与することが示唆された。

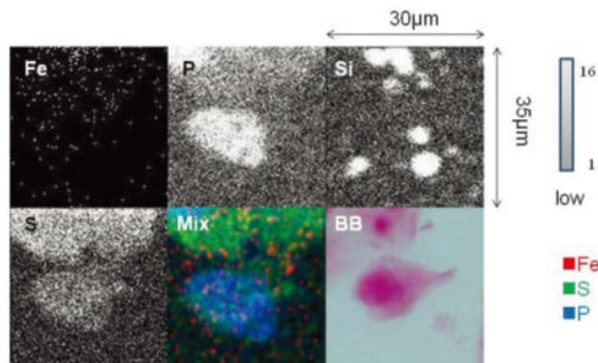


Fig. 1 In-air micro-PIXE analysis of an alveolar macrophage from the surfactant-rich area of PAP lung. The microbeam was focused on a 30 μm × 35 μm area of the lung to analyze the intracellular distribution of elements in an alveolar macrophage. Two-dimensional analysis was performed on the intracellular distribution and intensity of elements in an alveolar macrophage. The strength of Fe, P, Si, and S in lung tissue is shown by gray to white dots. Cell morphology was identified by the distribution of P located in the surfactant-rich area, which was identified by the distribution of S. The intracellular content and distribution of Fe, S and P in an alveolar macrophage are shown in mixed colors (Mix) as follows: Fe (red), S (green), and P (blue). A serial section of the area subjected to micro-PIXE showed a negative stained iron in a macrophage for Berlin blue (BB) (× 1000).

Reference

- 1) Y. Shimizu et al., Respir Res. 12(2013)88.

3 - 24 Analysis of Erythrocytes in Hepatitis C Patients Treated with Peg-interferon Using In-Air Micro-PIXE

S. Tomioka^{a)}, T. Nagamine^{a)}, T. Akutsu^{a)}, T. Satoh^{b)},
M. Koka^{b)} and T. Kamiya^{b)}

^{a)}Graduate School of Health Science, Gunma University,

^{b)}Department of Advanced Radiation Technology, TARRI, JAEA

Chronic hepatitis C patients treated with pegulated-interferon and ribavirin (Peg-IFN+RBV) and protease inhibitor (Peg-IFN+RBV+PI) are frequently associated with hemolytic anemia, whereas the mechanism of anemia is not fully understood. This study is aimed to analyze the elemental changes in erythrocytes in order to investigate the pathogenesis of anemia caused by combination of Peg-IFN and anti-viral drugs.

Eight patients with chronic hepatitis C (2 cases treated with Peg-IFN alone, 3 cases treated with Peg-IFN+RBV, 3 cases treated with Peg-IFN+RBV+PI), and three healthy controls were enrolled in this study. Whole blood was collected via peripheral vein, and the sample for PIXE analysis was prepared by the modified method of Ortega. Elemental distributions of erythrocytes were analyzed by In-Air Micro-PIXE at JAEA-Takasaki, Japan¹⁾.

The shape of erythrocytes, so-called the donut-like, became blurred markedly in Peg-IFN+RBV and Peg-IFN+RBV+PI cases, mildly in Peg-IFN cases. Dots of Cl, S and K distributed around a limb of erythrocyte, which fitted with the shape of erythrocytes in controls. In Peg-IFN cases, Cl, S, and K aggregated and diffused spreading over the erythrocytes. These elements tended to fall in pieces in the erythrocytes in Peg-IFN+RBV and Peg-IFN+RBV+PI cases (Fig. 1). Small granules of Ca were found in control erythrocytes, and granular size of Ca became larger in Peg-IFN+RBV and Peg-IFN+RBV+PI cases. Dots of Fe were distributed granularly dividing into 3-4 peace in normal erythrocytes. Typical donut-like distribution of Fe dots was diminished, and compensatory nodular or patchy aggregation of Fe dots was observed in Peg-IFN+RBV and Peg-IFN+RBV+PI cases. Distribution of P and Na in normal erythrocytes were similar to those of Peg-IFN alone, Peg-IFN+RBV and Peg-IFN+RBV+PI cases.

Dots of Mn in erythrocytes were decreased by Peg-IFN. Fe and Zn levels in erythrocytes were similar between controls and Peg-IFN alone, Peg-IFN+RBV and Peg-IFN+RBV+PI cases (Fig. 2). Cu levels in erythrocytes were increased in Peg-IFN+RBV+PI cases compared to controls.

In conclusion, the elemental changes in the erythrocytes in hepatitis C patients treated with Peg-IFN with or without anti-viral drugs, suggesting that some trace elementals may participate into the pathogenesis of anemia complicated with IFN therapy.

Reference

- 1) T. Nagamine et al., JAEA Takasaki Annu. Rep. 2011 (2013) 85.

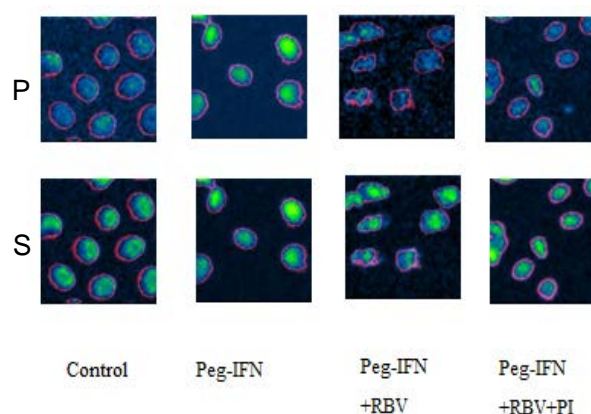


Fig. 1 Elemental maps of P and S within erythrocytes.

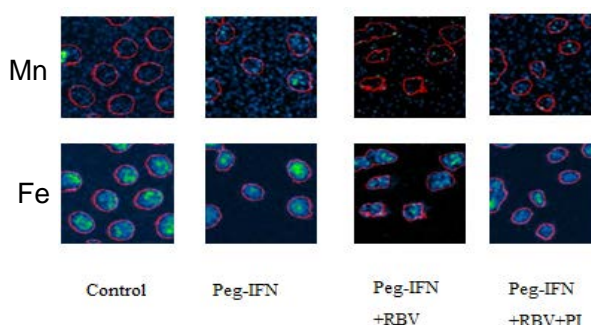


Fig. 2 Elemental maps of Mn and Fe within erythrocytes.

3 - 25

Trial for Targeting of Anticancer Drugs, Using Radiosensitive Immunolabelled Microcapsules

S. Harada^{a)}, S. Ehara^{a)}, K. Ishii^{b)}, T. Satoh^{c)}, T. Kamiya^{c)} and M. Koka^{c)}

^{a)}Department of Radiology, School of Medicine, Iwate Medical University,

^{b)}Department of Quantum Science and Energy Engineering, Tohoku University,

^{c)}Department of Advanced Radiation Technology, TARRI, JAEA

We have been developing the targeting of anticancer drug using microcapsules that release anticancer drugs with response to radiation^{1, 2)}. First, the microcapsules are delivered in capillaries around the tumors. Second, the tumors are irradiated and the microcapsules release anticancer drugs. Finally, released anticancer drugs act synergistically with radiation, resulting in increased anticancer effect, and localization of anticancer drugs by microcapsules reduces adverse effects¹⁾.

We have previously developed such liquid-core microcapsules using alginate polymerized with Fe^{2+} and hyaluronic acid. Radiation causes the conversion of hyaluronic acid into acetyl-glucosamine, while alginate- Fe^{2+} is depolymerized and exchanges Fe^{2+} for Fe^{3+} . This technique permits the encapsulation of carboplatin (Platinum containing anticancer drugs) and labeling of capsules with the $\alpha\text{v}\beta 3$ antibody²⁾.

Recent reports have shown that the $\alpha\text{v}\beta 3$ antibody is produced in the vascular endothelium of metastatic tissues of mammary tumors³⁾. By labeling the radiosensitive microcapsule with $\alpha\text{v}\beta 3$ antibody, which contains carboplatin, the intravenously injected microcapsules may then accumulate in capillaries around the tumor, through an antigen-antibody reaction with the $\alpha\text{v}\beta 3$ antibody. In this study, accumulation of microcapsules to mammary tumor through antigen-antibody reaction of $\alpha\text{v}\beta 3$ was tested.

The mixture of 0.2% alginate and 0.1% hyaluronic acid was prepared and 5mg Carboplatin (Pt containing anticancer drug) and 1 g L-ascorbic acid were added. A droplet of this mixture was sonicated using an ultrasound disintegrator and atomized to yield a 0.1 mol solution of CaCl_2 and FeCl_2 supplemented with 5 μg $\alpha\text{v}\beta 3$ under vibration^{1, 2)}.

The generated capsules observed in micro PIXE camera at TIARA were shown in Fig. 1A, basing on Fe and Pt distribution of microcapsules. Their mean diameter was $0.78 \pm 0.054 \mu\text{m}$. 1×10^{10} of microcapsules were injected through tail vein of C3He/N mice with MM 48 (mice mammary tumor) in their left hind leg. The microcapsules were allowed to interact with $\alpha\text{v}\beta 3$ for 6 hours. Then the tumors were taken and covered with dry ice powder, and cut into 3 μm thick slices and routinely processed to micro PIXE samples. Then number of trapped capsules through antigen-antibody reaction of $\alpha\text{v}\beta 3$ was counted within $25 \times 25 \mu\text{m}$ views of micro PIXE camera (Fig. 1A). The number of microcapsules that was trapped in tumor vessels were shown in Fig. 2. The trapped microcapsules significantly increased relative to $\alpha\text{v}\beta 3$ unlabeled

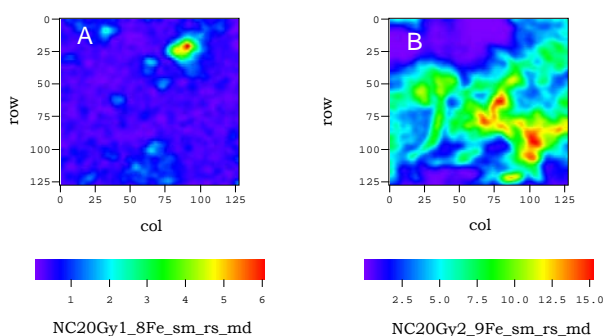


Fig. 1 Fe & Pt distribution by micro PIXE camera. A: Before irradiation, B: After irradiation.

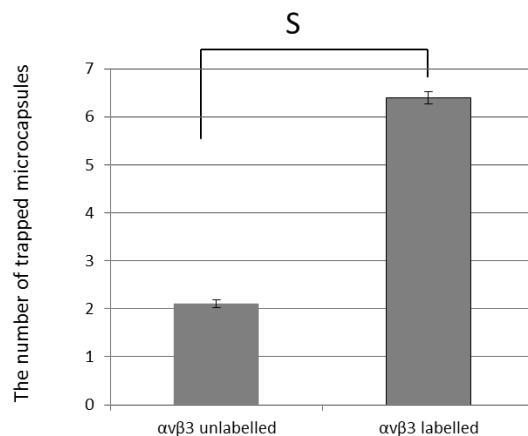


Fig. 2 Accumulation of microcapsules through antigen-antibody reaction of $\alpha\text{v}\beta 3$. S: Significantly different.

microcapsules. A single dose of 10 or 20 Gy X-rays (100 keV) were given to those accumulated microcapsules. The microcapsules released carboplatin with response to radiation, which occurred for $78.2 \pm 2.3\%$ of microcapsules in 10 Gy and $86.2 \pm 4.9\%$ of those in 20 Gy (Fig. 1B). This may lead to new method for targeting anticancer drug by radiation.

References

- 1) S. Harada et al., Int. J. Radiat. Oncol. Biol. Phys. 75(2) (2009) 455-62.
- 2) S. Harada et al., Int. J. PIXE 20 (1&2) (2009) 29-36.
- 3) W. Gong et. al., Int. J. Cancer 123 (2008) 702.

3 - 26 Development of Method for Plant Material Analysis by Micro-PIXE (Particle Induced X-ray Emission)

T. Yamamoto, H. Noda, J. Furukawa and S. Satoh

Life and Environmental Sciences, University of Tsukuba

Plants need various trace elements and the measurement of those contents and the localization analysis in plant tissue are very important to identify its functions. Some elements can visualize by chemical staining, but these methods have low resolution and can detect only one element. Micro-PIXE (Particle Induced X-ray Emission) method can detect multi-elements at the same time and visualize with high resolution image, so it is very useful for identifying where the elements localize. In micro-PIXE, especially which set samples on atmospheric pressure condition, various types of sample preparations are acceptable for the analysis. In this study, we analyzed paraffin embedded section and frozen section of plant sample to compare the difference of the sample preparations, and to clarify the most suitable condition for micro-PIXE at TIARA.

For the paraffin section, rice leaves were fixed by phosphate buffer containing glutaraldehyde and paraformaldehyde, and were dehydrated by ethanol and n-butyl alcohol. After that, rice leaves were embedded in paraffin and sliced to 15 μm sections by microtome. For freeze section, fresh rice leaves were embedded in the compound for freeze section, and sliced to 5 μm sections by freezing microtome. Each section was put on polycarbonate film and exposed by 3 MeV H^+ beam, then characteristic X-ray was detected. In paraffin sections, silicon (Si), calcium (Ca) and manganese (Mn) were detected by 3 min exposure, and potassium (K) and zinc (Zn) were detected by 60 min exposure (Fig. 1). In freeze sections, Si, K, Ca and Mn were detected by 6 min exposure (Fig. 2). Silicon was observed at surface of leaf and Ca was visible as dots at inside of rice leaf, and there were no

differences in their localizations between paraffin section and freeze section. Manganese was co-localized with Ca at the inside of rice leaf in paraffin section, while, in the freeze section, a part of Mn was not co-localized with Ca. Potassium detected in paraffin section was co-localized with Si, however, in freeze section, it localized at whole of tissue. Zinc localized at vascular tissue, phloem, and basal part of motor cells.

From these results, differences of detected elements by the preparation method and exposure time were shown. It is considerable that the difference by the exposure time depends on content of element, but the difference in the preparation methods was caused by the chemical form of elements in the plant tissue. To make paraffin section, plant tissue was soaked in fixing solution, so in this process soluble-form elements may be leaked outside of plant tissue and only insoluble-form elements remain in plant tissue. To make freeze section, fresh plant tissue was embedded in compound and rapidly frozen, so both soluble- and insoluble-form elements remain in plant tissue. Therefore, it might be possible to estimate the chemical forms of elements in plant tissue by comparing the results obtained from paraffin and freeze section. In fact, it is known that Si and Ca mainly exist as insoluble-form in plant tissue, consisted with the results of our study.

From these results, micro-PIXE analysis can be applicable to rice leaves by using paraffin and freeze section, and is a promising tool for estimating the chemical form of each element in the plant tissue. Consideration of conditions for various plant materials is now in progress.

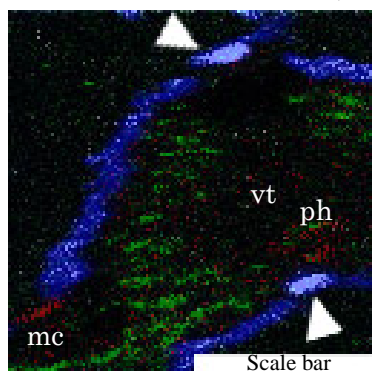


Fig. 1 Micro-PIXE image of rice leaf with paraffin section. Exposure time was 60 min. Blue: Si, Green: Ca, Red: Zn, White: K. vt: vascular tissue, ph: phloem, mc: motor cell. Arrow heads indicate co-localization of Si and K. Scale bar is 100 μm .

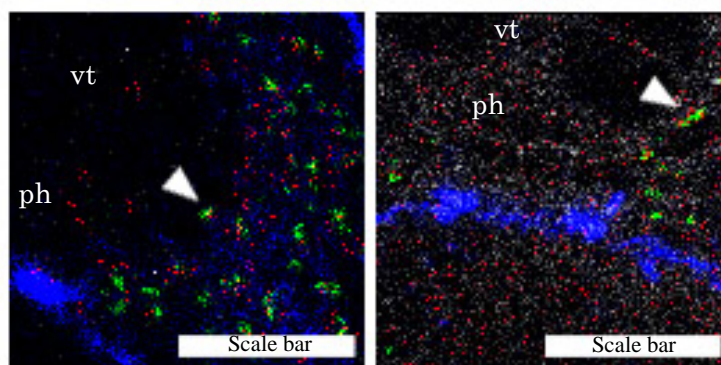


Fig. 2 Micro-PIXE image of rice leaf with paraffin and freeze section. Exposure time was 3 min for paraffin section and 6 min for freeze section. Blue: Si, Green: Ca, Red: Mn, White: K. vt: vascular tissue, ph: phloem. Arrow heads indicate co-localization of Si and K. Scale bars are 50 μm .

3 - 27 Sensitivity of Micro Beam PIXE System in TIARA for Several Trace Elements and Determination of Elemental Abundances in a Small Organism

Y. Iwata^{a)}, M. Katada^{a)}, T. Kamiya^{b)} and T. Satoh^{b)}

^{a)} Department of Chemistry, Faculty of Education and Human Studies, Akita University,

^{b)} Department of Advanced Radiation Technology, TAARI, JAEA

Standard Reference Material (SRM) for determination of trace elements in biological materials was made by macro porous cation-exchange resin (Macro-Prep 25S). Sulfur is main inorganic element in the resin and its concentration was determined by dry digestion / volumetric titration with the standard Ba^{2+} solution as SO_4^{2-} . The resin was suspended in the standard solution containing the known amount of trace elements. The concentration of those elements in the resin was 0-270 ppmv. Individual particle of the resin was subjected to 3 MeV proton bombardments by micro beam system of TIARA. PIXEana program was used to analyze peak count for each characteristic X-ray. Sensitivity for Al, S, Ca, Mn, Fe, Co, Ni, Cu, Zn, Sr and Pb for Si(Li) and PureGe detectors were calculated by elemental abundance in the resin and dose of proton. The sensitivity value was applied for determination of elemental abundances in a small organism.

1. 序 PIXE分析における装置の校正や分析値の相互比較のために、イオン交換樹脂中に分析目的元素を正確量含有する標準物質 (SRM) を開発してきた。これまで、粒径 7-11 μm のマクロポーラス型イオン交換樹脂に、生体関連元素の Al, Ca, Mn, Fe, Co, Ni, Cu, Zn, Sr, Pt および Pb を一定量含む SRM を調製し、特性 X 線強度と元素添加量とから、TIARA マイクロPIXE システムにおける Si(Li) 検出器による元素分析感度を求めた^{1,2)}。今回は、陽イオン交換樹脂中の硫黄含有量を化学分析で求め、これをもとに S の分析感度を求めた。また、新規導入された重元素分析用の PureGe 検出器による分析感度を求めた。これらの分析感度から微小生物のシオミズツボワムシ (*Brachionus Plicatilis*, ワムシ) に含まれる元素含有量を TIARA マイクロPIXE システムで定量したので報告する。

2. 実験 SRM の調製 前報同様、マクロポーラス型陽イオン交換樹脂 Macro Prep 25S (粒径 25 μm , BIORAD) に、樹脂体積あたりの含有量を 0 - 270 ppmv と段階的に変化させた 6 種類の SRM を調製した²⁾。

SRM 中の硫黄の定量 一定体積 (0.36 mL) のイオン交換樹脂を酸素フラスコ燃焼法により灰化し、硫黄分を 3% 過酸化水素水に SO_4^{2-} として吸収させた。この SO_4^{2-} は、Sulfonazo III を指示薬とし、0.01 mol/L Ba^{2+} 標準溶液を用いてマイクロビュレットを用いて滴定した³⁾。

微小生物の照射試料調製 体長 300 - 350 μm のワムシは、人工培養した微細藻類 (*Nannochloropsis* sp.) を給餌し、人工海水中で培養した。このワムシ 1 個体を Polycarbonate 膜に付着させ、照射試料とした。

マイクロPIXE 分析 TIARA マイクロPIXE システムにて、3 MeV H^+ ビームをサブミクロンに絞って照射した。スキヤンエリアは、イオン交換樹脂の場合、 $29 \times 29 \mu\text{m}$ 、ワムシの場合は $200 \times 200 \mu\text{m}$ とし、大気中 300 - 400 nC の照射を行った。解析は、PIXEana で行った。

3. 結果と考察 SRM 中の S 含有量 4 回の定量分析の結果、イオン交換樹脂中の体積あたりの S の含有量は、 $2056 \pm 19 \mu\text{g/mL}$ と極めて精度良く求まった。

分析感度の定量化 前報²⁾と同様の方法で、樹脂の体積から元素量、断面積から照射電荷量および特性 X 線のカウントから、元素 1 pg あたり 1 nC 照射による特性 X 線のカウント数を求め、前報の結果と合わせて示した (Table 1)。試

料間の変動が 20-30% 程度とやや大きい、Si(Li) 検出器では 2009 年の結果と ± 1 標準偏差で一致した。平均値では、Pb 以外の元素で今回の結果が 10-40% 高くなった。また、PureGe 検出器による Mn, Fe, Co, Ni, Cu, Zn, Sr および Pb の検出感度を求めた。これらは、Si(Li) 検出器より約 4 倍大きかった。

今回の感度測定により Fig. 1 に示すワムシの口部分 ($50 \times 50 \mu\text{m}$) の元素存在量を求めた。その結果、S:110, Ca:41, Fe:1.2, Cu:0.1 および Sr:0.8 とそれぞれ pg 単位で求めた。

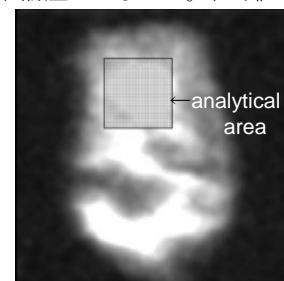


Fig. 1 Elemental mapping for S in *Brachionus Plicatilis* and analytical area for elemental abundances. Image Size : $200 \times 200 \mu\text{m}$.

Table 1 Analytical sensitivity for several elements by microbeam PIXE in TIARA.

	Sensitivity/Count $\text{pg}^{-1} \text{nC}^{-1}$ (n)				
	Si(Li) *	Si(Li) **	PureGe*		
Al	100 ± 16 (14)	80 ± 19 (17)	ND		
S	74 ± 13 (13)	ND	ND		
Ca	71 ± 14 (14)	60 ± 14 (18)	ND		
Mn	38 ± 5 (3)	27 ± 7 (9)	140 ± 22 (3)		
Fe	33 ± 11 (7)	25 ± 6 (9)	130 ± 23 (7)		
Co	24 ± 10 (6)	16 ± 7 (8)	91 ± 40 (6)		
Ni	15 ± 6 (8)	13 ± 3 (8)	65 ± 11 (8)		
Cu	18 ± 7 (6)	11 ± 3 (8)	65 ± 22 (6)		
Zn	10 ± 2 (8)	8.0 ± 1.9 (8)	62 ± 11 (8)		
Sr	1.2 ± 0.6 (8)	0.9 ± 0.4 (9)	4.7 ± 1.3 (8)		
Pb	1.0 ± 0.3 (14)	1.4 ± 0.3 (17)	5.3 ± 1.5 (14)		

* This work, **Measured at 2009²⁾.

References

- 1) Y. Iwata et al., JAEA Takasaki Annu. Rep. 2007 (2008) 173.
- 2) Y. Iwata et al., JAEA Takasaki Annu. Rep. 2009 (2011) 118.
- 3) 日本薬局方 (第16改正).

3 - 28 Synthesis of Radiohalogen-labeled Peptide with High Affinity to HER2/neu Receptor

I. Sasaki^{a)}, K. Yamada^{b)}, S. Watanabe^{a)}, H. Hanaoka^{c)}, Y. Sugo^{a)},
H. Oku^{b)} and N. S. Ishioka^{a)}

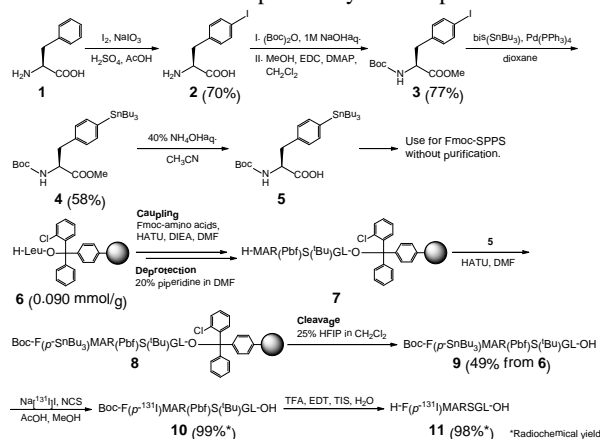
^{a)}Medical and Biotechnological Application Division, QuBS, JAEA, ^{b)}Graduate School of Engineering, Gunma University, ^{c)}Graduate School of Pharmacy, Chiba University

Radioisotope (RI)-labeled peptides with high affinity to receptors overexpressing on the surface of tumor cells are promising for applications in nuclear medicine such as diagnostic radiography (positron emission tomography (PET) and single photon emission computed tomography (SPECT)) and radiotherapy¹⁾. MARSGL (H-Met¹-Ala²-Arg³-Ser⁴-Gly⁵-Leu⁶-OH), a linear peptide consisting of six amino acids, has high affinity to HER2/neu receptor overexpressing in various cancer cells²⁾. Radiohalogens (radionuclides) such as radioiodine and radiobromine are versatile for clinical imaging and therapeutic applications³⁾. Thus, radiohalogenated MARSGL may have potential for clinical applications for HER2/neu overexpressing tumors. In this study, we designed a radioiodinated peptide, F(*p*-¹³¹I)MARSGL, in which phenylalanine labeled with ¹³¹I (*t*_{1/2} = 8.0 d) at the *para* position of the aromatic ring is introduced into the *N*-terminal of MARSGL. Although electrophilic destannylation is one of the most useful methods for radiohalogenation of aromatic compounds, radiohalogenated peptides prepared via electrophilic destannylation have hardly been reported. Therefore, we report synthesis of a stannylated peptide, Boc-F(*p*-SnBu₃)-MAR(Pbf)S(^tBu)GL-OH, by solid phase peptide synthesis (SPPS), and subsequent radioiodination to obtain F(*p*-¹³¹I)MARSGL via electrophilic destannylation.

Synthesis of F(*p*-¹³¹I)MARSGL is outlined in Fig. 1. **2** was prepared by iodination of phenylalanine in the presence of I₂ and NaIO₃ in 70% yield. **2** was acylated with (Boc)₂O and then converted to the methyl ester using an EDC-DMAP method to afford **3** in 77% yield. Stannylation of **3** was carried out via Pd(0)-catalyzed coupling reaction with bis(tributyltin) as reported previously⁴⁾. The desired compound (**4**) prepared in 58% yield was then saponified in the presence of NBu₄OH aqueous solution to yield **5**. These compounds were used for SPPS without further purification since a SnBu₃ group is sensitive to acidic conditions. A stannylated peptide (**9**) was synthesized via conventional Fmoc-SPPS using H-Leu-2-chlorotrityl resin (**6**, substitution: 0.90 mmol/g resin). Fmoc-SPPS usually requires strong acid for cleavage from resin and removal of protection groups in side chains, but a SnBu₃ group is quite sensitive under acid conditions. Therefore, we chose the strategy in which a stannylated peptide was cleaved without deprotection by using weakly acidic conditions before radioiodination. Cleavage of the stannylated peptide was investigated by using three acidic conditions; 25% HFIP in CH₂Cl₂ (A), 10% AcOH and 10% TFE in CH₂Cl₂ (B), and

0.5% TFA in CH₂Cl₂ (C). In the HPLC analysis of each solution after cleavage, the peak corresponding with the stannylated peptide was observed in two cases (A and B), while the peak of the stannylated one was not detected in the case of the solution of C. Based on the result, cleavage from the resin by treatment with the solution 25% HFIP in CH₂Cl₂, and following purification by gel filtration chromatography using Sephadex LH-20 was conducted. As a result, HPLC fractionation gave the desired precursor **9** in 49% yield from **6**. The protected radioiodinated peptide (**10**) was synthesized in the presence of Na¹³¹I and NCS. In the HPLC analysis, radiochemical yield in this step was 99%, indicating that radioiodination of the peptide progressed almost quantitatively via electrophilic destannylation. **11** was then obtained by treatment with deprotection reagents, and then purified with solid phase extraction followed by HPLC fractionation. The overall yield from the radioiodination of **9** was 95%. Thus, these results clearly indicated that the desired compound was obtained successfully in good yield.

In conclusion, a stannylated peptide used for radiohalogen labeling was successfully prepared via Fmoc-SPPS using H-Leu-2-chlorotrityl resin. The radioiodinated peptide was obtained via electrophilic destannylation in very high radiochemical yield. We are pursuing *in vitro* evaluation using HER2/neu overexpressing cancer cell lines to show possibility as radiopharmaceuticals.



References

- 1) S. Samnick et al., J. Nucl. Med. (2009) 2025-32.
- 2) M. Houimel et al., Int. J. Cancer (2001) 748-55.
- 3) Y. Arano et al., J. Med. Chem. (1994) 2609-18.
- 4) D. Wilbur et al., Bioconjugate Chem. (1993) 574-80.

3 - 29 Complexation of Lutetium-177 with Bifunctional Chelators in the Presence of Competing Metals

S. Watanabe, K. Hashimoto and N. S. Ishioka

Medical and Biotechnological Application Division, QuBS, JAEA

Lutetium-177 is considered to have potential for application in radioimmunotherapy because it emits β -particles ($E_{\beta, \max} = 498$ keV) suitable to penetrate small tumors and its physical half-life of 6.734 days is long enough for ^{177}Lu -labeled antibodies to accumulate to tumor sites. In addition, real time imaging of biodistribution can be done by using the γ -rays ($E_{\gamma} = 113$ keV and 208 keV) emitted from ^{177}Lu , whose energies are particularly suitable for imaging by single photon emission computed tomography.

We have succeeded in the production of high purity no-carrier-added ^{177}Lu of capable of labeling antibodies using reversed-phase ion-pair liquid chromatography¹⁾. Usually, as bifunctional chelating agents of the labeling antibodies, DOTA (1,4,7,10-tetraazacyclododecan- $\text{N}, \text{N}', \text{N}'', \text{N}'''$ -tetraacetic acid) and DTPA (diethylenetriamine- $\text{N}, \text{N}', \text{N}'', \text{N}'''$ -pentaacetic acid) are mainly used. Therefore, we carried out the labeling experiment of ^{177}Lu -DOTA-antibody by using the ^{177}Lu produced in our method in that study. As a result, it was found that metallic impurities such as Ca, Fe and Zn inhibited the complexation between ^{177}Lu and DOTA. However, the details of the inhibition by the metallic impurities have not been understood. Therefore, in the present study, the ^{177}Lu complexation of DOTA and DTPA was investigated by the addition of competing metals, Ca, Fe and Zn.

The ^{177}Lu used in this experiment was produced by $^{176}\text{Lu}(\text{n}, \gamma)^{177}\text{Lu}$ process. For the experiment of ^{177}Lu complexation of DOTA and DTPA, to the mixture of 5 μL of the ^{177}Lu solution (5.0×10^{-5} M as Lu) and 5 μL solution of the competing metal (Ca(II), Fe(II) or Zn(II)) in a prescribed concentration, 0.875 μL of acetate buffer (3 M, pH = 6.0) was added. After that, a 10 μL solution of DOTA or DTPA (5.0×10^{-5} M) was added. After incubating for 1.5 hours at 40 $^{\circ}\text{C}$, the complexation yield, which was defined as a percentage of the radioactivity of ^{177}Lu -DOTA or ^{177}Lu -DTPA to that of ^{177}Lu used for the complexation, was determined by thin layer chromatography on silica gel ITLC using aqueous ammonia : methanol : water (0.2 : 2 : 4) as a developing solvent. The unreactive ^{177}Lu remained at the origin point of a silica gel ITLC strip and the ^{177}Lu -DOTA or ^{177}Lu -DTPA moved to the solvent front.

Figure 1(a) shows the results of ^{177}Lu complexation of DOTA and DTPA by the addition of Ca(II). The ^{177}Lu complexation yield of DOTA decreased with increasing $[\text{Ca(II)}]/[\text{Lu}]$, while that of DTPA remained high even at $[\text{Ca(II)}]/[\text{Lu}] = 50$. This result indicates that ^{177}Lu complexation of DOTA was more inhibited by Ca(II) than

that of DTPA.

The results of ^{177}Lu complexation by the addition of Fe(II) and Zn(II) are shown in Figs. 1(b) and 1(c). The ^{177}Lu complexation yields of both DOTA and DTPA decreased with increasing $[\text{Fe(II)}]/[\text{Lu}]$ and $[\text{Zn(II)}]/[\text{Lu}]$. From comparison between DOTA and DTPA, the decrease of the complexation yield of DOTA was rather steep compared with that of DTPA in both cases of Fe(II) and Zn(II). Therefore, the inhibition for the ^{177}Lu complexation of DOTA was larger than that of DTPA.

Consequently, the ^{177}Lu complexation of DOTA was more inhibited by Ca(II), Fe(II) and Zn(II) than that of DTPA. Therefore, it was found that DTPA is advantageous for ^{177}Lu complexation compared with DOTA in the presence of competing metals, Ca, Fe and Zn.

Reference

- 1) S. Watanabe et al., Jpn. Patent Applic., 2010-223827.

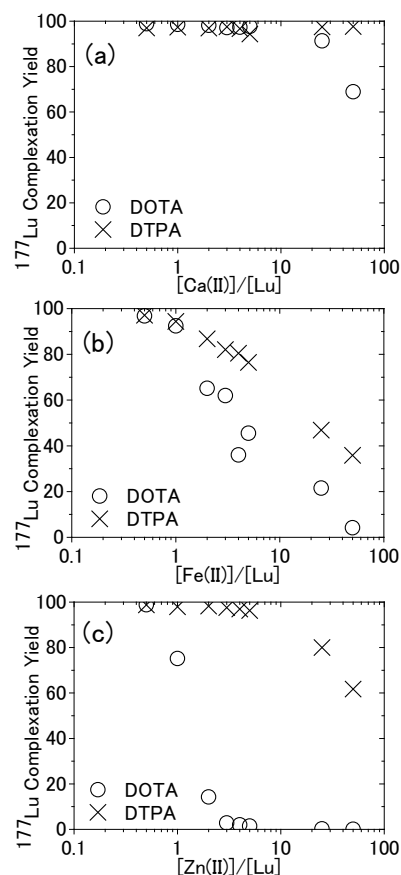


Fig. 1 ^{177}Lu complexation yield of DOTA and DTPA by the addition of metallic impurities. (a) Ca(II), (b) Fe(II) and (c) Zn(II).

3 - 30 Production of ^{13}N -labeled Nitrogen Gas Tracer for the Imaging of Nitrogen Fixation in Soybean Nodules

S. Ishii^{a)}, M. Igura^{a)}, Y.-G. Yin^{a)}, N. V. P. Hung^{a,b)}, N. Suzui^{a)}, N. Kawachi^{a)},
A. Koyanagi^{a)}, T. Ohyama^{b)} and S. Fujimaki^{a)}

^{a)}Medical and Biotechnological Application Division, QuBS, JAEA,

^{b)}Graduate School of Science and Technology, Niigata University

Nitrogen is the most important nutrient for the plants. Soybean can utilize nitrogen from atmospheric N_2 fixed by nodules which are symbiotic organs of leguminous plants with soil bacteria, rhizobia.

In the beginning of this research project, we set our methodological goal to visualize and analyze the nitrogen fixation in the nodules and subsequent nitrogen transport to the aerial part in a plant using ^{13}N and PETIS (positron-emitting tracer imaging system). Previously, we have developed a method of production of highly purified ^{13}N -labelled nitrogen gas tracer using gas chromatography and successfully visualized nitrogen fixation in intact nodules¹⁾. However, the yields of the tracer were only a few ten megabecquerels and too low to visualize the transport of fixed nitrogen to the aerial part. Therefore, we have been trying to improve the production method to gain much higher radioactivity with consideration of the very short half-life of ^{13}N (10 min)²⁾. In this study, we tested a new technique to turn the main by-product [^{13}N]N₂O into the desired product [^{13}N]N₂ directly.

^{13}N was produced using the system indicated Fig. 1. CO₂ was filled in a target chamber and irradiated with proton ions at electric current of 5 μA for 10 min delivered from the cyclotron (TIARA). Approximately 200-300 MBq in total of [^{13}N]N₂O and [^{13}N]N₂ were generated at the end of bombardment. The irradiated target gas was

collected into a plastic bag and added with nonradioactive N₂ gas. CO₂ in the gas was absorbed by soda-lime filled in a quartz tube. [^{13}N]N₂O in the remained gas was reduced into [^{13}N]N₂ by Cu powder heated at 600 °C with electric furnace (Fig. 1). Finally, approximately 150-200 MBq of ^{13}N was collected and the composition of tracer gas was checked with gas chromatography. As shown in Fig. 2, only N₂ (at 2 min) but neither CO₂ (at 12 min) nor N₂O (at 17 min) was detected. Therefore, it was confirmed that highly pure and radioactive [^{13}N]N₂ tracer was obtained (Fig. 2).

This gas was fed to the underground part of a soybean plant, and serial images by PETIS were collected for 1 h (360 frames \times 10 seconds). As a result, signals of ^{13}N were observed in the stem (Fig. 3). In other words, the transport of the fixed nitrogen was successfully visualized with PETIS (Fig. 3).

In conclusion, we successfully established a new production method of ^{13}N -labeled nitrogen gas tracer for the imaging analysis of nitrogen fixation and subsequent transport in soybean.

References

- 1) S. Ishii et al., Soil Sci. Plant Nutr. 55 (2009) 660-66.
- 2) S. Ishii et al., JAEA Takasaki Annu. Rep. 2011 (2013) 90.

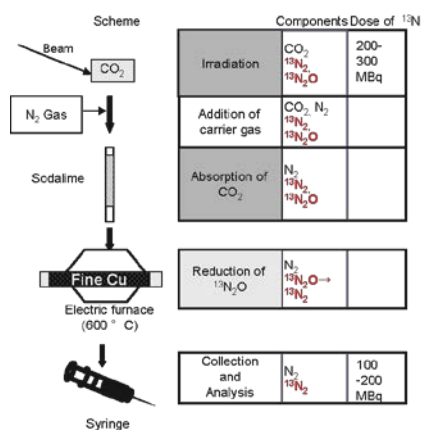


Fig. 1 Scheme of the new production method of ^{13}N -labeled N₂ tracer gas.

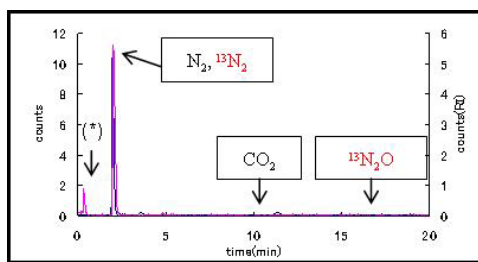


Fig. 2 Chromatogram of obtained gas. The peak at 0.5 min (*) was from electric noise.

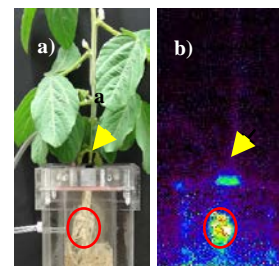


Fig. 3 a) Field of view and b) result of PETIS experiment. Red ellipses indicate the place of nodules and yellow arrowheads indicate the stem.

3 - 31

Analysis of the Effect of O₂ Partial Pressure on Nitrogen Fixation in Soybean Plant Using Positron-emitting Tracer

N. V. P. Hung^{a,b)}, S. Ishii^{a)}, N. Suzui^{a)}, N. Kawachi^{a)}, Y. G. Yin^{a)}, A. Koyanagi^{a,c)},
T. Ohyama^{b)} and S. Fujimaki^{a)}

^{a)}Medical and Biotechnological Application Division, QuBS, JAEA,

^{b)}Graduate School of Science and Technology, Niigata University,

^{c)}Faculty of Industrial Science and Technology, Tokyo University of Science

Oxygen plays the dilemmatic roles in biological nitrogen fixation process. It is necessary for the respiration of bacterioids in nodules but it has also strong negative influence on nitrogenase, which catalyzes the synthesis of ammonium from atmospheric N₂. To sustain the symbiotic nitrogen fixation process, legume nodules have to adapt their roles in regulating internal O₂ concentration in order to optimize cell condition in nodules.

So far, the studying of effects of O₂ levels on nitrogen fixation was based mainly on measurement using the acetylene reduction. This is a simple, inexpensive and highly sensitive method for studying of nitrogen fixation activity in plants but it only shows the change of acetylene to ethylene and not provides the real rate of nitrogen fixation directly. In the present study, the effects of O₂ levels on nitrogen fixation were visualized by a positron-emitting tracer imaging system (PETIS), which is an advanced technology developed for studying of plant nutrition. This technique can provide the capacity to visualize the dynamic transport and allocation of metabolites at large distance scales and consequently gives information for understanding the whole-plant physiological response to environmental change in real time. We successfully visualized the N fixation in soybean using PETIS in a previous study (Ishii et al., 2009).

In this study, the soybean (*Glycine max* [L.] Merr. cv. Williams) plants were inoculated with *Bradyrhizobium japonicum* and cultivated with a hydroponic nutrient solution without nitrogen. Soybean plants at 26 days after sowing were treated with 50 mL of mixed gas containing [¹³N]N₂ tracer and various proportions (0%, 10%, 20%) of oxygen. The fed gas was kept for 10 minutes in the acrylic box containing the underground part of the plant. PETIS imaging was performed when [¹³N]N₂ tracer was introduced in the acrylic box. A frame of the imaging was obtained in every 10 seconds and the measurement was continued for 1 hour. The PETIS images were reconstructed and analyzed by ImageJ software.

The integrated images (Fig. 1) after flushing out of the tracer gas show strong signal on the nodules and faint signal on the stem. The time-activity curves (Fig. 2) show that nitrogen fixation activity at nodules was highest with 20% O₂ and lowest with 0% O₂, and it was not significantly different between 0% O₂ and 10% O₂ in these experiments.

This result indicates that nitrogen fixation activity of soybean nodules was limited by the decline in rhizosphere O₂ and was fully depressed under low O₂ levels below 10% although it was not completely inhibited.

References

- 1) S. Ishii et al., Soil Sci. Plant Nutr. 55 (2009) 660-66.
- 2) W. S. Rasband, ImageJ, U. S. National Institutes of Health, USA (1997-2012). <http://imagej.nih.gov/ij/>.

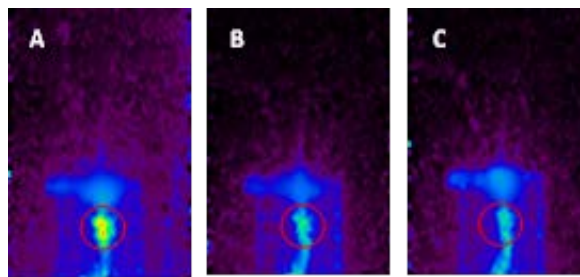


Fig. 1 PETIS images of ¹³N activity in soybean nodules at different O₂ compositions. A, 20% O₂, B, 10% O₂, C, 0% O₂. Red circles indicate nodule region used for time-course analysis.

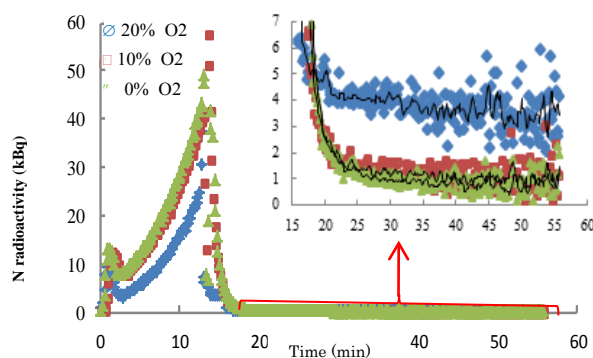


Fig. 2 The time-activity curves of ¹³N radioactivity in nodules after feeding of [¹³N]N₂ tracer gas under various O₂ levels.

3 - 32 RI Imaging Method to Analyze a Process of Radiocesium Contamination of Plants and to Develop Phytoremediation Techniques

N. Kawachi^{a)}, Y.-G. Yin^{a)}, N. Suzui^{a)}, S. Ishii^{a)}, H. Watabe^{b)},
S. Yamamoto^{c)} and S. Fujimaki^{a)}

^{a)}Medical and Biotechnological Application Division, QuBS, JAEA, ^{b)}Graduate School of Medicine, Osaka University, ^{c)}Graduate School of Medicine, Nagoya University

Because of the accident at the Fukushima Daiichi Nuclear Power Plant of the Tokyo Electric Power Company, Inc., an extensive area of agricultural fields was contaminated with radioactive materials. There are still major concerns of elevated rates of ambient radiation dose in the neighboring areas around the nuclear power plant and potential pollution in agricultural products. Cs-137 is the most of soil contaminant, which was reported to have a 16-18 years half-life in agricultural fields affected by physical decay and soil erosion. Therefore, further research is required on the behavior of radiocesium and its transfer from contaminated soil to agricultural products.

Previously, we employed RI imaging method to quantitatively assess the uptake of cadmium. Cadmium is one of the major soil pollutants in the world, and we successfully elucidated the mechanism of transport of cadmium in the rice plants from root to shoot¹⁾. The RI image data analyzed the absorptive function of a high cadmium-accumulating rice cultivar, and also evaluated the function of a cleanup ability of phytoremediation with a high cadmium-accumulating rice cultivar²⁾. We lead up to the similar approach of RI imaging is competent in determining the distribution of radiocesium in soil and plants; in other words, we could analyze radiocesium dynamics in the soil-plant relationship and construct a “platform” for developing an application technology on the basis of cesium kinetics in plants and environments.

In this study, we selected a gamma camera (Fig. 1) for gamma ray imaging of Cs-137 emitting at 662 keV. Gamma camera is a common modality in biological and medical imaging experiments but it is generally difficult to apply for imaging against high-energy gamma rays over 364 keV. A pinhole collimator was fabricated with heavy metal of tungsten to avoid the penetration and scattering of gamma rays, since high-energy incident gamma ray originates from Cs-137 tracer inside a test plant. A gadolinium oxyorthosilicate (GSO) scintillator with a thickness of 15 mm and a flat panel position sensitive photomultiplier tube were adapted to the gamma camera to obtain adequate high sensitivity. Giant knotweed (*Reynoutria sachalinensis*), which has potential as a cleanup plant with high uptake capacity for cesium, was grown in hydroponic solutions. After exposed to approximately 400 kBq of Cs-137, images were taken for 15 h. Sequential images reveal the changing distribution of cesium into the plant from the hydroponic solutions via the root system.

We have indicated real-time visualization of uptake of radiocesium within an intact plant in the first time successfully (Fig. 2). Further, we believe that our technique will be valuable for research on environmental pollution caused by radioactive materials.

References

- 1) S. Fujimaki et al., Plant Physiol. 152 (2010) 1796.
- 2) S. Ishikawa et al., BMC Plant Biol. 11 (2011) 172.

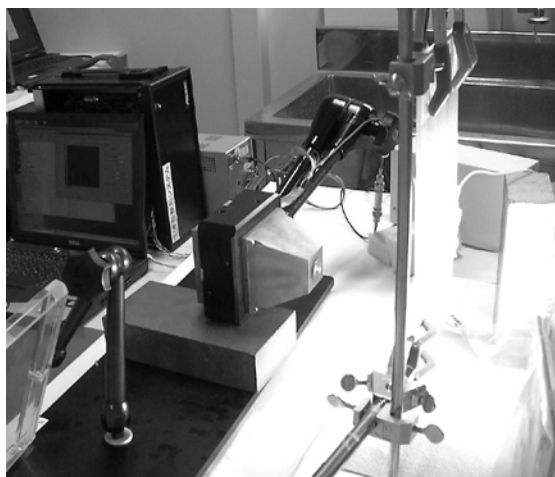


Fig. 1 Photograph of Gamma Camera we have developed.

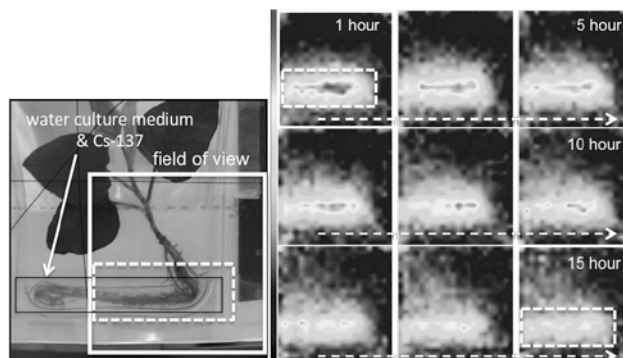


Fig. 2 Square in photograph of Giant knotweed indicates a field of view of the gamma camera (left), and dynamic images of Cs-137 kinetics for 15 h (Right).

3 - 33

Whole-plant Imaging of ^{107}Cd Distribution Using Positron-emitting Tracer Imaging System

N. Suzui^{a)}, Y.-G. Yin^{a)}, M. Igura^{b)}, S. Ishii^{a)}, N. Kawachi^{a)},
S. Ishikawa^{b)} and S. Fujimaki^{a)}

^{a)} Medical and Biotechnological Application Division, QuBS, JAEA,

^{b)} Soil Environment Division, National Institute for Agro-Environmental Science

We have conducted noninvasive imaging of cadmium (Cd) in intact plants using positron-emitting tracer imaging system (PETIS) and ^{107}Cd ($t_{1/2} = 6.5$ h) for understanding the mechanism of Cd translocation in plants. In our previous imaging experiment, ^{107}Cd tracer has been fed to the root of large plants such as rice, and obtain the serial images of ^{107}Cd distribution in the underground parts (roots and culture solutions) or the aerial parts (shoots or grains)¹⁾. However, whole-plant images of ^{107}Cd distribution in both underground and aerial parts have not been obtained because the field of view (FOV) of PETIS is small (120 mm in width, 187 mm in height). In this study, we fed ^{107}Cd to dwarf plants, *Sedum plumbizincicola* and visualized Cd dynamics in a whole plant within the FOV of PETIS.

Sedum plants were cultured hydroponically in 1/2-Hoagland solutions. ^{107}Cd tracer was produced and purified at TIARA as described previously²⁾, and fed to the solutions containing 25 MBq of ^{107}Cd and 0.1 μM nonradioactive Cd. The dynamics of ^{107}Cd in intact sedum plants were monitored by PETIS for 30 hours.

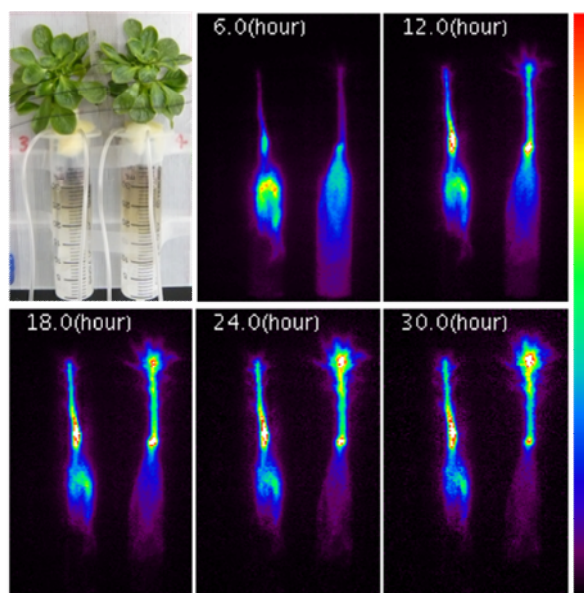


Fig. 1 Serial images of ^{107}Cd distribution in the underground and aerial parts.

Figure 1 shows the serial PETIS images of ^{107}Cd distribution in the whole sedum plants. The whole physiological process, i.e., Cd uptake from culture solution, translocation from root to shoot and accumulation in shoot, were successfully visualized in a single image. Figure 2 shows quantitative analysis of ^{107}Cd distribution in the root and the shoot. The time courses of Cd amounts demonstrated that the half amount of Cd fed to the solution was taken up by the root within 2 hours, and the two-thirds amount (2 nmol) was accumulated in the shoot after 30 hours. These results imply the whole-plant imaging represents a reliable method for the quantitative analysis of Cd dynamics. In fact, this method has shed light on the positive effect of nitrate on Cd uptake, transport and accumulation in *S. plumbizincicola*³⁾.

References

- 1) S. Ishikawa, N. Suzui et al., BMC Plant Biol. (2011) 172:1-12.
- 2) S. Fujimaki et al., Plant Physiol. 152 (2010) 1796-806.
- 3) P. Hu, Y.-G. Yin et al., Environ. Sci. Pollut. Res. 20(2013)6306.

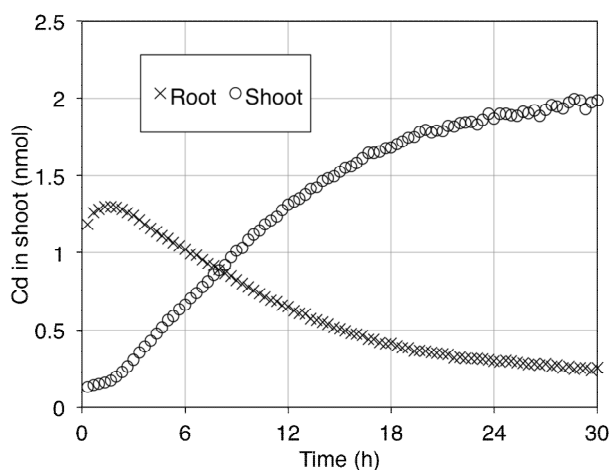


Fig. 2 Time course of Cd amount in the region of root and shoot. A total of 3 nmol of Cd (0.1 μM) was fed to the solution at the beginning of the experiment.

3 - 34 Development of Ion Beam Breeding Technology in Plants and Creation of Useful Plant Resources

Y. Hase^{a)}, S. Nozawa^{a)}, I. Asami^{b)}, Y. Tanokashira^{c)}, Y. Matsuo^{d)},
A. Kanazawa^{e)}, K. Honda^{f)} and I. Narumi^{a)*}

^{a)}Medical and Biotechnological Application Division, QuBS, JAEA, ^{b)}Aichi Agricultural Research Center, ^{c)}Kagoshima Biotechnology Institute, ^{d)}Saga Prefectural Agricultural Fruit Tree Experiment Station, ^{e)}Research Faculty of Agriculture, Hokkaido University,

^{f)}Faculty of Agriculture and Life Science, Hirosaki University,

*Present affiliation: Faculty of Life Sciences, Toyo University

This study is aimed to develop ion beam breeding technology and useful plant resources. In particular, our current research is focused on the step-wise improvement of traits in ornamental plants. We also focus on improvement of trees and functional ingredients in crops because little knowledge has been accumulated in this area. Here, we describe recent progress made in these studies.

Chrysanthemum variety ‘Princess (tentative name)’, which has characteristic petal shape in the outer part of a flower head, was irradiated with carbon ions. As shown in Fig. 1A, petal shape variation in the branches of petal apex was observed in the regenerated plants. Finally, 4 mutant lines that have characteristic petals in a whole part of the flower head were selected from about 1,500 regenerated plants. The trial growing of one of the mutant lines in FY2012 in Aichi prefecture was received well. Further characterization of the other mutant lines will be performed.

We previously produced a new chrysanthemum variety ‘Aladdin’ that has a lesser number of axillary buds than ‘Jimba’, a leading variety of chrysanthemum. We carried out further improvement of ‘Aladdin’, because the flowering of ‘Aladdin’ often delayed under a low temperature condition. The cultured leaves of ‘Aladdin’ were irradiated again with carbon ions. Nine mutant lines were selected that flowered 12-13 days earlier than ‘Aladdin’ under a low temperature condition. Since the number of axillary buds of these mutant lines was generally low for the propagation of seedlings in practical use, we are trying re-irradiation of these mutant lines. The growth of regenerated plants was not bad even though they experienced three-time irradiation in total from the starting material ‘Jimba’. So far, 21 candidate lines were selected for further characterization.

We are developing the ion beam breeding technology in Citrus plants as a model for trees. The cut surfaces of hypocotyls were exposed to carbon ions and the regenerated plants were grown. There was a large difference in radiation sensitivity among 7 kinds of commercial varieties. The regeneration rate after 10 Gy irradiation was more than 90% in ‘Kawano-Natsudaidai’ but was less than 10% in Trifoliate orange. Mutant plants with shorter internode were successfully obtained in ‘Imamura-unshu’ (Fig. 1B). Nobiletin, one of the citrus flavonoids, has been suggested to have many potential health benefits. Nobiletin content was measured in mutant population of ‘Shiikwaasaa’ (*Citrus*

depressa)’ and ‘Yuzu’. So far mutant candidate whose nobiletin content was twice that of the original strain were obtained in ‘Shiikwaasaa’.

Soybean is an important crop that provides food, oil, forage and industrial raw materials. Genome sequence of soybean revealed that ~75% of genes were present in multiple copies. It is likely that gene duplication lowers the efficiency of mutant production. We carried out a detailed analysis of mutagenic effect of carbon ions in soybean. We identified chlorophyll-deficient mutants in the M₂ generation of plants irradiated at 2.0-7.5 Gy. We examined whether seed components were altered in these mutants. We analyzed contents of isoflavones, proteins, fatty acids and starch in dried seeds. We found a decrease in isoflavone content, an increase in protein content, and both an increase and a decrease in fatty acid content in the mutants. These mutants potentially confer genetic changes that are useful for improving seed components. In addition to these mutants, we have detected mutants that have an altered morphology or altered maturity traits. We will maintain these mutants and analyze the stability of the observed changes.

In order to create useful plant resources in terms of functional ingredients, dry seeds of traditional pepper variety ‘Hirosaki Zairai’ in Aomori, were irradiated with carbon ions. Several mutant candidates, which showed increased blanching, fleshy fruits and shorter internodes, were obtained in M₂ generation. Phenotypic analyses in M₃ generation suggested that the increased blanching phenotype was under the control of a single recessive gene, while the hereditary pattern of the other mutant traits was unclear. Further analysis will be performed to confirm the hereditary pattern of the mutant traits.



Fig. 1 (A) Petal shape variation observed in chrysanthemum variety ‘Princess (tentative name)’ irradiated with carbon ions. (B) Short-internode mutant of ‘Imamura-unshu’ (left) and the original variety (right).

3 - 35 Ion Beam Breeding of Rice for the Mutation Breeding Project of the Forum for Nuclear Cooperation in Asia (FNCA)

A. Tanaka^{a)}, S. Nozawa^{a)*}, Y. Hase^{a)}, I. Narumi^{a)**}, H. Ishikawa^{b)} and A. Koike^{b)}

^{a)}Medical and Biotechnological Application Division, QuBS, JAEA, ^{b)}Nuclear Safety Research Association, *Present affiliation: Department of Advanced Radiation Technology, TARRI, JAEA, ** Faculty of Life Sciences, Toyo University

1. Introduction

Ion beams have been utilized for the Sub-Project on Composition or Quality in Rice (FY 2007-2012) under the Mutation Breeding Project of the Forum for Nuclear Cooperation in Asia (FNCA) of MEXT (Ministry of Education, Culture, Sports, Science and Technology) since 2009¹⁾. This sub-project contributes to increase food production and to improve food quality in Asia, by developing new rice mutant varieties that are more resistant to disease, insects, and drought, or give higher yields and offer higher quality. Seven participating countries, i.e., Bangladesh, China, Indonesia, Korea, Malaysia, The Philippines, and Vietnam joined this project and irradiated seeds of their own rice varieties with ion beams.

2. Materials and Methods

Hulled dry seeds of rice varieties of participating countries were exposed to 320 MeV carbon ions at TIARA with individual optimal doses to induce mutation. After irradiation, seeds were sent back to the participating countries and investigated for mutation induction.

At the FNCA workshop on Mutation Breeding held in Thailand in February 2012, we have deeply discussed the appropriate population size for mutation induction and concluded that at least several seeds from each 5 panicles from each 1,000 M₁ plants (5,000 initial mutated cells) should be harvested in order to obtain mutation efficiently.

3. Results and Discussion

In FY2012, most of participating countries completed to decide the optimal dose for mutation induction for each rice variety and harvested offsprings such as M₂, M₃ and their descendants. For example, in Vietnam, 40 Gy and 60 Gy were adopted as optimal doses for Khandan and Bacthom varieties, respectively, and interesting mutant lines, which show high yield, early maturation, tolerant to disease, or semi-dwarf, were obtained in M₃ lines. In the Philippines, M₄ selected lines derived from IR72 variety irradiated with 20 or 40 Gy showed distinct features such as early maturing (one week earlier than the control), short, or high tillering with long panicle.

In Bangladesh, a salt tolerant but highly photoperiod sensitive and tall local variety, Ashfal, and popular and early maturation variety BRRI dhan29 were investigated. In the M₁ offspring of Ashfal, several photo-insensitive mutants have been obtained, some of which show slender grains (Fig. 1 left). The two mutants produce higher yield and mature earlier at all locations than BRRI dhan29. These

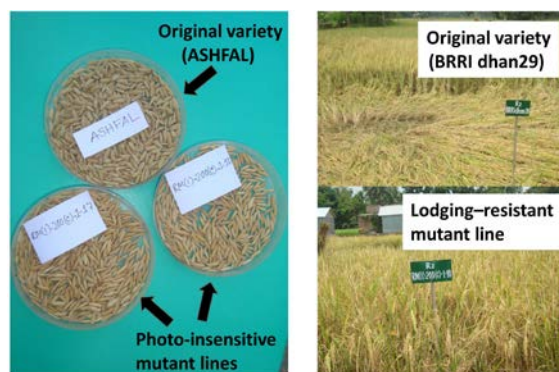


Fig. 1 Left: Slender grain and photo-insensitive mutants obtained from Ashfal variety. Right: High yield and lodging-resistant mutant (lower) obtained from BRRI dhan29 variety (upper).

mutants are also shorter in height and thus lodging resistant, and have similar grain quality as BRRI dhan29 (Fig. 1, right).

In Malaysia, 31 selected mutant lines (ML1-31) were obtained in M₃ derived from MR219 variety irradiated with 60 Gy (Fig. 2). In these mutant lines, the differences in culm length, days to flowering, number of tiller, number of panicle, 1,000 grain weight, total grain yield, etc. were observed. These results indicated that ion beams caused some great performance changing in the agronomic traits as compared to the control.

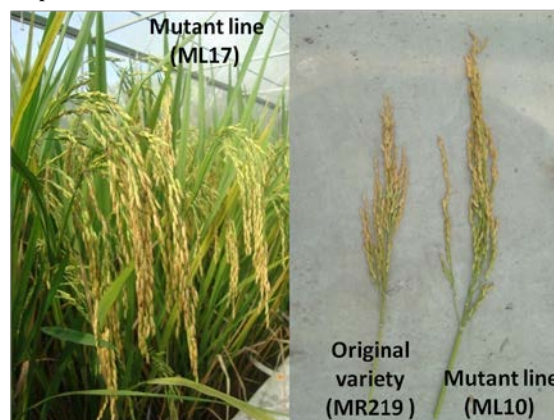


Fig. 2 Left: A higher number of grain mutant obtained from MR219 variety. Right: A longer panicle mutant obtained from MR219 variety.

Reference

- 1) A. Tanaka et al., JAEA Takasaki Annu. Rep. 2011 (2013) 96.

3 - 36 Generating New Chrysanthemum Plant Varieties Using Ion Beams

A. Zaiton^{a)}, A. H. Affrida^{a)}, S. Shakinah^{a)}, M. Nurul Hidayah^{a)},
S. Nozawa^{b)}, I. Narumi^{b)}*, Y. Hase^{b)} and Y. Oono^{b)}

^{a)} Agrotechnology and Biosciences Division, Malaysian Nuclear Agency,

^{b)} Medical and Biotechnological Application Division, QuBS, JAEA,

*Present affiliation: Faculty of Life Sciences, Toyo University

Chrysanthemum is among the most important cut flowers in Malaysia especially for export market¹⁾. The main problem for chrysanthemum in Malaysia is the lack of new varieties to meet the ever-changing customer demands. In chrysanthemum production, demands are high for new cultivars with good horticultural traits such as unique flower colour, shape, plant architecture and leaf morphology. Ion beam mutagenesis, in combination with *in vitro* organ cultures, is known to be very effective in producing new cultivars with novel traits and wider mutation spectrum²⁾. In this project, organ cultures of several chrysanthemum varieties were irradiated at various doses with 320 MeV ¹²C⁶⁺ ions, regenerated into plantlets and screened for morphological variations.

This report discusses irradiation experiments for nodal cultures of chrysanthemum Pink variety (Fig. 1). *In vitro* stems were cut into single nodes (0.5 cm in length) and cultured on 6-cm sterile petri dishes containing half MS³⁾ hormone-free medium approximately 5 days before irradiation. Irradiation was carried out at doses of 0, 0.5, 0.8, 1, 2, 3, 5, 8, 10, 15, 20, and 30 Gy. Following irradiation, the cultures were transferred onto fresh half MS medium and incubated at 25±2 °C under 16-h photoperiod for multiplication. Data on the survival of cultures, regenerated shoot height and number of leaves were taken 8 weeks after irradiation.



Fig. 1
Chrysanthemum morifolium pink.

Table 1 shows the percentage of survived nodes at all doses 8 weeks after irradiation. No significant difference was observed in terms of survival percentage in nodes irradiated at doses 2 Gy and below, which recorded between 86-100% of survival. The figures however drastically dropped to 60% at 3 Gy and further reduced to less than 50% at doses 5 Gy and higher, indicating that the sensitivity of nodes to ion beam irradiation is similar to that of their ray floret counterparts⁴⁾.

Table 1 Percentage of node survival 8 weeks after irradiation.

Dose (Gy)	Survival %	Dose (Gy)	Survival %
0	87 ^{ab}	5	47 ^{cd}
0.5	100 ^a	8	33 ^{cde}
0.8	87 ^{ab}	10	40 ^{cde}
1	93 ^a	15	33 ^{cde}
2	100 ^a	20	13 ^e
3	60 ^{bc}	30	27 ^{de}

* Data followed by the same letters are not significantly different, according to Duncan's New Multiple Range Test ($P < 0.05$).

In terms of mean shoot height and number of leaves generated in survived nodal shoots (Figs. 2 and 3), it was also observed that 5 Gy was a cut-off dose value since the figures recorded at 5 Gy and higher showed a drastic decrease of more than 50% for all categories.

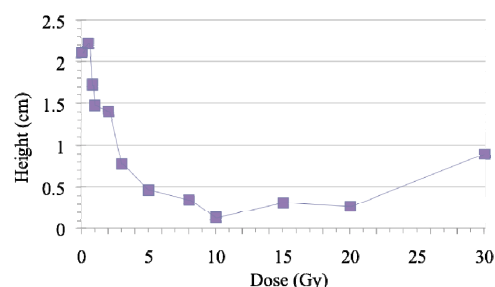


Fig. 2 Average shoot height in irradiated nodes at week 8.

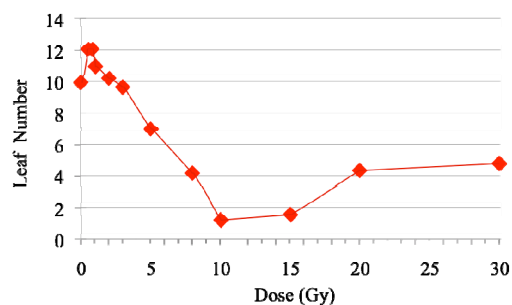


Fig. 3 Average leaf number in irradiated nodes at week 8.

References

- 1) H. Noor Auni et al., Economic Technol. Management Rev. 3 (2008) 75.
- 2) S. Nagatomi et al., Inst. Radiat. Breeding Technical News No. 65 (2003).
- 3) T. Murashige et al., Physiol. Plant. 15 (1962) 473.
- 4) A. Zaiton et al., JAEA Takasaki Annu. Rep. 2011 (2013) 97.

3 - 37 Mutational Effects of Carbon Ions near the Range End in Arabidopsis

Y. Hase, S. Nozawa and I. Narumi*

Medical and Biotechnological Application Division, QuBS, JAEA,

*Present affiliation: Faculty of Life Sciences, Toyo University

To date, little is known about the mutational effects of ion beams near the range end in plants. In previous studies, we showed that the carbon ions near the range end, which have a mean LET of 425 keV/μm (C (425)), had higher cell killing effect and induced more irreparable DNA lesions compared to 208 MeV carbon ions with a mean LET of 113 keV/μm (C (113))¹⁾. We examined the mutations occurred in the Arabidopsis *GLI* gene with the emphasis on large deletions. The frequency of glabrous mutant sectors, which is caused by inactivation of *GLI* gene, was not significantly different between C (425) and C (113), while the C (425) induced large deletions (> ~5 kb) more frequently by 6 times than C (113)^{2, 3)}. These results suggested that the frequency of large deletions is affected by LET. In the present study, we prepared the polymorphic DNA markers and evaluated the total size of deletions in a 9.4-Mb region around the *GLI* gene, which corresponds to about 40% of total length of chromosome 3.

Arabidopsis seeds obtained by crossing the wild type (ecotype: Columbia (Col)) with *gli-1* mutant (background ecotype: Landsberg *erecta*) were used to detect glabrous mutant sectors. Genomic DNA was extracted from leaf tissues of the glabrous mutant sectors. Twenty of polymorphic DNA markers that can distinguish the wild type and *gli-1* sequence were prepared to evaluate the total size of deletions. The polymorphic sites on the Col chromosome were considered to be deleted if no or very little signal for Col sequence was detected against a signal for *gli-1* sequence. Mutations that have deletion in either one or both of the nearest DNA markers (3.9 kb upstream and 2.8 kb downstream of *GLI* gene) were further examined to evaluate the total size of deletions.

The estimated size of a deletion induced by C (113) was 1-2 Mb (Fig. 1). In the case of C (425), one out of 7 deletions was less than 20 kb, while the others were larger than 200 kb. Total size of the largest deletion was estimated to be more than several Mb. Similar results were obtained in the case of neon ions with a mean LET of 352 keV/μm (Ne (352)). These results suggest that deletions larger than 200 kb are often induced by the ion beams with a LET higher than 100 keV/μm.

To further examine the LET dependency of the types of mutations, we examined the radiation sensitivity of the material seeds for six kinds of ion beams and gamma rays (Fig. 2). The effects of survival reduction clearly depended on the LET.

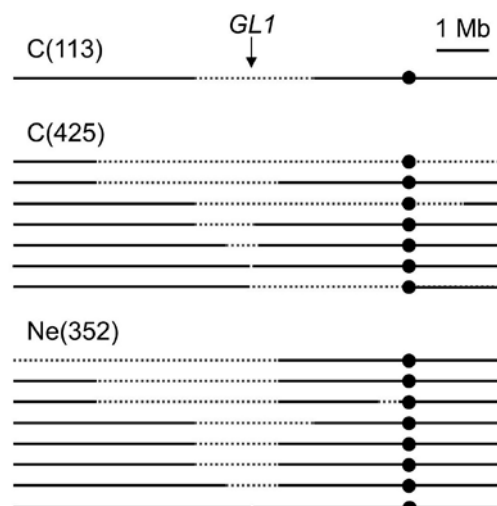


Fig. 1 Schematic representation of deleted region deduced from loss of heterozygosity for DNA markers. Horizontal lines represent chromosomes and dotted lines represent deleted regions. Black circles represent centromeres. Arrow indicates the position of *GLI* gene.

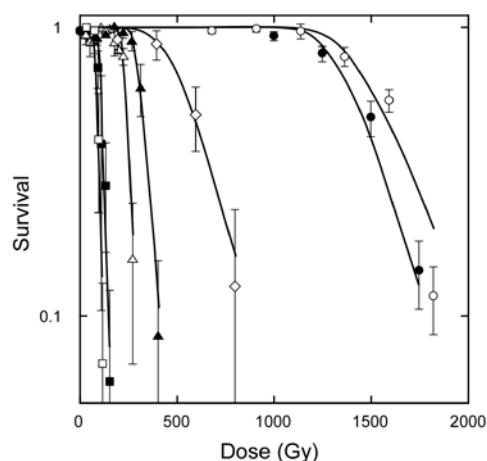


Fig. 2 Dose response curves for survival rate of irradiated seeds. ●, ⁶⁰Co gamma rays; ○, He (mean LET, 8.3 keV/μm); ◇, He (30); ▲, C (78); △, C (113); ■, C (425); □, Ne (352).

References

- 1) Y. Hase et al., JAEA Takasaki Annu. Rep. 2010 (2012) 103.
- 2) Y. Hase et al., Mutat. Res. 731 (2012) 41.
- 3) Y. Hase et al., JAEA Takasaki Annu. Rep. 2011 (2013) 98.

3 - 38 Homologous Recombination Induced by Low-dose Radiations in Arabidopsis

T. Uchida^{a)}, M. Teranishi^{b)}, Y. Hase^{a)}, M. Endo^{c)}, S. Toki^{c,d)},
J. Hidema^{b)} and A. N. Sakamoto^{a)}

^{a)}Medical and Biotechnological Application Division, QuBS, JAEA, ^{b)}Graduate School of Life Sciences, Tohoku University, ^{c)}Agrogeomics Research Center, National Institute of Agrobiological Sciences, ^{d)}Kihara Institute of Biological Research, Yokohama City University

Ion beams have been used as effective mutagens in plant breeding. Highly efficient mutagenic character of ion beams seems to be due to their energy deposit manner. Namely, ion beams deposit energy locally on chromosome, which induces irreparable DNA damage such as double-strand breaks (DSBs) or clustered DNA damage. However, little is known about cellular mechanism(s) by which DNA damage is converted into a mutation(s) in plant cells.

To study the mechanism(s) responsible for mutagenesis in plants, we utilized a transgenic Arabidopsis line harboring a GUS-based homologous recombination (HR) marker¹⁾. The marker line has a split GUS gene integrated in the genome that is inactive as is (Fig. 1). When a recombination occurs between the homologous sequences, an active GUS gene is reconstructed, which produces indigo-blue pigment in the presence of the substrate. We irradiated the HR marker lines with low dose of γ -rays or ion beams, which do not reduce the growth of plants, and examined the effects on HR activity.

Arabidopsis seeds were sown on a nutritive agar plate in 60-mm plastic petri dish and grown under 16h-light/8h-dark cycle at 23 °C for 10 days. The plants were irradiated with 25 Gy of γ -rays from ⁶⁰Co, or 15 and 25 Gy of 107 MeV ⁴He²⁺ from AVF cyclotron. After irradiation, the plants were grown under the same condition for another 7 days. All aerial parts of plants were collected and subjected to GUS-staining to detect HR events.

When the plants were grown without radiations, the average HR events per plants were 2.53 ± 0.12 . Twenty-five Gy of γ -ray irradiation increased the HR events to 3.56 ± 0.19 . By 15 and 25 Gy of 107 MeV ⁴He²⁺, the HR events per plants were 3.75 ± 0.22 and 6.29 ± 0.27 ,

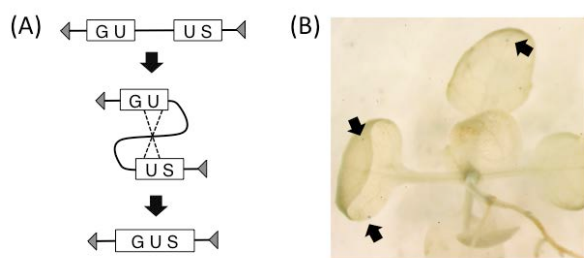


Fig. 1 Detection of homologous recombination (HR). (A) Reconstruction of an active GUS gene by HR, (B) Blue GUS⁺ sectors on plant tissues.

respectively. The results indicate that the 107 MeV ⁴He²⁺ has higher HR-inducing effect than the same dose of γ -rays (Fig. 2). The 15 Gy of 107 MeV ⁴He²⁺ induced comparable HR events as 25 Gy of γ -rays. In our preliminary data, the 107 MeV ⁴He²⁺ induced 1.4 times more DNA breaks [DSB + single strand breaks (SSBs)] than γ -rays per 1,000 Gy (Teranishi et al., unpublished). The higher HR activity after the 107 MeV ⁴He²⁺ irradiation may reflect this higher number of DNA breaks in Arabidopsis genome.

DSBs are thought to be repaired by HR or non-homologous end-joining (NHEJ) pathway in plant cells. Analyzing the sequence change in radiation-induced mutations suggested that NHEJ pathway is involved in the mutagenesis process²⁾. On the other hand, HR pathway utilizes undamaged homologous sequence to synthesize new DNA strand, thus less mutagenic than NHEJ. However, recombination between para-homologous sequences possibly induces drastic change of the chromosome(s). Our result indicated that HR activity was induced after low-dose irradiation. It is possible that HR pathway affects the DNA repair process. Further analysis would clarify the role of HR in radiation-induced mutagenesis in higher plants. Also, the HR-detecting marker could be a useful tool to monitor the biological effects of low-dose radiation.

References

- 1) H. Gerbi et al., EMBO Rep. 2 (2001) 287-91.
- 2) R. Yoshihara et al., Int. J. Radiat. Biol. 86 (2010) 125-31.

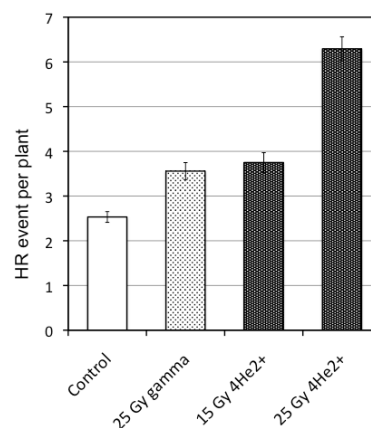


Fig. 2 HR events induced by γ -rays or 107 MeV ⁴He²⁺. The average HR events detected per plant was shown as the mean ± SEM.

3 - 39 Screening of Salt Tolerant Mutants by Combination of Radiation Mutagenesis and *In vitro* Regeneration in Lombardy Poplar (*Populus nigra*)

K. K. Biswas, Y. Hase, I. Narumi* and Y. Oono

Medical and Biotechnological Application Division, QuBS, JAEA,

*Present affiliation: Faculty of Life Sciences, Toyo University

Species of the genus *Populus* are ecologically important trees and often serving as a vegetative pioneer species because of their fast growth rates. The rapid growth of poplar is dependent on access to sufficient water in plantation sites and this is problematic. To overcome this problem, a forward genetics approach has been taken for developing salt/drought tolerant mutants by combination of radiation mutagenesis and *in vitro* regeneration in *Populus*. There is evidence that induced mutation with radiation mutagenesis has a great potential to produce new cultivars with wider mutation spectrum¹⁾.

Stem explants grown from newly developed canes of 3- to 4-month-old poplar plants were cultured in growth regulator-supplemented Murashige and Skoog (MS) medium and subjected for 320 MeV $^{12}\text{C}^{6+}$ ion-beam or gamma-ray irradiation in a dose-dependent manner. We found that 2.5 Gy of ion beams and 5 Gy of gamma rays have a minimum effect on regeneration ratio and growth of new shoots. Thus, we used these dosages for mutagenesis²⁾.

To establish screening system, above 1-cm-long regenerated shoots were cultured in a series of rooting media supplemented with different concentrations of NaCl. We found that regenerated non-irradiated shoots failed to produce roots in rooting medium supplemented with 75 mM or above concentration of NaCl (Table 1). Thus, for 1st screening, regenerated plants derived from ion-beam- or gamma-ray-irradiated tissues were grown on vermiculite until 8 weeks, and stem segments (6 cm) of these plants were then cultured in rooting medium with 75 mM NaCl. Root development efficiency of culture was monitored for 4 weeks. Using this system, a total of 5,500 regenerate plants was evaluated (Table 2). In first screening, we found five candidates of mutant, named *gamma1* to 5, which were developed root system in this medium. However, in second screening, about 25% stem segments of *gamma1* and *gamma5* produced roots in above medium (Fig. 1), but none of the stem segments from *gamma2*, 3 and 4 produced roots in same medium. Thus, *gamma1* and *gamma5*, obtained from gamma ray irradiation, might be the candidates of putative salt tolerant mutants that we are trying to isolate.

The screening system we mentioned above is based on root induction ability of the regenerate “shoots” to NaCl-supplemented rooting medium. To achieve more relevant and convincing results, we also developed *in vitro* regeneration system from “root” explants of the *gamma1*

(Fig. 1B) and *gamma5* mutants. Hopefully, this system may increase root induction ability of the mutants to salt medium.

Table 1 Root induction of regenerated non-irradiated shoots in NaCl-supplemented rooting medium.

NaCl (mM)	No. of regenerate shoots tested	No. of root producing shoots	% of root producing shoots
0	30	30	100
25	30	30	100
50	30	30	100
60	30	14	47
75	30	0	0
85	30	0	0
100	30	0	0
150	30	0	0

Table 2 Summary of 1st screening.

Mutagen	Dose (Gy)	No. of regenerate plants tested	No. of putative mutants
Carbon ion	2.5	741	0
Carbon ion	3	753	0
Gamma rays	5	2093	3
Gamma rays	7	1995	2

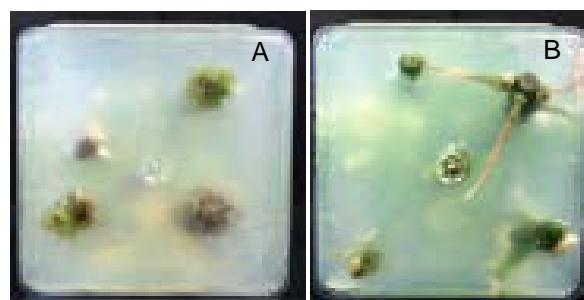


Fig. 1 The *gamma1* mutant developed roots in 75 mM NaCl-supplemented rooting medium. A: wild type; B: *gamma1*.

References

- 1) S. Nagatomi et al., Acta Horticult. 508 (2000) 69.
- 2) K. K. Biswas et al., Am. J. Plant Sci. 3 (2012) 1181.

3 - 40 Effects of Gamma-ray Irradiation on Oxalate Metabolism in *Rumex obtusifolius* L.

S. Kitano^{a)}, A. Miyagi^{a)}, Y. Oono^{c)}, Y. Hase^{c)}, I. Narumi^{c)}*,
H. Uchimiya^{b)} and M. Kawai-Yamada^{a, b)}

^{a)} Graduate School of Science and Engineering, Saitama University,

^{b)} Institute for Environmental Science and Technology, Saitama University,

^{c)} Medical and Biotechnological Application Division, QuBS, JAEA,

* Present affiliation: Faculty of Life Sciences, Toyo University

Rumex obtusifolius (Polygonaceae) highly accumulates soluble oxalate in leaves. Animals should restrict their intake of oxalate because high level of oxalate causes the poisoning. Therefore, *R. obtusifolius* well growing in the meadow is a target of weeding. In this study, we aimed to develop a low oxalate *R. obtusifolius* plant that can be used as a pasture by radiation breeding. Plants from seeds irradiated with several doses of gamma rays were used to analyze the radiation effect on oxalate content and other metabolite profiles. As a result, the oxalate content in leaves was decreased by gamma-ray irradiation. Plants with low oxalate content commonly contained increased level of amino acids and reduced level of organic acids.

エゾノギンギシ(タデ科)はヨーロッパ原産の多年生草本である。繁殖力が強く牧草地に繁茂する性質があり、播種やバイオマス維持等のコスト削減が見込めることから、新規の牧草としての利用が期待できる。しかし、この植物の代謝的特徴として、葉に可溶性シュウ酸を高蓄積することが知られている¹⁾。シュウ酸は動物が過剰摂取をすると害になる。そのため、エゾノギンギシを牧草飼料とするためには、葉の低シュウ酸化が必須である。本研究では、低シュウ酸化個体作出に向けて、ガンマ線のシュウ酸動態等への影響解析を行った。

まず、0-500 Gy の⁶⁰Co ガンマ線を照射したエゾノギンギシの種子を発芽させ、第3葉を回収した。50%エタノールによって葉の代謝物を抽出し、キャピラリー電気泳動-質量分析装置を用いてシュウ酸含有量の測定を行った(Fig. 1)。ガンマ線非照射個体に比べ、照射個体では葉のシュウ酸含有量が減少することが明らかになった。

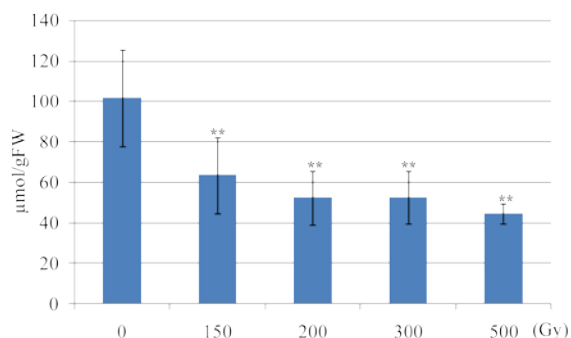


Fig. 1 Oxalate contents in leaves of *R. obtusifolius* irradiated with gamma rays. Seeds irradiated with 0-500 Gy of gamma rays were germinated and the third leaves were used for oxalate measurement (**= $p < 0.01$).

さらに、シュウ酸含有量の違いがその他の代謝物に及ぼす影響を明らかにするため、シュウ酸含有量が多い個体(80-100 μg/FW)、平均的な個体(50-78 μg/FW)、少ない個体(19-45 μg/FW)をそれぞれ 10 サンプルずつ選抜し、計 30 サンプルのメタボローム解析を行った。代謝物データ

を用いたヒートマップは代謝物量を正視化することで個体間における代謝物の多少を示したもので、多い代謝物が赤、少ない代謝物が緑で表わされている(Fig. 2A)。また、代謝物間の関係を調べるためにヒートマップのデータをもとに階層的クラスター解析を行い、樹形図を作成した(Fig. 2B)。その結果、シュウ酸含有量の少ない個体では共通してグルタミン、グルタミン酸、アスパラギンなどのアミノ酸が増加し、2-オキシグルタル酸やリンゴ酸などの有機酸が減少する傾向が見られた。ガンマ線照射によって TCA サイクルからアスパラギン酸及びグルタミン酸生合成方向への代謝動態変化が促進されたと考えられる。

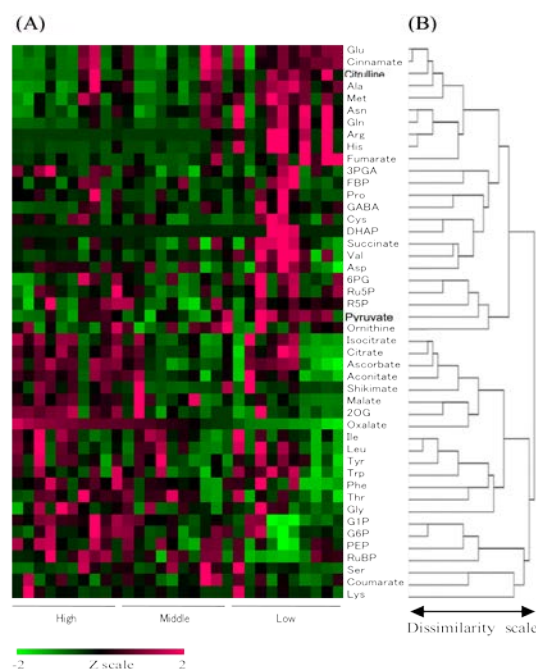


Fig. 2 (A) Heat map of metabolites in leaves of *R. obtusifolius*. (B) Hierarchical classification of metabolites in leaves of *R. obtusifolius*.

Reference

- 1) A. Miyagi et al., Metabolomics 6 (2010) 497.

3 - 41 Determination of the Carbon Ion Beam Irradiation Condition for Barley

T. Iimure^{a)}, T. Hoki^{a)}, Y. Hase^{b)}, S. Nozawa^{b)}, I. Narumi^{b)}, M. Kihara^{a)} and K. Ogushi^{a)}

^{a)} Bioresources Research and Development Department, Sapporo Breweries Ltd.,

^{b)} Medical and Biotechnological Application Division, QuBS, JAEA

To determine ideal condition of ion beam irradiation for barley grains, the carbon ion beam whose LET (Linear Energy Transfer) was 127 (C-127) and 275 (C-275) keV/μm was applied and the variation of the germination rate, initial plant growth, the survival rate by cultivars and by irradiation doses was observed. As a result, no difference was observed among six cultivars tested and the survival rates gradually decreased as to the irradiation doses. It was suggested from the relationship between the irradiation doses and the survival rate that the ideal irradiation doses at which the survival rate was around 80% were 10 Gy and 4 Gy for C-127 and C-275 irradiation, respectively.

オオムギへのイオンビーム照射に関する報告例は少ない。本研究ではビール醸造用オオムギのミュータントパネルの構築、およびビール醸造品質に関与する遺伝子の変異個体取得を目指し、オオムギへの適切なイオンビーム照射条件を決定することを目的とした。

イオンビームとして、TIARA のエネルギーの異なる 2 種類の炭素イオン(種子中の平均 LET: 127 keV/μm(C-127) 及び 275 keV/μm(C-275))を用いた。イオンビーム照射条件の決定は以下の 3 つのステップで行った。

① 試験 1: 初期スクリーニング(品種: 系統 A)

C-127: 0, 25, 50, 100, 150, 200 Gy

C-275: 0, 10, 20, 40, 80, 120 Gy

② 試験 2: イオンビーム感受性の大麦品種間差調査(系統 A を含む 6 品種・系統)

C-127: 0, 5, 10, 20, 40, 60, 80, 100, 120, 140 Gy

③ 試験 3: 最終スクリーニング(品種: 系統 A)

C-127: 0, 4, 8, 12, 16, 20 Gy

C-275: 0, 1, 2, 4, 8, 12 Gy

イオンビーム照射後の発芽率および生存率等の調査を行った後、適切な照射条件を決定した。

試験 1 では、対照と比較して、いずれのイオンビーム照射区とも生育が認められず、ほとんどの個体は生存しなかった (Fig. 1)。つまり本条件におけるイオンビーム照射区では発芽はするものの、致死的な変異導入により、それ以上の生育が困難であったと考えられる。このことから、イオンビーム照射による感受性のオオムギ品種間差が存在する、もしくは本試験でのイオンビーム照射は強度が強すぎることが考えられた。

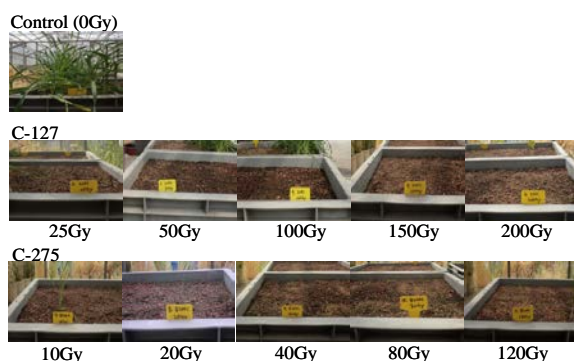


Fig. 1 The dose effect of C-127 and C-275 irradiation on the initial plant growth of barley cultivar A.

試験 2 では、初期生育はいずれの品種・系統とも 5~10 Gy 程度までは対照と大差がないが、20 Gy を超えると葉の伸長が悪くなり、40 Gy を超えると、土の中で死滅していた (Fig. 2)。以上の結果から、C-127 でのイオンビーム線量による初期生育に大きな品種間差はなく、適正な線量は 0-20 Gy の間であることが示唆された。

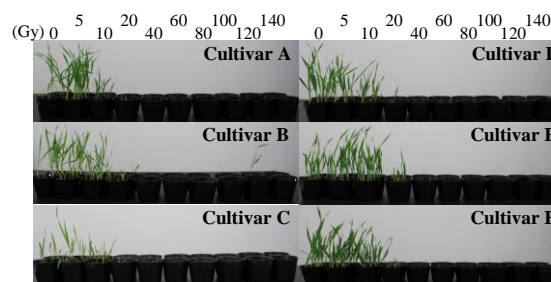


Fig. 2 The variation of the initial plant growth among barley cultivars by different irradiation doses of C-127.

試験 3 では、イオンビームの適切な照射線量を決定するために、試験 1 より線量が低い条件を設定し、生存率を調査した (Fig. 3)。C-127 では 8 Gy までは生存率に大きな差は見られなかったが、8 Gy 以上の線量では、線量の増加とともに生存率が低下し、20 Gy では全く生存しなかった。C-275 では、線量の増加とともに生存率が低下した。本結果から、生存率 80% 前後の処理区、つまり C-127 は 10 Gy、C-275 は 4 Gy が効率的な変異導入に適切な線量であると考えられた。

本研究成果は独立行政法人日本原子力研究開発機構の先端研究施設共用促進事業によるものである。

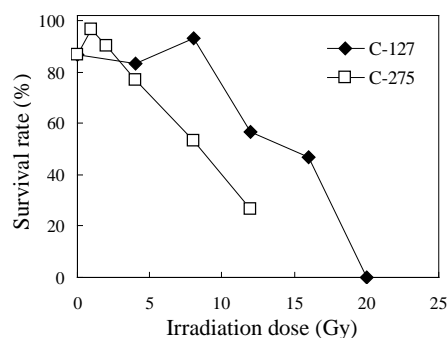


Fig. 3 The relationship between the irradiation doses and the survival rates.

3 - 42

Mutagenic Effect of Carbon Ion Beams in *Deinococcus radiodurans*

K. Satoh^{a)}, T. Onodera^{a,b)}, K. Takeda^{a,c)} and I. Narumi^{a)*}

^{a)}Medical and Biotechnological Application Division, QuBS, JAEA,

^{b)}Graduate School of Life Sciences, Tokyo University of Pharmacy and Life Sciences,

^{c)}United Graduate School of Agricultural Science, Tokyo University of Agriculture and Technology, *Present affiliation: Faculty of Life Sciences, Toyo University

Introduction

Ionizing radiation induces DNA double-strand breaks (DSBs), which is a particularly serious form of DNA damage and has especially deleterious effects in cells. Ion beams have high linear energy transfer (LET, keV/μm) and give DNA damage containing DSBs locally (clustered damage) than gamma rays do. *Deinococcus radiodurans* exhibits extraordinary resistance to the lethal effects of ionizing radiations. This resistance has been attributed to its highly proficient DNA repair capacity¹⁾. Previously, it had been reported that the DNA repair mechanism of *D. radiodurans* is not necessarily “error-free” since there were an increase in rifampicin-resistant mutant frequency depending on radiation doses of ion beams and gamma rays²⁾. In this study, we investigated mutant frequencies of two different antibiotic-resistant mutants for carbon ion beams in *D. radiodurans* and identified the mutation sites in the antibiotic-resistant mutants.

Experimental procedures

D. radiodurans cells were grown, harvested, resuspended and frozen as described previously²⁾. Freeze-dried cells were irradiated with ¹²C⁵⁺ ion beams (220 MeV; 121.8 keV/μm) accelerated by an AVF cyclotron at JAEA. The irradiation dose ranged from 2 to 15 kGy. Irradiated cells were cultivated at 30 °C in TGY broth with agitation to early stationary phase. Cells were harvested, diluted appropriately with 10 mM sodium phosphate, spread onto either TGY agar or TGY agar supplemented with streptomycin (2 μg/mL), and incubated at 30 °C for 3 or 4 days prior to the enumeration of colonies. The mutant frequency was determined by calculating the number of streptomycin-resistant (Sm^R) colonies divided by the total number of viable cells. To isolate the *rpsL* locus, PCR was carried out using PrimeSTAR GXL with the purified genomic DNA from Sm^R mutant as a template. To identify the mutation sites in the *rpsL* locus, DNA sequencing was carried out using BigDye Terminator Sequencing Kit with the PCR products. The sequence of the *rpsL* locus was compared to the wild-type sequence using software packages SeqMan Pro and Genetyx-Mac.

Results and discussion

The cells exhibited sensitivities to ¹²C⁵⁺ ion beams depending on radiation dose (Fig. 1). Streptomycin is one of the antibiotics that inhibit protein synthesis by directly

interacting with small ribosomal protein S12 encoded by *rpsL* gene. By genetically altering the *rpsL* gene in genome, Sm^R mutant can be generated. Like the previous study²⁾, the Sm^R mutant frequencies increased depending on radiation dose (Fig. 1). The highest Sm^R mutant frequencies were observed at a dose range that give 10⁻¹ to 10⁻² of surviving fraction. It seems that this dose range is the best dose to generate the mutants of interest for research and breeding purpose. Four kinds of mutation sites at the *rpsL* locus were determined from 8 Sm^R mutants. The first mutation from a mutant was identified as an A:T to C:G transversion at position 128 in the *rpsL* gene. The second mutation from 2 mutants was identified as an A:T to G:C transition at position 128. The third mutation from 2 mutants was identified as an A:T to G:C transition at position 262. The fourth mutation from 3 mutants was identified as an A:T to G:C transition at position 263. These mutations cause amino acid substitutions at position 43 (Lys to Thr or Arg) and 88 (Lys to Glu or Arg) in the S12 protein, respectively. The two hot spots at Lys43 and Lys88 in the S12 protein might be a binding target of streptomycin or adjacent to the center of streptomycin interaction with the ribosome.

References

- 1) I. Narumi, Trends Microbiol. 11 (2003) 422.
- 2) K. Satoh et al., JAEA Takasaki Annu. Rep. 2011 (2013) 103.

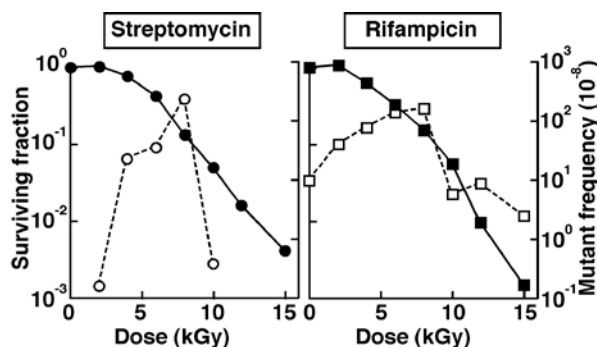


Fig. 1. Survival curves and antibiotics-resistant mutant frequencies for carbon ion beams. Closed and open symbols indicate surviving fraction and mutant frequency, respectively.

3 - 43 Genetic Analysis of Novel DNA Cross-link Repair Genes Common to *Deinococcus* and *Thermus*

T. Onodera^{a,b)}, K. Satoh^{a)}, T. Ohta^{b)} and I. Narumi^{a)*}

^{a)}Medical and Biotechnological Application Division, QuBS, JAEA,

^{b)}Graduate School of Life Sciences, Tokyo University of Pharmacy and Life Sciences,

*Present affiliation: Faculty of Life Sciences, Toyo University

Introduction

The *ygjD* and *yeaZ* orthologs are highly conserved in eubacteria, and the former is also widely found in the genomes of archaea and eukaryotes. These orthologs are known as essential genes for *Escherichia coli*, *Synechocystis* sp. PCC6803 and *Thermus thermophilus*. It was recently reported that the *ygjD* and *yeaZ* orthologs were related to DNA metabolism in *E. coli*¹⁾, mitochondrial DNA maintenance and transcriptional regulation in *Saccharomyces cerevisiae*²⁾. However, their functions are still poorly understood. *Deinococcus radiodurans* and *T. thermophilus* possess the both orthologs hereafter *Drygjd*, *DryeaZ*, *TygdjD* and *TtyeaZ*, respectively. We have reported that the *Drygjd* and *DryeaZ* disruptants show extreme sensitivity to mitomycin C (MMC), which causes interstrand DNA cross-links³⁾. In this study, we constructed *TygdjD* and *TtyeaZ* gene expression plasmids and the resultant plasmids were introduced into the *Drygjd* and *DryeaZ* disruptant strains (Δ *Drygjd* and Δ *DryeaZ*). To investigate whether *ygjD* and *yeaZ* orthologs share the common function in *D. radiodurans* and *T. thermophilus*, these generated strains were challenged by MMC.

Experimental procedures

We constructed two plasmids as follows. PCR fragment containing the structural gene of *TygdjD* was inserted into an *NdeI*-*BamHI* site of pRGL1 carrying the *D. radiodurans* *groE* promoter to yield plasmid pGroTygdjD. PCR fragment containing the structural gene of *TtyeaZ* was inserted into an *NdeI*-*BamHI* site of pRGL1 to yield plasmid pGroTtyeaZ. *Drygjd* and *DryeaZ* disruptant strains were transformed with the above-mentioned plasmids. These complementation strains were cultivated at 30 °C in TGY broth (0.5% tryptone-peptone, 0.1% glucose and 0.3% yeast extract) supplemented with 3 µg/mL of chloramphenicol. For MMC treatment, 20 µg/mL of MMC was directly added to the culture. Cells were incubated at 30 °C and withdrawn at various time points. After the treatments, cells were diluted with 10 mM sodium phosphate buffer, drop onto TGY agar, and incubated at 30 °C for 2 days prior to the enumeration of colonies.

Results and discussion

Two gene disruptant strains (Δ *Drygjd* and Δ *DryeaZ*) and a double disruptant strain (Δ *Drygjd DryeaZ*) exhibited extreme sensitivity to MMC compare to the wild-type strain (WT) (Fig. 1)³⁾. Δ *Drygjd* carrying *TygdjD* expression

plasmid was partially complemented to the wild-type phenotype (Fig. 2A). Δ *DryeaZ* carrying *TtyeaZ* expression plasmid also showed the same result as the complementation test by *TygdjD* gene (Fig. 2B). These results suggest that *Drygjd* and *DryeaZ* genes share common function or operation with *TygdjD* and *TtyeaZ* genes. However, *TygdjD* and *TtyeaZ* proteins could not entirely complement the function of *Drygjd* and *DryeaZ* proteins. Because the optimal growth temperature of *D. radiodurans* and *T. thermophilus* is 30 and 70 °C, respectively, we speculated that the original activity of *TygdjD* and *TtyeaZ* proteins was not fully exerted in *Drygjd* and *DryeaZ* disruptant strains.

References

- 1) J. I. Handford et al., J. Bacteriol. 191 (2009) 4732.
- 2) J. Obero et al., Nucleic Acids Res. 37 (2009) 5343.
- 3) T. Onodera et al., Extremophiles, 17 (2013) 171.

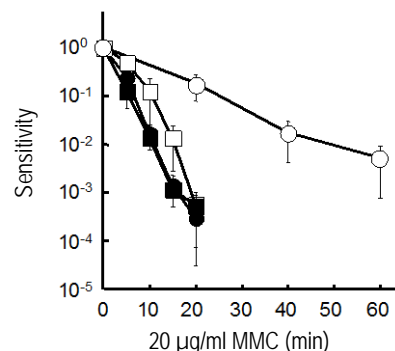


Fig. 1 Sensitivity of *Drygjd* and *DryeaZ* disruptant strains to MMC. Symbols: open circles, WT; filled circles, Δ *Drygjd*; open squares, Δ *DryeaZ*; closed squares, Δ *Drygjd DryeaZ*.

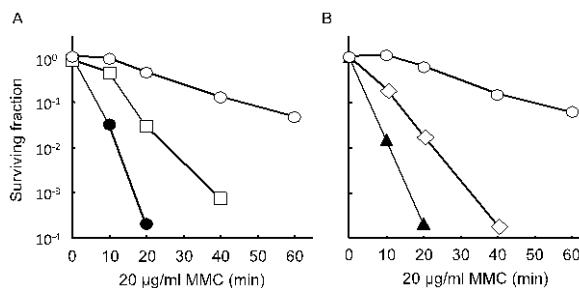


Fig. 2 Complementation tests of *Drygjd* and *DryeaZ* disruptant strains for MMC challenge. (A) Symbols: open circles, WT carrying pRADN1 (vector); filled circles, Δ *Drygjd* carrying pRADN1; open squares, Δ *Drygjd* carrying pGroTygdjD. (B) Symbols: open circles, WT carrying pRADN1; filled triangles, Δ *DryeaZ* carrying pRADN1; open diamonds, Δ *DryeaZ* carrying pGroTtyeaZ.

3 - 44 Molecular Analysis of Heavy Ion Induced Mutations in Budding Yeast *S. cerevisiae*

Y. Matuo^{a)}, Y. Izumi^{a)}, Y. Hase^{b)}, A. N. Sakamoto^{b)}, S. Nozawa^{b)},
I. Narumi^{b)*} and K. Shimizu^{c)}

^{a)}Research Institute of Nuclear Engineering, University of Fukui,

^{b)}Medical and Biotechnological Application Division, QuBS, JAEA,

^{c)}Radioisotope Research Center, Osaka University,

*Present affiliation: Faculty of Life Sciences, Toyo University

The ion beams have been widely used as the mutagen for developing new varieties of plants and bacteria^{1,2)}. To investigate the nature of mutations induced by accelerated ions in eukaryotic cells, the effects of carbon-ion irradiation were compared with those of gamma-ray irradiation in the budding yeast *Saccharomyces cerevisiae*. Carbon-ion irradiation ($^{12}\text{C}^{5+}$, 220 MeV) at 100 Gy increased the mutation frequency in *URA3* gene 100 times as compared to the spontaneous mutation frequency. The types of base changes consisted of transversion (68.7%), transition (13.7%) and deletion/insertion (17.6%). Most of the transversion mutations were G:C to T:A and all the transition mutations were G:C to A:T. We found that the base change mutations were often induced in 5'-ACA-3' and 5'-ACT-3' sequences. The most remarkable feature of the mutations induced by carbon ions was that the mutation sites were localized near the linker regions of nucleosomes, whereas mutations induced by gamma rays were located uniformly throughout the gene³⁾.

We hypothesized that the locus of mutations might be concerned with the nucleosome structure. Studies of the nucleotide excision repair and photorepair suggested that the DNA damage was repaired slowly on the nucleosomes but was repaired quickly on the linkers⁴⁾. We designed new experiment to clarify this hypothesis. The yeast strain that has *URA3* gene with altered nucleosome structure was generated by genetic modification using pAUR112 plasmid and Aureobasidin transformation system (TaKaRa). The yeast cells were irradiated with carbon ions (LET 107 keV/ μm) with the dose of 100 Gy.

Figure 1 shows the mutation spectrum in the *URA3* gene and Table 1 shows the summary of the sequence analyses. It is likely that locus of mutations occurred in the *URA3* with altered nucleosome structure is inconsistent with those in the wild type, suggesting that the locus of mutations depends on the nucleosome structure. We will accumulate the data further to examine the above hypothesis.

References

- 1) A. Tanaka et al., J. Exp. Bot. 53 (2002) 683.
- 2) T. Masubuchi et al., JAEA Takasaki Annu. Rep. 2011 (2013) 110.
- 3) Y. Matuo et al., Mutat. Res. 602 (2006) 7.
- 4) R. E. Wellinger et al., EMBO. J. 16 (1997) 5046.
- 5) S. Tanaka et al., J. Mol. Biol. 257 (1996) 919.

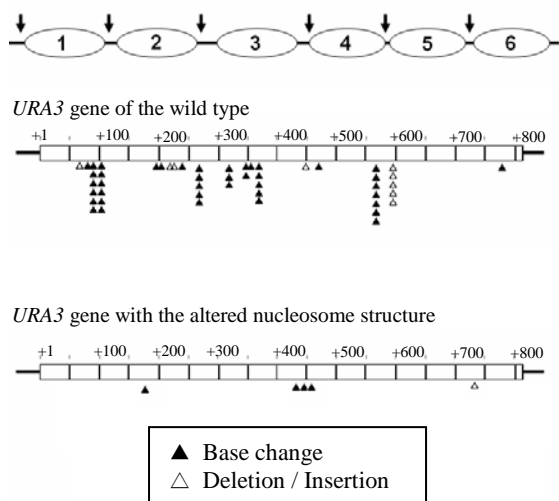


Fig. 1 Mutation spectrum induced by carbon-ion irradiation in yeast. Arrows indicate the position of linker DNA of the wild type⁵⁾. Numbers refer to the nucleotide position of *URA3* gene. +1 is the A of the initiation codon ATG.

Table 1 DNA sequence context of mutations in *URA3* caused by carbon ion beam.

Position	Change	Sequence context
+167	G to A	AAT TTG TTT
+417	A to T	AGA AGT AGC
+419	T to A	AGA AGT AGC
+421	A to G	TGA AGC AAC
+720	Insert A	AAA <u>↑</u> GGG AAG

Arrow indicates the insertion site.

3 - 45 Improvement of Endophytic Bacteria Using Ion Beams and Application of Bio-pesticide with Plant Growth Promoter Made from Oligo-chitosan

M. Aino^{a)}, K. Satoh^{b)}, I. Narumi^{b)*}, N. Nagasawa^{c)}, F. Yoshii^{c)} and M. Taguchi^{c)}

^{a)}Hyogo Prefectural Center for Agriculture, Forestry and Fisheries, ^{b)}Medical and Biotechnological Application Division, QuBS, JAEA, ^{c)}Environment and Industrial Materials Research Division, QuBS, JAEA, *Present affiliation: Faculty of Life Sciences, Toyo University

The endophytic bacteria produce various kinds of bioactive substances, by which the plants grow well and exhibit resistance to diseases and environmental stress. In this study, 300 isolates that were derived from *Pseudomonas fluorescens* strain FPH9601 irradiated with carbon ion beams were tested for inhibitory effect of tomato bacterial wilt. We could successfully obtain 24 mutants that have enhanced suppressiveness against the tomato bacterial wilt. In the meantime, chitosan is a linear polysaccharide composed of randomly distributed β -(1-4)-linked D-glucosamine (deacetylated unit) and N-acetyl-D-glucosamine (acetylated unit). Low molecular weight chitosan (oligo-chitosan), which can be obtained by γ -ray irradiation of chitosan in diluted solutions, has potential uses in agriculture. In the field condition, the suppression effect against the pathogen significantly increased when tomato was treated with oligo-chitosan and endophytic bacteria.

生物農薬の原体微生物 *Pseudomonas fluorescens* FPH9601 菌株を用いて、イオンビーム突然変異育種のための最適線量を求めたところ、300 Gy の照射線量において最も変異株の出現率が多いことが判明した。今回は、検定数を増やし変異株の選抜を行った。一方、植物に生理活性を有するオリゴキトサンを用いて、*P. fluorescens* FPH9601 菌株のトマト青枯病発病抑制効果の増強が可能かどうかを検討した結果、ポット試験において、高い増強効果が認められた。今回は、圃場条件においてもその併用効果が得られるかどうかを検討した。

1) イオンビーム照射による内生細菌の改良

供試内生細菌は *P. fluorescens* FPH9601 菌株を用い、標準寒天培地上で 28 °C、24 時間培養後、滅菌蒸留水に懸濁した。懸濁液(約 10^8 cfu/mL) 2 mL を直径 47 mm の酢酸セルロースメンブランフィルター (ADVANTEC 社) でろ別した。ろ別後、直ちに直径 60 mm シャーレにフィルターを入れ、凍結乾燥を行った。保護剤等は添加せず行った。凍結乾燥後、シャーレ上面をカプトン膜で覆った。イオンビーム照射は TIARA の AVF サイクロトロンを用い、 $^{12}\text{C}^{5+}$ (220 MeV) で 300 Gy を照射した。照射試料を滅菌蒸留水と共に試験管に入れ、30 分間振とう後、懸濁液を標準寒天培地上に塗布した。28 °C、48 時間後に生じたコロニーを 15% グリセロール溶液に懸濁し、一旦、-80 °C で保存した。凍結保存 300 菌株をシードリングバイオアッセイチャンバー法で、トマト青枯病に対する発病抑制効果を検定した。

親株の健全株数を基準にして照射株の健全株の比率を Fig. 1 に示した。健全株比率が 2 倍以上の菌株 24 菌株を得ることができた。

2) 内生細菌とオリゴキトサンとの併用効果

供試内生細菌は *P. fluorescens* FPH9601 菌株を用い、標準培地平板で 24 時間培養後にかきとり、トマト(品種: 大型福寿) 種子にバクテリアゼーションした。育苗培土を充填したセルトレイ(200 穴)に播種し、ガラスハウス内で約 25 日間育苗した。汚染程度の異なる青枯病汚染圃場(多発生、中発生)に定植し、定植 7 日後から 5 日間隔で地上部へオリゴキトサン水溶液(100 ppm)を散布した。試験区は 1 区 9 株、3 反復とした。オリゴキトサンは原子力機構作製のオリゴキトサン・エチルアルコール溶液を用い、原液を 1/3 に濃縮

し、エタノールを完全に除去した。調査は肉眼で萎凋症状を確認し、発病株率及び防除価((対照の発病株率-処理区の発病株率)/対象の発病株率 \times 100)を算出した。

FPH+オリゴキトサン散布区において、多発生圃場では、発病遅延効果とやや低いが発病抑制効果が認められた(Fig. 2)。中発生圃場では、防除価 50 程度(定植 41 日後)の発病抑制効果が確認された。本結果から、内生細菌に感染したトマトを定植後、地上部へのオリゴキトサンを散布することにより内生細菌の効果増強が確認されたが、圃場の青枯病菌の汚染程度が高くなるに従ってその効果が低くなった。

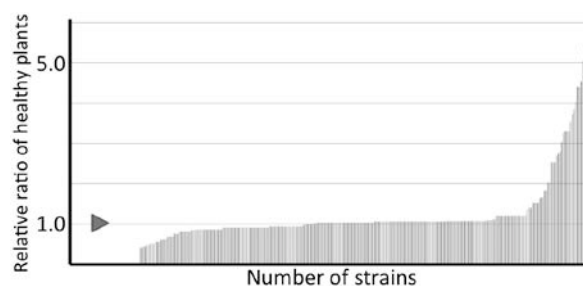


Fig. 1 Suppression effect of occurrence of tomato bacterial wilt by *P. fluorescens* FPH9601 mutagenized with carbon ion beams.

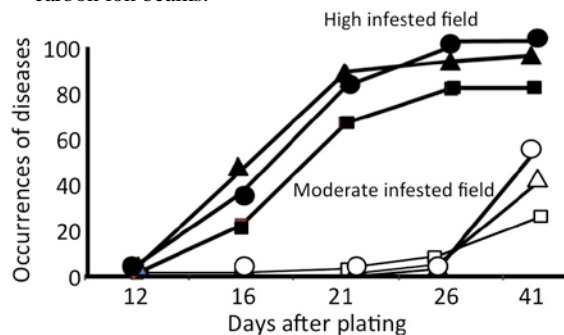


Fig. 2 The suppression effect of combination of oligo-chitosan and endophytic bacteria. Symbols: circles, control; triangles, oligo-chitosan; squares, oligo-chitosan + endophytic bacteria.

3 - 46

Identification of DNA Mutation Sites in a High Temperature Tolerant Mutant of *Bradyrhizobium japonicum* USDA110 Generated by Ion-beam Irradiation

K. Takeda^{a,b)}, K. Satoh^{b)}, I. Narumi^{b)*}, N. Ohkama-Ohtsu^{c)} and T. Yokoyama^{c)}

^{a)}United Graduate School of Agricultural Science, Tokyo University of Agriculture and Technology,

^{b)}Medical and Biotechnological Application Division, QuBS, JAEA,

^{c)}Institute of Agriculture, Tokyo University of Agriculture and Technology,

*Present affiliation: Faculty of Life Sciences, Toyo University

In Asian countries, in order to increase crop yield under low input of chemical fertilizers, many researchers in agricultural institutes are trying to develop biofertilizers. However, several researchers point out constraints on application of biofertilizers. Major constraint of biofertilizer utilization in agricultural practice is a viability loss of beneficial microorganisms in biofertilizers caused by high temperature and drought stress during both storage and transportation. Therefore, we have tried to improve high temperature tolerance of *Bradyrhizobium japonicum* USDA110, which is a superior inoculant to soybean in temperate area. Consequently, we have obtained a high temperature tolerant mutant that can survive at 42 °C for at least 7 days, and named it as M14.

As shown in Fig. 1, the mutant M14 formed smooth colonies with glossy white color like wild type (WT). The colony size of M14 was little smaller than that of WT when incubated at 30 °C. The generation time of M14 at 30 °C was 7.2 h, which was about 1.2 h longer than that of WT (6.0 h). As for symbiotic functions with soybean (*Glycine max* cv. Enrei), there was not much difference on nodulation ability between M14 and WT.

The genome sequence of M14 was determined by a whole-genome shotgun strategy. The pyrosequencing data were accumulated using a GS Junior System (Roche Applied Science, Mannheim, Germany) according to the supplier's protocol. Then, the data were mapped to the reference sequence of strain USDA110 (WT) using a GS Reference Mapper software. About 99.5% of the reference sequence was covered with the M14 sequence.

Genome comparison between strain USDA110 (WT) and the high temperature tolerant mutant M14 revealed a large-scale structural change in the circular DNA genome of M14. Namely, a DNA region at the coordinates 4,029,222-5,299,699 (1,270,478 bp) was inverted. This region contained 8 tRNAs and 1,139 genes with various functions (Fig. 2). In addition, 84 mutations such as base substitutions, insertions and deletions were found in M14. Although the inverted region was corresponded to only 14% of whole genome size, 40% of 84 mutations were located in this region. This bias could indicate the association between the inversion occurrence and the increase of mutations. In the meantime, 56 out of 84 mutations were distributed in 48 structural genes, and the other 28 were located in non-coding

regions. Forty-three out of 48 structural genes had some influences on the process of translating protein, and caused amino acid substitutions and frameshift mutations. The acquirement of high temperature tolerance in M14 could be attributed to a large-scale inversion or small-scale mutations in the inverted region, or both.

Now, we are on the process of confirming these mutations one by one using Sanger sequencing. In addition, we intend to analyze gene expression by cDNA microarray in order to find out how these mutations effect on transcriptional level.

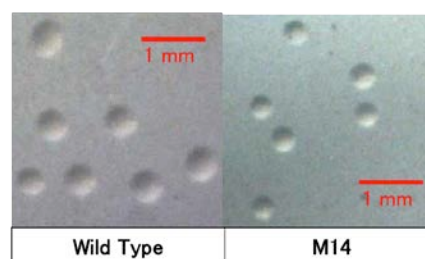


Fig. 1 Colony morphology of *B. japonicum* after cultivating at 30 °C for 4 days.

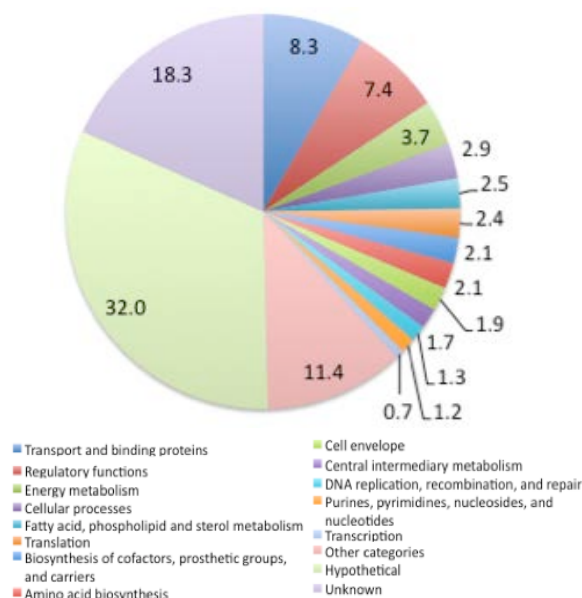


Fig. 2 The functional classification of the genes in the 1.27-Mbp inverted region.

3 - 47 Simultaneous Saccharification and Fermentation from Ionic Liquid-pretreated Biomass Using Ionic Liquid-tolerant Yeast Mutant

K. Ninomiya^{a)}, S. Omote^{a)}, K. Satoh^{b)}, I. Narumi^{b)*} and N. Shimizu^{a)}

^{a)}Division of Material Engineering, Graduate School of Natural Science and Technology, Kanazawa University, ^{b)}Medical and Biotechnological Application Division, QuBS, JAEA,

*Present affiliation: Faculty of Life Sciences, Toyo University

Simultaneous saccharification and fermentation from ionic liquid-pretreated biomass was carried out using ionic liquid-tolerant yeast that was obtained from the mutant population prepared by irradiation with carbon ion beams (220 MeV $^{12}\text{C}^{5+}$, 100 Gy). By using the ionic liquid-tolerant yeast strain, we could simplify the washing procedure of ionic liquid-pretreated biomass prior to the simultaneous saccharification and fermentation.

【緒言】木質系(リグノセルロース)バイオマスをから、酵素糖化・微生物発酵をへてエタノール等の有用代謝産物を生産する際に問題となるのが、リグノセルロースの強固な構造(セルロース繊維間の水素結合による結晶構造やリグニンのネットワーク構造)が糖化酵素のアクセスを阻害するという問題である。そのため、リグノセルロース系バイオマスの場合では、酵素前処理が必要となる。従来、酸やアルカリ、そして高圧・高温条件下で前処理が行われていたが、エネルギーコストや糖の過分解が問題となっていた。

近年、木質系バイオマスを、常圧・温和な条件で溶解し、セルロースを非結晶化させる『イオン液体』を用いた糖化前処理が注目されている^{1,2)}。しかし、バイオマス前処理に使用されるイオン液体は、一般的に毒性が高いため、前処理バイオマスからイオン液体を洗浄する際に生じる大量の洗浄廃液が問題となっている。

そこで本研究では、イオン液体に耐性を示す変異酵母株をイオンビーム照射変異集団から選抜し、イオン液体で前処理したバイオマスについて異なる洗浄回数を用意し、同時糖化発酵試験を行った。

【実験方法】使用菌株及びイオンビーム照射: 酵母 *Saccharomyces cerevisiae* MT8-1 株を用いた。酵母の培養は YPD 培地を用いて 30 °C で行った。また、MT8-1 株に炭素イオン (220 MeV $^{12}\text{C}^{5+}$) を 100 Gy 照射し、変異株集団を調製した。イオン液体耐性酵母は、所定の濃度のイオン液体を添加した YPD 液体培地で馴化培養後、寒天培地上で選抜した。

バイオマスおよびイオン液体: リグノセルロース系バイオマスには 1 mm に粉碎した竹を用いた。90 °C で 12 h 乾燥させてから使用した。バイオマス前処理用のイオン液体として 1-ethyl-3-methylimidazolium acetate を用いた。

イオン液体による前処理: バイオマス:イオン液体の重量比が 1:10 になるよう混合し、110 °C で 16 h 加熱前処理を行った。前処理したバイオマスはイオン液体に溶解しているため、貧溶媒として蒸留水 50 mL を加え析出させた。サンプルは遠心分離し、固液分離・洗浄する操作を 2 回、または 5 回繰り返して行い、イオン液体の除去を行った。回収したバイオマスは 90 °C を保ったインキュベーター内で 12 h 乾燥させた。同時糖化発酵には乾燥後の前処理バイオマスを使用した。

同時糖化発酵: 前処理バイオマスを唯一の炭素源として酵素と酵母を用いて同時糖化発酵を行った。YP 液体培地

に、前処理バイオマス 50 g/L、メイセラゼ (明治製菓 6,200 U/g) 5 g/L、酵母 100 g-wet/L となるように加え、30 °C で 96 h 醗酵を行った。エタノール濃度はガスクロマトグラフィーを用いて測定し、前処理バイオマスから生産できる理論エタノール量との比よりエタノール収率を算出した。

【結果と考察】イオン液体を用いて 16 h 加熱前処理し、その後 2 回もしくは 5 回洗浄したバイオマスを用いて同時糖化発酵を行った。Figure 1 にエタノール収率を示す。野生酵母 MT8-1 株を用いた同時糖化発酵では、5 回洗浄の場合と比較し、2 回洗浄しかしていない場合では、エタノール収率が半減した。これは、イオン液体前処理バイオマスの洗浄回数を減らしたことにより、同時糖化発酵の反応液中に持ち込まれたイオン液体が増加し、それにより酵母が阻害されたためと考えられる。一方、イオン液体耐性酵母株 MT8-1m 株を用いた同時糖化発酵では、5 回洗浄の場合と比較し、2 回洗浄しかしていない場合でも、エタノール収率が減少しなかった。これは、イオン液体前処理バイオマスの洗浄回数を減らしたことにより、増加した持ち込みイオン液体に対して、酵母が耐性を示した結果と考えられる。しかしながら、変異導入そのものによるエタノール生産レベルの低減が見られた。以上、イオン液体耐性酵母を用いることにより、イオン液体前処理後のバイオマスの洗浄回数を低減し、廃液量を削減できることが示唆された。

References

- 1) R. P. Swatloski, et al., J. Am. Chem. Soc. 124 (2002) 4974.
- 2) I. Kilpeläinen, et al., J. Agric. Food Chem. 55 (2007) 9142.

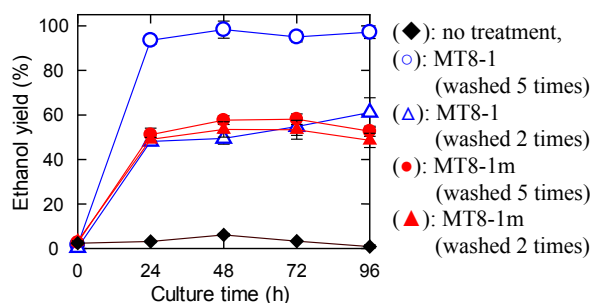


Fig. 1 Time course of ethanol yield during simultaneous saccharification and fermentation.

3 - 48 Benomyl-tolerant Mutation of Entomopathogenic Fungi Induced by Carbon Ion Beams

T. Saito^{a)}, Y. Fitriana^{a)}, K. Satoh^{b)} and I. Narumi^{b)*}

^{a)}Faculty of Agriculture, Shizuoka University, ^{b)}Medical and Biotechnological Application Division, QuBS, JAEA, *Present affiliation: Faculty of Life Sciences, Toyo University

Entomopathogenic fungi, *Isaria fumosorosea* and *Beauveria bassiana*, are important agents to control insect pests, but the fungi could be negatively affected by conventional fungicides for plant diseases such as powdery mildew. The purpose of this study is to generate mutants highly tolerant to benomyl, a major fungicide, using carbon ion beams. We have obtained some benomyl-tolerant mutants and examined the tolerant levels to benomyl, response to other fungicides, and virulence to target insects. It has been shown that β -tubulin of fungi are involved in resistance to benzimidazole fungicides such as benomyl. In this study, in order to identify the mutation sites of β -tubulin in the benomyl-tolerant mutants, we determined the nucleotide sequences of β -tubulin locus and compared with those of the wild-type strains. In *B. bassiana* mutants, the mutation was identified to be an A:T to C:G transversion at position 924 in the β -tubulin gene. This mutation causes an amino acid substitution at position 198 (Glu to Ala) in the β -tubulin protein. This site might be a binding target of benomyl or adjacent to the center of benomyl interaction with the β -tubulin. On the other hand, in *I. fumosorosea* mutants, the β -tubulin sequences were identical to that of the wild-type, suggesting that other mechanisms might be responsible for the benomyl tolerance. These results suggest that mechanisms of benomyl tolerance were different between *I. fumosorosea* and *B. bassiana*.

昆虫病原糸状菌を用いて害虫を防除する微生物的防除法は殺菌剤と併用しにくいという難題を抱えている。この抜本的な解決策として、殺菌剤耐性という新機能を有する昆虫病原糸状菌を創出することが考えられる。本研究の目的は、炭素イオンビームの照射による突然変異育種技術を用いて、殺菌剤耐性の昆虫病原糸状菌 (*Beauveria bassiana* 及び *Isaria fumosorosea*) 変異体を創出することである。

これまでの研究によって、両菌種ともベノミル剤耐性変異体が得られ、耐性レベルの詳細、他剤に対する耐性、病原力の変化などについて明らかにした¹⁻³⁾。ここでは、ベノミル耐性に関与していると考えられている β チューブリン遺伝子の解析を行った。

B. bassiana は親株と 2 種のベノミル耐性変異株、*I. fumosorosea* は親株と 4 種のベノミル耐性変異株を供試した。各菌株は、サブロー寒天培地で 3 日間培養したコロニーから分生子を採集し、Fast DNA SPIN Kit (MP Biomedicals)を用いてゲノム DNA を抽出した。ゲノム DNA をテンプレートとして、*B. bassiana* は *Ex Taq* DNA Polymerase (Takara Bio)、*I. fumosorosea* は PrimeSTAR GXL DNA Polymerase (Takara Bio)を用いて、 β チューブリン遺伝子領域を増幅した。PCR 産物は、電気泳動によりサイズを確認した後、MinElute PCR Purification Kit (Qiagen)を用いて精製した。DNA シークエンス解析は、PCR 産物をテンプレートとして、BigDye Terminator Cycle Sequencing Kit (Applied Biosystems) 及び ABI Prism 377 DNA Sequencer を用いて行った。 β チューブリン遺伝子領域の塩基配列を SeqMan Pro (DNASTAR) と GENETYX-MAC (GENETYX) のソフトウェアを用いて解析し、変異部位を同定した。

電気泳動解析の結果、*B. bassiana* (親株及び 2 種の変異株) 及び *I. fumosorosea* (親株及び 4 種の変異株) において、目的サイズの β チューブリン遺伝子領域の増幅を確認した (それぞれ 1,428 及び 1,424 bp) (Fig. 1)。

DNA 塩基配列解析の結果、*B. bassiana* 変異株では決定した β チューブリン遺伝子領域の 924 番目の塩基 A が C

に変異しており、これにより β チューブリンの 198 番目のアミノ酸が Glu から Ala に変化していると推定された。 β チューブリン遺伝子の同部位での突然変異によるベノミル耐性獲得の事例は、植物病原菌や NaNO_2 によって誘導された *B. bassiana* 変異株でも過去に報告されている^{4,5)}。一方、*I. fumosorosea* の β チューブリン遺伝子領域の塩基配列解析の結果、親株と変異株では、推定されるアミノ酸配列が同一であることから、*I. fumosorosea* のベノミル耐性には別のメカニズムが関与していると考えられる⁶⁾。

以上のことから、*B. bassiana* と *I. fumosorosea* のベノミル耐性発現に関わるメカニズムは遺伝子レベルで異なることが明らかとなった。今後、*I. fumosorosea* におけるベノミル耐性獲得のメカニズムを究明したい。

References

- 1) T. Saito et al., JAEA Takasaki Annu. Rep. 2009 (2011) 76.
- 2) T. Saito et al., JAEA Takasaki Annu. Rep. 2010 (2012) 112.
- 3) T. Saito et al., JAEA Takasaki Annu. Rep. 2011 (2013) 109.
- 4) R. M. Davidson et al., J. Phytopathol. 154 (2006) 321.
- 5) G. Zou et al., Environ. Microbiol. 8 (2006) 2096.
- 6) T. T. Song et al., J. Appl. Microbiol. 112 (2011) 175.

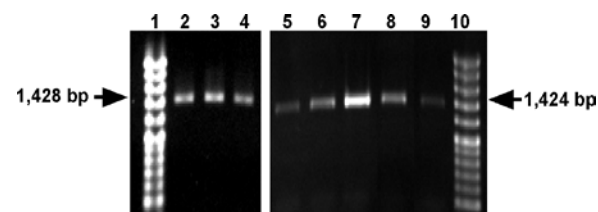


Fig. 1 PCR amplification of β -tubulin gene in *B. bassiana* and *I. fumosorosea*. Lanes 1 and 10, DNA ladder marker; lane 2, *B. bassiana* wild-type; lanes 3 and 4, *B. bassiana* mutants; lane 5, *I. fumosorosea* wild-type; lanes 6 to 9, *I. fumosorosea* mutants. Arrows indicate predicted PCR product sizes.

3 - 49 Mutation Analysis of High Ethyl Caproate Producing Sake Yeasts Generated by Ion Beam Breeding

T. Masubuchi^{a)}, R. Ueda^{b,c)}, O. Kamiyama^{a)}, H. Ikenaga^{b)}, K. Satoh^{c)} and I. Narumi^{c)*}

^{a)}Gunma Industrial Technology Center, ^{b)}Maebashi Institute of Technology,

^{c)}Medical and Biotechnological Application Division, QuBS, JAEA,

*Present affiliation: Faculty of Life Sciences, Toyo University

We have previously obtained high ethyl caproate producing Sake yeasts “No.227” and “No.1333” by ion beam breeding. The fatty acid synthase genes (*FAS1* and *FAS2*) and the fatty acid esterase genes (*EHT1* and *EEB1*) might be involved in the higher production of ethyl caproate in the mutant strains. In this study, to identify the mutation sites of the mutant strains, each gene locus was sequenced and compared with corresponding sequences in the parental strain “Kyokai-901”. For the *EHT1*, *EEB1* and *FAS1* loci, all the mutations found in mutant strains are nonsense mutations, suggesting that these mutations did not involved in the higher production of ethyl caproate. On the other hand, strains No.227 and No.1333 carried G/A and A/A mutations at nucleotide position 3,748 as heterozygous and homozygous states, respectively. This result strongly suggested that the higher production of ethyl caproate in strains No.227 and No.1333 is attributed to a dominant mutation in *FAS2* gene.

群馬県では、オリジナルの吟醸用清酒酵母を開発するために、イオンビーム育種による新たな吟醸用清酒酵母の開発を行ってきた。これまでに、吟醸酒特有の香気成分であるカプロン酸エチルを高生産する優良清酒酵母 (No.227 及び No.1333 株) を選抜した (Table 1)¹⁾。イオンビーム育種によって優良形質を持った清酒酵母が得られた一方で、優良な変異株を選抜するためには多大な労力を要するのが現状である。そこで、本研究では、イオンビーム育種により作出した清酒酵母のゲノム DNA 塩基配列解析によるカプロン酸エチルを高生産する要因を明らかにするとともに、優良な変異株を早期選抜できる DNA マーカーの開発が可能か検討した。

カプロン酸エチルは、脂肪酸生合成経路で生成・蓄積したカプロン酸とアルコール発酵によって生成したエタノールがエステル縮合することで生成され、その生合成には脂肪酸合成酵素 *FAS1* 及び *FAS2*、脂肪酸エステル化酵素 *EHT1* 及び *EEB1* が関与する。そこで、イオンビーム育種に用いた親株 (きょうかい 901 号)、イオンビーム育種により作出した優良酵母 (No.227 及び No.1333 株) 及びエチルメタンスルホン酸 (EMS) を変異原として作出した既存のカプロン酸エチル高生産酵母 (KAZE-2 号) の 4 株について解析を行った。各々の酵母よりゲノム DNA を抽出し、これを鋳型として、*EHT1*、*EEB1*、*FAS1* 及び *FAS2* 遺伝子領域を増幅し、ダイレクトシーケンス解析を行った。決定した各遺伝子領域の塩基配列は、親株と 3 種のカプロン酸エチル高生産酵母の塩基配列の比較を行い、変異部位を同定した。

EHT1、*EEB1* 及び *FAS1* 遺伝子領域の DNA 塩基配列解析の結果、親株と変異株では推定されるタンパク質のアミノ酸配列に相違が見られず、これらの遺伝子の変異はカプロン酸エチルの高生産に関与していないと考えられた。一方、3 種のカプロン酸エチル高生産清酒酵母において、*FAS2* 遺伝子の 3,748 番目の塩基 G が A に変異しており (KAZE-2 号及び No.227 株はヘテロ変異)、これにより *FAS2* タンパク質の 1,250 番目のアミノ酸が Gly から Ser に変化していると推定された (Fig. 1)。以上のことから、*FAS2* 遺伝子のたった 1 カ所の点突然変異によって生じた変異型 *FAS2* タンパク質の働きによってカプロン酸の生産量が向上し、カプロン酸エチルの高生産に繋がっていると考えら

れた。また、カプロン酸エチル生産量が最も多かった No.1333 株 (Table 1) では、この部位での *FAS2* 遺伝子の突然変異が対立遺伝子の両方に生じていた (Fig. 1)。このことから、選抜方法を工夫することで、優性形質のホモ化によるカプロン酸エチル生産の強化が可能と考えられた。*FAS2* 遺伝子の同部位での突然変異によるカプロン酸エチル生産能向上の事例は過去にも報告されている^{2, 3)}。

本研究によって、イオンビーム突然変異育種により作出した優良清酒酵母は、変異型 *FAS2* 遺伝子を持つことで有用形質としてカプロン酸エチルを高生産することを明らかにした。また、DNA マーカーによる優良変異体の早期選抜は、変異箇所の組合せを利用することで可能であると考えられた。

References

- 1) 増淵 隆 et al., 放射線と産業 128 (2010) 43.
- 2) R. Akada et al., J. Biosci. Bioeng. 92 (2001) 189.
- 3) 堤浩子, 生物工学 89 (2011) 717.

Table 1 Ethyl caproate in Sake by test brewing, 2010.

Strain No.	Ethyl caproate* (ppm)
KAZE-2	5.6
No.227	7.4
No.1333	11.0

*The production amount of ethyl caproate in Kyokai-901 (parental strain) was estimated at about 1.5 ppm under the same condition.

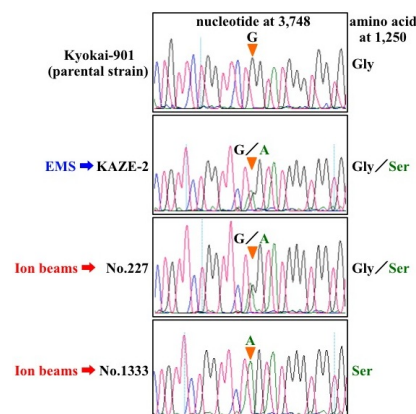


Fig. 1 Sequence analysis in *FAS2* gene.

3 - 50 Role of DNA Repair and Effect of Herbal Extract on LOH Induced by Ion Beam Radiations in *Saccharomyces cerevisiae*

T. Nunoshiba^{a)}, Y. Sakata^{a)}, A. Yamauchi^{a)}, K. Satoh^{b)}, T. Onodera^{b)} and I. Narumi^{b)*}

^{a)}International Christian University, ^{b)}Medical and Biotechnological Application Division, QuBS, JAEA, *Present affiliation: Faculty of Life Sciences, Toyo University

The LOH (loss of heterozygosity) induction by various ion beam radiations was investigated in diploid *Saccharomyces cerevisiae*. The ion beams $^{12}\text{C}^{5+}$, $^{12}\text{C}^{6+}$, $^4\text{He}^{2+}$ and $^{40}\text{Ar}^{13+}$ at the lowest dose (75, 75, 200 and 150 Gy, respectively), which had 30–50% lethality, induced LOH with 10-fold higher frequency. The LOH induction was predominantly (~90%) resulted from homologous recombination. Pol ζ may be involved in the induction of LOH by ion beam radiations, because in the strain lacking Rev3, only slight induction of LOH was observed. In addition, the effects of 14 herbal extracts were examined on ion-beam radiation induced LOH, and ethanol extract of *Eucalyptus regnans* possessed inhibitory effect on LOH induced by $^{12}\text{C}^{5+}$ ion-beam radiation with the manner dependent on doses of extract.

生物は常に DNA に損傷を被る環境に曝されており、生命維持や種の保存はいかなる仕組みで損傷 DNA を効率良く正確に修復するかに懸かっている。生命維持の根幹機能であるゲノム情報の維持機構を明らかにすることは、巧妙な生命現象を理解する上で非常に重要である。放射線による微生物ゲノムへの影響を我々は 2 倍体出芽酵母のヘテロ接合性喪失 (LOH: loss of heterozygosity) を指標として検討してきた。この菌株では LOH 誘発頻度とともに起こった LOH が 2 次的な突然変異によるのか、相同組換えに依存する遺伝子変換や交叉によるのか、または染色体の不均衡な分配に起因する染色体喪失によるのかも推定することができる。この系を用い、イオンビームによって出芽酵母のゲノムやゲノム維持機構への影響に関する基礎的知見を得ることとともに、DNA 修復や損傷乗り越え DNA 合成酵素の役割についても検討した結果、野生株の場合、非照射が概ね 2.5×10^{-4} であるのに対し、 $^{12}\text{C}^{5+}$ 及び $^{12}\text{C}^{6+}$ は照射最小線量の 75 Gy でともに 4.7×10^{-3} と 10 倍以上の頻度で LOH を誘発し、 $^4\text{He}^{2+}$ についても照射最小線量の 200 Gy で 4.6×10^{-3} と約 10 倍、 $^{40}\text{Ar}^{13+}$ でも最小線量の 150 Gy で 2.4×10^{-3} と 10 倍の頻度で LOH を誘発し、いずれの場合もそれ以上の線量による大きな LOH 誘発頻度の上昇は見られなかった。観察された LOH の 90% 程度は相同組換え依存の遺伝子変換や交叉によるもので、染色体の不均衡分配によるものはわずか 10% 程度であった。また DNA 脱塩基 (AP) 部位の DNA 修復に関わる AP endonuclease (Apn1) 欠損株、translesion DNA polymerase である Pol η (Rad30) 及び Pol ζ (Rev3) 欠損株についても検討したところ、Apn1 欠損株及び Rad30 欠損株についてはいずれの核種でも野生株と大きな差は見られなかったが、Rev3 欠損株では、非照射で 1.4×10^{-3} と他の株より LOH が高頻度であるものの、照射によっても 75 及び 150 Gy でそれぞれ 2–3 倍の LOH 誘発しか見られず、これらの LOH 誘発に translesion DNA polymerase Pol ζ の関与がうかがえ、特に核種による違いは見られなかった。現在、出芽酵母で確認されているもう一つの AP endonuclease Apn2 の欠損株や、Rev3 欠損株と他の DNA 修復欠損株との 2 重欠損株などを作製し、さらにイオンビームのゲノム情報維持への影響や LOH 誘発における DNA 修復や損傷乗り越え DNA 合成酵素の役割について検討を加える予定である。

次にイオンビームに対する防護効果を示す物質を検索する目的で、 $^{12}\text{C}^{5+}$ 照射による LOH 誘発への 14 種の植物エ

タノールエキスの効果を調べた。cellulose ester membrane filter 上で $^{12}\text{C}^{5+}$ を 300 Gy 照射した 10^7 細胞の酵母細胞を回収し、その回収した細胞 20 μL を 50 μL の植物エキスとともに YPD 培地 2 mL に加え、30 $^{\circ}\text{C}$ 、17 h 培養したのち、栄養培地と選択培地に撒いて LOH 誘発頻度を求めた。その結果、ツバキ種子、アズキ、カキドオシ、ユーカリで抑制が観察され、特にカキドオシ、ユーカリでは、無添加では 4.4×10^{-3} であった LOH が、カキドオシでは 1.8×10^{-4} に、ユーカリ添加では 4.3×10^{-4} にまで抑制した (Fig. 1A)。また UV 照射による LOH 誘発へのカキドオシ、ユーカリの効果を調べたところ、カキドオシのみに同様の抑制効果が見られた (Fig. 1B)。その機構を明らかにするためこのエキスの成分を調べたところ、溶媒に butylene glycol が含まれていることがわかり、butylene glycol の細胞増殖抑制のため見かけ上 LOH 抑制に見えたものと考えられる。一方、ユーカリは細胞増殖にはほぼ影響を与えず、また添加量に伴う効果の増大が確認できたことから (Fig. 1C)、このエキス成分が効果を示していると考えられる。しかしながら照射前の前処理による抑制効果は全く認められなかった。今後、この抑制効果の機構について、組換えや損傷乗り越え DNA 合成、DNA 修復への影響を視野に、検討したい。

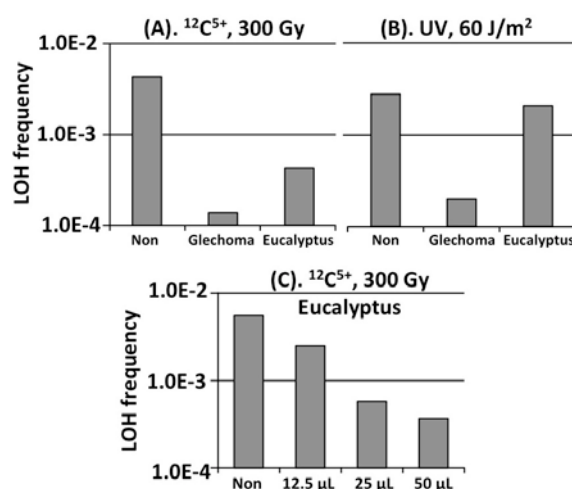


Fig. 1 Effect of herbal extract on LOH induction. A) LOH was induced by 300 Gy of $^{12}\text{C}^{5+}$ radiation. B) LOH was induced by 60 J/m² of UV. C) Dose dependent inhibitory of eucalyptus on $^{12}\text{C}^{5+}$ induced LOH.

4. Advanced Materials, Analysis and Novel Technology

4-01	Preparation of Gasochromic MoO ₃ Films by Reactive Sputtering Deposition	123
	S. Yamamoto, T. Hakoda and M. Yoshikawa	
4-02	1D Protein and Sugar Nanostructures by Single Particle Reactions	124
	S. Seki, K. Takano, M. Omichi, A. Asano, H. Marui and M. Sugimoto	
4-03	Formation of Ag Nanoparticles on Poly(vinylpyrrolidone) Nanowire Fabricated by SPNT	125
	S. Tsukuda, M. Sugimoto, A. Idesaki, M. Yoshikawa, S. Seki and S.-I. Tanaka	
4-04	Formation of Poly(vinylpyrrolidone) Nanofiber Containing Platinum Particles	126
	M. Sugimoto, R. Takahashi, S. Tsukuda, M. Yoshikawa, S. Seki and S. Tanaka	
4-05	Production of Nano-sized Platinum-particle Films Using Low Energy Electron Beams	127
	T. Hakoda, S. Yamamoto, H. Aritani and M. Yoshikawa	
4-06	Wetting Phenomena of Polycarbosilane Solution	128
	A. Takeyama, M. Sugimoto and M. Yoshikawa	
4-07	Investigation of Permeation Mechanism through Zeolite Membranes by Using Ion Beam Irradiation	129
	M. Nomura, R. Ono, D. Tamashiro and M. Sugimoto	
4-08	Control of Spatial Crosslinking Reaction in Polymer Film by Ion and Electron Beam Irradiation	130
	S. Tsukuda, M. Sugimoto, A. Idesaki, M. Yoshikawa, S. Seki and S.-I. Tanaka	
4-09	Effect of Irradiation Ions on Critical Fluence of Changing to Amorphous from Crystalline SiC Nanotubes	131
	T. Taguchi, S. Yamamoto and K. Yamaguchi	
4-10	Thermo-Optic Switch Consisting of Mach-Zehnder Polymer Waveguide Drawn Using Proton Beam Writing	132
	K. Miura, T. Satoh, Y. Ishii, M. Koka, H. Kiryu, Y. Ozawa, A. Kubota, T. Ohkubo, A. Yamazaki, W. Kada, A. Yokoyama, T. Kamiya and O. Hanaizumi	
4-11	Hydriding Property of Hydrogen Storage Alloy by Charged Particle Under Different Irradiation Environment	133
	H. Abe, K. Muraki, M. Kishimoto, H. Uchida and T. Ohshima	
4-12	Micropatterning on Fluoropolymer Surface Using Proton Beam Writing and Nitrogen Ion Beam Irradiation	134
	A. Kitamura (Ogawa), T. Sato, M. Koka, T. Kamiya and T. Kobayashi	
4-13	Fabrication of a Flexible Dielectrophoretic Device Using Proton Beam Writing	135
	G. Ayugase, D. Terajima, H. Nishikawa, T. Satoh, Y. Ishii and T. Kamiya	

4-14	Li-ion Battery Characterization by Ion Beam Analysis	136
	K. Mima, K. Fujita, Y. Kato, S. Nakai, H. Sawada, A. Yamazaki, C. Okuda, Y. Ukyo, Y. Uchimoto, Y. Orikasa, K. Yamamoto, T. Kamiya, R. Gonzalez and I. M. Perlado	
4-15	Atomistic Transformation Processes Induced by the Interaction of Implanted N-ions with Ti Thin Films	137
	Y. Kasukabe, H. Shimoda, S. Yamamoto and M. Yoshikawa	
4-16	Ion Beam Analysis of Quaternary Heusler Alloy $\text{Co}_2(\text{Mn}_{1-x}\text{Fe}_x)\text{Si}(111)$ Epitaxially Grown on Ge(111)	138
	Y. Maeda, K. Narumi, S. Sakai, K. Hamaya and M. Miyao	
4-17	Non-thermal Equilibrium Crystal Structure of FeRh Intermetallic Compound Irradiated with Energetic Heavy Ions	139
	A. Hashimoto, Y. Kaneno, T. Matsui, Y. Saitoh and A. Iwase	
4-18	Magnetic Patterning of FeRh Thin Films by Energetic Light Ion Microbeam Irradiation and Their XMCD-PEEM Observation	140
	T. Koide, T. Satoh, M. Koka, Y. Saitoh, T. Kamiya, T. Ohkouchi, M. Kotsugi, T. Kinoshita, T. Nakamura, A. Iwase and T. Matsui	
4-19	Transmission Properties of a 4-MeV C^+ Ion Beam Entering a Curved Insulating Channel	141
	K. Motohashi, Y. Saitoh, N. Miyawaki, Y. Matsuo and T. Kamiya	
4-20	Cathodoluminescence of He^+ -ion-implanted Feldspars	142
	H. Nishido, M. Kayama, S. Toyoda and K. Komuro	
4-21	Control of Photoluminescent Properties of Si-O-C Materials by Irradiation of Various Particle Beams	143
	M. Narisawa and M. Sugimoto	
4-22	Contribution of Aeolian Dust in Ichinomegata Estimated from Electron Spin Resonance Signal Intensity and Crystallinity of Quartz	144
	K. Nagashima and R. Tada	
4-23	Development of Spin-polarized Positron Beam and Its Application to Spintronics Study	145
	A. Kawasuso, M. Maekawa, Y. Fukaya, H. J. Zhang and H. Li	
4-24	Complementary Study of Vacancy Defects in Si Substrates by Using SPM and EBIC Method	146
	M. Maekawa and A. Kawasuso	
4-25	Positron Annihilation Lifetime Study of Cation Vacancies in Electroceramics	147
	M. Ryu and T. Suzuki	
4-26	Yield of Transient Species in NaBr Aqueous Solution Irradiated with Pulsed H^+ , C^{5+} and Ne^{8+} Ions	148
	K. Iwamatsu, M. Taguchi, Y. Sugo, S. Kurashima, S. Yamashita and Y. Katsumura	

4-27	Transient Absorption Spectra of Biphenyl-Dodecane Solution Measured by Microsecond Ion Pulse Radiolysis	149
	T. Kondoh, K. Iwamatsu, M. Taguchi, S. Kurashima, J. Yang, K. Kan, H. Shibata and Y. Yoshida	
4-28	Observation of Scintillation Behavior under Pulsed Ion Beam Irradiation	150
	M. Koshimizu, M. Taguchi, S. Kurashima and K. Asai	
4-29	Solvent Effect on Copolymerization of Maleimide with Styrene Induced by Ion Beam Irradiation	151
	S. Nakagawa, M. Taguchi and A. Kimura	
4-30	Measurements of Low Energy Neutron Spectra Using the TOF Method in Quasi-monoenergetic Neutron Fields at TIARA	152
	T. Matsumoto, A. Masuda, H. Harano, Y. Tanimura, M. Yoshizawa, H. Seito and K. Mizuhashi	
4-31	Measurement of Lineal Energy Distributions for Energetic Ion Beams Using a Wall-less Tissue Equivalent Proportional Counter	153
	S. Tsuda, T. Sato and T. Ogawa	
4-32	Fabrication of UV Curable Resin Based Microscopic Devices Using External Scanning Proton Microbeam	154
	T. Sakai, R. Yasuda, H. Iikura, T. Nojima, M. Matsubayashi, M. Koka, T. Satoh, T. Ohkubo and Y. Ishii	
4-33	Preliminary Study on 3D Proton Lithography Using 300 kV Compact Focused Gaseous Ion Beam System	155
	T. Ohkubo, Y. Ishii, Y. Miyake and T. Kamiya	
4-34	Research and Development of an Ultra-high-energy Neutrino Detector Using Radar Reflection in Rock Salt and Ice	156
	M. Chiba, T. Kamijo, T. Tanikawa, F. Yabuki, H. Yano, M. Utsumi and M. Fujii	
4-35	Effect of Low Irradiation Temperature on the Gamma-ray Response of Clear Polymethylmethacrylate Dosimeter, Radix W	157
	H. Seito, Y. Nagao, T. Ichikawa, M. Iwasaki, Y. Sato, T. Agematsu, H. Kaneko, H. Watanabe and T. Kojima	
4-36	Analysis of Phase Bunching in AVF Cyclotron	158
	N. Miyawaki, S. Kurashima, H. Kashiwagi, S. Okumura, K. Yoshida, Y. Yuri, T. Yuyama, T. Ishizaka, I. Ishibori and T. Nara	
4-37	Status Report on Technical Developments of Electrostatic Accelerators	159
	K. Yamada, Y. Saitoh, Y. Ishii, S. Matoba, A. Chiba, A. Yokoyama, A. Usui, T. Satoh, T. Ohkubo and S. Uno	
4-38	Fast Single-ion Hit System for Heavy-ion Microbeam at TIARA Cyclotron (VI)	160
	W. Yokota, T. Satoh, S. Okumura, S. Kurashima, N. Miyawaki, H. Kashiwagi, K. Yoshida, M. Koka, A. Yokoyama, W. Kada and T. Kamiya	

4-39	Development of a Microwave Ion Source for Industrial Applications	161
	N. Takahashi, H. Murata, H. Mitsubori, T. Soga, Y. Aoki, J. Sakuraba, T. Kato, N. Sakudo, K. Yamada and Y. Saitoh	
4-40	Beam Intensity Distribution Measurement Using a Fluorescent Screen for Formation of a Uniform Ion Beam	162
	T. Yuyama, Y. Yuri, T. Ishizaka, I. Ishibori and S. Okumura	
4-41	Response of Gafchromic Films to Energetic Ion Beams	163
	Y. Yuri, T. Ishizaka, T. Yuyama, I. Ishibori and S. Okumura	
4-42	Development of Scintillator for Detention of Single-ion	164
	A. Yokoyama, W. Kada, T. Satoh, M. Koka, S. Yamamoto, T. Kamiya and W. Yokota	
4-43	Focused Microbeam Irradiation Effects in Transmission CVD Diamond Film Detectors	165
	T. Kamiya, W. Kada, N. Iwamoto, S. Onoda, V. Grilj, N. Skukan, T. Makino, M. Koka, T. Satoh, T. Ohshima and M. Jakšić	
4-44	Development of a New Ion Microbeam Analysis Technique: Ion Luminescence Microscopic Imaging and Spectroscopy	166
	W. Kada, A. Yokoyama, M. Koka, T. Satoh and T. Kamiya	
4-45	Coulomb Explosion Process in Collision of a Swift Cluster Ion with Gas Target	167
	A. Chiba, K. Narumi, K. Yamada, S. Matoba and Y. Saitoh	
4-46	Study of Ion Induced Luminescence from Sapphire Irradiated with Swift Cluster Ion Beams	168
	H. Shibata, Y. Saitoh, A. Chiba, K. Yamada, K. Narumi and M. Taguchi	
4-47	Electronic Stopping Power of Al and Si for Swift Carbon Cluster Ions with Average Charge Reduction	169
	T. Kaneko, K. Ihara, F. Miyahara, Y. Saitoh, A. Chiba and K. Narumi	
4-48	Comparison of Positive Secondary Ion Emission Yields for PMMA between Low Energy Bi and C ₆₀ Ion Impacts	170
	K. Hirata, Y. Saitoh, A. Chiba, K. Yamada, S. Matoba and T. Kamiya	
4-49	Vicinage Effect on Secondary-electron Yield from Carbon Foils Bombarded with 62.5-250-keV/u H ₂ ⁺ and C ₂ ⁺ Ions	171
	K. Narumi, A. Chiba, K. Yamada, S. Matoba, Y. Saitoh	
4-50	Production of Fast C ₆₀ Microbeam Using the Capillary-beam Focusing Method	172
	H. Tsuchida, T. Majima, S. Tomita, K. Sasa, K. Narumi, Y. Saitoh, A. Chiba, K. Yamada, K. Hirata, H. Shibata and A. Itoh	
4-51	Ion Tracks in Amorphous Si ₃ N ₄ Films Produced by Sub MeV C ₆₀ Ion	173
	K. Nakajima, Y. Morita, M. Suzuki, K. Narumi, Y. Saitoh, K. Hojou, M. Tsujimoto, S. Isoda and K. Kimura	

4 - 01

Preparation of Gasochromic MoO_3 Films by Reactive Sputtering Deposition

S. Yamamoto, T. Hakoda and M. Yoshikawa

Environment and Industrial Materials Research Division, QuBS, JAEA

Liquid organic-hydrides such as cyclohexane, decalin are promising carriers of hydrogen gas with dehydrogenation processes for hydrogen fuel cells. However, organic-hydrides are highly flammable and volatile. The monitoring of leakage of hydrogen and organic-hydride gases at storage or usage sites is strongly required for safe operation. In explosive atmospheres, optical gas detection with gasochromic materials such as tungsten trioxide (WO_3)¹⁾ and molybdenum trioxide (MoO_3) is more appropriate because they have not any ignition sources such as electrical circuits. Nevertheless, the correlation between crystal structure and gasochromic properties in MoO_3 is not well understood in comparison with that of WO_3 .

In the present study, we prepared MoO_3 films using a reactive sputtering deposition on SiO_2 substrates at different substrate temperatures and annealing temperatures to clarify preparation conditions and crystal structure for optical detection of hydrogen and organic-hydride. The reactive sputtering deposition was performed by a magnetron sputtering source with Mo metal target in an argon and oxygen mixture. The substrates were maintained at temperatures of RT-400 °C during the deposition. Annealing of the deposited films was carried out at temperature up to 400 °C for 1h in air. To evaluate the gasochromic coloration of MoO_3 films, the films were coated with a Pt layer by the sputtering method. And then, optical transmittance spectra (wavelength: 400-1000 nm) were measured using a spectrometer while nitrogen gas including 1% hydrogen (1% H_2/N_2) and nitrogen gas including 5% cyclohexane, respectively. The films were characterized using scanning electron microscopy (SEM), X-ray diffraction (XRD) and Rutherford backscattering

spectroscopy (RBS). The RBS analysis using a 3 MV single-stage-accelerator at JAEA Takasaki was employed to determine the composition and thickness of films.

The results of the optical transmittance spectra measurements of the films exposing to hydrogen, significant optical transmittance changes were observed in MoO_3 films deposited at 300 °C and subsequent annealed at 250 °C. Figure 1 shows a typical optical transmittance change ratio of Pt(5 nm)/ MoO_3 (180 nm)/ SiO_2 substrate at 130 °C by 5% cyclohexane/ N_2 with a gas flow rate of 100 sccm (standard cc/min). The change in optical transmittance of the Pt/ MoO_3 film decreases gradually at a wavelength of around 900 nm with an increasing exposure time. Figure 2 shows the SEM images of the Pt/ MoO_3 films, MoO_3 films were deposited at 300 °C and different annealing temperature (a) 250 °C, (b) 400 °C, respectively. Flake grain structure which is unsuitable for optical measurements was observed in MoO_3 films annealed at higher than 350 °C. The results of XRD indicated the MoO_3 film deposited at 300 °C and annealed at 250 °C has (011)-oriented monoclinic structure and the film annealed at 400 °C has (010)-oriented orthorhombic structure. It seems that crystal structure of MoO_3 may contribute to formation of flake structure of the films. In summary, we found that (011)-oriented monoclinic MoO_3 films prepared with deposition temperature of 300 °C and annealing temperature at 250 °C have potential for optical detection of hydrogen and organic-hydrides.

Reference

- 1) S. Yamamoto et al., JAEA Takasaki Annu. Rep. 2011 (2013) 117.

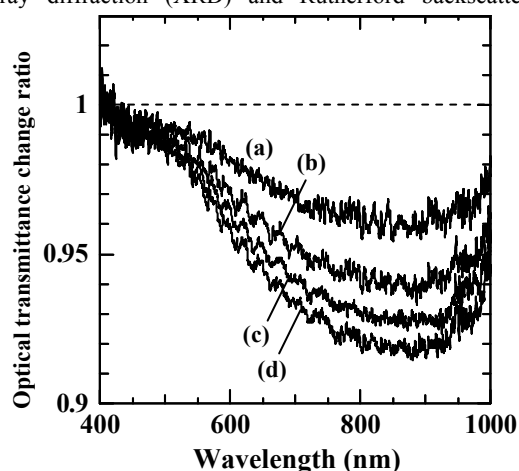


Fig. 1 Change ratio of optical transmittance induced by 5% cyclohexane/ N_2 exposure. (a)5 min, (b)10 min, (c)15 min, (d)20 min.

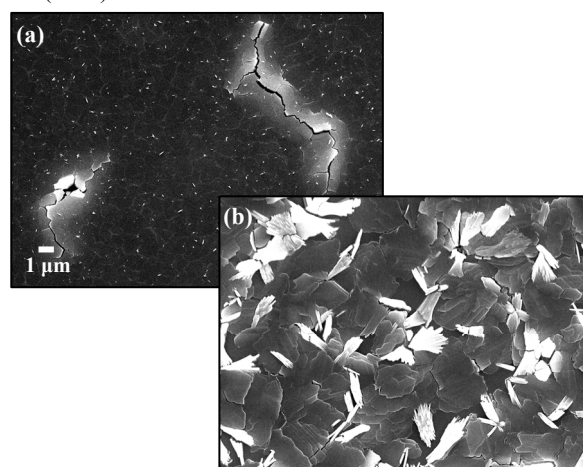


Fig. 2 SEM images of the Pt/ MoO_3 films, MoO_3 films were deposited at 300 °C and annealing temperatures (a) 250 °C, (b) 400 °C, respectively.

4 - 02

1D Protein and Sugar Nanostructures by
Single Particle ReactionsS. Seki^{a)}, K. Takano^{a)}, M. Omichi^{a)}, A. Asano^{b)}, H. Marui^{a)} and M. Sugimoto^{b)}^{a)}Department of Applied Chemistry, Graduate School of Engineering, Osaka University,^{b)}Environment and Industrial Materials Research Division, QuBS, JAEA

Ion-beam irradiation of films based on polymeric materials has been shown to cause cross-linking reactions, leading to the formation of a polymer gel containing 1D-nanostructures, known as nanowire. A single ion particle can fabricate one nanostructure along its trajectory; this methodology is referred to as the single particle nano-fabrication technique (SPNT)¹⁾. Polymeric materials with an alkyne moiety have the ability to easily introduce functionality by the formation of a strong covalent linkage. The copper(I)-catalyzed Huisgen 1,3-dipolar cycloaddition of alkyne and azide, called the “Click reaction”²⁾, has recently been revealed to be an important modification technique because this reaction can result in high yields under mild and with ease of operation. Herein, we report a fabrication technique with the concept of “a nanowire produced by a particle”, released from these limitations, using “Clickable” nanowires to construct highly controlled biological macromolecular materials.

Poly(styrene-*co*-4-ethynylstyrene) (PSES) with an alkyne “Click” function was synthesized by a nitroxide-mediated controlled/living radical polymerization. PSES ($M_n = 15,200 \text{ g mol}^{-1}$, PDI=1.31) and polystyrene (PS) ($M_n = 13,200 \text{ g mol}^{-1}$, PDI=1.18) nanowires were fabricated using the SPNT with an irradiation of 450 MeV $^{129}\text{Xe}^{23+}$ particles at $3.0 \times 10^8 \text{ ions cm}^{-1}$. PS was used for comparison. The cross-sectional radius of PSES and PS nanowires was estimated to be 13.2 nm and 4.7 nm, respectively, measured by an atomic force microscope (AFM). The nanowire size was revealed to have good correlation with the spatial distribution of deposited energy in an ion track by a penetrating ion particle, the parameters of the target materials, and the efficiency of cross-linking reactions. Semi-empirical modeling of the PSES nanowire size gives estimates of the cross-linking efficiency of $G_{\text{PSES}}(x)$ as > 3 (100 eV^{-1}), which is a higher value compared to PS with $G_{\text{PS}}(x) > 0.4$ (100 eV^{-1}).

In order to fabricate the 1D-protein nanowires, avidin can be introduced to the surface of PSES nanowires by using avidin-biotin affinity after the biotinylation reaction (Fig. 1). Figures 1 (ii) and (iii) show the nanowires before and after modification of avidin, respectively. The radii of the nanowires were evaluated to be 16.4 nm and 27.1 nm respectively from the cross-sectional profiles in Fig. 1 (iv). This value difference in the radii nearly corresponds to the size of avidin³⁾. When the biotinylation process was not carried out, the radius of the nanowires hardly changed (r was 17.1 nm). These results indicate that a mono-layer of avidin is formed on the surface of the nanowire by the

avidin-biotin interaction, as shown in Fig. 1 (v)⁴⁾. The PSES nanowires can produce not only 1D-protein nanowires, but also 2D-protein sheets by modifying the assembly structure of the nanowires. This is the first report of bio-macromolecular materials arranging a protein onto highly controlled structures composed of 1D-nanowires.

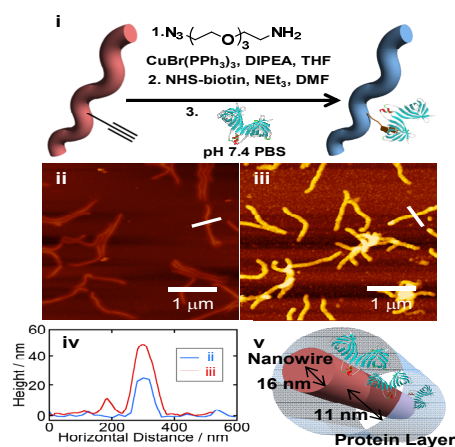


Fig. 1 (i) Scheme for fabrication of the protein nanowires by using chemical modification and avidin-biotin system. (ii) AFM micrograph of nanowires based on a PSES film prepared by exposure to 490 MeV $^{192}\text{Os}^{30+}$ particles at $1.0 \times 10^8 \text{ ions cm}^{-2}$. (iii) AFM micrograph of modified nanowires. The surfaces were modified with avidin. (iv) Cross-sectional profiles of nanowires based on PSES before and after modification. (v) A visualization of a bio-macromolecular nanowire covered with avidin.

The alkyne moieties have two important roles: improving the cross-linking efficiency for radiation and introducing functional materials with Click reactions. Fabrication of 1D-nanowires and highly controlled 2D-arrays of bio-macromolecules can be carried out by simple surface modification and assembly of PSES nanowires. SPNT with the “top-down” technique was thus used to fabricate the 1D-nanostructure, which maintained the function of the base material. The surface of the nanowires can acquire any functionality using chemical and biological modifications. This represents a step in fusing “top-down” and “bottom-up” approaches, providing the foundation for the development of a new strategy for the architectures of nanosized functional materials via radiation chemistry.

References

- 1) S. Seki et al., Adv. Mater. 13 (2001) 1663.
- 2) H. C. Kolb et al., Angew. Chem. Int. Ed. 40 (2001) 2004.
- 3) L. Pugliese et al., J. Mol. Biol. 231 (1993) 698.
- 4) A. Asano, et al., J. Phys. Chem. C 116 (2012) 17274.

4 - 03

Formation of Ag Nanoparticles on Poly(vinylpyrrolidone) Nanowire Fabricated by SPNT

S. Tsukuda^{a)}, M. Sugimoto^{c)}, A. Idesaki^{c)}, M. Yoshikawa^{c)}, S. Seki^{b)} and S.-I. Tanaka^{a)}

^{a)}Institute of Multidisciplinary Research for Advanced Materials, Tohoku University,

^{b)}Division of Applied Chemistry, Graduate School of Engineering, Osaka University,

^{c)}Environment and Industrial Materials Research Division, QuBS, JAEA

Heavy-ion beams are used for high-density energy deposition in polymeric materials. Ion irradiation at low fluence without overlapping between ion tracks produces single ion events in the target materials. Single ion bombardment can release active intermediates at high density within a limited area along the single ion track. In crosslinking-type polymers, the crosslinking reactions along the ion track result in the formation of a cross-linked nanogel (nanowire) in the thin films. The non-crosslinked area can be removed by development procedure, utilizing the change in solubility due to the gelation of polymer. This technique (called as Single particle nanofabrication technique (SPNT)) is useful to fabricate one dimensional polymer nanowires¹⁻³⁾. In this paper, we demonstrated that silver nanoparticles were formed on nanowires based on poly(vinylpyrrolidone) fabricated by SPNT through the reduction of AgNO_3 . The number and size of silver nanoparticles were also controlled by reduction conditions.

PVP films were prepared on Si substrates by spin coating technique. The thin films were exposed to beams of 490 MeV $^{192}\text{Os}^{30+}$ at the TIARA cyclotron accelerator facility of the Japan Atomic Energy Agency (JAEA). After irradiation, a non-cross-linked polymer was removed by development using IPA. PVP nanowires were successfully fabricated and isolated on Si substrate by irradiation and wet-development procedures. The substrates coated with a layer of PVP nanowires were immersed into a solution containing AgNO_3 and capping reagents. The reduction of AgNO_3 was carried out at 80 °C for 1-60 minutes, respectively. After each immersing time, the samples were rinsed with pure water to stop the reduction reaction and dried. Observation was subsequently carried out using SEM.

The Ag nanoparticles were formed on PVP nanowires by the reduction of AgNO_3 as shown in Fig. 1. The number of Ag nanoparticles increased depending on reaction time from 10 to 60 minutes. The sizes of Ag nanoparticles were also changed by reduction time. The sizes were measured using TEM and plotted in Fig. 2. The average sizes were also increasing in immersing times in AgNO_3 solution.

Therefore, it is suggested that the surface modification of PVP nanowires by the Ag nanoparticles can be controlled by changing the immersing time.

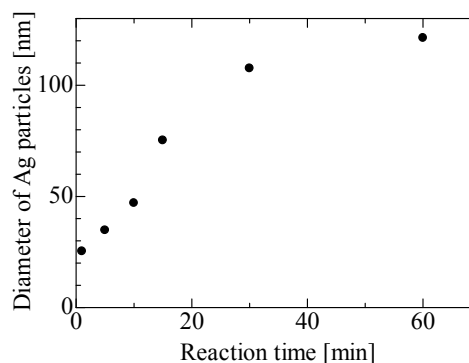


Fig. 2 The diameter of Ag nano-particles formed by immersing the samples in a solution with AgNO_3 at 80 °C for 1-60 minutes. The sizes were measured by TEM observation.

References

- 1) S. Seki et. al., Adv. Mater. 13 (2001) 1663-65.
- 2) S. Tsukuda, et al., Appl. Phys. Lett. 87 (2005) 233119-1-3.
- 3) S. Tsukuda, et al., J. Photopolym. Sci. Technol. 22 (2009) 245-48.

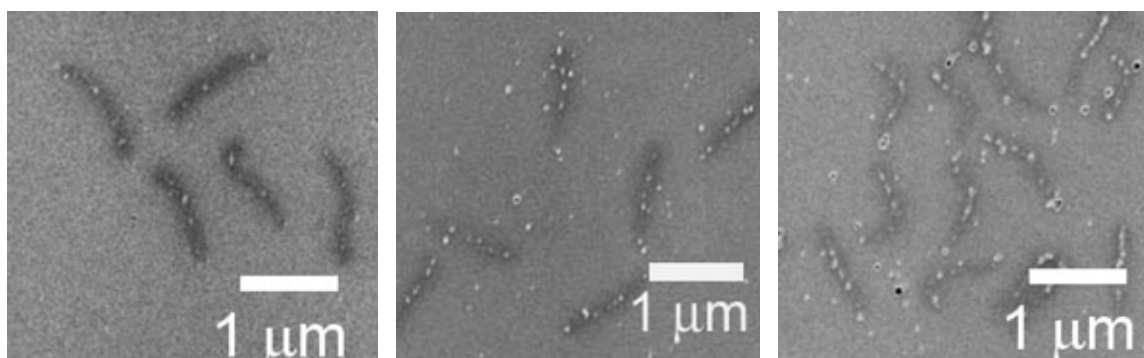


Fig. 1 SEM images of Ag nanoparticles on PVP nanowires. The PVP nanowires were prepared by SPNT on Si substrates. The formation of Ag nanoparticles was carried out by immersing the samples in a solution with AgNO_3 at 80 °C for (a) 10, (b) 30, and (c) 60 minutes.

4 - 04

Formation of Poly(vinylpyrrolidone) Nanofiber Containing Platinum Particles

M. Sugimoto^{a)}, R. Takahashi^{b)}, S. Tsukuda^{b)}, M. Yoshikawa^{a)}, S. Seki^{c)} and S. Tanaka^{b)}

^{a)}Environment and Industrial Materials Research Division, QuBS, JAEA,

^{b)}Institute of Multidisciplinary Research for Advanced Materials, Tohoku University,

^{c)}Department of Applied Chemistry, Osaka University

Ion beams are used for high-density energy deposition in polymer materials. Single ion bombardment can release active intermediates at high density within a limited area along the single ion track. In crosslinking-type polymers, the crosslinking reactions along the ion track result in the formation of a cross-linked part in the thin films. Developing irradiated samples using an organic solvent to remove a non-cross-linked polymer affords isolated nanofiber with controlled size and number density^{1, 2)}. This direct fabrication technique of polymer nanofiber is called single particle nanofabrication technique (SPNT). Based on the concept of single-track gelation, this study presents formation of nanofiber based on poly(vinylpyrrolidone) (PVP) containing Platinum (Pt) nanoparticles and we also report their radii dependence on hexachloroplatinic(IV) acid (H₂PtCl₆) concentration.

Poly(vinylpyrrolidone) was dissolved in 2-propanol at 5 mass%, then H₂PtCl₆ was also dissolved at 1.0-10 mass% as against PVP. These solutions were spin coated on a Si substrate. The thin film of PVP was subsequently placed in a vacuum chamber and irradiated to 490 MeV ¹⁹²Os³⁰⁺ beams at ion fluence of $1.0 \times 10^7 \sim 1.0 \times 10^9$ ions/cm². The irradiated films were treated using 2-propanol for 60 sec. and the insoluble irradiated part of the film was developed as nanofibers. The sizes and shapes of the nanofibers were observed using Scanning Probe Microscopy (SPM : Seiko Instruments Inc. SPA-400) using dynamic force microscope method. The size of cross-section of nanofiber was defined as an average radius of cross-sectional measurements.

The nanofibers were successfully formed on the Si substrate by irradiation to PVP thin films, and then Pt nanoparticles were found in these nanofibers by TEM observation. Figure 1 shows SPM micrographs of the

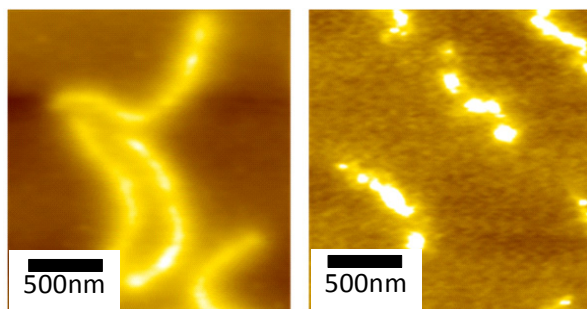


Fig. 1 SPM micrographs of PVP nanofiber containing Pt nanoparticles. Each concentration of H₂PtCl₆ in PVP thin films is (a):1.0 mass% (b):7.5 mass%, respectively.

nanofibers synthesized from PVP with the concentration of 1.0 and 7.5 mass% of H₂PtCl₆. In the case of 7.5 mass% of H₂PtCl₆, the shape of the nanofiber was discontinuous, additionally in the case of 10 mass% of H₂PtCl₆, nanofibers were not observed. Figure 2 shows dependence of the radii of PVP nanofibers containing Pt nanoparticles on the concentration of H₂PtCl₆. The radii of nanofibers decrease with an increase in the H₂PtCl₆ concentration. Furthermore, it was observed a tendency to decrease of the length of the nanofibers with increasing in the H₂PtCl₆ concentration, although the nanofiber should become the same length synthesized from the thin film with the same thickness. These results mean the decrease in the cross-linking efficiency of PVP, because Pt nanoparticles prevent the cross-linking reactions between each PVP polymer chains as obstacles. However we found that the radius of nanofiber increase by additional crosslinking using gamma or electron beam irradiation subsequently to ion beam irradiation³⁾, therefore cutting of the nanofibers containing high amount of the nanoparticles may be able to suppress by applying this technique.

This synthesis method will enable to fabricate the nanofiber with supreme large specific surface containing catalyst elements; therefore it has been expected as high efficiency catalyst and adsorption materials.

References

- 1) S. Seki et al., Adv. Mater. 13 (2001) 1663-65.
- 2) M. Sugimoto et al., Ceramic Trans. 213 (2010) 105-11.
- 3) S. Tsukuda et al., J. Photopolym. Sci. Technol. 23 (2010) 231-34.

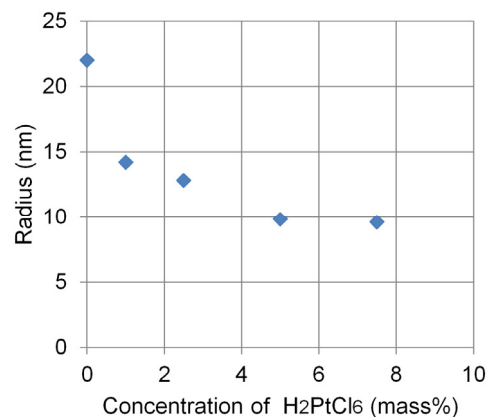


Fig. 2 Dependence of the radii of PVP nanofiber containing Pt nanoparticles on H₂PtCl₆ concentration.

4 - 05 Production of Nano-sized Platinum-particle Films Using Low Energy Electron Beams

T. Hakoda^{a)}, S. Yamamoto^{a)}, H. Aritani^{b)} and M. Yoshikawa^{a)}

^{a)}Environment and Industrial Materials Research Division, QuBS, JAEA,

^{b)}Department of Applied Chemistry, Saitama Institute of Technology

Reduction of noble metal ions and subsequent production of noble metal particles in a solution has been performed as a radiation-induced precipitation (RIP) method using high energy ionizing radiation such as a few MeV electron beams (EBs) and ^{60}Co γ -rays. The size of produced particles is reported to be smaller as increasing the dose rate of ionizing radiation^{1,2)}. Electron beams with energies below 300 keV, low energy EBs, have been frequently used for surface modification because they have shorter penetration range and can irradiate at higher dose rates. Application of such low energy EBs to the RIP method has a possibility of producing film matter that consists of noble metal particles at the surface of the solution. In the present study, this possibility was examined using a few ten keV EBs for PtCl_6^{2-} ion solutions.

A solution containing 1 mmol/L PtCl_6^{2-} ion and 0.5-20 v% ethanol, which plays OH-radical scavengers and Pt-particle stabilizing surfactants, was prepared as a sample solution. The sample solution (10 mL) was irradiated with 55-keV and 0.17-mA EBs for 20 s with introducing nitrogen gas between an irradiation window and the sample solution. The absorbed dose of irradiated layer of the sample solution is estimated to be 770 kGy from deposited EB energy and an electron penetration range of 20 μm . The morphology of products on the solution was observed by Transmission Electron Microscope (TEM) analysis after fixation on glassy carbon (GC) substrates. The Pt yield in the products was measured by Rutherford Backscattering Spectrometry (RBS).

Black-colored matter was produced at the surface of the sample solution after EB irradiation at 0.5-20 v% ethanol concentrations. The films were attached to the surface of

GC substrates and rinsed with water to remove PtCl_6^{2-} and PtCl_4^{2-} ions. The RBS spectrum is shown in Fig. 1 for the films/GC substrates under 0.5 v% ethanol condition. This spectrum suggests that the films exclusively contained Pt and hardly contained O-containing chemicals produced from H_2O and ethanol.

The peak area corresponding to Pt atoms was examined for the films prepared from different ethanol concentrations. The peak area lineally decreased with ethanol concentration up to 10 v% and seemed to reach a constant value at 10-20 v%. Lower concentrations of ethanol such as 0.5 v% accelerate the formation of Pt films on the sample solution.

The Pt-films produced at a 0.5 v% ethanol concentration were observed by TEM after loading to the surface of TEM collodion membranes. The TEM image (Fig. 2) showed that the films had network structure having connected Pt particles with sizes of 2-5 nm. This result suggests that the Pt particles with sizes of 2-5 nm are produced through the reduction of PtCl_6^{2-} ions at the surface of the solution. These Pt particles coagulated each other to form such structure.

The obtained results suggest that low energy EBs can be applied to the production of nano-sized noble metal particle films as new application of RIP method.

A part of this study was supported by an MEXT Grant-in-Aid for Scientific Research (C). (No. 23560936).

References

- 1) S. Seino et al., J. Nanopart. Res. 10 (2008) 1071.
- 2) T. Hakoda et al, JAEA Takasaki Annu. Rep. 2011 (2013) 121.

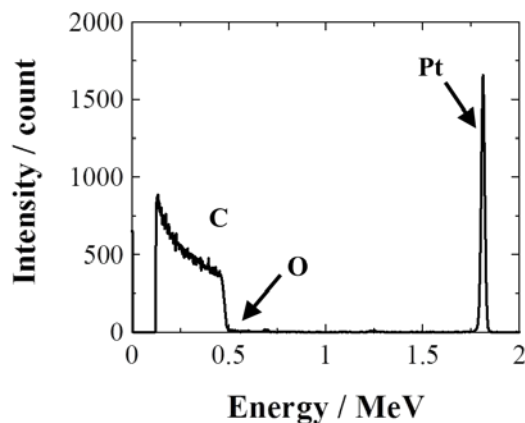


Fig. 1 RBS spectra for film matter produced at the surface of EB-irradiated water containing 1 mmol/L Pt and 0.5 v% ethanol.

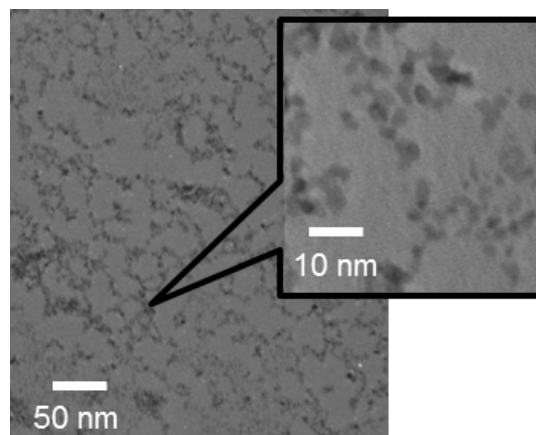


Fig. 2 A TEM image of Pt films on the surface of EB irradiated water containing 1 mmol/L Pt and 0.5 v% ethanol.

4 - 06

Wetting Phenomena of Polycarbosilane Solution

A. Takeyama, M. Sugimoto and M. Yoshikawa

Environment and Industrial Materials Research Division, QuBS, JAEA

Chemically and thermally stable polymer-derived silicon carbide (SiC) membranes have been received attention for use of hydrogen separation¹⁾. The membrane is a thin SiC film derived from polymer precursor, polycarbosilane (PCS) film. We previously prepared the SiC film for the hydrogen separation by employing our developed method to form defect-free PCS film on porous support²⁾. Since the PCS film was formed on porous alumina (Al_2O_3) support using dilute PCS solution, it is necessary for improvement of the coating method to reveal wetting phenomena of PCS solution. In order to evaluate wetting phenomena of PCS solution, firstly, we measured surface tension of PCS solution by maximum bubble pressure method³⁾, secondary, contact angles between PCS solution or cyclohexane and Al_2O_3 substrates were measured.

Figure 1 shows scheme of the bubble pressure method. The end of the capillary tube was located at the depth h from the surface of the solution. Bubble was generated on the tip of capillary tube immersed in the PCS solution by pressurized nitrogen. As pressure inside the tube was raised, bubble grows and finally detached from the tube. When the bubble was detached, maximum bubble pressure P was followed the equation below;

$$P = 2\gamma/r + \rho gh$$

where, r : radius of the capillary tube, ρ : density, γ : surface tension of the solution and g : gravity. Measurement was carried out at room temperature, 299 K with monitoring bubble pressure by a capacitance manometer gauge.

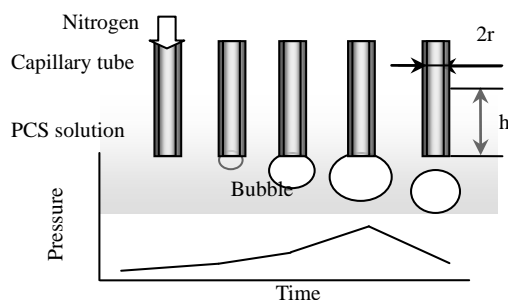


Fig. 1 Dependence of bubble pressure on time.

Table 1 Surface tensions of PCS solutions and cyclohexane.

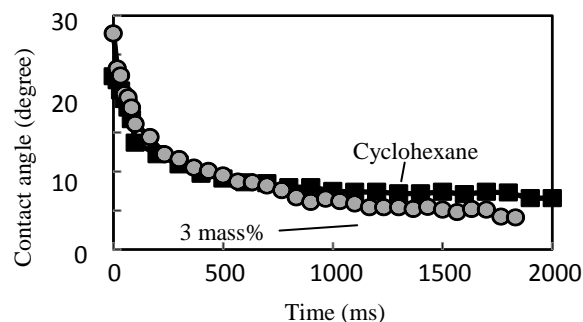
Solution	Surface tension (mN/m)
Cyclohexane	24.0
3 mass%	20.8
5 mass%	22.3
10 mass%	25.3
12 mass%	26.7

Table 1 shows the values of surface tensions measured for PCS solutions, which were usually used for coating of PCS film, and cyclohexane as a solvent. Surface tension of cyclohexane of 24.0 mN/m is quite comparable with literature data, 24.20 mN/m at 297.82 K⁴⁾. Though our data was slightly smaller than the literature one, deviation was within 1%. While, surface tensions of PCS solutions were increased from 20.8 to 26.7 mN/m with increasing the concentration of PCS solution. As is known that liquid with low surface tension wets the surface of a material well, accordingly, it is expected 3 mass% PCS solution wets Al_2O_3 better than 10 mass% solution or cyclohexane.

Figure 2 shows dynamic contact angles between either 3 mass% PCS solution or cyclohexane and Al_2O_3 substrate. At the origin of the plot, each liquid is dispensed on Al_2O_3 (single crystalline sapphire, m -plane) substrate. Lower contact angle for 3 mass% solution observed at more than 1,500 ms was explained by lower surface tension of 3 mass% solution than that of cyclohexane. On the basis of this experimental result, surface tension data and Young's equation, we could estimate the contact angle of 10 mass% solution more or less 10 degrees. This estimation enabled us to avoid measuring contact angle for 10 mass% solution with extreme difficulty, because the solution easily formed a lump of PCS at the tip of the dispenser and scarcely dispensed. Dynamic contact angles measured for other sapphire substrates with either crystalline plane of a - or r -plane were almost the same as that measured for m -plane. In conclusion, it is confirmed that PCS-cyclohexane solutions whose concentration up to 10 mass% wet Al_2O_3 well.

References

- 1) R.A. Wach et al., Mat. Sci. Eng. B 140 (2007) 81.
- 2) A. Takeyama et al., Mater. Trans. 52 (2011) 1276.
- 3) A. W. Adamson et al., Phys. Chem. Surf. (2007).
- 4) H. Kahl et al., J. Chem. Eng. Data 48 (2003) 580.

Fig. 2 Contact angles between either 3 mass% PCS solution or cyclohexane and Al_2O_3 .

4 - 07

Investigation of Permeation Mechanism through Zeolite Membranes by Using Ion Beam Irradiation

M. Nomura^{a)}, R. Ono^{a)}, D. Tamashiro^{a)} and M. Sugimoto^{b)}^{a)} Department of Applied Chemistry, Shibaura Institute of Technology,^{b)} Environment and Industrial Materials Research Division, QuBS, JAEA

Hydrophilic zeolite membranes such as a mordenite membrane have been developed for water permselective membranes from alcohol aqueous solution¹⁾. Usually, a zeolite membrane is a polycrystalline structure. There are two kinds of pathways through zeolite membranes. One is intracrystalline pathways that molecules pass through the inside of zeolite pores. Other is intercrystalline pathways that molecules pass through the outside of zeolite crystals. In this study, effects of ion beam irradiation on hydrophilic mordenite zeolite membranes were investigated as one of the physical post-treatment to improve the water flux through the membrane. The ion beam trucks through the mordenite membranes must be the intercrystalline pathways.

Mordenite zeolite membranes were synthesized with mordenite seed crystals on porous α -alumina disk substrates (ϕ : 13 mm, 150 nm pore size: Noritake Co.) based on the recipe described in the former literature¹⁾. Ion beam irradiation was carried out using $^{192}\text{Os}^{30+}$ ion at 490 MeV by using a cyclotron. The irradiation fluence was at 1.0×10^{10} ions cm^{-2} (membrane A) or 3.0×10^{10} ions cm^{-2} (membrane B), respectively. The permeation properties through the obtained membranes were evaluated by isopropyl alcohol (IPA)/water pervaporation (PV). IPA/water PV was employed at 80 wt% of IPA at 75 °C.

Figure 1 shows the transmission electron microscope (TEM) images of the surface and cross-sectional views of the membrane B. White circles about ϕ 7.7 nm of the diameter were found from the surface image shown in Fig. 1 (a). These circles were the ion tracks damaged by the Os irradiation. The density of the white circles was about 2.3×10^{10} cm^{-2} from the low magnification image. This fluence was the same order to the irradiation fluence (3.0×10^{10} ions cm^{-2}) measured by using a Faraday cup. The straight line was found from the cross-sectional view shown in Fig. 1 (b). The width of the line was approximately 8 nm, which is almost the same as the circle size in the surface view.

Figure 2 shows the IPA/water PV results through the membrane A and the membrane B. Initially, water selectivity was 7600 with $0.069 \text{ kg m}^{-2} \text{ h}^{-1}$ of the flux through membrane A and 2700 with $0.088 \text{ kg m}^{-2} \text{ h}^{-1}$ for membrane B. There was no significant permselectivity difference found after irradiation at 1.0×10^{10} ions cm^{-2} . Total flux improved by approximately 84 % by keeping the high water selectivity above 1,200 through membrane B. The flux of IPA component increased from $3.3 \times 10^{-5} \text{ kg m}^{-2} \text{ h}^{-1}$ to $1.3 \times 10^{-4} \text{ kg m}^{-2} \text{ h}^{-1}$ by the irradiation. The flux of the water component changed for $0.074 \text{ kg m}^{-2} \text{ h}^{-1}$ by the irradiation. If all flux difference was due to the

new pathways made by the Os ion tracks, the water permselectivity through the new pathways was calculated as 730. This shows that the pathways outside the mordenite crystals were water permselective.

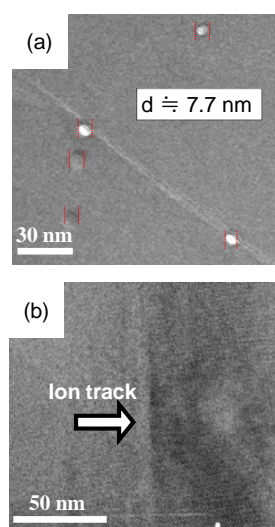


Fig. 1 TEM images of the surface view (a) and the cross-sectional view (b) for the membrane B (irradiation fluence: 3.0×10^{10} ions cm^{-2}).

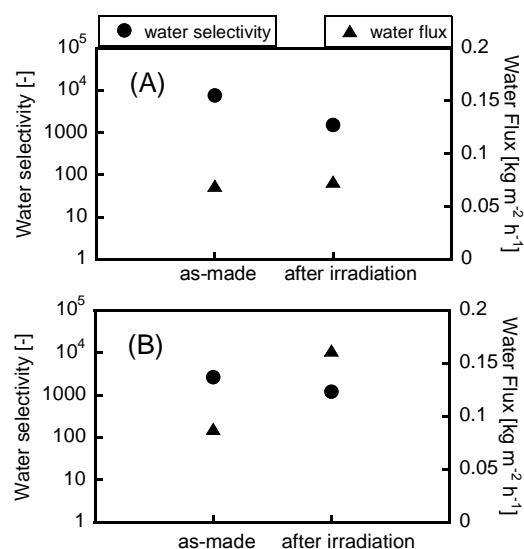


Fig. 2 IPA/water PV results before and after the irradiation for the mordenite membranes. (A) 1.0×10^{10} ions cm^{-2} , (B) 3.0×10^{10} ions cm^{-2} .

Reference

1) M. Matsukata et al., J. Membr. Sci. 316 (2008) 18-27.

4 - 08 Control of Spatial Crosslinking Reaction in Polymer Film by Ion and Electron Beam Irradiation

S. Tsukuda^{a)}, M. Sugimoto^{c)}, A. Idesaki^{c)}, M. Yoshikawa^{c)}, S. Seki^{b)} and S.-I. Tanaka^{a)}

^{a)}Institute of Multidisciplinary Research for Advanced Materials, Tohoku University,

^{b)}Division of Applied Chemistry, Graduate School of Engineering, Osaka University,

^{c)}Environment and Industrial Materials Research Division, QuBS, JAEA

Radiation processing of polymeric materials is one of the main modifications in certain modern technologies. The main chemical effects are chain scission and crosslinking reactions resulting in enhanced or reduced solubility. Heavy-ion beams are used for high-density energy deposition in polymeric materials, and the effects of ion beams differ markedly from those for low-energy ionizing radiation such as γ -ray and electron beams. In heavy-ion beam processes, the ionization and excitation processes that occur in ion tracks result in the generation of active intermediates at high density, leading to chemical reactions. Thus, the ion irradiation of cross-linked type polymers produced 1-d nano-gel (nanowires) by local cross-linking reactions along in an ion track¹⁻³⁾. In this study, ion beam firstly irradiated to poly(vinylpyrrolidone) (PVP) films in order to form nanowires. Additionally, electron beam irradiation to the same film was carried out in order to control the local crosslinking reaction around nanowires. The change of radial sizes which depended on the dose was quantitatively measured, and we discussed in terms of radiation induced gel formation.

PVP was dissolved in isopropanol (IPA) at 5 wt% with crosslinking agent. PVP films were prepared on Si substrates by spin coating technique. The thin films were exposed to beams of 490 MeV $^{192}\text{Os}^{30+}$ at the TIARA cyclotron accelerator facility of the Japan Atomic Energy Agency (JAEA). The ion irradiated films were also exposed to electron beam with the dose from 40 to 470 kGy. After irradiation, a non-crosslinked polymer was removed by development using IPA. The direct observation of the surface of the substrates were performed using an atomic force microscope (AFM Seiko Instruments Inc.(SII

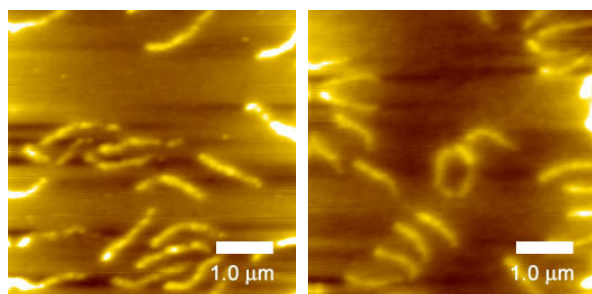


Fig. 1 AFM micrographs of nanowires based on PVP. The nanowires were formed by 490 MeV Os ion beam irradiation at 1.0×10^8 ions/cm², and additional electron beam irradiation with the dose of (a) 40 and (b) 320 kGy, respectively.

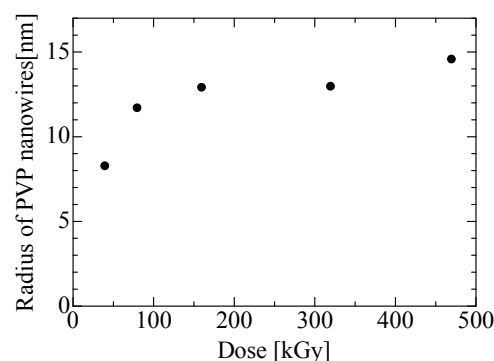


Fig. 2 The radii of PVP nanonanowires formed by ion and electron beam irradiation. The sizes were measured by AFM. The electron beam irradiation was carried out with the dose 40 - 320 kGy, respectively.

SPI-4000). The value of radial size is defined as an average radius of cross-sectional measurements of a nanowire.

Figure 1 shows results of ion beam and additional electron beam irradiation with 40 and 320 kGy, respectively. The nanowires formed by electron beam irradiation with 40 kGy were partially degraded and separated in the structures. In contrast, the continuous structures were observed with increase of radiation dose as shown in Fig. 1(b). The radii of PVP nanowires were measured using AFM and plotted in Fig. 2. The average radius of nanowires was increased with the dose of electron beam. These results indicate the electron beam irradiation produces homogeneous crosslinking reactions throughout films, and the cross-linking reactions inner or around the nanowires. Therefore, the stable nanowires were formed by increase of crosslinking points within a nanowire. The radius of cross-section of nanowire was also increased with an increase of the radiation dose by the cross-linking reactions between the boundary of original nanowires and around polymer chains. It is suggested that electron beam irradiation was useful to precisely control local crosslinking reaction around a nanowire.

References

- 1) S. Seki et. al., Adv. Mater. 13 (2001) 1663-65.
- 2) S. Tsukuda, et al., Appl. Phys. Lett. 87 (2005) 233119-1-3.
- 3) S. Tsukuda, et al., J. Photopolym. Sci. Technol. 22 (2009) 245-48.

4 - 09 Effect of Irradiation Ions on Critical Fluence of Changing to Amorphous from Crystalline SiC Nanotubes

T. Taguchi^{a)}, S. Yamamoto^{b)} and K. Yamaguchi^{a)}

^{a)} Materials Science Research Division, QuBS, JAEA,

^{b)} Environment and Industrial Materials Research Division, QuBS, JAEA

Since the discovery of carbon nanotubes (CNTs) in 1991, a lot of new one-dimensional nanostructured materials such as nanotubes, nanorods and nanowhiskers for potential applications have been synthesized by significant number of researchers. Some of them have reported that many nanomaterials such as TiC, NbC, BN, SiO₂ and GaN nanostructures are fabricated from CNTs as the template. SiC is one of the most important wide-band-gap semiconducting materials for high temperature and high power. And SiC is also one of the most important structural materials at high temperature. Therefore, SiC offers exciting opportunities in electronic devices and in structural materials at high temperature. We have reported that the polycrystalline C-SiC coaxial nanotubes, which were CNTs sheathed with SiC layer, and that polycrystalline single-phase SiC nanotubes were formed^{1,2)}. Furthermore, the amorphous SiC nanotubes were successfully synthesized by the ion irradiation of the polycrystalline SiC nanotubes at 100 °C³⁾. However, the critical fluence of changing to amorphous SiC nanotubes from polycrystalline SiC nanotubes has not been investigated yet. The purpose of this study is, therefore, to investigate the effect of irradiation ions on the critical dose of changing to amorphous SiC nanotubes.

Carbon nanotubes (GSI Creos Corporation, Tokyo, Japan) were used as the template. The C-SiC coaxial nanotubes were synthesized by heating CNTs with Si powder (The Nilaco Corporation, Tokyo, Japan) at 1,200 °C for 100 h in a vacuum. Single-phase SiC nanotubes were formed by the heat treatment of C-SiC coaxial nanotubes at 600 °C for 2 h in air. The single-phase SiC nanotubes dispersed in ethanol were deposited on nickel grid sample holder for transmission electron microscope (TEM)

observation. These nickel grid sample holders deposited with single-phase SiC nanotubes were irradiated with 3-MeV Ni²⁺ or Au²⁺ ions at 100 °C. The ion fluence ranges of Ni or Au ions were 1.7×10^{19} - 7.4×10^{19} or 2.9×10^{17} - 1.5×10^{19} ions/m², respectively.

Figures 1 and 2 showed TEM images and the corresponding electron diffraction patterns of SiC nanotubes irradiated with 4.8×10^{19} Ni ions/m² and 2.9×10^{18} Au ions/m² at 100 °C, respectively. According to these TEM images, polycrystalline SiC nanotubes were completely transformed to amorphous SiC nanotubes by both Ni and Au ions irradiation. The critical Ni ions fluence and displacement damage of changing to amorphous SiC nanotubes were 4.8×10^{19} ions/m² and 1.5 dpa, respectively. On the other hand, the critical Au ions fluence and displacement damage of changing to amorphous SiC nanotubes were 2.9×10^{18} ions/m² and 0.5 dpa, respectively. Both critical ion fluence and displacement damage decreased with increasing the atomic weight of irradiation ions. The reason is considered that the damage area induced by one ion increased with increasing the atomic weight of irradiation ion. These results indicate that the irradiation with heavier ions causes the amorphization of polycrystalline SiC nanotubes at the lower fluence and displacement damage.

References

- 1) T. Taguchi et al., J. Am. Ceram. Soc. 88[2] (2005) 459-61.
- 2) T. Taguchi et al., Physica E 28[4] (2005) 431-38.
- 3) T. Taguchi et al., JAEA Takasaki Annu. Rep. 2009 (2011) 127.

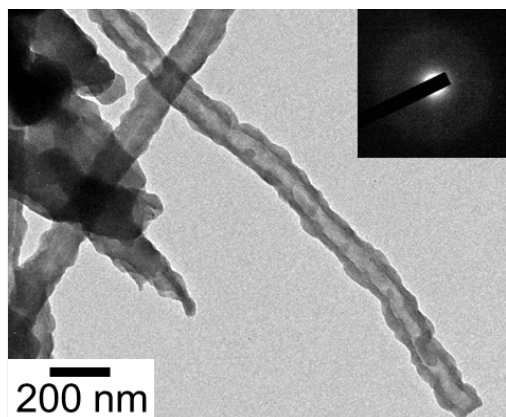


Fig. 1 TEM image and the corresponding electron diffraction pattern of SiC nanotubes irradiated with 4.8×10^{19} Ni ions/m².

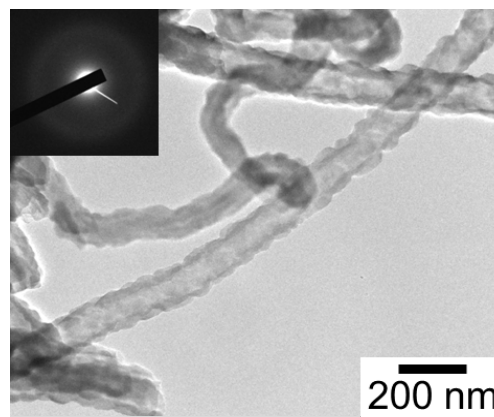


Fig. 2 TEM image and the corresponding electron diffraction pattern of SiC nanotubes irradiated with 2.9×10^{18} Au ions/m².

4 - 10 Thermo-Optic Switch Consisting of Mach-Zehnder Polymer Waveguide Drawn Using Proton Beam Writing

K. Miura^{a)}, T. Satoh^{b)}, Y. Ishii^{b)}, M. Koka^{b)}, H. Kiryu^{a)}, Y. Ozawa^{a)}, A. Kubota^{a)},
T. Ohkubo^{b)}, A. Yamazaki^{b)}, W. Kada^{b)}, A. Yokoyama^{b)}, T. Kamiya^{b)} and O. Hanaizumi^{a)}

^{a)}Graduate School of Engineering, Gunma University,

^{b)}Department of Advanced Radiation Technology, TARRI, JAEA

Proton beam writing (PBW) has recently attracted much attention as a next-generation micro-fabrication technology. This is a direct-drawing technique and does not need any masks to transfer micro-patterns to sample surfaces. Optical waveguides can be directly drawn in PMMA using PBW because the refractive index of PMMA can be increased by proton irradiation. In our previous works, we demonstrated the first single-mode straight-line, Y-junction, and Mach-Zehnder (MZ) type PMMA-based waveguides fabricated using PBW and working at $\lambda = 1.55 \mu\text{m}$ ^{1, 2)}. They are important components for constructing MZ type thermo-optic switches for optical-fiber telecommunication systems³⁾.

Our purpose is to realize this type of optical switch, schematically illustrated in Fig. 1, utilizing PBW. One waveguide arm is equipped with a thin-film heater on the upper cladding that operates as a phase shifter. The phase shifter can introduce a difference in light-propagation phase $\Delta\phi$ between the two arms by changing the refractive index of one arm waveguide by manipulating the thermo-optic effect of a polymer material. The optical switch will be an ON state when the phase difference $\Delta\phi = 0$ and an OFF state when $\Delta\phi = \pi$. In this study, we attempted to fabricate a MZ type thermo-optic switch utilizing PBW.

A 15- μm -thick silicon-dioxide (SiO_2) film was deposited as an under-cladding on a silicon (Si) substrate (20 mm \times 40 mm \times 0.5 mm¹⁾) using radio-frequency magnetron sputtering. A PMMA film was spin-coated onto the SiO_2 film. The total thickness of the PMMA film was $\sim 10 \mu\text{m}$. A core of a waveguide was drawn in the PMMA film using a 3-MV single-ended accelerator. The proton (H^+) beam energy was 1.7 MeV, and the beam current was $\sim 50 \text{ pA}$. The beam diameter was focused to $\sim 1 \mu\text{m}$, and the total dose was set to 100 nC/mm². A MZ waveguide was produced by symmetrically coupling two Y junctions with a core with $w = 8 \mu\text{m}$ in order for it to work as a single-mode waveguide, and we set its branching angle to 2° in order to obtain a low branching loss. The two Y-junction waveguides were drawn by controlling both H^+ beam scanning and stage translation. A 10- μm -thick PMMA film is subsequently deposited again on the sample as an over-cladding by spin-coating under the same conditions as the first PMMA layer.

We formed a titanium (Ti) thin-film heater and aluminum (Al) electrodes on the surface of the MZ waveguide. The layout of the heater and electrodes was optimized by Hiratani *et al.* using heat-transfer analysis to effectively

utilize heat from the Ti heater and Al electrodes⁴⁾. They were formed using conventional photolithography and wet-etching processes. First, a 300-nm-thick Ti or Al thin film is deposited on the waveguide by vacuum evaporation. Next, a commercial positive photoresist film is spin-coated onto the metal film, and the resist is exposed by UV light through a photomask. After development, a Ti or Al thin film is patterned by wet etching. Finally, the resist is removed by UV exposure without the photomask and development.

Figure 2 plots the relative output intensity of the sample versus applied electric power to the heater at $\lambda = 1.55 \mu\text{m}$. An ON/OFF ratio of 9.0 dB and a switching power of 43.9 mW were obtained. The ON/OFF ratio needs to be around 20 dB, but the switching power is lower than for conventional silica-based switches. In commercially available silica-based devices, the electric power consumption of one element is typically from 100 to 200 mW³⁾.

References

- 1) K. Miura *et al.*, Key Eng. Mater. 497 (2012) 147.
- 2) K. Miura *et al.*, Key Eng. Mater. 534 (2013) 158.
- 3) K. Watanabe *et al.*, NTT Tech. Rev. 8 (2010) 1.
- 4) Y. Hiratani *et al.*, Tech. Rep. IEICE OPE2004-220 (2005) 13, in Japanese.

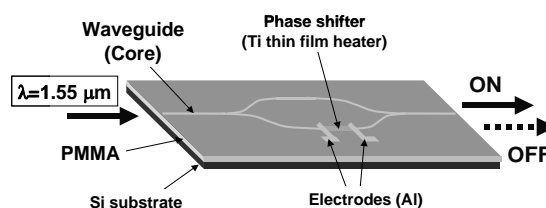


Fig. 1 Schematic of a MZ type thermo-optic switch.

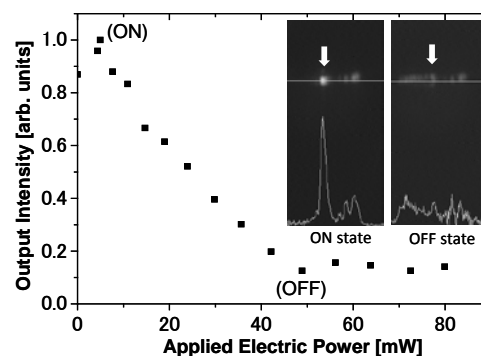


Fig. 2 Relative output intensity ($\lambda = 1.55 \mu\text{m}$) versus applied electric power to the heater.

4 - 11 Hydriding Property of Hydrogen Storage Alloy by Charged Particle Under Different Irradiation Environment

H. Abe^{a)}, K. Muraki^{b)}, M. Kishimoto^{b)}, H. Uchida^{c)} and T. Ohshima^{a)}

^{a)}Environment and Industrial Materials Research Division, QuBS, JAEA,

^{b)}Course of Applied Science, Graduate School of Engineering, Tokai University,

^{c)}Department of Energy Science and Engineering, School of Engineering, Tokai University

In this study, we examined the effect of electron irradiation to the surface of a Mm-Ni based hydrogen storage alloy on the initial activation. We made surface analysis of the alloy samples by electron spectroscopy for chemical analysis (ESCA) indicated non-stoichiometric oxides of rare earths such as LaO_x and CeO_x , which seemed responsible for the promotion of the dissociation rate of H_2O , and according enhancement of electrochemical hydrogen absorption rate. This paper demonstrates an effective surface treatment of electron irradiation, which induces catalytic activations of rare earth oxides in the alloy surface.

The hydrogen storage alloy forms an oxide or a hydroxide layer on the surface in the atmosphere or a low vacuum. In the hydrogen absorption from the H_2 gas or in electrochemical process, the surface oxide layers strongly inhibit the dissociation of H_2 molecules or H_2O molecules. In order to reduce such inhibitive effects, we have investigated various surface modifications of hydrogen storage alloys by alkaline (Li, Na and K) treatments¹⁾, HF treatment²⁾ and ion irradiations³⁾.

A negative electrode material of Ni-MH battery a Mm-Ni based hydrogen storage alloy, $\text{MmNi}_{3.48}\text{Co}_{0.73}\text{Mn}_{0.45}\text{Al}_{0.34}$ ($\text{Mm} = \text{La}_{0.35}\text{Ce}_{0.65}$), was prepared by arc melting. The alloy was then flushed to produce powder samples by cyclic hydriding and dehydriding treatments. The produce powder samples had an average grain size of about 38 μm . The powder was then pressed under a pressure of 7 t/cm² to prepare a pellet sample with a size of 12 mm ϕ and 1.2 mm thickness as cathode, $\text{Ni}(\text{OH})_2$ as an anode, for the measurement of hydriding rate in electrochemical process alloys. Surface modifications were made by electron irradiation and alkaline treatment. Electron irradiation onto the surface for a sample was made in an acceleration energy

of 2 MeV, and a dose of $1 \times 10^{17} \text{ cm}^{-2}$ in the atmospheric air, in a vacuum ($\sim 2 \text{ Pa}$) and in a He gas atmosphere using a 2 MV Cockcroft-Walton electron accelerator. For the electrochemical measurements of initial hydrogen absorption reaction rate of the electron irradiated and un-irradiated samples, the rate of hydriding of the samples were measured in a 6 M-KOH using the open cell at a constant voltage -0.93 V at a temperature of 298 K, from 0 to 120 min. The pellet samples after the irradiation treatment were subjected to the microstructure observation by scanning electron microscopy (SEM), and the depth profile analyses by ESCA.

Figure 1 shows results of ESCA depth profile analyses with respect to distributions of oxygen and Ni atoms in the surface region of samples (a), (b), (c) and (d) before electrochemical process. Sample (d) irradiated in the atmosphere exhibited the highest oxygen concentration in the surface among the samples. Sample (c) irradiated in low vacuum exhibited also high oxygen concentrations, however, lower than that of sample (d). Compared with these samples, sample (b) irradiated in the He gas and sample (a) without irradiation show low oxygen concentrations in the surface. These results indicate the difference in the surface composition in the atmosphere or low vacuum. From results of sample (b), the He gas was found to inhibit surface oxidation during electron irradiation effectively. For all samples, Ni atoms in the surface seem totally oxidized.

Electron irradiation was very effective in the improvement of the initial activation of the Mm-Ni based alloy by electrochemical process at 298 K when, prior to hydrogen absorption, the irradiation to the alloy surface was made in the atmosphere or low vacuum with relatively high oxygen partial pressures. The irradiation to the alloy surface induces morphological modifications of the surface, and the formation of non-stoichiometric oxides of Ce or La in the surface. These oxides contribute to the promotion of the dissociation of H_2O molecules, and results in the improved initial activation in electrochemical process. However, no improvement in the electrochemical hydrogen absorption was found for the Mm-Ni based alloy with electron irradiations in the He gas. These alloys surface were covered with thin layers of stoichiometric oxides such as CeO_2 and NiO which have no contribution to the dissociation of H_2O molecules at room temperature.

References

- 1) H. Uchida et al., J. Alloys and Comp. 253-254 (1997) 525.
- 2) H. Uchida et al., J. Alloys and Comp. 253-254 (1997) 547.
- 3) H. Abe et al., Nucl. Instrum. Meth. B 206 (2003) 224.

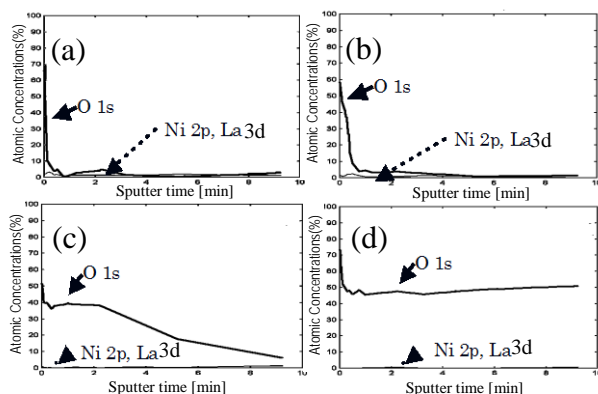


Fig. 1 ESCA depth profile analyses for sample irradiated (a) sample without irradiation, (b) in the He gas, (c) in low vacuum, (d) in the atmosphere.

4 - 12 Micropatterning on Fluoropolymer Surface Using Proton Beam Writing and Nitrogen Ion Beam Irradiation

A. Kitamura (Ogawa)^{a)}, T. Sato^{a)}, M. Koka^{a)}, T. Kamiya^{a)} and T. Kobayashi^{b)}

^{a)}Department of Advanced Radiation Technology, TARRI, JAEA,

^{b)}Advanced Science institute, RIKEN

Polytetrafluoroethylene (PTFE, $-(CF_2-CF_2)_n-$) and fluorinated ethylene propylene (FEP, $-(CF_2-CF_2)_n-(CF_2-CF(CF_3))_m-$) are known commercially under the trade name Teflon. They exhibit several desirable properties for the fabrication of microelectromechanical systems and biochemical tools. Using keV nitrogen ion beam irradiation, needle-like protrusions are created at a high density over the entire irradiated area¹⁾. These unique surfaces are useful in cell culture dishes, because cells can attach and spread on top of the protrusions²⁾. Therefore, it is important to enhance this cytological feature of the Teflon surface for the further development of biotechnology. In order to arrange cells on such a unique surface, micropatterning of Teflon is one of the best approach. In this study, several flat patterns were created between micro-protrusions on FEP surface using proton beam writing (PBW) and subsequent nitrogen ion beam irradiation. High-energy protons (e.g., 500 keV to 3 MeV) penetrate deeply into materials with depositing their energy along their trajectory. These properties of an MeV proton beam was used to create patterns between the micro-protrusions formed via keV ion beam irradiation.

First, a FEP sheet (100- μ m-thick, Daikin Industries) was irradiated by a 3.0 MeV focused proton beam from a 3-MV single-ended accelerator. The diameter of a proton beam was approximately 1 μ m, and the beam current was set at 200 pA. The fluence was varied between 2.5×10^{11} and 2.5×10^{13} ions/cm² by changing the exposure time. The beam was scanned over 50 μ m² patterning area. Next, to form dense micro-protrusions on the surface, the scanned surfaces were subsequently irradiated with a 250 keV N₂⁺ ion beam using a 400-kV implanter³⁾. The surface were observed with an optical microscope (SZX16, Olympus Corp.) and an scanning electron microscope (SEM) (TM3000, Hitachi High-Tech. Corp.). The molecular configuration of the samples was analyzed using attenuated total reflectance/Fourier transform infrared (ATR/FT-IR) spectroscopy (FT-700, HORIBA, Ltd.).

When the fluence of PBW and subsequent 250 keV N₂⁺ ion beam irradiation were 1.3×10^{12} ions/cm² and 2.0×10^{15} ions/cm², respectively, the surface morphology changed as shown in Fig. 1. Smooth areas were formed between dense micro-protrusions, and their size corresponded to that of the patterns by PBW. Therefore, the formation of the smooth areas was explained as follows. When PBW was carried out on an original FEP surface, radical fragments were generated in the scanned areas due to irradiation-induced scission of the main polymer chains.

During subsequent N₂⁺ ion beam irradiation, the scanned areas were only evaporated because the temperature of the sample was raised without formation of micro-protrusions.

New bonds (C=C, COOH, C=O, COO, and -OH) were detected locally in the patterned areas with an ATR/FT-IR analysis. They were formed by reactions of radicals with oxygen when the samples were exposed to air. Their new bonds help cells attach to the surface, and it has already been confirmed that fibroblast cells can also attach and spread on top of micro-protrusions²⁾. Therefore, patterned FEP surfaces can be used in three-dimensional cell culture dishes.

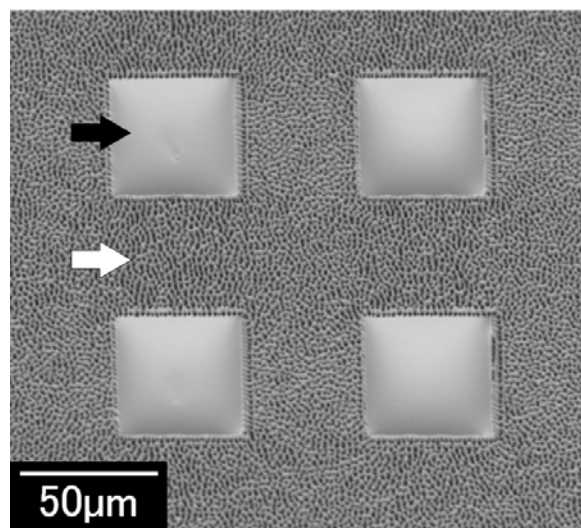


Fig. 1 SEM image of FEP surface patterned using a 3 MeV proton micro beam followed by irradiation with a 250 keV N₂⁺ ion beam. The white and black arrows indicate the surfaces irradiated only by the N₂⁺ ion beam and the patterned areas, respectively.

References

- 1) A. Kitamura et al, Surf. Coat. Technol. **203** (2009) 2406-09.
- 2) A. Kitamura et al, Surf. Coat. Technol. **206** (2011) 841-44.
- 3) A. Kitamura (Ogawa) et al, Nucl. Instrum. Meth. Phys. Res. B 314(2013)82.

4 - 13 Fabrication of a Flexible Dielectrophoretic Device Using Proton Beam Writing

G. Ayugase^{a)}, D. Terajima^{a)}, H. Nishikawa^{a)}, T. Satoh^{b)}, Y. Ishii^{b)} and T. Kamiya^{b)}

^{a)}Department of Electrical Engineering, Shibaura Institute of Technology,

^{b)}Department of Advanced Radiation Technology, TARRI, JAEA

Aiming at development of a flexible dielectrophoretic (DEP) device equipped with 3D-pillar arrays, we studied fabrication processes of a high-aspect-ratio pillar arrays on polyethylene terephthalate (PET) films using proton beam writing. The high-aspect-ratio pillar arrays of epoxy were successfully fabricated by applying an appropriate post-exposure bake process on the SU-8 film onto the PET with transparent indium tin oxide (ITO) electrodes, which were patterned prior to PBW.

誘電泳動デバイスにプロトンビーム描画(PBW: Proton Beam Writing)を用いた高アスペクト比誘電体ピラーアレイを誘電泳動デバイスに組み込むことで、電界強度の差を生じさせ、高効率な生体微粒子の捕集効果を報告してきた¹⁾。従来の研究では、Siやガラスといった基板上にデバイス作製を行って来た。近年は、検査デバイスに樹脂基板を用いることで、デバイス全体を柔構造化し、曲面を有する部位に設置することが可能になる。また、安価な樹脂を用いることで、低コストな使い捨てデバイスとしての利用により、今後、誘電泳動デバイスの普及につながると考えられる。

本研究課題では、PBWを用いて高アスペクト比構造を作りこむことにより、ガラス基板上に形成してきた3次元誘電泳動デバイスを、柔軟性と透明性に優れたPETフィルム上に作製し、フレキシブルで高効率、低コストの誘電泳動デバイスの作製を目的とする。

誘電体ピラーの作製には、ネガ型の感光性樹脂SU-8 3025 (MicroChem 社製)を使用した。まず脱脂洗浄したPETフィルム上に15 μm 膜厚のSU-8をスピンコート法にて成膜し、原子力機構高崎TIARAもしくは芝浦工大フレキシブル実装工学研究センター設置のPBW装置にて照射(ビームエネルギー1.0 MeV、ビーム径1.3 μm 、試料電流 5.0 pA、照射量10~90 nC/mm²)を行った。その後、化学増幅作用を有する光酸発生剤を含むレジストに有効な露光後の熱処理であるPEBを温度65 $^{\circ}\text{C}$ にて3分間行った。専用現像液(MicroChem社製 SU-8 Developer)に浸漬し現像後、2-propanolでリンスした。

フレキシブル誘電泳動デバイスの電極には、誘電泳動効果を外部からの観察を可能にするため、透明導電膜であるITOを用いた。ポジ型感光性樹脂のOFPR-5000LB (東京応化工業(株)製)を塗布したITO付きPETフィルムをUV露光後(照射量:12.5 mJ/cm²)、現像した。その後、

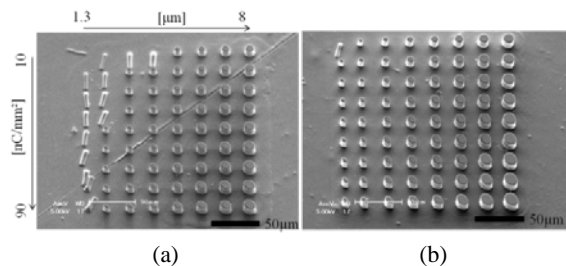


Fig. 1 Scanning electron microscope (SEM) images of SU-8 Pillar array on the PET film obtained for samples (a) with and (b) without post exposure bake at 65 $^{\circ}\text{C}$ for 3 minutes in air.

ITO エッチング液(関東化学(株)製)によりギャップ状の電極をパターンニングした。

Figure 1にPETフィルム上の誘電体ピラー構造の作製結果を示す。直径の異なるピラーアレイに対し、現像した結果をFig. 1に示す。ここでは照射量10~90 nC/mm²にて、(a)PEB無し、および(b)PEB65 $^{\circ}\text{C}$ を3分間行った場合の各ピラーのSEM像を示す。Figure 1(a)よりPEBを行わない場合、一部の高照射量のピラー構造は形成されたものの、最小径の2.0 μm 描画径のピラーは照射量によらず倒壊することがわかる。PEBを行った場合、Fig. 1(b)より照射量、20 nC/mm²で実寸が1.9 μm 径のピラーを倒壊することなく、作製できた。

Figure 2に2.0 μm 描画径でPBWにより描画したピラーの現像後の実寸の照射量依存性を示す。いずれの場合も照射量の増加に伴い解像度が劣化し、設計値より大きくなる。例えば、PEB 65 $^{\circ}\text{C}$ では照射量20 nC/mm²にて1.9 μm であるのに対し、照射量90 nC/mm²では3.8 μm となり、設計値に対しピラー径が2倍に増大した。これより、ピラーの倒壊を防ぐためのPEBを行うと架橋が促進し、その強度は向上するが、ピラーの直径は設計値より大きくなることに留意する必要がある。

本基板を用いた予備的実験により、誘電泳動デバイスとしての基本的な機能を確認している。今後は、よりピラー径が小さく、アスペクト比の向上を目指した照射条件およびプロセスの検討を行う予定である。

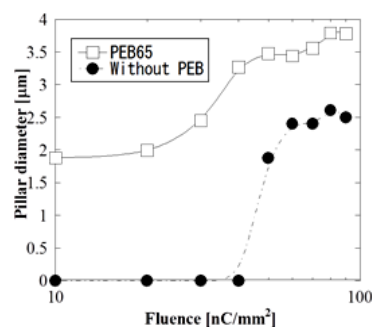


Fig. 2 Actual diameters obtained for pillars with a written diameter of 2.0 μm under different fluence after development with and without PEB. The pillar diameters of zero indicate that no pillar arrays were formed without collapse after development.

Reference

- 1) Y. Furuta et al., Microelectr. Eng. 86 (4-6) (2009) 1396-1400.

4 - 14 Li-ion Battery Characterization by Ion Beam Analysis

K. Mima^{a)}, K. Fujita^{a)}, Y. Kato^{a)}, S. Nakai^{a)}, H. Sawada^{b)}, A. Yamazaki^{c)}, C. Okuda^{b)},
Y. Ukyo^{b)}, Y. Uchimoto^{d)}, Y. Orikasa^{d)}, K. Yamamoto^{d)}, T. Kamiya^{c)},
R. Gonzalez^{e)} and I. M. Perlado^{e)}

^{a)}The Graduate School for the Creation of New Photonics Industries,

^{b)}Toyota Central R&D Labs. Inc., ^{c)}Department of Advanced Radiation Technology,
TARRI, JAEA, ^{d)}The Graduate School of Human and Environment Science, Kyoto University,

^{e)}Instituto de Fusión Nuclear, Universidad Politécnica de Madrid

Li-ion batteries are attractive candidates for portable consumer electronics, electric vehicles, and so on, since they can provide high energy and high power densities. Li-ion batteries consist of a positive and a negative electrode separated by an electrolyte layer, which must be an ionic conductor and electronic insulator. Once positive and negative electrodes are linked by an external circuit, spontaneous electrochemical reactions take place, in which chemical energy is transformed into electrical energy. These reactions involve the lithium-ion diffusion between the positive and the negative electrodes. Therefore, the performance of a Li-ion battery strongly depends on the characteristic of the electrodes and in particular on the Li-ion diffusion capabilities. Because of this reason the study of the Li distribution in the positive electrode is one of the main points of concern in further battery development.

The use of μ -Ion Beam Analysis (IBA) with scanning procedures allows studying elemental concentration distributions with high lateral resolution (in the μm range). We investigated the Li and Ni distribution for as-received and charged positive electrode containing $\text{Li}_x\text{Ni}_{0.8}\text{Co}_{0.15}\text{Al}_{0.05}\text{O}_2$ ($0.75 \leq x \leq 1.0$) microparticles as active

material by using particle induced γ -ray emission (PIGE) and particle induced X-ray emission (PIXE) at TIARA, respectively. Li distribution maps of individual secondary particles (active material) are shown in the figures 1 and 2. The dependences of the Li distribution in a secondary particle as well as on electrode thickness are presented¹⁾.

The Fig. 1 shows that the Li concentration relative to the Ni distribution is uniform. On the other hand, the Li distribution in the thick electrode sample is found to be non-uniform, but it is relatively uniform in the thin sample. This is the first finding in the Li battery research, although it is predicted²⁾.

This work was performed under "Project for promotion of shared use of high technology research institute" for creation of research platform and sharing of advanced research infrastructure by ministry of education, culture, sports, science and technology.

References

- 1) J. Newman and K. E. Thomas-Alyea, *Electrochemical Systems*, John Wiley & Sons (2004).
- 2) K.Mima et al., *Nucl. Instrum. Meth. Phys. Res. B* 290 (2012) 79-84.

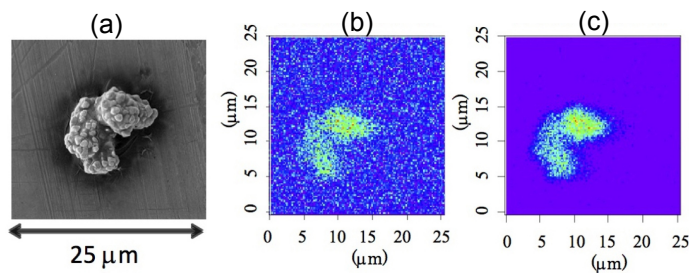


Fig. 1 Secondary particle images: (a) SEM image, (b) PIGE(Li) image, and (c) PIXE(Ni) image.

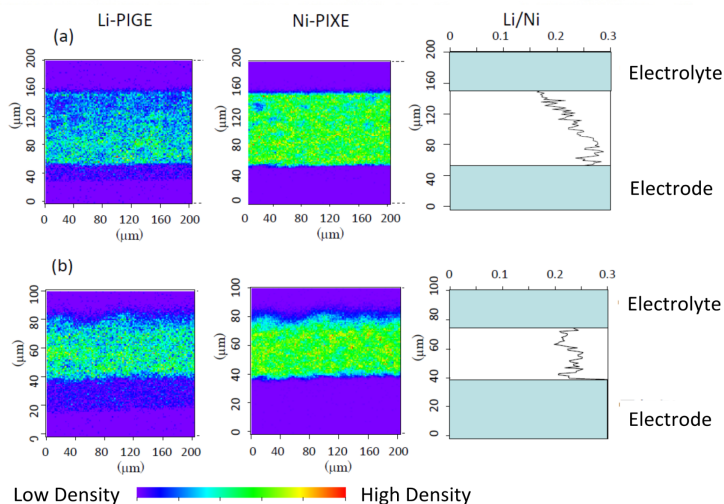


Fig. 2 Electrode thickness dependence of Li distribution.

4 - 15 Atomistic Transformation Processes Induced by the Interaction of Implanted N-ions with Ti Thin Films

Y. Kasukabe^{a,b)}, H. Shimoda^{b)}, S. Yamamoto^{c)} and M. Yoshikawa^{c)}

^{a)}Center for International Exchange, Tohoku University, ^{b)}Department of Metallurgy, Tohoku University, ^{c)}Environment and Industrial Materials Research Division, QuBS, JAEA

Non-stoichiometric titanium nitrides, TiN_y , have covalent properties as well as metallic and ionic properties, which make them fascinating for both fundamental research and technological applications. Recently, it has been revealed that the interesting physical properties are related to the crystallographic (preferred oriented) and electronic structures¹⁾. However, atomistic growth processes of TiN_y films due to ion implantation, especially correlations between implanted ions and deposited Ti films in the early N-implantation stage, have not been sufficiently studied. In order to clarify atomistic transformation processes of Ti films, in-situ observations by using transmission electron microscope (TEM) and electron energy loss spectroscopy (EELS) have been carried out, along with the characterization of the electronic structure by molecular orbital calculations.

The as-deposited Ti films on thermally cleaned NaCl substrates consisted of both TiH_x and hcp-Ti with some preferred orientations at RT. The N_2^+ ions with 62 keV were implanted into hcp-Ti and TiH_x with preferred orientations in the 400 kV analytic high resolution TEM combined with ion accelerators at JAEA-Takasaki²⁾.

In-situ TEM observations have revealed that the (110)-oriented TiN_y is formed by nitriding the (110)-oriented TiH_x in the band-like TEM contrast region of the as-deposited Ti film, whereas the (001)-oriented TiN_y is mainly formed by the transformation of the (03·5)-oriented hcp-Ti to (001)-oriented fcc-Ti. In-situ EELS observations have elucidated that the release of H atoms in TiH_x proceeds preferentially in the early N-implantation stage, and that in the subsequent N-implantation stage the electron density in the hybridized band by N 2p and Ti 3d-Ti 4p states increases gradually with increasing N-concentration, which means that the number of N atoms bonding to Ti atoms increases gradually. Comparison of the net areas of the energy loss peaks concerning N 1s (K) and Ti 2p (L2,3) electrons in electron energy loss spectra for TiH_x and hcp-Ti regions is shown in Fig. 1. From Fig. 1, it can be seen that, the difference of area ratio keeps a positive value with the increase in N-concentration until the concentration ratio N/Ti reaches near ~0.25. When the concentration ratio N/Ti is larger than 0.25, the difference of area ratio is not so clear, in other words, the values can be regarded as an average 0 within the limit of experimental errors. It can be considered that N atoms implanted into the Ti films can be located as the atoms dissolved randomly in the interstitial sites and those (bonded to Ti atoms) in the octahedral sites of each Ti

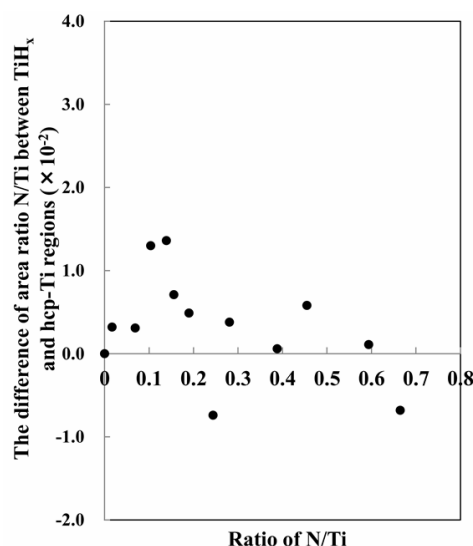


Fig. 1 Variation of the difference of the net areas of the energy loss peaks concerning N 1s (K) and Ti 2p (L2,3) electrons in electron energy loss spectra for TiH_x and hcp-Ti regions with the increase in the concentration ratio N/Ti. The vertical axis is the difference of the area ratios, (the area ratio for TiH_x region) - (that for hcp-Ti region).

sublattice (hcp or fcc-Ti). Considering the fast diffusion of N atoms in the interstitial sites in the Ti films, the amount of the dissolved N atoms in the interstitial sites in hcp-Ti and TiH_x regions during N-implantation is nearly the same. Therefore, the difference of the area ratio, N/Ti, between TiH_x and hcp-Ti regions at the initial implantation stage (less than N/Ti=0.25) in Fig. 1 indicates that there are more N atoms invading into the octahedral sites in the fcc-Ti sublattice of H-released TiH_x than those invading into the octahedral sites in hcp-Ti sublattice. On the other hand, the difference of the area ratio disappears when the N/Ti ratio exceeds ~0.25, which means that the amount of N atoms bonded to Ti atoms in hcp-Ti region becomes the same as that in TiH_x region in the further N-implantation stage. Here, we define N/Ti, 0.25 as a critical concentration ratio. Therefore, it is concluded that at N/Ti > ~0.25, the hcp-fcc transformation occurs collectively, when another N atom invades the neighboring octahedral site, and induces the growth (evolution) of nucleus of the hcp-fcc transformation.

References

- 1) S. Hao et al., Phys. Rev. B 74 (2006) 035424-1.
- 2) H. Abe et al., JAERI-Research 96-047 (1996) 1.

4 - 16 Ion Beam Analysis of Quaternary Heusler Alloy Co₂(Mn_{1-x}Fe_x)Si(111) Epitaxially Grown on Ge(111)

Y. Maeda^{a,b)}, K. Narumi^{b)}, S. Sakai^{b)}, K. Hamaya^{c)} and M. Miyao^{c)}

^{a)}Department of Computer Science and Electronics, Kyushu Institute of Technology, ^{b)}Department of Advanced Radiation Technology, TARRI, JAEA, ^{c)}Department of Electronics, Kyushu University

High tunnel magnetoresistance (TMR) effects in magnetic tunneling junctions (MTJs) have been achieved by using Co-based Heusler compounds. Recently, giant TMR ratio and its small temperature dependence were demonstrated simultaneously by carefully controlled fabrication conditions with adding a fourth element to the ternary Co-based Heusler-alloy electrodes of the MTJs.

Quaternary Heusler Alloy Co₂(Mn_{1-x}Fe_x)Si (CMFS)¹⁾ is one of the candidates for the electrodes on semiconductors and have been succeeded in epitaxial growth on Ge(111) by using low temperature MBE technique²⁾. This successful epitaxial growth may be supported by almost zero-lattice mismatching between CMFS ($a = 0.567$ nm)¹⁾ and Ge ($a = 0.5675$ nm).

In this study, quality and disordering due to static atomic displacement in CMFS/Ge(111) hybrid structures have been investigated by axial ion channeling measurements.

Fifty nm-thick CMFS alloy films with compositions of Co₂Mn_{0.5}Fe_{0.5}Si (0.5CMFS) and Co₂Mn_{0.25}Fe_{0.75}Si (0.75 CMFS) were epitaxially grown on Ge(111) substrates at 60 °C by a low temperature MBE deposition technique²⁾.

Two-MeV ⁴He⁺ Rutherford backscattering spectrometry (RBS) was measured at the backscattering angle of 165°. Along the zone axis Ge<111> and axial channeling dip curves were analyzed in order to obtain an accurate minimum yield (χ_{\min}) and a critical half angle ($\psi_{1/2}$).

Figures 1(a) and (b) show axial channeling dip curves at each CMFS/Ge heterointerface along a crystal axis of Ge<111> for (a) 0.5CMFS and (b) 0.75CMFS, respectively. The dip curves include all atoms because of impossible separation of ion yields due to neighbor atoms. In both curves, the minimum yields (χ_{\min}) at the <111> axis originate from ion scattering by Co atoms, while increase of yield near the axis may come from Fe. The χ_{\min} of 0.5CMFS was 0.035 (3.5%) which was smaller than 0.088 (8.8%) of 0.75CMFS. The χ_{\min} of DO₃-Fe₃Si, L2₁-Fe₂MnSi (FMS), and L2₁-Fe₂CoSi (FCS) epitaxially grown on Ge(111) were 0.013-0.045 (1.3-4.5%). The critical half angles ($\psi_{1/2}$) for both CMFS were 0.75-0.76° which were smaller than those of Fe₃Si (0.98°), Fe₂MnSi (0.85°), Fe₂CoSi (0.88°).

To discuss on disordering of atomic row, static atomic displacement $\langle u_s \rangle$ was deduced from analysis based on channeling parameters (χ_{\min} and $\psi_{1/2}$), the Debye model and the Barrette-Gemmell model³⁾.

It was found that 0.75CMFS at the interface had the largest $\langle u_s \rangle$ and the inside $\langle u_s \rangle$ became smaller than that at the interface. The $\langle u_s \rangle$ of CMFS/Ge interface was

relatively larger than those at other alloy cases. The same systematic behavior has been reported in FMS/Ge structures because of increase in lattice mismatch ($\delta < -0.06\%$) at their interfaces⁴⁾. The δ of 0.5CMFS/Ge and Co₂FeSi (CFS)/Ge may be -0.088% and -0.123% which are relatively larger than the δ of FMS/Ge. This difference in the δ between them can be reflected in the larger values of $\langle u_s \rangle$ of 0.5CMFS and CFS/Ge interfaces and their insides. This important fact teaches us that such a large atomic displacement of 0.012 nm ($\Delta \sim \langle u_s \rangle / a = 0.012 / 0.567 = 2.1\%$), which causes significant disordering of atomic row, is introduced during growth of 0.75CMFS on the Ge surface (~5 nm thick regions on Ge).

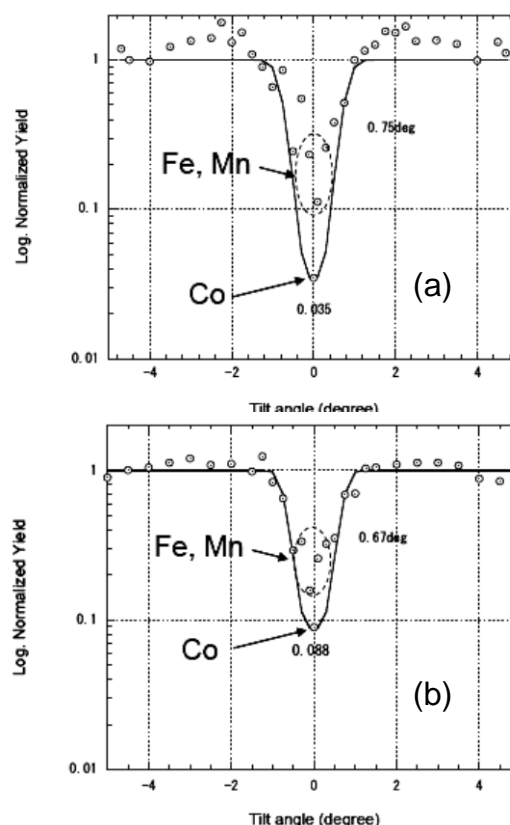


Fig. 1 Axial channeling dip curves at the CMFS/Ge heterointerfaces for (a) Co₂Mn_{0.5}Fe_{0.5}Si (0.5CMFS) and (b) Co₂Mn_{0.25}Fe_{0.75}Si (0.75CMFS).

References

- 1) B. Balke et al., Phys. Rev. B **74** (2006) 104405.
- 2) S. Yamada et al., J. Appl. Phys. **109** (2011) 07B113.
- 3) Y. Maeda et al., Thin Solid Films **519** (2011) 8461.
- 4) Y. Maeda et al., MRS Proc. **1119E** (2009) 1119-L05-02.

4 - 17

Non-thermal Equilibrium Crystal Structure of FeRh Intermetallic Compound Irradiated with Energetic Heavy Ions

A. Hashimoto^{a)}, Y. Kaneno^{a)}, T. Matsui^{b)}, Y. Saitoh^{c)} and A. Iwase^{a)}

^{a)}Department of Materials Science, Osaka Prefecture University,

^{b)}Research Organization for the 21st Century, Osaka Prefecture University,

^{c)}Department of Advanced Radiation Technology, TARRI, JAEA

1. Introduction

It is well known that FeRh intermetallic compounds show a structural transformation from B2 structure to A1 structure near the melting temperature. We have so far studied the effect of ion beam irradiation on the magnetic properties of this alloy¹⁻⁴⁾. In the present study, we focus on the effect of energetic ion irradiation on structural transformation and the hardness. Owing to this purpose, instead of Fe-50 at.% Rh alloy, we have used Fe-45 at.% Rh alloy which does not show any magnetic transitions and remains ferromagnetic below the Curie temperature⁵⁾.

2. Experimental procedure

Fe-45 at.% Rh bulk samples were irradiated at room temperature with 16 MeV Au⁵⁺ ions by using a tandem accelerator at Takasaki Advanced Radiation Research Institute, Japan Atomic Energy Agency (JAEA). Irradiation fluences used in the present experiment were 1×10^{12} , 5×10^{13} and 5×10^{14} /cm². The crystal structures of the irradiated and unirradiated samples were determined by using the X-ray diffraction (XRD).

3. Results and Discussion

Figure 1 shows the widely-scanned XRD spectra for the unirradiated and the irradiated samples as a function of diffraction angle, 2θ , for the four kinds of ion fluences. For the unirradiated sample, all the observed XRD peaks correspond to the B2 structure. But by the irradiation, diffraction peaks for A1 and L1₀ phases appear and their intensity increases with increasing the ion fluence.

The A1 phase is a stable phase only at high temperatures. The structural change from B2 to A1 has been observed so far in Fe₅₀Rh₅₀ irradiated with 10 MeV I (iodine) ions by means of EXAFS measurement⁶⁾. It is well known that the thermal spike effect occurs by energetic ion irradiations, leading to high temperature state in the materials⁷⁾. When a solid crystal is irradiated with energetic ions, the kinetic energy of moving ions is partially transferred to host atoms through the elastic collisions. The recoiled atoms transfer a part of their energy to other atoms. Hence a cascade evolves resulting in the formation of a highly disrupted and very hot region inside the solid, followed by rapid quenching. Thus, the A1 phase which should be stable only at high temperature is kept even at room temperature.

On the other hand, the process of the phase transformation from B2 to L1₀ is quite different from the case of B2 to A1 transformation. The atomic configuration

of the L1₀ structure can be constructed from four B2 unit cells. Namely, the transformation from B2 to L1₀ is a diffusion-less type (i.e., martensitic transformation). Although L1₀ phase doesn't exist in the phase diagram of Fe-Rh system, it has also been observed so far in the FeRh alloy by the high speed deformation⁸⁾. Therefore, this transformation is not the effect of the thermal spike effect but is the effect of high stress induced by high energy ions.

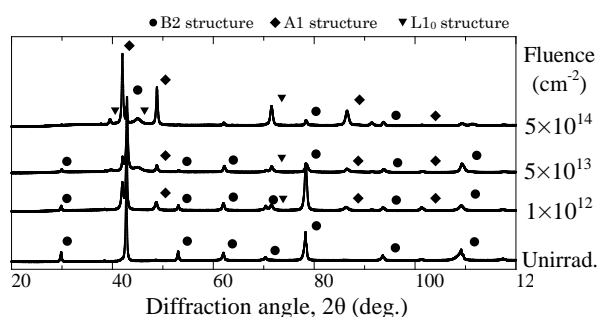


Fig. 1 XRD spectra as a function of diffraction angle, 2θ , for the unirradiated and irradiated Fe₅₅Rh₄₅.

4. Summary

In Fe₅₅Rh₄₅ intermetallic compound, 16 MeV Au ion irradiation induces two non-thermal equilibrium structures at room temperature. The A1 structure, which is the thermal-equilibrium phase at elevated temperatures is induced by the thermal spike effect. The L1₀ structure, which does not exist in the phase diagram is induced by the ion-irradiation stress effect.

References

- 1) M. Fukuzumi et al., Nucl. Instrum. Meth. B 245 (2006) 161-65.
- 2) A. Iwase et al., Nucl. Instrum. Meth. B 256 (2007) 429-33.
- 3) Y. Zushi et al., Nucl. Instrum. Meth. B 256 (2007) 434-37.
- 4) S. Kosugi et al., Nucl. Instrum. Meth. B 267 (2009) 1612-15.
- 5) O. Kubaschewski, IRON-Binary Phase Diagrams (Springer, Berlin, 1982) 121.
- 6) S. Kosugi et al., Nucl. Instrum. Meth. B 269 (2011) 869-72.
- 7) F. Seitz, J. S. Koehler, Solid State Physics (Academic, New York, 1956) (2) 305-448.
- 8) R. Oshima et al., Mater. Sci. Eng. A350 (2003) 139-44.

4 - 18

Magnetic Patterning of FeRh Thin Films by Energetic Light Ion Microbeam Irradiation and Their XMCD-PEEM Observation

T. Koide^{a)}, T. Satoh^{b)}, M. Koka^{b)}, Y. Saitoh^{b)}, T. Kamiya^{b)}, T. Ohkouchi^{c)},
M. Kotsugi^{c)}, T. Kinoshita^{c)}, T. Nakamura^{c)}, A. Iwase^{a)} and T. Matsui^{a)}

^{a)}Department of Materials Science, Osaka Prefecture University,

^{b)}Department of Advanced Radiation Technology, TARRI, JAEA,

^{c)}Hard-X-ray Spectroscopy Group & Spectroscopy Group II, JASRI-SPring8

Iron–rhodium (FeRh) alloy with B2 (CsCl-type) crystal structure has been studied intensively because of its unique magnetic behavior with a first order low temperature antiferromagnetic (AF)–high temperature ferromagnetic (FM) phase transition near room temperature¹⁾. We previously reported that the magnetic state of FeRh can be controlled by irradiation with ion beams of various energies ranging from GeV to keV²⁾. In addition, we also revealed that these magnetic modifications were related directly to the energy introduced by elastic collisions under ion beam irradiation, which generated lattice defects in B2-type FeRh³⁾. We investigated the possibility of magnetic patterning of FeRh thin films using energetic light ion microbeam irradiation with various shapes and dimensions. We report the magnetic domain structure of micrometer-sized FM regions observed by X-ray magnetic circular dichroism photoemission electron microscopy (XMCD–PEEM).

FeRh thin films were deposited on the MgO (100) substrate at 973 K by ion beam sputtering from an FeRh alloy target. H and He ion microbeam irradiation with 2 MeV was performed at JAEA-Takasaki to produce micron-sized magnetic patterns. XMCD-PEEM observation at the Fe L₂-L₃ absorption edge was performed at room temperature at BL25SU of SPring8 to confirm the synthesized magnetic patterns.

Figures 1(a)-(d) show the XMCD-PEEM images of the various micrometer sized patterns in FeRh film by using 2 MeV H ion microbeam. The bright regions are considered to have FM spin orders. In contrast, the gray areas have AFM spin order. Hence, the images shown in Figs. (a)-(c) reveal that micrometer sized magnetic patterns with designed shapes of dot, line and character can be successfully synthesized by using high energy light ion microbeam. The observed square regions with various gray scales in Fig 1(d) correspond to the irradiation patterns with different ion fluences from $2 \times 10^{16} \text{ cm}^{-2}$ (top) to $2 \times 10^{18} \text{ cm}^{-2}$ (bottom). Since the brightness of the PEEM images is strongly correlated with the magnetization of the samples, we reveal that the magnetic state in local regions of the FeRh thin films can be significantly controlled by changing the ion fluences.

References

- 1) M. Fallot et al., Rev. Sci. 77 (1939) 498.
- 2) A. Iwase et al., Nucl. Instrum. Meth. Phys. Res. B 256 (2007) 429-33.
- 3) S. Kosugi et al., Nucl. Instrum. Meth. Phys. Res. B 267 (2009) 1612-15.

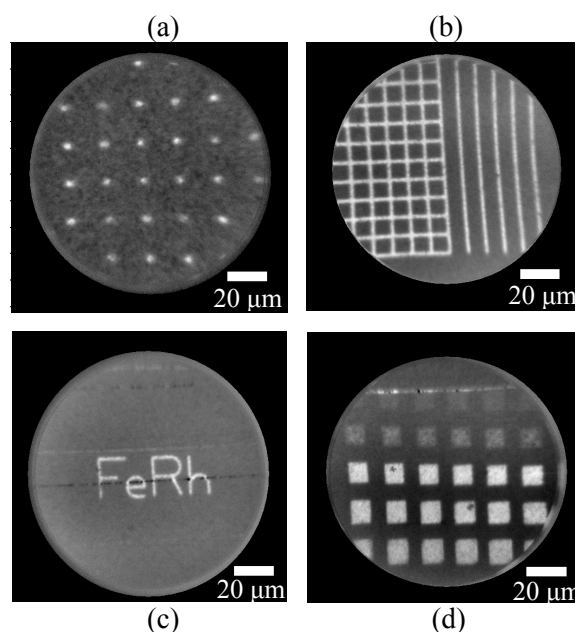


Fig. 1 XMCD-PEEM images of the various micro sized magnetic patterns by using 2 MeV H ion microbeam irradiations: (a) dot pattern, (b) grid pattern, (c) character patterns and (d) square patterns with different ion irradiation fluences.

4 - 19 Transmission Properties of a 4-MeV C^+ Ion Beam Entering a Curved Insulating Channel

K. Motohashi^{a)}, Y. Saitoh^{b)}, N. Miyawaki^{b)}, Y. Matsuo^{a)} and T. Kamiya^{b)}

^{a)} Department of Biomedical Engineering, Toyo University,

^{b)} Department of Advanced Radiation Technology, TARRI, JAEA

The efficient reflection of fast light ions by solid surfaces has recently attracted attention. Van Kan and Vis¹⁾ observed almost-complete reflection of a 2.5-MeV proton beam on a Au atomic surface layer at an incident angle of ~ 5 mrad, which was attributed to binary encounters between single protons and Au atoms. In focusing a 2-MeV He^+ -ion beam by means of tapered-glass capillary optics, Nebiki *et al.*²⁾ found that approximately 2% of the focused ions exited the outlet of the tapered-glass capillary without significant energy loss. Considering the inlet-to-outlet-area ratio ($\sim 1.4 \times 10^6$) of the capillary optics, this result corresponds to an enhancement in the ion-beam density by more than four orders of magnitude.

On one hand, charging on the surface is considered vital for the transmission of slow, highly charged ions through capillaries with inner insulating walls³⁾. It may be possible to guide not only light ions but also heavy ions like C, N, O, and other ions by electric field from the wall. If fast heavy-ion beams are guided by such charged insulating surfaces, they can be applied to various scientific and technological fields. In this study, we first investigate the transmission properties of a 4-MeV C^+ -ion beam entering a gap between a pair of cylindrical convex and concave glass lenses to inspect the possibility of guiding the fast, heavy-ion beam with the tilted curved surfaces.

A pair of cylindrical glass lenses was used as the walls of the curved insulating channel, as shown in Fig. 1. The setup basically consists of three parts: an aluminum electrode with an entrance hole, a cylindrical convex borosilicate-crown glass lens, and a cylindrical concave borosilicate-crown glass lens. The diameter of the entrance hole was 1.5 mm. The curvature of both lenses was

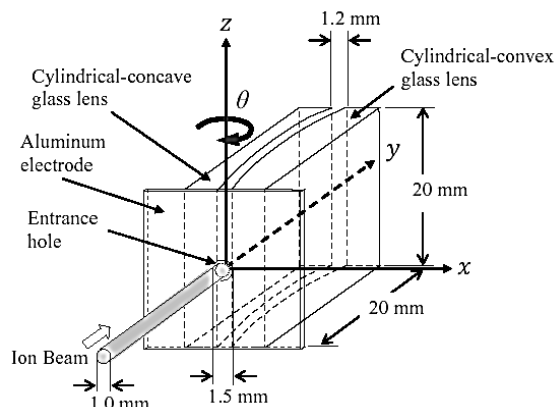


Fig. 1 Curved insulating channel formed by a pair of cylindrical convex and concave glass lenses.

155.70 mm. The convex and concave lenses face each other across a gap of 1.2 mm. The entire setup can be tilted around the z-axis, which passes through the center of the entrance hole. The tilt angle θ was defined to be positive for clockwise rotation. The depth and height of both cylindrical lenses were 20 mm. The entire setup was connected to a manipulator with three linear (x, y, and z) motions and one rotational (θ) motion. The transmission of the 4-MeV C^+ -ion beam as a function of the tilt angle θ was measured by a silicon surface barrier detector.

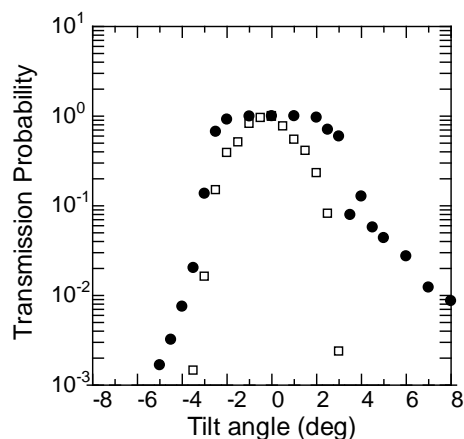


Fig. 2 Experimental results of ion-beam transmission (●) and He-Ne laser-beam transmission (□).

Ion-beam transmission is larger than the He-Ne laser-beam transmission at wider tilt angles ($|\theta| \geq 2^\circ$) as shown in Fig. 2. The ion-transmission probability is at least a factor of 2 - 100 times larger than that of the laser-beam transmission at the angle. The angular dependence of the ion-beam transmission is asymmetric. Transmission at a positive angle is larger than that at the opposite angle in the measurements. Transmission at $|\theta| \geq 2^\circ$ almost exponentially decreases with increasing $|\theta|$. Furthermore, no significant ion-energy loss occurs upon transmission for the angular range $-3^\circ \leq \theta \leq +3.4^\circ$. These results provide evidence that fast heavy-ion beams are guided by the curved surfaces⁴⁾.

References

- 1) J. A. van Kan and R. D. Vis, Nucl. Instrum. Meth. Phys. Res. B **109/110** (1996) 85.
- 2) T. Nebiki *et al.*, J. Vac. Sci. Technol. A **21** (2003) 167.
- 3) N. Stolterfoht *et al.*, Phys. Rev. Lett. **88** (2002) 133201.
- 4) K. Motohashi *et al.*, Jpn. J. Appl. Phys. **52** (2013) 076301.

4 - 20 Cathodoluminescence of He⁺-ion-implanted Feldspars

H. Nishido^{a)}, M. Kayama^{b)}, S. Toyoda^{c)} and K. Komuro^{d)}

^{a)}Research Institute of Natural Sciences, Okayama University of Science,

^{b)}Department of Earth and Planetary Systems Science, Graduate School of Science,
Hiroshima University, ^{c)}Department of Applied Physics, Okayama University of Science,

^{d)}Earth Evolution Sciences, University of Tsukuba

Cathodoluminescence (CL) is the emission of photons of UV to IR wavelengths from a material stimulated by an incident electron beam. CL properties of minerals depend on radiation dose of alpha particles, implying its geoscientific applications for geodosimetry and geochronology. CL microscopy and spectroscopy has been extensively investigated to clarify radiation-induced damages on quartz, zircon and cordierite and to estimate natural radiation dose on them, but less on feldspar in spite of an important rock-forming mineral.

The doses of natural radiation that has been accumulated by feldspar can be estimated using thermoluminescence (TL), Optical Stimulated Luminescence (OSL) and Electron Spin Resonance (ESR) spectroscopy. It is, however, necessary for estimating the dose by these methods to extract a large amount of mineral from the target sediment, so that these techniques are difficult to apply to micrometer sized grains. Cathodoluminescence (CL) spectroscopy provides useful information about the existence of radiation-induced defect centers in mineral, and with a spatial resolution of a few micrometers, suggesting a potential for geodosimetry and geochronometry with respect to a micron-ordered heterogeneous minerals or single grain analysis. In this study, CL of He⁺-ion-implanted feldspars at 4.0 MeV, corresponding to energy of α particle from radioactive decay of ²³⁸U and ²³²Th, were measured to clarify the effect of ion implantation on luminescent emissions.

CL analysis was carried out on unimplanted and He⁺-ion-implanted samples of single crystals of sanidine, orthoclase, microcline, amazonite, adularia, anorthoclase, albite, oligoclase, andesine, labradorite, bytownite, anorthite, celsian and hyalophane. He⁺ ion implantation was conducted perpendicular to their surface using a 3 MV tandem accelerator located at Takasaki Advanced Radiation Research Institute in JAEA. The specific dose density was set in the range from 2.18×10^{-6} to 6.33×10^{-4} C/cm². A scanning electron microscopy-cathodoluminescence (SEM-CL) analysis was carried out using a SEM (JEOL: JSM-5410) combined with a grating monochromator (Oxford: Mono CL2) to obtain CL spectra and images.

CL images of the cross-section samples of K-feldspars and Na-rich plagioclase show a bright luminescent band of ~14 μ m width as CL halo from the implanted surface, whereas those of adularia and Ca-rich plagioclase exhibit a dark line with ~1 μ m width on the bright luminescent background at ~12 to ~14 μ m beneath the implanted surface. CL spectra of K-feldspars commonly consists of emission bands at ~410 and 730 nm, where the former is assigned to Ti⁴⁺ impurity and/or Al-O⁻-Al/Ti defect, and the latter to Fe³⁺ impurity on the T1 and T2 sites. With an increase in radiation dose, the intensity of an emission band attributed to Al-O⁻-Al/Ti defect increases up to 1.07×10^{-4} C/cm², but those to others decrease. Adularia has a distinct emission band at ~600 nm caused by defect center, of which the intensity is reduced by the implantation. A yellow-orange emission from 500 to 600 nm is also recognized in He⁺-ion-implanted K-feldspars and then is assigned to radiation-induced defect center.

Deconvolution of the CL spectra can successfully separate this emission bands into Gaussian component at 2.09 eV, of which intensity correlates with radiation dose up to 6.33×10^{-4} C/cm²¹⁾. CL spectra of plagioclase reveals emission bands with peak wavelength centered below 300 nm assigned to Pb²⁺, and the bands peaked at ~320 and ~350 nm to Ce³⁺, ~380 nm to Eu²⁺, ~560 nm to Mn²⁺, ~740 nm to Fe³⁺, all of which the intensity decrease with the enhanced radiation dose. CL spectra of He⁺-ion-implanted plagioclase were deconvoluted into the emission component at 1.86 eV assigned to radiation-induced defect center. The emission intensity increases with radiation dose up to 6.33×10^{-4} C/cm². Taken together these results indicate that CL intensity may be used for a quantitative estimation of α radiation dose from natural radionuclides that alkali feldspars have experienced, as geodosimetry and geochronometry in the low radiation level for the blue emission assigned to Al-O⁻-Al/Ti defect center and in the wide-range radiation for the red emission to radiation-induced defect center²⁾.

References

- 1) M. Kayama et al., Phys. Chem. Minerals 17 (2013) 1.
- 2) M. Kayama et al., Geochronometria 40(2013)244.

4 - 21

Control of Photoluminescent Properties of Si-O-C Materials by Irradiation of Various Particle Beams

M. Narisawa^{a)} and M. Sugimoto^{b)}^{a)} Graduate School of Engineering, Osaka Prefecture University,^{b)} Environment and Industrial Materials Research Division, QuBS, JAEA

Two kinds of white of Si-O-C(-H) ceramics with reduced excess carbon contents were synthesized from a densely cross-linked polysiloxane particles. S800 was a sample decarbonized at 800 °C for 1 h, and showed blue emission under a UV light excitation. On the other hand, S1100 was a sample decarbonized at 1100 °C for 3 h, and showed white emission. These samples were exposed to proton beam or electron beam irradiations. At high dose (proton beam: $1 \times 10^{14}/\text{cm}^2$, electron beam: 3.95 MGy), white emission of S1100 decreased. The spectrum feature of S1100 was, however, not changed substantially, while the blue PL band of S800 showed a small shift to longer wavelength. Perhaps, reduction of white emission was caused by overlapping of new absorption band at near UV region.

近年、大阪府立大学の研究グループは、水素脱炭法を用いて、安価なポリシロキサン系前駆体から白色かつ特異な発光性を有する Si-O-C(-H)セラミックスの合成に成功した¹⁻³⁾。賦活化剤などを含まない単純な組成であることから、一般の蛍光塗料などの基材となるフィラーから、広い波長領域をカバーする LED 照明の発光層にいたる多様な用途が期待される。また発光機構として Si-O-C(-H)アモルファスの中に形成される酸素欠損などとの関連が示唆されている。本研究では、アモルファス中に欠陥を導入する効果があるプロトン照射、および電子線照射を行い、発光性を与える影響について定量的に調査した。水素を含む脱炭雰囲気にて、800 °C で 1 時間保持した試料を S800、1100 °C で 3 時間保持した試料を S1100 とする。PVA を全体に 5% 量加えて水中に分散した状態で、Si 基板上に塗布し、乾燥の後、プロトン照射 (1 MeV) を行った。S800 は青色、短寿命単一成分から成る発光を示すのに対し、S1100 は、水色短寿命および黄色長寿命の二つの発光成分を有し、両成分が合成されることによって、全体として白色発光を呈する。両試料ともに 1×10^{15} 個/cm² 照射の時点で黄変が見られ、さらに 6×10^{15} 個/cm² 照射の時点では灰黄色に色づく様子が見られた。

黄変が認められる直前の照射量として、 1×10^{13} 個/cm²、 3×10^{13} 個/cm²、 1×10^{14} 個/cm² を選択し、照射の後の発光の目視観察を行った結果を Fig. 1 に示す。S800 の発光には見た目には変化が見られないのに対し、S1100 の発光は照射量の増大とともに衰えが見られる。またこれらのサンプルに関して、PL 測定を行った結果を Fig. 2 に示す。照射量の増大に伴って、S800 の発光ピークの位置が、410 nm から 450 nm にシフトしている。一方、S1100 のスペクトルは見た目にはほとんど変化が見られない。S1100 の発光強度が全体として下がるのは、黄変の原因となる発光に寄与しない光吸収成分が増えているためと思われる。励起スペクトルの解析によれば、特に S1100 中の黄色長寿命成分は紫外から可視域にかけて広い範囲での吸収を有し、上記のような競合する波長での吸収成分の影響を受けて、光量が落ちやすいと考えられる。

一方、電子線 (2 MeV) 照射を行った場合にも、同様の傾向が認められた。照射量が増すにしたがって (0.395 - 3.95 MGy)、ピーク位置が長波長側にシフトするが、シフト量の少ない S1100 の方が発光強度の低下が著しい。(Fig. 3)

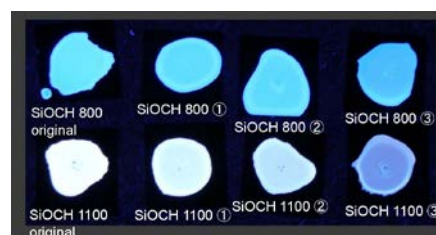


Fig. 1 Photo image of S800 (upper) and S1100 (lower) after the proton beam irradiation, Original, ① $1 \times 10^{13}/\text{cm}^2$, ② $3 \times 10^{13}/\text{cm}^2$, ③ $1 \times 10^{14}/\text{cm}^2$.

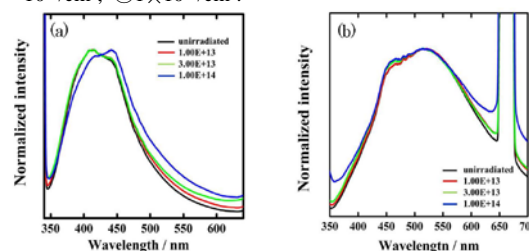


Fig. 2 PL spectra of S800 and S1100 after 1×10^{13} - $1 \times 10^{14}/\text{cm}^2$ proton beam irradiation, (a) S800, (b) S1100 (by S. Watase and K. Matsukawa, Osaka Municipal Technical Research Institute).

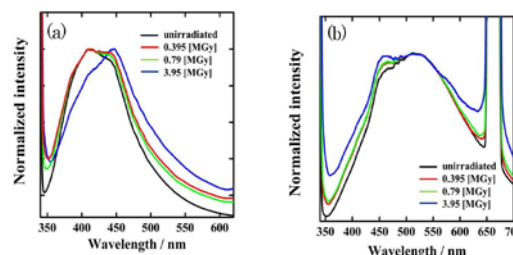


Fig. 3 PL spectra of S800 and S1100 after 0.395-3.95 MGy electron beam irradiation, (a) S800, (b) S1100 (by S. Watase and K. Matsukawa, Osaka Municipal Technical Research Institute).

放射線照射による見た目の発光の変化は、新たな光吸収成分の導入 (E' センター類似?) によって説明可能であることがわかった。短寿命の青色成分については、照射が発光中心の構造変化に影響している可能性がある。

References

- 1) M. Narisawa et al., J. Am. Ceram. Soc. 95 (2012) 3935.
- 2) M. Narisawa et al., Bull. Chem. Soc. Jpn. 85 (2012) 724.
- 3) 成澤雅紀他, セラミックスデータブック (工業製品技術協会) 40 (2012/2013) 132-35.

4 - 22 Contribution of Aeolian Dust in Ichinomegata Estimated from Electron Spin Resonance Signal Intensity and Crystallinity of Quartz

K. Nagashima^{a)} and R. Tada^{b)}

^{a)}Research Institute for Global Change, Japan Agency for Marine-Earth Science and Technology,

^{b)}Department of Earth and Planetary Sciences, Graduate School of Science, The University of Tokyo

The sediments from Ichinomegata, locates in the Oga peninsula, are expected to contain aeolian dust (Kosa) from Asian deserts which potentially records past variations in the Asian monsoon and the westerly jet. However, extracting information about aeolian dust from such lake sediments is difficult because the sediments also contain detrital material from the drainage areas of the lake. Here we try to extract the aeolian dust information in the sediments from Ichinomegata using Electron Spin Resonance signal intensity and Crystallinity of quartz.

日本の湖沼が世界で注目されている。その理由は過去数万年前にまで遡れる年縞(一年に一枚の縞模様)を形成する湖沼堆積物にある。年縞等によって入れられた非常に精度の高い年代目盛によって、福井県・水月湖や秋田県・一の目潟の湖底堆積物は、古気候研究の恰好の材料になっている。こうした年縞を持つ湖沼堆積物を用いて、東アジアの過去の気候変動の実態を解明し、そのメカニズムを検証するのが本研究の大きな目的である。

本研究で注目したのが、湖沼堆積物に含まれる黄砂である。東アジアの中緯度域には広大な砂漠域(たとえばタクラマカン砂漠やモンゴルのゴビ砂漠など)が広がり、これらの砂漠域から舞い上がった黄砂は、上空の偏西風に乗って日本や北太平洋、遠くはアメリカやヨーロッパまで運ばれる。日本の年縞堆積物から黄砂の情報を抽出することができれば、過去の東アジアの乾湿度や上空の大気循環の変遷を検証することができる。そこで、2012年8月に一の目潟で採取したグラビティコア(過去60年ほどの情報を持つ)を用いて、一の目潟の湖底堆積物中に黄砂がどの程度入っているのか、予察的な検証を行った。

黄砂の識別に際して注目したのが、石英の電子スピン共鳴(Electron Spin Resonance; ESR)信号強度および結晶化度(Crystallinity Index; CI)である。石英の E_1' 中心のESR信号強度は、石英中の酸素空格子量を反映しており、母岩の形成年代を反映する指標と考えられている¹⁾。一方、石英のCIは、石英の生成環境を反映する指標と考えられている²⁾。そこで我々はこれらの指標を組み合わせ、黄砂が堆積物に含まれているか否かの検証を行った。石英の E_1' 中心のESR信号強度が正確に酸素空格子量を反映するためには、石英試料に対して、事前に γ 線の照射を行い、更に加熱(300 °C)する必要がある。これは、 γ 線を照射することで石英中に十分な量の電氣的ホールが作られ、さらに加熱することで、電氣的ホールが酸素空格子へ移動し、石英中のすべての酸素空格子が E_1' 中心として存在するようになるためである。そこで本研究では、高崎量子応用研究所において2.5 kGyの⁶⁰Co- γ 線照射を行い、加熱した後、ESR分析を行った。

一の目潟コアに含まれる陸源碎屑物は直径0~300 μ mの粒子から構成されている。日本列島に降下した黄砂の粒径の直径が0~20 μ m程度であることから、20 μ m以上のほとんどが湖周辺から運ばれた碎屑物、一方、20 μ m以下の碎屑物には黄砂が含まれていることが期待される。そこで

本研究では20 μ m以上と4-20 μ m(0-4 μ mはESR・CI分析に適さないため取り除く)の2つにサイズを分けて、各々のサイズ画分に含まれる石英について ESR 信号強度およびCIの測定を行った。

ESR, CI の X-Y プロット(Fig. 1)に示されるように、4-20 μ m以下の石英は20 μ mの石英に比べ高いESR信号強度を持つことが分かった。主な砂漠(タクラマカン砂漠、ゴビ砂漠)の分布と比較した結果、一の目潟に堆積する4-20 μ mの石英の約10-30%(周辺からの石英の値を、ここでは仮に一の目潟>20 μ m 石英の値 ESR = 0.5 ± 0.2 , CI = 6.7 ± 0.5 とした)が黄砂由来の石英であると推測される。当初は、流入河川がないことから、一の目潟の細粒石英のほとんどが黄砂であることを予測していたが、本研究による検証から、黄砂は含まれるものの周辺から運ばれた石英粒子が大部分であることがわかり、黄砂の情報は石英の ESR, CI 結果を頼りに慎重に抽出する必要があることがわかった。

References

- 1) S. Toyoda, Ph. D. Thesis, Osaka University (1992) 106 pp.
- 2) K. Murata and M. Norman, Am. J. Sci. 276 (1976) 1120-30.
- 3) Y. Sun et al, Atmos. Environ. 41 (2007) 8537-48.

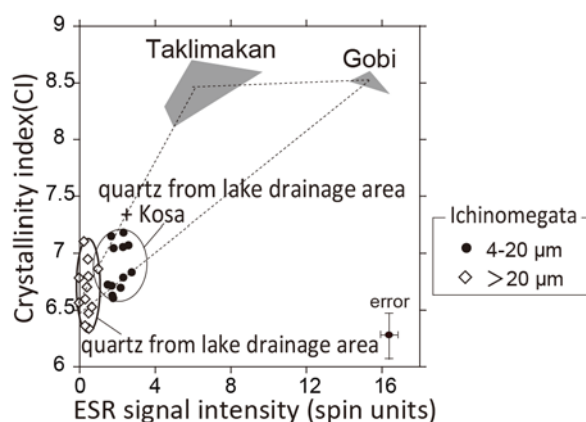


Fig. 1 The relationship between ESR signal intensity and Crystallinity of 4-20 μ m and >20 μ m fractions of samples from Ichinomegata core. Taklimakan Desert and Gobi are also shown as shaded areas³⁾.

4 - 23

Development of Spin-polarized Positron Beam and Its Application to Spintronics Study

A. Kawasuso, M. Maekawa, Y. Fukaya, H. J. Zhang and H. Li

Advanced Science Research Center, JAEA

In 2011 fiscal year, we accomplished the construction of a spin-polarized positron beam apparatus by producing the ^{68}Ge - ^{68}Ga source¹⁾. To establish the foundation of spin-polarized positron annihilation spectroscopy (SP-PAS), we have also studied some ferromagnets²⁾. In 2012 fiscal year, we have started the study of current-induced spin polarization on heavy metal surfaces³⁾.

Spin-up (down) positrons preferentially annihilate with spin-down (up) electrons into two-photons. Positrons and electrons having parallel spins annihilate into three-photons with a considerably smaller probability as compared to that of two-photon annihilation. Hence, in condensed matters, only two-photon annihilation is normally considered as annihilation events. The Doppler broadening of annihilation radiation (DBAR) spectrum (energy spectrum of two-photon annihilation) represents the electron momentum distribution. If both positrons and electrons are spin-polarized, the DBAR spectrum exhibits an asymmetry upon their spin-reversal. We demonstrated that, through this asymmetry, the ferromagnetic band structures of Fe, Co, Ni and Gd can be studied²⁾. Here, we further apply the above method to the Heusler alloys which are anticipated to have 100% spin polarization at the Fermi level. Figure 1 shows the change of the DBAR spectra under a magnetic field (1 T) obtained for Co_2MnAl (CMA), Co_2MnSi (CMS) and NiMnSb (NMS). These show different electron momentum distributions in magnetic field. The majority spin electrons of CMA have more d-like character. Replacing Al with Si, CMS tends to exhibit a little s-like character. In the case of NMS, the majority spin electrons are more s-like.

Current-induced spin polarization (CISP) on non-magnetic material surfaces has attracted much attention due to the rapid development of spintronics devices and

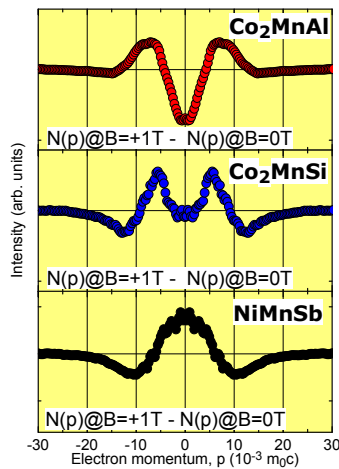


Fig. 1 Change of DBAR spectra in a magnetic field (1 T) obtained for the Co_2MnAl , Co_2MnSi and NiMnSb samples.

their underlying physics. Spin current arises from the spin-orbit (SO) interaction between the conduction electrons and nuclei, which then causes CISP. The Rashba SO interaction, which originates from space-reversal symmetry-breaking at a surface, gives rise to CISP near surfaces and interfaces. Recently, markedly large spin Hall effect and Rashba effect are observed for Pt and Au. Thus, it is particularly interesting to use newly developed surface-sensitive tools to investigate CISP on Pt and Au surfaces. Spin-polarized electrons can be detected through self-annihilation of positronium, which is a bound state of a positron and an electron. When positronium is emitted into vacuum, positrons pick up surface electrons near the Fermi level. The detection limit of spin polarization is low (10^{-3} (0.1%)) for normal positron spin polarization ($\sim 30\%$). These are major advantages for studying surface spin phenomena. Figure 2 shows the three-photon annihilation intensity of positronium generated on Pt and Au surfaces as a function of successive current reversal. The oscillations observed for the Pt surfaces indicate the occurrence of CISP. From the amplitudes of the oscillations, the spin polarizations were more than 1%. Possible reasons for this large CISP on the Pt surfaces are currently considered in relation to the Rashba effect and the ferromagnetism associated with the outermost surface state³⁾.

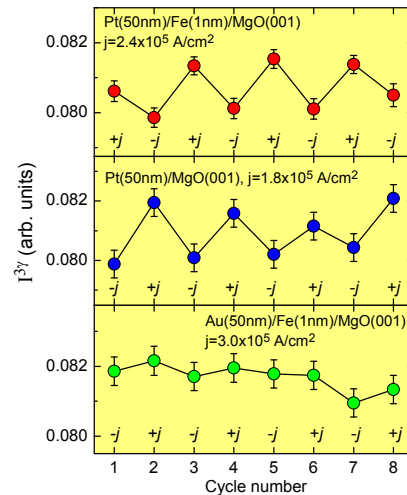


Fig. 2 Three-photon annihilation intensity upon successive current reversal observed for the Pt and Au surface. (j_+) and (j_-) denote the direction of current applied for the sample. Current and positron spin polarization directions are perpendicular to each other.

References

- 1) M. Maekawa et al., Nucl. Instrum. Meth. B **308** (2013) 9-14.
- 2) A. Kawasuso et al., Phys. Rev. B **85** (2012) 024417.
- 3) A. Kawasuso et al., J. Magn. Magn. Mater. **342** (2013) 139-43.

4 - 24

Complementary Study of Vacancy Defects in Si Substrates by Using SPM and EBIC Method

M. Maekawa and A. Kawasuso

Advanced Science Research Center, JAEA

Electron beam induced current (EBIC) method provides the spatial distribution of defects in semiconductors¹⁾. This method is based on a phenomenon that electron-hole pairs induced by electron bombardment in a depletion layer recombine at defects and hence the electric current is reduced near the defect region. Scanning positron microscope (SPM) is a powerful tool for observing spatial distribution of vacancy defects near the subsurface region. We have constructed a SPM by using a specially fabricated small source and a solid neon moderator²⁾. In our system, the simultaneous acquisition of the SPM and EBIC images is possible. In this work, a complementary study of vacancy defects in Si substrates by using SPM and EBIC method were carried out for the same samples.

Samples used in this work was *n*-type Si crystals (10 × 10 mm) with SiO₂ film of the thickness of 50 nm. Helium ion implantation was carried out through an aluminum mask with four holes. After implantation, Au gate electrodes and ohmic contacts were fabricated on the front sides and backsides of the sample. A focused positron and an

electron beam were scanned to obtain a special distribution of positron annihilation parameter (S-parameter) and an EBIC image.

Figure 1 shows the obtained EBIC and SPM images. In the ion-implanted regions, dark contrasts are observed when the gate bias, which induces the depletion layer, was applied. This means that implantation-induced defects act as carrier recombination centers. In the ion-implanted region, S parameter also increases. This is attributed to the annihilation of positrons at vacancy defects introduced by the ion implantation.

Figure 2 shows that the Doppler broadening of annihilation radiation (DBAR) spectrum obtained in the high S parameter region (inside the circle in Fig. 1) and several theoretical DBAR spectra of V2 (divacancy), V18 (vacancy cluster), V2+He and V2+2He (complex of divacancy and He atoms) defect structures³⁾. The experimental DBAR spectrum is differentiated by the spectrum of the unimplanted silicon. Similarly, the theoretical DBAR spectra are differentiated by the spectrum of the perfect Si. Within these models, the divacancy occupied by one He atoms (V2+He) better reproduces the experimental result.

The combined SPM and EBIC method which can provide spatial distribution of electrical active vacancy defects is expected to be an important evaluation tool in the semiconductor device process.

References

- 1) P. R. Wilshaw, Ultramicroscopy 31 (1989) 177.
- 2) M. Maekawa and A. Kawasuso, App. Surf. Sci. 255 (2008) 39-41.
- 3) M. Maekawa and A. Kawasuso, J. Phys. Conf. Ser. 225 (2010) 012032.

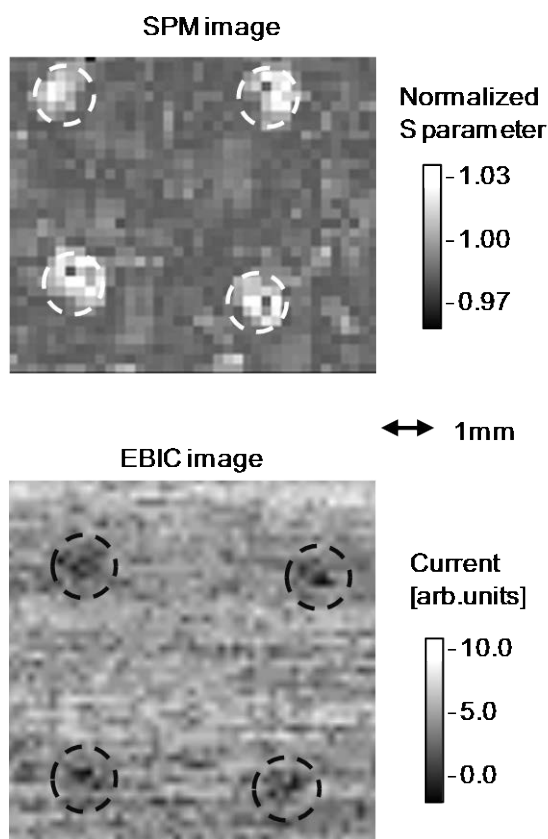


Fig. 1. Distributions of S parameter and corresponding EBIC image.

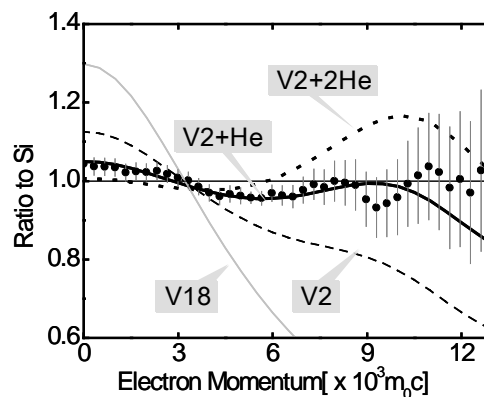


Fig. 2 DBAR spectrum in the high S parameter region. Theoretical curves for several defect structures are also shown.

4 - 25 Positron Annihilation Lifetime Study of Cation Vacancies in Electroceramics

M. Ryu and T. Suzuki

R & D Center, TAIYO YUDEN CO., LTD.

Atomic vacancies of oxide electro-ceramics are studied by Positron Annihilation Lifetime Spectroscopy (PALS). SrTiO_3 single crystals show three lifetime components corresponding to an average lifetime between bulk and V_{Ti} , and lifetimes for $V_{\text{Sr}}-V_{\text{O}}$ complexes and nanosize voids. Moreover, Li insertion of $\text{Li}_4\text{Ti}_5\text{O}_{12}$ used for anode material in the lithium ion battery is studied by PALS.

誘電体やセンサー、不揮発性メモリなど多くの電子デバイスへの応用が研究されている SrTiO_3 の物性は、添加物や空孔の濃度によって大きく変化する。 SrTiO_3 中の空孔について、陽電子寿命測定による評価を試みた。また、リチウム二次電池負極材料である $\text{Li}_4\text{Ti}_5\text{O}_{12}$ について、Li 挿入による陽電子寿命の変化を調べた。

陽電子寿命測定は、 ^{22}Na を同一の試料で挟む一般的な方法を用いた。試料として、 SrTiO_3 単結晶（フルウチ化学）を用いた。無添加の単結晶、La 0.075 wt%、La 0.38 wt%、Nb 0.1 wt%、Nb 0.2 wt% をそれぞれ添加した単結晶に加え、Ti 蒸着と真空熱処理で酸素欠損を導入した単結晶を測定した。 $\text{Li}_4\text{Ti}_5\text{O}_{12}$ は、固相合成した粉末を焼結してペレットとした後、金属 Li と電解液を用いて Li を挿入し、厚さ 100 μm のアルミラミネートフィルムでラミネート加工した。比較の為、Li 挿入無し・ラミネート無し試料と Li 挿入無し・ラミネート有り試料も測定した。

Figure 1 に各種 SrTiO_3 単結晶の陽電子の寿命 τ_1 、 τ_2 、 τ_b 、強度 I_2 を示す。 τ_b は 2 成分系での Trapping model から計算した¹⁾。 τ_1 について、無添加試料と比べ、元素を添加した試料は短い寿命を、酸素欠損導入試料は長い寿命を示した。 τ_2 について、元素を添加した試料は、無添加試料より長い寿命を示した。Nb 0.2 wt% 添加試料のみ、無添加試料と同じ寿命を示した。酸素欠損導入試料は、短い寿命を示した。 τ_2 は、第一原理計算²⁾より得られている V_{Sr} の寿命や関連する複合欠陥 $V_{\text{Sr-3O}}$ の寿命と同程度か、より長かった。より長い寿命は、より大きな複合欠陥、もしくは、 V_{Sr} とナノボイドの平均寿命の可能性を示唆している。全ての試料で、強度 0.5% 前後、寿命 4 ns 前後の τ_3 も測定されており、ナノボイドでのオルトポジトロニウムの形成を示唆している。空隙サイズとオルトポジトロニウムの寿命の関係式から、第三成分の空隙のサイズは 0.4~0.5 nm と推定される。酸素欠損導入試料での τ_2 の減少は、平衡電気伝導度測定の低酸素分圧条件と同様に、陽イオン空孔の減少を示していると考えられる。 τ_b について、無添加試料に比べ、La と Nb を添加した試料は短い寿命を示した。酸素欠損を導入した試料について、無添加試料と差がなかった。これらの τ_b は、第一原理計算²⁾のバルクの寿命と、 V_{Ti} の寿命の中間値であり、これらの平均寿命が測定されていると考えられる。この場合、単純な 2 成分系での Trapping model は成立しないが、定性的には、元素添加による τ_b の減少は、 V_{Ti} の減少を意味すると考えられる。これらの陽電子寿命測定の結果から、添加元素による V_{Ti} の減少と、ナノボイドの形成が示唆された。

$\text{Li}_4\text{Ti}_5\text{O}_{12}$ について、Li 挿入とラミネートの有無に関わらず、 τ_b は 210 ± 5 ps の範囲に収まった。この値は、 $\text{Li}_4\text{Ti}_5\text{O}_{12}$ のバルク中の消滅と考えられる。これに対し、Li の挿入によ

り、 τ_2 は 476 ± 45 ps から 428 ± 25 ps に減少、 I_2 は $13.2 \pm 2.1\%$ から $21.5 \pm 2.8\%$ に増加した。Li 挿入前の $\text{Li}_4\text{Ti}_5\text{O}_{12}$ について、ラミネートがないと τ_2 は 620 ± 76 ps、 I_2 は、 $2.0 \pm 0.6\%$ だった。 τ_2 は、ラミネートの有無により変化しており、 $\text{Li}_4\text{Ti}_5\text{O}_{12}$ 自体の寿命成分とラミネート自体の寿命成分が混ざっていると考えられる。試料を覆うラミネートは、Li 挿入反応後に装着された為、Li 挿入によるラミネート自体の構造変化はない。よって、陽電子寿命 τ_2 と強度 I_2 の変化は、Li 挿入による構造変化を捉えている可能性が高い。しかし、試料本来の寿命については、ラミネート由来の寿命成分が影響する為、本実験の範囲では得られなかった。

SrTiO_3 について、バルクの寿命成分と V_{Ti} の寿命成分は直接分離できなかったものの、それらの平均寿命の変化として捉えられた。 V_{Sr} に関連する寿命成分 τ_2 も測定されたが、ナノボイドとの平均寿命として測定されていると考えられる。時間分解能の問題から、各空孔の寿命の正確な測定は難しいものの、文献値との比較から、空孔量の変化を定性的に検出できたと考えている。更に、Li 二次電池負極材料である $\text{Li}_4\text{Ti}_5\text{O}_{12}$ の Li 挿入の有無による陽電子寿命の変化が捉えられた。

本研究成果は、独立行政法人日本原子力研究開発機構の先端研究施設共用促進事業によるものである。

References

- 1) M. J. Puska and R. M. Nieminen, Rev. Mod. Phys. **66** (1994) 841.
- 2) R. A. Mackie et al., Phys. Rev. B **79** (2009) 014102.

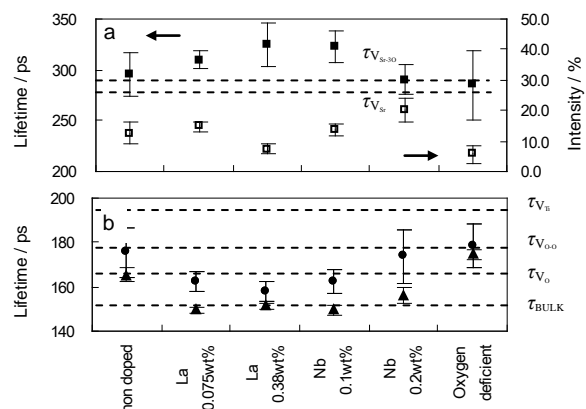


Fig. 1 Results of positron experiments in SrTiO_3 samples. a) τ_2 (filled square) and I_2 (open square), b) τ_1 (filled triangle) and τ_b (filled circle). Broken lines indicate calculated value from Ref. 2.

4 - 26 Yield of Transient Species in NaBr Aqueous Solution Irradiated with Pulsed H^+ , C^{5+} and Ne^{8+} Ions

K. Iwamatsu^{a,b)}, M. Taguchi^{a)}, Y. Sugo^{c)}, S. Kurashima^{d)},
S. Yamashita^{b)} and Y. Katsumura^{b)}

^{a)}Environment and Industrial Materials Research Division, QuBS, JAEA,

^{b)}The University of Tokyo, ^{c)}Medical and Biotechnological Application Division, QuBS, JAEA,

^{d)}Department of Advanced Radiation Technology, TARRI, JAEA

Heavy ion beams are well-known as high linear energy transfer (LET) radiations and induce specific irradiation effects differing from those of low LET radiations. These specific effects are attributed to initial dense and heterogeneous distributions along ions' trajectories¹⁾. The distributions depend on the energy and mass of the incident ions. Therefore, the systematic investigations by changing energy and mass are important. The LET effects have been investigated by using water and aqueous solutions in the past because water is considerable substance for the radiation biology. Hydroxyl radical ($\cdot OH$) is one of the most important water decomposition radicals. Reaction intermediates of $\cdot OH$ with solute were observed by the time-resolved spectroscopic method²⁾.

NaBr was selected as a probe reagent for $\cdot OH$ since $\cdot OH$ reacts with Br^- to produce $Br_2^{\cdot-}$, which has a large extinction coefficient ($\epsilon = 9000 \text{ M}^{-1}\text{cm}^{-1}$ at 375 nm)³⁾. NaBr aqueous solutions (0.009-900 mM) were irradiated with 10 μs pulsed ions (19.2 MeV/u H^+ , 15.8 MeV/u C^{5+} and 12.8 MeV/u Ne^{8+} ions) provided from an AVF cyclotron in TIARA facility. Absorbance of $Br_2^{\cdot-}$ at 375 nm was observed by the time-resolved spectroscopic method. Dependences of the absorbance on incident ion energy were investigated by setting Al films, which have several thicknesses, above sample cell.

The absorbance of $Br_2^{\cdot-}$ sharply increased within the ion pulse and then decreased bi-molecularly. The absorbance at the pulse end decreased with the decrease in the incident energy. Formation yield: $d(G(Br_2^{\cdot-})E)/dE$ (number of molecules per 100 eV) of $Br_2^{\cdot-}$ was estimated by

differentiating the fitting function of a number of $Br_2^{\cdot-}$ molecules to the ion energy. The formation yield of $Br_2^{\cdot-}$, which is strongly related to the amount of $\cdot OH$, increased with the increase in the energy and also decrease in the mass as shown in Fig. 1. When H, C and Ne ions have the same energy, their track radii are the same but the deposited energy density increases with the mass of the incident ions. The initial density of the produced $\cdot OH$ increases in response to a deposited energy density, and recombination reactions of radicals, for example, $\cdot OH + \cdot OH$, $\cdot OH + e^-_{aq}$ and $\cdot OH + \cdot H$, increase in an early time scale. Scavenging time of $\cdot OH$ by Br^- can be estimated from the concentration of NaBr and rate constant ($k = 1.1 \times 10^{10} \text{ M}^{-1}\text{s}^{-1}$). Here, the concentration was changed for changing the scavenging times in the range $10^{-10} - 10^{-5} \text{ s}$. The formation yield of $Br_2^{\cdot-}$ obtained for 10 MeV/u ions decreased from 1.7 to 0.1 in response not only to the ion mass but also the scavenging time (Fig. 2). The yield of $\cdot OH$ decreases as the elapsed time or as the deposited energy density increases¹⁾. Our results are consistent with them. Precise analyses to clarify the behavior of $\cdot OH$ in the track are in progress as a function of initial distribution of radicals and diffusion and reaction of radicals.

References

- 1) Jay A. LaVerne, Radiat. Res. 153 (2000) 487.
- 2) K. Iwamatsu et al., Trans. Mater. Res. Soc. Jpn. 36 (2011) 329.
- 3) M. Kelm and E. Bohnert, Forschungszentrum Karlsruhe GmbH, Karlsruhe (2004).ISSN 0947-8620.

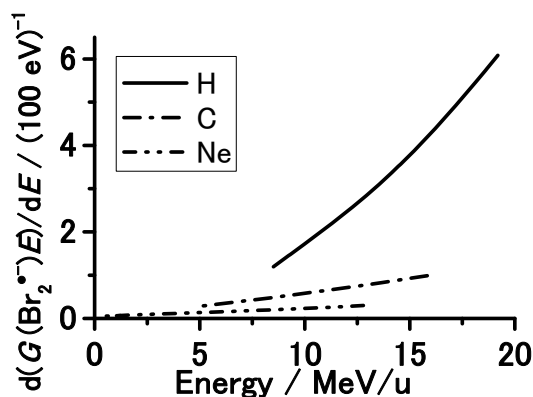


Fig. 1 Energy dependence of $Br_2^{\cdot-}$ yields estimated in 90 mM NaBr aqueous solution.

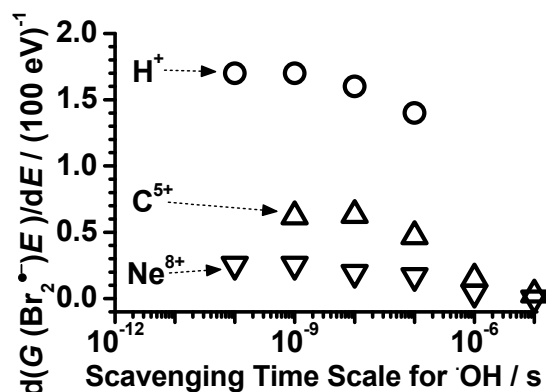


Fig. 2 Scavenging time dependence of $Br_2^{\cdot-}$ yields. Energy of each ion is 10 MeV/u.

4 - 27 Transient Absorption Spectra of Biphenyl-Dodecane Solution Measured by Microsecond Ion Pulse Radiolysis

T. Kondoh^{a)}, K. Iwamatsu^{b)}, M. Taguchi^{b)}, S. Kurashima^{c)}, J. Yang^{a)}, K. Kan^{a)},
H. Shibata^{a)} and Y. Yoshida^{a)}

^{a)} ISIR, Osaka University, ^{b)} Environment and Industrial Materials Research Division, QuBS, JAEA, ^{c)} Department of Advanced Radiation Technology, TARRI, JAEA

To reveal initial processes of ion beam induced track reactions in dodecane, microsecond time-resolved ion-pulse radiolysis system was developed at TIARA facility. Time dependent behaviors and transient spectra of optical absorption were measured in biphenyl-dodecane solution irradiated with 220 MeV C⁵⁺ ions.

重粒子線がん治療やイオンビーム照射による植物の品種改良、イオン注入による材料改質などの応用技術が注目されている。これらのイオンビーム応用技術は、高LET放射線であるイオンビームが生成する高密度イオン化効果によるものが多いが、イオンビームの高密度イオン化状態における活性種反応の初期過程の直接観測は困難なため詳細には理解されていない。高密度イオン化による活性種の時間挙動を解明するために、原子力機構の田口らは、チョッパーのゲート幅を変化させることにより、数千パルスにわたるパルス列を得てマクロパルスとして試料に照射し、マクロパルスのパルス幅より長い時間領域で活性種の光吸収時間挙動を観測可能なマイクロ秒重イオンパルスラジオリシスを開発した¹⁾。

我々は、代表的な非極性溶媒であり核燃料サイクルにおける抽出溶媒でもあるドデカンの分解及び水素発生の基礎過程の解明を目指しており、特に重イオンを照射した場合の高密度イオン化効果を解明するために、国内で唯一のマイクロ秒重イオンパルスラジオリシスシステムを用いた。前年度にも重イオンが誘起するピレン-ドデカン溶液中の過渡吸収を測定したが、単一波長での測定のため活性種の種類を同定できていなかった。今年度は、多波長で測定することにより、活性種を同定し、反応挙動を解明することを目的とした。

約1,000個のマイクロパルスを持つマクロパルスをHYポートに輸送し、試料に照射して溶媒の活性種や溶質との反応を誘起した。1,000パルス照射しても吸光度は 10^{-3} 以下であることが多く、これを観測するために分析光には高安定な半導体レーザーを用いた。

220 MeV C⁵⁺イオンビームを20 mM ビフェニル-ドデカン溶液に照射し、375 nm, 447 nm, 532 nmで測定した結果をFig. 1に示した。50 μ sまでに重イオンマクロパルスにより吸光度が増加した。375 nm ではパルスエンド直後から100 μ sにかけて吸光度の減衰が観測されたが、その後900 μ sに至るまでほぼ一定であった。一方532 nmでは、パルスエンドまで吸光度が増加し900 μ sまでほぼ減衰しなかった。447 nmでは光吸収がほとんど観測されなかった。

各波長における時間挙動から得たパルスエンドにおける過渡吸収スペクトルをFig. 2に示した。375 nm付近の光吸収帯は、その吸光度がビフェニル濃度に依存することや減衰の速度から、高密度イオン化状態による再結合を逃れた長寿命のビフェニル三重項励起状態と考えられる。しかしながら、完全な同定を行うためには400 nm付近で詳細に観測波長を変える、あるいは別の捕捉剤を加えた測定が必要である。532 nm付近の吸収帯はビフェニル濃度に依存しな

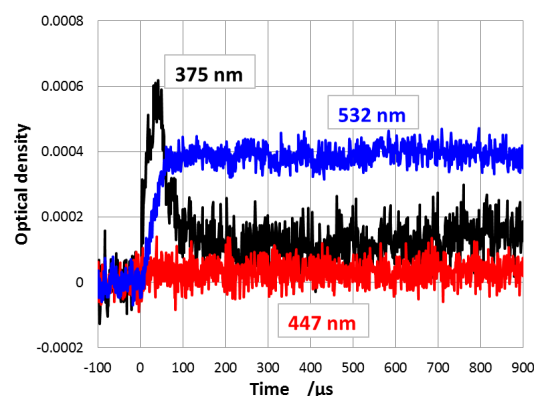


Fig. 1 Time dependent behaviors of 20 mM biphenyl dodecane solution at 375, 447 and 532 nm.

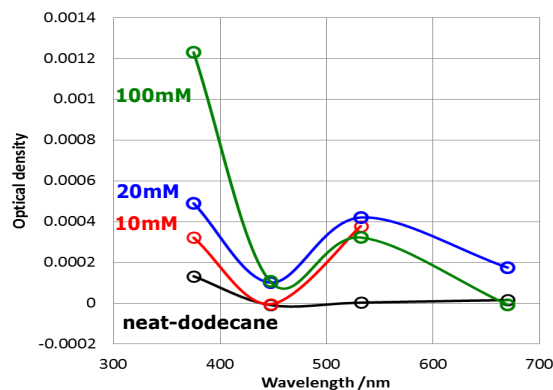


Fig. 2 Transient absorption spectra of biphenyl dodecane solution for different concentration of biphenyl.

いが線量依存性を示すことから、ビフェニルの反応生成物などと考えられる。また、以前の測定では447 nmにドデカンの過渡吸収を得たため、447 nmの吸光度については再測定を行う予定である。測定波長を変更する毎にプローブ光源を変えるため、イオンビームとプローブ光の重なり条件が変わった可能性があり、Fig. 2のスペクトルの形状解析には課題が残っている。このため、光源の変更を必要としない重イオンビーム誘起過渡スペクトル測定システムが必要である。ドデカンの活性種を同定するために、電子捕捉剤やカチオン捕捉剤を用いたスペクトル測定を予定している。

Reference

- 1) M. Taguchi et al., Radiat. Phys. Chem. 78 (2009) 1169-74.

4 - 28 Observation of Scintillation Behavior under Pulsed Ion Beam Irradiation

M. Koshimizu^{a)}, M. Taguchi^{b)}, S. Kurashima^{c)} and K. Asai^{a)}

^{a)}Department of Applied Chemistry, Graduate School of Engineering, Tohoku University,

^{b)}Environment and Industrial Materials Research Division, QuBS, JAEA,

^{c)}Department of Advanced Radiation Technology, TARRI, JAEA

A large number of novel scintillation materials for neutron detection have been developed due to recent demands for high-quality neutron detection techniques. In solid scintillators for neutron detection, neutrons are converted into energetic heavy charged particles via nuclear reaction, and scintillation is induced by such particles. The linear energy transfer (LET) of such particles is much higher than those of high energy photons or electrons. Such difference in LET may lead to different scintillation behaviors for detection events of high energy photons and neutrons, and discrimination of the neutron/photon detection events may be possible on the basis of the difference in the scintillation spectrum or decay behavior¹⁾. In order to develop novel scintillation materials enabling such discrimination, observation of scintillation behavior at high LET is indispensable.

In this study, we have attempted to observe scintillation decay under pulsed ion beam irradiation. The irradiation was performed by using the AVF cyclotron at TIARA. Samples were irradiated with a pulsed beam of 20 MeV H, 50 MeV He, or 220 MeV C, and scintillation time profile was recorded using a photomultiplier tube (HAMAMATSU, R7400) and a digital oscilloscope. The scintillation time profile was obtained as an average of detection signals of 1000 pulses. Wavelength-dependent time profile was obtained by using a band pass filter in the front of the PMT window. Figure 1 shows a schematic diagram of the measurement system.

Figure 2 shows the scintillation time profile of a plastic scintillator, BC400, under 220 MeV C irradiation. The full width at half maximum (FWHM) was approximately 5 ns. Taking into account of the scintillation rise time and decay time constant of 0.9 and 2.4 ns, respectively, in BC400, the time resolution was estimated to be significantly less than 5 ns. This time resolution is enough to observe the scintillation behavior of the time scale longer than several nanoseconds.

Figure 3 shows the scintillation time profiles under 220 MeV C irradiation of a Li-glass scintillator, GS20, at different wavelength region. The wavelength-dependent scintillation time profiles have successfully been observed by using band pass filters.

Reference

- 1) A. Yamazaki et al., Nucl. Instrum. Meth. Phys. Res. A 652 (2011) 435.

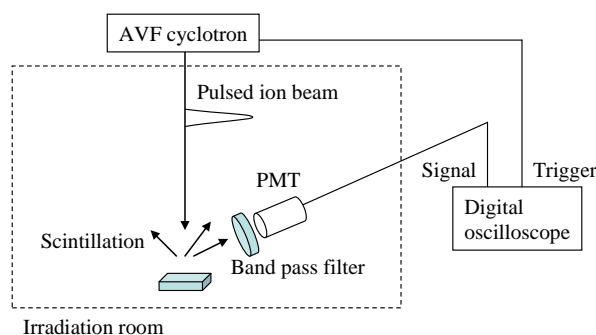


Fig. 1 Schematic diagram of measurement system.

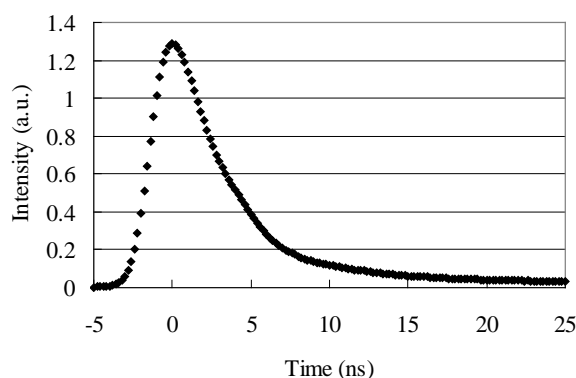


Fig. 2 Scintillation time profile of a plastic scintillator, BC400, under 220 MeV C pulsed beam irradiation.

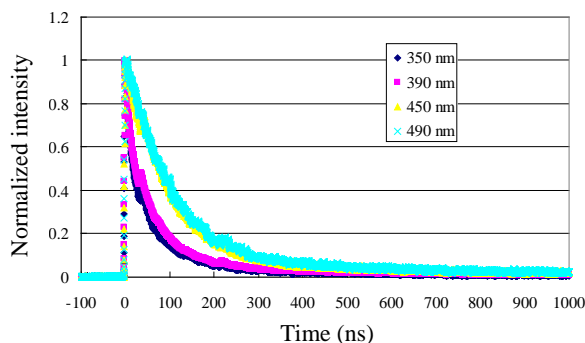


Fig. 3 Scintillation time profiles under 220 MeV C irradiation of a Li-glass scintillator, GS20, at different wavelength region.

4 - 29 Solvent Effect on Copolymerization of Maleimide with Styrene Induced by Ion Beam Irradiation

S. Nakagawa^{a)}, M. Taguchi^{b)} and A. Kimura^{b)}

^{a)}Tokyo Metropolitan Industrial Research Institute,

^{b)}Environment and Industrial Materials Research Division, QuBS, JAEA

The radiation-induced polymerization of styrene with maleimide was studied in methanol, ethanol, and 2-propanol solutions by irradiation of H-20 MeV, He-50 MeV, He-107 MeV and C-320 MeV. The polymer yield increased in the order of methanol, ethanol, and 2-propanol, depending on the reactivity of the solvent radical to initiate the polymerization. Though the polymer yield decreased with increasing LET value in 2-propanol, the yield by irradiation of He-50 MeV was the lowest in the methanol and ethanol solutions. Not only the LET value but also the specific energy of the ions and the reactivity of the solvent radical to initiate the polymerization will influence the polymer yield and the distribution of the molecular weight.

2-プロパノール中でマレイミド ($C_2H_2(CO)_2NH$) とスチレンを放射線共重合したところ、平均分子量およびポリマー生成量は線量率が減少するほど増加し、この効果は LET の大きい重イオンビームほど顕著であった。また、ポリマー生成量は LET が高いと減少するが、高 LET 線源により低線量率で照射すると高分子量のポリマーが生成することがわかった¹⁾。時間的空間的なラジカル分布が、ポリマーの分子量や生成効率に影響を与えると考えられる。一方、溶媒ラジカルのヒドロキシマレイミドへの付加反応の効率は 2-プロパノールに比較してメタノールでは 1/2 以下であった²⁾。そこで、溶媒ラジカルのマレイミド付加反応の効率が放射線重合に及ぼす影響について検討することとした。

マレイミドおよびスチレンをメタノール、エタノール、2-プロパノールに溶かし (各 0.5 mol/L)、窒素置換した試料に原子力機構高崎量子応用研究所において、イオンビーム (C-320 MeV, He-50, 107 MeV, H-20 MeV) を照射した。照射により白色微粒子が生成した。微粒子をメンブランフィルターで回収し、生成物の質量を測定した。また、テトラヒドロフランに溶解し、分子量分布をゲル浸透クロマトグラフで分析した。

Table 1 にイオンビーム 1 kGy あたりのポリマー生成量を示す。イオン種に関わらず、メタノール < エタノール < 2-プロパノールの順でポリマー生成効率が増加した。また、2-プロパノール中では照射イオンの LET が増加すると生成効率が低下するが、エタノールおよびメタノール中では、He-50 MeV の照射による生成効率が最も低かった。Figure 1 に、He-50 MeV ビームを 200~240 秒照射した試料の分子量分布を示す。エタノールおよびメタノール中では、保持時間 9 分程度の高分子量ポリマーと比較して、保持時間 10 分程度の低分子量ポリマーの生成割合が高いことがわかる。低分子量ポリマーの生成割合が大きいことが、ポリ

マー生成量が少なくなった一因と考えられる。高分子量ポリマーがポリマーラジカル同士の結合で生成するのに対し、低分子量ポリマーはポリマーラジカルと溶媒ラジカルの結合で生成したと考えられ、どちらが主反応となるかはポリマーラジカルと溶媒ラジカルの割合と分布に起因する。He-50 MeV は、他のイオン種と比較して一核子あたりのエネルギーが 1/2 程度でイオントラック半径が小さいため、初期ラジカル分布がより局在化していると考えられる。このため、重合の開始反応である溶媒ラジカルの付加反応が遅いと、ポリマーラジカルの相対的な濃度が低く溶媒ラジカルと結合する確率が増加し、低分子量ポリマーの生成割合が増加したと考えられる。

以上のように、放射線誘起ラジカル重合反応において LET のみならず、一核子あたりの初期エネルギーや溶媒ラジカルの付加反応速度がポリマー生成効率や分子量分布に影響を与えることがわかった。

References

- 1) S. Nakagawa, M. Taguchi, and A. Kimura, Radiat. Phys. Chem., 80 (2011) 1199-202.
- 2) S. Nakagawa, Radiat. Phys. Chem., 79 (2010) 705-09.

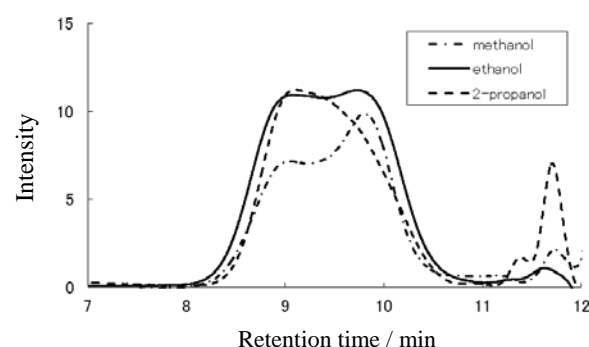


Fig. 1 The distribution of the molecular weight of the polymer obtained by irradiation of He-50 MeV.

Table 1 The yield of polymer by 1 kGy irradiation of ion beams.

Irradiation source	LET eV/nm	2-propanol	ethanol	methanol
H-20 MeV	2.2-13	3.7	2.9	1.6
He-107 MeV	7.1-60	2.21	1.14	0.50
He-50 MeV	13-100	1.07	0.52	0.22
C-320 MeV	75-600	0.71	0.71	0.38

Unit of the polymer yield: mg/mL/kGy

4 - 30 **Measurements of Low Energy Neutron Spectra Using the TOF Method in Quasi-monoenergetic Neutron Fields at TIARA**

T. Matsumoto^{a)}, A. Masuda^{a)}, H. Harano^{a)}, Y. Tanimura^{b)}, M. Yoshizawa^{b)},
H. Seito^{c)} and K. Mizuhashi^{c)}

^{a)}National Metrology Institute of Japan, National Institute of Advanced Industrial Science and Technology, ^{b)}Department of Radiation Protection, NSRI, JAEA,
^{c)}Department of Advanced Radiation Technology, TARRI, JAEA

Precise measurements for high-energy neutrons are important in studies on neutron dose estimation around large accelerator facilities such as J-PARC, nuclear data, exposure in aircrafts and neutron induced soft error rate in semiconductor devices. High energy quasi-monoenergetic neutron fields at energies of 45 MeV, 60 MeV and 75 MeV at the cyclotron facility TIARA are promising candidates for reference fields in order to calibrate measurement devices¹⁾. The peak neutron fluence was measured with a proton recoil telescope and a liquid scintillator^{1,2)}. However, it is also necessary to precisely evaluate neutron spectra of the low energy region in the field³⁾, because most of neutron dosimeters have large sensitivity for low energy neutrons. In TIARA, quasi-monoenergetic neutrons were produced by the $^7\text{Li}(p,n)$ reaction. In previous measurements with the TOF method, it is difficult to measure the neutron spectra below approximately 10 MeV by limitations for pulse intervals of ion beams from the AVF cyclotron and the distance from the neutron production target. In the present experiments, it was possible to measure the neutron spectrum below 10 MeV by the TOF method, because ion pulses with intervals over 1 μs from the AVF cyclotron were obtained by using S- and P-chopper systems developed by Kurashima et al⁴⁾. The neutron spectrum of low energy region in the field was measured by the TOF method. An organic liquid scintillator ($3'' \times 3''$ NE213) was used to measure neutron energy spectra above 1.5 MeV. A ^6Li -glass scintillator (GS20) was used to measure neutron energy spectra below 1.5 MeV. The NE213 and the ^6Li -glass scintillators were placed 6.5 m away from the target. The detection efficiency of the NE213 was determined by calculation with the SCINFUL-QMD code⁵⁾ as well as by calibration with mono-energetic neutrons at AIST. The detection efficiency of the ^6Li -glass scintillator was obtained from calibration using mono-energetic neutrons at AIST. Figure 1 shows the neutron spectra for 45 MeV and 60 MeV neutrons measured with the NE213 detector by the TOF method. Figure 2 shows the neutron spectrum measured with the NE213 and the ^6Li -glass scintillator. The neutron spectra in keV region are successfully obtained using the S- and P- chopper systems. The evaporation spectrum produced by the target is also shown around 1 MeV in Fig. 2. We will also obtain the neutron spectra measured with a Bonner sphere

spectrometer by means of an unfolding method. After measurements with the Bonner sphere spectrometer, the TOF and unfolding methods will be compared.

It is necessary to evaluate the low energy neutron spectra more precisely to improve the reliability of the experimental results.

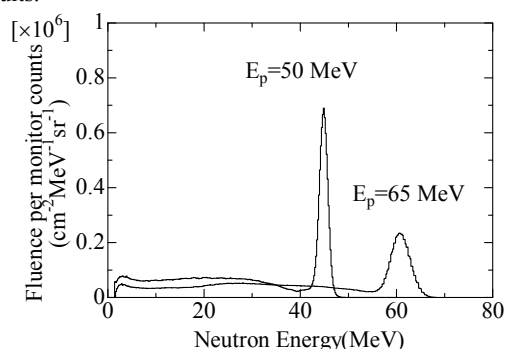


Fig. 1 Neutron spectra for proton energies of 50 MeV and 65 MeV measured with the NE213 scintillator by the TOF method.

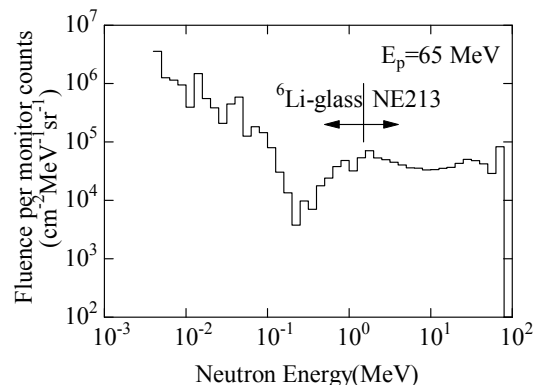


Fig. 2 Low energy neutron spectrum measured with the NE213 and the ^6Li -glass scintillators.

References

- 1) H. Harano et al., Radiat. Meas. 45 (2010) 1076.
- 2) Y. Shikaze et al., Nucl. Instrum. Meth. Phys. Res. A 615 (2010) 211.
- 3) A. Masuda et al., IEEE trans. Nucl. Sci. 59 (1) (2012) 161-66.
- 4) S. Kurashima et al., Proc. CYCLOTRONS 2010, MOPCP090 (2010).
- 5) D. Satoh et al., JAEA-Data/Code 2006-023 (2006).

4 - 31 Measurement of Lineal Energy Distributions for Energetic Ion Beams Using a Wall-less Tissue Equivalent Proportional Counter

S. Tsuda, T. Sato and T. Ogawa

Division of Environment and Radiation Sciences, NSED, JAEA

The biological effects of energetic ion beams have attracted attention, particularly in particle therapies and space activity. Deposit energy distribution in a microscopic site is basic information for evaluating the biological effects of energetic ion beams. In microdosimetry, lineal energy (y) is defined and used in the index of energy deposition in micrometer scale. Lineal energy can express each energy deposition in a microdosimetric scale by a single event of both incident primary heavy ions and secondary particles.

Microdosimetric deposit energy spectra have been measured for various energetic heavy ion beams using a wall-less tissue equivalent proportional counter (wall-less TEPC)^{1, 2)} and used for the verification of the microdosimetric function³⁾ for calculating y distributions incorporated in the PHITS code. In the previous studies, since uniformly spread beam were used to simulate a uniform irradiation to cells, the measured deposit energy spectra include the contribution of both incident heavy ion beams and secondarily produced electrons (delta rays). In this study, to investigate the radial dependence of y distributions, y distributions are measured in radial direction for energetic ions using the wall-less TEPC.

Figure 1 shows the experimental set-up in the HB1 course. The wall-less TEPC²⁾ has a transparent detection part composed of thin wires, the size of which is 3 mm in diameter and 3 mm high. The gas pressure inside the wall-less TEPC is kept at 13.3 kPa so as to simulate a site in tissue measuring 0.72 μm . In the standard position, the centers of the detection part in the wall-less TEPC and the beam monitor are set in a straight line on the trajectory of the incident ion beam. The vertical positions of the wall-less TEPC are changed to measure the y distributions

apart from the incident ion beam. The adjustment of height is performed using a lab jack with precision of 1 mm in the range of z from 2.5 to 15 mm.

The beam monitor consists of 16 plastic scintillation fiber (PSF) arrays. The cross-section of each PSF is 1 mm². By arranging two groups of 8 PSFs at right angles, the ion beam positions are monitored at intervals of 1 mm in 64 mm² area. The signals from the wall-less TEPC and the PSFs are simultaneously recorded on a digital storage oscilloscope. In terms of the energy calibration, a ²⁴⁴Cm alpha source equipped inside the wall-less TEPC is used before and after the irradiation.

Figure 2 presents the pulse height distributions measured at $z=0.0$ and 8.2 μm from the 320 MeV carbon ion beam path, shown in microdosimetric scale unit. In the distribution at $z=0.0$ μm , on the beam path, the peak of the incident carbon ions is clearly seen in the pulse height between 0.5 and 0.6 V. Since the size of the irradiated beam and the detection area are comparable, most of the energy depositions are due to the incident carbon beam. The shape of the pulse height distribution is similar to that of the chord length distribution of the cylindrical detection part. On the other hand, the energy deposition at 8.2 μm away from the beam path ranges up to 0.3 V but most of the signals are found in the range less than 0.1 V due to the contribution of delta rays. In the next experiment, y distributions under different gas pressures will be obtained for the carbon and other kinds of ion beams.

References

- 1) S. Tsuda et al., Phys. Med. Biol. 55 (2010) 5089.
- 2) S. Tsuda et al., J. Radiat. Res. 53 (2012) 264.
- 3) T. Sato et al., Radiat. Prot. Dosim. 122 (2006) 41.

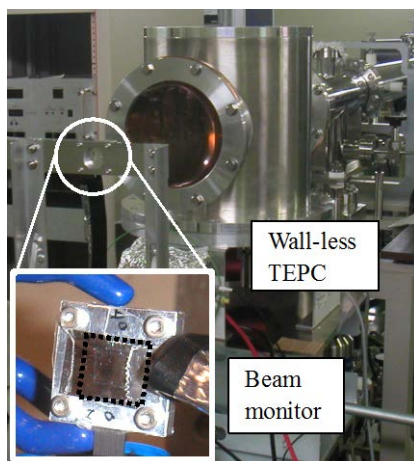


Fig. 1 Experimental set-up at the HB1 line.

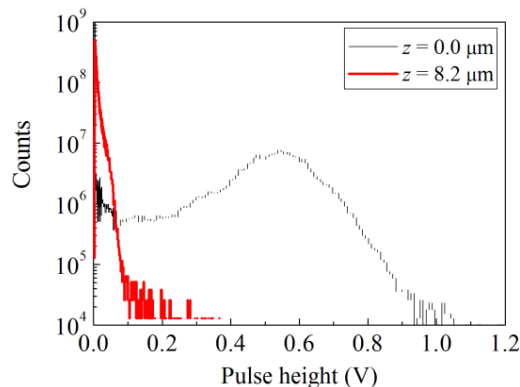


Fig. 2 Pulse height distributions for 320 MeV carbon ion beam, measured at the center of the detection part of the wall-less TEPC ($z=0.0$) and 8.2 μm apart from the beam path, in microdosimetric scale unit.

4 - 32 Fabrication of UV Curable Resin Based Microscopic Devices Using External Scanning Proton Microbeam

T. Sakai^{a)}, R. Yasuda^{a)}, H. Iikura^{a)}, T. Nojima^{a)}, M. Matsubayashi^{a)},
M. Koka^{b)}, T. Satoh^{b)}, T. Ohkubo^{b)} and Y. Ishii^{b)}

^{a)}Materials Science Research Division, QuBS, JAEA,

^{b)}Department of Advanced Radiation Technology, TARRI, JAEA

We have demonstrated micro-machining technique using a UV curable resin and external scanning proton microbeam. A fine hexagonal cylinder array (negative structure of honeycomb pattern) was successfully fabricated. The UV curable resin is very promising material for Proton Beam Writing technique.

1. はじめに

MeV エネルギーのプロトンビーム描画(PBW)による微細加工技術は、レジスト材料に対してアスペクト比の高い加工が可能であり、多くのイオンマイクロビーム施設で研究・利用が行われている。一方、紫外線硬化樹脂は、印刷や塗装などの工業分野で幅広く利用されており、光吸収による硬化が速く、常温常圧で透明な液体の硬化材である。

そこで、PBW 技術の新たな展開を図るため、TIARA 軽イオンマイクロビーム装置の大きな特徴である大気照射技術を活かして、紫外線硬化樹脂への直接描画を行い、新たな微細加工技術の開発を試みた。

2. 実験

紫外線硬化樹脂をマイクロ PIXE 分析用の試料ホルダー¹⁾に塗り、プロトンビームの描画照射を行った。試料のバックング材は 5 μm 厚のポリカーボネート膜であり、真空窓も兼ねている。また、使用した紫外線硬化樹脂は工芸用の市販品である。プロトンビームは、エネルギー 3 MeV、ビーム電流 1~2 pA、ビーム径約 1 μm である。照射パターンは六角柱構造体(ハニカム構造のネガ型、1ユニット 20 μm)であり、CAD ソフトで画像データを作成後、座標データに変換した²⁾。1点当たりの照射時間は 60 μs で、4 回繰り返し照射を行った。

照射後の試料はエタノールで洗浄し、未照射部分の紫外線硬化樹脂を取り除いた。

3. 結果と考察

Figure 1 に作製した六角柱構造体の顕微鏡写真を示す。照射パターン通りに硬化しているのが確認できる。また、バックング材との接合性も良く、1本1本の六角柱がきれいに直立している。

硬化に必要なビーム束(Fluence)は、PMMA 等のレジスト材料に比べ二桁程度低く、非常に感度が高いことが判った。また、照射後の処理もエタノールでの洗浄だけであるので、加工の簡便さという観点からも大変優れていることが判った。

以上の結果から、PBW 技術において、紫外線硬化樹脂は微細加工用のレジスト材料として極めて有効であることが確認できた。

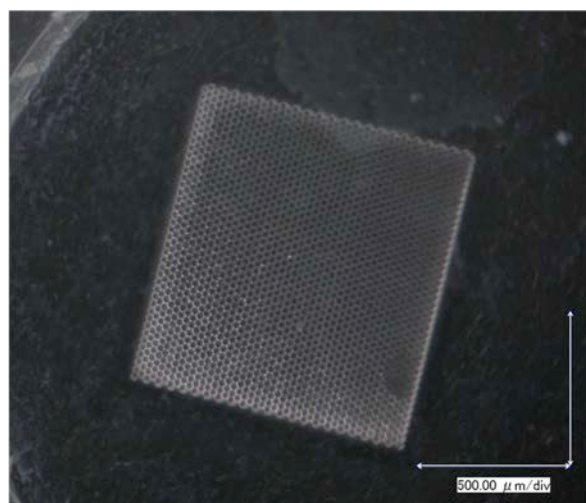


Fig. 1 Microscopic photograph of a fabricated fine hexagonal cylinder array made from a UV curable resin. The hexagonal cylinder is approximately 20 μm in diameter. The scale bars are 500 μm each.

4. 今後の予定

紫外線硬化樹脂は粘度のある液体であるため、機能性を有する粉末を混入することで、様々な機能を有する微細素子を作成することが可能であると思われる。今後は、ZnS (Ag) 等の蛍光体を混入した微細な構造を有する蛍光板の作製を予定しているが、触媒粉末等の利用など、新たな応用への展開が大いに期待できる。

References

- 1) T. Sakai et al., Nucl. Instrum. Meth. B 23 1 (2005) 112.
- 2) T. Sakai et al., JAEA Takasaki Annu. Rep. 2009 (2011) 172.

4 - 33 Preliminary Study on 3D Proton Lithography Using 300 kV Compact Focused Gaseous Ion Beam System

T. Ohkubo^{a)}, Y. Ishii^{a)}, Y. Miyake^{b)} and T. Kamiya^{a)}

^{a)}Department of Advanced Radiation Technology, TARRI, JAEA,

^{b)}Beam Seiko Instruments Inc.

Focused proton beam of several hundreds of keV with micrometer scale range become a powerful tool for high aspect ratio 3-Dimensional structures in proton lithography. Ion beam, especially proton beam, has longer penetration depth into a certain material than electron beam with the same kinetic energy has. When the proton beam's kinetic energy increases, the penetration depth becomes longer. Using different kinetic energy of proton beams for one sample in proton lithography, a three dimensional structure with high aspect ratio can be made by the beam writing directly.

A new 300 kV compact focused gaseous ion beam (gas-FIB) system with three-stage acceleration lens was constructed at JAEA. In the gas-FIB system, the ion is accelerated and focused by rotationally symmetric electrostatic lens without magnetic fields. Since the ion moves in the vicinity of the optical axis (z axis) in the cylindrical coordinates, the ion accordingly behaves in the paraxial approximation described as following equation, called as paraxial ray equation,

$$\frac{d^2 r}{dz^2} + \frac{1}{2V} \cdot \frac{dV}{dz} \cdot \frac{dr}{dz} + \frac{1}{4V} \cdot \frac{d^2 V}{dz^2} \cdot r = 0 \quad (1)$$

where V is the electric potential and then the focal length for a pair of electrodes f is described as follows,

$$f = \frac{4L}{\left(\frac{\varepsilon_{im}}{\varepsilon_{ob}} - 1 \right)} \quad (2)$$

where ε_{ob} and ε_{im} are the kinetic energies of ion beam in object and image sides and L is the distance between the electrodes. The focal length does not change while the kinetic energy ratio is constant, which was defined as the ratio of kinetic energy in object side to that in image side. Therefore, the beam is focused to the same point as long as keeping the ratio constant even if the kinetic energy is

changed. This is the key point of gas-FIB to be expected as a powerful tool for 3D fabrication. The penetration depth can be changed continuously by adjusting voltages of every electrode proportionally while proton beam is irradiated to a sample.

The preliminary experiments of formation of the focused gaseous ion beams were carried out to show the availability of the gas-FIB system as a writing tool for 3D proton lithography. Proton beam energy after the extraction stage and after the first acceleration stage was fixed to 0.6 keV and 2.5 keV, respectively. The beam energy after the second acceleration stage was fixed to ε_{ob} in eq. (2) as the kinetic energy ratio was kept. The final beam energy after third acceleration stage was changed around ε_{im} , for which 100 keV, 120 keV and 140 keV were selected to avoid electric discharge which caused breakdown of measurement devices. Beam diameter was determined using the knife-edge method, in which the beam current was measured by Faraday Cup, gradually cutting the beam by moving a knife-edge. Figure 1 shows the beam diameter as a function of the kinetic energy ratio in the third acceleration stage, (a) with the image side's kinetic energy of around 100 keV, (b) around 120 keV, (c) around 140 keV. Dotted line fitted to plots in those three graphs showed that minimal beam diameter was about 20 μm (FWHM) at the kinetic energy ratio of (a) 6.33, (b) 6.32 and (c) 6.30; in 0.5% difference. A difference of 0.5% for the kinetic energy ratio led to an expansion of only 4% for the beam size. Therefore, it was experimentally proved that the focal point was kept at the same position under changing the kinetic energy with keeping the kinetic energy ratio constant. This characteristic of the gas-FIB is a good point to advance the 3D proton lithography changing penetration depth in a sample by varying the beam energy.

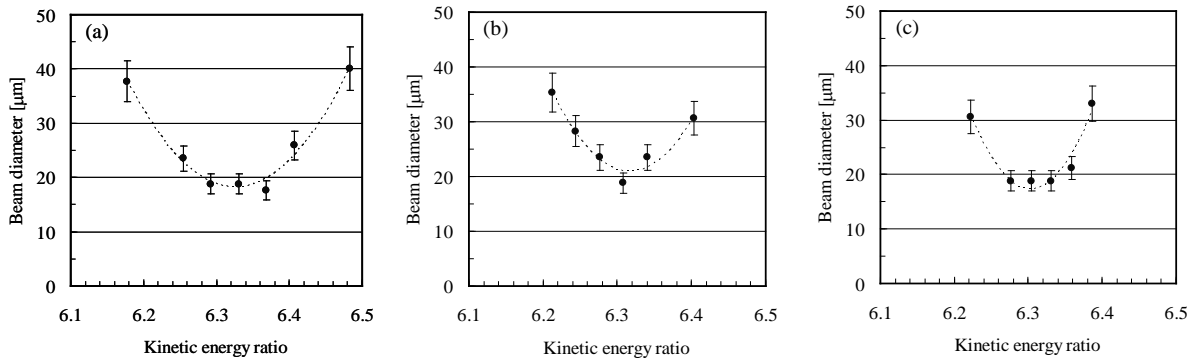


Fig. 1 The beam diameter as a function of the kinetic energy ratio of image side to object side in the third acceleration stage, (a) with the image side's kinetic energy of around 100 keV, (b) around 120 keV, (c) around 140 keV.

4 - 34 Research and Development of an Ultra-high-energy Neutrino Detector Using Radar Reflection in Rock Salt and Ice

M. Chiba^{a)}, T. Kamijo^{a)}, T. Tanikawa^{a)}, F. Yabuki^{a)}, H. Yano^{a)}, M. Utsumi^{b)} and M. Fujii^{c)}

^{a)}Graduate School of Science and Engineering, Tokyo Metropolitan University,

^{b)}Department of Applied Science and Energy Engineering, School of Engineering, Tokai University,

^{c)}School of Medicine, Shimane University

Berezinsky and Zatsepin predicted that ultra-high-energy neutrinos (UHEv's) would be produced at a collision of UHE-cosmic ray with the cosmic-microwave-radiation background in the universe¹⁾. In order to detect them we have searched for and found a radio-wave-reflection effect in rock salt and ice. A gigantic detector is needed for the detection due to the expected ultra-low flux of about $1 \text{ km}^{-2} \cdot \text{d}^{-1}$. When an UHEv interacts with rock salt or ice as a detection medium, a shower is generated. The energy of the UHEv shower converts finally to thermal energy through ionization processes. Consequently, the temperature rises along the shower produced by the UHEv. The refractive index rises as a function of the temperature. The irregularity of the refractive index in the medium for radio waves causes reflection. This reflection effect combined with long attenuation length of radio waves in rock salt and ice would yield a new method to detect UHEv's.

We report on a new experiment to measure power reflection fraction and phase of reflected radio wave from a dielectric medium which was irradiated by an electron beam filled in a coaxial tube (WX-20D) with a diameter of 20 mm and a length of 100 mm. We utilized a 2 MeV electron beam produced by a Cockcroft-Walton accelerator located at the Takasaki Advanced Radiation Research Institute of Japan Atomic Energy Agency. The electron beam was injected into an open end of the coaxial tube set in a dry-ice cooling box. The coaxial tube was filled with rock salt powder or ice. The temperature of salt powder or ice was measured by a chromel-alumel thermocouple positioned 2 mm from the surface of the open end. The refractive indices of rock salt powder and ice were measured by the reflection method in the coaxial tube yielding 1.79 ± 0.01 at 22°C and 1.76 ± 0.01 at -60°C , respectively.

The increase of the refractive index with respect to the temperature gave rise to 435 MHz radio-wave reflection. We observed the reflection effect including phase from ice as well as rock salt as shown in Fig. 1. A model calculation was done to confirm the cause of the radio wave reflection effect. We assumed that the temperature of the ice from the open end to 10 mm inner the coaxial tube was the same as the measured temperature at 2 mm from the open end. The power reflection fraction was calculated based on the telegrapher's equations and the result was in agreement with the Real Time Spectrum Analyzer (RSA) value within 50% during the irradiation and the shape was similar to the temperature as a function of time²⁾. We

calculated the power reflection fraction by the measured phase shift plotted as points in Fig. 1. They are somewhat scattered but coincide very well with the RSA data.

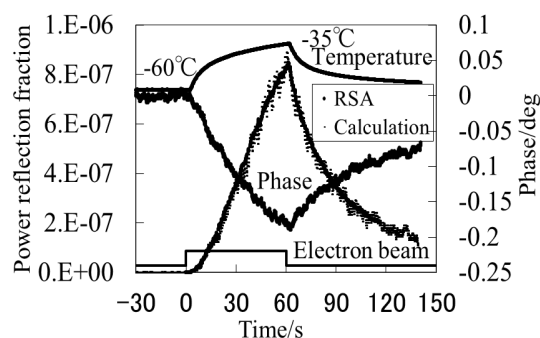


Fig. 1 Power reflection fraction with respect to time. During irradiation with the electron beam, the temperature of the ice target increased from -60°C to -35°C with time. The power reflection fraction measured by the RSA is plotted as small closed circles and increased from 0 to 8×10^{-7} with the temperature, and is compared with a calculation plotted as points utilizing the phase. The phase obtained from by the variable phase shifter decreased from 0° to -0.2° .

According to the coincidence of the reflection fraction between the measurement and the calculation deduced from the measured phase adding to the accordance to the model calculation, we could understand the reflection mechanism. A new radiation detector "Radar Chamber" is proposed not only for detection of UHEv's but also for applications using various dielectric media where the refractive indices change with temperature. It is not only for radiation detection but also for other purposes using materials with inhomogeneous refractive index in space and time. An important application for human-body imaging could be investigated at 10 MHz where the attenuation length is $\sim 5 \text{ cm}$. The good phase precision may afford a good position resolution.

References

- 1) Berezinsky and Zatsepin, Phys. Lett. B **28** (1969) 423.
- 2) M. Chiba et al., 5th Int. Workshop on Acoustic and Radio EeV Neutrino Detect. Activ. ARENA 2012 workshop (Erlangen, Germany), AIP Conf. Proc. 1535, 45-50 (2013); <http://dx.doi.org/10.1063/1.4807519>, <http://arxiv.org/abs/1307.1767>.

4 - 35 Effect of Low Irradiation Temperature on the Gamma-ray Response of Clear Polymethylmethacrylate Dosimeter, Radix W

H. Seito^{a)}, Y. Nagao^{a)}, T. Ichikawa^{b)}, M. Iwasaki^{b)}, Y. Sato^{b)}, T. Agematsu^{a)},
H. Kaneko^{a)}, H. Watanabe^{b)} and T. Kojima^{a)}

^{a)} Department of Advanced Radiation Technology, TARRI, JAEA, ^{b)} Radia Industry Co., Ltd

Radiation sterilization of pharmaceutical and biomedical products, and irradiation of fresh and frozen foodstuffs are achieved at low temperatures, often lower than 0 °C. For instance, sterilization of frozen foods such as chicken and shrimps, and bone graft prosthetic composite has been conducted in foreign irradiation facilities. The absorbed dose and temperature level of these radiation processing are usually doses of a few several kGy to a few hundreds kGy and mainly -80 to -20 °C (on the surface of frozen materials), respectively. Various types of dosimeters are used for the process control in the radiation processing. Among them, polymethylmethacrylate (PMMA) dosimeters are mainly used because of a wide measurable dose range, easy-handling and available cost¹⁾. The effect of dose rate and temperature during and after irradiation on the dose response of PMMA dosimeters has been ever studied under common atmospheric conditions at temperatures above 0 °C, prevailing in most irradiation facilities. However, the dose response under low temperature still has not been well-studied under different irradiation conditions.

In this study, for application of clear PMMA dosimeters to sterilization of food and biomedical materials, detailed effect of temperature during irradiation was studied at useful doses of 5, 10, 15, 25, 35 and 50 kGy, dose rate of 8.87 kGy/h, and at a temperature range of -73 to +21 °C. The gamma-ray irradiation was carried out using a ⁶⁰Co plaque source in dewar vessel packed with water (20 °C), ice (0 °C), ice mixed with calcium chloride (-20~-30 °C) or dry ice (-70~-80 °C). Clear PMMA dosimeter, Radix W (Batch E), was tested in this study. Irradiation of 4 dosimeters to each dose at each temperature was simultaneously done. Dose response is measured at 30 min after irradiation, in terms of optical density at 320 nm wavelength, and is expressed as net optical density per unit thickness. Optical density and thickness values are measured using a SHIMADZU spectrophotometer model UV-1700 and an ONO SOKKI micrometer model DG-825, respectively.

The temperature dependence of dose response for Radix W, in terms of the relative response as a function of the temperature during irradiation is shown in Fig. 1. At doses of 5, 10, 15, 25, 35 and 50 kGy, the dose response of Radix W linearly increased from -73 to +21 °C with a coefficient of approximately $+0.21 \pm 0.04$ %/°C, which agrees with the data obtained in the previous study at temperature range of -40~20 °C at 6 kGy²⁾. These results are plotted such that the relative dose for a dosimeter irradiated at 21 °C but

irradiated at some other temperature would have its apparent dose reading from the dose response curve multiplied by the coefficient (0.21 %/°C) in order to give the dose reading that is corrected for the temperature dependence.

Dose response curves measured in dose range from 5 to 50 kGy under different irradiation temperatures of +21, +1, -24 and -73 °C are shown in Fig. 2. The influence of irradiation temperature gradually becomes significant for higher doses. The coefficient of variation to show scattering in the dose response values among 4 dosimeters to each dose at each temperature during irradiation was between 0.22% and 1.30%. These results suggest that precise dose estimation of gamma-ray doses in the range of 5-50 kGy with careful use and proper calibration under conditions almost equivalent to those in practical applications can be achieved using Radix W dosimeter.

References

- 1) M. Takehisa et al., Radiat. Phys. Chem. 76 (2007) 1619.
- 2) H. Seito et al., Radiat. Phys. Chem. 78 (2009) 356.

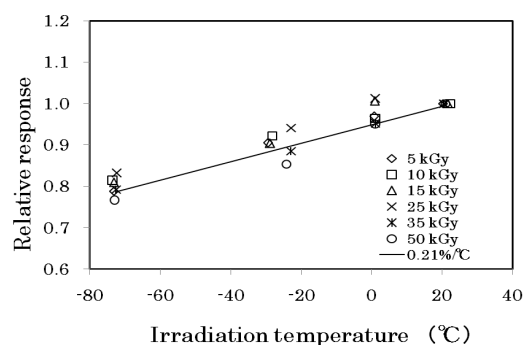


Fig. 1 Dose response of Radix W dosimeters as a function of irradiation temperature.

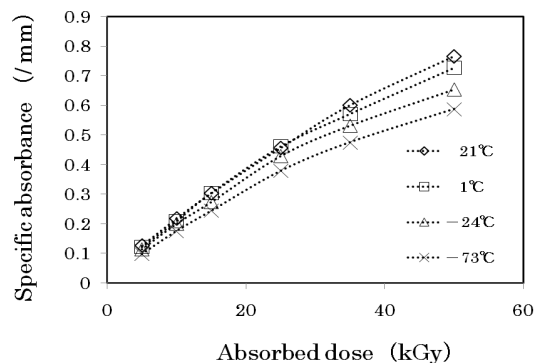


Fig. 2 Dose response curves of Radix W dosimeters at different irradiation temperatures.

4 - 36

Analysis of Phase Bunching in AVF Cyclotron

N. Miyawaki, S. Kurashima, H. Kashiwagi, S. Okumura, K. Yoshida, Y. Yuri,
T. Yuyama, T. Ishizaka, I. Ishibori and T. Nara

Department of Advanced Radiation Technology, TARRI, JAEA

Phase bunching in the central region of a cyclotron has been investigated in order to obtain a narrow beam phase width necessary for a high quality beam. The paper reports the condition of phase bunching evaluated by a simplified geometric trajectory analysis¹⁾ and its application to the JAEA AVF cyclotron. Moreover, a result of a preliminary measurement for phase bunching is indicated.

Phase bunching is generated by energy-gain modulation produced in a rising-slope region of the acceleration voltage waveform at the first acceleration gap. To evaluate the condition of phase bunching, we devised a simplified geometric trajectory analysis for the charged particles from the first to the second acceleration gap. The phase difference $\Delta\phi_{RF}$ of incident particles from the reference particle at the second acceleration gap is given by¹⁾,

$$\Delta\phi_{RF} = h \cdot \sin^{-1} \left\{ \left[\frac{\sqrt{1 - R_V \sin \phi_F}}{\sqrt{1 - R_V \sin(\phi_F + \Delta\phi_a)}} - 1 \right] \sin \theta_F \right\}, \quad (1)$$

where h is the acceleration harmonic number, R_V is the ratio of the peak acceleration voltage in the cyclotron to the extraction voltage of an ion source, θ_F is the span angle from the first to the second acceleration gap, $\Delta\phi_a$ is the phase difference at the first acceleration gap from the reference particle phase ϕ_F given by

$$\phi_F = -h \left(\theta_F - \frac{\theta_D}{2} \right), \quad (2)$$

where θ_D is the span angle of the dee electrode. In Eq. (1), the phase bunching or de-bunching condition is determined by the combination of four parameters: h , θ_F , θ_D and R_V . Optimum values of θ_F for phase bunching are limited by the relationship between h and θ_D , which is $90^\circ/h + \theta_D/2 \leq \theta_F \leq 180^\circ/h + \theta_D/2$, and $\sin \theta_F \leq 0$. Optimum values of R_V in the condition of phase bunching were between two and four, if $\Delta\phi_a$ was within 40 RF degrees.

The conditions to generate phase bunching in the JAEA AVF cyclotron with $\theta_D = 86^\circ$, $\theta_F = 118^\circ$ for $h = 1$ and 2, and $\theta_F = 78^\circ$ for $h = 3$ were calculated from Eq. (1). As a result, Fig. 1 shows the correlation between $\Delta\phi_a$ and the phase difference at the second acceleration gap $\Delta\phi_{2nd} = \Delta\phi_a + \Delta\phi_{RF}$ for $h = 1, 2$ and 3 with $R_V = 2.5$ in the cyclotron, respectively. Phase bunching appears in the region $|\Delta\phi_{2nd}| < |\Delta\phi_a|$, and this effect is maximized near the local minima of the curves in the figure. Then, phase bunching is generated for $h = 2$ and 3. For example, $\Delta\phi_a$ between -20 and 20 RF degrees for $h=2$ is narrowed to $\Delta\phi_{2nd}$ of 8 RF degrees. However, the case of $h=1$ is hardly generated because the slope of the curve depending on location and width of $\Delta\phi_a$ is almost 1.

In order to experimentally confirm the actual relation between $\Delta\phi_a$ and $\Delta\phi_{2nd}$ as shown in Fig. 1, both the

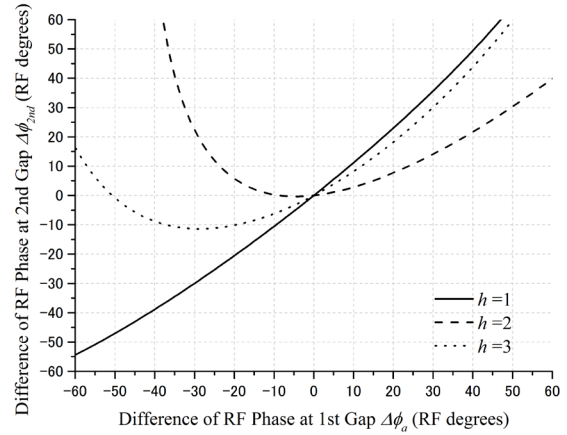


Fig. 1 Relation between $\Delta\phi_a$ and $\Delta\phi_{2nd}$ for $h=1, 2$ and 3 with $R_V=2.5$ in the JAEA AVF cyclotron. When the absolute value of the slope of the curve is smaller than 1, phase bunching is generated.

measurement of the beam phase distribution in the cyclotron and control of the initial beam phase are needed. Already phase bunching for the $h=2$ in the JAEA AVF cyclotron was confirmed by the estimation from both the simulation and the measurement of the phase distribution of the extracted beam from the cyclotron and the radial position of the slits in the cyclotron²⁾. However, it has not been observed directly because there is no method of the measurement of the beam phase distribution in the cyclotron. Therefore, the main-probe was improved by adding the measurement system with a plastic scintillator^{3,4)}. The initial phase of the injected beam into the cyclotron was controlled by adjusting the relative phase of the external buncher in the injection beam line. By using both of the main-probe and the external buncher, the beam phase distributions of a 260 MeV $^{20}\text{Ne}^{7+}$ ($h = 2$) with $R_V = 2.5$ was measured for three initial phases of 0 and ± 18.9 RF degrees. As a result, they were narrowed to ± 4 RF degrees or less, and were consistent with the calculation result shown in Fig. 1.

References

- 1) N. Miyawaki et al., Nucl. Instrum. Meth. A 715 (2013) 126.
- 2) N. Miyawaki et al., Nucl. Instrum. Meth. A 636 (2011) 41.
- 3) S. Kurashima et al., JAEA Takasaki Annu. Rep. 2008 (2009) 167.
- 4) N. Miyawaki et al., JAEA Takasaki Annu. Rep. 2007 (2008) 182.

4 - 37

Status Report on Technical Developments of
Electrostatic Accelerators

K. Yamada, Y. Saitoh, Y. Ishii, S. Matoba, A. Chiba, A. Yokoyama, A. Usui,
T. Satoh, T. Ohkubo and S. Uno

Department of Advanced Radiation Technology, TARRI, JAEA

Measurement of beam emittance of 3 MV single-ended accelerator by emittance monitor with wire method

The emittance monitor for 3 MV Single-ended Accelerator in TIARA is developed on the basis of measuring beam currents by moving a thin Cu wire toward crossing multi-ion beams passing through a multi-hole slit. The emittance of 1 MeV proton beam was measured as a performance test of the emittance monitor in the 2011 financial year¹⁾. The extraction voltage dependence of the emittance of the ion source placed in the accelerator was investigated in the 2012 financial year. The emittances were measured by changing the extraction voltages at 7.8, 8.4, 8.8 and 10 kV in the experiments. The wire was moved at the distance of 0.03125 mm per a step using a stepping motor from one side to the other side of the multi-beam. The relation between the extraction voltage and beam emittance is shown in Fig. 1. This figure shows that the emittance at the extraction voltage of 8.4 kV was a minimum value. The emittance was measured using SiO₂ luminescence induced by ion beam in the previous work²⁾. The emittances measured using the wire and the luminescence indicated the almost same tendency.

Measurement of cluster ion beam current

A fullerene ion beam current is usually measured using a high-aspect-ratio Faraday Cup (FC) because a bombardment of a fullerene ion generates not only secondary electrons but also secondary positive ions more than those of a monoatomic ion. However, the size of the high-aspect-ratio FC is too large to be installed in an existing beam transport line. We have developed a compact FC that was filled with needles on the bottom of the cup shown in Fig. 2, which is expected to be equivalent for a high-aspect-ratio FC. The aspect ratio which was calculated from the top of the needle was 2.1. The ion beam current of C₆₀⁺ ions at 100 keV generated by the 400 kV Ion Implanter was measured using the compact FC, a high-aspect-ratio FC of which aspect ratio is 15 and a conventional FC of which aspect ratio is 2.1 to compare the effect of the needles. The measurement value using the conventional FC with an electron suppressor was negative values because secondary positive ions were extracted. In contrast, the measurement value of the compact FC was equivalent with that of the high-aspect-ratio FC. These results indicate that the compact FC has an advantage to keep secondary ions from being extracted from the FC by comparing with the conventional FC.

Investigation of a charge exchange gas for cluster ion acceleration

We have investigated the charge exchange and destruction mechanism on the MeV energy cluster ions colliding with gas targets to select the suitable charge exchange gas which has a small destruction cross section (σ_d) and a large charge exchange cross section without destruction (σ_p). In this financial year, the destruction cross sections for $0.24v_B - 0.34v_B$ (v_B : Borh velocity) gold cluster ions Au_n ($n = 2, 3$) with metallic bond in collisions with a helium and a nitrogen gas targets were evaluated from a beam transmission through the tandem accelerator. As a result, it was revealed that there was no energy dependence of the cross sections in the energy range studied, whereas they depended on target gases and cluster sizes. These tendencies of gold cluster ions are consist with those of carbon cluster ions with covalent bond reported previously¹⁾.

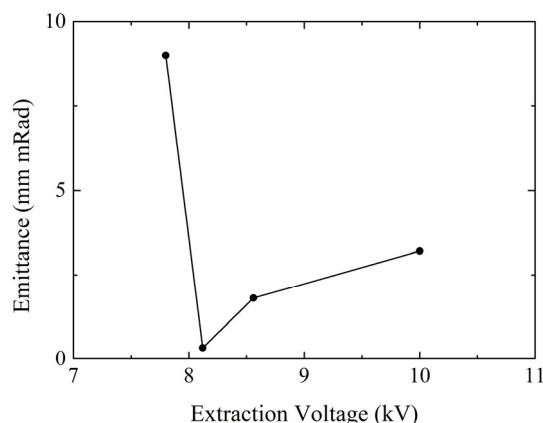


Fig. 1 The extraction voltage dependence of the emittance.

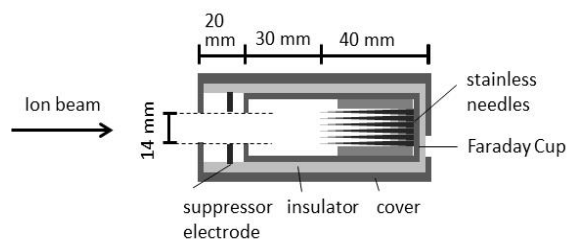


Fig. 2 The schematic diagram of the compact FC.

References

- 1) K. Yamada et al., JAEA Takasaki Annu. Rep. 2011 (2013) 155.
- 2) A. Yokoyama et al., JAEA Takasaki Annu. Rep. 2010 (2012) 158.

4 - 38 Fast Single-ion Hit System for Heavy-ion Microbeam at TIARA Cyclotron (VI)

W. Yokota, T. Satoh, S. Okumura, S. Kurashima, N. Miyawaki, H. Kashiwagi, K. Yoshida, M. Koka, A. Yokoyama, W. Kada and T. Kamiya

Department of Advanced Radiation Technology, TARRI, JAEA

The fast single-ion hit system on the HX course of the TIARA cyclotron¹⁾ was continuously improved for higher quality of microbeam and single-ion hit. A technique of real-time detection of single-ion-hit position has been realized and new microbeam of 320 MeV-¹²C was developed using this technique.

A scintillator of CaF₂:Eu of 0.5 mm as thick as ions stopped in it was examined in fiscal 2011 and scintillations were detected at a rate of several ions per second for 260 MeV-Ne. The scintillation detection system used in the experiment consisted of an optical microscope with a 10-power object lens, a CCD and an image intensifier with 1×10^6 magnifications (photon gain). The system was improved for higher sensitivity in fiscal 2012 by replacing the CCD with a EMCCD (Electron Multiplying CCD) with 8×10^5 magnifications (full-well capacity) operated at -25 °C and removing the image intensifier. The improvement has enabled us to detect a scintillation from CaF₂:Eu induced by an ion of 260 MeV-²⁰Ne. Figure 1 shows a sample map of hit positions detected by the system comparing with etch pits on CR-39 which was set beneath the CaF₂:Eu and hit by ions passing through it. About 80% of pit positions correspond to those of scintillations. The scintillations away from the pits by several tens of microns may be noises. The spatial resolution of the system was estimated from the distribution of the displacement of scintillation positions from the pits on an assumption that the pits show the actual hit points. The distributions of the displacement are shown in Fig. 2 and the resolution is 5 μ m in x-direction and 11 μ m in y-direction by full width at half maximum (FWHM).

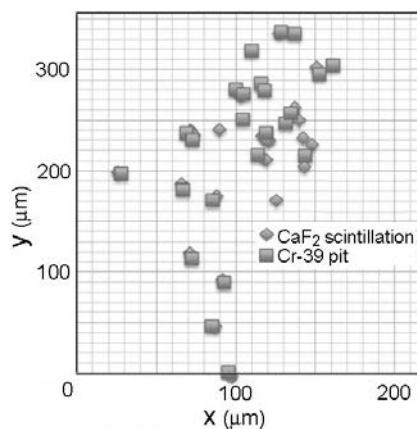


Fig. 1 Comparison of hit positions of 260 MeV-²⁰Ne ions detected by the developed system (diamonds) and a conventional method with CR-39 (squares).

The new microbeam development of 320 MeV-¹²C was started in fiscal 2010. The difficulty in formation to a microbeam arises from low intensity and low secondary electron emission rate of 320 MeV-¹²C. Therefore, a usual way to observe secondary electron image (SEM) of a copper grid cannot be used to observe beam size for formation tuning. The SEM images for 220 MeV and 320 MeV-¹²C beams are compared in Fig. 3. In the former, the intensity of secondary electrons is high enough to recognize a shape of the grid and tune to make the image clearer leads to a smaller beam. In the latter, on the other hand, the grid image is too faint with many noise signals no matter how the beam size is small, and further tune is impossible. The CaF₂:Eu system was therefore employed to monitor the beam shape at a rate of several ions per second, and 50 μ m \times 5 μ m beam was formed in fiscal 2011. The real-time detection of single-ion-hit has realized forming a microbeam of 320 MeV-¹²C with a smaller size. A microbeam with a size less than 10 μ m \times 10 μ m, which was estimated by the method mentioned in the previous section, was formed. The beam size is expected to be reduced further with finer tune.

Reference

- 1) W. Yokota et al., JAEA Takasaki Annu. Rep. 2011 (2013) 156.

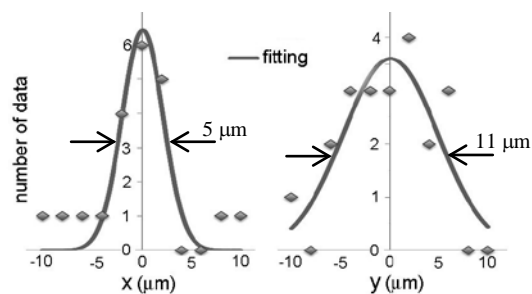


Fig. 2 Displacement distributions of scintillation positions from corresponding pit positions and their FWHM.

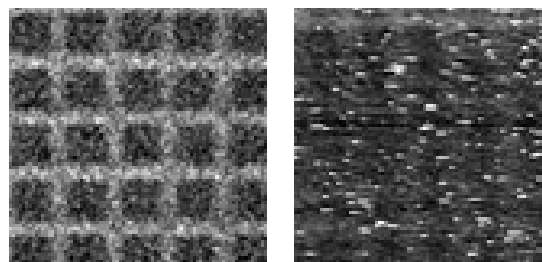


Fig. 3 Copper grid images drawn from secondary electrons by 220 MeV-¹²C (left) and 320 MeV-¹²C (right).

4 - 39

Development of a Microwave Ion Source for Industrial Applications

N. Takahashi^{a)}, H. Murata^{a)}, H. Mitsubori^{a)}, T. Soga^{a)}, Y. Aoki^{a)}, J. Sakuraba^{a)}, T. Kato^{a)},
N. Sakudo^{b)}, K. Yamada^{c)} and Y. Saitoh^{c)}

^{a)}Sumitomo Heavy Industries, Ltd.,

^{b)}Kanazawa Institute of Technology,

^{c)}Department of Advanced Radiation Technology, TARRI, JAEA

A microwave ion source is one of the long-life ion sources, because it is filamentless. We have been developing a microwave ion source for industrial applications such as ion implantation and heavy ion radiotherapy. As a result of evaluation of plasma density and ion current density, we have achieved more than 10^{12} cm^{-3} of plasma density and 100 mA/cm^2 of ion current density with Ar gas. We report spectra determined for Ar plasma with various magnetic field distributions and gas pressures, showing that almost all of produced ion was Ar^+ under our experimental conditions.

背景: マイクロ波イオン源は、その構造上、無電極であるため、他のバーナス型、PIG 型等のアーク放電型イオン源に対して、長寿命であることが期待される。また、これまでの研究事例から高密度プラズマの生成も確認されている。従って、成膜装置、粒子線がん治療装置、イオン注入装置など、多くの産業機器への適用が期待される。

そこで、前述の装置に用いることを目的とし、マイクロ波イオン源の開発を行っている。

住友重機械工業で、電磁石、プラズマチャンバー、引き出し電極、導波管、発振器で構成されるマイクロ波イオン源を製作した。電磁石は 2 つのスプリット型コイルから成り、コイル電流値、コイル間ギャップを変えることにより、チャンバー内の磁束密度が可変である。発振器の周波数は 2.45 GHz であり、最大出力は 1 kW である。また、導入ガスとしてアルゴン (Ar) を用い、ガス流量の調整は、マスフローコントローラで行う。

本装置の磁場分布、マッチングセクション、ガス流量を変えて、プラズマ密度、イオン飽和電流を測定した。その結果、アルゴンガスでプラズマ密度が 10^{12} cm^{-3} 以上、イオン電流密度が 100 mA/cm^2 以上になることを確認した。

以下に、本イオン源を TIARA 施設内のイオン源テストベンチに設置し、磁場分布などの各パラメーターを変えてイオン電流スペクトルを測定した結果を報告する。

実験環境: 実験は TIARA 施設内のイオン源テストベンチ内にて行った。テストベンチは、イオン源、加速電場、アイソツェレンズ、分析前ファラデーカップ、質量分析マグネット、分析後マグネットから構成される。本実験では、加速電圧は最大 10 kV であり、磁場分布、ガス流量およびマイクロ波出力を変え、全イオン電流及びイオン電流スペクトルの測定を行った。

結果と考察: Figure 1 に磁場分布を変えた時のイオン電流スペクトルの測定結果を示す。横軸は質量電荷比、縦軸はイオン電流である。図中(a)、(b)、(c)の時のプラズマチャンバー中心の軸方向磁場分布の計算値を Figure 2 にそれぞれ示す。MW はマイクロ波導入位置、EX はイオンビーム引き出し位置を示す。いずれの場合も磁束密度勾配は、マイクロ波導入側が高く、引き出し側に向かって一様減衰するように設定している。測定結果から、全ての磁場分布に対し

て、イオン電流スペクトルには Ar^+ イオンが圧倒的に多く含まれている事が分かった。これは、これらの磁場分布では、磁気ミラー構造のような荷電粒子を閉じ込める作用が無く、電子が多価イオンを生成するために十分なエネルギーをマイクロ波から吸収する前に、中性ガス等と衝突して、消失してしまうためだと考えられる。また、最もイオン電流が高い条件は、プラズマチャンバー内の磁束密度を最も高く設定した時であった。

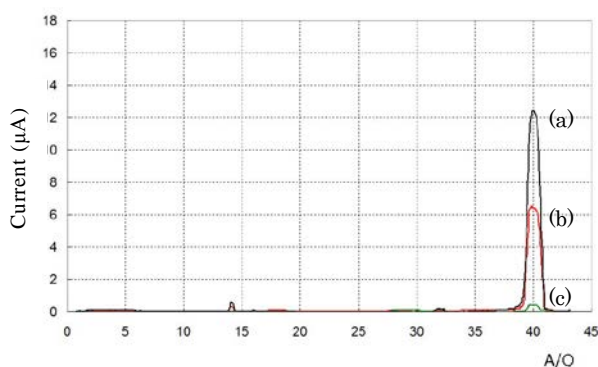


Fig. 1 Spectra of ion with Ar gas for various magnetic flux distributions shown in Fig. 2.

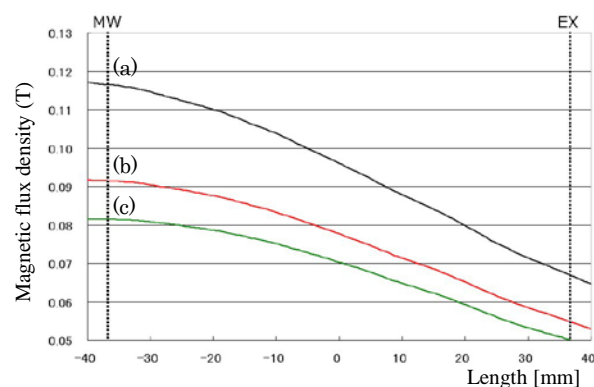


Fig. 2 Calculated magnetic flux density distributions in the plasma chamber.

4 - 40 Beam Intensity Distribution Measurement Using a Fluorescent Screen for Formation of a Uniform Ion Beam

T. Yuyama, Y. Yuri, T. Ishizaka, I. Ishibori and S. Okumura

Department of Advanced Radiation Technology, TARRI, JAEA

The LB line of the TIARA cyclotron has been continuously improved for more efficient R&D studies and utilization of uniform ion beams focused with multipole magnets. A vacuum pipe of a circular cross section was replaced with a pipe of a square larger cross section at the quadrupole magnets TTQ2 for higher transport efficiency of the beam with large emittance. A large turbo-molecular pump (1,000 L/s) was additionally installed before the target chamber. Sufficiently high vacuum pressure can be maintained in the LB line despite a target material that contains gas plentifully. With these improvements, uniform beam irradiation of 10-MeV protons can be now performed at a high fluence rate up to $2 \times 10^{11} \text{ cm}^{-2} \text{ s}^{-1}$, which makes space solar cell testing more efficient¹⁾. The effect of the multipole force on the beam intensity distribution was also studied in detail^{2,3)}. In the followings, experimental studies on the development of the beam intensity distribution measurement system⁴⁾ and on the formation of heavy-ion uniform beams are reported.

A beam intensity distribution measurement system, which is composed of two CCD cameras, fluorescent screens, and an image analysis program based on LabVIEW, was developed for real-time tuning of a uniform beam using multipole magnets. The characteristics of the system were investigated. Figure 1 shows the dependence of the fluorescent intensity on the fluence rate of the 10-MeV proton beam for DRZ-High (Mitsubishi Chemical) and AF995R (Desmarquest). The fluorescent intensity grew proportionally to the fluence rate of the beam at a low fluence rate and then was saturated. A similar tendency was observed for 520-MeV ^{40}Ar beams although the available fluence rate is about one order of magnitude lower than that of 10-MeV protons. Using the linear response region of the fluorescence, the relative intensity distributions were measured and compared with the measurement result using Gafchromic films. The response of the film to ion

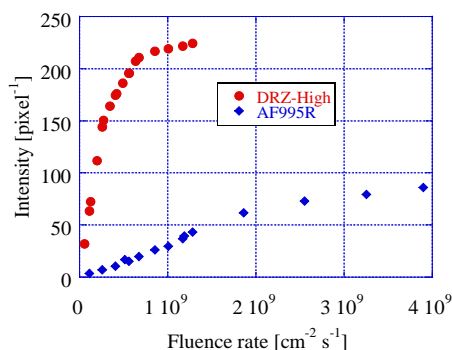


Fig. 1 Dependence of the fluorescent intensity on 10-MeV proton irradiation for the two screens.

irradiation was also explored⁵⁻⁷⁾. It was found that the optical density of the film linearly increased with the fluence of the beam at a low fluence. We confirmed that these distributions agreed well. The system is now applied to the uniform-beam formation using multipole magnets.

The formation of a uniform intensity distribution was investigated at the LB line for 150-MeV ^{40}Ar beams. The beam was first multiply-scattered using an aluminum foil of 1 μm thick in the first straight section after the cyclotron so that the initial complicated intensity profile was smoothed into a Gaussian-like profile. Then, the Ar beam was focused by two octupole magnets under the beam optics that suppresses horizontal-vertical coupling of the beam motion. The on-target distribution of the beam is shown in Fig. 2. The root-mean-square uniformity was 10% in the region of 7 cm \times 4 cm. A similar uniform distribution was obtained also for 520-MeV Ar beams⁸⁾. These uniform beams will be applied to the creation of functional polymer membranes, in which efficient ultra-low-fluence irradiation is required.

References

- 1) M. Imaizumi, Y. Yuri, P. R. Bolton et al., Proc. 38th IEEE Photovoltaic Specialists Conf. (2012) 2831.
- 2) Y. Yuri et al., J. Phys. Soc. Jpn. **81** (2012) 064501.
- 3) Y. Yuri, T. Yuyama, T. Ishizaka, I. Ishibori and S. Okumura, Proc. 3rd Int. Part. Accel. Conf. (2012) 1062.
- 4) T. Yuyama, Y. Yuri, T. Ishizaka et al., Proc. 1st Int. Beam Instrum. Conf. (2012) 246.
- 5) T. Ishizaka, K. Imai, Y. Yuri et al., Proc. 9th Annu. Meet. Part. Accel. Soc. Jpn. (2012) 594 [in Japanese].
- 6) Y. Yuri, T. Ishizaka, T. Yuyama, I. Ishibori, S. Okumura et al., Proc. 1st Int. Beam Instrum. Conf. (2012) 531.
- 7) Y. Yuri, T. Yuyama et al., Proc. 10th Int. Workshop Radiat. Eff. Semicond. Devices Space Appl. (2012) 97.
- 8) A. Kitamura (Ogawa), T. Yamaki, Y. Yuri et al., to be published in Nucl. Instrum. Meth. B.

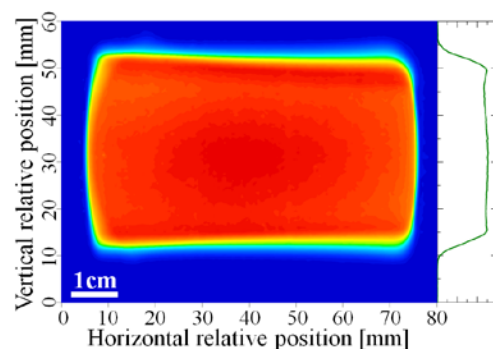


Fig. 2 Relative transverse intensity distribution of the 150-MeV ^{40}Ar beam, measured using a Gafchromic film HD-810.

4 - 41 Response of Gafchromic Films to Energetic Ion Beams

Y. Yuri, T. Ishizaka, T. Yuyama, I. Ishibori and S. Okumura

Department of Advanced Radiation Technology, TARRI, JAEA

It is required to precisely evaluate the large-area transverse intensity distribution of various ion beams applied to materials and biological research at the TIARA cyclotron. Gafchromic radiochromic films HD-810 and EBT2 (Ashland Inc.) are, thus, employed as a possible technique for measuring the beam intensity distribution. The optical-density response of the films was investigated for various ion beams¹⁻³⁾. In this study, the film response is further analyzed with absorbed dose through linear energy transfer (LET) of the beam⁴⁾.

The films were irradiated uniformly in a wide fluence range with 10-MeV ¹H, 520-MeV ⁴⁰Ar, and 450-MeV ¹²⁹Xe beams from the cyclotron. The irradiated films were read at a resolution of 127 dpi using general-purpose flat-bed scanners to digitize them into TIFF-formatted images with 16-bit RGB color intensity values. The optical density d_X was determined from the 16-bit intensity value I_X in a color channel X (red, green, or blue) by the equation: $d_X = \log_{10}(2^{16} - 1/I_X)$.

According to previous experimental results, the response curve of the films is strongly dependent on ion species as well as on the film type,¹⁻³⁾ the available linear-response range moves to the lower-fluence region for heavier-ion beams. This is probably due to the difference of the LET in the active layer of the film. To see this dependence, the particle fluence F is transformed into the dose D using the following relation: $D = c(LET/\rho)F$ where ρ is the density of the active layer of the film and c is a constant. The LETs of the beams at each layer of the films can be determined using SRIM code. For example, the average LETs in the active layer ($\rho = 1.08 \text{ g/cm}^3$) of HD-810 are 5.0×10^0 , 1.2×10^3 , and $1.1 \times 10^4 \text{ keV}/\mu\text{m}$ for the H, Ar, and Xe ion beams in the present case, respectively.

The response curves for the three ion species are plotted in Fig. 1 as a function of the average dose in the active layer of HD-810. Although the linear-response dose range is partially overlapped with the manufacturer's specifications (10~400 Gy) of the film for all three ion species, the dose-response curves shift slightly to the right for heavier-ion beams and the film response seems still dependent on ion species. In fact, the sensitivity of the film, defined here as an increment of the optical density per dose in the linear-response region, becomes lower for heavier-ion beams. This might be because, for a heavy ion with a higher LET, the local dose along the ion's trajectory is very high and the coloration in the microscopic region becomes saturated; a large part of the deposited dose does not contribute to the film coloration. The reduced sensitivity for a higher LET agrees well with a previous study⁵⁾.

As can be seen from Fig. 1, the response of the film is always linear in a low-dose (low-fluence) region where the optical density is well below unity. This feature gives us a handy technique to measure the relative intensity distribution of the beam directly from the optical density. It has been confirmed, through repeated experiments, that the present technique is useful for the measurement and evaluation of the intensity distribution of a large-area uniform beam formed with multipole magnets^{1-4, 6)}.

References

- 1) T. Ishizaka, K. Imai, Y. Yuri et al., JAEA Takasaki Annu. Rep. 2011 (2013) 157.
- 2) T. Ishizaka, K. Imai, Y. Yuri et al., Proc. 9th Annu. Meeting Part. Accel. Soc. Jpn. (2012) 594 [in Japanese].
- 3) Y. Yuri, et al., Proc. 1st Int. Beam Instrum. Conf. (2012) 531.
- 4) Y. Yuri et al., Nucl. Instrum. Meth. A 727 (2013) 40.
- 5) T. Kojima et al., Rad. Phys. Chem. 68 (2003) 975.
- 6) T. Yuyama, Y. Yuri et al., in this annual report.

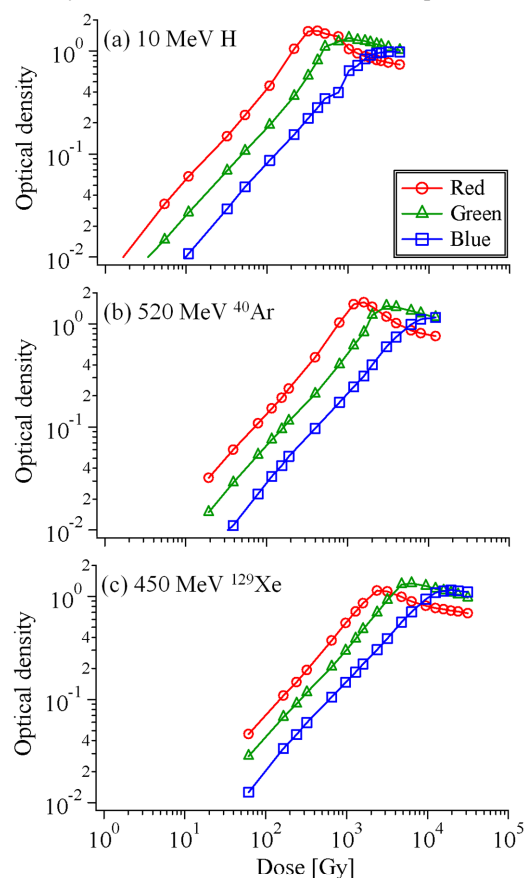


Fig. 1 Response curves of the Gafchromic film HD-810 for three different ion beams as a function of the dose in the active layer of the film. The LiDE50 (Canon) was used for film scanning.

4 - 42 Development of Scintillator for Detention of Single-ion

A. Yokoyama^{a)}, W. Kada^{a)}, T. Satoh^{a)}, M. Koka^{a)}, S. Yamamoto^{b)},
T. Kamiya^{a)} and W. Yokota^{a)}

^{a)}Department of Advanced Radiation Technology, TARRI, JAEA,

^{b)}Environment and Industrial Materials Research Division, QuBS, JAEA

Introduction

Single-ion hit for studies of microscopic irradiation experiment is utilized with spatial accuracy of a few micrometers by means of heavy ion microbeam of several hundred MeV at the TIARA cyclotron. High spatial accuracy for the real-time position detection of single-ion hit is essential in irradiation experiments of biological cells. A CR-39 plastic track detector is generally used as a position detector of single-ion hit. The tracks formed on it after chemical etching are observed by microscope. This procedure takes more than an hour and limits efficiency of therefore strongly required, and various scintillators are examined so far. It is taken notice of photostimulated luminescence (PSL) of $\text{Al}_2\text{O}_3\text{:C}$ in this study, which has accurate dose sensitivity ranging from 0.1 μGy to 10 Gy. Photostimulable sample are possible to be prepared by adjusting parameters such as the amount of implantation density of activators by means of the TIARA ion implanter and annealing condition.

The following two subjects were carried out in fiscal 2012. (1) Sample preparation of $\text{Al}_2\text{O}_3\text{:Eu}$, which emit strong luminescence by ion beam irradiation, to establish preparation method for PSL sample. (2) Measurement of Photoluminescence (PL) spectra of $\text{Al}_2\text{O}_3\text{:Eu}$.

Sample preparation

It is necessary to investigate how the luminescence intensity of prepared $\text{Al}_2\text{O}_3\text{:Eu}$ depends on ion implantation depth, density, annealing temperature and time. The optimal implantation depth (i.e. luminescence layer) and density were found for preparing sample in fiscal 2011¹⁾. The optimal “implantation layer” is triple layers of 70, 50 and 35 nm corresponding to three different Eu-beam energies, 350, 250 and 150 keV, respectively, and the optimal implantation density is $1.0 \times 10^{16} \text{ cm}^{-2}$. Annealing temperature and time were searched with the samples prepared using those results.

Photoluminescence measurement

Measurement of photoluminescence (PL), of which the intensity was correlated with that of PSL²⁾ was carried out to find the optimal annealing temperature and time. A continuous wave He-Cd laser at 325 nm was used as an excitation light and the PL signal was detected by a high sensitivity spectrometer based on cooled CCD in this measurement. First, the annealing temperature dependence of the PL intensity was measured for an-hour-annealed samples. The highest PL peak intensity was observed at

around 600 nm at 600 °C as shown in Fig. 1. Secondly, annealing time dependence of the PL from this sample was measured. The highest PL intensity was obtained from 0.5-hour-annealed sample (Fig. 2). It was found how the four parameters depend on PL intensity of prepared sample consequently.

This indicates PSL sample with high luminescence intensity is possible to be prepared using the same method. The prepared PSL sample is going to be used in the irradiation experiment of single-ion hit in fiscal 2013.

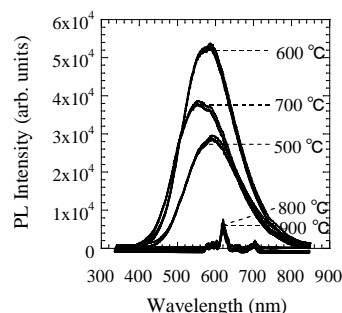


Fig. 1 Annealing temperature dependence of the PL intensity of $\text{Al}_2\text{O}_3\text{:Eu}$ annealed for an hour. The highest is at 600 °C.

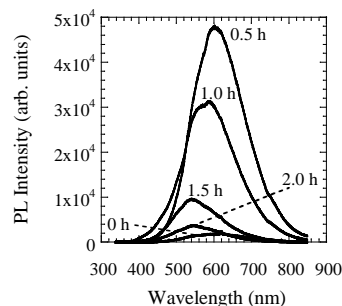


Fig. 2 Annealing time dependence of the PL intensity of $\text{Al}_2\text{O}_3\text{:Eu}$ annealed at 600 °C. The highest is for 0.5 hour.

Acknowledgment

We would like to gratefully thank Dr. Miura in Graduate School of Engineering, Gunma University for PL measurement. This work was supported by KAKENHI, Grant-in-Aid for Young Scientists (B) 23760837.

References

- 1) A. Yokoyama et al., JAEA Takasaki Annu. Rep. 2011 (2013) 159.
- 2) M. Takebe., Radiation 23 (2) (1995) 3-7.

4 - 43 Focused Microbeam Irradiation Effects in Transmission CVD Diamond Film Detectors

T. Kamiya^{a)}, W. Kada^{a)}, N. Iwamoto^{b)}, S. Onoda^{b)}, V. Grilj^{c)}, N. Skukan^{c,d)},
T. Makino^{b)}, M. Koka^{a)}, T. Satoh^{a)}, T. Ohshima^{b)} and M. Jakšić^{c)}

^{a)}Department of Advanced Radiation Technology, TARRI, JAEA, ^{b)}Environment and Industrial Materials Research Division, QuBS, JAEA, ^{c)}Rudjer Boskovic Institute, Croatia

1. Introduction

Diamond is a promising candidate for radiation detectors which are expected to have high charge collection efficiency (CCE), good thermal stability, and excellent radiation hardness. Therefore, the response of single crystal chemical vapor deposited (SC-CVD) diamond film made by focused ionized particle irradiation was investigated in order to evaluate the usage as a single ion hit detector for heavy ion microbeam from azimuthally varying field (AVF) cyclotron at the Takasaki Advanced Radiation Research Institute, Japan Atomic Energy Agency.

2. Materials and Methods

A SC-CVD diamond film wafer (4.6 mm × 4.6 mm) with thickness of approximately 50 μm were prepared by Diamond Detectors Ltd. Prior to the microbeam irradiation, the response to the charged particles were obtained as spectrum with ²⁴¹Am alpha-particle checking source. Charge collection efficiency (CCE) was reached equal to 100% at bias voltage of ±50 V. An energy resolution of 2% in a full width at half-maximum (FWHM) was sustained in an energy spectrum of alpha-particles from ²⁴¹Am with the total fluence of 10⁹ [particles/cm²].

The detector was then characterized by using an ion beam-induced charge (IBIC) system with a 3 MeV H⁺ microbeam and a transient ion beam-induced current (TIBIC) system with a 15 MeV O⁴⁺ microbeam at both the ion microbeam irradiation facilities of Rudjer Boskovic

Institute (RBI) and TIARA. The ranges of these ions were also calculated as 43 μm and 5.2 μm in diamond, respectively. Beam current was controlled as 100 cps with maximum scanning area of 800 μm × 800 μm. Three MeV H⁺ and 15 MeV O⁴⁺ microbeam probe was focused approximately 1 μm and 1.5 μm, respectively.

3. Results and Discussion

The 15 MeV O⁴⁺ microbeam irradiation on SC-CVD diamond film caused pulse height degradation as shown in Fig. 1. The irradiation was performed until a total fluence of 10⁹ [particles/cm²]. The significant and rapid decrease in the pulse height of the IBIC signals was observed in a range of 10⁸ [particles/cm²], whereas the signal responded satisfactorily to the alpha particles from ²⁴¹Am radiation source. However, the peak degradation was temporal and quickly recovered by releasing the detector from the bias voltages. This degradation was significant in areas damaged by previous ion irradiation. This degradation seems to be caused by an accumulated irradiation effect which can be explained by terms of polarization due to charge capture by defects in the SC-CVD diamond. Further analysis is in progress by using diamond films with different impurity densities.

Reference

- 1) W. Kada et al., Trans. Mater. Res. Soc. Jpn. 38 (2013) 279.

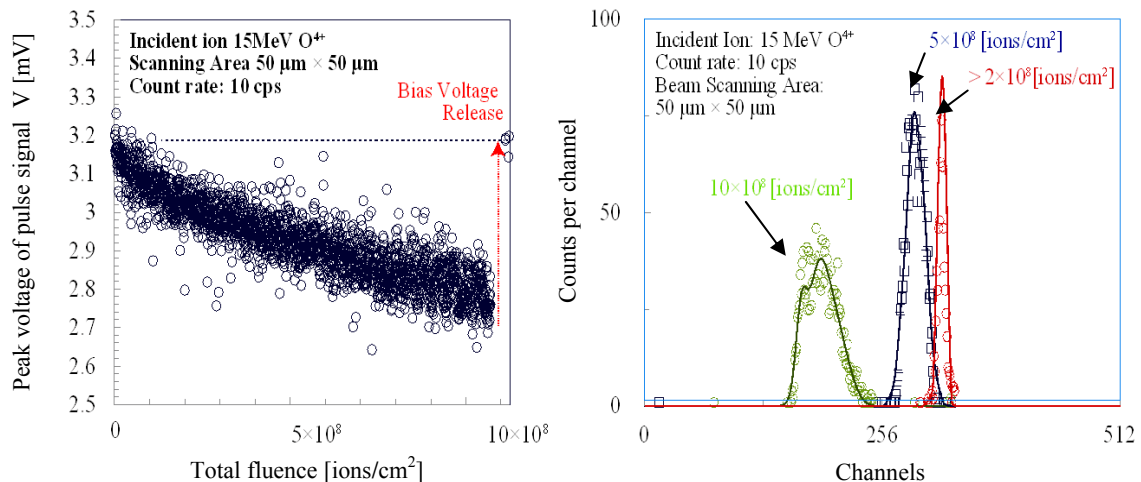


Fig. 1 (Left) The decrease in the pulse height spectra of the IBIC signals with the increase in the total fluence, (Right) IBIC spectra obtained at three different fluences.

4 - 44 Development of a New Ion Microbeam Analysis Technique: Ion Luminescence Microscopic Imaging and Spectroscopy

W. Kada, A. Yokoyama, M. Koka, T. Satoh and T. Kamiya

Department of Advanced Radiation Technology, TARRI, JAEA

1. Introduction

Huge efforts are being made to fulfill increasing interests of researchers in various field of science where precise chemical state analysis of organic/inorganic targets is desired for long time. Ion Luminescence (IL) analysis using ion microbeam probe has a potential to visualize distribution of specific chemical states in microscopic targets, which were not able to be characterized with conventional techniques. In this study, new IL analysis system with proton microbeam probe was developed to accomplish chemical state analysis and imaging of microscopic targets. Microscopic optics for IL was newly designed to obtain high resolution images and spectra.

2. Materials and Methods

Multi-wavelength optics for the spectroscopy of IL was designed and developed at the external microbeam chamber of the 3 MV single-ended accelerator. Whole IL optics was placed on the symmetric coordination to the Si(Li) X-ray detector. Spectroscopy of IL was enabled by introducing IL photons into a UV-Vis spectrometer (Spectra Corp Solid Lambda CCD). First, spectroscopy of IL was performed using high-efficiency gratings with the resolution of 0.8 nm at the effective wavelength ranging from 200 to 980 nm. IL is then detected by electrically-cooled back-thinned CCD sensor array (Hamamatsu Photonics S7031-1006) with high signal-to-noise ratio 10,000:1 for each photon signals. Thermal stability of the CCD sensor array was also improved by using peltier-cooler during measurements. Another photon-detector (photomultiplier head, Hamamatsu Photonics H10682-210) was used to obtain IL images by scanning microbeam. Output signals were processed with the same signal processing procedure of in-air micro PIXE analysis.

3. Results and Discussion

Figure 1 show an example and its expanded image of IL spectrum obtained from Al_2O_3 . Luminescent center of chromium, impurity in host crystal, was clearly distinguished from surroundings with resolution better than 5 nm. High-speed measurement enables us to obtain single IL spectrum in several milliseconds.

Database of IL was also prepared using particulate samples with known elemental and chemical states¹⁾. Particulate minerals were irradiated with a 3 MeV H^+ beam with a typical beam current of approximately 100 pA. Peak wavelengths of IL for specific inorganic (Table 1) or organic materials were gathered for the utilization of microscopic spectroscopy of IL. Further developments including improvements in optical throughput and detection efficiencies of IL are ongoing for the actual utilization of this IL analysis system for chemical state analysis in microscopic targets.

Reference

1) W. Kada et al., Int. J. PIXE, **22** (2012) 21-27.

Table 1 Examples of IL peak wavelength of crystalline targets.

Chemical compounds	Wavelength
SiO_2	460 nm
$\text{SiO}_2\cdot\text{Fe}, \text{Fe}^{3+}$	695 nm
CaSiO_3	556 nm
CaMgSiO_4	525 nm
CaCO_3	560 nm
$\text{Al}_2\text{O}_3\cdot\text{Cr}, \text{Cr}^{3+}$	689 nm

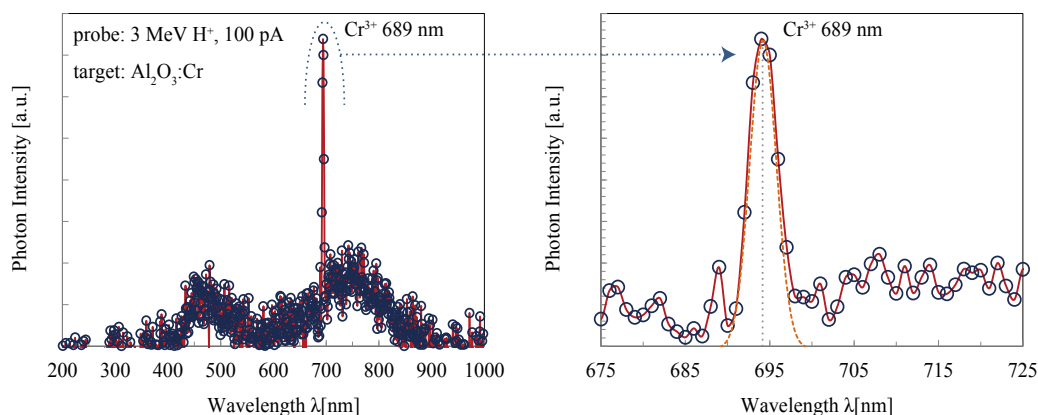


Fig. 1 Example (left) and its expanded image (right) of IL spectrum obtained from particulate targets of aluminum oxide. A sharp peak of chromium (Cr^{3+} , 689 nm) was well obtained.

4 - 45 Coulomb Explosion Process in Collision of a Swift Cluster Ion with Gas Target

A. Chiba, K. Narumi, K. Yamada, S. Matoba and Y. Saitoh

Department of Advanced Radiation Technology, TARRI, JAEA

Understanding the interaction of a cluster/molecular ion with a material such as a solid or a gas target contributes to the underlying studies not only on the atomic-molecular physics and the surface modification science but also on the formation of protostar and the origin of life. The cluster ion penetrating the material scarcely loses more than two outer electrons by the collision with target atoms when it is dissociated and spreads the interatomic distance between the constituent ions due to the Coulomb repulsion force. Such behavior of the cluster ions, which is called as a Coulomb explosion, is one of most significant processes in the interaction between cluster ions and the material. In this report, a part of the Coulomb explosion process is presented; it was obtained by analyzing the angular distributions of the constituent ions resulting from the dissociation of C_2^+ ions by the collision with an atom in the gas target.

A schematic drawing of the experimental setup is shown in Fig. 1. The intensity of the collimated pulsed beam of 6-MeV C_2^+ ions from 3-MV tandem accelerator of TIARA is adjusted so as to penetrate through an Ar gas target at the rate of a few ions per second. The Ar gas jet synchronized to the pulsed beam is discharged from the skimmer (1 mm × 3 mm) at a 9-Hz repetition rate. According to the density of the gas in the collision area, the collision frequency of the incident ions with target atoms is estimated to be about 1 time. The constituent ions resulting from gas-induced dissociation are deflected to the vertical direction in accordance with their charges by the electric field of the deflection plates located behind the gas target. The spatial arrangements of the deflected ions detected with a micro-channel plate equipped with a phosphor screen are stored as image data on an event-by-event basis.

A divergence angular distribution obtained from the spatial arrangements of the pairs of constituent ions in charge states $1+$, is plotted as the solid square symbols in Fig. 2. In terms of the geometry, the angular distribution for the diatomic molecule has a peak as shown in Fig. 2; the divergence angle configuring the peak is derived from the molecule of which the molecular orientation at the instant of dissociation has been perpendicular to the beam axis. Moreover, the divergence angle of the peak depends on the interatomic distance at the instant of dissociation. The angular distributions shown as histogram in the same figure was calculated with a particle trajectory simulation taking into account the molecular vibration; the solid and dotted line were obtained using the different distributions of interatomic distance at the instant of dissociation, shown as solid and dotted line in Fig. 3, respectively. Here, the distribution of interatomic distance indicated as dotted line

in Fig. 3 was acquired via the foil-transmission experiments for 6-MeV C_2^+ ions¹⁾. On the other hand, by assuming the solid line in Fig. 3, the calculated distribution of the divergence angle relatively well-reproduced the experimental result (shown as solid square in Fig 1). This result will enable us to describe more concretely the process leading to the dissociation from several excited electronic states of C_2^+ ions caused by the collision with an atom.

Reference

- 1) A. Chiba, et al., Nucl. Instrum. Meth. Phys. Res. B 269 (2011) 824.

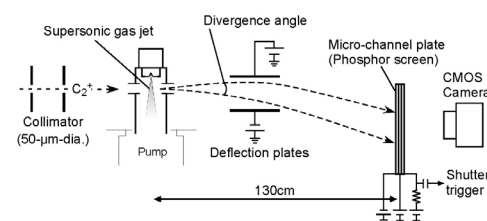


Fig. 1 Schematic drawing of experimental setup.

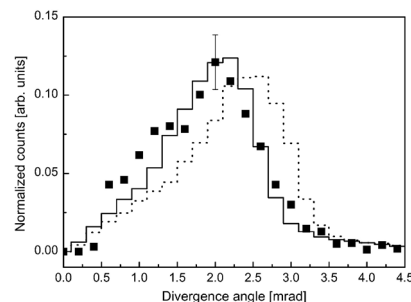


Fig. 2 Divergence angular distributions of constituent ions for 6-MeV C_2^+ ions passing through the Ar gas target. Experimental and calculation results are indicated as the solid square symbols and histograms, respectively (see text).

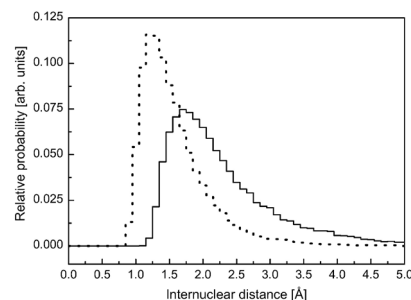


Fig. 3 Distributions of the interatomic distance at the instant of dissociation for C_2 ions. They were used as the initial condition for the trajectory simulations.

4 - 46 Study of Ion Induced Luminescence from Sapphire Irradiated with Swift Cluster Ion Beams

H. Shibata^{a)}, Y. Saitoh^{b)}, A. Chiba^{b)}, K. Yamada^{b)}, K. Narumi^{b)} and M. Taguchi^{c)}

^{a)}Graduate School of Engineering, Kyoto University,

^{b)}Department of Advanced Radiation Technology, TARRI, JAEA

The interaction of swift cluster ions with matter has been studied for these ten years, because it is strongly interesting that cluster ions bombard a very small area of a solid surface with many energetic atoms simultaneously and release large energy in the time range around pico-second. These situations cause non-linear effects or synergetic effects, which are not normally caused by a single atom collision with solid targets.

Our purpose of this study is to elucidate the characteristics of the interaction between energetic cluster ions and solids by means of measuring luminescence from solid surfaces irradiated with cluster ions. We report some results of luminescence measurement from sapphire target irradiated with carbon cluster ions.

Luminescent spectra from sapphire ($\alpha\text{-Al}_2\text{O}_3$) induced by 0.5~2.0 MeV/atom (42~168 keV/u) $\text{C}_1^+ \sim \text{C}_8^+$ ion irradiation were measured in the wavelength range of 250~800 nm at room temperature. Cluster ion beams accelerated by the TIARA 3 MV tandem accelerator were used for this study. Beam intensities were typically 2.5 nA for C_1^+ and 50 pA for C_8^+ ions at 0.5 MeV/atom. The luminescence measurement has been carried out by using an optical multichannel analyzer (Hamamatsu Photonics PMA11). Cluster ion size and energy dependences of incident cluster ion beams on luminescence yield have been measured. Two peaks around 326 and 411 nm were observed in ion induced luminescent spectra. Luminescence of 326 nm was identified as F^+ center, whose intensity grew up and decayed gradually with irradiation. Luminescence of 411 nm was F center, whose intensity grew up rapidly and decayed faster than F^+ center luminescence in time resolved observation¹⁾. Intensities of luminescence reached peaks with less fluence as the cluster size increased.

The incident cluster ion size dependence on the yield of the F^+ center luminescence from sapphire target with different incident energies is shown in Fig. 1. In this study the maximum intensity of luminescence was set as the luminescence yield, since the intensity of luminescence depended on the ion fluence. Each yield was compare to the yield for C_1^+ ion irradiation. Ratios R_n of luminescence yields from sapphire target irradiated with 0.5, 1.0, 1.5 and 2.0 MeV/atom $\text{C}_2^+ \sim \text{C}_8^+$ incident cluster ions to that for C_1^+ ion are described as $R_n = I(n) / nI(1)$, where n is number of cluster ion, $I(n)$ is the yield for C_n^+ cluster ion and $I(1)$ is the yield for C_1^+ ion. The luminescence yields increase as the cluster sizes increase for every incident energy, but the ratios R_n become almost less than unity. The ratio 'unity' means that the yield increases linearly as the cluster size increases.

This non-linearity also appears in the theoretical calculation of the stopping power ($S = -dE/dx$) for the united atom limit of cluster ions²⁾. The ratio R_n of stopping power of cluster ion to that of single atom ion describes as $R_n = S(n) / nS(1)$.

$$R_n = n \left((1 - \exp(-v/(nZ_1)^{2/3}v_0)) / (1 - \exp(-v/Z_1^{2/3}v_0)) \right)^2,$$

where v is the velocity of the projectile, v_0 is the Bohr velocity and Z_1 is the nuclear charge of the projectile. This value is independent to kinds of targets and depends on incident velocity only, if Z_1 will be fixed.

Though there is the difference between the values of the experimental data and that of the calculation data of stopping power for the united atom of the cluster ions, the tendency of experimental data resembles that of the calculated one.

This suggests that luminescence caused by irradiation defects directly relates the stopping power of incident cluster ion.

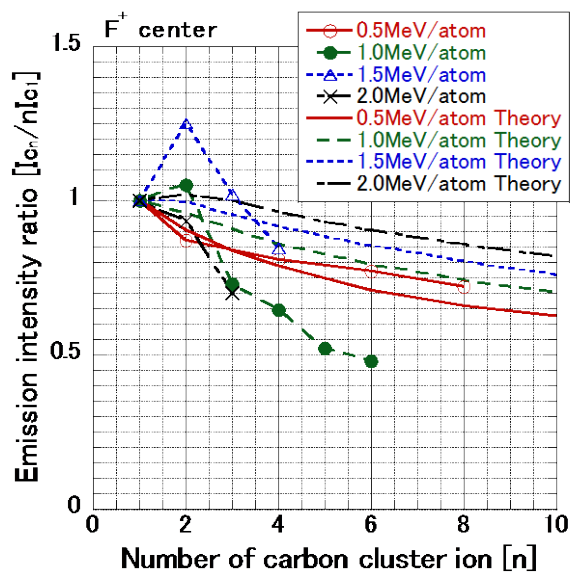


Fig. 1 The ratios of yields of luminescence from F^+ center of sapphire target irradiated with 0.5~2.0 MeV/atom $\text{C}_2^+ \sim \text{C}_8^+$ projectiles to that for C_1^+ ions in each energy indicate with continuous lines. Dashed and dotted lines show the theoretical stopping power calculation for the united atom of projectile.

References

- 1) Y. Aoki et al., Nucl. Instrum. Meth. Phys. Res. B 114 (1996) 276-80.
- 2) P. Sigmund et al., Nucl. Instrum. Meth. Phys. Res. B 112 (1996) 1-12.

4 - 47 Electronic Stopping Power of Al and Si for Swift Carbon Cluster Ions with Average Charge Reduction

T. Kaneko^{a)}, K. Ihara^{a)}, F. Miyahara^{a)}, Y. Saitoh^{b)}, A. Chiba^{b)} and K. Narumi^{b)}

^{a)}Graduate School of Science, Okayama University of Science,

^{b)}Department of Advanced Radiation Technology, TARRI, JAEA

Cluster-ion-solid interaction has attracted attention in that the irradiation effects are different from those expected in single-ion irradiation. The so-called cluster effects have been found in the average charge¹⁾, energy-loss¹⁾, and secondary electron emission²⁾ under MeV/atom carbon cluster impacts. In order to show a basic quantity in the cluster-solid interaction, we present the electronic stopping power of Aluminum and Silicone for swift carbon clusters together with the reductive effect in the cluster average charge^{1,3)}.

This theoretical research is composed of estimating the reduced average charges of constituent ions in a cluster and evaluating the electronic stopping power for a cluster, using the reduced average charges. The theoretical basis is to describe the incident cluster as an ensemble of partially stripped ions, where their charges are determined by the self-consistent cluster average-charge theory, and their spatial charge distribution is described in a statistical manner. The excitation of target electrons is treated in the dielectric formalism for an electron gas model. The dynamical responses of the conduction and shell electrons are treated with Lindhard dielectric function and the dielectric function in the wave-packet model, respectively¹⁾. The sum of those two contribution yields the stopping of the material.

Figures 1 and 2 show the electronic stopping power ratio, $S(n)/nS(1)$, of Al and Si target, respectively, for a carbon cluster C_n ion having a linear-chain structure with equal separation of $2.4 a_0$ (a_0 is the Bohr radius) to that for a C ion with an equivalent speed, as a function of ion speed in units of the Bohr speed v_0 . The solid line, the dotted line, the dot-dash line, dot-dot-dash line, and the dashed line refer to $n=2, 3, 4, 6$, and 10 , respectively. Here the so-called R_s values are assumed to be 2.070 for Al with three conduction electrons per atom, and 2.006 for Si with four conduction electrons, respectively. Regarding the inner-shell electrons, i.e., $1s, 2s$ and $2p$ electrons, the characteristic parameters were listed in ref. 4. In both figures, at a glance, one finds that $S(n)/nS(1)$ represents a remarkable super-linear dependence for each target over a wide range of speed. In the low speed region, on the other hand, the stopping power ratio shows the sub-linear dependence with increasing the number of constituent atoms in a cluster. In addition, the stopping ratio has a plateau up to $v/v_0=5$ and a rapid increase when the speed exceeds this value. This tendency, common to Al and Si targets, is attributed to excitation of the inner-shell electrons and a strong charge correlation in a moving cluster, regardless of linear-chain structure or ring structure. A plateau is not seen in carbon target. As for

the difference of $S(n)/nS(1)$ between linear- and ring-structure, we reported recently in ref. 5. Finally we are grateful for useful discussion of project members in collaboration.

References

- 1) T. Kaneko, Phys. Rev. A66, (2002) 052901.
- 2) S. Tomita et al., Phys. Rev. A73, (2006) 060901(R).
- 3) A. Chiba et al., Phys. Rev. A76 (2007) 063201.
- 4) T. Kaneko, At. Dat. Nucl. Dat. Tab. 53 (1993) 271.
- 5) T. Kaneko et al., Nucl. Instrum. Meth. Phys. Res. B 315(2013)76.

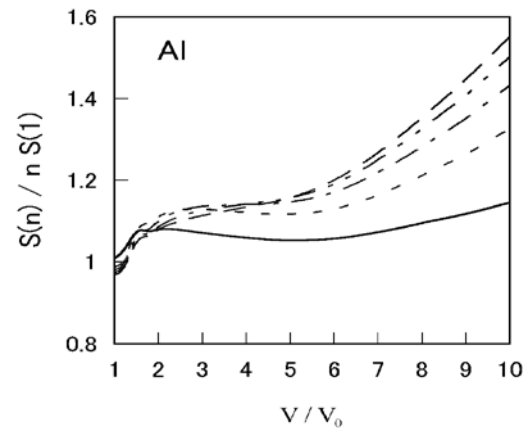


Fig. 1 Electronic stopping-power ratio of Al for a C_n cluster ion to that for a C ion cluster: solid line ($n=2$), dotted line ($n=3$), dot-dash line ($n=4$), dot-dot-dash line ($n=6$), and the dashed line ($n=10$).

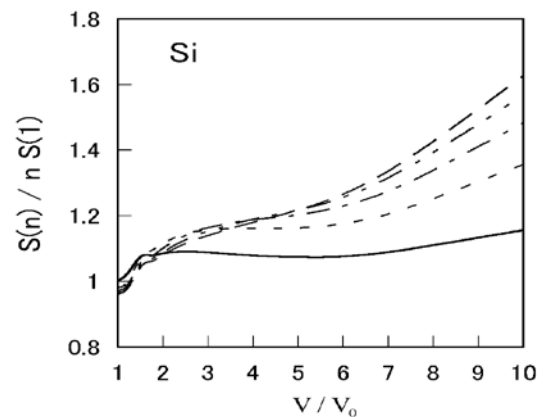


Fig. 2 Electronic stopping-power ratio of Si for a C_n cluster ion to that for a C ion cluster: solid line ($n=2$), dotted line ($n=3$), dot-dash line ($n=4$), dot-dot-dash line ($n=6$), and the dashed line ($n=10$).

4 - 48 Comparison of Positive Secondary Ion Emission Yields for PMMA between Low Energy Bi and C₆₀ Ion Impacts

K. Hirata^{a)}, Y. Saitoh^{b)}, A. Chiba^{b)}, K. Yamada^{b)},
S. Matoba^{b)} and T. Kamiya^{b)}

^{a)}National Institute of Advanced Industrial Science and Technology (AIST),
^{b)}Department of Advanced Radiation Technology, TARRI, JAEA

Secondary ions (SIs) are ejected from the surface when the primary ions bombard the target. Cluster ion impact on a target produces different SI emission yields compared with those for monoatomic ions because of their peculiar irradiation effects caused by simultaneous energy transfer from the constituent atoms of the cluster to a small area of the target surface. In this paper, we report comparison of SI emission yields from a Poly(methyl methacrylate) (PMMA) thin film target for incident ion impacts of lower energy monoatomic heavy ions (30 keV Bi⁺) and C₆₀ cluster ions by time-of-flight (TOF) SI mass analysis combined with SI electric current measurements. Bi ions with lower incident energy (several tenth keV) are widely used as primary ions of commercial SI mass spectrometers.

The PMMA thin-film target was produced by spin coating an dichlorobenzene solution of PMMA (Wako Pure Chemical Industries, Ltd.) on a silicon wafer. SI emission yield measurements for PMMA were performed using a TOF mass analyzer combined with pulsed ion beams produced by a 400 kV ion implanter of the Japan Atomic Energy Agency (JAEA)/Takasaki¹⁾, which has been described elsewhere²⁾. Cluster ion impacts on organic compounds are expected to give a relatively high total SI yield per impact because, in addition to the enhanced SI yield per incident atom, the number of incident atoms per impact for a cluster ion is cluster number times higher relative to that for the corresponding monoatomic ion³⁾. We used a SI counting system that can accurately obtain TOF SI mass spectra even when many SIs are detected for one pulse. For quantitative comparison of SI emission yields per incident ion impact, peak intensities of the TOF spectra were plotted by scaling the total count of each spectrum based on qI_s/I_o (q : incident ion charge number, I_o : incident beam electric current, I_s : positive SI current for each irradiation condition), respectively. I_o and I_s were measured by highly sensitive electrometers, respectively, connected to a Faraday cup and a movable metal plate with a grid.

Figure 1 shows the positive SI TOF spectra from m/z (mass to charge ratio) = 55 to 75 of PMMA for (a) 30 keV Bi⁺ and (b) 30 keV C₆₀⁺, respectively. The relative intensity on the vertical axis is proportional to the SI yield per incident ion impact, as the total counts of the spectra are scaled based on I_p/I_o as described above. The major peaks at $m/z=59$ and $m/z=69$ in the figure can be attributed to C₂H₃O₂⁺ and C₄H₅O⁺, respectively. The SI yields of the peaks for 30 keV C₆₀⁺ are much higher than those for

30 keV Bi⁺, showing that the C₆₀ impact provides the SIs more effectively than the impact of heavy monoatomic Bi with the same incident energy.

The SI yields are influenced by energy transfer processes and their deposited energy densities around the impact-points. In the previous paper, we reported that the SI yields for C₆₀ impacts increase with increasing incident energy and that the electronic process may dominantly contribute to the SI yields⁴⁾. In the present study, both the densities of the energies transferred to the target surface by the nuclear and electronic processes are higher for the C₆₀ impact than those for the Bi impact. Although the detailed mechanism for the higher SI yields for C₆₀ than that for Bi is currently unclear, the higher electronic energy density for the C₆₀⁺ impact than that for the Bi⁺ impacts may dominantly contribute to this mechanism in an analogy of the previous results.

References

- 1) Y. Saitoh et al., Nucl. Instrum. Meth. Phys. Res. A **452** (2000) 61.
- 2) K. Hirata et al., Nucl. Instrum. Meth. Phys. Res. B **266** (2008) 2450.
- 3) K. Hirata et al., Rev. Sci. Instrum. **82** (2011) 033101.
- 4) K. Hirata, et al., JAEA Takasaki Annu. Rep. **2008** (2009) 164.

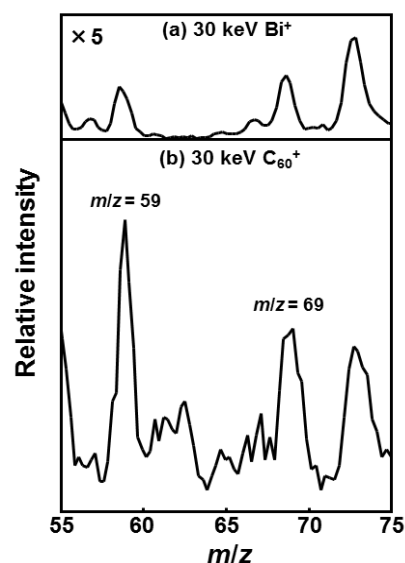


Fig. 1 Positive secondary ion TOF spectra of PMMA for (a) 30 keV Bi⁺, and (b) 30 keV C₆₀⁺. Peaks at $m/z=59$ and 69 are attributed to C₂H₃O₂⁺ and C₄H₅O⁺, respectively.

4 - 49 Vicinage Effect on Secondary-electron Yield from Carbon Foils Bombarded with 62.5-250-keV/u H_2^+ and C_2^+ Ions

K. Narumi, A. Chiba, K. Yamada, S. Matoba and Y. Saitoh

Department of Advanced Radiation Technology, TARRI, JAEA

Secondary-electron (SE) emission from a solid surface bombarded with fast charged particles is a very fundamental phenomenon and has been studied extensively for a long time; however, it is not still understood completely. Vicinage effect on the SE emission induced by swift molecular/cluster ions is one of the unresolved problems^{1,2)}. The previous reports including ours¹⁻⁵⁾ have suggested that the *transport* process of scattered electrons in a solid in the three-step model⁶⁾ plays an important role in the effect as well as the *production* process. In the present report, we demonstrate our internuclear-analysis of the effect on the SE emission induced by bombardment with H_2^+ and C_2^+ ions in the same velocity region.

62.5-250-keV/u H_2^+ and C_2^+ ions available at TIARA were incident on self-supporting amorphous carbon foils of 2-100 $\mu\text{g}/\text{cm}^2$ thickness, which were tilted by 45° to the beam axis. SE's emitted in the forward and backward directions from a carbon foil were detected with two microchannel-plate (MCP) detectors placed at the both sides of the target holder in parallel with the foil. Projectiles transmitted through the foil were detected with a solid-state detector (SSD) placed at the backside of the target holder on the beam axis, which made it possible to measure the energy and the number of the transmitted particles. The signal from each detector was stored in a PC in list mode. In order to evaluate the vicinage effect correctly, only MCP signals coinciding with the two-hydrogen or carbon signals were selected, and the pulse-height distributions of MCP were measured. The forward and backward SE yields per incident projectile were determined from the pulse-heights of the forward and backward MCP signals, respectively, which were proportional to the number of detected SE's.

In this report, only the measurement for the forward SE emission is discussed. The vicinage effect was evaluated with the ratio of the forward SE yields $R_2 = \gamma_2/2\gamma_1$, where γ_2 and γ_1 are SE yields induced by bombardment with diatomic and monatomic ions with the same velocity, respectively. As shown in Fig. 1, enhancement and suppression of SE emission have been observed for H_2^+ ions and C_2^+ ions, respectively. It should be noted that change of R_2 at the smaller internuclear distances than ~ 1 nm depends on the velocity; at the larger internuclear distances than ~ 1 nm, on the other hand, R_2 is almost constant and still not the unity. The former indicates that the change of R_2 could be attributed to the *production* process, because the vicinage effect on the energy loss, which determines the number of scattered electrons approximately, in this velocity region diminishes at the smaller internuclear distance than ~ 1 nm. The latter indicates the *transport* process is dominating at the larger internuclear distances where the vicinage effect on

the energy loss diminishes. We can conclude from the present internuclear-distance analysis that the vicinage effect on SE yield consists of two contributions, one in the *production* process and the other in the *transport* process. The effect in the *production* process is due to the effect on the energy-loss process of the projectile; on the other hand, the physical mechanism of the vicinage effect in the *transport* process is still an open question.

This work was supported in part by a Grant-in-Aid for Scientific Research (C) No. 22560833 from JSPS.

References

- 1) A. Billebaud *et al.*, Nucl. Instrum. Meth. B **112** (1996) 79.
- 2) H. Kudo *et al.*, Jpn. J. Appl. Phys. **45** (2006) L565.
- 3) H. Arai *et al.*, J. Phys. Soc. Jpn. **78** (2009) 104301.
- 4) Y. Takahashi *et al.*, EPL **88** (2009) 63001.
- 5) Y. Takahashi *et al.*, JAEA Takasaki Annu. Rep. 2009 (2011) 164.
- 6) E. J. Sternglass, Phys. Rev. **108** (1957) 1.

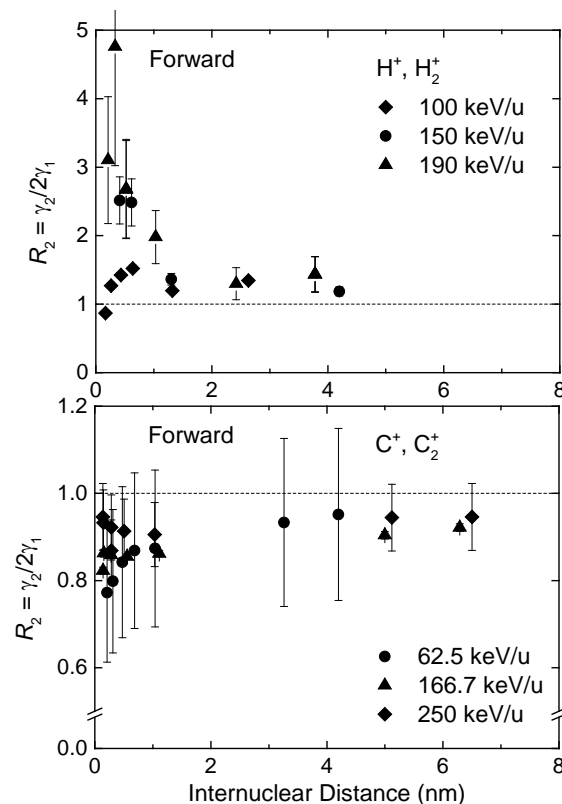


Fig. 1 Dependences of the ratio of the forward SE yields R_2 on the internuclear distance between the dissociated ions. The internuclear distance was estimated with simple trajectory calculation after the dissociation in the foil.

4 - 50

 Production of Fast C_{60} Microbeam Using the Capillary-beam Focusing Method

H. Tsuchida^{a)}, T. Majima^{a)}, S. Tomita^{b)}, K. Sasa^{c)}, K. Narumi^{d)}, Y. Saitoh^{d)}, A. Chiba^{d)},
K. Yamada^{d)}, K. Hirata^{e)}, H. Shibata^{f)} and A. Itoh^{f)}

^{a)}Quantum Science and Engineering Center, Kyoto University, ^{b)}Institute of Applied Physics, University of Tsukuba, ^{c)}Tandem Accelerator Complex, University of Tsukuba, ^{d)}Department of Advanced Radiation Technology, TARRI, JAEA, ^{e)}National Institute of Advanced Industrial Science and Technology (AIST), ^{f)}Department of Nuclear Engineering, Kyoto University

We apply the capillary beam-focusing method for the C_{60} fullerene projectiles in the velocity range 0.14-0.2 a.u. We studied the C_{60} transmission properties through a capillary, and measured the transmitted particle composition by using the electrostatic deflection method combined with the MCP imaging technique. The main transmission component was found to be primary C_{60} beams that are focused in the area equal to the capillary outlet diameter. We found that the C_{60} transmission fraction is considerably high in the present velocity range.

The experiment was performed at TIARA. Projectile beams of 360 keV C_{60}^{q+} ($q = 1, 2$) and 720 keV C_{60}^{2+} ions were collimated by two sets of slits and then transmitted through a capillary mounted on a high precision goniometer. We employed a borosilicate glass capillary with an outlet diameter of 5.5 μm . The capillary taper angle in the exit region was 0.1° or less. To analyze the outgoing ion species after passing through capillaries, the transmitted particles were deflected by an electric field. The deflected particles were detected by a rectangular (MCP) with a phosphor screen. The two-dimensional image spectra were recorded with a CMOS camera.

In Fig. 1 we present two-dimensional histogram (image spectra) of transmitted particle components. The y-axis projections are shown together on the left panel which indicates mass-to-charge distributions of transmitted particles. The electric field was applied in the downward direction in the image spectra. The spectra denoted by “total” shown in Figs. 1 (a) and (c) correspond to the data for all of the luminescence intensity signals from the MCP imaging detector. The spectra consist of the C_{60} primary ions (main components), charged fullerene-like fragments C_{60-2m} caused by successive C_2 emission (in the down part of the C_{60} peak), and neutrals. The beam spot size of C_{60} primary ions is almost the same as the capillary outlet diameter. As seen in Fig. 1 (c), the same features were observed for 720 keV C_{60}^{2+} projectiles with higher charge state at higher energy. Figures 1 (b) and (d) show image spectra only for detection of C_{60} and fullerene-like C_{60-2m} particles. In this measurement, we selected the signals of high luminescence intensity from the MCP detector. Relative peak intensity of primary C_{60} ions (or direct transmission fraction) are 92% and 84% for projectiles of 360 keV C_{60}^+ ions and 720 keV C_{60}^{2+} ions, respectively. This comparison indicates that the transmission fraction of

primary ions increases with decreasing the incident energy or projectile velocity. In comparison between “total” (Fig. 1 (a) and (c)) and “high luminosity” image spectra (Fig. 1 (b) and (d)), spot profiles for neutral particles are completely different. This difference is due to the contribution of small-sized neutral fragments. We also performed measurements of charged small fragments C_n^+ ($n = 1, 2, 3, \dots$) arising from the C_{60} multifragmentation by applying a weak electric field to the deflection plates. Such fragment ions cannot be observed within the experimental uncertainties.

The present results suggest that the capillary beam-focusing method is applicable for large molecular particles like a C_{60} fullerene. The application will lead to the development of new techniques for materials component analysis at the micro-scales, such as molecular mapping by secondary ion mass spectrometry (SIMS).

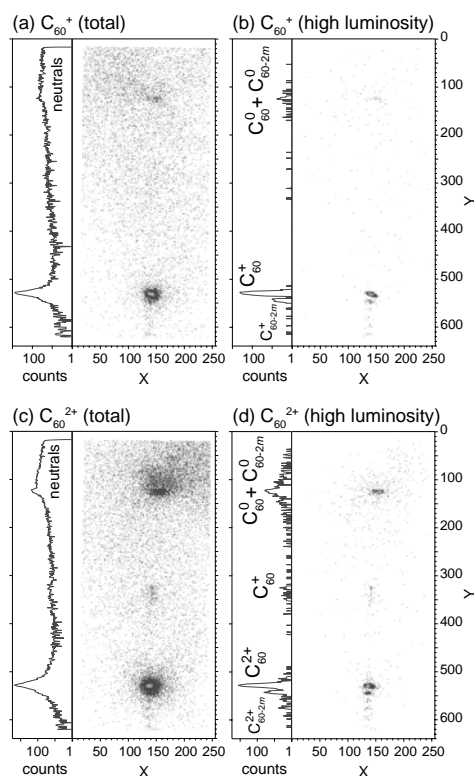


Fig. 1 Transmitted particle spectra measured with the MCP imaging detector for 360 keV C_{60}^+ (upper) and 720 keV C_{60}^{2+} (lower) passing through a capillary of 5.5 μm diameter. In the X and Y axes, one pixel is 0.127 mm.

4 - 51 Ion Tracks in Amorphous Si_3N_4 Films Produced by Sub MeV C_{60} Ion

K. Nakajima^{a)}, Y. Morita^{a)}, M. Suzuki^{a)}, K. Narumi^{b)}, Y. Saitoh^{b)}, K. Hojou^{c)},
M. Tsujimoto^{d)}, S. Isoda^{d)} and K. Kimura^{a)}

^{a)}Department of Micro Engineering, Kyoto University, ^{b)}Department of Advanced Radiation Technology, TARRI, JAEA, ^{c)}Advanced Science Research Center, JAEA,
^{d)}Institute for Integrated Cell-Material Sciences, Kyoto University

When an energetic ion passes through a material, an ion track may be produced along the ion path if the electronic stopping power S_e is larger than a material dependent threshold value¹⁾. Although there are a number of studies on the ion tracks produced in crystalline materials using transmission electron microscopy (TEM), there are only a limited number of TEM studies on the ion tracks in amorphous materials due to a lack of sufficient contrast. In this report, the ion tracks in amorphous Si_3N_4 films irradiated with 120-720 keV $\text{C}_{60}^{+,2+}$ ions were observed with TEM and high-angle annular dark field scanning transmission electron microscopy (HAADF-STEM). The radial density distribution of the ion track was derived from the observed HAADF-STEM images.

Self-supporting amorphous Si_3N_4 (a- Si_3N_4) films of thickness 20 nm were purchased from Silson Ltd, which were prepared by chemical vapor deposition on Si wafers. The a- Si_3N_4 films were irradiated with 120-720 keV $\text{C}_{60}^{+,2+}$ ions from the 400-kV ion implanter of TIARA to fluences $1\text{--}5 \times 10^{11}$ ions/cm². After the ion irradiation, TEM and HAADF-STEM observations were performed using a JEOL JEM-2200FS equipped with a field-emission gun operating at 200 kV.

Figure 1 shows an example of the observed HAADF-STEM image for a- Si_3N_4 irradiated with 720-keV C_{60}^{2+} ions. There are dark circular structures of almost uniform diameter of ~4 nm. The number of these structures agrees with the fluence of the C_{60}^{2+} ions, indicating that single C_{60}^{2+} impacts create individual circular

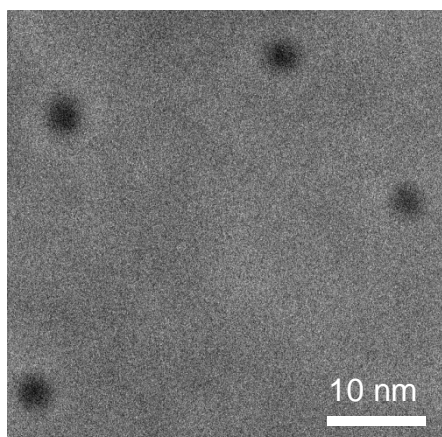


Fig. 1 HAADF-STEM image of an a- Si_3N_4 film irradiated with 720-keV C_{60}^{2+} ions to a fluence of $\sim 2 \times 10^{11}$ ions/cm².

structures. The radial density profiles of the ion tracks were derived from the observed HAADF-STEM images.

Figure 2 shows the obtained profiles for 360-keV, 540-keV and 720-keV C_{60}^{2+} impacts. The density is about 80% of the bulk density at the track center and increases with increasing distance r from the center. The low-density core is surrounded by a high-density shell of which the density is 1-2% larger than the bulk density. For comparison, radial density profiles of ion tracks in a- SiO_2 calculated by MD simulation at various electronic stopping powers²⁾ are also shown by short dashed lines. Although the material is different, the characteristic features (low-density core and surrounding high-density shell) are similar to the present observation. The observed stopping power dependence, however, is very different from the simulation. The observed profile changes only slightly when S_e changes from 6.8 (for 360-keV C_{60} ions) to 9.6 keV/nm (for 720-keV C_{60} ions) while the simulated profile changes significantly when S_e changes from 7.2 to 10.8 keV/nm. Considering that the total stopping of C_{60} ion is almost constant in this energy region (360-720 keV), the present result indicates that not only the electronic stopping power but also the nuclear stopping power plays an important role in the ion-track formation.

References

- 1) A. Meftah et al., Phys. Rev. B **49** (1994) 12457.
- 2) P. Kluth et al., Phys. Rev. Lett. **101** (2008) 175503.

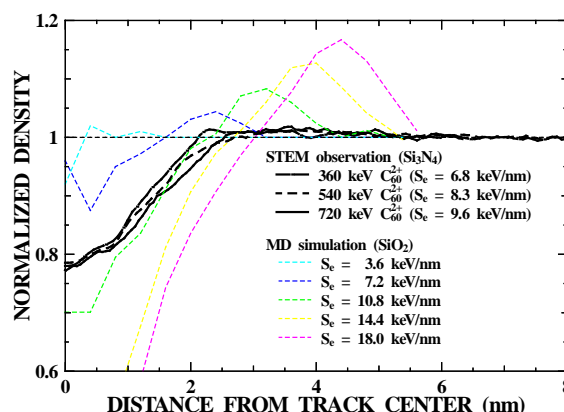


Fig. 2 Radial density profiles of the ion track obtained from the observed HAADF-STEM images of a- Si_3N_4 films irradiated with 360-keV (dot-dashed line), 540-keV (dashed line) and 720-keV C_{60}^{2+} ions (solid line).

This is a blank page.

5. Present Status of Irradiation Facilities 2011

5-01	Utilization Status at TIARA Facility	177
	Y. Haruyama, H. Takizawa, M. Hosono, K. Mizuhashi, Y. Nakamura, S. Kaneya, T. Asai, M. Kawabata and K. Imai	
5-02	Operation of the AVF Cyclotron	178
	I. Ishibori, S. Kurashima, K. Yoshida, T. Yuyama, T. Ishizaka, N. Miyawaki, H. Kashiwagi, Y. Yuri, S. Okumura, T. Nara, To. Yoshida, Tu. Yoshida, K. Akaiwa, S. Ishiro, S. Kanou, A. Ihara, K. Takano and H. Saitoh	
5-03	Operation of Electrostatic Accelerators	179
	S. Uno, A. Chiba, K. Yamada, A. Yokoyama, A. Usui, Y. Saitoh, Y. Ishii, T. Satoh, T. Ohkubo, T. Nara, T. Kitano, T. Takayama, S. Kanai, T. Orimo, Y. Aoki and N. Yamada	
5-04	Operation of the Electron Accelerator and the Gamma-ray Irradiation Facilities	180
	T. Agematsu, Y. Haruyama, H. Hanaya, R. Yamagata, H. Seito, Y. Nagao, H. Kaneko, T. Yamaguchi, N. Yagi, M. Takagi, I. Kawashima and S. Matsuzaki	
5-05	Utilization Status of the Electron Accelerator and the Gamma-ray Irradiation Facilities	181
	T. Agematsu, Y. Haruyama, H. Hanaya, R. Yamagata, H. Seito, Y. Nagao, H. Kaneko, T. Yamaguchi, N. Yagi, M. Takagi, I. Kawashima and S. Matsuzaki	
5-06	Radiation Control in TIARA	182
	Safety Section	
5-07	Radioactive Waste Management in TIARA	183
	M. Nabatame and T. Hosoi	
5-08	FACILITY USE PROGRAM in Takasaki Advanced Radiation Research Institute	184
	H. Yoshida, D. Ushijima and K. Shidomi	

This is a blank page.

5 - 01

Utilization Status at TIARA Facility

Y. Haruyama^{a)}, H. Takizawa^{a)}, M. Hosono^{a)}, K. Mizuhashi^{a)},
Y. Nakamura^{b)}, S. Kaneya^{b)}, T. Asai^{b)}, M. Kawabata^{b)} and K. Imai^{b)}

^{a)}Department of Advanced Radiation Technology, TARRI, JAEA,

^{b)}Takasaki Establishment, Radiation Application Development Association

1. Utilization Status

The shift of cyclotron utilization time assigned to the respective research fields is shown in Fig. 1. For recent 10 years, utilization time of cyclotron gradually decreased about 300 h from 2,500 h to 2,200 h. In FY (Fiscal year) 2012, this time was 2,243.5 hours. The biggest part of utilized scientific field was “Medical and Biotechnological application”, occupied 26% of whole utilization. The second largest part of “Basic technology” was 23%, and the ratio of “Outside utilization (common use)” was 17%.

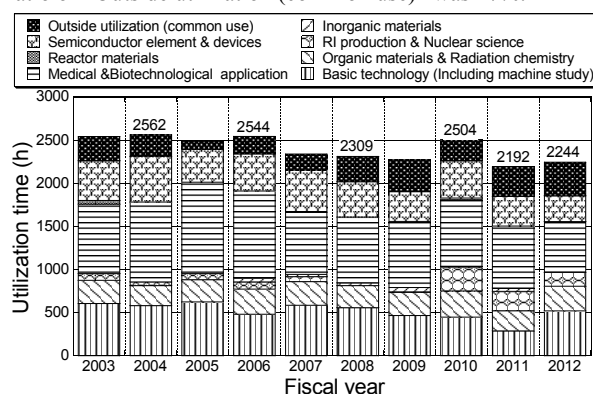


Fig. 1 Shift of cyclotron utilization time for recent 10 years.

In case of three electrostatic accelerators, the shift of total utilization time assigned to the respective research fields is also shown in Fig. 2. On the Contrary, this time slowly increased up to 480-490 days from 460 days during last 10 years. In FY 2012, this time attained to 490 days. The largest scientific field of “Basic technology” occupied about a half, besides the ratio of “Outside utilization” was 8.2%.

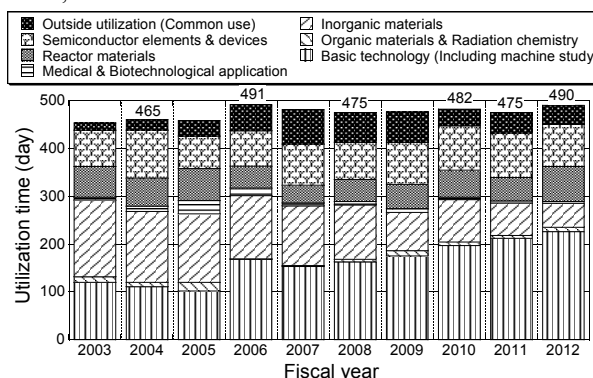


Fig. 2 Shift of total utilization time in three electrostatic accelerators during recent 10 years.

It seems that the influence induced by the huge earthquake and the severe accident of nuclear power station somewhat appears at FY 2011 as seen in Figs. 1 and 2.

Typical trend for last decade between the number of entire research visitors and research subjects applied to TIARA facility is shown in Fig. 3. After the visitors reached once at 1405 persons of maximum value in FY 2005, they rather rapidly decreased to about 800 ones. The main reason of this reduction has been thought that the support for user's travel fee was cut off completely in FY 2006. The number of research visitors and research subjects in FY 2012 was 840 and 128, respectively. Present situation may be seen at normal condition in consideration of recent tendency.

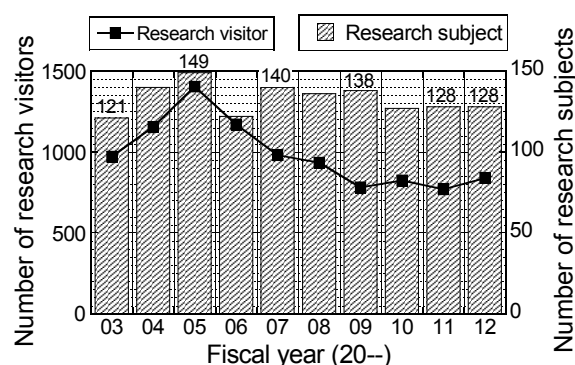


Fig. 3 Relationship between the number of research visitors and research subjects at TIARA facility.

Furthermore, twelve of total 128 research subjects included in research issues related to fatal accident at Fukushima Daiichi nuclear power station. These typical issues were as follows; remote robot system operated under extreme environment into high radiation and temperature, cadmium and cesium transition to human body from contaminated soil, radiation degradation of cesium adsorbent, rice breeding functioned with low cesium absorption, and so on.

In regard to the utilization form, both constructed ratios of JAEA internal and joint research use showed unexpectedly the same values which are about 41% in case of cyclotron and about 35% for electrostatic accelerators, respectively.

2. The others

Seventh Takasaki Advanced Radiation Research Symposium was held successfully on 11th to 12th in October, 2012 at Takasaki City Gallery. The number of presentations for oral and poster sessions was 19 and 142, respectively. Participants to this symposium were 526, which increased 66 persons in comparison with last meeting.

In addition, the JAEA Takasaki annual report 2011 summarized research results and activities at Takasaki Advanced Radiation Research Institute was also issued. This report contained 158 papers consists of 209 pages including 37 coloured sheets, and was printed as 600 books.

5 - 02

Operation of the AVF Cyclotron

I. Ishibori^{a)}, S. Kurashima^{a)}, K. Yoshida^{a)}, T. Yuyama^{a)}, T. Ishizaka^{a)}, N. Miyawaki^{a)},
H. Kashiwagi^{a)}, Y. Yuri^{a)}, S. Okumura^{a)}, T. Nara^{a)}, To. Yoshida^{b)}, Tu. Yoshida^{b)},
K. Akaiwa^{b)}, S. Ishiro^{b)}, S. Kanou^{b)}, A. Ihara^{b)}, K. Takano^{b)} and H. Saitoh^{b)}

^{a)}Department of Advanced Radiation Technology, TARRI, JAEA, ^{b)}Beam Operation Service, Co., Ltd.

Operation

The AVF cyclotron was smoothly operated in fiscal 2012. For comparison, it includes the data in fiscal 2011. The cumulative operation time was 69,092.3 hours and the total number of experiments was 9,788 from the first beam extraction in 1991 to March 2013.

Table 1 shows the statistics of the cyclotron operation of fiscal 2012. The total operation time amounted to 3,175.6 hours, and monthly operation times are shown in Fig. 1. The percentages of operation time of the year used for regular experiments, facility use program, the promotion of shared use program¹⁾, beam tuning, and beam development are 64.1%, 11.5%, 22.5%, and 2.0%, respectively. There was no cancellation of the experiments, which was caused by the machine troubles of the year.

Table 1 Statistics for cyclotron operation.

	2011	2012
Beam service time	2343.6 h	2398.5 h
Machine tuning	669.9 h	714.9 h
Beam development	24.9 h	62.2 h
Total operation time	3038.4 h	3175.6 h
Change of particle and/or energy	223 times	225 times
Change of beam course	274 times	273 times
Change of harmonic number	69 times	72 times
The number of experiments	522	547
Experiment cancelled due to machine trouble	0	0

Table 2 shows the operation time of the multi-cusp ion source for H⁺ and D⁺ production and two ECR ion sources for heavier ions. The ECR ion sources are used alternatively. The Operation time of the OCTOPUS ion source and multi-cusp ion source decreased and, the operation time of the HYPERNANOAGAN ion source increased compared to fiscal 2011. Fractional distribution of major ions used for experiments is shown in Fig. 2. Compared to usual, the ratio of H⁺ experiments decreased.

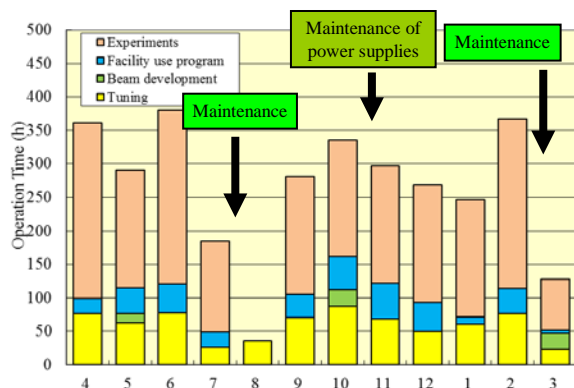


Fig. 1 Monthly operation time in fiscal 2012.

Table 2 Operation times of ion sources.

Ion source	Operation time 2011 (h)	Operation time 2012 (h)
Multi-cusp	957.2	821.3
ECR (OCTOPUS)	1249.2	1170.4
ECR(HYPERNANOAGAN)	1278.7	1833.9

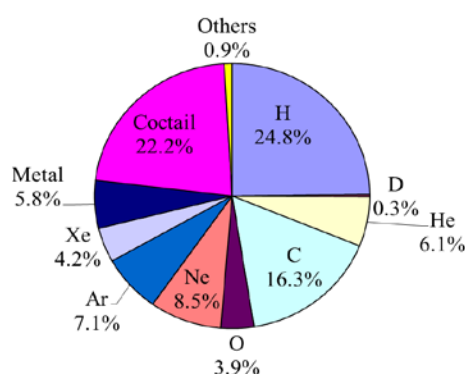


Fig. 2 Ion species used for experiments in fiscal 2012.

Maintenance

The regular yearly overhaul and maintenance were carried out. The major items were as follows: 1) Exchange of vacuum-tubes of the main amplifiers and contact-fingers for the outer tubes of the RF system, 2) Replacement of the cryogenic pumps in the cyclotron system, 3) Exchange of cooling fans for power supplies, 4) Inspection of the beam scanner power supplies and the radiation shield doors, 5) Routine maintenance of the power supplies, 6) Additional installation of the power supply for analyzing electromagnet in the injection system, 7) Fix of water leak from front baffle slit at the magnetic channel, 8) Repainting of the floor in the power supply room and the radiation shield doors.

Technical Development

New beam acceleration tests were carried out for 505 MeV ¹⁰²Ru²²⁺ and 40 MeV ⁴He²⁺. They are ready for use in experiments.

The condition of phase bunching is evaluated by a simplified geometric trajectory analysis, and was applied to the AVF cyclotron. A preliminary measurement for phase bunching was executed. In order to increase the transmission for uniform irradiation with heavy-ion beams in the LB course, a vacuum pipe with a large square section was installed. In the acceptance measurement system development, a circuit switching unit for the IST1 steering magnet was installed to select the power supplies. The detail is described elsewhere in this annual report.

5 - 03

Operation of Electrostatic Accelerators

S. Uno^{a)}, A. Chiba^{a)}, K. Yamada^{a)}, A. Yokoyama^{a)}, A. Usui^{a)}, Y. Saitoh^{a)}, Y. Ishii^{a)},
T. Satoh^{a)}, T. Ohkubo^{a)}, T. Nara^{a)}, T. Kitano^{b)}, T. Takayama^{b)}, S. Kanai^{b)},
T. Orimo^{b)}, Y. Aoki^{b)} and N. Yamada^{b)}

^{a)}Department of Advanced Radiation Technology, TARRI, JAEA,

^{b)}Beam Operation Service, Co., Ltd.

1. Operations and Status

Three electrostatic accelerators at TIARA were operated on schedule in fiscal year 2012 except changing its schedule by cancellations of users. The yearly operation time of the 3 MV tandem accelerator, the 400 kV ion implanter and the 3 MV single-ended accelerator were 2,073, 1,847 and 2,389 hours, respectively, in the same levels as the ordinary one. The tandem accelerator had no trouble, whereas the ion implanter and the single-ended accelerator stopped by any troubles for one day and four days, respectively. These lost days were compensated by operational extra days of yearly operating schedule of these accelerators. The accumulated operation time of these accelerators had been achieved at 38,671, 34,305 and 44,064 hours, since the operations were started. The monthly operation time of three electrostatic accelerators are shown in Fig. 1. The operation time in August, December and March was less than other one, because three accelerators were carried out scheduled maintenance in two weeks.

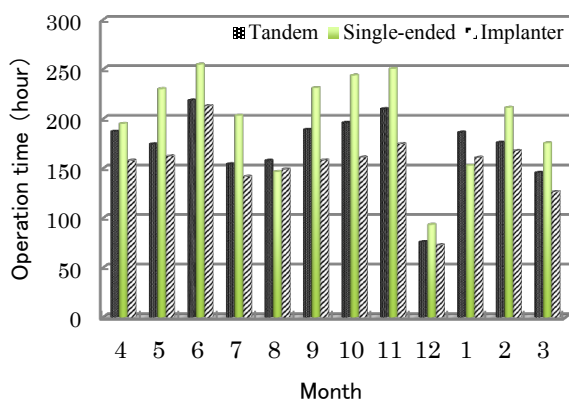


Fig. 1 Monthly operation time in FY 2012.

2. New Beam

The ion beam of tungsten (W) at 15 MeV was accelerated by the tandem accelerator, whose intensity was 20 nA at charge state of 4+, because of the request from a researcher in the field of nuclear fusion.

The molecular ion beam of helium hydride was generated by a mixed gas method using the Freeman type ion source with the ion implanter, because the users required irradiation of several cluster ions in order to study the irradiation effect with material. As a result, its intensity of beam was 50 nA at 200 kV.

3. Maintenance and Improvement

The thermal mechanical leak valve to regulate hydrogen gas for the RF ion source of the single-ended accelerator is shown Fig. 2. It became uncontrollable during the operation of its accelerator, though its valve was regularly replaced about 3,000 hours. The leak valve with a bracket was replaced with a new one. This gas flow rate is regulated through Joule heating, which is controlled by current whose limit amount of available to a maximum is 60 A. The cause of failure is considered to be the poor electrical connection between of the leak valve and a bracket. The RF ion source in the single-ended accelerator has this type of leak valves of the three sets to regulate hydrogen, deuterium and helium.

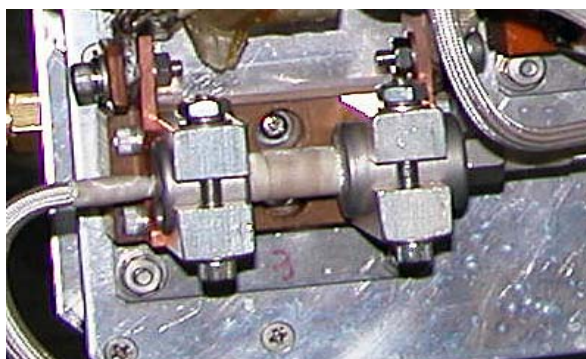


Fig. 2 Installed thermal mechanical leak valve.

The ion implanter has eight programmable logic controllers operated via three personal computers. The programmable logic controllers and the personal computers are connected through the Ethernet using the wiring of optical fibers. Although these devices are separately installed in the long distance, they are hardly affected by electrical noise. The multiport repeater which converts to optical fiber was replaced to the media converter. Because it failed by aging degradation. The media converter is not troubled with the setting place of the control console, because it is smaller than the multiport repeater. In addition, it scarcely fails because it has no air-cooling fan.

The programmable logic controllers for the ion implanter and the single-ended accelerator are planned to renew in fiscal year 2013. Therefore, these accelerators are expected to operate more stably and safely.

5 - 04 Operation of the Electron Accelerator and the Gamma-ray Irradiation Facilities

T. Agematsu^{a)}, Y. Haruyama^{a)}, H. Hanaya^{a)}, R. Yamagata^{a)}, H. Seito^{a)}, Y. Nagao^{a)},
H. Kaneko^{a)}, T. Yamaguchi^{b)}, N. Yagi^{b)}, M. Takagi^{b)}, I. Kawashima^{b)} and S. Matsuzaki^{b)}

^{a)} Department of Advanced Radiation Technology, TARRI, JAEA,

^{b)} Takasaki Establishment, Radiation Application Development Association (RADA)

1. Operation

The electron accelerator and the gamma-ray irradiation facilities were operated without serious trouble.

The electron accelerator was on service as scheduled 9:00~17:30 on Monday and Friday, and 8:30~23:00 from Tuesday to Thursday, to satisfy users' demand for operation time. The annual operation time of the electron accelerator in FY 2012 is 910 h, slightly decreased as compared with that in FY 2011, as shown in Fig. 1.

The ⁶⁰Co gamma-ray irradiation facilities consisting of three buildings with eight irradiation rooms cover a wide dose-rate range from 10⁻¹ Gy/h to 10⁴ Gy/h. The annual operation times for the first, the second cobalt irradiation facilities and the food irradiation facility are 15,738 h, 10,537 h and 7,871 h, respectively, as shown in Fig. 2.

2. Maintenance

2.1 Electron accelerator

The regular maintenance was carried out for 6 days in October to check the conveyor and doors of irradiation room. The old electrical parts inside the accelerator were replaced. When SF₆ gas in the accelerator vessel was

evacuated to be opened, the SF₆ gas withdrawal system, which was used for thirty two years, broke down on October 15, 2012. Although the gas got mixed with air and its density decreased to 90% from 98%, the accelerator could be continuously operated. The gas withdrawal system will be renewed in FY 2013.

2.2 Gamma-ray irradiation facilities

The periodical maintenance check mainly on mechanical system for radiation source transportation is performed every year on one of three gamma-ray irradiation facilities in turn. The maintenance checks of the first irradiation facility were done in July and August, 2012, with interruption of operation for eighteen days.

The new ⁶⁰Co sources were loaded for the irradiation room No.2 of the first irradiation facility to increase homogeneous irradiation area and dose rate. The three type sources were transferred to Japan Radioisotope Association for disposal. They were fifteen 30 cm-length pencil-type ⁶⁰Co sources, twelve globular ⁶⁰Co sources and five ¹³⁷Cs sources. There are consequently no sources of 30 cm-length pencil-type in the TARRI.

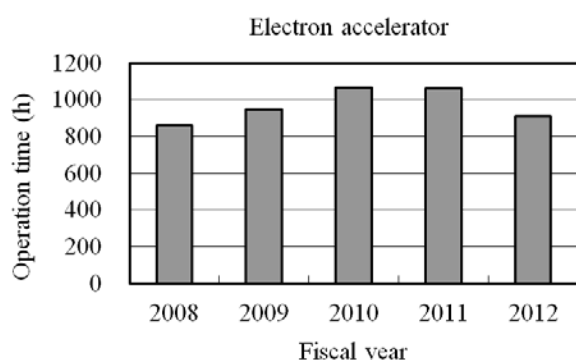


Fig. 1 Annual operation time of the electron accelerator.

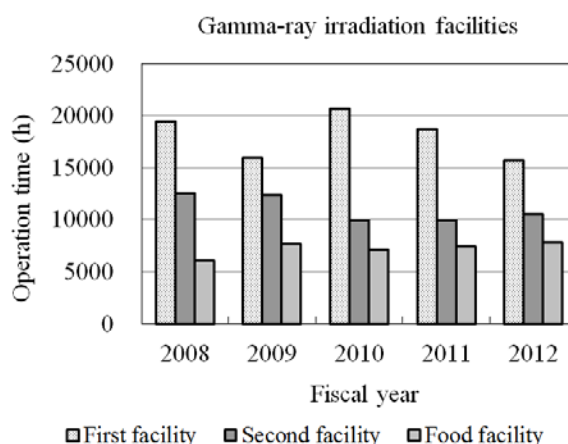


Fig. 2 Annual operation times of the ⁶⁰Co gamma-ray irradiation facilities.

5 - 05 Utilization Status of the Electron Accelerator and the Gamma-ray Irradiation Facilities

T. Agematsu^{a)}, Y. Haruyama^{a)}, H. Hanaya^{a)}, R. Yamagata^{a)}, H. Seito^{a)}, Y. Nagao^{a)}, H. Kaneko^{a)}, T. Yamaguchi^{b)}, N. Yagi^{b)}, M. Takagi^{b)}, I. Kawashima^{b)} and S. Matsuzaki^{b)}

^{a)}Department of Advanced Radiation Technology, TARRI, JAEA,

^{b)}Takasaki Establishment, Radiation Application Development Association (RADA)

The electron accelerator and three gamma-ray irradiation facilities were operated for various research subjects according to the operation plan in FY 2012 without serious trouble.

The irradiation time and the number of research subjects for each facility in FY 2012 are shown in Table 1. The accelerator mainly served for graft-polymerization for new material development, radiation effect study on semiconductors and various experiments of visiting users. The first cobalt irradiation facility mainly served for radiation-resistance testing of cables used in nuclear power plants and nuclear reactor facilities with a long irradiation period. The second cobalt irradiation facility, involving the irradiation room No.6 operated on hourly schedule, mainly served for development of new functional materials and other research subjects of visiting users. The food irradiation facility mainly served for development of detection method for irradiated foods and radiation resistance testing at lower dose rates.

Figure 1 shows the number of research subjects in each research field at each facility in FY 2008-2012. The number of research subjects at the electron accelerator in FY 2012 was similar to that in FY 2011. The number of research subjects at the gamma-ray

irradiation facilities slightly decreased year by year.

All of these research subjects, 14 ones at the electron accelerator and 93 ones at the gamma-ray irradiation facilities were relevant to the Fukushima Daiichi nuclear disaster.

Table 1 The irradiation time and the number of research subjects for each facility in FY 2012.

Research fields \ Facility	Electron accelerator		Gamma-ray irradiation facilities	
	Irradiation time (h)	Research subject	Irradiation time (h)	Research subject
Material processing	141.3	199	6561.1	299
Heat-resist material	142.7	39	0.0	0
Material for space	397.1	86	526.2	18
Nuclear facilities	0.0	0	30148.1	90
Environment	5.2	6	1902.1	52
Resources & Biotechnology	1.2	2	267.1	128
Basic technology	139.5	13	633.6	22
Joint use	82.9	29	23697.5	169
Total	910.0	374	63735.7	778

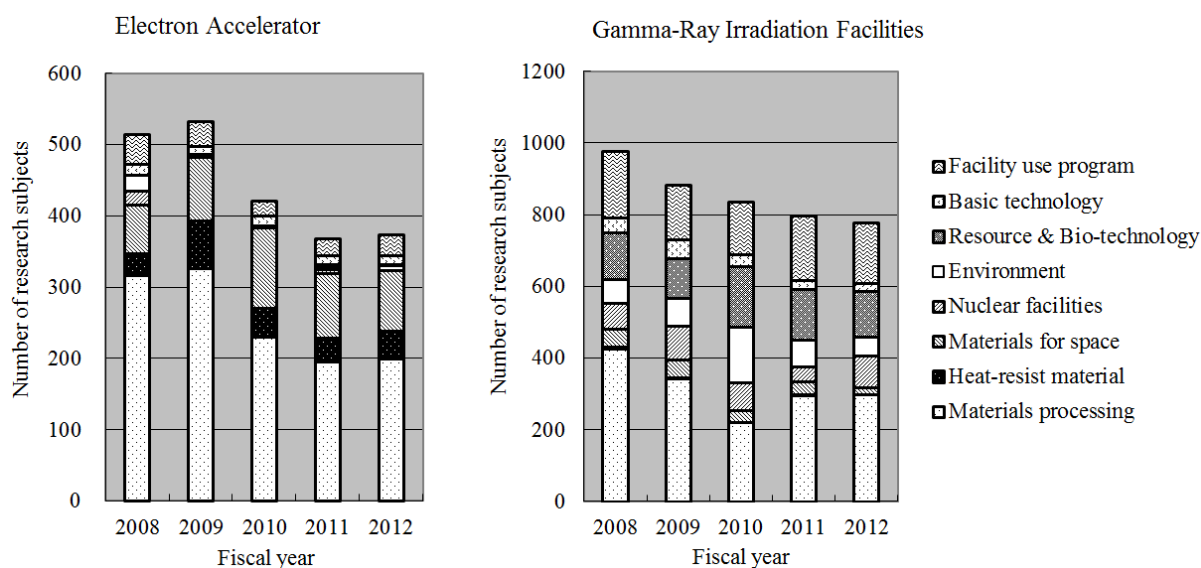


Fig. 1 The number of research subjects (FY 2008-2012).

5 - 06

Radiation Control in TIARA

Safety Section

Department of Administrative Services, TARRI, JAEA

1. Individual monitoring

(1) Individual monitoring for the radiation workers

Table 1 shows a distribution of effective dose of the radiation workers in FY 2012. The effective dose values of almost all radiation workers were below the detection limit (0.1 mSv).

The maximum dose was 0.3 mSv/y due to the overhaul of the TIARA AVF cyclotron.

Table 1 Distributions of the effective dose of the radiation workers in FY 2012.

Items		Number of persons in each periods				Total ^{*2}
		1st quarter	2nd quarter	3rd quarter	4th quarter	
Distribution range of effective dose	HE < 0.1	562	620	586	610	692
	0.1 ≤ HE ≤ 1.0	1	1	1	1	3
	1.0 < HE ≤ 5.0	0	0	0	0	0
	5.0 < HE ≤ 15.0	0	0	0	0	0
HE: Effective dose ^{*1} (mSv)						
Number of persons under radiation control (A)		563	621	587	611	695
Exposure above 1mSv	Number of persons (B)	0	0	0	0	0
	(B)/(A) × 100 (%)	0	0	0	0	0
Mass effective dose (Person · mSv)		0.1	0.2	0.1	0.1	0.5
Mean dose (mSv)		0.00	0.00	0.00	0.00	0.00
Maximum dose (mSv)		0.1	0.2	0.1	0.1	0.3

*1 The dose by the internal exposure was not detected.

*2 Net number.

(2) Individual monitoring for the visitors and others

Table 2 shows the number of persons who temporally entered the radiation controlled areas. The effective dose of all persons was less than 0.1 mSv.

Table 2 The number of persons who temporary entered the radiation controlled areas in FY 2012.

Periods	1st quarter	2nd quarter	3rd quarter	4th quarter	Total
Number of persons	768	1025	1326	1307	4426

2. Monitoring of radioactive gas and dust

Table 3 shows the maximum radioactive concentrations and total activities for radioactive gases released from the stack of TIARA, during each quarter of FY 2012.

Small amount of ⁴¹Ar, ¹¹C and ¹³N were detected during operation of the cyclotron or experiment, but the pulverized substances (⁶⁵Zn, etc.) were not detected.

Table 3 Monitoring results of released radioactive gases and dust in FY 2012.

Nuclide	Periods Items	1st quarter	2nd quarter	3rd quarter	4th quarter	Total
⁴¹ Ar	Maximum concentration	<1.4×10 ⁻⁴	<1.4×10 ⁻⁴	<1.4×10 ⁻⁴	<1.4×10 ⁻⁴	
	Activity	0	0	0	2.8×10 ⁷	2.8×10 ⁷
¹¹ C	Maximum concentration	<1.4×10 ⁻⁴	<1.4×10 ⁻⁴	<1.4×10 ⁻⁴	<1.4×10 ⁻⁴	
	Activity	1.8×10 ⁸	2.1×10 ⁷	1.3×10 ⁸	1.2×10 ⁷	3.4×10 ⁸
¹³ N	Maximum concentration	<1.4×10 ⁻⁴	—	<1.4×10 ⁻⁴	<1.4×10 ⁻⁴	
	Activity	2.0×10 ⁷	—	9.3×10 ⁷	6.9×10 ⁶	1.2×10 ⁸
⁶⁵ Zn	Maximum concentration	<6.5×10 ⁻¹⁰	<5.6×10 ⁻¹⁰	<4.5×10 ⁻¹⁰	<5.9×10 ⁻¹⁰	
	Activity	0	0	0	0	0

Unit : Bq/cm³ for Maximum concentration, Bq for Activity.

3. Monitoring for external radiation and surface contamination

External radiation monitoring was routinely carried out in/around the radiation controlled areas and surface contamination monitoring was also carried out. Neither unusual value of dose equivalent rate nor surface contamination was detected.

Figure 1 shows a typical example of distribution of the dose equivalent rate in the radiation controlled area of the cyclotron building.

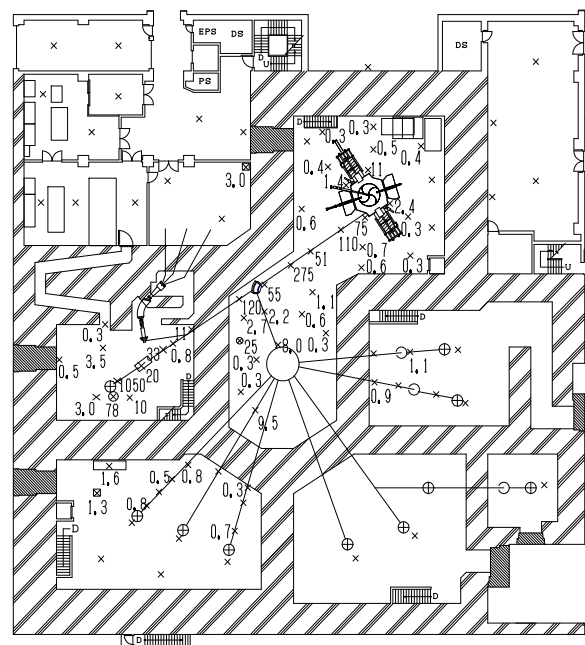


Fig. 1 Dose equivalent rate distribution in the radiation controlled area of the cyclotron building.

Measurement date : 5th, 25th and 26th March, 2013,

Measuring position : Indicated with × 1 m above floor,

Unit : μSv/h.

(The values are not indicated if they are less than 0.2 μSv/h.)

5 - 07

Radioactive Waste Management in TIARA

M. Nabatame and T. Hosoi

Department of Administrative Services, TARRI, JAEA

1. Management of radioactive wastes

The radioactive wastes generated in TIARA are managed by Utilities and Maintenance Section. The main radioactive wastes are the solid wastes generated from research experiments and the maintenance of the cyclotron. Other radioactive wastes are the liquid wastes such as inorganic waste fluids generated from research experiments and the air-conditioning machines in radiation controlled area. These wastes are managed according to their properties.

2. Solid radioactive waste

Table 1 shows the amounts of solid wastes at various properties and kinds generated in each quarter of FY 2012. The main solid waste is generated from research experiments and the maintenance of the cyclotron.

Combustible wastes are rubber gloves, paper, and clothes, etc. Incombustible wastes are metal pieces, the glasses, and contaminated parts.

3. Liquid radioactive waste

Table 2 shows the amounts of liquid wastes generated in each quarter of FY 2012. Most of liquid waste was inorganic waste water generated from chemical experiments and condensed water from operation of air conditioning units installed in each room of the first class radiation controlled area. The largest quantity of waste water in summer season (2nd quarter) is mainly due to condensed water. After treatment by evaporation, inorganic water is reused in the radiation controlled area. Only small amounts of concentrated liquid are generated from the evaporation.

Table 1 Radioactive solid wastes generated in FY 2012.

Items	Amounts	Amounts of generation in each periods (m ³)					Number of package /drum
		1st quarter	2nd quarter	3rd quarter	4th quarter	Total	
Category A*		0.10	0.83	0.32	0.26	1.51	
1)Combustible		0.06	0.28	0.26	0.16	0.76	4**
2)Incombustible		0.04	0.55	0.06	0.10	0.75	0
Compressible		0.04	0.14	0.06	0.10	0.34	2**
Filters		0	0.41	0	0	0.41	0
Incompressible		0	0	0	0	0	0
Ion exchange resin		0	0	0	0	0	0
Category B*		0	0	0	0	0	0

* defined by dose at the outer surface of container : (A) < 2 mSv/h ≤ (B),

** 200-liter drum.

Table 2 Radioactive liquid waste generated in FY 2012.

Items	Amounts	Amounts of generation in each periods (m ³)					Number of package /drum
		1st quarter	2nd quarter	3rd quarter	4th quarter	Total	
Category A*		10.21	18.29	2.54	1.14	32.18	
1)Inorganic		10.21	18.29	2.54	1.04	32.08	treatment
2)Organic		0	0	0	0	0	0
Organic		0	0	0	0	0	0
Oil		0	0	0	0	0	0
3)Sludge		0	0	0	0	0	0
4)Evaporation residue		0	0	0	0.1	0.1	1
Category B*		0	0	0	0	0	0

* defined by concentrations in Bq/cm³ (β, γ) : (A) < 3.7 × 10 ≤ (B) < 3.7 × 10⁴.

5 - 08 FACILITY USE PROGRAM in Takasaki Advanced Radiation Research Institute

H. Yoshida, D. Ushijima and K. Shidomi

Department of Advanced Radiation Technology, TARRI, JAEA

1. Introduction

The facilities of JAEA are widely opened to users in universities, public institutes, and industries, etc. Taking over the former system, FACILITY USE PROGRAM started in 2006, which is the system of facility use for the user's service on fee-charging basis. The open used facilities in Takasaki are Co-60 Gamma-ray Irradiation Facilities, Electron Accelerator, TIARA (Takasaki Ion Accelerators for Advanced Radiation Application), and some of the off-line analysis instruments.

In this program, the Research Proposals are examined carefully every half year from the standpoint of the availability and the validity of the experimental plan by the special committee. The facility usage fee has revised in FY2011. The details of the fee consist of handling fees, the irradiation fee, the expendables fee, radioactive waste disposal expenses and the additional charge. In case of Non-proprietary research, the users, who are exempted from the irradiation fee, should report the experimental results to JAEA. JAEA opens the reports to the public. Universities can also apply through another facility use program operated by the University of Tokyo. Such applications are accepted as priority case. Table 1 shows main classification of FACILITY USE PROGRAM.

Table 1 Main Classification of FACILITY USE PROGRAM.

Purpose	Research and Development			Except R&D
Classification	General		Priority case	Commercial
Result	Non-proprietary	Proprietary		
Referee	Yes	No		
Charge*	A	B		C

*A = handling fees + the expendables fee + radioactive waste disposal expenses,

B = handling fees + the irradiation fee,

C = handling fees + the irradiation fee + depreciation.

2. Use in FY2012

There were 19 applications of Research Proposals in FY2012 at Takasaki Institute, and 17 of them were as Non-proprietary use. Including the users from priority case and others, 276 applications from 86 users are accepted. Table 2 and Fig. 1 show user's classification for each facility and distribution of classification for FACILITY USE PROGRAM.

Table 2 User's classification for each facility.

User		University	Public Institute	Industries and others	Total
TIARA	AVF cyclotron	7	1	6	14
	3MV tandem accelerator	3	1	1	5
	3MV single-ended accelerator	2	0	0	2
	400kV ion implanter	3	0	0	3
Co-60 gamma-ray irradiation facilities		12	5	31	48
Electron accelerator		8	0	6	14
Total for each classification		35	7	44	86

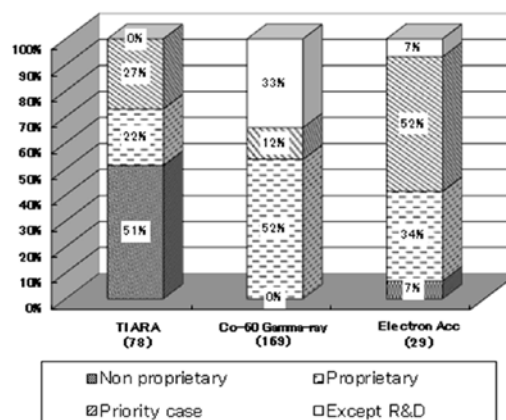


Fig. 1 Distribution of classification for FACILITY USE PROGRAM. The number of theme for each facility is shown in parentheses.

3. Public Relations

The information, such as an outline of this system, guidelines for applicants, format download etc. can be found on JAEA website as follows:

<http://sangaku.jaea.go.jp/3-facility/01-intro/index-02.html>.

“Project for Promotion of Shared Use of High Technology Research Institute” ended in FY2012, and “Project for Shared Use of High Technology Research Base and Platform Formation”, will start from FY2013, as one of the subsidiary project of Ministry of Education, Culture, Sports, Science and Technology (MEXT). This project intends that industrial users promote shared use of facilities, which accelerates the whole activity of science technology from basic research to innovation creation.

An outline of this project can be seen on website as follows: <http://www.taka.jaea.go.jp/innovation/index.html>

Appendices

Appendix 1 List of Publication	186
A1.1 Publication in Journal	186
A1.2 Publication in Proceedings	198
Appendix 2 List of Related Patents	205
Appendix 3 List of Related Press-Release and Television Broadcasting	207
Symbol used in the Appendix 1 to 3	209
Appendix 4 Type of Research Collaboration and Facilities Used for Research	210
Appendix 5 Examples of Typical Abbreviation Name for Organizations in Japan Atomic Energy Agency (JAEA)	212

Appendix 1. List of Publication

A 1.1 Publications in Journal

12J001 1-01 E

T. Ohshima, S. Sato, M. Imaizumi, T. Nakamura,
T. Sugaya, K. Matsubara and S. Niki

“Change in the Electrical Performance of GaAs
Solar Cells with InGaAs Quantum Dot Layers by
Electron Irradiation”

Sol. Energy Mater. Sol. Cells 108 (2013) 263-68.

12J002 1-02 C, T, S, I,

S. Sato and T. Ohshima

“Ion-Induced Changes in Semiconductor
Properties of Hydrogenated Amorphous Silicon”

Nucl. Instrum. Meth. Phys. Res. B 314 (2013)
153-57.

12J003 1-02 C, T, S, I,

S. Sato and T. Ohshima

“Electroic Transport Transition of Hydrogenated
Amorphous Silicon Irradiated with Self Ions”

IEEE Trans. Nucl. Sci. 60 (2013) 2288-99.

12J004 1-02 C, T, S, I,

S. Sato, H. Sai, T. Ohshima, M. Imaizumi,
K. Shimazaki and M. Kondo

“Temperature Influence on Perfomance
Degradation of Hydrogenated Amorphous
Silicon Solar Cells Irradiated with Protons”

Prog. Photovolt.: Res. Appl. 21 (2013) 1499-506.

12J005 1-02 C, T, S, I,

S. Sato, H. Sai, T. Ohshima, M. Imaizumi,
K. Shimazaki and M. Kondo

“Electric Properties of Undoped Hydrogenated
Amorphous Silicon Semiconductors Irradiated

with Self-Ions”

Nucl. Instrum. Meth. Phys. Res. B 285 (2012)
107-11.

12J006 1-05 E

I. Tsunoda, T. Nakashima, M. Naka, T. Idemoto,
M. Yoneoka, K. Takakura, K. Yoshino,
M.B. Gonzalez, E. Simoen,
C. Claeys and H. Ohyama

“Local compressive stress generation in electron
irradiated boron-doped Si_{0.75}Ge_{0.25}/Si devices”

Phys. Status Solidi C 9 (2012) 2058-61.

12J007 1-05 E

Y. Hirose, M. Warasawa, I. Tsunoda,
K. Takakura and M. Sugiyama

“Effects of Proton Irradiation on Optical and
Electrical Properties of Cu(In, Ga)Se₂ Solar Cells”

Jpn. J. Appl. Phys. 51 (2012) 111802.

12J008 1-05 E

J.M. Rafi, F. Campabadal, H. Ohyama,
K. Takakura, I. Tsunoda, M. Zabala,
O. Beldarrain, M.B. González, H. García,
H. Castán, A. Gómez and S. Dueñas

“2 MeV electron irradiation effects on the
electrical characteristics of metal-oxide-silicon
capacitors with atomic layer deposited Al₂O₃,
HfO₂ and nanolaminated dielectrics”

Solid-State Electron. 79 (2013) 65-74.

12J009 1-08

Abdelkader A.rrahmane, S. Koide, Sh. Sato,
T. Ohshima, A. Sandhu and H. Okada

“Robust Hall Effect Magnetic Field Sensors for

Operation at High Temperatures and in Harsh Radiation Environments”

IEEE Trans. Magn. 48 (11) (2012) 4421.

12J010 1-08

A. Abderrahmane, S. Koide, T. Tahara, S. Sato, T. Ohshima, H. Okada and A. Sandhu

“Effect of Proton Irradiation on 2DEG in AlGaIn/GaN Heterostructures”

J. Phys.: Conf. Series 433 (2013) 012011.

12J011 1-11 C

S. Onoda, T. Yamamoto, T. Ohshima, J. Isoya, T. Teraji and K. Watanabe

“Diamonds Utilized in the Development of Single Ion Detector with High Spatial Resolution”

Trans. Mater. Res. Soc. Jpn. 37 [2] (2012) 241-44.

12J012 1-12 E

J. Zhang, J. H. Shim, I. Niemeyer, T. Taniguchi, T. Teraji, H. Abe, S. Onoda, T. Yamamoto, T. Ohshima, J. Isoya and D. Suiter

“Experimental implementation of assisted quantum adiabatic passage in a single spin”
Phys. Rev. Lett. 110 (2013) 240501.

12J013 1-12 E

I. Niemeyer, J. H. Shim, J. Zhang, D. Suiter, T. Taniguchi, T. Teraji, H. Abe, S. Onoda, T. Yamamoto, T. Ohshima, J. Isoya, and F. Jelezko

“Broadband excitation by chirped pulses: application to single electron spins in diamond”
New J. Phys. 15 (2013) 033027.

12J014 1-12 E

Y. Kubo, I. Diniz, C. Grezes, T. Umeda, J. Isoya, H. Sumiya, T. Yamamoto, H. Abe, S. Onoda, T. Ohshima, V. Jacques, A. Dréau, J. -F. Roch, A. Auffeves, D. Vion, D. Esteve, and P. Bertet

“Electron spin resonance detected by superconducting qubit”

Phys. Rev. B 86 (2012) 064514.

12J015 1-12 E

N. T. Son, X. T. Trinh, L. S. Løvlie,

B. G. Svensson, K. Kawahara, J. Suda,

T. Kimoto, T. Umeda, J. Isoya, T. Makino,

T. Ohshima and E. Janzén

“Negative-U system of carbon vacancy in 4H-SiC”

Phys. Rev. Lett. 109 (2012) 187603.

12J016 1-17

岡 隆文、佐藤 智徳、山本 正弘

“ヒドラジンによる人工海水中の溶存酸素低減に及ぼすガンマ線の影響”

日本原子力学会和文論文誌、11 (2012) 249-54.

12J017 1-17

T. Motooka, T. Sato and M. Yamamoto

“Effect of gamma-ray irradiation on the deoxygenation of salt-containing water using hydrazine”

J. Nucl. Sci. Tech. 50 (2013) 363-68.

12J018 1-19 G

R. Yamada and Y. Kumagai

“Effects of Alumina Powder Characteristics on H₂ and H₂O₂ Production Yields in γ -Radiolysis of Qater and 0.4 M H₂SO₄ Aqueous Solution”

Int. J. Hydrogen Energy 37 (2012) 13272-77.

12J019 1-19 G

Y. Kumagai, A. Kimura, M. Taguchi,
R. Nagaishi, I. Yamagishi and T. Kimura
“Hydrogen Production in Gamma Radiolysis of
the Mixture of Mordenite and Seawater”
J. Nucl. Sci. Tech. 50 (2013) 130-38.

12J020 1-21 G

K. Yoshida, K. Kizu, H. Murakami, K. Kamiya,
A. Honda, Y. Ohnishi, M. Furukawa,
S. Asakawa, M. Kuramochi and K. Kurihara
“Feeder components and instrumentation for the
JT-60SA magnet system”
Fusion Eng. Des. 88 (2013) 1499-504.

12J021 1-25,1-38 G

A. Shimada, M. Sugimoto, H. Kudoh,
K. Tamura and T. Seguchi
“Radiation Ageing Technique for Cable Life
Evaluation of Nuclear Power Plant”
IEEE Trans. Dielectrics and Electrical Insulation
19 (2012) 1768-73.

12J022 1-25 G

T. Seguchi, K. Tamura, A. Shimada,
M. Sugimoto and H. Kudoh
“Mechanism of antioxidant interaction on polymer
oxidation by thermal and radiation ageing”
Radiat. Phys. Chem. 81 (2012) 1747-51.

12J023 1-25,1-38 G

M. Sugimoto, A. Shimada, H. Kudoh,
K. Tamura and T. Seguchi
“Product analysis for polyethylene degradation
by radiation and thermal ageing”
Radiat. Phys. Chem. 82 (2013) 69-73.

12J024 1-25,1-38 G

瀬口 忠男、田村 清俊、工藤 久明、島田 明彦、
杉本 雅樹、出崎 亮、大島 武、吉川 正人
“ケーブル絶縁材料の経年劣化研究”
JAEA-Review 2012-027 (2012).

12J025 1-25,1-38 G

瀬口 忠男、田村 清俊、渡士 克己、鈴木 雅秀、
島田 明彦、杉本 雅樹、出崎 亮、吉川 正人、
大島 武、工藤 久明
“原子力発電所用ケーブルの経年劣化メカニズ
ムの研究”
JAEA-Research 2012-029 (2012).

12J026 1-43 C

S. Kato, T. Yamaki, S. Yamamoto, T. Hakoda,
K. Kawaguchi, T. Kobayashi,
A. Suzuki and T. Terai
“Nanoparticle Formation by Tungsten Ion
Implantation in Glassy Carbon”
Trans. Mater. Res. Soc. Jpn. 38 (2013) 81-84.

12J027 1-43 C

S. Kato, T. Yamaki, S. Yamamoto, T. Hakoda,
K. Kawaguchi, T. Kobayashi,
A. Suzuki and T. Terai
“Preparation of Tungsten Carbide Nanoparticles
by Ion Implantation and Electrochemical Etching”
Nucl. Instrum. Meth. Phys. Res. B 314 (2013)
149-52.

12J028 1-45,1-46 C

A. Kitamura (Ogawa), T. Yamaki, Y. Yuri,
S. Sawada and T. Yuyama
“Microscopic Evaluation of the Absolute
Fluence Distribution of a Large-Area Uniform
Ion Beam Using the Track-Etching Technique”

Nucl. Instrum. Meth. Phys. Res. B 314 (2013) 47-50.

12J029 1-45 C

T. Yamaki, N. Nuryanthi, H. Koshikawa,
M. Asano, S. Sawada, S. Hasegawa,
Y. Maekawa, K.-O. Voss,
C. Trautmann and R. Neumann
“Investigation of Nanopore Evolution in
Track-Etched Poly(vinylidene fluoride)
Membranes”
Trans. Mater. Res. Soc. Jpn. 37 (2012) 223-26.

12J030 1-45 C

N. Nuryanthi, T. Yamaki, H. Koshikawa,
M. Asano, S. Sawada, S. Hasegawa,
Y. Maekawa and Y. Katsumura
“Ion-Track Membranes of Poly(vinylidene
fluoride): Etching Characteristics during
Conductometric Analysis”
Trans. Mater. Res. Soc. Jpn. 38 (2013) 105-8.

12J031 1-45 C

T. Yamaki, M. Asano, H. Koshikawa,
Y. Maekawa, D. Severin,
T. Seidl and C. Trautmann
“In-Situ Analysis of Ion-Beam-Induced
Degradation and Post-Irradiation Oxidation in
Poly(vinylidene fluoride)”
GSI Sci. Rep. 2011 (2012) 420.

12J032 1-45 C

T. Yamaki, M. Asano, H. Koshikawa,
Y. Maekawa, D. Severin,
T. Seidl and C. Trautmann
“Analysis of Ion-Beam Induced Degradation of
Poly(vinylidene fluoride) and Post-Irradiation

Treatment for Efficient Track Etching”
GSI Sci. Rep. 2012 (2013) 402.

12J033 1-45 C

T. Yamaki, N. Nuryanthi, H. Koshikawa,
M. Asano, S. Sawada, T. Hakoda, Y. Maekawa,
K.-O. Voss, D. Severin, T. Seidl,
C. Trautmann and R. Neumann
“Ion-Track Membranes of Fluoropolymers:
Toward Controlling the Pore Size and Shape”
Nucl. Instrum. Meth. Phys. Res. B 314 (2013)
77-81.

12J034 1-45 C

N. Nuryanthi, T. Yamaki, H. Koshikawa,
M. Asano, S. Sawada, S. Hasegawa,
Y. Maekawa and Y. Katsumura
“Applied-Voltage Dependence on
Conductometric Track Etching of
Poly(vinylidene fluoride) Films”
Nucl. Instrum. Meth. Phys. Res. B 314 (2013)
95-98.

12J035 2-01 E

N. H. Mohamed, M. Tamada,
Y. Ueki and N. Seko
“Emulsion graft polymerization of
4-chloromethylstyrene on kenaf fiber by
pre-irradiation method”
Radiat. Phys. Chem. 82 (2013) 63-68.

12J036 2-01 E

N. H. Mohamed, M. Tamada,
Y. Ueki and N. Seko
“Effect of partial delignification of kenaf bast
fibers for radiation graft copolymerization”
J. Appl. Polym. Sci. 127 (2013) 2891-95.

12J037 2-02 G

A. Iwanade, N. Kasai, H. Hoshina, Y. Ueki,
S. Saiki and N. Seko
“Hybrid grafted ion exchanger for
decontamination of radioactive cesium in
Fukushima Prefecture and other contaminated
areas”
J. Radioanal. Nucl. Chem. 293 (2012) 703-9.

12J038 2-03 G

H. Hoshina, N. Kasai, N. Seko and T. Shibata
“Synthesis of arsenic graft adsorbents in pilot scale”
Radiat. Phys. Chem. 81 (2012) 1033-35.

12J039 3-02 C

T. Ushigome, N. Shikazono, K. Fujii,
R. Watanabe, M. Suzuki, C. Tsuruoka,
H. Tauchi and A. Yokoya
“Yield of Single- and Double-Strand Breaks and
Nucleobase Lesions in Fully Hydrated Plasmid
DNA Films Irradiated with High-LET Charged
Particles”
Radiat. Res. 177 (5) (2012) 614-27.

12J040 3-05

T. Sakashita, M. Suzuki, N. Hamada,
Y. Shimozawa, K. Shirai-Fukamoto, Y. Yokota,
S. Hamada-Sora, T. Kakizaki, S. Wada,
T. Funayama and Y. Kobayashi
“Behavioral Resistance of *Caenorhabditis*
elegans Against High-LET Radiation Exposure”
Biol. Sci. Space 26 (2012) 7-11.

12J041 3-05

T. Sakashita, M. Suzuki, N. Hamada,
Y. Shimozawa, K. Shirai-Fukamoto, Y. Yokota,
S. Hamada-Sora, T. Kakizaki, S. Wada,

T. Funayama and Y. Kobayashi
“Effects of Low- and High-LET Radiation on the
Salt Chemotaxis Learning in *Caenorhabditis*
elegans”
Biol. Sci. Space 26 (2012) 21-25.

12J042 3-10

K. Akeo, N. Hamada, T. Funayama,
Y. Akeo and Y. Kobayashi
“Effects of Ion Beam Irradiation on the
Expression of Glutathione Peroxidase in
Cultured Human Retinal Vascular Endothelial
Cells Exposed to L-dopa”
Tissue Cult. Res. Comm. 32 (2013) 195.

12J043 3-13 C

白井 孝治
“重イオンビームを用いた昆虫細胞の放射線応
答と DNA 障害の修復機構の解析”
蚕糸・昆虫バイオテック(日本蚕糸学会) 81
181-86(総説).

12J044 3-17,3-18 G

岸田 敬吾、貝森 良彦、川村 翔栄、坂本 侑輝、
中村 秀夫、菊地 正博、下山 雄平、小林 泰彦、
鵜飼 光子
“照射処理により食品に誘導されるラジカルの
解析”
食品照射 47 (2012) 1-5.

12J045 3-17,3-18 G

亀谷 宏美、菊地 正博、等々力 節子、
古田 雅一、小林 泰彦、原 英之、下山 雄平、
鵜飼 光子
“Pulse-ESR と CW-ESR による照射黒コショウ中
のラジカルの緩和時間解析”
食品照射 47 (2012) 6-10.

12J046 3-17,3-18 G

M. Kikuchi, H. Kameya, Y. Shimoyama,
M. Ukai and Y. Kobayashi
“Electron-spin relaxation phenomena in
irradiated saccharides detected by pulsed electron
paramagnetic resonance spectroscopy”
Radiat. Phys. Chem. 81 (2012) 1639-45.

12J047 3-17,3-18 G

H. Kameya, M. Ukai and Y. Shimoyama
“An ESR Study of radiation induced radicals in
glucose polymer”
Radiat. Phys. Chem. 84 (2013) 232-34.

12J048 3-19

T. Satoh, M. Koka, W. Kada, A. Yokoyama,
T. Ohkubo, A. Yamazaki, Y. Ishii,
T. Kamiya and N. Kozai
“EFFECTIVENESS OF A COMBINATION OF
ML-EM AND STIM-CT IN PIXE-CT FOR
BIOLOGICAL SPECIMEN”
Int. J. PIXE 22 (2012) 73-80.

12J049 3-20

E. Sakurai, E. Sakurai, Y. Ueda and Y. Yagi
“Enhancing effect of zinc on L-histidine
transport in rat lung microvascular endothelial
cells”
Biol. Trace Elem. Res. 2011;142(3):713-22.

12J050 3-23 S

Y. Shimizu, S. Matsuzaki,
M. Mori and K. Dobashi
“Chronic exposure to particles caused
bronchioloalveolar carcinoma in a patient with
cryptogenic organizing pneumonia evaluated by
elemental analysis”

Immunopharmacol. Immunotoxicol.
2012 Feb ;34(1):170-3.

12J051 3-25 S

S. Harada, S. Ehara, K. Ishii, H. Yamazaki,
S. Matsuyama, T. Sato, T. Kamiya,
K. sera and Y. Saito
“Decreasing size of radiosensitive capsules from
micro to nano, and its increased antitumor effect
and decreasing adverse effect”
Int. J. PIXE 22 (2012) 57-64.

12J052 3-28 C

I. Sasaki, K. Yamada, Sh. Watanabe,
H. Hanaoka, Y. Sugo, H. Oku and N.S. Ishioka
“Synthesis of radiohalogen-labeled peptides with
high affinity to HER”/neu receptor”
Peptide Sci. 2012, K. Sugimura (Ed.),
Jpn. Peptide Soc. 157-60.

12J053 3-28 C

K. Yamada, S. Watanabe, Y. Ohshima,
H. Hanaoka, N. Tsukui, C. Takano,
A. Yamaguchi, H. Oku and N. S. Ishioka
“Synthesis and in vivo evaluation of
radiohalogen-labeled antitumor cyclic peptides”
Peptide Sci. 2011, K. Sakaguchi (Ed.),
Jpn. Peptide Soc. 287-90.

12J054 3-29 C

A. Achmad, H. Hanaoka, H. Yoshioka,
S. Yamamoto, H. Tominaga, T. Araki, Y. Ohshima,
N. Oriuchi and K. Endo
“Predicting cetuximab accumulation in KRAS
wild-type and KRAS mutant colorectal cancer
using ⁶⁴Cu-labeled cetuximab positron emission
tomography”

Cancer Sci. 103 (2012) 600-5.

12J055 3-33 C

鈴木 伸郎

“植物における放射性カドミウムの非破壊イメージング”

RADIOISOTOPES 62 (2013) 61-63.

12J056 3-33 C

S. Nakamura, N. Suzui, T. Nagasaka,
F. Komatsu, N.S. Ishioka, S. Ito-Tanabata,
N. Kawachi, H. Rai, H. Hattori,
M. Chino and S. Fujimaki

“Application of glutathione to roots selectively inhibits cadmium transport from roots to shoots in oilseed rape”

J. Exp. Bot. 64 (2013) 1073-81.

12J057 3-33 C

P. Hu, Y.-G. Yin, S. Ishikawa, N. Suzui,
N. Kawachi, S. Fujimaki, M. Igura, C. Yuan,
J. Huang, Z. Li, T. Makino, Y. Luo,
P. Christie and L. Wu

“Nitrate facilitates cadmium uptake, transport and accumulation in the hyperaccumulator *Sedum plumbizincicola*”

Environ. Sci. Pollut. Res. 20 (2013) 6306-16.

12J058 3-34

田之頭 優樹

“突然変異を利用した花きの新品種育成”

農業かごしま 2012 年 11~12 月号 (2012) 20-21

12J059 3-38 C,G

R. Yoshihara, S. Nozawa, Y. Hase, I. Narumi,
J. Hidema and A. N. Sakamoto

“Mutational effects of γ -rays and carbon ion

beams in *Arabidopsis* seedlings”

J. Radiat. Res. 54 (2013) 1050-56.

12J060 3-39 C,G

K. K. Biswas, T. Mohri, S. Kogawara, Y. Hase,
I. Narumi and Y. Oono

“An improved system for shoot regeneration from stem explants of Lombardy poplar (*Populus nigra* L. var. *italica* Koehne)”

Am. J. Plant Sci. 3 (2012) 1181-86.

12J061 4-01,4-05 S

五十住 幸大、箱田 照幸、山本 春也、
有谷 博文、吉川 正人

“低エネルギー電子線を用いた白金ナノ粒子の生成と触媒反応への応用”

Radioisotopes 61 (2012) 289-96.

12J062 4-04

Y. Maeyoshi, A. Saeki, S. Suwa, M. Omichi,
H. Marui, A. Asano, S. Tsukuda, M. Sugimoto,
A. Kishimura, K. Kataoka and S. Seki

“Fullerene nanowires as a versatile platform for organic electronics”

Nature Sci. Rep. 2, 600 DOI, 10.1038/srep00600 (2012).

12J063 4-04

A. Asano, M. Omichi, S. Tsukuda, K. Takano,
M. Sugimoto, A. Saeki and S. Seki

“Fabrication and Arrangement of "Clickable" Nanowires by the Single-Particle Nanofabrication Technique”

J. Phys. Chem. C 116 (32) (2012) 17274-79.

12J064 4-05 O

T. Hakoda, H. Igarashi, Y. Isozumi,

S. Yamamoto, H. Aritani and M. Yoshikawa
 “Gasochromic property of
 dehydrogenation-catalyst loaded tungsten trioxide”
 J. Phys. Chem. Solids 74 (2013) 200-4.

12J065 4-11 S

K. Miura, T. Satoh, Y. Ishii, H. Kiryu, Y. Ozawa,
 M. Kohka, K. Takano, T. Ohkubo, A. Yamazaki,
 W. Kada, A. Yokoyama,
 T. Kamiya and O. Hanaizumi
 “Fabrication of Mach-Zehnder polymer
 waveguides by a direct-drawing technique using
 a focused proton beam”
 Key Eng. Mater. 534 (2013) 158-61.

12J066 4-11 I

H. Abe, S. Orimo, M. Kishimoto, S. Aone,
 H. Uchida, H. Daido and T. Ohshima
 “Effects of an Ultra-Intense Laser Driven Proton
 Beam on the Hydriding Property of a Hydrogen
 Storage Alloy”
 Nucl. Instrum. Meth. Phys. Res. B. 307 (2013)
 218-20.

12J067 4-11 I

H. Abe, S. Aone, R. Morimoto,
 H. Uchida and T. Ohshima
 “Synergic Effects of Ion Irradiations (La, Ce)
 and Alkaline Pretreatment (KOH) on Hydriding
 Kinetic Property of a Mm-Ni Based Alloy”
 J. Alloys Comp. 580 (2013) S219-21.

12J068 4-12 S

A. Kitamura (Ogawa), T. Satoh, M. Koka,
 T. Kamiya and T. Kobayashi
 “Morphological change of PTFE by ion micro
 beam irradiation”

Trans. Mater. Res. Soc. Jpn. 32 (2012) 219-22.

12J069 4-12 S,I

A. Kitamura (Ogawa), T. Satoh, T. Kobayashi,
 M. Koka and T. Kamiya
 “Fabrication of Micropatterns on Teflon surface
 by Proton beam Writing and Nitrogen ion
 implantation”
 Trans. Mater. Res. Soc. Jpn. 38 (2013) 101-4.

12J070 4-12 I

A. Kitamura (Ogawa), T. Kobayashi, T. Satoh,
 M. Koka and T. Kamiya
 “Morphological change of self-organized
 protrusions of fluoropolymer surface by ion
 beam irradiation”
 Nucl. Instrum. Meth. Phys. Res. B 307 (2013)
 614-17.

12J071 4-12 S

A. Kitamura (Ogawa), T. Satoh, M. Koka,
 T. Kamiya and T. Kobayashi
 “Fabrication of Micro-prominences on PTFE
 Surface using Proton Beam Writing”
 Nucl. Instrum. Meth. Phys. Res. B 306 (2013)
 288-91.

12J072 4-12 S,I

A. Kitamura (Ogawa), T. Satoh, T. Kobayashi,
 M. Koka and T. Kamiya
 “Microfabrication on Teflon surface by
 MeV-proton-microbeam and
 keV-nitrogen-ion-beam irradiation”
 Nucl. Instrum. Meth. Phys. Res. B 307 (2013)
 610-13.

12J073 4-12 S,I

A. Kitamura (Ogawa), T. Kobayashi, T. Satoh,
M. Koka and T. Kamiya

“Modification of Teflon Surface by Proton
Microbeam and Nitrogen Ion Beam”

Nucl. Instrum. Meth. Phys. Res. B 314 (2013)
82-85.

12J074 4-13 S

K. Saito, H. Hayashi, H. Nishikawa

“Fabrication of curved PDMS microstructures on
silica glass by proton beam writing aimed for
micro-lens arrays on transparent substrates”

Nucl. Instrum. Meth. Phys. Res. B (2013)
in press.

12J075 4-14 S

K. Mima, R. Gonzalez-Arrabal, H. Azuma,
A. Yamazaki, C. Okuda, Y. Ukyo,
H. Sawada, K. Fujita, Y. Kato,
J. M. Perlado and S. Nakai

“Li distribution characterization in Li-ion
batteries positive electrodes containing
 $\text{Li}_x\text{Ni}_{0.8}\text{Co}_{0.15}\text{Al}_{0.05}\text{O}_2$ secondary particles ($0.75 \leq x \leq 1.0$)”

Nucl. Instrum. Meth. Phys. Res. B 290 (2012)
79-84.

12J076 4-15 I

Y. Kasukabe, H. Shimoda, Yu. Chen,
S. Yamamoto, M. Yoshikawa and Y. Fujino
“Characterization of Epitaxial Transformation
Phenomena Induced by the Interaction of
Implanted N-Ions with Ti Thin Films”
Nucl. Instrum. Meth. Phys. Res. B 315 (2013)
131-35.

12J077 4-16 S

B. Matsukura, Y. Hiraiwa, T. Nakajima,
K. Narumi, S. Sakai, T. Sadoh,
M. Miyao and Y. Maeda

“Self organization of FeGe/FeSi/FeGe layered
structures on Ge and their electrical conduction
properties”

Phys. Procedia 23 (2012) 21-24.

12J078 4-16 S

Y. Maeda, K. Nishimura, T. Nakajima,
B. Matsukura, K. Narumi and S. Sakai
“Enhancement of IR light emission from β -FeSi₂
nanocrystals embedded in Si”

Phys. Status Solidi (c) 9 (2012) 1888-91.

12J079 4-16 S

Y. Maeda, K. Nishimura, T. Nakajima,
B. Matsukura, K. Narumi and S. Sakai
“Photoluminescence property of carbon-doped
 β -FeSi₂ nanocrystals”

Phys. Status Solidi (c) 9 (2012) 1884-87.

12J080 4-19 T

K. Motohashi, Y. Saitoh,
N. Miyawaki and Y. Matsuo
“Transmission Properties of a 4-MeV C^+ Ion Beam
Entering a Narrow Gap Between Two Cylindrical
Glass Surfaces”
Jpn. J. Appl. Phys. 52 (2013) 076301.

12J081 4-20 T

S. Toyoda, F. Sato, H. Nishido,
M. Kayama and J. Ishibashi
“The alpha effectiveness of the dating ESR
signal in barite”
Radiat. Meas. 47 (2012) 900-2.

12J082 4-20 T

A. Gucsik, H. Nishido, K. Ninagawa, U. Ott,
A. Tsuchiyama, M. Kayama,
I. Simonia and J. Boudou
“Cathodoluminescence microscopy and
spectroscopy of micro- and nanodiamonds: An
implication for laboratory astrophysics”
Microsc. Microanal. 18 (2012) 1-7.

12J083 4-20 T

M. Kayama, H. Nishido, T. Sekine, T. Nakazato,
A. Gucsik and K. Ninagawa
“Shock barometer using cathodoluminescence of
alkali feldspar”
J. Geophys. Res. (Planets) 117 (2012) 1-13.

12J084 4-20 T

Sz. Nagy, S. Józsa, A. Gucsik, Sz. Bérczi,
K. Ninagawa, H. Nishido, M. Veres,
Á. Kereszturi and H. Hargitai
“Shock and thermal annealing history of the
ALH77005 Martian meteorite: a micro-Raman
spectroscopical investigation”
Cent. Eur. Geol. 55 (2012) 33-48.

12J085 4-20 T

M. Watanabe, K. Hoshino, K. Yamaguchi,
S. Kihata, O. Matsubaya,
H. Nishido and S. Ishihara
“Granitic pegmatite of the
Umanotani-Shiyoyama quartz-feldspar mine,
Shimane Prefecture, Southwest Japan”
Bull. Geol. Surv. Jpn. 62 (2012) 425-39.

12J086 4-20 T

T. Imayama, T. Takeshita, K. Yi, D. Cho,
K. Kitajima, Y. Tsutsumi, M. Kayama, H. Nishido,

T. Okumura, K. Yagi, T. Itaya and Y. Sano
“Two-stage partial melting and the different
cooling history within the Higher Himalayan
Crystalline Sequence in the far-eastern Nepal
Himalaya”
Lithos. 134 (2012) 1-22.

12J087 4-20 T

A. Gucsik, K. Tsukamoto, H. Nishido, H. Miura,
M. Kayama, K. Ninagawa and Y. Kimura
“Cathodoluminescence microcharacterization of
forsterite in the chondrule experimentally grown
under super cooling”
J. Lumin. 132 (2012) 1041-47.

12J088 4-20 T

H. Tissoux, P. Vonchet, F. Lacquement,
F. Prognon, D. Moreno, C. Falgueres,
J. Bahain and S. Toyoda
“Investigation on non-optically bleachable
components of ESR aluminum signal in quartz”
Radiat. Meas. 47 (2012) 894-99.

12J089 4-22 G

長島 佳菜、豊田 新
“風成塵から眺めた古気候研究”
エアロゾル研究 27(3) (2012) 284-91.

12J090 4-26

S. Yamashita, G. Baldacchino, T. Maeyama,
M. Taguchi, Y. Muroya, M. Lin, A. Kimura,
T. Murakami and Y. Katsumura
“Mechanism of Radiation-Induced Reactions in
Aqueous Solution of Coumarin-3-Carboxylic
Acid: Effects of Concentration, Gas and Additive
on Fluorescent Product Yield”
Free Radic. Res. 46 (2012) 861-71.

12J091 4-26

A. Kimura, M. Osawa and M. Taguchi
 “Decomposition of persistent pharmaceuticals in wastewater by ionizing radiation”
 Radiat. Phys. Chem. 81 (2012) 1508-12.

12J092 4-26

A. Hiroki, S. Yamashita, Y. Sato,
 N. Nagasawa and M. Taguchi
 “New polymer gel dosimeters consisting of less toxic monomers with radiation-crosslinked gel matrix”
 J. Phys.: Conf. Series, 444 (2013) 012028.

12J093 4-27 C

T. Kondoh, J. Yang, K. Norizawa, K. Kan,
 T. Kozawa, A. Ogata, S. Tagawa and Y. Yoshida
 “Femtosecond pulse radiolysis study of geminate ion recombination in biphenyl-dodecane solution”
 Radiat. Phys. Chem. 84 (2013) 30-34.

12J094 4-32 S

T. Sakai, R. Yasuda, H. Iikura, T. Nojima,
 M. Matsubayashi, W. Kada, M. Kohka, T. Satoh,
 T. Ohkubo, Y. Ishii and K. Takano
 “Micromachining of Commodity Plastics by Proton Beam Writing and Fabrication of Spatial Resolution Test-chart for Neutron Radiography”
 Nucl. Instrum. Meth. Phys. Res. B. 306 (2013) 299-301.

12J095 4-36 C

N. Miyawaki, M. Fukuda, S. Kurashima,
 H. Kashiwagi, S. Okumura,
 K. Arakawa and T. Kamiya
 “Short-time change of heavy-ion microbeams with different mass to charge ratios by scaling

method for the JAEA AVF cyclotron”
 Nucl. Instrum. Meth. Phys. Res. A 715 (2013) 126-31.

12J096 4-36 C

S. Kurashima, S. Okumura, N. Miyawaki,
 H. Kashiwagi, T. Satoh, T. Kamiya,
 M. Fukuda and W. Yokota
 “Short-time change of heavy-ion microbeams with different mass to charge ratios by scaling method for the JAEA AVF cyclotron”
 Nucl. Instrum. Meth. Phys. Res. B 306 (2013) 40-43.

12J097 4-40

Y. Yuri, T. Yuyama, T. Ishizaka,
 I. Ishibori and S. Okumura
 "Transformation of the transverse beam intensity distribution by sextupole focusing in a transport line"
 J. Phys. Soc. Jpn. 81 (2012) 064501.

12J098 4-45 T

A. Chiba, Y. Saitoh, K. Narumi, Y. Takahashi,
 K. Yamada and T. Kaneko
 “Quantitative evaluation of charge-reduction effect in cluster constituent ions passing through a foil”
 Nucl. Instrum. Meth. Phys. Res. B 315 (2013) 81-84.

12J099 4-47 T

T. Kaneko, K. Ihara and M. Kohno
 “Electronic stopping for swift carbon cluster ions connected with average charge reduction”
 Nucl. Instrum. Meth. Phys. Res. B 315 (2013) 76-80.

12J100 4-47 T

H. Ogawa, K. Sorai, S. Amano,
K. Ishii and T. Kaneko
“Secondary electron emission from a thin carbon
foil induced by H^+ , He_2^+ , and Li_3^+ at fixed
velocity of 1 MeV/u”
Nucl. Instrum. Meth. Phys. Res. B 315 (2013)
291-4.

12J101 4-48 T,I

K. Hirata, Y. Saitoh, A. Chiba,
K. Yamada and K. Narumi
“Time-of-flight secondary ion mass spectrometry
with energetic cluster ion impact ionization for
highly sensitive chemical structure
characterization”
Nucl. Instrum. Meth. Phys. Res. B 314 (2013)
39-42.

12J102 4-50 I

H. Tsuchida, T. Majima, S. Tomita, K. Sasa,
K. Narumi, Y. Saitoh, A. Chiba, K. Yamada,
K. Hirata, H. Shibata and A. Itoh
“Transmission properties of C_{60} ions through
micro- and nano-capillaries”
Nucl. Instrum. Meth. Phys. Res. B 315 (2013)
336-40.

12J103 4-50 I

H. Tsuchida, S. Tomita, K. Nishimura,
R. Murakoshi, M. Naitoh, K. Sasa, S. Ishii,
A. Yogo and A. Itoh
“Properties of fast carbon cluster microbeams
produced with a tapered capillary”
Nucl. Instrum. Meth. Phys. Res. B 293 (2012)
6-10.

12J104 4-50 I

J. Yokoe, H. Tsuchida, K. Nishimura,
R. Murakoshi, S. Mori, M. Naitoh,
T. Majima and A. Itoh
“Charge-state distributions of fast diatomic
carbon ions and dissociated fragments passing
through microcapillaries”
J. Phys. B 46 (2013) 115201.

12J105 4-51 I

K. Nakajima, Y. Morita, M. Suzuki, K. Narumi,
Y. Saitoh, N. Ishikawa, K. Hojou, M. Tsujimoto,
S. Isoda and K. Kimura
“Direct observation of fine structure in ion tracks
in amorphous Si_3N_4 by TEM”
Nucl. Instrum. Meth. Phys. Res. B 291 (2012)
12-16.

A 1.2 Publication in Proceedings

12C001 1-01 I, T, C, E

T. Nakamura, M. Imaizumi,
S. Sato and T. Ohshima
“Estimation Method for Radiation Resistance of
Multi-junction Solar Cells using I-V
Characteristics of Subcells”
Proc. 10th Int. Workshop Radiat. Eff. Semicond.
Devices Space Appl. [Tsukuba, Japan] (2012)
44-47.

12C002 1-01 I, T, C, E

T. Nakamura, M. Imaizumi,
S. Sato and T. Ohshima
“Change in I-V Characteristics of Subcells in a
Multi-junction Solar Cell due to Radiation
Irradiation”
Proc. 38th IEEE Photovoltaic Specialists Conf.
[Austin, USA] (2012) in Press.

12C003 1-01 C

M. Imaizumi, Y. Yuri, P. R. Bolton,
S. Sato and T. Ohshima
“Innovative Technologies on Proton Irradiation
Ground Tests for Space Solar Cells”
Proc. 38th IEEE Photovoltaic Specialists Conf.
[Austin, USA] (2012) in Press.

12C004 1-02 C, T, S, I

S. Sato, K. Beernink and T. Ohshima
“Proton Irradiation Effects on Amorphous
Silicon Triple-Junction Solar Cells”
Proc. 10th Int. Workshop Radiat. Eff. Semicond.
Devices Space Appl. [Tsukuba, Japan] (2012)
44-47.

12C005 1-03 C

A. Makihara, T. Yokose, Y. Tsuchiya,
Y. Miyazaki, H. Abe, H. Shindou,
T. Ebihara, A. Maru, K. Morikawa,
S. Kuboyama and T. Tamura
“Applicability of redundant pairs of SOI
transistors for analog circuits and their
applications to phase-locked Loop circuits”
IEEE Trans. Nucl. Sci. 60(1) (2013) 230-35.

12C006 1-05 E

R. Watanabe, Y. Nagaoka, T. Nakashima,
M. Yoneoka, I. Tsunoda, K. Takakura,
M.B. Gonzalez, E. Simoen and C. Claeys
“Electron irradiation degradation of gate length
modulated strained-Si pMOSFETs”
31st Electronic. Mater. Symp. (EMS-31),
Extended abstr. 31st Electron. Mater. Symp.
[Izu, Japan] 153-54.

12C007 1-05 E

T. Nakashima, I. Tsunoda, K. Takakura,
M. Yoneoka, H. Ohyama, N. Naka, K. Yoshino,
E. Simoen and C. Claeys
“Stress evaluation by Raman Spectroscopy in
2MeV electron irradiated SiGe/Si diodes”
31st Electron. Mater. Symp. (EMS-31),
Extended abstr. 31st Electron. Mater. Symp.
[Izu, Japan] 155-156.

12C008 1-05 E

S. Sakiyama, D. Tsumagari, M. Moriuchi,
K. Takakura, I. Tsunoda, M. Yoneoka,
H. Ohyama and T. Nakashima
“2 MeV Electron irradiation damage of

commercial JFET”

31st Electron. Mater. Symp. (EMS-31),
Extended abstr. 31st Electron. Mater. Symp.
[Izu, Japan] 157-158.

12C009 1-05 E

M. Moriuchi, K. Takakura,
I. Tsunoda and H. Ohyama
“Electron-irradiation damage of commercial
Monolithic Ceramic Capacitors”
31st Electron. Mater. Symp. (EMS-31),
Extended abstr. 31st Electron. Mater. Symp.
[Izu, Japan] 159-160.

12C010 1-05 E

M. Sugiyama, Y. Hirose, M. Warasawa,
I. Tsunoda and K. Takakura
“Degradation effects of proton and electron
irradiation for Cu(In,Ga)Se₂ solar cells”
18th Int. Conf. Ternary Multinary Comp.
[Salzburg, Austria].

12C011 1-05 E

T. Nakashima, M. Yoneoka, I. Tsunoda,
K. Takakura, M. Bargallo, Gonzalez, E. Simoen,
C. Claeys and K. Yoshino
“Ge content dependence of radiation damage in
Si_{1-x}Gex S/D p-MOSFETs”
18th Int. Conf. Ternary Multinary Comp.
[Salzburg, Austria].

12C012 1-05 E

M. Sugiyama, L.J. Sharon, D. Itakura,
Y. Hirose, I. Tsunoda,
K. Takakura and T. Itagaki
“Clarification of proton- and electron-irradiated
degradation mechanism of Cu(In, Ga)Se₂ solar

cells using impedance spectroscopy”

2012 MRS Fall Meeting & Exhibit.
[Boston, USA] (2012/11).

12C013 1-11 C

S. Onoda, H. Abe, T. Yamamoto, T. Ohshima,
J. Isoya, T. Teraji and K. Watanabe
“Development of Ion Photon Emission
Microscopy at JAEA”
Proc. 10th Int. Workshop Radiat. Eff. Semicond.
Devices Space Appl.
[Tsukuba, Japan] (2012/12) 93-96.

12C014 1-19 E

R. Nagaishi, Y. Kumagai, N. Aoyagi,
I. Yamagishi and K. Nishihara
“Studies of Irradiation Effects on Zeolite Wastes
after Decontamination of Radioactive Water”
4th Asia Pacific Symp. Radiat. Chem.
(APSRC-2012)
[Huangshan, China] (2012).

12C015 1-19 G

Y. Kumagai, A. Kimura, R. Yamada,
R. Nagaishi and M. Taguchi
“Production of Hydrogen and Hydrogen Peroxide
by γ -Radiolysis of Water in the presence of
Y-type Zeolite”
4th Asia Pacific Symp. Radiat. Chem.
(APSRC-2012)
[Huangshan, China] (2012).

12C016 1-19 G, E

I. Yamagishi, R. Nagaishi, A. Terada, Y. Kamiji,
C. Kato, K. Morita, K. Nishihara, Y. Tsubata,
W. Ji, H. Fukushima, S. Sato,
Y. Okagaki and M. Denton

“Safe Storage of Zeolite Adsorbents used for Treatment of Accident-generated Water at Fukushima Daiichi Power Station”
International Experts’ Meeting on Decommissioning and Remediation after a Nuclear Accident.

12C017 1-21. G

村上 陽之、古川 真人、本田 敦、吉田 清
“JT-60SA 超伝導マグネット計測系の設計”
低温工学・超伝導学会講演概要集 86 (2012) 219.

12C018 1-22 G

舟川 勲、鬼頭 誠、堀江 一志、渡辺 健、
沼尾 達弥、三枝 長生、増田 健康、東 克洋、
薮 健次、山縣 諒平
“合成高分子樹脂材料の放射線耐性評価”
土木学会第 68 回学術講演会講演概要集 V
(2013/9) V-387.

12C019 1-22 G

東 克洋、鬼頭 誠、堀江 一志
“ポリウレタン・ポリウレア材料の耐放射線性能評価”
2013 年度日本建築学会大会学術講演会概要
集 (2013/9) 1372.

12C020 1-23 G

伊藤 主税、西村 昭彦、大場 弘則、
若井田 育夫、内藤 裕之、杉山 僚、茶谷 恵治
“遠隔観察・分光技術を用いた炉内検査技術の
開発 (1)水中観察とレーザー分光が可能な新
型光ファイバプローブ”
日本原子力学会「2013 年春の年会」要旨集
(2013) G44.

12C021 1-23 G

C. Ito, H. Naito, K. Chatani, A. Nishimura,

A. Sugiyama, H. Ohba and I. Wakaida
“Development of In-vessel Inspection
Technology Using Remote Imaging and
Spectroscopy”
Int. Conf. Laser Appl. Nucl. Eng. (LANE’13)
[Yokohama, Japan] (2013) LANE2-4, 12.

12C022 1-30 T, S, I

Gwang-ho Kim, I. Ioka, T. Sawai,
K. Kiuchi and H. Tanigawa
“Microstructural Evolutions in G-Phase
Strengthened Ni-base Alloy under Multi-ion
Irradiation”
Nucl. Mater. Conf. (NuMat 2012) [Osaka, Japan]
(2012/10).

12C023 1-34 G

安倍 弘、佐野 雄一、星 真之、坂内 信行、
竹内 正行、荻野 英樹、青瀬 晋一
“放射線環境下における塩化物を含む溶液中で
の炭素鋼の腐食挙動”
日本原子力学会「2013 年春の年会」要旨集
[近畿大学] (2013).

12C024 1-44 C

N. Tanaka, T. Yamaki, M. Asano,
T. Terai and K. Onuki
“Membrane Performance on
Electro-Electrodialysis of HI-I2-H2O Mixture for
IS Process”
6th Int. Topical Meeting HTR2012
[Tokyo, Japan] (2012) HTR2012-2-006.

12C025 3-03 G

北村 智、鳴海 一成
“シロイヌナズナにおけるフラボノイド局在性とガ
ンマ線感受性との関係”

第 54 回日本植物生理学会年会要旨集 (2013) 268.

12C026 3-08 C

M. Tomita, H. Matsumoto, T. Funayama,
Y. Yokota, K. Otsuka,
M. Maeda and Y. Kobayashi
“Mechanisms of signal transduction activated by
heavy-ion microbeam induced bystander
responses”
50th Annu. Meeting Biophys. Soc. Jpn.
[Nagoya, Japan] (2012) S31.

12C027 3-11 C

久保 誠、高橋 昭久、馬 洪玉、中川 彰子、
吉田 由香里、古澤 佳也、小林 泰彦、
舟山 知夫、金井 達明、大野 達也、中野 隆史
“DNA 二本鎖切断修復を分子標的とした LET
依存的な殺細胞効果”
第 3 回国際放射線神経生物学学会大会 [沖縄]
(2013/01).

12C028 3-11 C

馬 洪玉、高橋 昭久、久保 誠、中川 彰子、
吉田 由香里、古澤 佳也、小林 泰彦、
舟山 知夫、金井 達明、大野 達也、中野 隆史
“ヒト肺がん細胞の炭素線治療における標的とし
ての NHEJ 修復”
第 15 回癌治療増感研究シンポジウム [奈良]
(2013/02).

12C029 3-11 C

高橋 昭久、久保 誠、馬 洪玉、中川 彰子、
吉田 由香里、古澤 佳也、小林 泰彦、
舟山 知夫、金井 達明、大野 達也、中野 隆史
“LET 依存的な殺細胞効果におよぼす DNA 二
本鎖切断修復の役割”
第 6 回 Quantum Medicine [茨城] (2013/03).

12C030 3-24 S

富岡 智、阿久津 泰斗、長嶺 竹明、
佐藤 隆博、江夏 昌志、神谷 富裕
“大気 micro-PIXE による貧血の病態解明”
—C型慢性肝炎患者のインターフェロン治療
における検討—
第 28 回 PIXE シンポジウム [東京] (2012) 23.

12C031 3-34 C

松尾 洋一、長谷 純宏、野澤 樹、
石地 耕太郎、竹下 大樹
“カンキツ類へのイオンビーム及びシンクロトロン
光照射による突然変異誘発”
第 8 回イオンビーム育種研究会要旨集 (2012)
19-20.

12C032 3-37 C

長谷 純宏
“イオンビームによる効率的な変異誘発技術の
開発”
第 51 回ガンマフィールドシンポジウム要旨集
(2012) 18-21.

12C033 3-38 C, G

R. Yoshihara, Y. Hase, S. Nozawa, I. Narumi,
K. Takimoto and A. N. Sakamoto
“Mutation Spectrum Analysis in Higher Plant”
EMBO Workshop “Genetic Stability and
Change: Genome Maintenance Mechanisms in
Plants” [Roscoff, France] (2012).

12C034 4-04 C

M. Sugimoto, M. Yoshikawa, S. Tsukuda,
S. Tanaka and S. Seki
“Radius control of Ceramic Nano Fiber
Synthesized from Precursor Polymer by two
steps irradiation method using ion and electron

beams”

IUMRS-Int. Conf. Electron. Mater.
(IUMRS-ICEM 2012) [Yokohama, Japan]
(2012/09).

12C035 4-04 C

K. Takano, A. Asano, Y. Maeyoshi, H. Marui,
M. Omichi, A. Saeki, S. Seki, T. Satoh, Y. Ishii,
T. Kamiya, M. Koka, T. Ohkubo, W. Kada,
M. Sugimoto and H. Nishikawa
“Three Dimensional Microprocessing for
Polymer Films by MeV Ion Beam Lithography”
IUMRS-Int. Conf. Electron. Mater.
(IUMRS-ICEM 2012) [Yokohama, Japan]
(2012/09).

12C036 4-10 S

K. Miura, T. Satoh, Y. Ishii, M. Kohka,
K. Takano, T. Ohkubo, A. Yamazaki, W. Kada,
A. Yokoyama, T. Kamiya, H. Kiryu,
Y. Ozawa and O. Hanaizumi
“Fabrication of polymer optical waveguides for
the 1.5- μ m band using proton beam writing”
IUMRS-Int. Conf. Electron. Mater.
(IUMRS-ICEM 2012) [Yokohama, Japan]
(2012/09).

12C037 4-10 I

K. Inada, A. Kawashima, K. Kanou, K. Noguchi,
K. Miura, O. Hanaizumi, S. Yamamoto,
K. Kawaguchi and M. Yoshikawa
“Photoluminescence properties of light-emitting
SiO₂ substrates implanted with Si and C ions”
4th Int. Conf. Adv. Micro-Device Eng.
[Kiryu, Japan] (2012) 44.

12C038 4-10 S

Y. Ozawa, A. Kubota, K. Miura, O. Hanaizumi,
K. Noguchi, T. Satoh, Y. Ishii, M. Kohka,
K. Takano, T. Ohkubo, A. Yamazaki, W. Kada,
A. Yokoyama and T. Kamiya
“Mach-Zehnder type thermo-optic switch
fabricated by proton beam writing”
4th Int. Conf. Adv. Micro-Device Eng.
[Kiryu, Japan] (2012) 47.

12C039 4-13 S

H. Hayashi, Y. Takeno and H. Nishikawa
“Microelectronic devices on polyimide substrate
processed by Proton Beam”
13th Int. Conf. Nucl. Microprobe Tech. Appl.
[Lisbon, Portugal] (2012/7) O-39, 50.

12C040 4-13 S

H. Nishikawa, S. Makita and Y. Harashima
“Micromachining of Polytetrafluoroethylene by
Direct Etching Using Proton Beam Writing”
13th Int. Conf. Nucl. Microprobe Tech. Appl.
[Lisbon, Portugal] (2012/7) O-42, 53.

12C041 4-13 S

K. Saito, H. Nishikawa and H. Hayashi
“Flexible optical components of silicone
fabricated by proton beam writing”
13th Int. Conf. Nucl. Microprobe Tech. Appl.
[Lisbon, Portugal] (2012/7) P-67, 140.

12C042 4-13 S

高橋 潤一、岩本 隆志、田邊 裕介、
西川 宏之、林 秀臣、石井 保行、
神谷 富裕、佐藤 隆博
“PB-LIGA を用いた局所インプリントプロセスと
その応用展開”

エレクトロニクス実装学会、第 22 回マイクロエレクトロニクスシンポジウム 2B1-2 (2012/9).

12C043 4-13 S

鮎瀬 銀也、寺島 大貴、西川 宏之、内田 諭
“プロトンビーム描画を用いたフレキシブル誘電泳動デバイス作製”
平成 25 年電気学会全国大会 3-101 (2013/3).

12C044 4-13 S

村上 了太、西川 宏之、石井 保行、神谷 富裕
“Si イオンを注入したシリコン熱酸化膜におけるナノ Si 形成の制御”
平成 25 年電気学会全国大会 2-095 (2013/3).

12C045 4-27 C

T. Kondoh, J. Yang, K. Norizawa, K. Kan,
T. Toigawa, H. Kobayashi, A. Ogata,
S. Tagawa and Y. Yoshida
“Femtosecond Pulse Radiolysis for Radiation Chemistry”
3rd World Class Institute Symp.
(WCI-Symp. 2012) [Seoul, Korea] (2012/11).

12C046 4-27 C

T. Kondoh, J. Yang, K. Norizawa, K. Kan,
T. Toigawa, H. Kobayashi, A. Ogata,
S. Tagawa and Y. Yoshida
“Geminate ion recombination and ultrafast charge transfer in n-dodecane studied by femtosecond pulse radiolysis”
Radiat. Chem. Gordon Res. Conf. (GRC)
[Andover, USA] (2012/07-08).

12C047 4-27 C

T. Kondoh, J. Yang, K. Norizawa, K. Kan,
T. Toigawa, H. Kobayashi, A. Ogata,

S. Tagawa and Y. Yoshida
“Geminate ion recombination and ultrafast charge transfer in n-dodecane studied by femtosecond pulse radiolysis”
4th Asia Pacific Symp. Radiat. Chem.
(APSRC-2012) [Huangshan, China]
(2012/10-11).

12C048 4-27 C

T. Kondoh, J. Yang, K. Norizawa, K. Kan,
H. Kobayashi, A. Ogata,
S. Tagawa and Y. Yoshida
“Femtosecond pulse radiolysis study of dodecane radical cation”
28th Miller Conf. Radiat. Chem.
[Dead Sea, Israel] (2013/03).

12C049 4-29 C, E

S. Nakagawa, M. Taguchi and A. Kimura
“Solvent effect on radiation induced polymerization”
Proc. 55th Annu. Meeting Jpn. Soc. Radiat. Chem. [Iwanuma, Japan] (2012/09).

12C050 4-33

T. Ohkubo, Y. Ishii, Y. Miyake and T. Kamiya
“Preliminary Study On Development Of 300 kV Compact Focused Gaseous Ion Beam System”
AIP Conf. Proc. 1525 (2013) 370-74.

12C051 4-36 C

N. Miyawaki, S. Kurashima,
H. Kashiwagi and S. Okumura
“Influence of the buncher on beam intensity and phase width in the JAEA AVF cyclotron”
Proc. 9th Annu. Meeting Part. Accel. Soc. Jpn.
(2012) 574-76.

12C052 4-36 C

H. Kashiwagi, S. Kurashima,
N. Miyawaki and S. Okumura
"Transverse-acceptance measurement system for
JAEA AVF cyclotron"
Proc. IBIC2012 (2012) TUPB65.

12C053 4-40 C

M. Imaizumi, Y. Yuri, P. R. Bolton,
S. Sato and T. Oshima
"Innovative technologies on proton irradiation
ground tests for space solar cells"
Proc. 38th IEEE Photovoltaic Specialist Conf.,
(2012) 2831-34.

12C054 4-40 C

Y. Yuri, T. Yuyama, T. Ishizaka,
I. Ishibori and S. Okumura
"Focusing charged particle beams using
multipole magnets in a beam transport line"
Proc. 3rd Int. Part. Accel. Conf. (2012) 1062-64.

12C055 4-40 C

T. Ishizaka, K. Imai, Y. Yuri, T. Yuyama,
I. Ishibori and S. Okumura
"Calibration of Gafchromic dosimetry films for
large-area ion-beam distribution measurement"
Proc. 9th Annu. Meeting Part. Accel. Soc. Jpn.
(2012) 594-96.

12C056 4-40 C

T. Yuyama, Y. Yuri, T. Ishizaka,
I. Ishibori and S. Okumura
"Real-time beam profile measurement system
using fluorescent screens"
Proc. 1st Int. Beam Instrum. Conf. MOPB75
246-48.

12C057 4-40 C

Y. Yuri, T. Ishizaka, T. Yuyama,
I. Ishibori and S. Okumura
"Use of Gafchromic films to measure the
transverse intensity distribution of a large-area
ion beam"
Proc. 1st Int. Beam Instrum. Conf. TUPB79
531-33.

12C058 4-40 C

Y. Yuri, T. Yuyama, T. Ishizaka,
I. Ishibori and S. Okumura
"Large-area uniform ion beam formed by the
nonlinear beam optics at the JAEA TIARA
Cyclotron"
Proc. 10th Int. Workshop Radiat. Eff. Semicond.
Devices Space Appl. (2012) 97-100.

12C059 4-45 T

千葉 敦也、斎藤 勇一、鳴海 一雅、
山田 圭介、金子 敏明
"薄膜を透過するクラスター構成イオンの核間距
離と電荷"
第25回「タンデム加速器およびその周辺技術の
研究会」報告集 [名古屋] (2012/7).

12C060 5-03 T, S, I

宇野 定則、千葉 敦也、山田 圭介、
横山 彰人、上松 敬、北野 敏彦、高山 輝充、
織茂 貴雄、金井 信二、青木 勇希、
山田 尚人、斎藤 勇一、石井 保行、
佐藤 隆博、大久保 猛
"TIARA 静電加速器の現状"
第25回「タンデム加速器およびその周辺技術の
研究会」報告集 [名古屋] (2012/7).

Appendix 2

List of Related Patents

12PAT001 1-03

“Single event effect tolerant SOI-based Inverter, NAND element, NOR element, semiconductor memory device and data latch circuit”

US patent No. US 7,504,850 B2.

(SOI-ASIC, HR5000S に適用)

12PAT002 1-03

“Single event effect tolerant latch circuit and flip-flop circuit,”

US patent No. US 7,576,583 B2.

(SOI-ASIC, SOI-FPGA, HR5000S に適用)

12PAT003 1-03

“シングルイベント耐性のラッチ回路”

公開番号:2009-105967

(SOI-ASIC, SOI-FPGA, HR5000S に適用)

12PAT004 1-45,4-40

古山 了、村木 勇三、長井 陽三、網野 一郎(日東電工(株))、百合 庸介、湯山 貴裕、石坂 知久、石堀 郁夫、吉田 健一(原子力機構・高崎研)、前川 康成、越川 博、八巻 徹也、浅野 雅春(原子力機構・量子ビーム)

「多孔性高分子フィルムの製造方法」

出願番号:特願 2013-066942 号

出願日:2013 年 3 月 27 日

12PAT005 1-45,4-40

古山 了、長井 陽三、森山 順一(日東電工(株))、百合 庸介、湯山 貴裕、石坂 知久、石堀 郁夫、吉田 健一(原子力機構・高崎研)、前川 康成、越川 博、八巻 徹也、浅野 雅春(原子力機構・

量子ビーム)

「多孔性高分子フィルムの製造方法および多孔性高分子フィルム」

出願番号:特願 2013-067306 号

12PAT006 1-45,4-40

古山 了、長井 陽三、森山 順一(日東電工(株))、百合 庸介、湯山 貴裕、石坂 知久、石堀 郁夫、吉田 健一(原子力機構・高崎研)、前川 康成、越川 博、八巻 徹也、浅野 雅春(原子力機構・量子ビーム)

「多孔性高分子フィルムの製造方法および多孔性高分子フィルム」

出願番号:特願 2013-066946 号

出願日:2013 年 3 月 27 日

12PAT007 2-01

植木 悠二、玉田 正男(原子力機構・量子ビーム)

「バイオディーゼル製造用触媒とその製造方法並びにバイオディーゼルの製造方法」

特許番号:第 5167110 号

12PAT008 2-02

岩撫 暁生、瀬古 典明、保科 宏行、植木 悠二、佐伯 誠一(原子力機構・量子ビーム)

「布状の放射性物質吸着材及びその製造方法」

出願番号:特願 2011-136558 号

出願日:2011 年 6 月 20 日

12PAT009 2-02,2-03,2-04

瀬古 典明、柴田 卓弥、岩撫 暁生、笠井 昇、植木 悠二、佐伯 誠一、保科 宏行(原子力機構・量子ビーム)、中野 正憲、近石 尚樹、

見上 隆志、村木 慎作(倉敷繊維加工(株))
「セシウム除去用フィルターカートリッジおよび
その製造方法」

出願番号 2012-23880 号

出願日:2012 年 10 月 30 日

12PAT010 3-40

大野 豊、鳴海 一成、長谷 純宏(原子力機構・
量子ビーム)、川合 真紀、北野 沙也佳、
宮城 敦子、内宮 博文(埼玉大学)
「シュウ酸濃度が低減された植物体の製造法」

出願番号:特願 2013-023290 号

12PAT011 4-11

織茂 聡、阿部 浩之(原子力機構・量子ビーム)、
大道 博行(原子力機構・敦賀本部レーザー共同
研究所)、内田 裕久(東海大・工)
「水素吸蔵材の製造方法、水素吸蔵材」

公開番号:2011-236446 号

出願番号:2010-106216 号

12PAT012 4-14

Y.Kato and K.Mima

Title: “Material Analysis by Using Laser Produced
Charged Particles”

Patent Application Number: 2011-227386,
227387, 227388

12PAT013 5-03

山田 圭介 (原子力機構・高崎研)
「イオン源の運転方法」

出願番号:特願 2013-20571 号

出願日:2013 年 2 月 5 日

Appendix 3

List of Related Press-release and Television Broadcasting

12NP001 1-25, 1-38

吉川 正人、杉本 雅樹、島田 明彦、宮下 敦巳
(原子力機構・量子ビーム)
「高分子系材料・機器の耐放射線性データベースを整備 ― 廃炉作業現場で使われる材料・機器の耐放射線性の評価検討に貢献―」
平成 24 年 6 月 1 日プレス発表
上毛新聞に掲載。

12NP002 2-02

「放射性セシウムが検出された井戸水を用いての除去試験について」
平成 24 年 9 月 11 日プレス発表
経済産業省からプレス発表。

12NP003 2-02

「水中の放射性セシウム除去用カートリッジを製品化 ― 電子線グラフト重合技術により高性能セシウム捕集材の開発に成功―」
2012 年 11 月 7 日プレス発表
倉敷繊維加工株式会社と共同でプレス発表。

12NP004 2-03, 2-04

内閣府原子力被災者生活支援チーム(試験に用いた吸着材の開発・試験実行者)(共同開発者)
「放射性セシウムが検出された井戸水を用いての除去試験について」
平成 24 年 9 月 11 日プレス発表
首相官邸ツイッターで紹介。

12NP005 2-03, 2-04

原子力機構・倉敷繊維加工
(製品化に用いた吸着材の開発者)(共同開発者)
「水中の放射性セシウム除去用カートリッジを製品化」
平成 24 年 11 月 7 日プレス発表
上毛新聞、織研新聞、日刊工業新聞、福島民友新聞、読売新聞に掲載。

12NP006 2-03, 2-04

原子力機構(製品化に用いた吸着材の開発者)(共同開発者)
「水中の放射性セシウム除去用カートリッジの実用化試験の開始について」
平成 25 年 3 月 7 日プレス発表
朝日新聞、読売新聞、福島民報に掲載。

12NP007 2-04

倉敷繊維加工(共同開発者)
「微量金属除去性能に優れたカートリッジフィルターを開発」
平成 24 年 11 月 29 日プレス発表。

12NP008 2-04

見上 隆志、中野 正憲(倉敷繊維加工(株))、
柴田 卓弥、瀬古 典明(原子力機構・量子ビーム)
「電子線グラフト繊維を用いた上水用カートリッジフィルター」
設備と管理(2013)4月号。

12NP009 3-49

原子力機構群・馬産業技術センター（共同発表した研究成果）

「群馬県の新しい吟醸用清酒酵母ができました！」

平成 24 年 12 月 10 日プレス発表

ぐんま経済新聞、化学工業日報、科学新聞、産経新聞、上毛新聞、朝日新聞、電気新聞、読売新聞、日経産業新聞、日本経済新聞、毎日新聞に掲載。

12NP010 4-14

平成 24 年 10 月 3 日プレス発表

「イオンマイクロビームを用いたリチウムイオン電池内部のリチウム分布の高分解能可視化に成功

中日新聞、日刊工業新聞、読売新聞、静岡新聞。

12TV001 1-18

（原子力機構（原科研福島特別チーム）、北海道大学）

「シリーズ原発事故（7）冷温停止状態 浮かび上がる課題」

平成 24 年 5 月 13 日（19 日）TV 放映, NHK サイエンス ZERO（No. 385）。

12TV002 4-22

～湖に眠る奇跡の堆積物～

NHK E テレ サイエンス ZERO 2013 年 1 月 16 日放映

（撮影協力：高崎量子応用研究所において、 γ 線照射を行った試料の年代分析結果が、一部放映される）。

Symbol used in the Appendix 1 to 3

An example of symbol expression is written as following.

12 **J** **102** **4-47** **T**
 ① ② ③ ④-⑤ ⑥

- ① Number of last two orders in fiscal year
- ② Kind of publication
 - J** : Publication in Journal
 - C** : Publication as Proceedings
 - NP** : Press-Release (Newspaper)
 - TV** : Television Broadcasting
 - PA** : Patent
- ③ Consecutive numbers for the kind of publication
- ④-⑤ Paper number
- ④ Classification number of research field
 - 1** : Space, nuclear and energy engineering
 - 2** : Environment conservation and resource exploitation
 - 3** : Medical and biotechnological application
 - 4** : Advanced materials, analysis and novel technology
- ⑤ Consecutive number every research field
- ⑥ Accelerators or irradiation facilities utilized for the research
 - C** : AVF Cyclotron
 - T** : 3 MV Tandem Electrostatic Accelerator
 - S** : 3 MV Single-ended Electrostatic Accelerator
 - I** : 400 kV Ion Implanter
 - E** : 2 MV Electron Accelerator
 - G** : Co-60 Gamma-ray Irradiation Facilities
 - O** : Off-line (Research without the utilization of irradiation facilities)

Appendix 4 Type of Research Collaboration and Facilities Used for Research

Paper No.	Type of Research Collaboration ^{*1}					Irradiation Facilities ^{*2}						Paper No.	Type of Research Collaboration ^{*1}					Irradiation Facilities ^{*2}					
	Joint Res.	Entr. Res.	Coop. Res.	JAEA Inter.	Ext. Use	C	T	S	I	E	G		Joint Res.	Entr. Res.	Coop. Res.	JAEA Inter.	Ext. Use	C	T	S	I	E	G
1-01	●					◎	◎		◎	◎		2-01				●						◎	
1-02				●		◎	◎	◎	◎			2-02				●						◎	
1-03	●					◎						2-03	●									◎	◎
1-04	●						◎					2-04	●									◎	
1-05					●					◎		2-05	●									◎	
1-06				●		◎	◎					2-06				●						◎	
1-07				●OL								2-07	●										◎
1-08	●								◎			2-08				●							◎
1-09					●	◎						2-09	●									◎	
1-10					●		◎																
1-11				●		◎						3-01				●			◎				
1-12	●								◎			3-02				●		◎					
1-13				●							◎	3-03				●							◎
1-14			●					◎				3-04				●		◎					
1-15		●									◎	3-05	●					◎					
1-16				●							◎	3-06				●		◎					◎
1-17				●							◎	3-07	●					◎					
1-18				●							◎	3-08	●					◎					
1-19				●						◎	◎	3-09	●					◎					
1-20		●									◎	3-10	●					◎					
1-21				●							◎	3-11	●					◎					
1-22					●						◎	3-12	●					◎					
1-23				●							◎	3-13	●					◎					
1-24	●										◎	3-14	●					◎					
1-25				●OL								3-15	●					◎					
1-26				●			◎	◎	◎			3-16				●		◎					
1-27			●				◎	◎	◎			3-17	●									◎	◎
1-28				●			◎					3-18	●									◎	◎
1-29				●			◎	◎	◎			3-19			●				◎				
1-30				●			◎	◎	◎			3-20			●				◎				
1-31				●			◎	◎	◎			3-21			●				◎				
1-32				●			◎	◎	◎			3-22			●				◎				
1-33				●							◎	3-23			●				◎				
1-34				●							◎	3-24			●				◎				
1-35				●			◎	◎	◎			3-25			●				◎				
1-36					●						◎	3-26			●				◎				
1-37				●				◎	◎			3-27			●				◎				
1-38				●							◎	3-28	●					◎					
1-39	●										◎	3-29				●		◎					
1-40	●										◎	3-30	●					◎					
1-41				●						◎	◎	3-31	●					◎					
1-42				●						◎	◎	3-32	●					◎					
1-43	●					◎		◎	◎			3-33	●					◎					
1-44				●							◎	3-34	●					◎					
1-45				●		◎						3-35	●					◎					
1-46				●		◎						3-36				●		◎					

Paper No.	Type of Research Collaboration ^{*1}					Irradiation Facilities ^{*2}						Paper No.	Type of Research Collaboration ^{*1}					Irradiation Facilities ^{*2}					
	Joint Res.	Entr. Res.	Coop. Res.	JAEA Inter.	Ext. Use	C	T	S	I	E	G		Joint Res.	Entr. Res.	Coop. Res.	JAEA Inter.	Ext. Use	C	T	S	I	E	G
3-37				●		◎					◎	4-24				●					◎		
3-38				●		◎					◎	4-25					●						
3-39				●		◎					◎	4-26				●		◎					
3-40	●					◎					◎	4-27	●					◎					
3-41					●	◎						4-28	●					◎					
3-42				●		◎					◎	4-29	●					◎				◎	
3-43				●							◎	4-30	●					◎					
3-44	●					◎						4-31				●		◎					
3-45	●					◎						4-32				●			◎				
3-46	●					◎						4-33				●OL							
3-47	●					◎						4-34					●					◎	
3-48	●					◎					◎	4-35	●										◎
3-49	●					◎						4-36				●		◎					
3-50	●					◎						4-37				●			◎	◎	◎		
												4-38				●		◎					
4-01				●				◎	◎			4-39				●OL							
4-02					●	◎						4-40				●		◎					
4-03					●	◎						4-41				●		◎					
4-04	●					◎						4-42				●			◎	◎			
4-05				●				◎		◎		4-43	●					◎					
4-06				●OL								4-44				●			◎				
4-07					●	◎						4-45			●			◎					
4-08					●	◎						4-46			●			◎					
4-09				●			◎		◎			4-47			●			◎					
4-10	●							◎	◎			4-48			●			◎		◎			
4-11	●								◎	◎		4-49			●			◎		◎			
4-12				●				◎	◎			4-50			●					◎			
4-13	●						◎	◎				4-51	●							◎			
4-14					●			◎															
4-15					●				◎			5-01						◎	◎	◎	◎		
4-16	●				●			◎				5-02						◎					
4-17	●					◎						5-03							◎	◎	◎		
4-18					●			◎				5-04										◎	◎
4-19	●					◎						5-05										◎	◎
4-20					●	◎						5-06						◎	◎	◎	◎		
4-21					●	◎				◎		5-07						◎	◎	◎	◎		
4-22					●						◎	5-08						◎	◎	◎	◎	◎	◎
4-23				●				◎	◎			Total	55	2	17	64	19	65	32	38	32	22	39
^{*1} Type of Research Collaboration Joint Res. : Joint research with external users Entr. Res. : Research entrusted to JAEA Coop. Res. : Cooperative research with plural universities through The University of Tokyo JAEA Inter. : JAEA internal use Ext. Use : Common use based on "JAEA-facility-use program" and "Common promotion project" supported from MEXT OL : Off line (Research without the use of irradiation facilities)												^{*2} Utilization of Irradiation Facilities C : AVF Cyclotron System T : 3 MV Tandem Electrostatic Accelerator S : 3 MV Single-ended Electrostatic Accelerator I : 400 kV Ion Implanter E : 2 MV Electron Accelerator G : Co-60 Gamma-ray Irradiation Facilities											

Appendix 5 Examples of Typical Abbreviation Name for Organizations in Japan Atomic Energy Agency (JAEA)

◆Directorate, Center, Institute, etc.

QuBS (量子ビーム応用研究部門): Quantum Beam Science Directorate

NSED (原子力基礎工学研究部門): Nuclear Science and Engineering Directorate

FRDD (核融合研究開発部門): Fusion Research and Development Directorate

GIRDD (地層処分研究開発部門): Geological Isolation Research and
Development Directorate

ANSRD (次世代原子力システム研究開発部門): Advanced Nuclear System Research
and Development Directorate

NCBD (バックエンド推進部門): Nuclear Cycle Backend Directorate

NSRC (安全研究センター): Nuclear Safety Research Center

NFCEL (核燃料サイクル工学研究所): Nuclear Fuel Cycle Engineering Laboratories

NERCC (原子力エネルギー基盤連携センター): Nuclear Engineering Research
Collaboration Center

NHARC (原子力水素・熱利用研究センター): Nuclear Hydrogen and Heat Application
Research Center

J-PARC (J-PARC センター): J-PARC Center

TARRI (高崎量子応用研究所): Takasaki Advanced Radiation Research Institute

NSRI (原子力科学研究所): Nuclear Science Research Institute

ORDC (大洗研究開発センター): Oarai Research and Development Center

KPSI (関西光科学研究所): Kansai Photon Science Institute

◆Division, Unit, Department, etc.

- ・量子ビーム応用研究部門、環境・産業応用量子ビーム技術研究ユニット
⇒ Environment and Industrial Materials Research Division, QuBS, JAEA
- ・量子ビーム応用研究部門、医療・バイオ応用量子ビーム技術研究ユニット
⇒ Medical and Biotechnological Application Division, QuBS, JAEA
- ・量子ビーム応用研究部門、量子ビーム材料評価・構造制御技術研究ユニット
⇒ Materials Science Research Division, QuBS, JAEA
- ・量子ビーム応用研究部門、レーザー応用技術研究ユニット
⇒ Laser Application Technology Division, QuBS, JAEA
- ・原子力基礎工学研究部門、環境・放射線科学ユニット
⇒ Division of Environment and Radiation Sciences, NSED, JAEA
- ・原子力基礎工学研究部門、燃料・材料工学ユニット
⇒ Division of Fuels and Materials Engineering, NSED, JAEA

- ・原子力基礎工学研究部門、原子力化学ユニット
⇒ Division of Chemistry for Nuclear Engineering, NSED, JAEA
- ・核融合研究開発部門、ITER プロジェクトユニット
⇒ ITER Project Unit, FRDD, JAEA
- ・核融合研究開発部門、トカマクシステム技術開発ユニット
⇒ Tokamak System Technology Unit, FRDD, JAEA
- ・核融合研究開発部門、六ヶ所 BA プロジェクトユニット
⇒ Rokkasho BA Project Unit, FRDD, JAEA
- ・先端基礎研究センター
⇒ Advanced Science Research Center, JAEA
- ・原子力科学研究所、放射線管理部
⇒ Department of Radiation Protection, NSRI, JAEA
- ・原子力科学研究所、福島技術開発特別チーム
⇒ Fukushima Project Team, NSRI, JAEA
- ・大洗研究開発センター、高速実験炉部
⇒ Experimental Fast Reactor Department, ORDC, JAEA
- ・大洗研究開発センター、福島燃料材料試験部
⇒ Fukushima Fuels and Materials Department, ORDC, JAEA
- ・原子力水素・熱利用研究センター、水素利用研究開発ユニット
⇒ Hydrogen Application Research and Development Division, NHARC, JAEA
- ・高崎量子応用研究所、放射線高度利用施設部
⇒ Department of Advanced Radiation Technology, TARRI, JAEA
- ・J-PARC センター、加速器ディビジョン
⇒ Accelerator Division, J-PARC, JAEA
- ・J-PARC センター、安全ディビジョン
⇒ Safety Division, J-PARC, JAEA
- ・安全研究センター、軽水炉長期化対応研究ユニット
⇒ LWR Long-term Reliability Research Unit, NSRC, JAEA
- ・地層処分研究開発部門、地層処分基盤研究開発ユニット
⇒ Geological Isolation Research Unit, GIRDD, JAEA
- ・核燃料サイクル工学研究所、サイクル工学試験部
⇒ Nuclear Cycle Engineering Department, NFCEL, JAEA
- ・核燃料サイクル工学研究所、プルトニウム燃料技術開発センター
⇒ Plutonium Fuel Development Center, NFCEL, JAEA
- ・核燃料サイクル工学研究所、再処理技術開発センター
⇒ Tokai Reprocessing Technology Development Center, NFCEL, JAEA
- ・核燃料サイクル工学研究所、福島技術開発試験部
⇒ Department of Fukushima Technology Development, NFCEL, JAEA

- ・ 次世代原子力システム研究開発部門、燃料材料技術開発ユニット
⇒ Fast Reactor Fuels and Materials Technology Development Unit, ANSRD, JAEA
- ・ バックエンド推進部門、バックエンド技術開発ユニット
⇒ Nuclear Cycle Backend Technology Development Unit, NCBD, JAEA
- ・ 産学連携推進部
⇒ Industrial Collaboration Promotion Department, JAEA

国際単位系（SI）

表 1. SI 基本単位

基本量	SI 基本単位	
	名称	記号
長さ	メートル	m
質量	キログラム	kg
時間	秒	s
電流	アンペア	A
熱力学温度	ケルビン	K
物質량	モル	mol
光度	カンデラ	cd

表 2. 基本単位を用いて表されるSI組立単位の例

組立量	SI 基本単位	
	名称	記号
面積	平方メートル	m ²
体積	立法メートル	m ³
速度	メートル毎秒	m/s
加速度	メートル毎秒毎秒	m/s ²
波数	毎メートル	m ⁻¹
密度, 質量密度	キログラム毎立方メートル	kg/m ³
面積密度	キログラム毎平方メートル	kg/m ²
比体積	立方メートル毎キログラム	m ³ /kg
電流密度	アンペア毎平方メートル	A/m ²
磁界の強さ	アンペア毎メートル	A/m
量濃度 ^(a) , 濃度	モル毎立方メートル	mol/m ³
質量濃度	キログラム毎立法メートル	kg/m ³
輝度	カンデラ毎平方メートル	cd/m ²
屈折率 ^(b)	(数字の) 1	1
比透磁率 ^(b)	(数字の) 1	1

(a) 量濃度 (amount concentration) は臨床化学の分野では物質濃度 (substance concentration) ともよばれる。

(b) これらは無次元量あるいは次元 1 をもつ量であるが、そのことを表す単位記号である数字の 1 は通常は表記しない。

表 3. 固有の名称と記号で表されるSI組立単位

組立量	SI 組立単位			
	名称	記号	他のSI単位による表し方	SI基本単位による表し方
平面角	ラジアン ^(b)	rad	1 ^(b)	m/m
立体角	ステラジアン ^(b)	sr ^(c)	1 ^(b)	m ² /m ²
周波数	ヘルツ ^(d)	Hz		s ⁻¹
力	ニュートン	N		m kg s ⁻²
圧力, 応力	パスカル	Pa	N/m ²	m ⁻¹ kg s ⁻²
エネルギー, 仕事, 熱量	ジュール	J	N m	m ² kg s ⁻²
仕事率, 工率, 放射束	ワット	W	J/s	m ² kg s ⁻³
電荷, 電気量	クーロン	C		s A
電位差 (電圧), 起電力	ボルト	V	W/A	m ² kg s ⁻³ A ⁻¹
静電容量	ファラド	F	C/V	m ⁻² kg ⁻¹ s ⁴ A ²
電気抵抗	オーム	Ω	V/A	m ² kg s ⁻³ A ⁻²
コンダクタンス	ジーメンズ	S	A/V	m ⁻² kg ⁻¹ s ³ A ²
磁束	ウェーバ	Wb	Vs	m ² kg s ⁻² A ⁻¹
磁束密度	テスラ	T	Wb/m ²	kg s ⁻² A ⁻¹
インダクタンス	ヘンリー	H	Wb/A	m ² kg s ⁻² A ⁻²
セルシウス度 ^(e)	セルシウス度 ^(e)	°C		K
光束度	ルーメン	lm	cd sr ^(c)	cd
照射度	ルクス	lx	lm/m ²	m ⁻² cd
放射性核種の放射能 ^(f)	ベクレル ^(d)	Bq		s ⁻¹
吸収線量, 比エネルギー分与, カーマ	グレイ	Gy	J/kg	m ² s ⁻²
線量当量, 周辺線量当量, 方向性線量当量, 個人線量当量	シーベルト ^(g)	Sv	J/kg	m ² s ⁻²
酸素活性化	カタール	kat		s ⁻¹ mol

(a) SI接頭語は固有の名称と記号を持つ組立単位と組み合わせても使用できる。しかし接頭語を付した単位はもはやコヒーレントではない。

(b) ラジアンとステラジアンは数字の 1 に対する単位の特別な名称で、量についての情報をつたえるために使われる。実際には、使用する時には記号rad及びsrが用いられるが、習慣として組立単位としての記号である数字の 1 は明示されない。

(c) 測光学ではステラジアンという名称と記号srを単位の表し方の中に、そのまま維持している。

(d) ヘルツは周期現象についてののみ、ベクレルは放射性核種の統計的過程についてののみ使用される。

(e) セルシウス度はケルビンの特別な名称で、セルシウス温度を表すために使用される。セルシウス度とケルビンの単位の大きさは同一である。したがって、温度差や温度間隔を表す数値はどちらの単位で表しても同じである。

(f) 放射性核種の放射能 (activity referred to a radionuclide) は、しばしば誤った用語で"radioactivity"と記される。

(g) 単位シーベルト (PV.2002,70,205) についてはCIPM勧告2 (CI-2002) を参照。

表 4. 単位の中に固有の名称と記号を含むSI組立単位の例

組立量	SI 組立単位		
	名称	記号	SI 基本単位による表し方
粘着力のモーメント	パスカル秒	Pa s	m ⁻¹ kg s ⁻¹
表面張力	ニュートンメートル	N m	m ² kg s ⁻²
角速度	ニュートン毎メートル	N/m	kg s ⁻²
角加速度	ラジアン毎秒	rad/s	m m ⁻¹ s ⁻¹ =s ⁻¹
角速度	ラジアン毎秒毎秒	rad/s ²	m m ⁻¹ s ⁻² =s ⁻²
熱流密度, 放射照度	ワット毎平方メートル	W/m ²	kg s ⁻³
熱容量, エントロピー	ジュール毎ケルビン	J/K	m ² kg s ⁻² K ⁻¹
比熱容量, 比エントロピー	ジュール毎キログラム毎ケルビン	J/(kg K)	m ² s ⁻² K ⁻¹
比エネルギー	ジュール毎キログラム	J/kg	m ² s ⁻²
熱伝導率	ワット毎メートル毎ケルビン	W/(m K)	m kg s ⁻³ K ⁻¹
体積エネルギー	ジュール毎立方メートル	J/m ³	m ⁻¹ kg s ⁻²
電界の強さ	ボルト毎メートル	V/m	m kg s ⁻³ A ⁻¹
電荷密度	クーロン毎立方メートル	C/m ³	m ⁻³ s A
表面電荷	クーロン毎平方メートル	C/m ²	m ⁻² s A
電束密度, 電気変位	クーロン毎平方メートル	C/m ²	m ⁻² s A
誘電率	ファラド毎メートル	F/m	m ⁻³ kg ⁻¹ s ⁴ A ²
透磁率	ヘンリー毎メートル	H/m	m kg s ⁻² A ⁻²
モルエネルギー	ジュール毎モル	J/mol	m ² kg s ⁻² mol ⁻¹
モルエントロピー, モル熱容量	ジュール毎モル毎ケルビン	J/(mol K)	m ² kg s ⁻² K ⁻¹ mol ⁻¹
照射線量 (X線及びγ線)	クーロン毎キログラム	C/kg	kg ⁻¹ s A
吸収線量率	グレイ毎秒	Gy/s	m ² s ⁻³
放射線強度	ワット毎ステラジアン	W/sr	m ⁴ m ⁻² kg s ⁻³ =m ² kg s ⁻³
放射輝度	ワット毎平方メートル毎ステラジアン	W/(m ² sr)	m ² m ⁻² kg s ⁻³ =kg s ⁻³
酵素活性濃度	カタール毎立方メートル	kat/m ³	m ⁻³ s ⁻¹ mol

表 5. SI 接頭語

乗数	接頭語	記号	乗数	接頭語	記号
10 ²⁴	ヨ	Y	10 ⁻¹	デシ	d
10 ²¹	ゼ	Z	10 ⁻²	センチ	c
10 ¹⁸	エ	E	10 ⁻³	ミリ	m
10 ¹⁵	ペ	P	10 ⁻⁶	マイクロ	μ
10 ¹²	テ	T	10 ⁻⁹	ナノ	n
10 ⁹	ギ	G	10 ⁻¹²	ピコ	p
10 ⁶	メ	M	10 ⁻¹⁵	フェムト	f
10 ³	キ	k	10 ⁻¹⁸	アト	a
10 ²	ヘ	h	10 ⁻²¹	ゼプト	z
10 ¹	デ	da	10 ⁻²⁴	ヨクト	y

表 6. SIに属さないが、SIと併用される単位

名称	記号	SI 単位による値
分	min	1 min=60s
時	h	1 h =60 min=3600 s
日	d	1 d=24 h=86 400 s
度	°	1°=(π/180) rad
分	′	1′=(1/60)°=(π/10800) rad
秒	″	1″=(1/60)′=(π/648000) rad
ヘクタール	ha	1 ha=1 hm ² =10 ⁴ m ²
リットル	L, l	1 L=1 l=1 dm ³ =10 ³ cm ³ =10 ⁻³ m ³
トン	t	1 t=10 ³ kg

表 7. SIに属さないが、SIと併用される単位で、SI単位で表される数値が実験的に得られるもの

名称	記号	SI 単位で表される数値
電子ボルト	eV	1 eV=1.602 176 53(14)×10 ⁻¹⁹ J
ダルトン	Da	1 Da=1.660 538 86(28)×10 ⁻²⁷ kg
統一原子質量単位	u	1 u=1 Da
天文単位	ua	1 ua=1.495 978 706 91(6)×10 ¹¹ m

表 8. SIに属さないが、SIと併用されるその他の単位

名称	記号	SI 単位で表される数値
バール	bar	1 bar=0.1 MPa=100 kPa=10 ⁵ Pa
水銀柱ミリメートル	mmHg	1 mmHg=133.322 Pa
オングストローム	Å	1 Å=0.1 nm=100 pm=10 ⁻¹⁰ m
海里	M	1 M=1852 m
バイン	b	1 b=100 fm ² =(10 ⁻¹² cm) ² =10 ⁻²⁸ m ²
ノット	kn	1 kn=(1852/3600) m/s
ネーパ	Np	SI単位との数値的な関係は、 対数量の定義に依存。
ベレル	B	
デジベール	dB	

表 9. 固有の名称をもつCGS組立単位

名称	記号	SI 単位で表される数値
エル	erg	1 erg=10 ⁻⁷ J
ダイン	dyn	1 dyn=10 ⁻⁵ N
ポアズ	P	1 P=1 dyn s cm ⁻² =0.1 Pa s
ストークス	St	1 St=1 cm ² s ⁻¹ =10 ⁻⁴ m ² s ⁻¹
スチルブ	sb	1 sb=1 cd cm ⁻² =10 ⁴ cd m ⁻²
フオット	ph	1 ph=1 cd sr cm ⁻² 10 ⁴ lx
ガリ	Gal	1 Gal=1 cm s ⁻² =10 ⁻² ms ⁻²
マクスウェル	Mx	1 Mx=1 G cm ² =10 ⁻⁸ Wb
ガウス	G	1 G=1 Mx cm ⁻² =10 ⁻⁴ T
エルステッド ^(c)	Oe	1 Oe ≡ (10 ³ /4π) A m ⁻¹

(c) 3 元系のCGS単位系とSIでは直接比較できないため、等号「 ≡ 」は対応関係を示すものである。

表 10. SIに属さないその他の単位の例

名称	記号	SI 単位で表される数値
キュリー	Ci	1 Ci=3.7×10 ¹⁰ Bq
レントゲン	R	1 R = 2.58×10 ⁻⁴ C/kg
ラド	rad	1 rad=1 cGy=10 ⁻² Gy
レム	rem	1 rem=1 cSv=10 ⁻² Sv
ガンマ	γ	1 γ=1 nT=10 ⁻⁹ T
フェルミ	f	1 フェルミ=1 fm=10 ⁻¹⁵ m
メートル系カラット		1 メートル系カラット = 200 mg = 2×10 ⁻⁴ kg
トル	Torr	1 Torr = (101 325/760) Pa
標準大気圧	atm	1 atm = 101 325 Pa
カロリ	cal	1 cal=4.1858 J (「15°C」カロリー) , 4.1868 J (「IT」カロリー) 4.184 J (「熱化学」カロリー)
ミクロン	μ	1 μ =1 μm=10 ⁻⁶ m

